Magnetic resonance imaging of respiratory mechanics

Tanguy Boucneau

UNIVERSITÉ PARIS SUD
Comprendre le monde, construire l'avenir

Magnetic resonance imaging of respiratory mechanics

Thèse de doctorat de l'Université Paris-Saclay
préparée à l'Université Paris-Sud

École doctorale n°575
Electrical, Optical, Bio-physics and Engineering (EOBE)
Spécialité de doctorat: Imagerie et physique médicale

Thèse présentée et soutenue à Orsay, le 3 juillet 2019, par

Tanguy Boucneau

Composition du Jury :

Dominique Chapelle Directeur de recherche, INRIA (M3DISIM)	Président
Najat Salameh Professeure, University of Basel, Switzerland (AMT Lab)	Rapporteure
Pierre-André Vuissoz Ingénieur de recherche, Université de Lorraine (IADI)	Rapporteur
Thomas Similowski PU-PH, Hôpital Pitié Salpétrière (UMRS 1158)	Examinateur
Brice Fernandez Lead scientist, GE Healthcare (Applications & Workflow)	Co-encadrant
Xavier Maître Chargé de recherche, CNRS (IR4M)	Co-encadrant
Luc Darrasse Directeur de recherche, CNRS (IR4M)	Directeur de thèse

TABLE OF CONTENTS

ACKNOWLEDGEMENTS

When I started my Ph.D. project three years ago, I was motivated by the application of physics, but also mathematics, engineering and computer programming in innovative projects that would bring advances in medical imaging, and more generally in patient diagnosis and management. I totally trust on this scientific approach of medicine, and more particularly on the importance we should give to rigorous physical measurements in patient care.

I had the opportunity to conduct my Ph.D. thesis at IR4M, a laboratory which definitely understood that a medical imaging machine is at first a measurement system designed to probe specific physical quantities. Of course, I would like to thank all my colleagues at IR4M for letting me carry on fantastic research projects, for letting me develop and test my ideas and for helping me and supporting me in my projects. However, I would like to thank them for defending every day the role of fundamental sciences in reliable medicine, and therefore putting physics, biology, mathematics and computer sciences at the beginning of any trustful medical device or practice.

In this lab, I would like to thank two persons in particular. The first one is Xavier Maître, my academic Ph.D. supervisor. For years ago now, as I was carrying out my first MRI research projects in San Francisco, we were yet discussing about future research projects together. When we met for the first time, he directly understood my scientific and personal goals and was really motivated to undertake research projects with me. This resulted in a Master thesis that was directly followed by this Ph.D. thesis. Maybe the most exciting aspect of working with Xavier is that he always let me develop my ideas and let me carry on my own projects, but always giving me valuable advices and recommendations. This gave me the opportunity to discover a lot of things in many domains, and go far beyond what I expected at the beginning of the collaboration. Furthermore, we had the opportunity to collaborate during two years on Art-Science projects at the sas>105. This artistic and scientific mediation project was really meaningful and rewarding and gave me the opportunity to meet fantastic people. The second person I would like to acknowledge is Luc Darrasse, my Ph.D. director. As Xavier, Luc has always believed in my vision and supported my research projects. I definitely admire both the human and scientific qualities of Luc and I think they are both of the highest importance for IR4M. He has always accepted people as they are and encouraged them to give their best in their research projects. This is in my opinion how every fruitful research project should start.

One of my goals in this Ph.D. project was to develop industrial collaborations. This was well understood by Xavier and Luc and it was decided to build these links with the industry. It was an ideal moment to do it as a new PET/MR machine built by GE Healthcare arrived in the lab. We decided to start collaborations with GE Healthcare, and several people at GE as Dr. Henri Souchay and Dr. Serge Muller highly encouraged us to go on this way and helped us to create the links between the company and our lab. I want to sincerely thank them for this help. Of course, a third person I want to thank from GE Healthcare is Brice Fernandez, my industrial Ph.D. supervisor. During the three years of Ph.D. thesis, Brice and I spent a lot of time working together, either around the PET/MR machine or trying to debug a code, and it was a great pleasure to collaborate with him. Thanks to Brice, I learnt a lot of things concerning the use of the PET/MR machine, but also on pulse sequence development, computer programming and also on how GE Healthcare was leading research projects and was developing collaborations with academic partners. Brice is a great expert in MRI pulse sequences and applications, and it was an amazing experience to develop my projects with him. It even led to a collaborative project with his research team in Munich (see AZTEK, Chapter 2 Section 4 of this manuscript). For this collaboration, I had the opportunity to meet Dr. Timo Schirmer, Dr. Anne Menini and Dr. Florian Wiesinger from GE Healthcare. Thanks to them, I learnt a lot of things on ZTE imaging, which was very useful to carry on my research projects. I want to sincerely thank them for this collaboration.

In terms of external collaborations also, I really want to warmly thank Dr. Peder Larson from the University of California – San Francisco, who gave me the possibility to use his 3D UTE MRI pulse sequence for my Ph.D. project. Most of the experiments made during my Ph.D. thesis were performed thanks to this pulse sequence. This is not the first time I acknowledge him as he was my supervisor during the internship I did in California just before my Master thesis, and as he taught me a lot of valuable things about MRI. Also, I would like to thank all the people with whom I interacted for scientific collaborations. In particular, I want to sincerely acknowledge Dr. Thomas Similowski, Dr. Pierantonio Laveneziana and Dr. Christian Straus from the Hôpital Pitié-Salpétrière, but also Dr. Georges Caillibotte, Dr. Marine Pichelin, Dr. Ira Katz, Dr. Spyridon Montesantos from Air Liquide, Dr. Dominique Chapelle, Dr. Philippe Moireau, Dr. Martin Genet, Dr. Irène Vignon-Clementel, Dr. Celine Grandmont and Cecile Patte from INRIA, and Dr. Bernard Van Beers, Dr. Philippe Garteiser and Dr. Marion Tardieu from LBI for their great interest on my functional lung imaging and MR elastography projects.

Of course, a great part of the fruitful projects developed during this Ph.D. thesis were possible thanks to the many discussions, collaborations, recommendations and help from many people at IR4M, but also at the IMIV lab. I would like to particularly thank Georges Willoquet, Rose-Marie Dubuisson, Laurène Jourdain, Catherine Sébrié, Pierre Gasner, Jean-Luc Gennisson, Anthony Novell, Geneviève Guillot, Jean-Christophe Ginefri, Marie Poirier-Quinot, Emmanuel Durand, Florent Besson, Nathalie Lassau, Stéphanie Pitre-Champagnat, Ingrid Leguerney, Caroline Caramella, Corinne Balleyguier, Jacques Bittoun and Albine Pinseel at IR4M, and Vincent Lebon, Claire Pellot-Barakat, Claude Comtat, Simon Stute, Marina Filipovic-Pierucci, Christophe Nioche, Charles Truilet, Irène Buvat, Niccolo Fuin, Vincent Brulon, Lionel Kallou and Michael Soussan at IMIV for the great quality of our scientific discussions and collaborations and the great moments we spent together during these three years. More globally, I would like to thank all the people working at SHFJ for the great moments we spent together during these three years. In particular, I would like to thank all the other Ph.D. students and post-docs with whom we shared pleasant moments, and more particularly my office colleagues: Khalil Rachid, Jinlong Yue, Hongchen Wang, Felicia Julea, Fatiha Andoh, Nicolas Chanet, Isabelle Saniour and Lena Nohava. It was a great pleasure to work with you every day.

To finish, I would like to thank my family, and in particular my spouse Camille, my parents and my grandparents for their unfailing support during these three years and for their interest and curiosity about my thesis project.

RESUME DU MANUSCRIT EN FRANÇAIS

1. INTRODUCTION

Pour de nombreuses maladies pulmonaires, nous observons l'altération de certains aspects de la mécanique respiratoire. Dans le cas de l'emphysème pulmonaire par exemple, l'altération des parois alvéolaires a un effet direct sur la ventilation pulmonaire, et donc sur la fonction du poumon. Autre exemple, dans un cas de fibrose radique, la présence de collagène rigidifie localement le poumon, ce qui impactera sa déformation lors de la respiration. Nous partons de l'hypothèse que cette étroite relation entre mécanique respiratoire et pathologie pulmonaire pourrait-être la source de biomarqueurs d'intérêt. Nous entendons par-là essentiellement deux aspects de la mécanique respiratoire :

- **Le comportement mécanique du poumon :** cet aspect de la mécanique respiratoire touche à la déformation locale et tridimensionnelle du poumon lors de manœuvres respiratoires. Une fois modélisé d'un point de vue mathématique et discrétisé d'un point de vue numérique, nous allons montrer qu'il est possible d'extraire des paramètres d'intérêt à partir de ces champs de déformation au sein du parenchyme pulmonaire. Par exemple, il sera possible d'estimer certains aspects régionaux de la ventilation, à partir desquels nous espérons détecter des zones emphysémateuses par exemple.
- **Les propriétés mécaniques du poumon :** cet aspect de la mécanique respiratoire touche au comportement du parenchyme pulmonaire lorsque qu'une contrainte externe lui est appliquée. En tant que matériau viscoélastique, le parenchyme pulmonaire voit l'émergence de forces internes s'opposant à sa déformation par une force externe (élasticité) ainsi qu'une diffusion interne de quantité de mouvement, ce qui donne naissance à des phénomènes d'hystérésis au cours du cycle respiratoire au sein de sa relation contrainte-déformation (viscosité). Ainsi, une mesure locale de la dureté du poumon pourrait nous permettre de détecter et caractériser des zones de fibrose radique.

Afin d'étudier ces deux aspects de la mécanique respiratoire, nous avons besoin de méthodes de mesure qui permettraient à la fois de visualiser de manière tridimensionnelle l'anatomie du poumon et le changement de sa structure au cours de la respiration, mais aussi de venir sonder à l'échelle régionale ses propriétés viscoélastiques. Pour ce faire, le domaine de l'imagerie médicale semble tout indiqué grâce aux possibilités de mesures physiques localisées dans le corps humain qu'offre cette famille de techniques. Cependant, aucune modalité d'imagerie médicale n'est parfaite. Alors que la tomodensitométrie, ou scanner médical, permet d'obtenir des images finement résolues et contrastées du parenchyme pulmonaire, son utilisation sur de longues durées (notamment plusieurs périodes respiratoires) est aujourd'hui freinée par l'irradiation excessive du patient qu'impose cette technique. De plus, le scanner n'offre aujourd'hui aucune solution de mesure des propriétés mécaniques des tissus biologiques. De même, alors que des techniques non-irradiantes comme l'échographie proposent aujourd'hui des solutions de quantification des propriétés mécaniques, leur utilisation reste très limitée pour le poumon en raison de ses grandes dimensions et de sa protection par la cage thoracique.

L'imagerie par résonance magnétique (IRM) nous semble être aujourd'hui la meilleure solution pour répondre à notre problème. Offrant tout à la fois des contrastes riches au sein des tissus mous et une fine résolution spatiale, cette modalité est non-irradiante pour le patient et permet des applications avancées comme l'élastographie par résonance magnétique, une technique permettant de mesurer les propriétés viscoélastiques des tissus directement à partir d'images IRM d'organes excités mécaniquement. Cependant, l'IRM du poumon reste très difficile aujourd'hui, et ce pour trois raisons principales :

- **La faible densité du parenchyme pulmonaire :** L'IRM du proton reposant essentiellement sur la présence de molécules d'eau au sein des tissus biologiques, le signal de résonance magnétique nucléaire (RMN) mesuré lors du processus d'imagerie est proportionnel à la densité de proton, elle-même intimement liée à la densité du tissu chez les organes mous. Or, le poumon étant structuré par un arbre de voies aériennes se terminant par des millions d'alvéoles pulmonaires remplies d'air, le signal récupéré pour l'imagerie du poumon est faible et varie au cours du cycle respiratoire. Une IRM de poumon acquise à l'aide d'une séquence IRM standard souffrira donc d'un très faible rapport signal sur bruit, ce qui compliquera la visualisation de détails anatomiques au sein du parenchyme pulmonaire.
- **Les courts temps de relaxation T_2^* au sein du parenchyme pulmonaire :** En IRM, T_2^* représente la durée de vie du signal RMN à la suite d'une excitation radiofréquence (RF) et sans application de champ magnétique externe autre que le champ magnétique principal $\overrightarrow{B_0}$ du système d'imagerie. Il s'agit donc de la durée pendant laquelle une mesure de signal RMN est possible après excitation RF. Dans la plupart des tissus biologiques, T_2^* est de l'ordre de quelques dizaines de millisecondes. Cependant, dans le poumon et à 3 T, ce temps de relaxation est plutôt de l'ordre de la demi-milliseconde. Cela rend la mesure de signaux IRM complexe dans le poumon car l'encodage de la position des spins au sein de l'organe ainsi que la récupération du signal doivent être effectués en moins de quelques millisecondes.
- **Le mouvement respiratoire :** Si l'organe d'intérêt bouge au cours du processus d'imagerie, des artéfacts de mouvement apparaissent au sein des images finales, ce qui dégrade la qualité de leur interprétation. Pour résoudre ce problème, il est possible d'acquérir l'image au cours d'une apnée. Dans ce cas, seules de courtes durées d'acquisition sont permises et il est impossible d'étudier le comportement dynamique du poumon au cours de la respiration. Or, il s'agit ici de changer de paradigme, de voir le mouvement physiologique non pas comme une difficulté du processus d'imagerie mais bien comme une source d'information pour nos perspectives diagnostiques. Pour cela, une stratégie de prise en compte, de mesure et de correction de ce mouvement sera nécessaire au cours du processus d'imagerie.

Afin de résoudre les deux premiers problèmes, deux séquences IRM semblent particulièrement adéquates : la séquence Ultrashort Time-Echo (UTE) et la séquence Zero Time-Echo (ZTE). Ces deux séquences IRM partagent de nombreuses similarités (voir Figure 1) : une acquisition radiale de l'espace de Fourier de l'image, une courte durée de lecture du signal ainsi qu'une limitation au maximum de la durée entre l'excitation RF du tissu et la mesure du signal RMN. Cette durée, couramment appelée temps d'écho (TE), peut alors atteindre des valeurs de l'ordre de la dizaine de microsecondes, alors que les TE les plus courts rencontrés en IRM sont rarement inférieurs à la milliseconde. Ces TE ultracourts permettent alors de récupérer une grande amplitude de signal RMN malgré la faible densité tissulaire et les courts temps de relaxation : une image par résonance magnétique du poumon devient alors possible. Cependant, le troisième problème reste à régler : le mouvement physiologique. Encore une fois, il ne s'agit pas de voir le mouvement respiratoire comme un problème dès lors qu'il constitue une source d'information capitale pour les grandeurs physiques que l'on souhaite quantifier. Il ne s'agit donc pas de l'empêcher ou de l'atténuer, mais bien de le mesurer et de l'étudier. Pour cela, la séquence UTE possède des propriétés très intéressantes : en plus d'être robuste vis-à-vis de certains artéfacts de mouvement, elle permet intrinsèquement de mesurer à chaque répétition de la séquence (à chaque TR) le signal au centre de l'espace de Fourier de l'image, qui n'est autre que le signal moyen envoyé par l'intégralité des tissus biologiques après excitation RF et capté par les antennes de réception. Ce signal (parfois appelé « Signal DC ») correspond donc au signal moyen d'une image par résonance magnétique qui serait acquise instantanément à chaque répétition de séquence. Lors de la respiration, ce signal sera modulé en raison de plusieurs facteurs (mouvement du tissu sous les profils de sensibilité d'antenne, modulation de la charge de l'antenne …). Représenté au cours du temps, ce signal DC oscille donc à la manière de la respiration et constitue donc une méthode de mesure du mouvement respiratoire intrinsèque au processus d'imagerie.

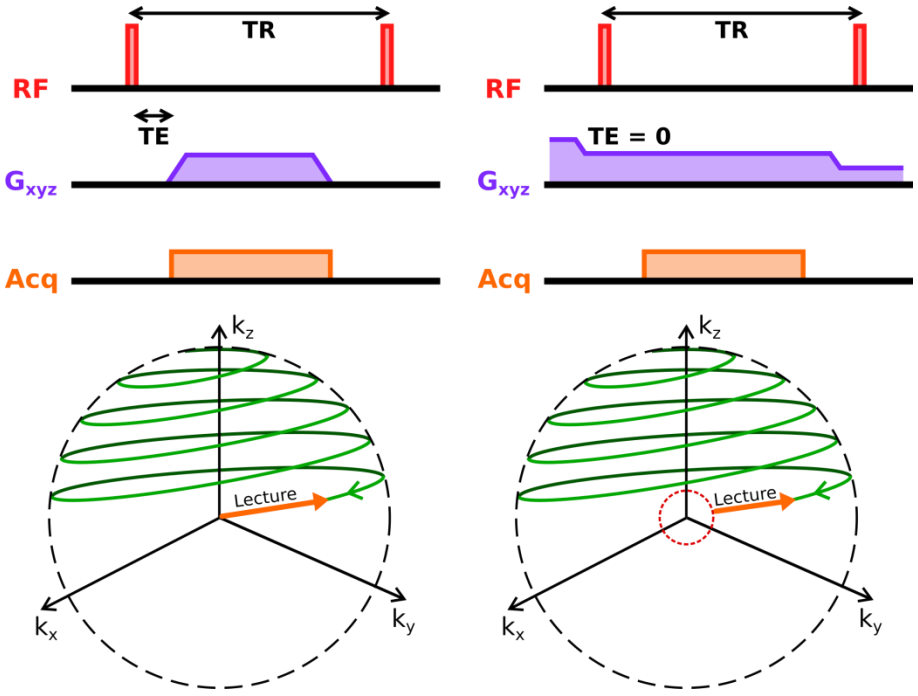

Figure 1 : Chronogrammes et trajectoires des séquences UTE (à gauche) et ZTE (à droite). La séquence ZTE étant exécutée à l'aide de gradients de lecture continus en temps, la zone centrale de l'espace de Fourier n'est pas acquise et les directions de rayons acquis successivement ne doivent pas être trop différentes les unes des autres.

2. DEVELOPPEMENTS INNOVANTS DANS LE DOMAINE DU SUIVI ET DE LA CORRECTION DE MOUVEMENT EN IRM

2.1. SNIF : SELF-NAVIGATOR INTELLIGENT FILTER

Cependant, que contient vraiment le signal DC ? Expérimentalement, nous observons un signal évoluant avec la respiration mais entaché par ce qui semble être un bruit haute-fréquence en temps. Néanmoins, nous nous sommes demandés si cette perturbation haute fréquence était uniquement du bruit ou contenait un biais de mesure modélisable et corrigible. Pour cela, nous avons modélisé l'évolution temporelle du signal DC, S_{DC}, comme étant l'addition et la convolution de plusieurs termes :

$$S_{DC} = S_m + S_0 \star h$$

Dans le modèle précédent, S_m représente le signal relatif au mouvement respiratoire, appelé signal de « Self-navigation ». Ce signal, qui nous intéresse dans une perspective de correction de mouvement ultérieure, contient également des informations sur le mouvement cardiaque. Il est cependant entaché de deux termes parasites convolués entre eux :

- S_0 : Ce terme représente un effet hors-centre de l'espace de Fourier, c'est-à-dire, un biais de mesure lié à un échantillonnage du signal DC décalée par rapport au centre de l'espace de Fourier de l'image. Il explique donc une part de la variation inter-répétition du signal mesuré.
- h : Ce terme représente un effet d'histoire de spin. En effet, lors d'une répétition du processus d'imagerie, le signal mesuré dépend des spins excités et encodés lors de la répétition en cours mais également du

signal généré par l'aimantation transverse résiduelle produite lors des précédentes répétitions. Nous modélisons ici cette histoire d'aimantation transverse par un filtre linéaire.

L'extraction de S_0 et de h à partir de S_{DC} nous permet alors d'extraire S_m « intelligemment », c'est-à-dire, en prenant en compte la physique sous-jacente et non pas en utilisant de manière aveugle d'un filtre passe-bas. Ce système de filtrage du signal DC a ainsi été appelé « Self-Navigator Intelligent Filter », ou SNIF. Nous avons montré, en particulier grâce à une analyse de Fourier, que les différentes harmoniques temporelles des mouvements respiratoire et cardiaque étaient extraites du bruit de fond, ce qui n'aurait pas été possible par l'utilisation d'un filtre linéaire par exemple (voir Figure 2). Nous avons également vérifié que les composantes mesurées de h vérifiaient le principe de causalité pour l'effet modélisé, ce qui semble indiquer la pertinence de notre modèle.

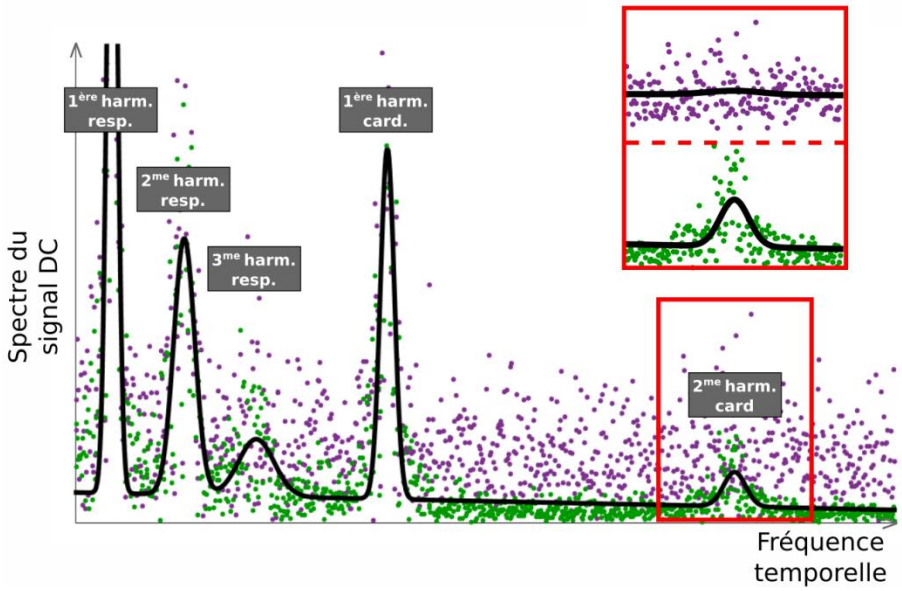

Figure 2 : Spectre du signal DC avant (magenta) et après (vert) l'application de SNIF. Le bruit de fond est diminué, ce qui laisse entrevoir la seconde harmonique du mouvement cardiaque auparavant cachée par le bruit de fond.

2.2. SNOZE : SELF-NAVIGATION FROM OFF-CENTER ZTE EVOLUTION

Ainsi, il est facile de suivre les mouvements physiologiques en UTE : il suffit d'étudier l'évolution temporelle du signal mesuré au début de chaque rayon d'espace de Fourier acquis au cours des répétitions. Mais qu'en est-il de la ZTE ? En effet, la ZTE diffère de la UTE sur ce point : les rayons acquis sont partiels (voir Figure 1) et le centre de l'espace de Fourier de l'image n'est mesuré que lors d'une séquence d'imagerie complémentaire. Il est donc impossible d'utiliser la même technique de self-navigation qu'en UTE. Cependant, à chaque répétition de la séquence ZTE, des mesures de signal sont effectuées à proximité du centre de l'espace de Fourier. Il est donc probablement possible d'extraire un signal de self-navigation à partir de ces points de mesure. Dans la version standard de la ZTE, lorsque les rayons de l'espace de Fourier sont caractérisés par leurs coordonnées sphériques, les deux angles polaire et azimutal, nommés respectivement θ et φ, présentent des évolutions temporelles très distinctes : alors que θ évolue lentement et monotoniquement (de 0 à π radians) au cours de l'acquisition ZTE, φ varie rapidement et de manière répétée entre $-\pi$ et π (voir Figure 3). Il est ainsi possible de dresser une relation bijective entre θ et le temps tout au long de l'acquisition, et ce pour chaque valeur de φ.

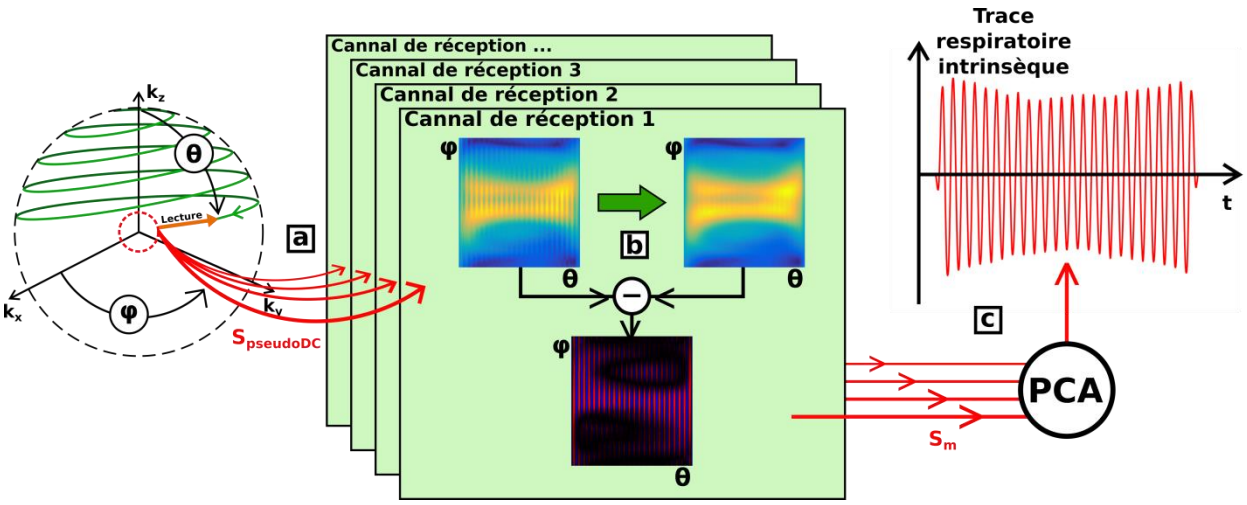

Figure 3 : Schéma de fonctionnement de la méthode SNOZE. a) Interpolation des données temporelles dans l'espace (θ, φ) ; b) Filtrage passe haut des données selon θ ; c) Analyse en composantes principales afin d'extraire la trace respiratoire finale.

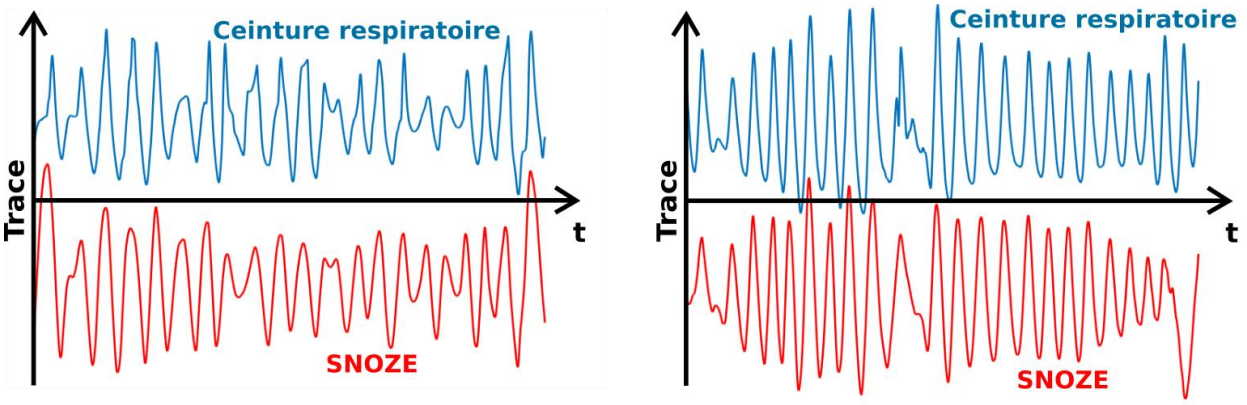

Figure 4 : Comparaison des traces respiratoires obtenues à l'aide d'une ceinture respiratoire et de la méthode SNOZE sur deux patients (l'un à gauche et l'autre à droite).

Cette relation bijective entre le temps et une coordonnée angulaire dans l'espace de Fourier nous a permis de développer SNOZE, « Self-Navigation from Off-center ZTE Evolution ». Basée sur la représentation dans l'espace (θ, φ) des données acquises à proximité du centre de l'espace de Fourier de l'image, cette méthode fait apparaitre des modulations de signal IRM liées au mouvement respiratoire (voir Figure 3). En appliquant un filtrage passe-haut et une analyse en composantes principales sur ces données, il est possible d'extraire une trace de self-navigation pour le mouvement respiratoire en ZTE, qui est similaire à celle extraite du centre de l'espace de Fourier en UTE. Ces traces ont été comparées à celles obtenues sur fantôme mais également sur patient à l'aide d'une ceinture respiratoire (protocole PROMISE conduit par le Dr. Michael Soussan, voir Figure 4).

2.3. AZTEK : ADAPTIVE ZTE K-SPACE TRAJECTORIES

Cependant, la mesure d'une trace respiratoire, qu'elle soit intrinsèque à l'acquisition des données ou non, n'est pas suffisante pour empêcher l'apparition d'artéfacts de mouvement dans les images. En effet, une deuxième étape consistant à corriger ces effets de mouvement à partir de la trace respiratoire est nécessaire. Une méthode simple, appelée « gating » rétrospectif, consiste à trier les données brutes (de l'espace de Fourier) en fonction de la phase

respiratoire au cours de laquelle elles ont été acquises, puis de reconstruire séparément les images correspondant à ces différentes phases du mouvement physiologique. Cependant, l'application d'un gating rétrospectif sur les données ZTE conduit très souvent à une espace de Fourier incomplet, avec des zones sur-échantillonnées et d'autres vides de signal. Après reconstruction, des artéfacts basse-fréquence de sous-échantillonnage apparaissent alors dans l'image finale corrigée du mouvement, ce qui détériore grandement son potentiel diagnostique. Ces vides de signal apparaissent en ZTE à cause de la trajectoire très spécifique de cette séquence, et en particulier à cause de la coordonnée de rayon θ évoluant lentement et monotoniquement au cours de l'acquisition, ce qui impose un lien fort entre les coordonnées de l'espace de Fourier et le temps.

Il serait préférable d'utiliser une trajectoire qui découplerait le temps et l'ordre d'acquisition des rayons dans l'espace de Fourier de l'image. Cependant, il est tout de même nécessaire de garder une certaine continuité directionnelle dans les rayons acquis successivement, la séquence ZTE étant appliquée à l'aide de gradients de lecture continus et non pulsés (voir Figure 1). Cette adaptation aux exigences de la ZTE et à la correction du mouvement respiratoire par gating rétrospectif est le point de départ d'une trajectoire développée lors de ma thèse. Cette nouvelle trajectoire, nommée AZTEK, pour « Adaptive ZTE K-space », a l'ambition de répondre au cahier des charges initial (découplage du temps et de l'ordre d'acquisition des rayons + continuité temporelle des directions de rayons acquis) mais aussi de s'adapter à n'importe quel rythme de mouvement physiologique. Cette dernière partie n'a été que théorisée et seul le développement de la trajectoire et ses premiers tests ont été effectués lors de la thèse.

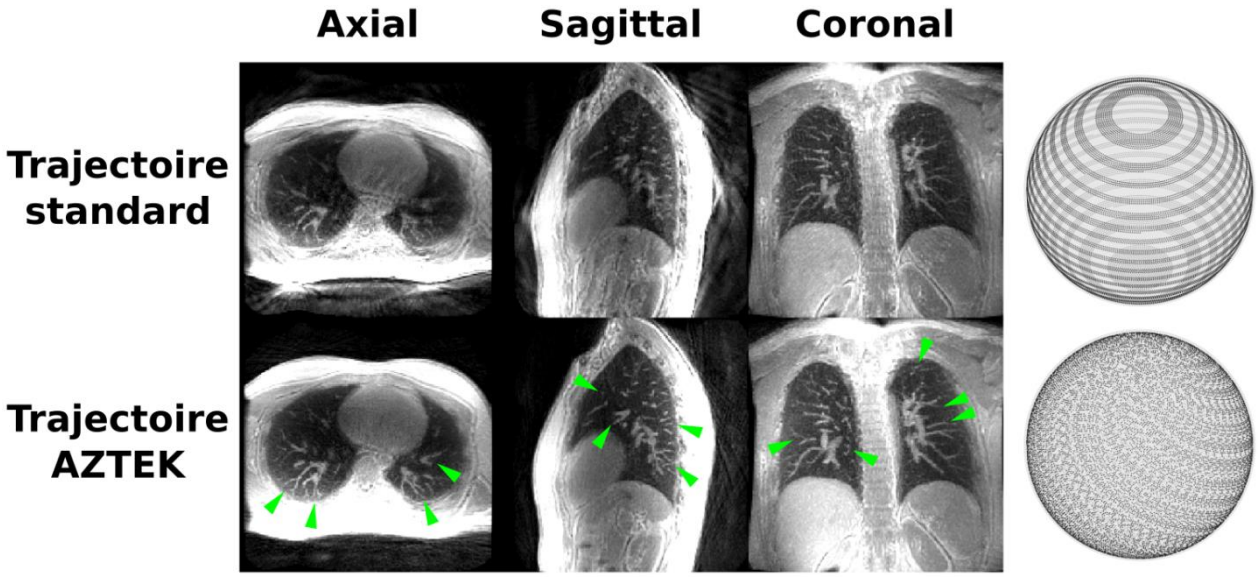

Figure 5 : Images ZTE obtenues à l'aide de la trajectoire standard et de la trajectoire AZTEK. A droite de la figure sont représentées des vues 3D du remplissage de l'espace de Fourier après gating rétrospectif.

Le développement de AZTEK part d'une inversion des rôles entre θ et φ : θ varie à présent rapidement, alors que φ varie lentement. De plus, trois paramètres ont étés implémentés pour le contrôle de l'évolution temporelle des directions de rayons acquis : AZTEK-Twist, AZTEK-Shuffle et AZTEK-Speed, contrôlant respectivement la torsion des arcs de la trajectoire, la variation en θ d'un arc à l'autre et la vitesse à laquelle est parcourue chaque arc. En réglant correctement ces trois paramètres, il est possible d'obtenir une couverture uniforme de l'espace de Fourier après l'application d'une gate rétrospective. L'adaptation théorisée dans la thèse portera sur le choix automatique des valeurs attribuées à ces trois paramètres pour adapter au mieux la trajectoire à n'importe quelles caractéristiques de mouvement physiologique (rythme, périodicité …). Des acquisitions ZTE sur fantôme, sur volontaire sain mais

également sur patient (protocole IMAHTEP conduit par le Dr. Florent Besson) ont été réalisées avec les trajectoires standard et AZTEK et ont validé le potentiel de la trajectoire AZTEK pour l'imagerie ZTE du poumon corrigée du mouvement (voir Figure 5).

A présent que nous maîtrisons un peu mieux l'imagerie par résonance magnétique dynamique du poumon, il nous est possible d'étudier les deux aspects de la mécanique respiratoire cités précédemment : le comportement mécanique et les propriétés mécaniques du parenchyme pulmonaire.

3. ETUDE DU COMPORTEMENT MECANIQUE DU POUMON : LA SPIROMETRIE PAR RESONANCE MAGNETIQUE 3D

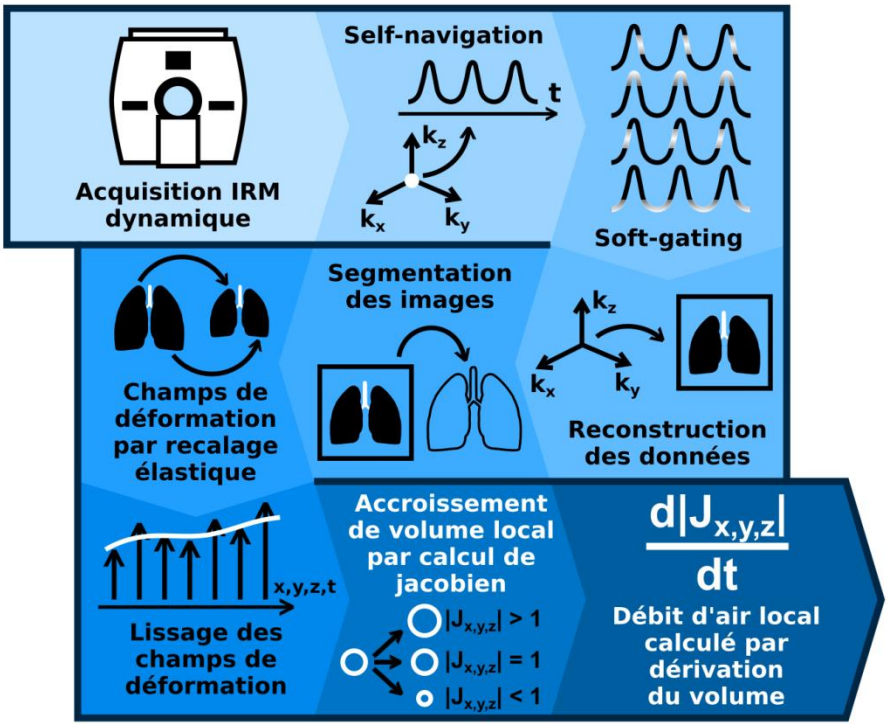

Figure 6 : Schéma décrivant l'acquisition et le post-traitement des données pour notre application « 3D Magnetic Resonance Spirometry ».

En ce qui concerne l'étude du comportement mécanique du poumon, nous avons développé un protocole complet d'imagerie thoracique et de post-traitement d'image dédié à l'extraction de paramètres d'intérêt quantifiant le comportement mécanique du poumon au cours de la respiration. Ce protocole, illustré en Figure 6, a été appelé « 3D Magnetic Resonance Spirometry », la spirométrie étant l'une des principales techniques utilisées aujourd'hui en routine clinique pour l'évaluation globale de la fonction pulmonaire.

L'inconvénient de la spirométrie est sa globalité : il est impossible d'extraire les propriétés fonctionnelles d'une région particulière du poumon car seule une mesure globale n'est possible. Par l'analyse de champs de déformation du parenchyme pulmonaire extraits des images dynamiques 3D UTE, nous avons montré qu'il était possible d'effectuer des mesures d'accroissement local de volume d'air dans le poumon. Leur analyse en temps nous donne alors accès à des mesures de débits d'air régionaux le long du cycle respiratoire. Il est alors possible

d'extraire et de représenter le même résultat qu'en spirométrie standard, c'est-à-dire, un cycle débit-volume d'air au sein du poumon, mais à l'échelle locale et en trois dimensions (voir Figure 7).

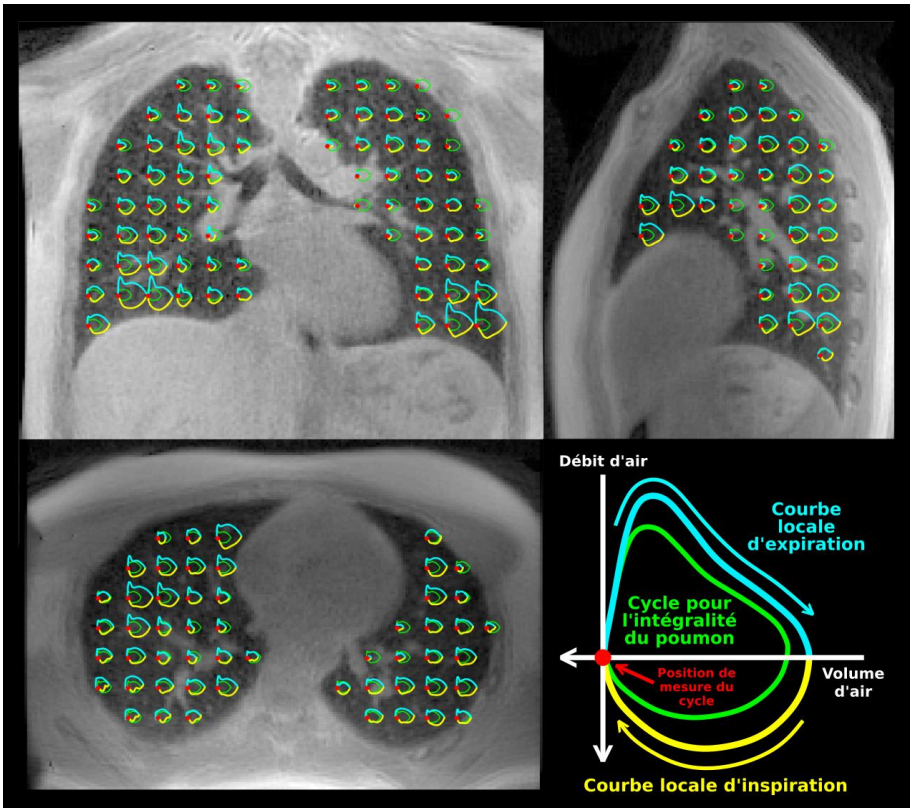

Figure 7 : Images de spirométrie par résonance magnétique 3D avec légende d'interprétation en bas à droite de la figure.

Nous avons également montré que la spirométrie n'était qu'une partie des informations qu'il était possible d'extraire des données initiales. Cette information est certainement la plus parlante pour les pneumologues mais n'est pas la seule qui puisse être extraite. Ainsi, nous avons montré qu'il était possible d'étudier les trajectoires locales suivies par le parenchyme pulmonaire, d'extraire les différentes composantes du tenseur de déformation local, d'étudier l'anisotropie et les directions principales de déformation ainsi que de mettre en évidence des phénomènes d'hystérésis apparaissant au sein du cycle respiratoire pour différentes quantités. A présent, la question à se poser porte sur l'intérêt clinique de telles mesures : même si cette analyse mécanique complète du mouvement respiratoire est très intéressante d'un point de vue physique, qu'en est-il de son potentiel clinique ? Pour cela, seules des réflexions approfondies avec des spécialistes de la physiologie et de la pathologie pulmonaire, couplées à des essais sur volontaires sains et sur patients, pourront éclaircir le sujet.

Dans cette analyse du comportement mécanique du poumon, un élément capital n'est pas pris en compte : les forces. Or, les déformations analysées précédemment, source de ventilation pulmonaire, sont contrôlées par des forces générées à l'extérieur du poumon (par le diaphragme et les muscles intercostaux essentiellement) qui se traduisent par des contraintes au sein du parenchyme pulmonaire (pression, cisaillement …). Jusqu'à présent, nous étions sensibles aux effets associés au comportement mécanique (déformation, ventilation …) mais pas aux causes (forces, contraintes …). Ce problème pourrait être adressé grâce à l'étude du deuxième aspect de la mécanique respiratoire : la mesure des propriétés mécaniques du parenchyme pulmonaire.

4. ETUDE DES PROPRIETES MECANIQUES DU POUMON : L'ELASTOGRAPHIE PAR RESONANCE MAGNETIQUE

Par le terme « propriétés » mécaniques du poumon, nous entendons essentiellement deux aspects : l'élasticité (ou dureté), qui fait le lien entre la contrainte et la déformation d'un matériau, et la viscosité, qui relie cette contrainte au taux de cisaillement du matériau. A partir de la connaissance de ces propriétés à l'échelle locale et de la mesure de l'évolution des déformations présentée précédemment, il serait alors possible de mesurer des forces et ainsi compléter notre étude de la mécanique respiratoire. Pour cela, l'IRM pourrait être d'une grande utilité grâce à l'une de ses applications : l'élastographie par résonance magnétique.

Cette technique consiste à ajouter des gradients d'encodage du mouvement à une séquence IRM standard et à générer des ondes mécaniques au sein de l'organe d'intérêt. Si ces gradients d'encodage du mouvement sont insérés entre l'impulsion d'excitation RF et la fenêtre d'acquisition des données, mais aussi appliqués en phase avec les ondes de cisaillement générées dans l'organe, il est possible de mesurer de manière quantitative les déplacements micrométriques au sein des tissus biologiques. L'analyse de la propagation des ondes, en particulier la mesure de leur vitesse de propagation et de leur atténuation, permet alors de remonter aux propriétés mécaniques que l'on souhaite mesurer. Cependant, pour le poumon, nous sommes confrontés à un problème majeur : à cause des T_2^* très courts présents au sein du poumon, il est difficile d'insérer un gradient d'encodage du mouvement entre l'impulsion d'excitation et l'acquisition des données. Cette stratégie provoquerait un allongement du TE incompatible avec l'imagerie du parenchyme pulmonaire. Une autre stratégie doit donc être envisagée.

Au cours de ma thèse, une nouvelle technique d'élastographie a été développée. Cette technique possède plusieurs propriétés intéressantes. En particulier, elle offre la possibilité de réaliser l'élastographie de matériaux à courts T_2^*, mais aussi de réduire la durée totale de l'acquisition d'un facteur 5 en moyenne. Cependant, le dépôt prochain d'un brevet portant sur cette technique ne nous permet pas de divulguer d'avantage d'informations sur cette nouvelle stratégie pour le moment. Cette nouvelle technique a été testée sur fantôme et sur volontaire sain et s'annonce très prometteuse à la fois pour l'élastographie du poumon mais également pour l'élastographie d'autres organes.

En conclusion, cette thèse nous a permis de mesurer le potentiel de l'IRM pour l'étude de la mécanique respiratoire, à la fois concernant l'analyse du comportement mécanique du poumon mais aussi la quantification de ses propriétés viscoélastiques. Cette approche biomécanique du diagnostic de la pathologie pulmonaire par IRM du proton est encore récente mais semble ouvrir la voie vers la mesure de nouveaux biomarqueurs de l'état physiopathologique du poumon.

INTRODUCTION

Medical imaging is probably one of the most valuable and impressive recent advances in medical practice.

It is of primary importance to consider physical phenomena and physical measurement at the basis of any reliable medical practice, either in diagnosis, therapy or treatment follow-up. The notion of physical measurement is not new as it has been practiced for several centuries by natural scientists to better understand their environment. However, the idea of simultaneously measuring the same physical quantity in an extended region of space is quite recent, and it can be challenging to find a non-invasive and reliable strategy to obtain, at the same time as the measurement process, the spatial positions where the physical parameters were measured. To take only one example that will be largely discussed in this manuscript, Magnetic Resonance Imaging (MRI) consists in measuring electromagnetic waves produced by nuclei through Nuclear Magnetic Resonance (NMR) phenomena in the body of a patient and localizing the sources from where the waves were emitted. Therefore, two strategies need to be developed and put together: one to reveal and enhance this physical phenomenon and another one to localize and characterize the sources from where the electromagnetic waves are emitted. This technique has the great advantage to non-invasively produce images of the inside of the body, but also to enable the measurement of special physical quantities or physiological phenomena that were not assessable before.

The lung is an organ of the greatest importance in the human body. Thanks to the gas exchange possibilities it enables, it is the only interface between the human body and its environment for dioxygen consumption and carbon dioxide evacuation. However, because of its low density and short NMR relaxation times, and because of the effects of respiratory motion in MR images, it is today one of the most challenging organs to study with proton MRI. This is problematic because MRI would offer the possibility to study the pulmonary anatomy, the physical and physiological processes occurring inside the organ, but also to detect lung diseases and assess the pathophysiological state of the organ.

In this manuscript, we will see that proton lung MRI is possible today thanks to advanced image acquisition and post-processing strategies dedicated to this type of organ. Moreover, we will see that most interesting aspects of the lung, anatomy, function, pathology, are closely related to lung mechanics, which covers at the same time the mechanical behavior of the organ (how it moves, how its shape changes along time, how it inflates, …) but also its mechanical properties (how elastic or viscous the organ is). Finally, we will see that these two aspects of lung mechanics can be directly assessed thanks to dedicated proton MRI acquisition protocols and post-processing strategies. This is therefore very promising for the future of pulmonology.

The assessment of pulmonary mechanical behavior and properties with MRI is quite new, and the only proposed strategies to do it are found in a quite small number of scientific publications. These strategies need to be further developed and discussed and tools need to be built, both for imaging protocols and for post-processing tasks. This is where my PhD thesis starts. I have worked during my three-year research project on magnetic resonance imaging of respiratory mechanics. This manuscript is composed of an extended bibliographic study, both on pulmonology and on medical imaging techniques to study the lung, and of the technological solutions I developed, tested and validated to answer to scientific and medical questions on respiratory mechanics and lung pathophysiology.

In the first chapter of this manuscript, I give a review of the basic information on lung structure and function, of the main techniques used today to diagnose pulmonary diseases, and I explain why we should focus on lung mechanics to assess its pathophysiological state. Then, I explain the fundamental concepts of magnetic resonance imaging, and exhibit its interest for the non-invasive assessment of many physical quantities inside the human body. Finally,

I introduce the challenges of lung MRI and give solutions to the encountered problems through two MRI pulse sequences adapted to lung imaging: Ultrashort Echo Time (UTE) and Zero Echo Time (ZTE) pulse sequences.

The second chapter of this manuscript is focused on the notion of physiological motion. After presenting the usual techniques developed to track motion and avoid motion related artifacts in MR images, and after introducing and explaining the notions of surrogate signal and self-navigation, I propose three innovations for motion tracking and correction in UTE and ZTE imaging. The first one is a Self-Navigator Intelligent Filter, or SNIF, that aims at understanding and correcting the high-frequency 'noise' observed sometimes in the UTE DC-signal, often used as a self-navigator. The second one is a Self-Navigator from Off-center ZTE Evolution, or SNOZE, which is an algorithm that aims at extracting a self-navigation signal from ZTE k-space data, as it can be done in UTE. The third one is an Adaptive ZTE K-space trajectory, or AZTEK, which is a k-space trajectory designed to be adapted to both ZTE pulse sequence recommendations and motion correction with retrospective gating.

In the third chapter of this manuscript, I focus on the primary aspect of respiratory mechanics: the mechanical behavior of the lung. To study this aspect, I give a review of the literature on MR imaging techniques that were developed for the assessment of the different aspects of lung function. I give a special attention to methods based on the measurement of motion components inside the lung (especially deformation and velocity fields), and explain the assets of this family of techniques. Then, I introduce a full MR image acquisition and post-processing strategy designed to measure the mechanical behavior of the lung and extract relevant potential biomarkers based on pulmonary biomechanics. This advanced technique, called 3D Magnetic Resonance Spirometry, is shown to extract a great variety of physical quantities of interest, and leads to results in accordance with the literature on lung physiology.

Finally, the fourth chapter of this manuscript is dedicated to the second aspect of respiratory mechanics: the mechanical properties of the lung. After introducing the fundamental physical and technological concepts of elastography, both in the field of ultrasound and MR imaging, I explain the challenge of MR elastography in the lung and describe why it is impossible to implement standard elastography techniques with UTE and ZTE imaging. To tackle this issue, I propose a totally new paradigm to perform MR elastography and show the very first promising results we obtained with this technique.

CHAPTER 1 - THEORETICAL BASES: THE LUNG IN MAGNETIC RESONANCE IMAGING

IN THIS CHAPTER, WE WILL INTRODUCE THE BASIC CONCEPTS AND VOCABULARY THAT WILL BE NEEDED FOR THE REST OF THIS MANUSCRIPT. FIRST, WE WILL INTRODUCE A BASIC KNOWLEDGE ABOUT LUNG ANATOMY, FUNCTION, PATHOLOGIES AND DIAGNOSIS TECHNIQUES. AFTER THIS, WE WILL STUDY THE BASIC PRINCIPLES OF MAGNETIC RESONANCE IMAGING, OR MRI, FROM ITS PHYSICAL ORIGINS TO ITS MAIN APPLICATIONS IN CLINICAL ROUTINE AND RESEARCH. TO FINISH, WE WILL FOCUS ON THE ISSUES OF LUNG MRI AND STUDY THEIR POSSIBLE SOLUTIONS THROUGH ADVANCED MRI PULSE SEQUENCES. THIS WILL BE THE STARTING POINT FOR THE EVALUATION OF RESPIRATORY MECHANICS WITH MAGNETIC RESONANCE IMAGING.

SECTION 1 THE HUMAN LUNG

IN HUMAN CELLS, DIOXYGEN IS CONSUMED DURING THE PRODUCTION OF ENERGY FROM NUTRIENTS AND CARBON DIOXIDE IS PRODUCED ALONG THIS CHEMICAL REACTION. THIS PROCESS IS CALLED CELLULAR RESPIRATION AND IS PART OF THE CELL METABOLISM. THESE DIOXYGEN AND CARBON DIOXIDE ARE RESPECTIVELY EXTRACTED FROM THE ENVIRONMENT AND EVACUATED THROUGH A SECOND RESPIRATION PROCESS CALLED PHYSIOLOGICAL RESPIRATION. THIS EXCHANGE PROCESS IS PROVIDED BY THE LUNG, AND THE TERM 'VENTILATION' IS OFTEN USED TO DESIGNATE MORE PRECISELY THE GAS, SAY THE AIR, RENEWAL PROCESS INSIDE THE LUNG NEEDED FOR THE GAS EXCHANGE. IN THE ENTIRE MANUSCRIPT, 'RESPIRATION' AND 'RESPIRATORY' WILL REFER ONLY TO THIS SECOND PROCESS. IN THIS FIRST SECTION, A BRIEF DESCRIPTION OF LUNG ANATOMY, FUNCTION AND DISEASE, AND THEIR RELATIONSHIP TO LUNG MECHANICAL PROPERTIES, IS GIVEN.

1. ANATOMY OF THE HUMAN LUNG

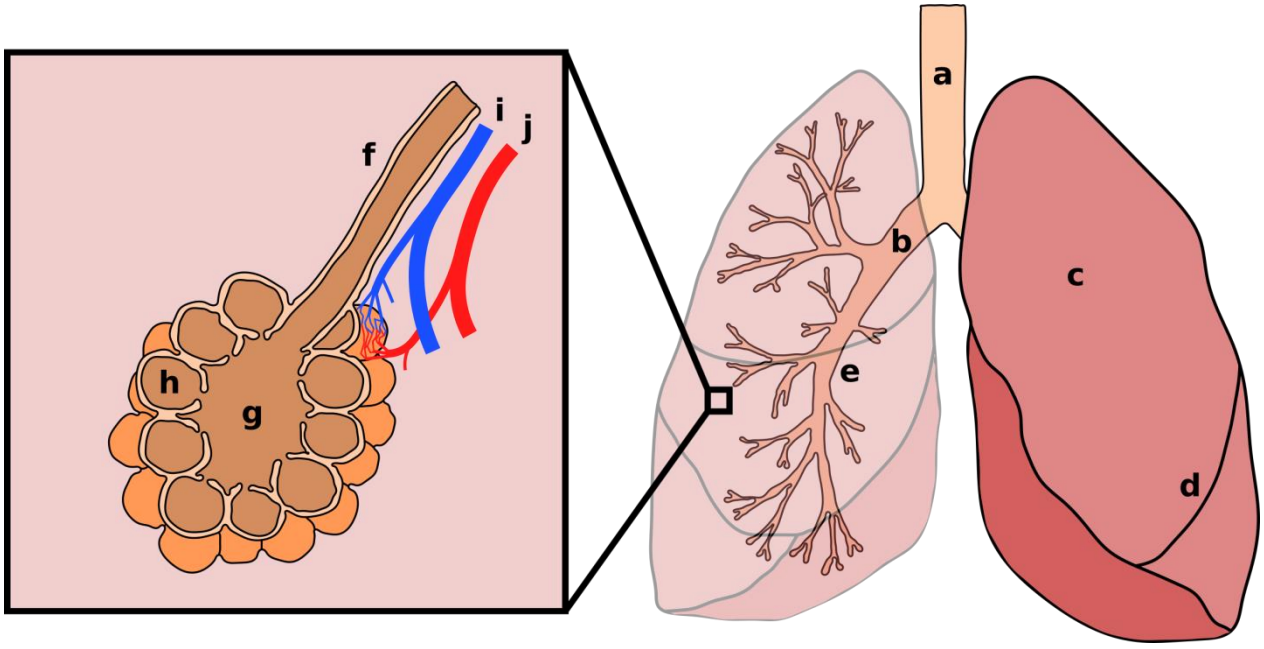

Figure 1.1: Schematic representation of the human lung anatomy.

Morphologically speaking, the human lung is located inside the thoracic cage[1]. Starting from the larynx and going caudally, the organ is composed of the trachea (see **Figure 1.1a**), which is the main air duct, that divides in two primary bronchi (see **Figure 1.1b**), the first generation of air ducts, and terminates into two 'lungs' (see **Figure**

[1] Susan Standring, *Gray's Anatomy International Edition: The Anatomical Basis of Clinical Practice* (Elsevier Health Sciences, 2015).

1.1c), the same term being used to designate either the whole organ or its two main parts, each of them fitting inside an independent pleural cavity. These cavities are covered with a membrane called parietal pleura. The two lungs are also covered with a membrane called visceral pleura. The space between those two pleurae is filled with a liquid called pleural liquid. The region between the two lungs, containing the trachea and the primary bronchi, but also the heart and the esophagus, is called the mediastinum. The right lung is composed of three lobes (upper, medium and lower) and the left lung of two lobes (upper and lower), each lobe being separated from the others by fissures (oblique and horizontal for the right lung and oblique for the left lung, see **Figure 1.1d**). The diaphragm spreads below the inferior surface of the lung, caudally to the parietal pleura.

Inside the two lungs, several interleaved functional systems can be distinguished:

- The bronchial tree, that includes the trachea and the two primary bronchi, is composed of successive generation of air ducts. The primary bronchi split into secondary bronchi (see **Figure 1.1e**), which split into tertiary bronchi, and so on until reaching bronchioles through several other generations of bronchi, forming the gas conductive zone of the bronchial tree. Distally to this conductive zone, we find the respiratory zone composed of respiratory bronchioles, alveolar ducts (see **Figure 1.1f**) and alveolar sacs (see **Figure 1.1g**) containing alveoli (see **Figure 1.1h**), where gas exchanges occur. In human lungs, the bronchial tree is composed approximatively of 23 generations of air ducts from the primary bronchi to the alveoli.

- The pulmonary circulation system, that brings deoxygenated blood from the right ventricle of the heart to the lung alveoli through the pulmonary arteries (see **Figure 1.1i**), that subdivides into small capillaries, and brings back to the left atrium of the heart oxygenated blood through the pulmonary veins (see **Figure 1.1j**) after the gas exchange processes occurred in the alveoli. Those processes are possible thanks to the close proximity between the alveolar walls, or septa, and the capillaries.

- The bronchial circulation system, part of the systemic circulation system, brings to the lower respiratory tract and the visceral pleura oxygenated blood for lung cell nutrition purposes. This blood is taken directly from the aorta and conducted to the lung cells through the bronchial arteries. The deoxygenated blood is then conducted out of the lung essentially through the pulmonary veins described above, but also through dedicated veins called bronchial veins.

- The nervous system, formed by nerves of the autonomic nervous system, controls the constriction of the bronchi and the secretion of mucus.

These different systems in the lung work together to ensure the lung function.

2. FUNCTION OF THE HUMAN LUNG

As stated above, the main function of lung is the gas exchange between the human body and the environment. The lung extracts dioxygen from the inhaled air and releases carbon dioxide produced by the different cells of the organism. These exchanges are permitted during the ventilation process, which is the renewal of gas inside the lung airways. This ventilation process is enabled by the respiratory cycles, during which the whole lung deforms (change in volume and shape) because of the air going in and out of the lung alveoli. All this process is explained by respiratory mechanics.

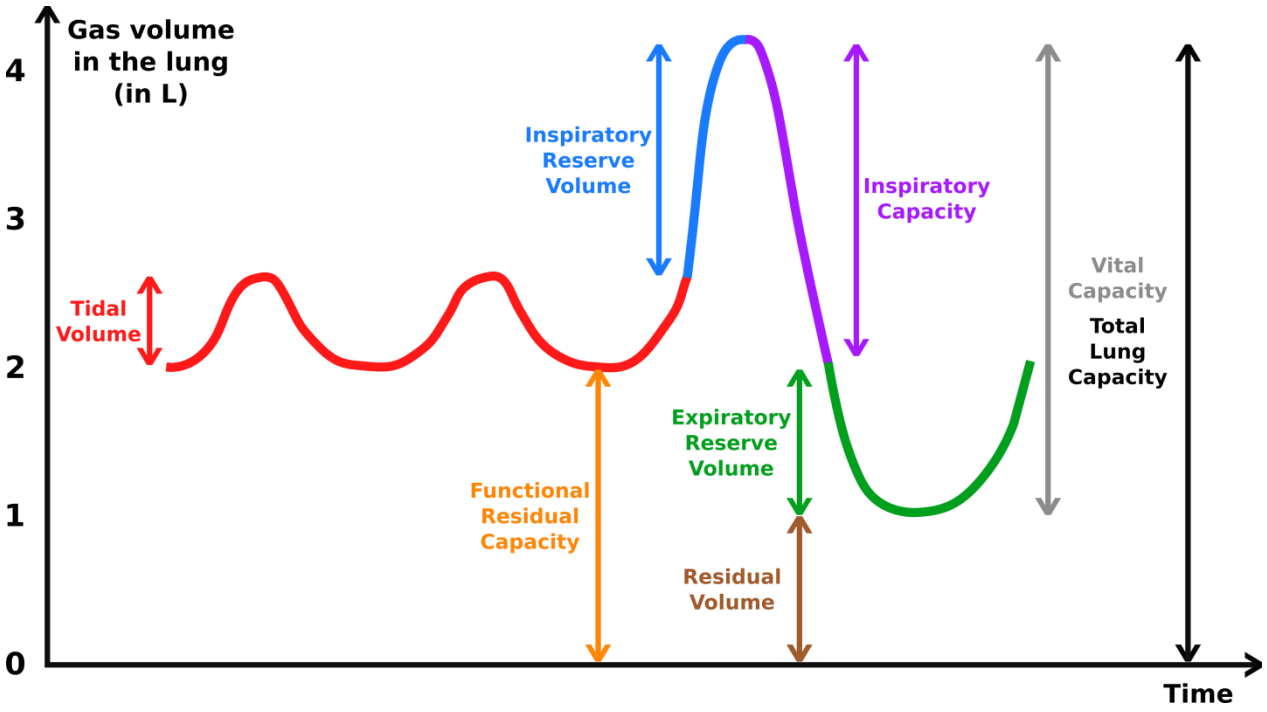

Figure 1.2: Chronogram of pulmonary respiration for nominal breathing over tidal volumes (red) with functional residual capacity and full breathing with additional inspiratory reserve volume (blue), inspiratory capacity (purple), expiratory reserve volume (green) and residual volume (brown).

Here is a presentation of the phenomena underlying the mains steps of a respiratory cycle:

- During an inspiration, a volume of air goes from the environment to the inside of the lung. This process is enabled by the increase of the thorax size in different directions. The principal increase direction occurs in the superior-inferior direction thanks to the contraction of the diaphragm: when this muscle of respiration contracts, the lung is pulled caudally and the organs present inside the abdomen are pushed toward the feet. The second diameter increase can be observed in the anterior-posterior direction because of the contraction of external intercostal muscles, in particular in the case of a deep inspiration: when these muscles contract, the rib cage is pulled upwards, which increases the distance between the spine and the sternum. Those two effects induce a depression inside the lung with respect to the environment, which makes the air go inside the lung through the mouth or the nose. It has been shown that lung alveolar walls are covered by a surfactant fluid, called pulmonary surfactant, which decreases the surface tension of alveoli, making easier for the lung to inflate and helping for the homogeneity of this inflation in all parts of the lung[2] [3]. Because of the action of these different muscles, the inspiration process is said to be active. In the case of a normal inspiration, the volume of air going inside the lung, called the tidal volume (see **Figure 1.2**, in red), is around 0.5 L, making the total volume of air inside the lung varying approximatively from 2 to 2.5 L. In the case of a very deep inspiration, other muscles, called 'accessory muscles of respiration', essentially in the neck and around the thoracic cage, are contracted. In the case of a full forced inspiration,

[2] R. J. King, "Pulmonary Surfactant," *Journal of Applied Physiology* 53, no. 1 (July 1, 1982): 1–8, https://doi.org/10.1152/jappl.1982.53.1.1.

[3] Melissa L. Siew et al., "Surfactant Increases the Uniformity of Lung Aeration at Birth in Ventilated Preterm Rabbits," *Pediatric Research* 70, no. 1 (July 2011): 50–55, https://doi.org/10.1203/PDR.0b013e31821be094.

the total gas volume inside the lung, called the total lung capacity (see **Figure 1.2**, in black), is usually comprised between 4 and 6 L.

- At the end of the inspiration, the gas inside the alveoli is a mixture of the air inhaled during this last inspiration and the air inhaled during previous ones. Once the alveoli are inflated, the gas exchanges are passively performed thanks to gas diffusion through which equilibrium is found to equalize the partial pressures of dioxygen and carbon dioxide between the alveoli and the blood capillaries surrounding the alveoli. The partial pressure of dioxygen being higher in the alveolus compared to the capillary, a global flow of dioxygen is observed from the alveolus to the capillary. To the contrary, because the partial pressure of carbon dioxide is higher in the capillary compared to the alveolus, a global flow of carbon dioxide is observed from the capillary to the alveolus. When the partial pressures of gas are equal between the two sides of the alveolus wall, the diffusion process is still ongoing at the same exchange rate but the different partial pressures do not change anymore: the equilibrium state is reached. In practice, 0.25 s of contact between the air inside the alveolus and the blood inside the capillary is needed to reach this equilibrium state at each respiratory cycle in the human lung. The physical proximity of both healthy alveoli and bold capillaries is needed for this gas exchange and is usually referred as ventilation-perfusion, or V/Q, matching[4].

- The expiration process, in the case of a healthy human subject spontaneously breathing, is a passive phenomenon. At the end of inspiration, the whole thorax is set in a state out of the mechanical equilibrium: the lung is mechanically stressed, the rib cage was moved cranially and the organs located below the lung (liver, spleen, …) are compressed. This state out of the mechanical equilibrium can be held by keeping the different muscles for the respiration, principally the diaphragm and the external intercostal muscles, activated. In this situation, an apnea or breathhold is performed. If their contraction is released, we observe passive elastic recoil from the different elements of the thorax: from the lung, because of its own elasticity, but also from the thoracic cage and the organs located caudally to the lung (liver, spleen, …). It involves an increased pressure inside the lung compared to the environment, which makes the deoxygenated and carbonated gas going outside of the lung. Thanks to the presence of pulmonary surfactant, alveoli are not collapsing at the end of the expiration process. Nevertheless, the expiration process can become an active process, in the case of some diseases or if the subject decides to control it, for example in the case of a forced exhalation. In this case, several other abdominal muscles and internal intercostal muscles are contracted, which cranially pushes the organs located below the lung and increases the pressure inside its entire parenchyma. Because of this pressure increase, the air goes outside of the lung. It needs to be noted that even at the very end of a total forced expiration process, some gas remains inside the lung: this volume of air is called the residual volume (see **Figure 1.2**, in brown), and is approximatively equal to 1 liter.

In the case of a healthy human subject freely breathing, the respiratory cycles are performed spontaneously by the subject. The rhythm and amplitude of the cycles are controlled by the brainstem and the regulation is performed essentially from a measure of the partial pressure of carbon dioxide in the blood thanks to chemoreceptors located in the aortic arch, in the carotids and in the medulla oblongata[5]. The rhythm and amplitude of breathing can also be

[4] SK Jindal Gupta PS Shankar, Suhail Raoof, Dheeraj, *Textbook of Pulmonary and Critical Care Medicine Vols 1 and 2* (Jaypee Brothers Publishers, 2011).

[5] Patrice G. Guyenet, "Regulation of Breathing and Autonomic Outflows by Chemoreceptors," in *Comprehensive Physiology* (American Cancer Society, 2014), 1511–62, https://doi.org/10.1002/cphy.c140004.

affected by efforts and emotions[6]. Usually, in the case of a healthy human subject freely breathing, the time spent with lungs deflated is longer than the one with the lung inflated[7].

The human lung plays also support and/or secondary roles. The most important one is surely the protection of the organism from the infection due to the inhalation of dust particles and microorganisms, like bacteria for example. The protection is ensured mainly through the mucociliary clearance[8]: the surface of the lung airways is covered by cilia carrying mucus and animated by a synchronic beating. The mucus is able to catch the intrusive particles or microorganisms and the coordinated beating of cilia sets them into motion from the lung to the mouth of the subject, where they can be either expectorated or swallowed and eliminated through the gastric process. Additionally, the secretion of other protective molecules and the presence of immune cells at the surface of the airway walls contribute to the protection of the lung[9]. As a remark, because of the decrease in size of these airways at each successive generation of bronchi and bronchioles, particles and microorganism cannot reach the alveoli if they are not small enough[10]. Finally, lung plays many other roles important for the global organism function (regulation of the blood pressure[11], speech[12], …).

One or several of these vital lung functions can be affected in the case of a patient suffering from a lung disease.

3. THE MAIN RESPIRATORY DISEASES IN HUMAN

Human lung can be affected by numerous illnesses that are not specific to the lung (cancer, idiopathic fibrosis, sarcoidosis, embolism, edema, …). Moreover, the lung function can be altered by causes that do not affect the lung itself directly (obesity, scoliosis, muscular and/or nervous diseases, …). For that reason, it can be difficult to give an overview of the pathology of the lung structure and/or function. One possibility is to classify them in groups depending on the part of the lung that is affected (upper airways, bronchi, bronchioles, alveoli, pleura, …). We can also consider their main cause (smoking, air pollution, hygiene, …). Here, I decided to focus only on respiratory diseases, which directly affect lung function in terms of gas exchange. These diseases can be classified into three classes: obstructive, restrictive and mixed lung diseases. The study of these diseases is called pulmonology.

[6] Frans A. Boiten, Nico H. Frijda, and Cornelis J. E. Wientjes, "Emotions and Respiratory Patterns: Review and Critical Analysis," *International Journal of Psychophysiology* 17, no. 2 (July 1, 1994): 103–28, https://doi.org/10.1016/0167-8760(94)90027-2.

[7] Martin J. Tobin et al., "Breathing Patterns: 1. Normal Subjects," *CHEST* 84, no. 2 (August 1, 1983): 202–5, https://doi.org/10.1016/S0012-3692(15)33498-X.

[8] "Mucociliary Clearance in the Airways. | American Journal of Respiratory and Critical Care Medicine," accessed January 3, 2019, https://www.atsjournals.org/doi/abs/10.1164/ajrccm.154.6.8970383?journalCode=ajrccm.

[9] L. P. Nicod, "Lung Defences: An Overview," *European Respiratory Review* 14, no. 95 (December 1, 2005): 45–50, https://doi.org/10.1183/09059180.05.00009501.

[10] G Oberdörster, J Ferin, and B E Lehnert, "Correlation between Particle Size, in Vivo Particle Persistence, and Lung Injury.," *Environmental Health Perspectives* 102, no. Suppl 5 (October 1994): 173–79.

[11] Walter F. Boron and Emile L. Boulpaep, *Medical Physiology, 2e Updated Edition E-Book: With STUDENT CONSULT Online Access* (Elsevier Health Sciences, 2012).

[12] Hixon Thomas J., Goldman Michael D., and Mead Jere, "Kinematics of the Chest Wall during Speech Production: Volume Displacements of the Rib Cage, Abdomen, and Lung," *Journal of Speech and Hearing Research* 16, no. 1 (March 1, 1973): 78–115, https://doi.org/10.1044/jshr.1601.78.

Obstructive lung diseases are characterized by an obstruction of the lung airways. It can affect bronchi, bronchioles or even alveoli. Here is a list of the principal pathologies referred as obstructive lung diseases:

- **Asthma**[13]**:** This pathology is characterized by the hyperresponsivity of lung airways. For that reason, the airways suffer from inflammation and produce an important quantity of mucus. Moreover, we observe a hyperplasia and a constriction of the smooth muscles in the airway walls. All those phenomena produce a narrowing of the airways, making the breathing work difficult.

- **Chronic bronchitis**[14]**:** This pathology is characterized by an inflammation of the bronchi and an hyper-secretion of mucus, that tends to obstruct the lung airways. The equivalent pathology for bronchioles is called bronchiolitis.

- **Bronchiectasis**[15]**:** This irreversible disease is characterized by a permanent dilatation of the bronchi. Its direct effect is the narrowing of the lung airways.

- **Pulmonary emphysema**[16]**:** This pathology is characterized by a destruction of the alveoli walls. Because of related loss of lung elasticity, the direct consequence for surrounding alveoli is a decreased expansion leading to a reduced local ventilation. If the emphysema is severe, it can also decrease importantly the gas exchange surface of the lung, making the gas exchange function more difficult to perform.

Chronic bronchitis and pulmonary emphysema are parts of the same group of illnesses called COPD, for Chronic Obstructive Pulmonary Disease[17]. Patients affected by this category of diseases can suffer both from chronic bronchitis and emphysema. Asthma is differentiated from COPD essentially because of its reversibility, even if COPD can sometimes show signs of reversibility.

Restrictive lung diseases[18] are characterized by a restriction of lung expansion, leading most importantly to lung volumes that are reduced during inspiration. This category of respiratory defects can be related to various organs and parts of the body. For example:

- It can be related to a degradation of thoracic or muscular walls or environment, for example in the case of scoliosis, obesity or myopathy.

- It can be related to the affection of the lung parenchyma, for example in the case of radiation-induced or idiopathic lung fibrosis, benign or malignant tumor or lesion in the lung parenchyma or lung sarcoidosis.

---

[13] Peter J. Barnes, "Asthma Mechanisms," *Medicine* 44, no. 5 (May 1, 2016): 265–70, https://doi.org/10.1016/j.mpmed.2016.02.020.

[14] Victor Kim and Gerard J. Criner, "The Chronic Bronchitis Phenotype in COPD: Features and Implications," *Current Opinion in Pulmonary Medicine* 21, no. 2 (March 2015): 133–41, https://doi.org/10.1097/MCP.0000000000000145.

[15] Angeline Lazarus, Janet Myers, and Gregory Fuhrer, "Bronchiectasis in Adults: A Review," *Postgraduate Medicine* 120, no. 3 (January 1, 2008): 113–21, https://doi.org/10.3810/pgm.2008.09.1912.

[16] Masashi Takahashi et al., "Imaging of Pulmonary Emphysema: A Pictorial Review," *International Journal of Chronic Obstructive Pulmonary Disease* 3, no. 2 (June 2008): 193–204.

[17] Peter J. Barnes et al., "Chronic Obstructive Pulmonary Disease," *Nature Reviews Disease Primers* 1 (December 3, 2015): 15076, https://doi.org/10.1038/nrdp.2015.76.

[18] Nina Saxena, "Restrictive Lung Disease," in *The Perioperative Medicine Consult Handbook*, ed. Molly Blackley Jackson, Somnath Mookherjee, and Nason P. Hamlin (Cham: Springer International Publishing, 2015), 199–202, https://doi.org/10.1007/978-3-319-09366-6_32.

- Finally, it can be related to a nervous system affection, for example in the case of respiratory defects caused by Parkinson's disease, multiple sclerosis or poliomyelitis.

Mixed lung diseases share the characteristics of obstructive and restrictive lung diseases. Hence, we observe both an obstruction of lung airways and a decrease in lung expansion. It can be related to a combination of several pathologies, for example, a chronic bronchitis (obstructive lung disease) for a patient affected by scoliosis (restrictive lung disease).

Many diagnosis techniques are used today in clinical routine to assess the quality of lung function and characterize a possible lung disease.

4. PULMONARY FUNCTION TESTS AND OTHER STANDARD PULMONOLOGY EXAMS IN CLINICAL ROUTINE

As explained previously in this chapter, normal lung function supports several distinct but simultaneous processes, which are to occur during breathing:

- providing dioxygen to the organs of the body and evacuating the carbon dioxide they produce in the environment, the first required step is a flow of gas inflating and deflating the different regions of the lung. This gas circulation process is referred to as ventilation.

- the exchange of dioxygen and carbon dioxide between gas and blood is made through a diffusion process through the alveolar-capillary membrane. This process is referred to as gas transfer.

- the blood newly enriched in dioxygen needs to be evacuated from the lung in order to let inflowing blood rich in carbon dioxide perform gas exchange too. This results in the circulation of blood in the lung, which is referred to as perfusion.

Those three processes are needed for a healthy function of the lung, and are generally fulfilled in the whole volume of the organ. If one of those three processes is deficient in one given region of the lung, global lung function can be partly altered. From this point of view, it can be deduced that the evaluation of one of those three processes (lung ventilation, gas transfer and blood perfusion around the alveoli) can help characterizing lung function, and therefore on the pathophysiological state of the organ. Complete information on lung function and pathology can be obtained by studying those three processes with spatial sensitivity, in order to discriminate between different regions of the lung.

To evaluate the pulmonary function and to diagnose the pathophysiological state of the lung in humans, various procedures and techniques are used today in clinical routine by pulmonologists and practitioners. The aim of these techniques is to measure physical parameters able to characterize lung function, either globally or locally, and either related to lung ventilation, gas transfer, or perfusion. In the following, we will study the global and the local methods and see what each of them measure.

4.1. GLOBAL MEASUREMENTS OF LUNG FUNCTION

As far as the global methods are concerned, the most important techniques used in clinical routine are gathered under the name 'respiratory function testing'. This family of techniques aims at measuring lung volumes (tidal volume, inspiratory reserve volume, expiratory reserve volume and residual volume, see **Figure 1.2**), lung capacities (total lung capacity, inspiratory capacity, functional residual capacity, and vital capacity, see **Figure 1.2**), inspiratory

and expiratory air flows and pressures, and also the global quality of gas exchange and blood composition. In these techniques, the three processes that characterize lung function are tested within the entire organ.

4.1.1. MEASUREMENT OF RECRUITABLE LUNG VOLUMES

A spirometer is a system able to measure inspiratory and expiratory gas volumes, gas flows and therefore recruitable lung volumes beyond the residual volume[19]. It is usually composed of a disposable mouthpiece and a measurement station. In a standard spirometry procedure, the patient holds the mouthpiece with his lips and freely breathes through it. After several respiratory cycles of free breathing permitting to measure the tidal volume, the patient is asked to inhale as deeply as he can and to blow the gas out of his lung as fast as possible. The result can be represented as a volume-time curve (representing the gas volume as a function of time) and/or, more commonly, as a flow-volume loop (representing the gas flow, which is the first time derivative of gas volume, as a function of gas volume during the forced respiratory cycle). The shape of this loop gives information about an eventual decrease in air flow during forced expiration, often explained by an obstructive lung disease, and/or a decrease in lung volumes and capacities, often explained by a restrictive lung disease (see **Figure 1.3**). Just by analyzing the global shape of this flow-volume loop, the pulmonologist is able to evaluate the global pathophysiological state of the lung in terms of ventilation.

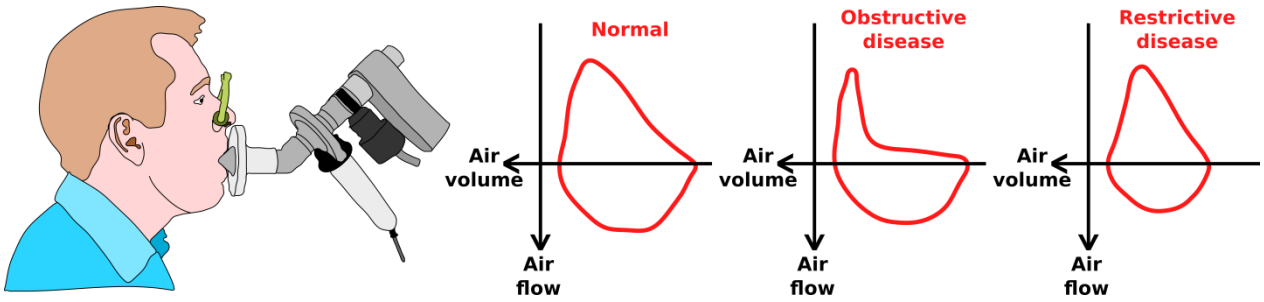

Figure 1.3: Illustration of a spirometry exam and presentation of the shape of the flow-volume loop for two common types of lung diseases.

From a more quantitative point of view, several indices can be calculated from this flow-volume loop and can be used for disease diagnosis and staging:

- The Tiffeneau-Pinelli index, which is the Forced Expiratory Volume in one second divided by the Forced Vital Capacity (FEV1/FVC). This index is decreased in patients suffering from obstructive lung diseases in comparison to normal subjects. In patients suffering from restrictive lung diseases, it remains normal or increases sometimes.

- The Forced Expiratory Flows (FEF) and Forced Inspiratory Flows (FIF) at different fractions of the forced vital capacity (often 25%, 50% and 75% of FVC).

- The Peak Expiratory Flow (PEF), which is the maximal air flow measured during the forced expiration period.

[19] M. R. Miller et al., "Standardisation of Spirometry," *European Respiratory Journal* 26, no. 2 (August 1, 2005): 319–38, https://doi.org/10.1183/09031936.05.00034805.

To increase its robustness, this procedure is often repeated several times. Spirometry can also be performed under other conditions: after the administration of a bronchodilator (to test the reversibility of an obstructive disease), during or after a physical effort (to study the alteration of effort dependent indexes measured with spirometry), after the administration of a pharmacological or a physical stress (called bronchial provocation testing, to evaluate an eventual hyperresponsivity of the lung) or after the administration of a treatment (corticoids, for example, to challenge the therapeutical action). Moreover, if spirometry measurements are associated to pressure measurement thanks to the use of a pressure transducer, the change in lung volume can be represented as a function of the pressure at the mouth and the lung compliance can be measured by estimating the slope of this curve[20]. Finally, this type of measurement can also be performed under a mechanical excitation produced by an oscillatory pressure signal to obtain information on both lung compliance and reactance through techniques known as forced oscillation techniques (FOT)[21]. The latter provides information that is directly related to lung mechanical properties and will be studied in details in the last chapter of this manuscript.

4.1.2. MEASUREMENT OF NON-RECRUITABLE LUNG VOLUMES

To measure non-recruitable lung volumes (residual volume, functional residual capacity and total lung capacity, see **Figure 1.2**), several techniques can be implemented[22]. A first technique is called plethysmography and is based on the measurement of volume and pressure changes in a sealed chamber as the patient breathes through a mouthpiece. The measurement of the lung volumes is based on Boyle's law (pressure × volume = constant for a given amount of gas at a given temperature). A second technique is called helium dilution technique, and is based on the measurement of the concentration of helium in a mixture made of oxygen and helium. As the patient is breathing the mixture, because the lung contains no helium at the beginning of the experiment and because the total amount of helium involved in the experiment is known, a lung volume that takes into account the residual volume can be estimated. Another technique, called nitrogen washout, is able to measure the anatomic dead spaces in the lung (spaces occupied by trachea, bronchi and bronchioles, which do not participate in the gas exchange) by making the patient breathing pure dioxygen and measuring along the respiratory cycles the quantity of nitrogen leaving the lung. Finally, lung volumes can also be assessed by medical imaging, and in particular X-ray imaging. Once again, those measurements of lung volumes and gas flows are only sensitive to ventilation, but neither to gas transfer nor blood perfusion in the lung parenchyma.

4.1.3. OTHER GLOBAL MEASUREMENT OF LUNG FUNCTION PROCESSES

Other global measurement techniques are also performed in clinical routine to assess the other processes involved in the lung function. For example, by measuring the diffusing capacity of carbon monoxide (DLCO) during a single inspiration-breath hold-expiration cycle of a known quantity of carbon monoxide, it is possible to evaluate the permeability of the alveolar wall to the gas exchange by measuring the partial pressures of CO before and after the cycle[23]. Moreover, arterial blood gas composition can be explored by sampling and analyzing a small quantity of blood to evaluate the global quality of gas exchanges for a given patient. Analyzes of bronchoalveolar lavage fluids

[20] Eduardo Salazar and John H. Knowles, "An Analysis of Pressure-Volume Characteristics of the Lungs," *Journal of Applied Physiology* 19, no. 1 (January 1, 1964): 97–104, https://doi.org/10.1152/jappl.1964.19.1.97.

[21] Bill Brashier and Sundeep Salvi, "Measuring Lung Function Using Sound Waves: Role of the Forced Oscillation Technique and Impulse Oscillometry System," *Breathe* 11, no. 1 (March 1, 2015): 57–65, https://doi.org/10.1183/20734735.020514.

[22] J. Wanger et al., "Standardisation of the Measurement of Lung Volumes," *European Respiratory Journal* 26, no. 3 (September 1, 2005): 511–22, https://doi.org/10.1183/09031936.05.00035005.

[23] J. M. B. Hughes and D. V. Bates, "Historical Review: The Carbon Monoxide Diffusing Capacity (DlCO) and Its Membrane (Dm) and Red Cell (Θ·Vc) Components," *Respiratory Physiology & Neurobiology* 138, no. 2 (November 14, 2003): 115–42, https://doi.org/10.1016/j.resp.2003.08.004.

and lung biopsy samples can also be performed to obtain more detailed information about a given pathology. Finally, polysomnography[24] consists in performing a great number of various measurements (ECG, EEG, lung air flow measurement, …) as the patient is sleeping in order to detect and characterize respiratory tract related sleep disorders, for example sleep apnea. Those last techniques are more specific to a given category of pathologies and go beyond our analysis in terms of ventilation, gas transfer and perfusion.

4.2. LOCAL MEASUREMENTS OF LUNG FUNCTION

The different techniques presented in 4.1 have great advantages: they are robust, often simple and available in clinical routine. However, they all show an important drawback: they only give a global estimation of lung function, in the sense that they are not sensitive to the spatial location of any lung defect. These techniques are not even able to distinguish between left and right lung function. Because many lung diseases affect specific regions of the lung (as pulmonary embolism, emphysema or lung cancer, for example), it seems worthwhile to develop new techniques that would be sensitive to lung function defects in terms of ventilation, gas transfer, and perfusion, but also to the location of the diseased regions inside the organ. This possibility would give more sensitive measurements (because they would average the measurement on smaller regions of the lung, and not on the entire organ), would make possible the detection and characterization of several types of pathologies or diseased regions at the same time and would inform on the location and extent of diseases in the perspective of a targeted therapy, for example.

As far as local methods are concerned, they are all based on medical imaging[25]. From a general point of view, medical imaging can be considered as the spatially localized measurement of a physical or a pathophysiological parameter. This physical parameter can be an intensity of X-rays attenuated by the patient's body, as it is done in conventional radiography. From this type of measurement, a linear attenuation coefficient of biological tissues can be estimated for X-rays, as it is done in Computed Tomography (CT). If an exogenous radioactive tracer is injected in the patient and is able to radiate gamma rays directly or indirectly, the concentration of this tracer can be estimated from the intensity of the emitted gamma rays, as it is done in scintigraphy, Single Photon Emission Computed Tomography (SPECT) or in Positron Emission Tomography (PET). Other physical phenomena, as the reflection of ultrasound waves in echography or the production of nuclear magnetic resonance electromagnetic waves in Magnetic Resonance Imaging (MRI), as seen previously, can be measured and localized in space to produce medical images. An optical probe can even be inserted in a natural cavity of the patient to observe directly the light reflected and diffused by the surface of an organ: this is the principle of endoscopy.

4.2.1. STRUCTURAL IMAGING OF THE LUNG

Today, in clinical routine, the main medical imaging techniques performed to establish a lung diagnosis are conventional radiography, CT, scintigraphy, SPECT, PET and bronchoscopy (endoscopy inside the first generations of bronchi, up to several millimeters in diameter). Conventional X-ray radiography can be used to observe the walls and heterogeneous structures of organs inside the thorax as 2-dimensional projection images. The measurement relies on the differences in density between neighbor organs and structures. Moreover, this technique can be useful to characterize pneumonia, emphysema and different types of lesions. CT gives anatomical images of the lung comparable to the ones obtained in conventional radiography but with the advantage to discriminate the

[24] Konrad E. Bloch, "Polysomnography: A Systematic Review," *Technology and Health Care* 5, no. 4 (January 1, 1997): 285–305.
[25] Jerrold T. Bushberg and John M. Boone, *The Essential Physics of Medical Imaging* (Lippincott Williams & Wilkins, 2011).

measurement along the third dimension of space by exploiting the image acquisition and reconstruction principles of tomography. This makes the detection of lesions or diseased tissues easier, and often more precise and more sensitive. Scintigraphy is able to give, on a bi-dimensional image, the location and the importance of the tissue uptake of a given radiopharmaceutical tracer. SPECT and PET are able to give similar results but in 3D by exploiting the principles of tomographic reconstruction. The information obtained will depend on the injected tracer and its administration method. For example, information about lung cell metabolism can be obtained during a ^{18}F-FDG PET exam. This information is valuable in the case of cancer diagnosis and therapy follow-up[26]. Finally, during a bronchoscopy exam, a bronchoscope is introduced in the lung airways through the patient's mouth or nose to visualize the surface of those airways. This procedure can be valuable to detect in real-time small bleedings, cancer lesions[27] or inflammation, for example.

4.2.2. FUNCTIONAL IMAGING OF THE LUNG

The possibilities offered by medical imaging are wide and it would be difficult to detail all the possibilities offered by this family of techniques in the field of ventilation, gas transfer and perfusion assessment in the lung. As a summary, every imaging method sensitive to any of the three functional processes presented at the beginning of this subsection, but also to other abnormal characteristics in the lung (presence of a lesion, abnormal metabolism, abnormal tissue texture, …) is valuable for the evaluation of the pathophysiological state of the lung.

Ventilation-perfusion ratio is efficiently mapped by V/Q scintigraphy[28] or V/Q SPECT[29] [30]. These two techniques will be introduced together as SPECT is the 3D extension of scintigraphy, and is thus based on the same physical phenomena and acquisition method. V/Q stands for Ventilation/Perfusion ratio, with the lung ventilation expressed in liters of gas per minute, and being globally around 4 L/min in healthy adults at rest for the entire lung, and the perfusion expressed in liters of blood per minute, and being globally around 5 L/min in healthy adults at rest for the entire lung. This V/Q ratio is therefore a dimensionless quantity reaching a global mean value around 0.8 in healthy adults at rest, and represents the ideal situation of global V/Q matching: ventilation and perfusion are globally adapted to each other, which enables the optimal gas exchange.

In a V/Q scintigraphy or SPECT exam, the ventilation maps result from the administration of an aerosol of radionuclides (based on Tc99m, for example), which get distributed throughout the airways, whereas the perfusion maps result from an intravenous injection of a radionuclide, which remains in the vascular system. Both ventilation and perfusion images are obtained with one (scintigraphy) or multiple (SPECT) projections images acquired thanks to a gamma camera. The comparison of both images and even the calculation of a V/Q map can be performed to obtain a global analysis of the ventilation-perfusion matching quality in a given patient (see **Figure 1.4**).

---

[26] James W. Fletcher et al., *Recommendations on the Use of 18F-FDG PET in Oncology*, n.d.

[27] Timothy C. Kennedy, Stephen Lam, and Fred R. Hirsch, "Review of Recent Advances in Fluorescence Bronchoscopy in Early Localization of Central Airway Lung Cancer," *The Oncologist* 6, no. 3 (January 6, 2001): 257–62, https://doi.org/10.1634/theoncologist.6-3-257.

[28] "Value of the Ventilation/Perfusion Scan in Acute Pulmonary Embolism: Results of the Prospective Investigation of Pulmonary Embolism Diagnosis (PIOPED)," *JAMA* 263, no. 20 (May 23, 1990): 2753–59, https://doi.org/10.1001/jama.1990.03440200057023.

[29] Patrick Reinartz et al., "Tomographic Imaging in the Diagnosis of Pulmonary Embolism: A Comparison Between V/Q Lung Scintigraphy in SPECT Technique and Multislice Spiral CT," *Journal of Nuclear Medicine* 45, no. 9 (January 9, 2004): 1501–8.

[30] Gregory G. King, Benjamin Harris, and Sriram Mahadev, "V/Q SPECT: Utility for Investigation of Pulmonary Physiology," *Seminars in Nuclear Medicine*, SPECT V/Q Imaging of the Lungs, 40, no. 6 (November 1, 2010): 467–73, https://doi.org/10.1053/j.semnuclmed.2010.07.006.

V/Q is usually not uniform throughout the lung. When regionally measured and calculated through local air volume per minute and local blood volume per minute, the local V/Q matching can be more or less optimal with respect to the lung regions. In particular, for a healthy human in upright position, ventilation and perfusion are known to reach higher values close to the base of the lung in comparison to the apex, essentially because of gravity. Concerning ventilation, the basal region is more subject to gravity than the apical region (and is therefore called the dependent region in upright position), which makes this former region more easily distensible than the latter. Basal regions therefore ventilates more efficiently than apical ones, as explained and demonstrated by Bryan *et al.*[31]. Concerning perfusion and because of gravity, it is more difficult for the blood to reach regions located above the heart than below in upright position[32] [33]. Because perfusion is more sensitive to gravity than ventilation, this leads to higher apical V/Q ratio compared to basal V/Q ratio in upright position in general[34] [35]. More recent studies however mitigate the role of gravity in the distribution of ventilation and perfusion in the lung, in particular for positions other than upright and by looking at the heterogeneity at smaller spatial scales[36] [37] [38] [39].

The V/Q ratio can also vary locally throughout the lung because of regional anatomical particularities and also because of lung disease. In the two extreme cases[40], first, if a given region is perfused but not ventilated (because of chronic bronchitis or asthma, for example), its V/Q is close to 0 and the region is called a blood shunt. Inversely, second, if a given region is ventilated but not perfused (because of pulmonary embolism or emphysema, for example), its V/Q becomes very high and the region is called an alveolar dead space (as it does not contribute to the gas transfer, like the previously described anatomic dead space that was referring to the volume occupied by the conducting airways). In all the intermediate situations between those two extreme cases, and for V/Q values that are shifted from the normal value obtained for a given region, we talk about V/Q mismatch or V/Q defect. This V/Q mismatch is therefore a good indicator of the functional and pathophysiological state of the lung. Nevertheless, as it was defined, V/Q does not take into account the gas diffusion process through the alveolus-

[31] A C Bryan, J Milic-Emili, and D Pengelly, "Effect of Gravity on the Distribution of Pulmonary Ventilation.," *Journal of Applied Physiology* 21, no. 3 (May 1, 1966): 778–84, https://doi.org/10.1152/jappl.1966.21.3.778.

[32] N R Anthonisen and J Milic-Emili, "Distribution of Pulmonary Perfusion in Erect Man.," *Journal of Applied Physiology* 21, no. 3 (May 1, 1966): 760–66, https://doi.org/10.1152/jappl.1966.21.3.760.

[33] Klaus W. Stock et al., "Demonstration of Gravity-Dependent Lung Perfusion with Contrast-Enhanced Magnetic Resonance Imaging," *Journal of Magnetic Resonance Imaging* 9, no. 4 (1999): 557–61, https://doi.org/10.1002/(SICI)1522-2586(199904)9:4<557::AID-JMRI8>3.0.CO;2-Y.

[34] C. J. Martin and A. C. Young, "Ventilation-Perfusion Variations Within the Lung," *Journal of Applied Physiology* 11, no. 3 (November 1, 1957): 371–76, https://doi.org/10.1152/jappl.1957.11.3.371.

[35] J. B. West and C. T. Dollery, "Distribution of Blood Flow and Ventilation-Perfusion Ratio in the Lung, Measured with Radioactive CO2," *Journal of Applied Physiology* 15, no. 3 (May 1, 1960): 405–10, https://doi.org/10.1152/jappl.1960.15.3.405.

[36] T. S. Hakim, R. Lisbona, and G. W. Dean, "Gravity-Independent Inequality in Pulmonary Blood Flow in Humans," *Journal of Applied Physiology* 63, no. 3 (September 1, 1987): 1114–21, https://doi.org/10.1152/jappl.1987.63.3.1114.

[37] R. W. Glenny et al., "Gravity Is a Minor Determinant of Pulmonary Blood Flow Distribution," *Journal of Applied Physiology* 71, no. 2 (August 1, 1991): 620–29, https://doi.org/10.1152/jappl.1991.71.2.620.

[38] Robb W. Glenny et al., "Gravity Is an Important but Secondary Determinant of Regional Pulmonary Blood Flow in Upright Primates," *Journal of Applied Physiology* 86, no. 2 (February 1, 1999): 623–32, https://doi.org/10.1152/jappl.1999.86.2.623.

[39] I. Galvin, G. B. Drummond, and M. Nirmalan, "Distribution of Blood Flow and Ventilation in the Lung: Gravity Is Not the Only Factor," *BJA: British Journal of Anaesthesia* 98, no. 4 (April 1, 2007): 420–28, https://doi.org/10.1093/bja/aem036.

[40] P. D. Wagner, H. A. Saltzman, and J. B. West, "Measurement of Continuous Distributions of Ventilation-Perfusion Ratios: Theory," *Journal of Applied Physiology* 36, no. 5 (May 1, 1974): 588–99, https://doi.org/10.1152/jappl.1974.36.5.588.

capillary membrane and thus the possibility to effectively perform gas exchange. Moreover, in the case of both abnormally low ventilation and perfusion in a given lung region, normal V/Q values can be reached thanks to the compensation between the two physical quantities, which necessitates to evaluate ventilation and perfusion values separately too.

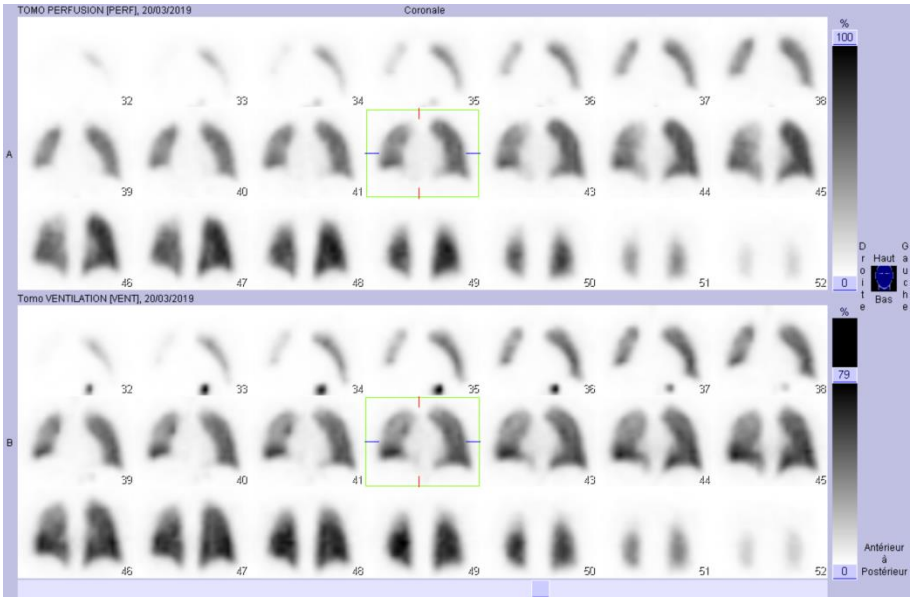

Figure 1.4: Typical V/Q maps of a standard clinical V/Q SPECT exam. The coronal perfusion images are represented in the top part of the figure and the corresponding ventilation images are represented in the bottom part. Note the greyscales on the right putting in evidence the mean V/Q around 0.8 (79% for ventilation and 100% for perfusion). Note also the black spot observed on several views of the ventilation maps. It corresponds to radioactive gas that entered inside the stomach of the patient during gas inhalation. This V/Q SPECT exam was recently performed at Service Hospitalier Frédéric Joliot (SHFJ), Orsay, France.

5. THE RELATIONSHIP BETWEEN LUNG MECHANICS, FUNCTION AND PATHOLOGY

Mechanics is the field of physics that studies the behavior of physical bodies when subjected to forces, in particular in terms of their displacement, deformation and interaction with their environment. In this way, lung is a very complex but rich object to study from a mechanical point of view:

- During the inspiration, the diaphragm and the thoracic cage apply forces and set boundaries to the lung, decreasing the surface force, or pressure, applied by the gas inside the lung and deforming it at different space scales as the organ inflates. For a given pressure inside the alveoli, the local tissue deformation pattern depends on the local elastic property of the lung tissue, of the thoracic cage and of the organs located caudally to the lung, but also on the opposite action of surface tension forces created by the alveoli wall but decreased thanks to the presence of pulmonary surfactant. The global effect of these elastic forces and surface tension forces gives the compliance introduced in 4.1.1. Moreover, resistance forces applied on the entering gas by the lung airways along the whole respiratory tract and the viscosity property of the lung tissue increase the mechanical work to provide in order to inflate the lung.

- During the expiration, the lung goes back to its mechanical rest state thanks to the elastic recoil of all the organs of the thorax and the abdomen, which were displaced and deformed during the inspiration

process. As it is observed during inflation, surface tension properties, airway resistance and viscosity of lung parenchyma play important roles in the time evolution of the lung's deformation field during its deflation.

As we can see, lung main function, which is the gas exchange in alveoli through cycles of lung inflation and deflation, is directly related to lung mechanics: a modification of either the elasticity or viscosity of the lung tissue and its surrounding environment, of the airway resistance or the surface tension properties of alveoli will produce direct effects on the time evolution of the deformation field of the lung parenchyma and, therefore, in its regional ventilation distribution and time evolution along the respiratory cycle.

We have seen throughout this section that most lung pathologies affect one or several of these mechanical properties of the lung. Just to remind a few examples:

- In asthma, we observe a narrowing of lung airways, which produces an increase of the resistance forces applied by the airways to the inflating and deflating air circulating in those airways.
- In emphysema, alveoli walls are locally altered, affecting directly both the elasticity and surface tension properties of lung parenchyma in the diseased regions.
- In idiopathic or radiation-related lung fibrosis, fibrous conjunctive tissue appears in the lung parenchyma, and affects directly its elasticity, making the tissue stiffer[41].
- In lung cancer, one or several soft tissue masses appear in the lung parenchyma. Those lesions usually do not share the same elasticity and viscosity compared to their surrounding lung tissue[42].

If we link these observations to what we explained just above, we observe an interesting relationship between:

- lung mechanical properties,
- lung mechanical behavior, which is a direct function of the mechanical properties,
- lung function, itself depending partly on the mechanical behavior, and on the deformation field of the lung parenchyma, in particular,
- and lung disease, that modifies lung mechanical properties, and thus its mechanical behavior and function.

For that reason, lung mechanical properties and lung mechanical behavior appear to be relevant sets of physical parameters to consider and estimate in order to probe lung function, detect pulmonary pathologies and characterize them. Lung mechanics, in terms of both mechanical properties and behavior, appears to bring a hopeful set of biomarker candidates for lung diagnosis in most of its common pathologies that are known today in human. As we will see in the next chapters, a great number of measurement techniques (spirometry, plethysmography, forced oscillations technique, …) are available in clinical routine to probe certain aspects of lung mechanics and extract information about lung function. However, because those behaviors and properties can vary throughout the lung, which can explain different pathophysiological states within the same organ (some regions of

[41] Rebecca G. Wells, "Tissue Mechanics and Fibrosis," *Biochimica et Biophysica Acta (BBA) - Molecular Basis of Disease*, Fibrosis: Translation of basic research to human disease, 1832, no. 7 (July 1, 2013): 884–90, https://doi.org/10.1016/j.bbadis.2013.02.007.

[42] Sui Huang and Donald E. Ingber, "Cell Tension, Matrix Mechanics, and Cancer Development," *Cancer Cell* 8, no. 3 (September 1, 2005): 175–76, https://doi.org/10.1016/j.ccr.2005.08.009.

the lung are affected while others are healthy), it would be important to obtain a spatial information with those potential biomarkers so as to know where they were measured, in the perspective to create a medical image spatially mapping those biomarkers.

Thanks to the spatial discretization inherent to medical imaging measurements, exploiting a modality from this family of techniques appears to be a promising strategy to probe the lung mechanics locally. In the following section, we will study the principles of one particular medical imaging modality which could be valuable to study lung mechanics at the regional scale: magnetic resonance imaging.

SECTION 2 MAGNETIC RESONANCE IMAGING

MAGNETIC RESONANCE IMAGING (MRI) IS A NMR-BASED MEDICAL IMAGING TECHNIQUE INVENTED IN 1973, WHICH UNDERWENT A VERY QUICK DEVELOPMENT OVER THE LAST 45 YEARS. MORE THAN A SIMPLE INNOCUOUS TECHNIQUE TO MAKE ANATOMICAL IMAGES WITH UNMET SOFT-TISSUE CONTRASTS WITHOUT IONIZING RADIATIONS, THE LATEST DEVELOPMENTS OF THIS MODALITY ENABLE THE ASSESSMENT OF ARTERIOVENOUS BLOOD VELOCITIES (MAGNETIC RESONANCE ANGIOGRAPHY), THE MAPPING OF WATER MOLECULES DIFFUSION COEFFICIENTS (DIFFUSION MRI), THE STUDY OF TISSUE'S BLOOD PERFUSION (PERFUSION MRI) OR AGAIN THE VISUALIZATION OF THE ACTIVATED PARTS OF THE BRAIN DURING A GIVEN ACTIVITY (BRAIN FUNCTIONAL MRI). AND THIS LIST IS NOT EXHAUSTIVE.

1. PHYSICAL PRINCIPLES OF NUCLEAR MAGNETIC RESONANCE (NMR)

1.1. THE BEHAVIOR OF AN ISOLATED SPIN IN A MAGNETIC FIELD

Every particle can be associated to a spin property, which is its intrinsic quantum angular momentum. It is characterized by the spin number, I, taking only integer or half-integer values, and is modeled by the angular momentum vector $\vec{I}$, with quantized components along any direction of space. If we measure the component I_z of $\vec{I}$ along the spatial z axis, it takes only discrete values given by $I_z = m\hbar$, where m is the magnetic quantum number of the particle, varying between $+I$ and $-I$ with integer intervals. Thus, for a particle of spin number I, we can measure $2I + 1$ possible values for I_z.

Concerning nucleons, protons and neutrons, from which atom nuclei are constituted, both are characterized by a spin number I equal to $1/2$: they are said to be of spin one-half and are called fermions. From the Pauli Exclusion Principle and the fundamental composition of nucleons, and because protons and neutrons are distinguishable particles, it can be shown that every nucleus composed of an odd number of protons and/or neutrons possesses a non-zero spin number. Water molecules in biological tissues possess two hydrogen atoms. The nucleus of an hydrogen atoms, ^{1}H, is made of one proton and zero neutron, and therefore possesses a spin one-half with $I_z = \pm \hbar/2$.

In the following, because most biological tissues are essentially made of water, and because our goal is to explain the medical application of these physical principles, we will consider only the particular case of ^{1}H Nuclear Magnetic Resonance (NMR), even if other isotopes, like ^{3}He, ^{13}C and ^{31}P, have also a non-zero spin and can lead to the same physical phenomena and NMR measurements.

We have in this case, for ^{1}H:

- A spin-up state, characterized by:

$$I_z = +\hbar/2 \quad \textbf{Eq. 1.1}$$

- A spin-down state, characterized by:

$$I_z = -\hbar/2 \quad \textbf{Eq. 1.2}$$

A magnetic dipole $\vec{\mu}$ can be associated to this spin $\vec{I}$ according to this expression:

$$\vec{\mu} = \gamma \vec{I} \quad \textbf{Eq. 1.3}$$

where γ is the gyromagnetic ratio of ^{1}H, and thus:

$$\mu_z = \gamma I_z \quad \textbf{Eq. 1.4}$$

where μ_z is the component of $\vec{\mu}$ along the z axis.

If the magnetic field of the nucleus environment is 0, the two spin states are said to be degenerated, meaning that they are characterized by the same energy. When a uniform and stationary magnetic field $\overrightarrow{B_0}$, considered to be oriented along the z axis, is applied to the ^{1}H nucleus, the degeneracy is lifted and two different energies must be considered for the two eigen quantum states described above.

As the energy of a magnetic dipole $\vec{\mu}$ in a magnetic field $\overrightarrow{B_0}$ is given by:

$$E = -\vec{\mu} \cdot \overrightarrow{B_0} \quad \textbf{Eq. 1.5}$$

we observe:

- One state of low energy E_1, for which the magnetic dipole $\vec{\mu}$ is parallel to the magnetic field $\overrightarrow{B_0}$:

$$\mu_z = +\gamma\hbar/2 \quad \textbf{Eq. 1.6}$$

- One state of high energy E_2, for which the magnetic dipole $\vec{\mu}$ is anti-parallel to the magnetic field $\overrightarrow{B_0}$:

$$\mu_z = -\gamma\hbar/2 \quad \textbf{Eq. 1.7}$$

and the energy difference between these two states is given by:

$$\Delta E = E_2 - E_1 = \gamma\hbar\left|\overrightarrow{B_0}\right| \quad \textbf{Eq. 1.8}$$

At thermal equilibrium and for a biological tissue, only a tiny difference exists between the number of spins in the parallel state and the ones in the anti-parallel state: for one million of protons, the difference between the number of protons in a parallel state and in an anti-parallel state in a magnetic field of 3 T is about 12 at room temperature. This difference is proportional to the magnetic field at low magnetic field strengths and room temperature. It is possible to change a spin in the parallel state into an anti-parallel state through an interaction between the nucleus carrying the spin and a photon of energy ΔE corresponding to the energy difference between the two spin quantum states described in **Eq. 1.1** and **Eq. 1.2**.

As the relation between the energy E_0 and the angular frequency ω_0 of a photon is given by $E_0 = \hbar\omega_0$ (Planck-Einstein relation), the resonance condition for the excitation to be performed is given by:

$$\omega_0 = \gamma\left|\overrightarrow{B_0}\right| \qquad \textbf{Eq. 1.9}$$

Moreover, in a magnetic field, the spins follow a precession motion called Larmor precession. It can be shown, by solving the equation given by the Ehrenfest theorem with the components of $\vec{\mu}$ orthogonal to $\overrightarrow{B_0}$ and the Hamiltonian for the interaction between $\vec{\mu}$ and $\overrightarrow{B_0}$, that the angular frequency of this precession is also equal to $\omega_0 = \gamma\left|\overrightarrow{B_0}\right|$.

1.2. THE BEHAVIOR OF A BIOLOGICAL TISSUE SUBJECT TO EXTERNAL MAGNETIC FIELDS

If we consider now several protons from an homogeneous biological tissue in the same magnetic field $\overrightarrow{B_0}$ and interacting with a radiofrequency (RF) electromagnetic wave (or photon flow, from a quantum mechanics point of view) tuned at Larmor frequency and characterized by the magnetic field $\overrightarrow{B_1}$ orthogonal to $\overrightarrow{B_0}$, a resonance condition is verified between the RF field and the magnetic dipoles. In this case, spins in the parallel state become able to absorb the energy of RF photons, which can be seen as an excitation of the spins in a parallel state to the anti-parallel state. However, this idea of state transition for one given spin is false from a quantum mechanics point of view. In general, the spin is set in a superposition of the two quantum states described in **Eq. 1.1** and **Eq. 1.2**. Nevertheless, this idea of transition between two quantum states, which is halfway between the classical and the quantum points of view, is often used to explain NMR phenomena.

If the tissue magnetization $\vec{M}$ is introduced, defined as the sum of all the individual $\vec{\mu}$ local magnetic moments in a localized infinitesimal volume of biological tissue divided by this given infinitesimal volume, this spin excitation phenomenon will be macroscopically characterized by:

- A decrease of the longitudinal magnetization amplitude M_z, the component of $\vec{M}$ parallel to $\overrightarrow{B_0}$ and conventionally along the z axis direction. If the RF field is applied with a strong amplitude and/or during a long period of time, an inversion of this longitudinal magnetization can occur.

- An increase of the transverse magnetization amplitude M_{xy}, the component of $\vec{M}$ perpendicular to $\overrightarrow{B_0}$ and conventionally in the (Oxy) plane. This transverse component describes a vector $\overrightarrow{M_{xy}}$, the projection of $\vec{M}$ in the (Oxy) plane, that rotates in this plane at Larmor frequency. This increase in transverse magnetization amplitude is directly related to the decrease in longitudinal magnetization amplitude explained just above: $\vec{M}$ is rotated by a given flip angle, and M_z and M_{xy} are respectively proportional to the cosine and the sine of this angle.

Thus, the interaction between a biological tissue in a magnetic field $\overrightarrow{B_0}$ and a RF electromagnetic field tuned at the Larmor frequency of the spins in the biological tissue will be characterized by a rotation of the total magnetization vector $\vec{M}$ around the time-varying RF magnetic field vector $\overrightarrow{B_1}$, resulting in a double rotation of $\vec{M}$ around $\overrightarrow{B_0}$ and $\overrightarrow{B_1}$ directions (see **Figure 1.5**).

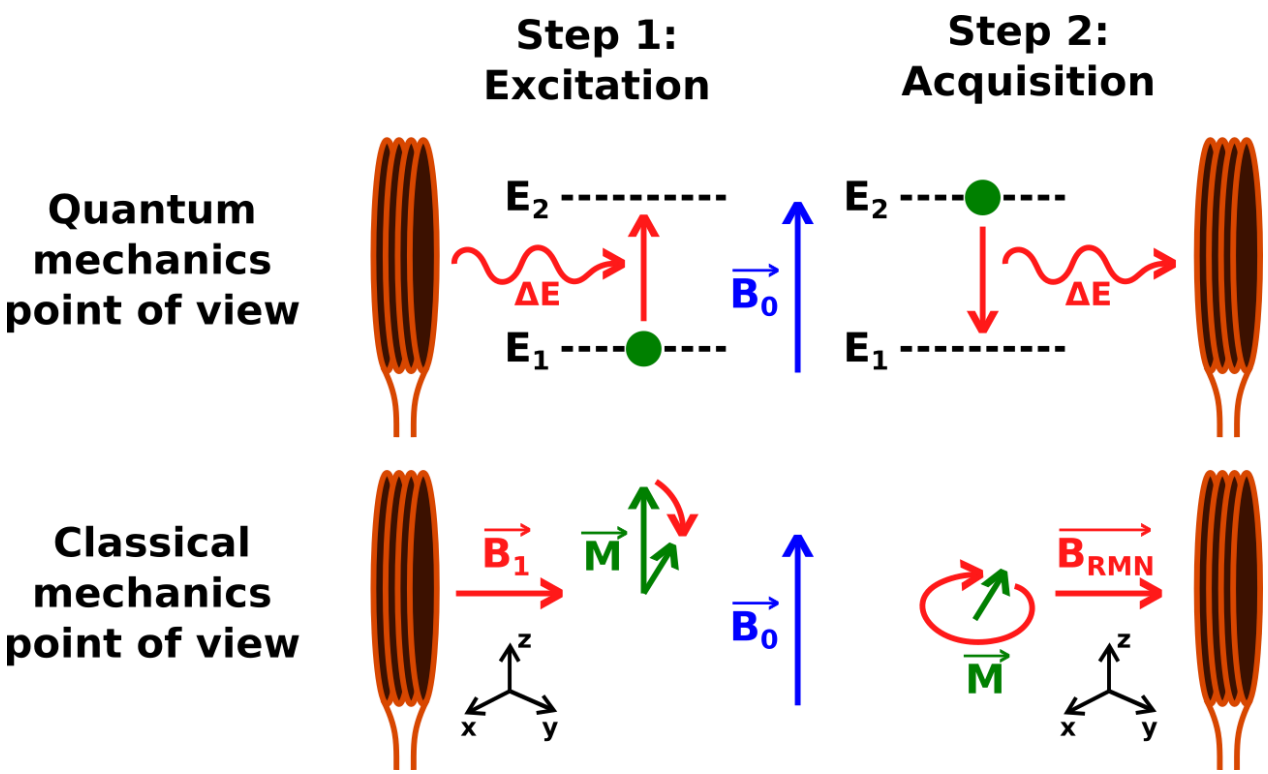

Figure 1.5: Schematic representation of the two major steps of a NMR experiment for a π/2 RF pulse, material excitation and data acquisition, from a quantum mechanics point of view and from a classical mechanics point of view.

In electromagnetism, from the classical mechanics point of view, the induction principle says that a magnetic dipole moving in space produces an electromagnetic wave. Here, because $\overrightarrow{M_{xy}}(t)$ keeps following a Larmor precession in the (Oxy) plane after the RF excitation, a RF wave at the same Larmor frequency and phase is produced and radiates from the biological tissue. At the scale of each individual spin and from a quantum mechanics point of view, after being excited, a spin in an anti-parallel state goes back to a parallel state by emitting a photon of angular frequency ω_0 and of energy $\Delta E = \hbar\omega_0 = \gamma\hbar\left|\overrightarrow{B_0}\right|$ (see **Figure 1.5**). Once again, the quantum point of view is simplified here, as each spin is actually set in a superposition of the two eigen quantum states. This phenomenon, composed of an excitation step and a relaxation step, is called ^{1}H Nuclear Magnetic Resonance (^{1}H-NMR).

After the excitation, the magnetization vector $\vec{M}$ will therefore concurrently relax to its initial value at thermal equilibrium (see **Figure 1.6**):

- The longitudinal magnetization M_z will increase in amplitude along time to reach its equilibrium value. This temporal evolution, driven by the relaxation process from an excited state to a more stable state, can be characterized by an exponential function of time constant T_1: this is the T_1 relaxation, or spin-lattice relaxation process.

- The transverse magnetization M_{xy} will decrease in amplitude along time to a null value. This temporal evolution, driven by the local dephasings between the different spins caused by spin-spin interactions and

$\overrightarrow{B_0}$ field spatial inhomogeneity, is characterized by an exponential function of time constant T_2^*: this is the T_2^* relaxation.

- If the $\overrightarrow{B_0}$ field was perfectly homogeneous in space or if the $\overrightarrow{B_0}$ field inhomogeneities could be compensated (with a 180° RF pulse for example), only spin-spin interactions would drive the transverse magnetization relaxation, and the associated time constant is written T_2: this is the T_2 relaxation, or spin-spin relaxation process.

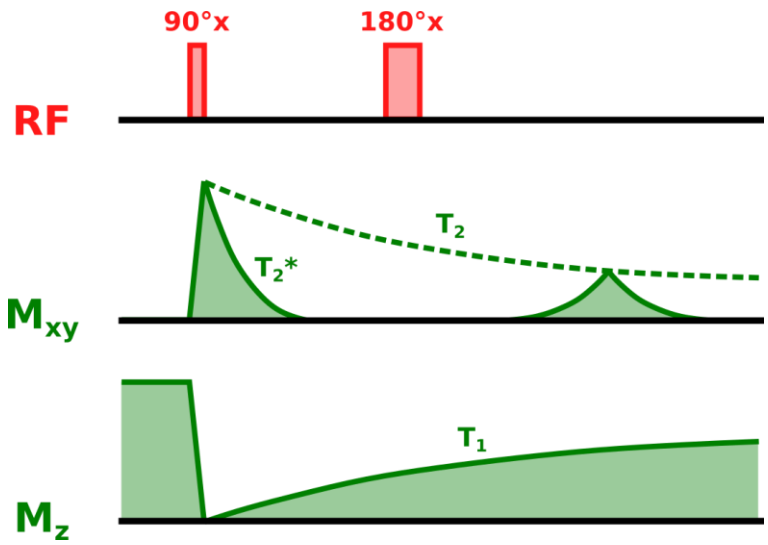

Figure 1.6: Time evolution of the different component of the magnetization vector $\vec{M}$ and definition of the time constants T_1, T_2 and T_2^*.

As mentioned just above, there are two types of dephasing causes explaining the T_2^* decay:

- Intrinsic inhomogeneities, causing a dephasing between spins because of the interactions between neighbor spins.
- Extrinsic inhomogeneities, causing a dephasing between spins because of stationary magnetic field inhomogeneities ($\overrightarrow{B_0}$ field imperfections, magnetic susceptibility effects, …).

T_1, T_2 and T_2^* values depend mainly on tissue characteristics (molecular composition, microscopic structure, …), tissue orientation (magic angle effect leading to a T_2 increase in tendons, …) and magnetic field characteristics ($\overrightarrow{B_0}$ field strength, $\overrightarrow{B_0}$ spatial homogeneity, …). Nevertheless, the relation $T_1 > T_2 > T_2^*$ is always verified. In biological tissues, we observe a great diversity of relaxation time values, ranging approximatively from a few tens of milliseconds to several seconds for T_1, from 1 ms to a few hundreds of milliseconds for T_2 and from a few tens of microseconds to a few tens of milliseconds for T_2^*.

The electromagnetic wave, radiating from the biological tissue and produced through NMR, experimentally looks like a sinusoidal signal oscillating at Larmor frequency, and decreasing exponentially in amplitude along time with a time constant equal to T_2^*: this signal is called the Free Induction Decay (FID). This electromagnetic wave can be recorded by inducing an electromotive force in a loop of conducting material (a receiving coil) electronically tuned

at Larmor frequency and exploited here to measure the NMR response of the tissue. This response signal is therefore transformed in an electrical signal that is recorded, digitized and stored in a computer memory.

2. FROM NMR TO MAGNETIC RESONANCE IMAGING (MRI)

We have seen previously that medical imaging consists in measuring a physical quantity produced through a physical phenomenon in the body of a patient. If we are able to localize and differentiate the signals produced by different regions of a biological tissue, it will be possible for us to represent a characteristic component of the NMR signal (magnitude or phase, for example) as a function of the spatial position of the region producing this signal thanks to a representation scale, giving an image of the information carried by the NMR signals regionally radiated by the biological tissue. This step is the only gap between standard NMR measurements and Magnetic Resonance Imaging, or MRI. In this subsection, the usual techniques to localize tridimensionally the sources of NMR signal in biological tissues will be presented.

Previously, we have seen that RF excitation of a biological tissue can only be done on-resonance: the frequency of the RF excitation wave must be equal to the Larmor frequency in the tissue. Moreover, we have seen that the NMR signal is emitted with the same characteristics as the Larmor precession of the magnetization $\vec{M}$ in the tissue: same frequency and same phase. In this subsection, we will see that we can exploit these properties of the acquired NMR signal to localize its source in space and produce an image.

2.1. THE CONCEPT OF SLICE SELECTION IN MRI

If a spatially linear and temporally constant magnetic field gradient oriented in one direction of space is superimposed to the $\overrightarrow{B_0}$ field during RF excitation at $\omega_{RF} = \omega_0$, the Larmor frequency of the biological tissue will accordingly vary along this direction, from $\omega_0 - \Delta\omega$ to $\omega_0 + \Delta\omega$, with $\Delta\omega$ depending on the strength of the magnetic field gradient and on the size of the biological tissue sample in the direction under consideration. Because of the need to be on-resonance to excite the tissue and produce a NMR signal, only the spins located in the plane centered on the biological tissue and orthogonal to the gradient direction will be excited because their Larmor precession frequency is equal to ω_{RF}. Experimentally, the excitation is performed with a RF pulse with a finite duration, thus characterized by an excitation bandwidth $\delta\omega$, which is inversely proportional to the timespan of the RF pulse. For that reason, only the spins located in the slab verifying a Larmor frequency comprised between $\omega_{RF} - \delta\omega$ and $\omega_{RF} + \delta\omega$ will be excited and will produce a FID, and the other spins are left in their original quantum state.

With this technique that consists in applying a linear magnetic field gradient during the RF excitation, we are able to select one slice of tissue from which an NMR signal will be produced: this is called slice selection (see **Figure 1.7**). To select a slice in another direction, we just need to change the direction of the gradient. If we want to modify the thickness of the slice, the best way to achieve it is to modify the gradient strength (for example, if the gradient strength is multiplied by two, the slice thickness will be divided by two, and inversely). If we now want to modify the position of the slice along the gradient direction, the best solution remains to modify the RF excitation frequency ω_{RF}: a decrease in excitation frequency will move the slice in the direction of the lower amplitudes of magnetic field (lower Larmor frequency), and inversely. This solution is thus very flexible to select any slice of the biological tissue sample from which we can produce a 2D image. The acquisition of 2D images from several parallel slices gives us the possibility to acquire a full 3D volume (stack of 2D slices) of biological tissue. In the following, we will see how to localize the sources of signal along the two spatial dimensions included in this selected plane.

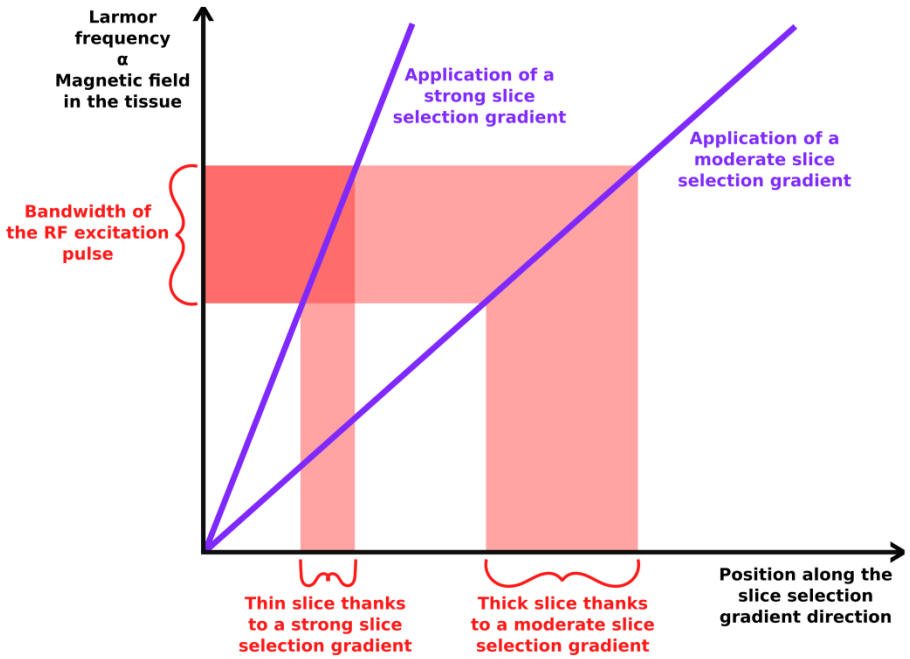

Figure 1.7: Excitation of a slice of biological tissue and control of the slice thickness thanks to the use of a slice selection gradient.

2.2. THE CONCEPTS OF FREQUENCY AND PHASE ENCODING IN MRI

Now consider that we apply the same type of magnetic field gradient during the signal acquisition in one of the directions included in the previous plane. In this situation, the FID is not looking like an exponentially decaying sinusoidal signal oscillating at Larmor frequency, but will be a continuous sum of oscillating signals with frequencies varying from $\omega_0 - \Delta\omega$ to $\omega_0 + \Delta\omega$. In this case, we observe a bijective relationship between the frequency of the NMR signal produced by a tiny part of the biological tissue (equal to the new Larmor frequency for the corresponding spins) and its location along the gradient direction. The position of signal sources is therefore encoded directly in the Larmor frequency of the spins: this technique is therefore called frequency encoding (see **Figure 1.8**).

Concerning the position encoding along the third direction of space, it is not possible to use a frequency encoding strategy because the simultaneous application of two stationary gradients oriented along different directions results in one global gradient, which therefore encodes along only one direction. We can propose to apply a gradient for a short time before the signal acquisition instead of during this readout. In this case, after the application of this gradient, all the spins induce a NMR signal oscillating at the same temporal frequency, but not at the same phase. This can be understood by the fact that the spins performed a different time evolution before the signal acquisition during the application of the gradient pulse. Regions of biological tissue located at extreme positions along the gradient direction perform an increase in angular frequency equal to $\Delta\omega$ during a time Δt. The phase increase in the acquired signal is therefore equal to $\Delta\varphi = \Delta\omega\,\Delta t$ for the spins located at those extreme positions. The biological tissue sample is therefore producing signal components with phase varying from $\varphi_0 - \Delta\varphi$ to $\varphi_0 + \Delta\varphi$ depending on where the spins are located along the axis corresponding to the direction of the gradient pulse, and φ_0 being the phase of signal components without applying the additional gradient. Once again, we

observe a bijective relationship between the phase of the NMR signal produced by a tiny part of the biological tissue and its location along the gradient direction. The position of signal sources is thus directly encoded in the phase of Larmor precession of spins: this technique is therefore called phase encoding (see **Figure 1.8**).

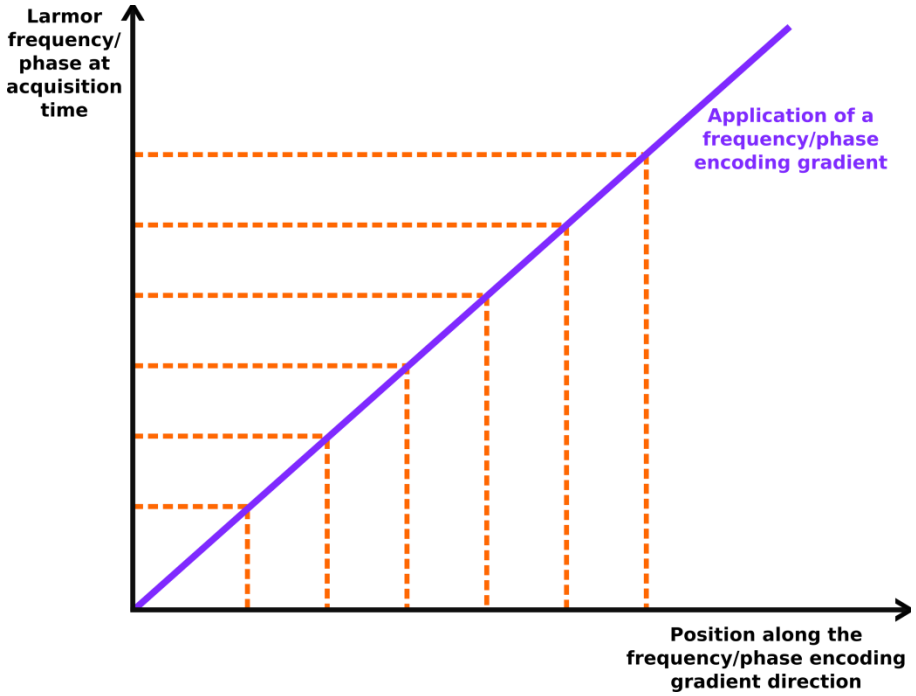

Figure 1.8: Principle of the frequency encoding of spin position.

For a biological tissue sample, it is therefore possible to encode the spatial localization of the sources of NMR signal just by applying (see **Figure 1.9**):

- concomitantly to the RF excitation pulse, a slice selection gradient pulse,
- between tissue excitation and signal readout, a phase encoding gradient pulse along one direction included in the slice, and,
- during the signal acquisition, a frequency encoding gradient pulse along the direction included in the slice and orthogonal to the phase encoding gradient direction.

We are thus able to fully encode the spatial positions of NMR signal sources in the three directions of space thanks to a succession of RF and gradient pulses along time. This set of RF pulses, gradient pulses and data acquisition widows, with chosen durations, amplitudes and frequencies, is called pulse sequence, and is today the way used in clinical routine to produce a magnetic resonance image from the NMR electromagnetic waves produced by the body of a patient once positioned in a strong magnetic field $\overrightarrow{B_0}$.

In the next subsection, we will see how to do it in practice.

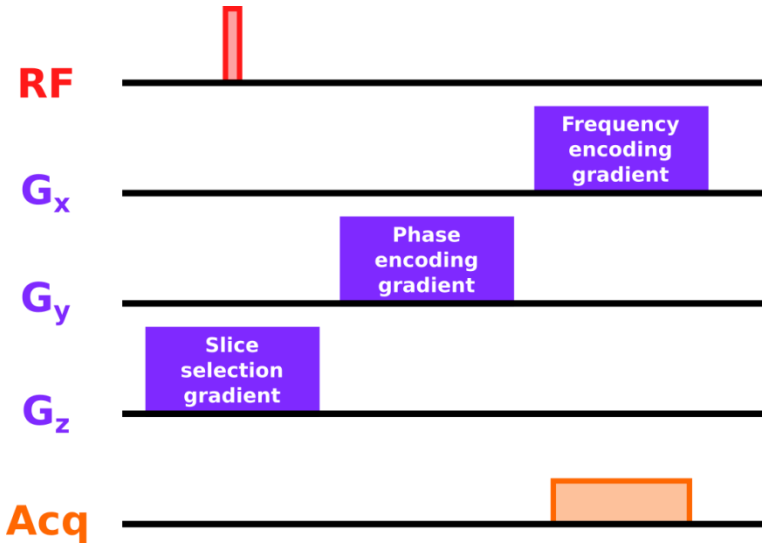

Figure 1.9: Position in the pulse sequence of the three position encoding gradients: slice selection gradient, frequency encoding gradient and phase encoding gradient.

3. DESCRIPTION OF BASIC MRI HARDWARE SET AND PULSE SEQUENCE

3.1. THE MAIN HARDWARE PARTS OF A MRI MACHINE

A clinical MRI machine is composed of several coils enabling the generation of the different magnetic fields required for the production of NMR signals and the encoding of the spatial positions from which they were emitted:

- **The main magnetic field coil:** This coil produces the main magnetic static field $\overrightarrow{B_0}$. Because of the very high amplitude of this field (between 1.5 T and 3 T in clinical practice), this coil is most of the time made up of a superconducting material. Some machines use a resistive coil or a permanent magnet, but only for lower magnetic fields.

- **The gradient coils:** They are organized in pairs of coils in a configuration inspired by Maxwell configuration (z direction, which is also conventionally the direction of $\overrightarrow{B_0}$) or Golay configuration (x and y directions, both orthogonal to the z direction) to produce magnetic field gradients in the x, y, and z directions.

- **The shim coils:** These coils improve the homogeneity of the main magnetic field across the biological sample before an acquisition, which is necessary to enhance the final image quality.

- **The transmit coil:** This coil produces the $\overrightarrow{B_1}$ RF pulses. One coil of this type is usually inserted into the MRI machine, and is called body coil. Other transmit coils can be used to address more specific regions of the body (knee or head typically). More recently, transmit coil arrays were proposed to perform parallel transmission with several coil elements at the same time.

- **The receive coil:** This coil receives the NMR signals coming from biological tissues after an excitation. Some receive coils can also transmit the $\overrightarrow{B_1}$ RF pulses and act as a transmit/receive coil (it is usually the

case for the body coil presented just above). Today, a lot of MRI reception antennas are constituted of a great number (up to 64 in practice today) surface coil elements, which acquire the NMR signals coming from the body in parallel with different non-uniform spatial sensitivity profiles. They are called reception phased array coils.

In the clinical field, the most standard field strengths for MRI machines are 1.5 T and 3.0 T. In the research field, in particular for preclinical research, it is possible to find MRI machines with a magnetic field strength of 7.0 T or even more, up to 21.1 T.

3.2. THE NOTION OF K-SPACE IN MRI

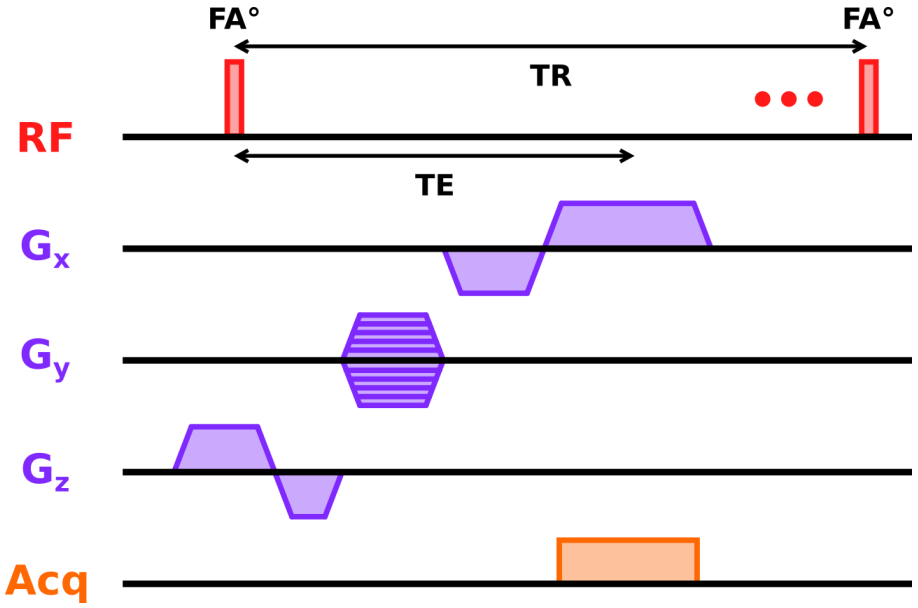

Figure 1.10: Chronogram of a standard gradient echo pulse sequence.

Let us consider the pulse sequence represented in **Figure 1.10**, featuring chronologically a RF excitation pulse concomitant to a slice selection gradient in the z axis, a phase encoding gradient in the y direction, of duration Δt_y, characterized by an amplitude G_y such that the local variation in magnetic field it creates at position y be equal to $G_y y$, and a signal readout window starting at time T concomitant to a frequency encoding gradient in the x direction, characterized by an amplitude G_x such that the local variation in magnetic field it creates at position x be equal to $G_x x$. Let $S(x, y)$ be the continuous complex amplitude function (including magnitude and phase) representing the monochromatic complex exponential NMR signal at time T in the slice of biological tissue selected by the slice selection gradient pulse. If we consider that there is no T_2^* decay of NMR signal during the data acquisition window, the value of the FID (we will keep this name, even if the precession is not free anymore) measured at time $t > T$ during the acquisition window on the volume V of biological tissue corresponding to the excited slice can be written:

$$FID(t) \propto \iint_{\{x,y\} \in V} S(x, y) \exp\left(-i \left(\gamma G_x x t + \gamma G_y y \Delta t_y\right)\right) dx dy \qquad \textbf{Eq. 1.10}$$

In **Eq. 1.10**, $\gamma G_x x$ represents the variation of Larmor angular frequency because of the application of the frequency encoding gradient G_x during signal readout, and $\gamma G_y y \Delta t_y$ represents the variation of Larmor precession phase because of the application of the phase encoding gradient G_y during a period Δt_y before signal readout. If we write $k_x = \gamma G_x t$ and $k_y = \gamma G_y \Delta t_y$, we obtain:

$$FID\big(k_x(t), k_y\big) \propto \iint\limits_{\{x,y\}\in V} S(x,y) \exp\Big(-i\left(k_x(t)x + k_y y\right)\Big)\, dxdy = \mathcal{F}[S(x,y)](k_x(t), k_y) \qquad \textbf{Eq. 1.11}$$

with $\mathcal{F}$ being the bidimensional spatial Fourier transform of $S(x,y)$, and with k_x and k_y being the spatial angular frequencies in the bidimensional plane (Oxy) along the directions given by the frequency encoding gradient and the phase encoding gradient respectively. If the FID function values are known for all the values of k_x and k_y, a function proportional to $S(x,y)$ can therefore be obtained by calculating the bidimensional inverse Fourier transform $\mathcal{F}^{-1}$ of the FID function represented in **Eq. 1.11**:

$$S(x,y) \propto \mathcal{F}^{-1}[FID\big(k_x, k_y\big)](x,y) \qquad \textbf{Eq. 1.12}$$

We can demonstrate that this relation is still correct in the case of discrete representations of $S(x,y)$ and of $FID\big(k_x, k_y\big)$, x and y being in this case discrete positions in space, and k_x and k_y being discrete angular spatial frequencies. At signal acquisition time, the FID values at N_x discrete k_x values for a given k_y value are acquired in one signal readout thanks to the pulse sequence introduced in **Figure 1.10**, N_x being the size of the S and FID matrices along their first dimension (the frequency or readout direction).

To obtain the full FID matrix, which is needed to calculate the full S matrix, we need to repeat this pulse sequence N_y times, N_y being the size of the S and FID matrices along their second dimension, with the same number of different amplitudes of phase encoding gradient permitting to reach the N_y required values of k_y. Once we acquired all the elements of the FID matrix, we just need to compute its 2D discrete inverse Fourier transform to obtain the matrix S. This last step is often called the image reconstruction step. S is then our complex 2D magnetic resonance image and FID, its Fourier transform, is usually called k-space of the MRI image. By representing graphically, thanks to a given color-scale or gray-scale for example, either the values of the complex modulus or argument of S obtained at each discrete position (x,y), we obtain respectively the MR magnitude and phase images of our biological tissue sample.

3.3. THE DIFFERENT FAMILIES OF MRI PULSE SEQUENCES

The pulse sequence we just studied is called a gradient echo pulse sequence. This name comes from the fact that a gradient echo is created at the center of the acquisition window thanks to the dephasing gradient pulse applied just before the refocusing frequency encoding gradient pulse: because the area of the refocusing part of the frequency encoding gradient is twice the area of its dephasing part applied just before, the spin dephases and then rephases completely at the exact center of the acquisition window, where we can thus see a maximum of signal called echo. An echo can also be produced in MRI with a RF pulse: if a refocusing 180° RF pulse (a RF pulse that inverses the sign of the different component of magnetization) is inserted at equal time distance between the RF excitation pulse (or a previous echo) and the readout gradient center, a new type of echo, called spin echo, superimposes with the previously described gradient echo. The RF excitation pulse is usually here a 90° RF pulse that flips all the longitudinal magnetization in the selected slice of the biological tissue sample into the transverse plane. The pulse sequence is therefore called a spin echo pulse sequence, even if a gradient echo is still produced.

If we want to obtain a 3D image of the biological tissue sample under consideration, three main possibilities can be explored:

- The first one is to repeat the same imaging procedure several times with a different RF excitation frequency to excite different slices of the biological tissue. Each 2D image is then reconstructed separately with a 2D discrete inverse Fourier transform as explained with **Eq. 1.12**. We refer to this procedure as a 2D multi-slice MRI acquisition. These slices can either be acquired successively or, more advantageously in terms of total scan time, be acquired in an interleaved manner.

- The second one is usually referred to as simultaneous multi-slice[43]. By using a RF pulse containing different frequency and phase components, it is possible to excite several 2D slices at the same time and separate them during the reconstruction.

- The third solution is to modify the pulse sequence by removing the slice selection gradient along z, keeping a frequency encoding strategy along the x axis and developing a phase encoding strategy on both y and z axes. In this case, we need to acquire a tridimensional matrix $FID(k_x, k_y, k_z)$, which represents a tridimensional k-space that can be reconstructed by applying a 3D discrete inverse Fourier transform (**Eq. 1.10**, **Eq. 1.11** and **Eq. 1.12** are generalizable in 3D). We refer to this procedure as a 3D MRI acquisition.

3.4. CARTESIAN K-SPACE SAMPLING SCHEMES IN MRI

Usually, the $N_x \times N_y$ points in the N_z 2D k-spaces, or the $N_x \times N_y \times N_z$ points in the 3D k-space, are chosen equally spaced or not in the spatial frequency domain along the different k-space dimensions: these measurements are said to be performed on a Cartesian grid. In this case, the image reconstruction process can be performed numerically by applying a 2D or 3D inverse Fast Fourier Transform (FFT) to the k-space matrix. The values of N_x, N_y and N_z are thus chosen as a function of the final image matrix size we want to obtain.

To control the Field Of View (FOV), which is the region over which the image is recorded, and in particular its size in the different dimensions of space, we need to modify the spatial frequency distance between the k-space points. For example, for a fixed frequency encoding gradient amplitude and duration, a twice larger sampling rate during signal readout (and a twice larger N_x value to cover the whole acquisition window and the same region of k-space) results in a twice larger FOV size along the frequency encoding direction, without modifying the image voxel size. The sampling rate during signal readout is usually expressed as the readout bandwidth (BW), which is the inverse of the time duration between two measurements of adjacent k-space points during signal readout. Another way to understand the readout bandwidth is to see it as the span of the range of Larmor frequencies in the FOV while the readout gradient is turned on: at a given sampling rate, if the readout gradient amplitude is increased, the span of the Larmor frequency range is increased by the same ratio in the whole biological tissue sample but, because of the decrease in FOV size as the frequency encoding gradient amplitude increases, the range of Larmor frequencies in the FOV remains the same and corresponds to BW. A last thing to know about the readout bandwidth is that an increase in BW degrades the Signal-To-Noise Ratio (SNR) of the image, which is the ratio between the informative signal amplitude in the image divided by the background noise. Indeed, the NMR measurement, as any other physical quantity measurement, is tainted by a multi-factorial noise (resistive noise of the reception antenna, thermal noise, electronic noise, digital noise, …), which is translated in image noise after the reconstruction step.

[43] David J. Larkman et al., "Use of Multicoil Arrays for Separation of Signal from Multiple Slices Simultaneously Excited," *Journal of Magnetic Resonance Imaging* 13, no. 2 (2001): 313–17, https://doi.org/10.1002/1522-2586(200102)13:2<313::AID-JMRI1045>3.0.CO;2-W.

This decrease in SNR is explained by the fact that more noise is acquired for the same amount of useful signal when BW is increased. In the y direction, the FOV size can be doubled by increasing twice the number of phase encoding steps while keeping the same extremal phase encoding amplitudes (for the acquisition of the first and last FIDs of a linearly filled 2D Cartesian k-space matrix, for example).

The voxel size in one given dimension can be set by modifying the maximal spatial frequency distance along this dimension between the k-space points and the k-space center, characterized by $k_x = k_y(= k_z) = 0$: as k-space values are sampled far from the k-space center, potential high spatial frequency information will be obtained, which decreases the voxel size of the image (but does not necessarily increase the spatial resolution of the image itself, in particular if this high spatial frequency information is hidden into background noise). To obtain a lower voxel size, at a fixed readout bandwidth, higher amplitude encoding gradients will be needed. In this case, because the matrix size is kept, the FOV is reduced. With this same strategy, to keep the same FOV with a decreased voxel size, the readout bandwidth and the matrix size need to be increased too (see **Figure 1.11**).

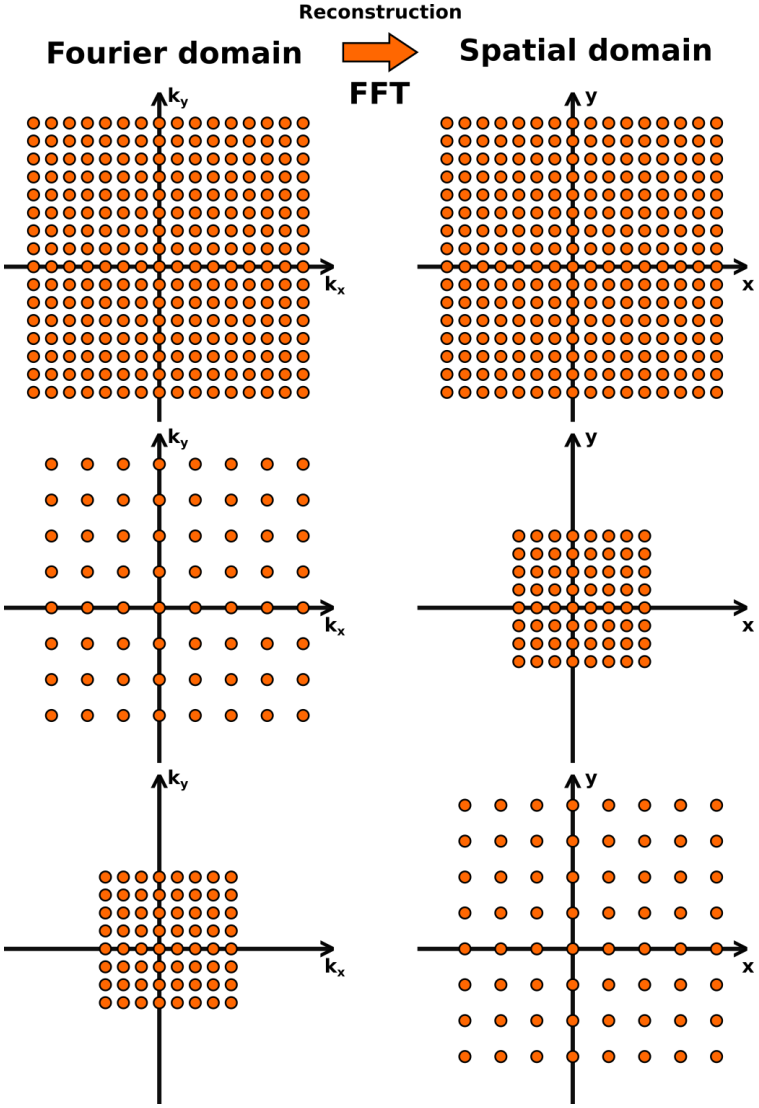

Figure 1.11: Relationship between spatial frequencies, field of view and voxel size.

3.5. NON-CARTESIAN K-SPACE SAMPLING SCHEMES IN MRI

In the more general case, we are neither asked to follow a Cartesian grid nor using phase encoding steps. We can imagine the k-space to be acquired through pure frequency encodings along freely drawn curves in the 2D or 3D Fourier domain of the final image, usually referred to as views. The combination of all these curves needed for the imaging process is called trajectory. In this case, $k_x(t)$, $k_y(t)$ and $k_z(t)$ are all piecewise continuous functions of time, with one continuous piece per readout. The pulse sequence designer is then free to cover the k-space surface or volumes as he or she desires. He or she can choose to follow, for example, radii in k-space starting from its center and finishing in the outer part of k-space: this is called a radial trajectory, and needs constant gradient amplitude values along readout. Another strategy would be to describe at each readout period a spiral starting from the center of k-space and finishing in the outer k-space part: this is called a spiral trajectory, and needs oscillating gradient amplitude values along readout. We can also imagine the acquisition of a whole k-space with only one RF excitation followed by one readout window. In this case, the trajectory needs to cover the whole k-space in only one view: this is what is done in single-shot Echo Planar Imaging (EPI) pulse sequences, for example (see **Figure 1.12**).

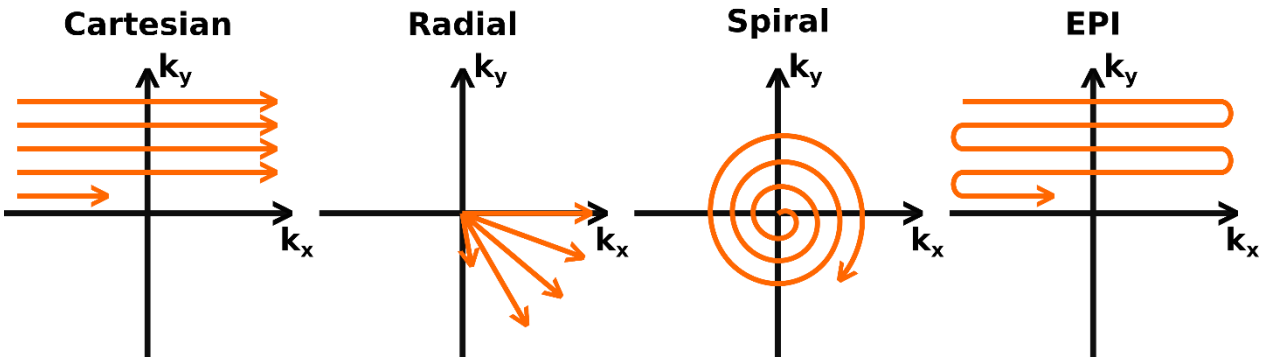

Figure 1.12: Examples of 2D Cartesian and non-Cartesian k-space trajectories.

The only limits of MRI sequence trajectory design are gradient limits in terms of maximal amplitudes and maximal rates of amplitude variation along time (called slew rate), and also, of course, the pulse sequence designer imagination. The difficult step is the image reconstruction step: because the k-space points are not acquired on a Cartesian grid anymore, the standard 2D or 3D inverse FFT algorithms cannot be directly applied. In the case of non-Cartesian trajectories, more developed reconstruction methods need to be used. For example, it is possible to use a direct regridding, based on the interpolation of the non-Cartesian k-space measurements on a Cartesian grid, that can thereafter be reconstructed by applying the inverse FFT. Another example is to directly apply a non-uniform FFT (or NUFFT[44]) on the non-Cartesian k-space data. Those methods are usually based on the iterative resolution of an inverse problem that tries to find the image that best fits to the k-space measurements and sometimes that verifies other conditions, usually called priors.

[44] J. A. Fessler and B. P. Sutton, "Nonuniform Fast Fourier Transforms Using Min-Max Interpolation," *IEEE Transactions on Signal Processing* 51, no. 2 (February 2003): 560–74, https://doi.org/10.1109/TSP.2002.807005.

4. MANAGEMENT OF MR IMAGE CONTRAST

4.1. PRINCIPLES OF MR CONTRAST MANAGEMENT

In this subsection, we will explore what MR properties and acquisition parameters control the aspect of our image S, and in particular the contrast of its magnitude $|S|$. To do this, we first need to introduce several standard acquisition parameters that control the gradient echo pulse sequence studied above (see **Figure 1.10**):

- The time duration between the application the RF excitation pulse and the acquisition of the most central points of k-space at each readout is called the Echo-Time, and is written TE. This is the time to wait after the excitation to reach the center of the gradient echo.

- The time duration between two successive RF pulses that excite the same biological tissue region (which is important to precise in the case of a multi-slice acquisition that interleaves in time the repetitions for the different slices to exploits the dead times and reduce the global scan time) is called the Repetition Time, and is written TR.

- The angle in space at which the global magnetization vector $\vec{M}$ is flipped from its thermal equilibrium direction by each RF excitation pulse is called the Flip Angle, and is written FA. This angle is a function of the amplitude, the duration and the envelope shape of the RF excitation pulse.

It is easy to guess that $|S|$ will depend first on the proton density of the biological tissue under consideration: a proton density ρ which is twice higher will produce, for the same pulse sequence, twice the NMR signal. Nevertheless, proton density does not vary a lot between the different tissues of the human body but for particular organs like bones or lungs. Therefore, the proton density contrast in MR images is not always interesting to study. Moreover, spin relaxation effects will affect a lot the signal produced by biological tissue and the relationship with the related density, which is a chance because of the great variety of values found for the different relaxations time in soft biological tissues, as stated in 1.2. For that reason, it is necessary to know how to control and exploit these NMR relaxation related contrast possibilities to increase the diagnostic potential of medical MR images.

Let us see what changes in terms of magnitude image contrast when the pulse sequence parameters seen just above are modified (see **Figure 1.13**):

- If the TE value is increased, biological tissues with different transverse relaxation time values, T_2^*, have more time to relax, which emphasizes the contrast in the signal value between tissues with different characteristic times for this relaxation process. For that reason, an increase of TE is said to increase the T_2^* weighting of gradient echo images. To the contrary, a decrease in TE decreases the T_2^* weighting. For spin-echo sequences, the same effect is obtained but with T_2 weighting instead of T_2^*. As seen in 3.3, the 180° refocusing RF pulse between the 90° RF excitation pulse and the acquisition window removes, more generally reduces, the effects coming from extrinsic inhomogeneities in the transverse relaxation phenomena.

- If the TR value is decreased, we can observe more important spin saturation effects: if the TR is short with respect to T_1, the biological tissue magnetization may not have the time to come back to its thermal equilibrium state, creating an accumulation effect along repeated RF excitations and thus reducing the amplitude of the NMR signal. For a given TR value, this effect will be more important for tissues with long T_1 values compared to tissues with short T_1 values, because these short T_1 tissues have the time to

recover their longitudinal magnetization between each excitation pulse. For that reason, a decrease of TR is said to increase the T_1 weighting of magnitude MR images. To the contrary, an increase of TR is said to decrease the T_1 weighting.

- If the FA is increased (only for gradient echo pulse sequences; spin echo pulse sequences are most of the time performed with a 90° RF excitation pulse), the same T_1 dependent saturation effect as for a decrease of TR can be observed. For that reason, an increase of FA is said to increase the T_1 weighting of gradient echo images, and a decrease of FA is said to decrease the T_1 weighting.

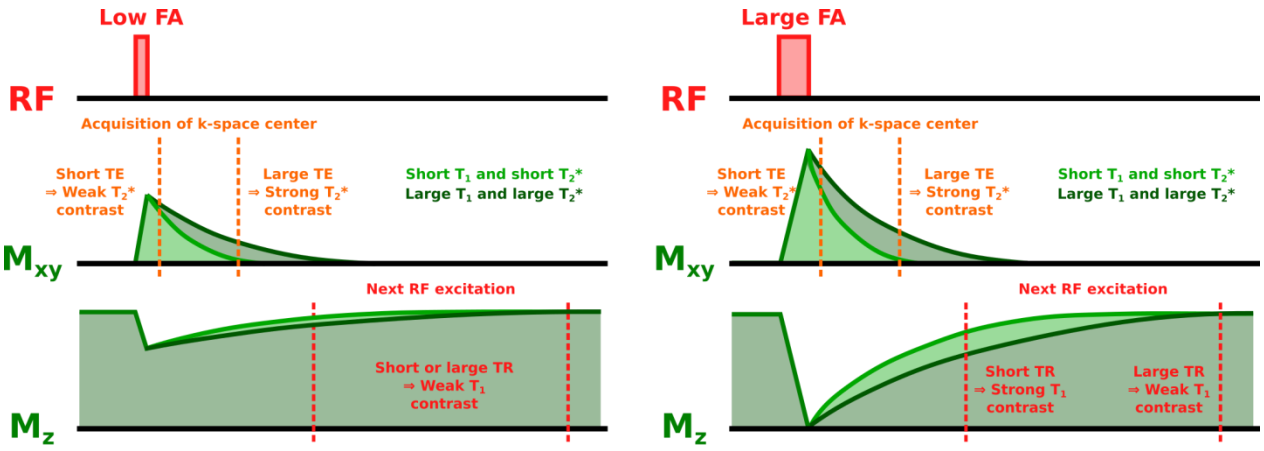

Figure 1.13: Control of the magnitude image contrast in gradient echo imaging.

Gradient echo pulse sequences being designed to reduce the total scan time compared to spin echo sequences, an increase of TR is not usually applied in practice with this type of sequence to control the contrast. By taking into account the previous consideration:

- **If we want to obtain a T_1 weighted image:**
    - We use a short TE and a large FA in gradient echo pulse sequences.
    - We use a short TE and a short TR in spin echo pulse sequences.
- **If we want to obtain a T_2^* or T_2 weighted image:**
    - We use a large TE and a short FA in gradient echo pulse sequences (in this case, we obtain a contrast driven by T_2^*).
    - We use a large TE and a large TR in spin echo pulse sequences (in this case, we obtain a contrast driven by T_2).
- **If we want to obtain a ρ weighted image:**
    - We use a short TE and a short FA in gradient echo pulse sequences.
    - We use a short TE and a large TR in spin echo pulse sequences.

Concerning the MR phase image, where the argument of the MR complex image is represented, one sequence parameter can be tuned to control its contrast: if the TE is increased, the excited spins, that can be considered all in phase just after the RF excitation, will have more time to dephase because of local magnetic field inhomogeneities (slightly off-resonance Larmor precession, magnetic susceptibility effects, …). For that reason, at signal readout time, the phase contrast increases with TE.

4.2. ADVANCED ASPECTS OF MR CONTRAST MANAGEMENT

If we want to control more precisely the magnitude image contrast, one solution is to use preparation pulses, which are small pulse sequences applied just before the RF excitation. For example, we can use:

- An inversion preparation pulse, which consists of a 180° RF pulse, followed by a waiting duration before the RF excitation pulse called inversion time. A standard role of this pulse is to obtain a stronger T_1 contrast in the image. By tuning precisely the inversion time, it is even possible to suppress the signal coming from a tissue with a known T_1 value. We can then obtain images with the signal coming from fat tissues being suppressed (STIR technique[45]) or with the signal coming from liquids being suppressed (FLAIR technique[46]).

- A spectrally selective preparation pulse, which attenuates the signal coming from a frequency shifted component (fat for example, that does not resonate at the exact same frequency as water) by applying a saturation pulse tuned at this special frequency (chemical shift selective fat saturation[47], for example).

Gradient echo pulse sequences being usually performed with short TR values, transverse magnetization may remain important just before the next RF excitation pulse. If this remaining signal created to acquire a previous k-space view is acquired at the same time as a new k-space view, it can produce artifacts in the final image. To solve this problem, two main solutions are usually implemented[48]:

- A spoiling strategy can be implemented, which consists in changing at each repetition the phase of the RF excitation pulse (RF spoiling) and/or performing magnetic field gradients (called spoiler or killer) just before the next RF excitation pulse (gradient spoiling). In this case, the transverse magnetization coherences between repetitions are disrupted. This strategy is implemented in the SPGR (or FLASH) pulse sequence, for example.

- A refocusing strategy can be implemented, which consists in implementing refocusing gradients before and/or after the readout gradient to make use of the transverse magnetization remaining at the end of each repetition for the next one. In this case, the transverse magnetization coherences between repetitions are preserved and exploited. This strategy is implemented in SSFP (or FIESTA) pulse sequences, for example.

---

[45] G. M. Bydder et al., "The Short TI Inversion Recovery Sequence—An Approach to MR Imaging of the Abdomen," *Magnetic Resonance Imaging* 3, no. 3 (January 1, 1985): 251–54, https://doi.org/10.1016/0730-725X(85)90354-6.

[46] B. De Coene et al., "MR of the Brain Using Fluid-Attenuated Inversion Recovery (FLAIR) Pulse Sequences.," *American Journal of Neuroradiology* 13, no. 6 (November 1, 1992): 1555–64.

[47] A. Haase et al., "1 H NMR Chemical Shift Selective (CHESS) Imaging," *Physics in Medicine & Biology* 30, no. 4 (1985): 341, https://doi.org/10.1088/0031-9155/30/4/008.

[48] Brian Hargreaves, "Rapid Gradient-Echo Imaging," *Journal of Magnetic Resonance Imaging* 36, no. 6 (2012): 1300–1313, https://doi.org/10.1002/jmri.23742.

Fast versions of the gradient echo and spin echo pulse sequences are also available. They are usually based on the acquisition of several lines of k-space from a single RF excitation pulse. To perform this, an echo train (spin echo train or gradient echo train) is created. The type of pulse sequence that exploits this technique at its best is surely Echo Planar Imaging (EPI) pulse sequences[49] for the gradient echo family and Fast Spin Echo (or FSE) pulse sequences for the spin echo family. In these cases, a full 2D k-space can be acquired in one or a small number of RF excitations and echo-trains.

In all those more complicated pulse sequences, contrast management will be often more complicated to understand (mixture of ρ, T_1 and T_2/T_2^* weightings, involvement of other acquisition parameters or MR signal characteristics, …). It makes MRI a very rich and highly tunable and flexible technique for medical imaging, and it definitely makes its great clinical value today. MRI contrast can even go beyond those purely anatomical imaging considerations and measure various physical parameters of great clinical value. Let's take a brief tour of them.

5. ADVANCED APPLICATIONS OF MRI: BEYOND PURE ANATOMICAL IMAGING

Here is a non-exhaustive list of the main advanced MRI applications that give the possibility to the clinician to go beyond anatomical images:

5.1. EXPLOITATION OF INTRINSIC AND EXTRINSIC CONTRAST AGENTS IN MRI

To enhance the image contrast, the clinician can decide to inject in the patient's blood a liquid modifying the surrounding MR properties of tissue. The most widely used contrast agent is based on the NMR action of gadolinium chelates[50]. The main effect of gadolinium consists in a T_1 shortening. At high concentration, it also decreases the T_2/T_2^*. Globally, it increases the NMR signal (in particular in T_1 weighted images) at low concentration but decreases the NMR signal if its local concentration is too high (in particular in T_2/T_2^* weighted images). The presence of a contrast agent in arterial and venous blood can be exploited to specifically image arteries and veins: it is called MR angiography[51]. In this case, special imaging protocols are used to enhance, in the image, the signal coming from blood vessels without enhancing the signal coming from the other tissues: this is why we usually talk about bright blood MR angiography.

Another way to perform MR angiography is to exploit the saturation effect on tissues around blood vessels. This effect is not the same for the fluid in blood vessels because of its circulation in and out of the excited slice or volume. In this case, blood plays the role of an intrinsic contrast agent and Time-Of-Flight (TOF) MR angiography[52] is performed. With the same type of effect but on the blood itself, if the saturation is performed thanks to a pre-saturation band created by a saturation pulse with a localized effect in space, dark blood MR angiography[53] is performed.

---

[49] M. K. Stehling, R. Turner, and P. Mansfield, "Echo-Planar Imaging: Magnetic Resonance Imaging in a Fraction of a Second," *Science* 254, no. 5028 (October 4, 1991): 43–50, https://doi.org/10.1126/science.1925560.

[50] Peter Caravan et al., "Gadolinium(III) Chelates as MRI Contrast Agents: Structure, Dynamics, and Applications," *Chemical Reviews* 99, no. 9 (September 1999): 2293–2352, https://doi.org/10.1021/cr980440x.

[51] Frank R. Korosec et al., "Time-Resolved Contrast-Enhanced 3D MR Angiography," *Magnetic Resonance in Medicine* 36, no. 3 (1996): 345–51, https://doi.org/10.1002/mrm.1910360304.

[52] D Saloner, "The AAPM/RSNA Physics Tutorial for Residents. An Introduction to MR Angiography.," *RadioGraphics* 15, no. 2 (March 1, 1995): 453–65, https://doi.org/10.1148/radiographics.15.2.7761648.

[53] R R Edelman et al., "Extracranial Carotid Arteries: Evaluation with 'Black Blood' MR Angiography.," *Radiology* 177, no. 1 (October 1, 1990): 45–50, https://doi.org/10.1148/radiology.177.1.2399337.

Concerning extrinsic contrast agents, like gadolinium for example, another widely used application is perfusion imaging. Injected as a bolus, the time evolution of the contrast agent concentration in an organ of interest can be followed by repeating the acquisition of the same image with a controlled time interval between the images. It is then possible to perform Dynamic Contrast Enhanced MRI (DCE-MRI)[54], based on the T_1 shortening in tissues caused by the gadolinium injection and followed with T_1 weighted images repeated at large time intervals, or Dynamic Susceptibility Contrast (DSC-MRI)[55], based on the T_2/T_2^* shortening in tissues caused by the gadolinium injection and followed with T_2/T_2^* weighted rapidly repeated images. As previously introduced with dark blood MRI, it is possible to use pre-saturation bands to use the blood itself as an intrinsic contrast agent giving information about perfusion: it is called Arterial Spin-Labeling MRI (ASL-MRI)[56].

5.2. MOTION SENSITIZATION IN MRI

To make the image contrast sensitive to motion effects, one widely-used possibility is to modify the pulse sequence to include motion encoding gradients. This strategy is usually performed by applying a pair of opposite gradient lobes in a gradient echo sequence (or identical gradient pulses on both sides of the refocusing pulse in spin echo sequences). If a spin is animated by a motion (caused by flow, diffusion, deformation of biological tissue, …) along the direction given by the motion encoding gradient and during the time between the application of the two lobes of this gradient, the phase of its Larmor precession accumulated during the application of the first lobe is not compensated by the application of the second lobe. In the case of a motionless spin, the motion encoding gradient does not alter the Larmor phase of the spin.

This phenomenon can be exploited in a type of MR angiography called phase contrast MR angiography[57]: in this technique, the velocity component of the blood flow along the motion encoding direction axis is directly encoded in the MR image phase. We can therefore obtain a quantitative map of flow velocities in an organ. In the case of a diffusive motion of water molecules in an organ, the same type of sequence can be used. Because of the random walk motion followed by each water molecule, the effect is not seen as a coherent MR phase shift anymore but as a decoherence in the phases of neighboring spins. This is thus visible as a decrease in MR magnitude signal intensity, similar to the one that would be obtained with a shorter T_2/T_2^*, for the tissue being subject to diffusion. This technique is called diffusion MRI[58]. Because this diffusion can be probed in different directions of space (the direction of the motion encoding gradient), diffusion anisotropy, as it can be observed in the white matter of the brain or in some muscles for example, can be additionally probed by analyzing, as a whole, a set of images acquired with different direction of motion encoding gradients. This leads to diffusion tensor imaging (DTI), from which advanced data processing algorithms can extract the path of the different white matter or muscle fibers: this technique is called tractography, and is useful in order to analyze the structural connections between the different parts of the brain.

---

[54] Paul S. Tofts et al., "Estimating Kinetic Parameters from Dynamic Contrast-Enhanced T1-Weighted MRI of a Diffusable Tracer: Standardized Quantities and Symbols," *Journal of Magnetic Resonance Imaging* 10, no. 3 (1999): 223–32, https://doi.org/10.1002/(SICI)1522-2586(199909)10:3<223::AID-JMRI2>3.0.CO;2-S.

[55] K. Welker et al., "ASFNR Recommendations for Clinical Performance of MR Dynamic Susceptibility Contrast Perfusion Imaging of the Brain," *American Journal of Neuroradiology* 36, no. 6 (June 1, 2015): E41–51, https://doi.org/10.3174/ajnr.A4341.

[56] A. R. Deibler et al., "Arterial Spin-Labeling in Routine Clinical Practice, Part 1: Technique and Artifacts," *American Journal of Neuroradiology* 29, no. 7 (August 1, 2008): 1228–34, https://doi.org/10.3174/ajnr.A1030.

[57] Saloner, "The AAPM/RSNA Physics Tutorial for Residents. An Introduction to MR Angiography."

[58] Denis Le Bihan, "Looking into the Functional Architecture of the Brain with Diffusion MRI," *Nature Reviews Neuroscience* 4, no. 6 (June 2003): 469–80, https://doi.org/10.1038/nrn1119.

A last technique based on the use of motion encoding gradients is Magnetic Resonance Elastography (MRE)[59]: in the MR phase image contrasted by the use of motion encoding gradients, we are able to depict the shear wave patterns induced by a mechanical exciter in the organ of interest. The analysis of these waves in terms of propagation velocity (and sometimes also linear attenuation coefficient) makes us able to measure the intrinsic elasticity (and sometimes also the intrinsic viscosity) of the biological tissue. This technique will be discussed more deeply later in this manuscript.

5.3. BRAIN FUNCTIONAL MRI

A last technique that will be rapidly discussed in this part is BOLD functional MRI (fMRI)[60]. This technique consists in probing the functional activity of the brain (contrary to DTI and tractography, that are sensitive to its structural architecture) by exploiting the difference in T_2/T_2^* between tissues perfused by oxygenated and deoxygenated blood, and called Blood Oxygen Level Dependent (BOLD) effect[61]. Indeed, when a region of the brain is functioning, a vasodilation is locally observed to supply the dioxygen needs of this region. This increase in amount of oxygenated blood is, in practice, more important than the real metabolic needs of brain cells. For that reason, brain region activation leads to a local higher tissue concentration of oxyhemoglobin, decreasing the relative concentration of deoxyhemoglobin, a paramagnetic molecule that disturbs the local magnetic field in the brain and thus decreases the local T_2/T_2^* value of tissue. For that reason, the activation of a region in the brain produces a signal increase in T_2/T_2^* weighted images acquired as the region is activated.

The standard way to practice fMRI consists in rapidly repeating the same imaging pulse sequence to capture the time evolution of MR signal in the brain. This protocol brings two principal types of application. The first one, called resting-state fMRI[62] [63], consists in analyzing the acquired images together and detect the statistically representative similarities in signal evolution between voxels. With the hypothesis that regions that are functionally connected perform the same BOLD effect evolution along time, this post-processing step gives the possibility to visualize the different functional networks of the brain during rest. The second one, usually referred to as task fMRI, consists in performing during the imaging protocol a set of stimuli, called paradigm, designed to test which regions of the brain are activated for a given stimulus[64]. A great variety of stimuli can be tested: visual, audio, olfactory, or even based on a complex activity involving the interaction between several senses (playing a game, answering to questions, …).

Many other applications are still under research validation and development today, and new promising ones are still discovered nowadays. This huge variety of possibilities offered by MRI makes it one of the most versatile

[59] R. Muthupillai et al., "Magnetic Resonance Elastography by Direct Visualization of Propagating Acoustic Strain Waves," *Science* 269, no. 5232 (September 29, 1995): 1854–57, https://doi.org/10.1126/science.7569924.
[60] S. Ogawa et al., "Intrinsic Signal Changes Accompanying Sensory Stimulation: Functional Brain Mapping with Magnetic Resonance Imaging," *Proceedings of the National Academy of Sciences* 89, no. 13 (July 1, 1992): 5951–55, https://doi.org/10.1073/pnas.89.13.5951.
[61] S. Ogawa et al., "Brain Magnetic Resonance Imaging with Contrast Dependent on Blood Oxygenation," *Proceedings of the National Academy of Sciences* 87, no. 24 (December 1, 1990): 9868–72, https://doi.org/10.1073/pnas.87.24.9868.
[62] Bharat Biswal et al., "Functional Connectivity in the Motor Cortex of Resting Human Brain Using Echo-Planar Mri," *Magnetic Resonance in Medicine* 34, no. 4 (1995): 537–41, https://doi.org/10.1002/mrm.1910340409.
[63] Frederik Barkhof, Sven Haller, and Serge A. R. B. Rombouts, "Resting-State Functional MR Imaging: A New Window to the Brain," *Radiology* 272, no. 1 (July 1, 2014): 29–49, https://doi.org/10.1148/radiol.14132388.
[64] A. M. Blamire et al., "Dynamic Mapping of the Human Visual Cortex by High-Speed Magnetic Resonance Imaging," *Proceedings of the National Academy of Sciences* 89, no. 22 (November 15, 1992): 11069–73, https://doi.org/10.1073/pnas.89.22.11069.

diagnostic tools in the clinical environment. However, while most organs can be observed and diagnosed today with MRI, several ones remain difficult to study with this imaging modality. This is the case of the lung for example, and we will see why in the next section.

SECTION 3 THE LUNG: A CHALLENGING ORGAN FOR MRI

AS SEEN IN THE FIRST SECTION OF THIS CHAPTER, THE LUNG IS A VITAL ORGAN IN THE HUMAN BODY. THROUGH ITS MAIN FUNCTION, WHICH IS GAS EXCHANGE BETWEEN THE ORGANISM AND ITS ENVIRONMENT, WORKING TOGETHER WITH THE HEART, IT CONSTITUTES ONE OF THE MOST IMPORTANT ELEMENTS IN BODY FUNCTION. WE SAW THAT THIS ORGAN CAN BE AFFECTED BY VARIOUS DISEASES, WHICH MOST OF THE TIME DIRECTLY AFFECT THE GAS EXCHANGE PROCESS AND THEREFORE PREVENT THE LUNG FROM FUNCTIONING CORRECTLY, WHICH CAN BE CRITICAL FOR PATIENT'S HEALTH AND WELLNESS. PREVIOUSLY, WE HAVE ALSO SEEN THE GREAT VALUE OF MRI. THROUGH ITS ABILITY TO GIVE HIGH QUALITY IMAGES REFLECTING THE INTRINSIC GREAT VARIABILITY IN NMR PROPERTIES OF BIOLOGICAL TISSUES, AND ITS HIGH FLEXIBILITY ENABLING THE DEVELOPMENT OF ADVANCED MR APPLICATIONS ABLE TO QUANTIFY VARIOUS PHYSICAL PARAMETERS AND PHYSIOLOGICAL PHENOMENA, MRI HAVE QUICKLY BECOME OVER THE LAST 40 YEARS ONE OF THE MOST VALUABLE TOOL IN CLINICAL ROUTINE TO EXPLORE MOST OF THE ORGANS IN HUMAN AND UNDERSTAND THEIR PATHOLOGIES. IN THIS SECTION, WE WILL STUDY THE CASE OF LUNG MRI, AND FIRST TRY TO UNDERSTAND THE CHALLENGES ENCOUNTERED WITH THIS ORGAN.

1. THE THREE CHALLENGES OF LUNG MRI

As it was previously presented in this manuscript, lung is a complex organ both in terms of structure and function. As a reminder, lung is made of a generative airway tree, starting at the larynx with the trachea then dividing into bronchi, that subdivide into smaller bronchi, bronchioles, alveolar ducts, alveolar sacs, and terminating with several hundreds of millions of alveoli through which gas exchange is performed. Moreover, the lung is also made of several generative arterial and venous trees, starting with the main arteries and veins of the human body (aorta, vena cava, pulmonary artery and vein) and finishing in either nutritive ducts for lung tissues or in millions of capillaries that surrounds the alveoli to bring them the carbon dioxide to evacuate and to capture the dioxygen that will be delivered to all the body cells. This function cannot be performed through a pure diffusive phenomenon of the exchanged gas through the alveoli walls. To perform its function correctly, the lung needs to create a circulation of air inside the bronchi, bronchioles and alveoli, called pulmonary ventilation. This ventilation, as we saw previously, is ensured by deforming the lung parenchyma quasi-periodically and this deformational motion is intimately related to lung function.

The morphofunctional characteristics of the lung induce three important consequences for lung MRI, which can be seen as challenges at first glance.

1.1. THE PROBLEM OF LOW TISSUE DENSITY IN THE LUNG

The first challenge concerns the low and dynamic tissue density in the lung parenchyma. As stated in the first section of this chapter, lung is made of numerous airways filled of air, the relative proportion of air being higher at the end of inspiration than at the end of expiration. However, we have seen that ^{1}H NMR and MRI in biological

tissues are based on the important quantity of water available in most biological tissues, in particular inside the cells. Moreover, we have seen that the signal measured in one voxel is directly proportional to the proton density at its location, written ρ, and thus proportional to the volume of water present in the biological sample corresponding to the voxel.

Because any representative sample of lung parenchyma will globally be composed of comparable volumes of tissue and air, the MR signal amplitude produced by a lung parenchyma sample will be lower than the one produced by the same volume of a plain tissue sharing the same other MR properties as the lung. The mean proton density within the entire lung was measured to be around 0.29 times the proton density of a muscle at the end of inspiration, which is known to have a water density of 75%[65]. This low proton density results in a low SNR in the MR image, which can compromise the depiction of details in the lung image and thus the diagnostic value of a lung MR image.

1.2. THE PROBLEM OF ULTRASHORT RELAXATION TIMES IN THE LUNG

The second challenge concerns the complex multi-scale airway structure of the respiratory tract. Because of the numerous generations of air ducts of different sizes in the lung and the huge number of alveoli, the lung features an important air-tissue interface surface relatively to its tissular volume, estimated to be between 40 and 100 square meters[66] for a tissular volume between 600 and 1000 mL[67] [68]. The magnetic susceptibility of most biological tissues is very different from the magnetic susceptibility of a gas. This magnetic susceptibility of a material characterizes its ability to get magnetized as it experiences a magnetic field. Because this is exactly the case for a biological tissue from which we want to produce a MR image, and because of this difference between water and air, those two media get differently magnetized. Because the magnetization of a medium changes the local magnetic field strength or, to be physically speaking more accurate, the magnetic induction strength inside it, the local magnetic field in pure biological tissue will be slightly different to the one in the gas, creating local magnetic field gradients inside the lung at space scales usually below the voxel size. Those local magnetic field gradients disturb the spatial homogeneity of the magnetic field in the lung: we thus observe a tissue-induced magnetic field inhomogeneity.

This induced magnetic field inhomogeneity is therefore an extrinsic magnetic field inhomogeneity that amplifies the discrepancy between T_2 and T_2^* in the lung parenchyma: a good order of magnitude of T_2^* in the lung parenchyma is known to be around 1-2 ms at clinical MRI magnetic field strength, while T_2 can be 60 times higher and T_1 very long, around 800 milliseconds[69] [70]. With standard MRI pulse sequences, the TE is often superior to a

[65] Hiroto Hatabu et al., "T2* and Proton Density Measurement of Normal Human Lung Parenchyma Using Submillisecond Echo Time Gradient Echo Magnetic Resonance Imaging," *European Journal of Radiology* 29, no. 3 (March 1, 1999): 245–52, https://doi.org/10.1016/S0720-048X(98)00169-7.
[66] William M. Thurlbeck, "The Internal Surface Area of Nonemphysematous Lungs," *American Review of Respiratory Disease* 95, no. 5 (May 1, 1967): 765–73, https://doi.org/10.1164/arrd.1967.95.5.765.
[67] M. F. Petrini, B. T. Peterson, and R. W. Hyde, "Lung Tissue Volume and Blood Flow by Rebreathing Theory," *Journal of Applied Physiology* 44, no. 5 (May 1, 1978): 795–802, https://doi.org/10.1152/jappl.1978.44.5.795.
[68] J. D. Armstrong et al., "Lung Tissue Volume Estimated by Simultaneous Radiographic and Helium Dilution Methods.," *Thorax* 37, no. 9 (September 1, 1982): 676–79, https://doi.org/10.1136/thx.37.9.676.
[69] Grzegorz Bauman et al., "Pulmonary Relaxometry with Inversion Recovery Ultra-fast Steady-state Free Precession at 1.5T," *Magnetic Resonance in Medicine* 77, no. 1 (January 1, 2017): 74–82, https://doi.org/10.1002/mrm.26490.
[70] Jiangsheng Yu, Yiqun Xue, and Hee Kwon Song, "Comparison of Lung T2* During Free-Breathing at 1.5T and 3.0T with Ultrashort Echo Time (UTE) Imaging," *Magnetic Resonance in Medicine : Official Journal of the Society of*

few milliseconds in gradient echo pulse sequences and superior to ~10 milliseconds in spin echo pulse sequences. It is therefore difficult to obtain an NMR signal from tissues with T_2 values under 10 ms[71]. The measured signal is therefore usually very low and hidden in the image noise, making the lung parenchyma details usually invisible because of the poor SNR.

Moreover, because of the fast signal decay, the standard assumption of null transverse relaxation effects during the signal readout (between the beginning and the end of the data acquisition window) usually fails for the lung parenchyma. It results in an important and unpredicted signal decrease during the MR signal readout. It leads to a wider point spread function in the image matrix, which depends on the T_2^* value of the biological tissue, the time duration of the signal acquisition window and the trajectory that is followed in k-space for the pulse sequence under consideration. This effect deteriorates the spatial resolution of the image only in the lung parenchyma. A standard lung MR image thus features several spatial resolutions depending directly on the T_2^* value of the tissue under consideration. Concerning the lung parenchyma, this effect decreases even more its MR image quality.

1.3. THE CHALLENGE OF PHYSIOLOGICAL MOTIONS INSIDE THE THORAX

The third challenge concerns motions. We have seen that lung is a living organ always in motion. Moreover, in the thorax, the heart is also in continuous motion and it creates blood flows in the arteries and veins in the lung and in the close environment of the organ. Lung and heart motions are usually quasi-periodic motions with a mean pseudo-period around 3-5 seconds (12-20 cycles per minutes) for the lung and 0.75-1 second (60-80 bpm) for the heart[72]. The blood motion depends on the type of vessels in which the blood circulates: the blood flow is usually pulsatile in the arteries and quasi-stationary in the veins. Generally speaking, if an organ is in motion during a MRI acquisition, motion artifacts can be observed in the image[73]. The aspect of those motion artifacts depends on the type of motion that occurs, but also on the MRI pulse sequence, and in particular its time parameters (TE, TR, …) and the trajectory followed in k-space. For example, standard pulse sequences with a Cartesian sampling of k-space and quasi-periodic motions usually result in images showing ghosting artifacts. In the case of a radial sampling of k-space, the same motion will lead to artifacts looking more like a smoothing around the moving organs.

For that reason, if motions are not taken into account in the imaging process of a human thorax, motion artifacts appear on the images and reduce their diagnostic value. When imaging rate cannot compete with the motion dynamics, the universal strategy to avoid or reduce motion artifacts in medical images consists in, first, capturing the motion, and second, establishing a strategy during any elementary part of the imaging process (image acquisition, image reconstruction, …) either to freeze, correct or compensate for the motion upon what was measured during the first step. The different strategies that are used and developed today to deal with motion in MRI will be presented and discussed in detail in the second chapter of this manuscript.

Lung MRI is therefore not as straightforward as it can be for other organs like the brain. To perform relevant medical images of the lung, in particular in terms of SNR, spatial resolution, and motion resolution and artifacts,

---

Magnetic Resonance in Medicine / Society of Magnetic Resonance in Medicine 66, no. 1 (July 2011): 248–54, https://doi.org/10.1002/mrm.22829.

[71] P. D. Gatehouse and G. M. Bydder, "Magnetic Resonance Imaging of Short T2 Components in Tissue," *Clinical Radiology* 58, no. 1 (January 2003): 1–19, https://doi.org/10.1053/crad.2003.1157.

[72] "Vital Signs," Cleveland Clinic, accessed January 5, 2019, https://my.clevelandclinic.org/health/articles/10881-vital-signs.

[73] Mark Hedley and Hong Yan, "Motion Artifact Suppression: A Review of Post-Processing Techniques," *Magnetic Resonance Imaging* 10, no. 4 (January 1, 1992): 627–35, https://doi.org/10.1016/0730-725X(92)90014-Q.

strategies need to be developed to go beyond standard MRI pulse sequences and adapt the modality to the special characteristics of the lung.

2. SUB-MILLISECOND TE RADIAL PULSE SEQUENCES

As seen previously, in the particular case of lung in MRI, we have to deal with three challenges:

- the low proton density ρ of the lung parenchyma;
- the low transverse relaxation times T_2/T_2^* in the lung parenchyma;
- the motion of the lung, the heart and the blood in the thorax.

An ideal pulse sequence would then be a sequence with a very high sensitivity to the MR signals produced by the nuclear spins in the lung (to compensate for the low ρ values), with a TE value being as short as possible (to minimize the SNR decrease related to the low values of T_2/T_2^*), an acquisition window duration as short as possible (to minimize the spatial resolution degradation related to the low values of T_2^*, but being careful not to increase the readout bandwidth too much to avoid a decrease in SNR), and which produces a low amount of motion artifacts and/or provides a method to solve easily the problem of motion (to avoid thoracic motions related artifacts in the MR images).

2.1. INTRODUCTION OF UTE AND ZTE PULSE SEQUENCES

To solve those issues and try to find the ideal MRI pulse sequence for lung imaging, we first need to change paradigms. In standard MRI pulse sequences, signal acquisition is based on the production of an echo, that needs at least a gradient dephasing immediately followed by a readout/refocusing gradient. Moreover, the RF excitation is usually performed with a 'sinc shaped' RF pulse, or a more complex pulse designed with the Shinnar-Le Roux (SLR) algorithm[74] for example, simultaneously to a slice selecting gradient that needs to be refocused just after its application in order to obtain a well-defined slice in the image domain. Finally, k-space acquisition is done on a Cartesian grid, by using both frequency and phase encoding gradients, which is convenient in terms of data acquisition control and flexibility, but also in terms of image reconstruction through the application of a simple FFT algorithm. All these standard characteristics avoid the possibility to obtain a TE value below approximatively one millisecond. However, we will see in the following that we do not really need all those features to create an image.

Previously, we have seen that any trajectory can be followed in k-space. To keep a good image quality without under-sampling artifacts, it will be necessary to ensure a uniform coverage of k-space, in particular without leaving 'holes' in k-space, where the signal would not be acquired. A dephasing gradient is used before the readout gradient in Cartesian imaging to read a full k-space line, on both sides of its center. If we remove it, only half of the k-space (the 'right' part of the k-space) will be acquired. One possibility is to acquire this half of the k-space and to apply exactly the same pulse sequence with sign inverted readout gradients. This strategy gives the possibility to reduce the time duration between the RF excitation pulse and the acquisition of the center part of k-space. The TE is therefore shorten by removing the dephasing gradient in the frequency encoding direction and by acquiring the most central points of the k-space at the beginning of the acquisition window.

[74] J. Pauly et al., "Parameter Relations for the Shinnar-Le Roux Selective Excitation Pulse Design Algorithm (NMR Imaging)," *IEEE Transactions on Medical Imaging* 10, no. 1 (March 1991): 53–65, https://doi.org/10.1109/42.75611.

Moreover, we are not forced to acquire the image in slices by measuring N_z 2D k-spaces. We can remove the slice selection gradient, adapt the trajectory and acquire a 3D k-space. Furthermore, the use of a phase encoding strategy is not necessary. We can just read center-out radii in k-space by applying a pure readout gradient composed of a stationary combination of G_x, G_y and G_z amplitudes at each repetition, and by changing these amplitudes during the acquisition to cover the whole k-space volume that is needed to avoid under-sampling artifacts. This type of pulse sequence, using only frequency encoding gradients along 3D center-out radii in k-space with no slice-selection or volume-selection, is usually called 3D radial pulse sequence.

In this type of pulse sequence, which is very similar to the very first one developed by Lauterbur in 1973[75], FIDs are directly measured and neither a gradient echo nor a spin echo needs to be produced: this is a clear change of paradigm compared to Cartesian pulse sequences. Nevertheless, we still call 'Echo-Time', or TE, the time between the tissue RF excitation and the signal readout, even if there is no echo. The advantage of removing all the unnecessary gradients (slice selection gradients and its refocusing lobe, phase encoding gradient and the dephasing lobe of the readout gradient) gives us the possibility to move the acquisition of the k-space center, which is done at the very beginning of the readout gradient and acquisition window, closer to the RF excitation pulse, which reduces considerably the TE and maximizes the image overall contrast.

The TE value can be even decreased by optimizing the duration of the RF excitation pulse: to do so, the best way is to use a 'square pulse', usually called 'hard pulse', which excites the whole resonant biological tissue sample covered by the excitation coil. For a given flip angle, this type of pulse is experimentally shorter than any 'sinc shaped' pulses or SLR pulses, for example. By further reducing its duration, one may be limited in flip angle because of hardware constraints, which is not a real problem here because it gives us the possibility to reduce the TR value too, without neither spin saturation effects nor Specific Absorption Rate (SAR) overtake. This key strategy is exploited in two very interesting and very similar pulse sequences called Ultrashort Echo-Time pulse sequence, or UTE, and Zero Echo-Time pulse sequence, or ZTE.

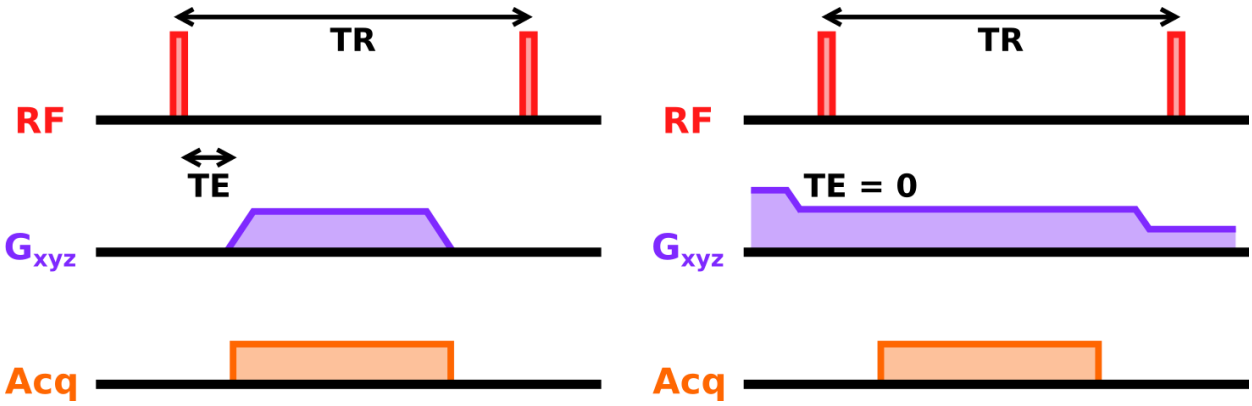

Figure 1.14: Chronograms of the UTE (left) and ZTE (right) pulse sequences.

A 2D version of UTE exists, using a slice selection gradient and half RF-pulses, and also 3D versions using a k-space trajectory which is radial along x and y and Cartesian along z, and usually referred to as 'stack of stars'. Moreover, for 3D versions of UTE pulse sequences, RF excitation can also be performed through a 'minimum-phase slab selective pulse' together with a slab selection gradient, which is similar to a slice selection gradient but with a lower

[75] P. C. Lauterbur, "Image Formation by Induced Local Interactions: Examples Employing Nuclear Magnetic Resonance," *Nature* 242, no. 5394 (March 1973): 190–91, https://doi.org/10.1038/242190a0.

gradient amplitude to select a 'slab', or a 'thick slice' of biological tissue, on which a 3D k-space is acquired. In the following, only 3D radial sequences featuring square/hard RF excitation pulses and without any slice or slab selection gradients will be discussed. In ZTE, only hard pulses are used for tissue excitation. We will see why later. Because of its appearance in a 3D graphical representation, the 3D radial trajectory is also called 'kooshball' trajectory.

UTE and ZTE pulse sequences, as said just before, are very similar (see **Figure 1.14**): they both provide a very high MR signal sensitivity because the acquisition is performed as soon as possible after the excitation, leading to a minimal incoherent dephasing of spins and a maximal amount of signal, which maximizes the image SNR. For that reason, they are particularly adapted to compensate for the low proton density ρ of the lung parenchyma and to capture its quickly decaying MR signals because of the very short T_2^* values it features. The two first challenges (i.e. short T_2^* and low proton density) of lung MRI are thus advantageously addressed. The value of such pulse sequences in short T_2^* materials is demonstrated in **Figure 1.15**.

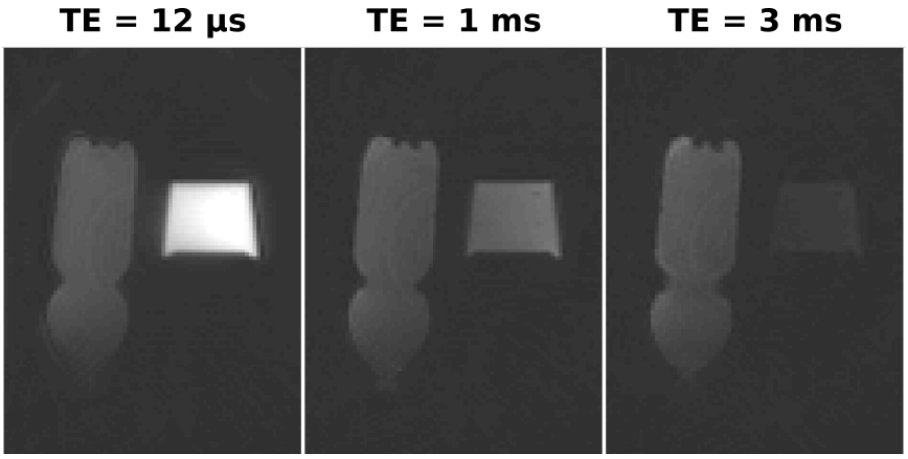

Figure 1.15: Images obtained with our UTE sequence on a bottle of water (on the left, long T_2^* of several tens of milliseconds) and on a piece of rubber (on the right, short T_2^* around 1 ms). At ultrashort TE, we clearly observe a very intense signal coming from the piece of rubber. This signal almost disappears when TE reaches a few milliseconds. The MR signal coming from the bottle of water remains almost the same over this range of TE values. For these acquisitions, TR and FA were set to 5 ms and 8° respectively.

In terms of image contrast, because of their intrinsic short TE values and low FA values, UTE and ZTE images appear naturally with a proton density contrast (and sometimes a little bit of T_1 contrast if FA is large and TR is short, as in **Figure 1.15**). Because proton density contrast is not the most useful one for medical diagnosis, UTE and ZTE pulse sequences provide preparation pulses to modify the contrast:

- It is possible to apply an inversion pulse before the RF excitation to add an inversion recovery property to UTE and ZTE, leading to a strong T_1 contrast.
- It is possible to apply a long T_2 suppression pulse, also called magnetization transfer pulse, which is a frequency shifted pulse aiming at saturating short T_2 components (which have large MR

excitation/emission bandwidth because of their short T_2^*) in tissues to transfer their magnetization to a neighbor long T_2 component and saturate it. These pulses give the possibility to obtain a T_2^* contrast[76].

- It is possible to apply a spectrally selective fat saturation pulse to saturate specifically fatty tissues in order to decrease their signal. The NMR signal of fat can indeed be very high in UTE and ZTE because of its high proton density and short T_1.

- Finally, it is possible to produce perfusion weighted images with an Arterial Spin Labelling (ASL) technique: an image, where out-of-FOV flowing spins are saturated, is subtracted to a non-saturated image[77].

2.2. MAIN DIFFERENCES BETWEEN UTE AND ZTE PULSE SEQUENCES

Despite of their numerous similarities, UTE and ZTE pulse sequences differ on a few aspects that need to be described. All those details are related to the readout gradients of both sequences. In UTE, the readout gradient is ramped-up just after the RF excitation and ramped-down just after the end of the signal readout. Signal readout often starts during frequency encoding gradient ramping to obtain a TE value as short as possible. In ZTE, in comparison to UTE, there is no readout gradient ramp-up and ramp-down. The signal readout is performed through a permanent frequency encoding gradient, which thus cannot be seen as pulsed, as it is the case in most standard MRI pulse sequences, and which is incrementally modified between the repetitions on the three gradient axes. One immediate effect of these small increments of gradient is the very low amount of sound produced when the pulse sequence is applied. In MRI, this sound is essentially generated by gradient ramping-up and down. These increments are moreover applied at the end of signal readout and before the next RF tissue excitation. This very particular way to apply readout gradients in ZTE implies several consequences for MR signal production and image acquisition compared to UTE. These differences are discussed in a great number of technical papers about UTE[78] [79] and ZTE[80] [81] [82] [83] [84] and are summarized below.

The first specificity of ZTE compared to UTE is the need to apply an excitation pulse with a large excitation bandwidth. Indeed, in UTE, the RF excitation pulse is applied to excite spins that precess at the same Larmor

[76] R. M. Henkelman, G. J. Stanisz, and S. J. Graham, "Magnetization Transfer in MRI: A Review," *NMR in Biomedicine* 14, no. 2 (2001): 57–64, https://doi.org/10.1002/nbm.683.
[77] Deibler et al., "Arterial Spin-Labeling in Routine Clinical Practice, Part 1."
[78] C J Bergin, J M Pauly, and A Macovski, "Lung Parenchyma: Projection Reconstruction MR Imaging.," *Radiology* 179, no. 3 (June 1, 1991): 777–81, https://doi.org/10.1148/radiology.179.3.2027991.
[79] Damian J. Tyler et al., "Magnetic Resonance Imaging with Ultrashort TE (UTE) PULSE Sequences: Technical Considerations," *Journal of Magnetic Resonance Imaging* 25, no. 2 (February 1, 2007): 279–89, https://doi.org/10.1002/jmri.20851.
[80] S. Hafner, "Fast Imaging in Liquids and Solids with the Back-Projection Low Angle ShoT (BLAST) Technique," *Magnetic Resonance Imaging* 12, no. 7 (January 1, 1994): 1047–51, https://doi.org/10.1016/0730-725X(94)91236-P.
[81] David P. Madio and Irving J. Lowe, "Ultra-Fast Imaging Using Low Flip Angles and Fids," *Magnetic Resonance in Medicine* 34, no. 4 (October 1995): 525–529, https://doi.org/10.1002/mrm.1910340407.
[82] Yaotang Wu et al., "Density of Organic Matrix of Native Mineralized Bone Measured by Water- and Fat-Suppressed Proton Projection MRI," *Magnetic Resonance in Medicine* 50, no. 1 (July 1, 2003): 59–68, https://doi.org/10.1002/mrm.10512.
[83] Dean O. Kuethe, Natalie L. Adolphi, and Eiichi Fukushima, "Short Data-Acquisition Times Improve Projection Images of Lung Tissue," *Magnetic Resonance in Medicine* 57, no. 6 (June 1, 2007): 1058–64, https://doi.org/10.1002/mrm.21230.
[84] Markus Weiger et al., "ZTE Imaging in Humans," *Magnetic Resonance in Medicine* 70, no. 2 (August 1, 2013): 328–32, https://doi.org/10.1002/mrm.24816.

frequency in the entire biological tissue sample. Experimentally, the Larmor frequency can vary a little bit between spins in this biological tissue sample because of B_0 inhomogeneities and the presence of frequency shifted components compared to free water, as it can be found in fatty tissues for example. Usually, an excitation bandwidth of approximatively 1000 Hz is sufficient to excite a slice or a slab of tissue[85]. The width of this slice/slab is determined by the choice of the slice/slab selection gradient amplitude. In ZTE, as it was explained just above, the RF excitation pulse is applied while the frequency encoding readout gradient is on, which imposes an excitation of spins that precess over a wide range of Larmor frequencies. More quantitatively speaking, and as explained earlier, the range of these precession frequencies in the FOV under consideration is equal to the readout bandwidth BW. For that reason, an excitation bandwidth at least equal to the readout bandwidth needs to be performed in order to ensure a uniform excitation of the piece of biological tissue comprised in the FOV. We also understand why slice or even slab selection is difficult in ZTE and why ZTE is always applied as a 3D MRI imaging technique. To perform such a wide bandwidth for tissue excitation, two main methods can be found in the literature[86]:

- The first one is based on the application of a very short square/hard pulse with a carrier frequency on resonance with the spins located in the FOV. The temporal Fourier transform of such an excitation pulse shows that its bandwidth around the carrier frequency is inversely proportional to its width in time. This type of pulse gives the possibility, after a fast transmit/receive (T/R) switching, to perform immediately the acquisition of data. Nevertheless, because of hardware constraints, this type of pulse can never achieve a flip angle FA much greater than a few degrees.

- The second one is based on the application of a swiped frequency pulse, in which the carrier frequency is modulated along time to linearly sweep from low to high temporal frequency. This type of pulse is much longer than the previous type. For that reason, and because the excitation frequency is varying along time, data acquisition can be performed during the excitation[87].

In this manuscript, we will only consider the first method for tissue excitation.

The second particularity of ZTE compared to UTE concerns the k-space trajectories followed by both sequences. In UTE, k-space radii are drawn from its center to the periphery of k-space. This is made possible by acquiring the very first data point of each radius while the readout gradient is starting to ramp-up at each repetition. In ZTE, because readout gradients are just incremented at the end of each repetition and because the tissue is excited during the application of this gradient, the center of k-space needs to be acquired at the center time of the RF excitation, which is technically impossible. For that reason, when the acquisition window starts to sample the FID, the first acquired k-space points are already out of the k-space center. At the end of the acquisition, it results in a sampled k-space spherical 'hole' located at the center of k-space and where data is missing (see **Figure 1.16**).

[85] Pauly et al., "Parameter Relations for the Shinnar-Le Roux Selective Excitation Pulse Design Algorithm (NMR Imaging)."

[86] Markus Weiger, Klaas P. Pruessmann, and Franciszek Hennel, "MRI with Zero Echo Time: Hard versus Sweep Pulse Excitation," *Magnetic Resonance in Medicine* 66, no. 2 (August 1, 2011): 379–89, https://doi.org/10.1002/mrm.22799.

[87] Djaudat Idiyatullin et al., "Fast and Quiet MRI Using a Swept Radiofrequency," *Journal of Magnetic Resonance* 181, no. 2 (August 1, 2006): 342–49, https://doi.org/10.1016/j.jmr.2006.05.014.

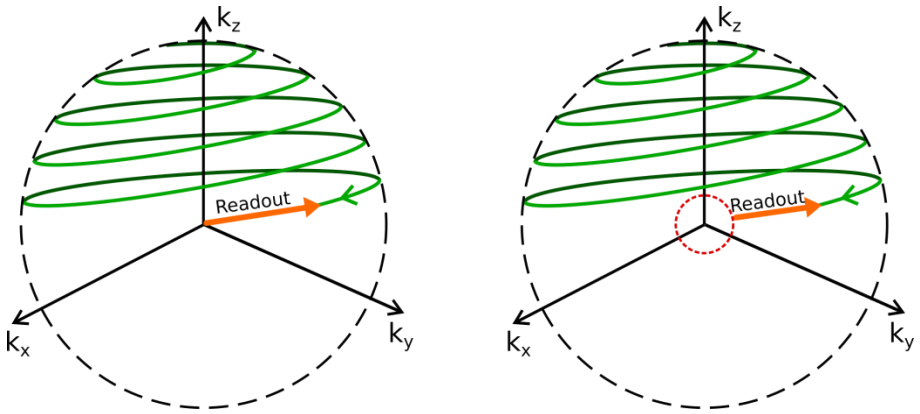

Figure 1.16: Standard 3D radial 'kooshball' trajectories followed in UTE (left) and ZTE (right) pulse sequences.

Nevertheless, the actual center of k-space is 'crossed' by the k-space trajectory at the exact same moment the RF excitation pulse is applied, and only at this particular moment because of the application of a continuous readout gradient. For that reason, the time duration TE between the center of the RF excitation pulse and the virtual acquisition of the k-space center is equal to zero, which has led to the somewhat misleading name of this sequence (Zero TE). For that reason, contrary to UTE, which usually reaches very short TE values around tens of microseconds and featuring an image contrast that corresponds to this value of TE, ZTE images feature an image contrast corresponding to a null TE, but only for tissues being excited and producing an MR signal (which is not always the case because of spin dephasing during excitation for very short T_2^* tissues, resulting in a decreased actual flip angle compared to the prescribed flip angle) and for which signals are at least partly acquired in the acquisition window. This last consideration can be illustrated by a very short T_2^* tissue or material (i.e. T_2^* < 1 µs) that would produce a tiny MR signal because of its inefficient excitation and that would not be even acquired because the T_2^* is shorter than the T/R switching time duration of the MRI machine (around 10 µs): in this case, even if we have a zero TE contrast, this very short T_2^* tissue cannot be seen in the image, which puts the concept of 'zero TE' in perspectives. Even for T/R switching durations of the order of T_2^*, enabling the acquisition of signal from the material under consideration, this T_2^* decay will remain strong during the signal acquisition, leading to a deterioration of the image spatial resolution and compromising the possibility to even see correctly the tissue in the image, as explained in 1.2. If the number of missing points at the center of k-space is too important, the image cannot be correctly reconstructed from the acquired k-space. In this case, several solutions can be considered:

- A first one consists in estimating the missing k-space points either by considering the acquired values of their neighbors or by assuming prior image characteristics.
- A second one is based on the acquisition of the missing data with the same type of trajectory but with reduced readout gradient amplitudes and a lower number of radii: this method is usually called WASPI.
- A third method consists in performing a pointwise acquisition of the missing points in k-space with a NMR signal spatial localization only based on phase encoding: this method is usually called PETRA.

If one of those previous methods needs to be performed to avoid low spatial frequency artifacts in the final image, it cannot be done within the acquisition of the outer k-space domain but as an offline process or as an additional pulse sequence implementation. Moreover, before image reconstruction, an additional processing step is needed in order to merge both parts of k-space: the acquired outer k-space part and the estimated or acquired center k-space region part.

The third specificity of ZTE compared to UTE is the global constraints imposed by the continuous readout gradients. Because these gradients are incremented instead of being ramped-up and down at each repetition, it is difficult to perform more things than just exciting the tissue and acquire the signal. For example, it is difficult to apply a crusher at the end of each repetition to spoil the remaining transverse magnetization. For that reason, the only way to avoid image artifacts because of this remaining transverse magnetization is to choose small increments of readout gradients at the end of each repetition: in this case, the remaining signal created during the previous repetitions and measured during the actual repetition results from spins that go on dephasing, thus producing a negligible signal. In this situation, we observe that readout gradients play also a role of crusher. Another constraint is the difficulty to apply preparation pulses to perform, for example, inversion recovery or chemical shift selective fat saturation. One possible solution to this problem is to divide the pulse sequence into segments of several tens of repetitions inside which the readout gradient is slightly incremented at the end of each repetition (see **Figure 1.14**, on the right) and at the end of which the readout gradient is ramped-down, before being ramped-up for the next segment. Between two segments, it is then possible to include one or several preparation pulses[88].

To wrap up the comparison, in UTE, there is an intrinsic solution to the third challenge we mentioned about MR lung imaging, which is related to the physiological motions inside the thorax during the acquisition, in particular respiratory and cardiac motions. First, radial trajectories are known to be very robust to motion artifacts, as explained in the next chapter. Moreover, thanks to this radial trajectory followed in k-space during an UTE acquisition, an easy solution is provided to follow this motion along the whole duration of the acquisition and directly from k-space data.

In the next chapter, we will see how this is working, what type of information we can obtain from this technique and how we can then avoid motion artifacts in the images. We will also understand how these strategies can be adapted to ZTE to a certain extent. All these considerations will be taken into account, amongst others, to choose the best pulse sequence between UTE and ZTE for one given lung MRI application.

[88] Florian Wiesinger et al., "Zero TE MR Bone Imaging in the Head," *Magnetic Resonance in Medicine* 75, no. 1 (January 1, 2016): 107–14, https://doi.org/10.1002/mrm.25545.

CHAPTER 2 - INNOVATIVE DEVELOPMENTS IN THE FIELD OF SELF-NAVIGATION AND SELF-GATING FOR UTE AND ZTE IMAGING OF THE LUNG

IN THIS CHAPTER, WE WILL FIRST INTRODUCE THE NOTIONS OF MOTION FIELD, MOTION MODEL, SURROGATE SIGNAL AND SELF-NAVIGATION. THROUGH A FEW REPRESENTATIVE EXAMPLES OF MOTION CORRECTION TECHNIQUES TAKEN FROM THE LITERATURE, WE WILL SEE THE CENTRAL ROLE OF THE SURROGATE SIGNAL IN MOTION CORRECTED MRI. THEN, WE WILL STUDY THE IMPROVEMENT BROUGHT BY THREE INNOVATIONS DEVELOPED DURING THIS THESIS. THE FIRST ONE, CALLED SNIF, IS A METHOD AIMING AT FILTERING THE SELF-NAVIGATION SIGNAL EXTRACTED FROM QUASI-RANDOM UTE ACQUISITION. THE SECOND ONE, CALLED SNOZE, IS A METHOD THAT EXTRACTS A SELF-NAVIGATOR FROM ZTE ACQUISITIONS SIMILARLY TO WHAT CAN BE DONE IN UTE. FINALLY, THE THIRD ONE, CALLED AZTEK, IS A NEW K-SPACE TRAJECTORY DESIGNED TO BE ADAPTED BOTH TO ZTE PULSE SEQUENCE REQUIREMENTS AND MOTION CORRECTION.

SECTION 1 MOTION TRACKING AND CORRECTION IN MRI

PERFORMING MRI OF THE RESPIRATORY MECHANICS REQUIRES DEALING WITH MOTION IN THE COURSE OF THE IMAGING PROCESS. IN THIS FIRST SECTION, WE WILL SEE ABOUT WHAT MOTIONS WE ARE TALKING AND WHY IT IS IMPORTANT TO TAKE THEM INTO ACCOUNT. ON THE WAY, WE WILL DESCRIBE THE DIFFERENT TECHNIQUES AVAILABLE IN CLINICAL ROUTINE OR PROPOSED IN THE LITERATURE.WE WILL EVENTUALLY SEE THAT MOTION IS NOT ONLY A CHALLENGE TO OVERCOME BUT ALSO AN OPPORTUNITY TO ACCESS TO NEW INFORMATION. WE WILL INTRODUCE A VERY IMPORTANT CONCEPT IN THE FIELD OF MOTION TRACKING AND MOTION MODELLING: THE SURROGATE SIGNAL.

1. MOTION IN MRI: A SOURCE OF TROUBLESOME ARTIFACT OR USEFUL CLINICAL INFORMATION?

Motion is a displacement of matter from one spatial position to another one during a given period of time and relatively to a reference frame. For a given material system, composed of one or several bodies, the motion can be rigid and therefore described through translations and rotations. In this case, the global position and the orientation of the system are changed but neither its shape nor the relative positions of the different bodies composing the system are modified. The motion can be non-rigid and include changes in the relative positions of bodies or even changes in the shape of the bodies, which is usually referred to as deformation. This definition does not include any concept of force or stress. Therefore, the concept of motion comes from kinematics, a branch of mechanics.

When a MRI acquisition is performed on living tissues or phantoms, motion can occur at different scales, from physical motions of body parts at macroscopic scales to the diffusion of water molecules at microscopic scales. Moreover, as it will be seen in the last chapter of this manuscript, motion can be induced by an external source for excitation and measurement purposes. In this special case, motion is not proper to the subject under consideration but induced to it. From a very applicative point of view in the field of MRI, those different types of motions can be classified, but not exclusively, into two main categories:

- **Deleterious motions:** One very large field of research in MRI, and in medical imaging more generally, consists in studying the negative impact of motions on the imaging procedure and mostly to find technical solutions to reduce or suppress their effects on images. As addressed later in this chapter, motions inside or surrounding the subject or organ of interest can induce motion artifacts in the final images so motion correction or compensation strategies are needed to avoid them. For example, a significant displacement of the body part under consideration during the MRI exam can produce a drastic degradation of the MR image quality. To preserve it, a strategy needs to be developed either to avoid this type of motion during the imaging process or to correct it either prospectively during the acquisition process or retrospectively afterwards.

- **Informative motions:** Several other fields of research in MRI focus on the study of motion either physiological or physical. They aim at developing techniques not to suppress their effects but to emphasize their effects and study them. They usually promote techniques to enhance these motions of interest in the

MR images and quantitatively measure them with MRI. For example, the diffusion of water molecules within tissues can be of great interest to detect and characterize some diseases (strokes, for example), but also to indirectly study the microstructure of tissues. Basic MR imaging techniques are poorly sensitive to diffusion processes. By implementing motion encoding gradients to the MR pulse sequence, diffusion of water molecules becomes quantifiable and advanced acquisition and post-processing strategies were developed to extract the diffusion motion.

The concept of motion can be detrimental or beneficial in MRI depending on the subject of interest, but also on the related methodological approach. In this way, diffusion motion discussed just above can also be problematic in pure anatomical MRI for example, as this motion may lead to signal amplitude decreases in the final image through the unavoidable use of position encoding gradients. In this manuscript, the subject of interest is the study of respiratory mechanics with MRI. As explained in the first chapter of this manuscript, the notion of respiratory dynamics refers to two main topics that were shown to be potentially related to lung function and pathophysiological state:

- **Mechanical behavior of the lung:** Estimated essentially through the study of pulmonary physiological motions, this topic will be covered in the third chapter of this manuscript.
- **Mechanical properties of the lung:** Estimated essentially through mechanical tests performed onto the lung, this topic will be covered in the fourth chapter of this manuscript.

Lung MRI is challenging because of physiological motions, especially respiratory and cardiac motions. In these lines, different types of motions in the lung, physiologically and remotely induced, will be studied here with MRI. In this manuscript, a third type of motion, related to flowing blood, will be minimally studied. As discussed later, this motion has a limited impact on the developed imaging techniques.

A dual role is played by respiratory motion, which will be at the same time a challenge to address and a source of information to explore. However, as many advanced MRI applications, the study of mechanical behavior and mechanical properties of the lung will be based on standard MRI pulse sequences made originally to perform anatomical images. Because anatomical imaging is, in the general case, concerned by the problem of motion artifacts, and in particular respiratory and cardiac motions artifacts, the first step of the doctoral project will be to find adapted solutions to deal with those two motions, and in particular with respiratory motion.

2. THE BASIC CONCEPTS OF MOTION CORRECTION IN MRI AND THE PRIMORDAL ROLE OF THE SURROGATE SIGNAL

Respiratory and cardiac motions are of the same type: they are both macroscopic physiological motions characterized by a deformation varying quasi-periodically with time. Hence, similar strategies can be considered to overcome their effects on anatomical images. One thing to keep in mind is that, because of the physical proximity of the lung and the heart in the human body, mutual deformations are generated by the two organs. The great difference between those two motions is found, as previously seen, in their motion periods: around 3-5 seconds for the lung and 0.75-1 second for the heart in healthy human adult. Besides, the subject can willingly take control over the respiratory motion by contracting the diaphragm and intercostal muscles whereas she or he does not have direct access to control the heart motion as it is induced by the depolarization of myocardial cells.

2.1. MATHEMATICAL MODELING OF A MOTION

A good and largely approved model to represent the evolutions along space and time of respiratory and cardiac motions is to define one, and only one, 3D vector field $\vec{u}(X,Y,Z,t)$. In this representation, X, Y and Z represent spatial positions in a given 3D coordinate system. This system is usually chosen as a direct orthonormal coordinate system, the same as the one in which the spatial components of $\vec{u}$, written u_x, u_y and u_z, will be described. t represents the time passed from a given time origin, which can be chosen as the beginning of the MR acquisition for example. Because only the subject located inside the MRI machine is considered, the spatial coordinates introduced above are usually defined only in the image FOV.

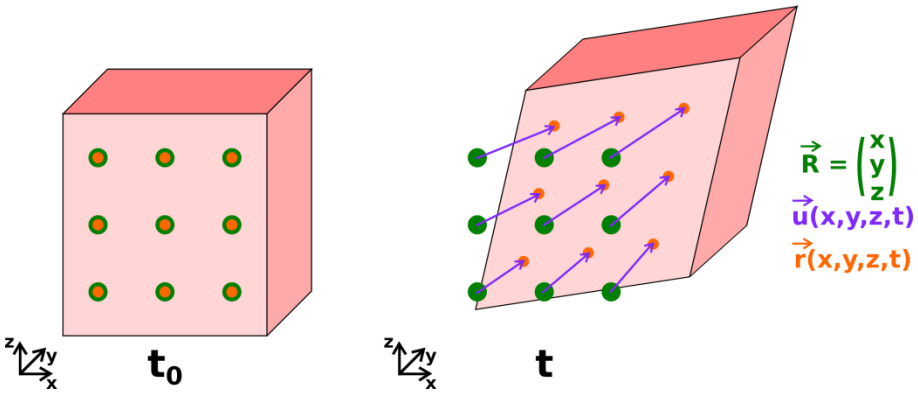

Figure 2.1: Illustration of the Lagrangian formulation of motion fields and definition of the main vector fields related to this representation.

To make the link between the abstract mathematical object $\vec{u}$ and the underlying physics, $\vec{u}(X,Y,Z,t)$ should be seen as the displacement of the infinitesimal volume of matter which was located at spatial coordinates (X,Y,Z) at time t_0. At this special time, taken as a reference, the vector field $\vec{u}$ is therefore null everywhere in the subject. This type of description is usually referred to as Lagrangian formulation (contrary to the Eulerian formulation). In this type of description, each infinitesimal volume of matter is 'followed' along time relatively to a reference state reached (or not, in a more general case) at a given reference time point t_0. More explicitly, if $\vec{R} = \begin{bmatrix} X \\ Y \\ Z \end{bmatrix}$ represents the position vector of a given infinitesimal volume of matter at time t_0, the position vector of this same volume of matter at time t is given by (see **Figure 2.1**):

$$\begin{aligned} \vec{r}(X,Y,Z,t) &= \begin{bmatrix} x(X,Y,Z,t) \\ y(X,Y,Z,t) \\ z(X,Y,Z,t) \end{bmatrix} \\ &= \vec{R} + \vec{u}(X,Y,Z,t) \\ &= \begin{bmatrix} X + u_x(X,Y,Z,t) \\ Y + u_y(X,Y,Z,t) \\ Z + u_z(X,Y,Z,t) \end{bmatrix} \end{aligned} \qquad \textbf{Eq. 2.1}$$

This vector field is not necessarily spatially continuous: 'sliding' motions may exist (which will be useful to represent the motion at the interface between the parietal pleura and the visceral pleura in the thorax, or the motion at the interface between the lung and the heart, for example). However, for physical purposes (infinite velocities and accelerations do not exist in physics), the different spatial components of this vector field will vary quite regularly

along time (at least C^2 in time). Usually, the vector field $\vec{u}(X,Y,Z,t)$ will be referred to as the motion field or the displacement field in the following and in the literature, whereas $\vec{r}$ is usually called deformation field. Finally, it is important to consider that this representation is a simplified model: diffusion of water molecules within the tissue for example is not included. Nevertheless, this representation is far sufficient for our applications.

2.2. THE EFFECTS OF MOTION IN MRI

2.2.1. INTRA-VIEW AND INTER-VIEW EFFECTS OF MOTION

An MR image is generated after recording temporal signals along an acquisition process, referred in the previous chapter to as views, with one view every TR. Within some approximations, those views were shown to be subsets of the k-space for one given MR image. If enough different views, or subsets of k-space, are recorded during the acquisition process, and if those views cover sufficiently well the k-space at coordinates where information corresponding to the reciprocal image of interest is found, it becomes possible to reconstruct a MR image. However, the different measurement points from the many views acquired during the imaging process must correspond to subsets of the same k-space, thus related to the same MR image. If a motion occurs during the acquisition, those considerations may be compromised. More precisely, it is necessary to distinguish between two types of effects[89] [90]:

- **Intra-view effects:** Those effects appear when a motion occurs during one repetition in the pulse sequence, and in particular during the position encoding and acquisition of one view[91]. Because of the relatively slow time evolutions of the motions under consideration here (respiratory and cardiac motions) and thanks to the very short TR values we will use in the following, we will neglect those effects.

- **Inter-view effects:** Those effects appear when a motion occurs between repetitions in the pulse sequence, and thus between the acquisitions of different views[92]. In a simple approach, the different views are acquired from different spatial spin configurations because of motion, and therefore correspond to different static MR images. When image reconstruction is performed after data acquisition, those different subsets of k-space are not coherent to each other anymore, leading to undesired effects in the image domain, which are usually referred to as motion artifacts.

[89] Mark Hedley and Hong Yan, "Motion Artifact Suppression: A Review of Post-Processing Techniques," *Magnetic Resonance Imaging* 10, no. 4 (January 1, 1992): 627–35, https://doi.org/10.1016/0730-725X(92)90014-Q.
[90] Qing-San Xiang and R. Mark Henkelman, "K-Space Description for MR Imaging of Dynamic Objects," *Magnetic Resonance in Medicine* 29, no. 3 (1993): 422–28, https://doi.org/10.1002/mrm.1910290324.
[91] Van J. Wedeen, Richard E. Wendt, and Michael Jerosch-Herold, "Motional Phase Artifacts in Fourier Transform MRI," *Magnetic Resonance in Medicine* 11, no. 1 (1989): 114–20, https://doi.org/10.1002/mrm.1910110110.
[92] Pippa Storey et al., "Band Artifacts Due to Bulk Motion," *Magnetic Resonance in Medicine* 48, no. 6 (2002): 1028–36, https://doi.org/10.1002/mrm.10314.

2.2.2. NOTIONS OF MOTION BLURRING ANG GHOSTING IN MRI

In the final MR image, the (inter-view) motion artifacts appear through two different visible effects[93] [94]:

- **Motion blurring:** This effect is characterized by a local degradation in image spatial resolution, which becomes worse than the voxel size. Thus, boundaries between different types of tissues or organs, which would be sharp without motion, now appear more diffuse. Moreover, small objects in close spatial proximity that were distinguishable in the MR image without motion now cannot be separated, and they even sometimes become invisible. This blurring appears in the direction of motion.

- **Motion ghosting:** The term ghosting refers to the presence of mirage structures appearing in the image and usually corresponding to objects in motion whose representations in the image repeat in the directions orthogonal to the views. Because 2D MR imaging is usually performed in Cartesian mode by acquiring views in k-space with different amplitudes of phase encoding gradients, the ghosts usually appear along the phase encoding direction. The appearance of those structured repetitions (sharp ghosts or more diffuse artifacts) and their spatial localization are related to both the time evolution of the motion causing this artifact and to the rate at which the views are acquired (usually related to the TR).

2.3. BASIC TECHNIQUES TO AVOID MOTION ARTIFACTS IN MR IMAGES

2.3.1. NATURAL ROBUSTNESS TO MOTION ARTIFACTS OF UTE AND ZTE PULSE SEQUENCES

For our applications in lung imaging, we focus on two pulse sequences: Ultrashort Time-Echo (UTE) and Zero Time-Echo (ZTE). Those two pulse sequences share one common feature: the purely radial exploration of a 3D k-space. Therefore, the views take the form of radii in k-space starting from the low spatial frequency center (or close to the center for ZTE) of k-space and finishing in the high spatial frequency domain of the k-space. This strategy uniquely based on frequency encoding, in comparison to the standard method combining frequency and phase encoding in 2D or 3D Cartesian acquisitions, is highly relevant for moving organs in the sense that the obtained images are usually robust to motion artifacts. This robustness can be explained along the following three aspects[95]:

- The first one is related to the oversampling of the k-space center. This oversampling occurs because every view record information in the central region of k-space. In a basic radial sampling scheme, the exact center of k-space is even sampled at each pulse sequence repetition. Whereas in Cartesian imaging, the sampling density in k-space is the same everywhere, it is oversampled at the center of k-space in radial imaging, which leads to averaging effects between the different states of motion, in particular for the bulk motion of large organs.

- The second one is related to the appearance of ghosting motion artifacts in radially acquired images. As seen in 2.2.2, motion artifacts in standard Cartesian imaging appear as blurring in the direction of motion and ghost images along the directions orthogonal to the acquisition of each view, which is often the phase encoding direction. In radial acquisitions, there is no phase encoding and the direction of each view in the

[93] Michael L. Wood and R. Mark Henkelman, "MR Image Artifacts from Periodic Motion," *Medical Physics* 12, no. 2 (1985): 143–51, https://doi.org/10.1118/1.595782.
[94] L Axel et al., "Respiratory Effects in Two-Dimensional Fourier Transform MR Imaging.," *Radiology* 160, no. 3 (September 1, 1986): 795–801, https://doi.org/10.1148/radiology.160.3.3737920.
[95] G. H. Glover and J. M. Pauly, "Projection Reconstruction Techniques for Reduction of Motion Effects in MRI," *Magnetic Resonance in Medicine* 28, no. 2 (1992): 275–89, https://doi.org/10.1002/mrm.1910280209.

k-space is different for each view. For that reason, the intensity corresponding to motion ghosts in radial imaging is spread in the entire image surface or volume and is thus diluted in the entire image. The artifacts are thus less visible compared to the ones obtained in Cartesian imaging, where the artifact intensity is only oriented along one direction and appears as coherent ghost structures. Motion ghosts in radial imaging usually appears as radial streaks, with an intensity lower close to the moving object and which increases far from this object.

- The third aspect is related to the location where the ghosting motion artifacts are observed. It can be shown that streaks are more intense in the direction orthogonal to motion. For that reason, the streaks are usually out of the organs and thus do not hinder the detection of structures or lesions of interest.

Nevertheless, even if the ghosting artifacts are not such a problem for our two sequences of interest, motion blur remains. For that reason, if the motion is not taken into account either during the acquisition or during the reconstruction process, small structures and other image features characterized by high spatial frequencies will not be detected. In the following, we will thus study the different strategies available to limit motion blurring, from the more basic to the more advanced ones.

2.3.2. REDUCTION OF PHYSIOLOGICAL MOTION AMPLITUDE

Motion blurring increases with the motion amplitude of a given organ (of the lung or the heart in our case). One solution to decrease this effect is to reduce the motion amplitude. This can be done by asking to the patient to perform one or several breath-holds during the imaging process. The patient can also be asked to slowly breathe and to inhale only small volumes of air. One last solution to reduce respiratory motion can be to restrain the subject by strapping the chest to the MRI bed.

However, those techniques require either the patient's cooperation or tolerance. Moreover, it concerns only motions that can be controlled, like the respiratory motion for example, but not cardiac motion. Furthermore, in our applications, we want to suppress the motion artifacts in the images, not the motions themselves because these motions are a valuable source of information. Consequently, those methods are not suited to our project but are usually considered in clinical routine for standard thoracic and abdominal imaging exams.

2.3.3. SPECIAL CASE OF ULTRAFAST MR IMAGING TECHNIQUES

Another technique does not consist in avoiding the motion itself but in being at the same motion field state for each view. A way to do it is to use ultra-fast imaging techniques, like EPI for example, in order to acquire one single image in a period of time shorter that the characteristic evolution time of motion. However, those ultrafast imaging techniques are usually limited to 2D imaging, and 3D imaging can only be assessed by repeating the same 2D acquisition techniques several times in this situation. This leads to a 'motion freezing' for each 2D image but not for the entire 3D image at the exact same motion field state.

2.3.4. PROSPECTIVE AND RETROSPECTIVE GATING TECHNIQUES

Another approach relies on the repetition of the motion. The motion may be 'freezed' by organizing the acquisition and/or the reconstruction process in order to have virtually no motion in the body of the patient within the data set. Those techniques are usually referred to as gating or binning techniques and give the possibility to artificially 'freeze' the motion. There are essentially two types of gating (see **Figure 2.2**):

- **Prospective gating:** MR data is acquired only when the motion field reaches a given state. For example, this state can be the end of expiration for respiratory motion or the diastole for the heart motion. The

major part of the strategy is thus concentrated on the image acquisition process, which is composed of an alternation between data acquisition periods and waiting periods.

- **Retrospective gating:** MR data is acquired in continuous mode, without any motion consideration. However, during the reconstruction step, the acquired data are sorted into gates (or bins), with one motion gate per representative motion field state. The different motion gates are then reconstructed separately to give one separate image per motion gate. For that reason, the major part of the strategy is concentrated in post-processing steps, even if techniques exist to take into account the motion during the acquisition process too (in cine cardiac imaging for example, where the same view in k-space is acquired several times during one heart beat in order to have enough data at the end of the acquisition to reconstruct properly each prospective motion gate).

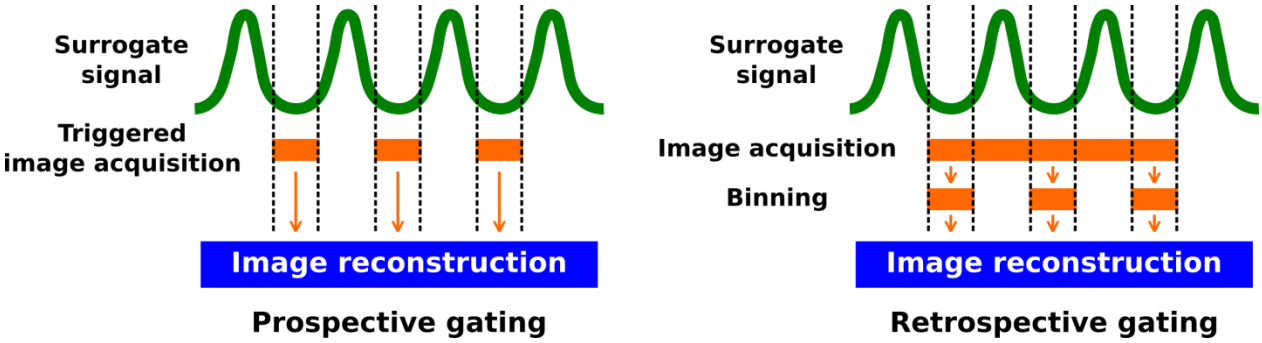

Figure 2.2: Illustration of the principles of prospective and retrospective gating techniques.

These two techniques are particularly adapted to lung and heart motions because of their quasi-periodicity: approximatively the same motion field states are retrieved at each motion cycle. Enough data can thus be accumulated for one or several motion gates, either in prospective or retrospective mode. However, for both types of motion and for the two strategies described above, it is necessary to know how the motion field evolves along time to properly perform any gating. But the motion field itself is a very complex vector field and it cannot be easily measured in the general case. Thankfully, respiratory and cardiac motions are quasi-periodic. Therefore the information upon the motion field state is redundant and can be largely 'compressed' in one or several temporally varying signals, which are sometimes referred to as surrogate signals.

2.3.5. NOTION OF SURROGATE SIGNAL

A surrogate signal, in its general form, can be defined as a temporally varying signal which is highly correlated to the time evolution of the motion field of an organ. For example, the time evolution of the periphery of the thorax and/or the abdomen of a patient can be considered as a surrogate signal for respiratory motion. A perfect surrogate signal would be a signal that varies with the motion field with a one-to-one correspondence between them. Usually, such a perfect surrogate signal does not exist but the one-to-one relationship can be an approximation, which is sometimes sufficient to solve a given problem. Another solution might be to use several surrogate signals from simultaneous different measurement sources in order to get a closer one-to-one correspondence between the actual motion field and the set of surrogate signals. Because of their capital role in gating processes (and also in other motion correction methods, as explained below), we will further study the concept of surrogate signal later.

2.4. ADVANCED TECHNIQUES TO AVOID MOTION ARTIFACTS IN MR IMAGES

So far, only techniques to freeze or attenuate the motion either mechanically or virtually have been discussed. Those techniques do not 'compensate' for the motion or 'correct' the motion, but just attenuate its effects in images by acting on the motion itself or by adapting the imaging process to its basic temporal features. Theoretically, it has been demonstrated that if the vector field $\vec{u}$ is known for each voxel position and for the time position of each view, the motion artifacts can be directly corrected in the acquired k-space before the reconstruction[96]. This does not depend neither on the type of motion nor on the type of pulse sequence under consideration but the motion field needs to be known during the entire data acquisition process. And it is very difficult if not impossible to entirely measure the 3D motion field in the region of interest at the same time as the MR data. A simplifying model of the motion may be used instead.

2.4.1. NOTION OF MOTION MODEL

An excellent review on respiratory motion models was written several years ago by McClelland *et al.*[97]. This review introduces very well the concept of respiratory motion model both for diagnostic medical imaging and interventional imaging. It provides an overview of the research projects that were held over the last 15 years in this domain. Moreover, most of the concepts introduced in this review are adapted to cardiac motion. In the following, I will make a non-exhaustive summary of this review by focusing on our purposes and give a list of the most remarkable examples of model based motion correction techniques.

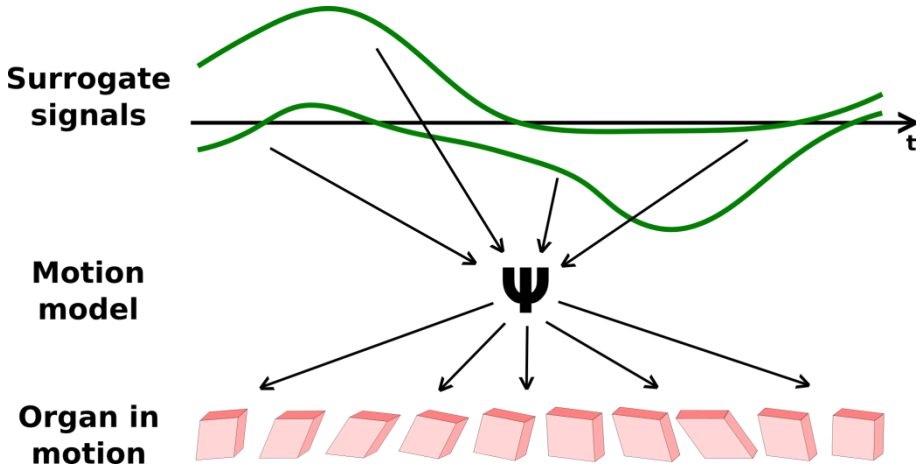

Figure 2.3: Definition of a motion model Ψ.

This review defines a motion model as a process Ψ that takes some surrogate data for input and produces some motion estimates for output (see **Figure 2.3**). To build a motion model, four choices are usually made:

1. The choice of one or several surrogate signals,
2. The choice of a simplified representation for the motion,

[96] P. G. Batchelor et al., "Matrix Description of General Motion Correction Applied to Multishot Images," *Magnetic Resonance in Medicine* 54, no. 5 (November 2005): 1273–1280, https://doi.org/10.1002/mrm.20656.
[97] J. R. McClelland et al., "Respiratory Motion Models: A Review," *Medical Image Analysis* 17, no. 1 (January 2013): 19–42, https://doi.org/10.1016/j.media.2012.09.005.

3. The choice of a method to estimate the relationship between the surrogate signal(s) and the motion representation, and
4. The choice of the relationship between the surrogate signal(s) and the motion representation.

2.4.2. MOTION CORRECTION TECHNIQUES BASED ON THE CONSTRUCTION OF A MOTION MODEL

Once the choices above are made and once the MR exam to correct from the motion is chosen, the motion model needs to be constructed and applied to the imaging process. Four main strategies can be considered:

- **Constructing the motion model before the MR acquisition and then applying it during the data acquisition process:** This type of approach is usually referred to as a prospective. In this case, the first step consists in constructing the motion model. It is usually based on the acquisition of temporally resolved medical images (ultra-fast MRI, CT, …) at the same time as one or several surrogate signals. From those two sets of data, surrogate and motion data, the motion model is constructed by estimating the relationship between both. The second step consists in applying in 'real-time' the motion model during the image acquisition process. As explained in the first chapter, the geometrical parameters of the MR image (slice position and width, FOV position and size, …) can be modulated by tuning the RF excitation frequency and the amplitude of the position encoding gradients. It is thus possible, thanks to the instantaneous value of the surrogate signal(s), to estimate the instantaneous motion field, from which an optimal setting of RF and gradients can be deduced for the view to be acquired in order to compensate for the motion. After the acquisition, the acquired k-space will be, in the ideal case, free of motion artifacts and can thus be directly reconstructed by applying a standard reconstruction algorithm. However, the motion correction remains limited to affine motion fields (translations, rotations, zoom and shearing). The first technical implementation of such a prospective motion correction technique was proposed by Nehrke *et al.*[98], based on observations made ten years before by Wang *et al.*[99]. The aim of their work was to correct the quasi-translational motion of the heart induced by respiration. To correct for this motion, which is supposed to be purely affine, a calibration sequence generating series of low-resolution 3D images with a good time resolution, is first applied before making the link between several surrogates signals (navigator echoes here) and the patient specific motion field estimated from these images. On each 3D low-resolution image, as described above, the motion is frozen. Once the motion model is learnt, it can be used in any MR pulse sequence to correct the position encoding gradients and RF excitation pulses in 'real-time' from the same surrogate signals measured and analyzed during the MR acquisition.

- **Constructing the motion model before the MR acquisition and then applying it during a post-processing step:** This type of approach is usually referred to as a retrospective. In this case, the first step consists in learning the motion model, as explained in the first strategy. However, instead of directly using it in the acquisition process, the imaging data and the surrogate signal(s) are just acquired continuously without taking into account the surrogate signal(s). The motion model is then exploited to estimate the time evolution of the motion field during the image acquisition thanks to the surrogate signal(s). The motion estimation is thus done as a post-processing step. Finally, the estimated motion field can be exploited to correct for the motion artifacts directly in the image k-space before or during the reconstruction. The

[98] Kay Nehrke and Peter Börnert, "Prospective Correction of Affine Motion for Arbitrary MR Sequences on a Clinical Scanner," *Magnetic Resonance in Medicine* 54, no. 5 (2005): 1130–38, https://doi.org/10.1002/mrm.20686.
[99] Yi Wang, Stephen J. Riederer, and Richard L. Ehman, "Respiratory Motion of the Heart: Kinematics and the Implications for the Spatial Resolution in Coronary Imaging," *Magnetic Resonance in Medicine* 33, no. 5 (1995): 713–19, https://doi.org/10.1002/mrm.1910330517.

advantage compared to the previous technique is that non-affine motion fields can be taken into account (which is more relevant for respiratory and cardiac motions) and it can be done for any standard pulse sequence. This strategy is well explained by Odille *et al.*[100] for respiratory motion correction. In their study, and similarly to what was proposed previously in prospective motion correction, a fast pulse sequence (bSSFP) was used to obtain 3.6 2D images per second during several periods of motion as a calibration step. An elastic motion model based on the displacement of control points chosen on a Cartesian grid was learned between these quasi-instantaneous images and the corresponding surrogate signals composed of the outputs of two respiratory belts (one for the thorax and one for the abdomen), one ECG system and their first time derivatives. For this, it was supposed that the motion of any control point along any spatial direction could be approximated as a linear combination of the surrogate signals, the coefficients of this linear combination being the parameters to learn during the model building step. Moreover, it was supposed that two neighboring control points should follow similar displacements, which was explained by the continuous elastic properties of the material, and introduced as a regularization term in the motion model learning process. This model was then exploited to retrospectively correct the motion during the image reconstruction process by taking as inputs the acquired k-space data of interest and the same surrogates signals acquired during the acquisition process.

- **Constructing the motion model during the acquisition process:** In this case, the acquisition of data dedicated to the construction of the motion model and to the generation of the final MR image is done simultaneously. Sometimes, data needed to build the motion model is extracted from the imaging data itself. In this case, the calibration step that was seen in both techniques described above is not needed here. This strategy was implemented for PROPELLER (Periodically Rotated Overlapping ParallEL Lines with Enhanced Reconstruction) MRI[101]. In this technique, k-space data is acquired with a very special trajectory composed of segments usually referred to as 'blades'. Those blades are composed of several Cartesian k-space lines spanned around the center of k-space and oriented along one given direction. The k-space is fully covered by acquiring several blades with different orientations. During the acquisition of each blade, the central region of k-space is sampled and a low-resolution image can be estimated from it. As a post-processing step, k-space center position, bulk rotations, bulk translations and through plane motion can be corrected within the Fourier domain thanks to this frequently sampled region around the k-space center. A motion-corrected image is thus reconstructed from the corrected k-space. Another more advanced way to do it is to include the correction of motion artifacts directly within the image reconstruction step, as proposed in the Augmented SENSE reconstruction method[102]. The effectiveness of this strategy was proven for head motion but also for the respiratory-induced motion of the heart. Finally, a 'real-time' estimation of a motion model can be imagined in order to make prediction on future physiological motion cycles and therefore perform optimized prospective gating, as it was demonstrated a few years ago for cardiac imaging[103].

[100] Freddy Odille et al., "Generalized MRI Reconstruction Including Elastic Physiological Motion and Coil Sensitivity Encoding," *Magnetic Resonance in Medicine* 59, no. 6 (2008): 1401–11, https://doi.org/10.1002/mrm.21520.
[101] James G. Pipe, "Motion Correction with PROPELLER MRI: Application to Head Motion and Free-Breathing Cardiac Imaging," *Magnetic Resonance in Medicine* 42, no. 5 (1999): 963–69, https://doi.org/10.1002/(SICI)1522-2594(199911)42:5<963::AID-MRM17>3.0.CO;2-L.
[102] Roland Bammer, Murat Aksoy, and Chunlei Liu, "Augmented Generalized SENSE Reconstruction to Correct for Rigid Body Motion," *Magnetic Resonance in Medicine* 57, no. 1 (January 2007): 90–102, https://doi.org/10.1002/mrm.21106.
[103] Brice Fernandez et al., "Adaptive Black Blood Fast Spin Echo for End-Systolic Rest Cardiac Imaging," *Magnetic Resonance in Medicine* 64, no. 6 (2010): 1760–71, https://doi.org/10.1002/mrm.22566.

- **Constructing the motion model during a post-processing step:** In this last case, the acquisition of imaging data with one or several surrogate signals is done in a standard way. However, both the estimation of the motion model and its exploitation are performed during the same post-processing task. One of the best examples of this strategy is the technique referred to as GRICS (Generalized Reconstruction by Inversion of Coupled Systems)[104]. In this algorithm, both the motion model and the motion-corrected image are iteratively estimated from the same k-space dataset, the corresponding surrogate signals and an initial motion model, estimated either from a calibration step as seen above or progressively estimated without prior knowledge thanks to a multi-resolution strategy. The elastic motion model is similar to the one described above for retrospective motion correction, but it is included in the multi-resolution strategy instead of being applied on a Cartesian grid of control points. Two coupled inverse problems are thus solved at the same time and lead to the desired optimally motion-corrected image and an optimal motion model directly estimated from the imaging data. The efficiency of this technique was demonstrated for the correction of respiratory motion on ECG trigged thoracic MR acquisitions in free-breathing.

The previous description of motion correction techniques is not supposed to give an exhaustive panel of what has been developed in the field during the last decades of research in model-based motion correction but instead to understand representative examples of what is possible. A common element is found in every model-based motion correction technique: the surrogate signal. To avoid motion artifacts in the images, it was explained that gating methods were based on the acquisition of a surrogate signal during the image acquisition. This signal could be used either in prospective or retrospective gating techniques. For that reason, any motion correction technique either based on a gating strategy or a motion model will depend on the efficient measurement of a surrogate signal that needs to be highly correlated to the evolution of the motion field within the organ of interest, and if possible with a one-to-one relationship between this surrogate signal and the actual motion field in the subject.

3. SURROGATE SIGNALS FOR RESPIRATORY AND CARDIAC MOTIONS AND PRINCIPLES OF SELF-NAVIGATION

Again, this part is not to be exhaustive on the many existing techniques to record a surrogate signal but to provide the main strategies that can be found in clinical routine and in the literature. First, a good surrogate signal needs to be highly correlated to the physiological motions that need to be corrected. Second, the surrogate signal should be easy to measure with a sufficient temporal resolution. Furthermore, in a MR environment, the chosen strategy needs to be compatible with the proximity to strong magnetic fields. Globally, motion tracking strategies can be divided into two groups:

- Techniques based on the use of an external hardware system during MR acquisition.
- Techniques based on the acquisition of MR signal directly thanks to the MRI machine.

3.1. TECHNIQUES BASED ON THE USE OF EXTERNAL HARDWARE PARTS

Techniques based on the use of an external hardware system are usually sensitive to only one type of motion (respiratory motion or cardiac motion). A brief description of the principal systems able to track the two types of motion is given in the following.

[104] Freddy Odille et al., "Generalized Reconstruction by Inversion of Coupled Systems (GRICS) Applied to Free-Breathing MRI," *Magnetic Resonance in Medicine* 60, no. 1 (2008): 146–57, https://doi.org/10.1002/mrm.21623.

Here is a list of the principal external hardware systems able to track respiratory motion[105]:

- **Respiratory bellows**[106]**:** This system, available on most MRI machines, consists of a bag filled of air and attached around the body of the patient (thorax or abdomen usually) thanks to a belt. This system is also usually referred to as respiratory belt or abdominal belt. When the patient breathes, the air pressure inside the bag changes and a pressure sensor measures its variations along time, which is thus related to respiratory motion.

- **Spirometry**[107]**:** The principles of spirometry and its use for lung function testing were introduced in the first chapter. Here, it is only considered as a device able to measure gas volumes and gas flows inflating and deflating the lung during breathing. The time evolution of this volume and/or the flow (which is the first time derivative of volume) can be directly used as a surrogate signals for respiratory motion.

- **Skin surface position measurement systems**[108]**:** By using an optical system based on a time-of-flight camera, on an infrared camera coupled with a reflective marker (as in the Real-Time Position Management™ system commercialized by Varian), on a laser or on electromagnetic fields, it is possible to follow along time the spatial position of one or several points located on the chest wall and/or the abdomen of the patient.

For the heart, here is a list of the principal external hardware systems able to track cardiac motion:

- **Electrocardiograph (ECG)**[109]**:** This system, which is added on many MRI machines, is composed of electrodes, positioned on the chest wall, directly on the skin surface, which record the electrical activity of the heart. The evolution of this electrical activity gives indirect information of the heart motions.

- **Photoplethysmograph (PPG)**[110]**:** This system, which is also available on many MRI machines, is based on the principle of the pulse oximeter. This pulse oximeter measures, with a photodiode, the absorption of the light generated by a light emitting diode. In clinical medical imaging routine, such a system is positioned at the patient's finger. The absorption of the light is directly correlated to the oxygen saturation of the blood, which varies through the cardiac cycle.

However, none of the systems described above is perfect. In particular, measurements based on phenomena occurring outside the patient's body (respiratory bellow, skin surface position measurements, …) never fully reflect the internal motion of organs inside the body. Moreover, systems based on air displacements (bellows, spirometry,

[105] J. R. McClelland et al., "Respiratory Motion Models: A Review," *Medical Image Analysis* 17, no. 1 (January 2013): 19–42, https://doi.org/10.1016/j.media.2012.09.005.

[106] Claudio Santelli et al., "Respiratory Bellows Revisited for Motion Compensation: Preliminary Experience for Cardiovascular MR," *Magnetic Resonance in Medicine* 65, no. 4 (2011): 1097–1102, https://doi.org/10.1002/mrm.22687.

[107] M. R. Miller et al., "Standardisation of Spirometry," *European Respiratory Journal* 26, no. 2 (August 1, 2005): 319–38, https://doi.org/10.1183/09031936.05.00034805.

[108] Hadi Fayad et al., "Technical Note: Correlation of Respiratory Motion between External Patient Surface and Internal Anatomical Landmarks," *Medical Physics* 38, no. 6Part1 (2011): 3157–64, https://doi.org/10.1118/1.3589131.

[109] Alfred P. Fishman and Dickinson W. Richards, "Electrocardiography," in *Circulation of the Blood: Men and Ideas*, ed. Alfred P. Fishman and Dickinson W. Richards (New York, NY: Springer New York, 1982), 265–351, https://doi.org/10.1007/978-1-4614-7546-0_5.

[110] John Allen, "Photoplethysmography and Its Application in Clinical Physiological Measurement," *Physiological Measurement* 28, no. 3 (February 2007): R1–R39, https://doi.org/10.1088/0967-3334/28/3/R01.

…) may suffer from air leaks, mis-positioning, and thus to biases in the measurement. This leads to a decrease in correlation between the surrogate signal and the motion field. Even systems more closely related to obvious physiological phenomena (ECG, EEG, …) usually produce delayed outputs with respect to the actual motion (particularly for the PPG, because of the distance between the heart and the finger where the measurement is performed) and never offer the expected one-to-one relationship with the internal motion field. However, this relationship can be more closely obtained by combining several external hardware systems (by exploiting several respiratory belts and ECG systems differently set up, and by taking into account the first time derivative of their outputs, for example).

3.2. TECHNIQUES BASED ON THE ACQUISITION OF MR SIGNAL

Some other techniques are based on the measurement of MR signal directly with the MRI machine. It has the advantage to be free of supplementary hardware equipment and to yield an inside output that is usually more closely related to the internal motion of organs, to reduce drastically the time delay between the actual motion field and the measurement, and to be able to measure both respiratory and cardiac motion components at the same time. A first sub-category of techniques based on MR measurements could be referred to as 'N-Dimensional navigator-echoes'. A navigator-echo can be defined as a short time MR acquisition sequence which is interleaved with the actual MR image acquisition, and implemented with a sufficient temporal rate to track the motion evolution of a given part of the body.

3.2.1. 1D NAVIGATOR

The most standard navigator-echo is the 1D navigator-echo, usually simply referred to as navigator. It consists in a short pulse sequence during which is acquired either:

- one 1D projection[111] [112] [113] [114]: this projection is obtained by calculating the 1D Fourier transform of one line of k-space passing through the center of k-space. This line is sometimes called center k-space line or CKL.

- or, more commonly, one small 'column' of MR signal[115] [116]: this column of signal can be acquired by using, for example, spatially selective RF pulses to excite only one particular region of the body.

At the end of the image acquisition process, the image k-space is obtained with the time varying 1D signal measured from the patient's body. Usually, the projection or column of MR signal is measured at a spatial position where motion occurs and oriented in a direction along which the signal changes with motion. For example, the

[111] Richard S. Hinks, Monitored echo gating for the reduction of motion artifacts, United States US4761613A, filed August 12, 1987, and issued August 2, 1988, https://patents.google.com/patent/US4761613A/en.
[112] Thomas A. Spraggins, "Wireless Retrospective Gating: Application to Cine Cardiac Imaging," *Magnetic Resonance Imaging* 8, no. 6 (January 1, 1990): 675–81, https://doi.org/10.1016/0730-725X(90)90001-I.
[113] Sergio Uribe et al., "Whole-Heart Cine MRI Using Real-Time Respiratory Self-Gating," *Magnetic Resonance in Medicine* 57, no. 3 (2007): 606–13, https://doi.org/10.1002/mrm.21156.
[114] Freddy Odille et al., "Model-Based Reconstruction for Cardiac Cine MRI without ECG or Breath Holding," *Magnetic Resonance in Medicine* 63, no. 5 (2010): 1247–57, https://doi.org/10.1002/mrm.22312.
[115] Yu L. Liu et al., "A Monitoring, Feedback, and Triggering System for Reproducible Breath-Hold MR Imaging," *Magnetic Resonance in Medicine* 30, no. 4 (1993): 507–11, https://doi.org/10.1002/mrm.1910300416.
[116] Y Wang et al., "Navigator-Echo-Based Real-Time Respiratory Gating and Triggering for Reduction of Respiration Effects in Three-Dimensional Coronary MR Angiography.," *Radiology* 198, no. 1 (January 1, 1996): 55–60, https://doi.org/10.1148/radiology.198.1.8539406.

most common way to set a navigator is to localize the column between the lung and the liver and to orient it along the superior-inferior axis (see **Figure 2.4**). With this setup, the sharp spatial transition between the low MR signal coming from the lung and the high MR signal coming from the liver can be tracked along time and is usually well correlated to the respiratory motion field in the patient's body. The navigator can also be set close to the myocardium wall in order to follow cardiac motion. It is even possible to follow several navigators during the same pulse sequence.

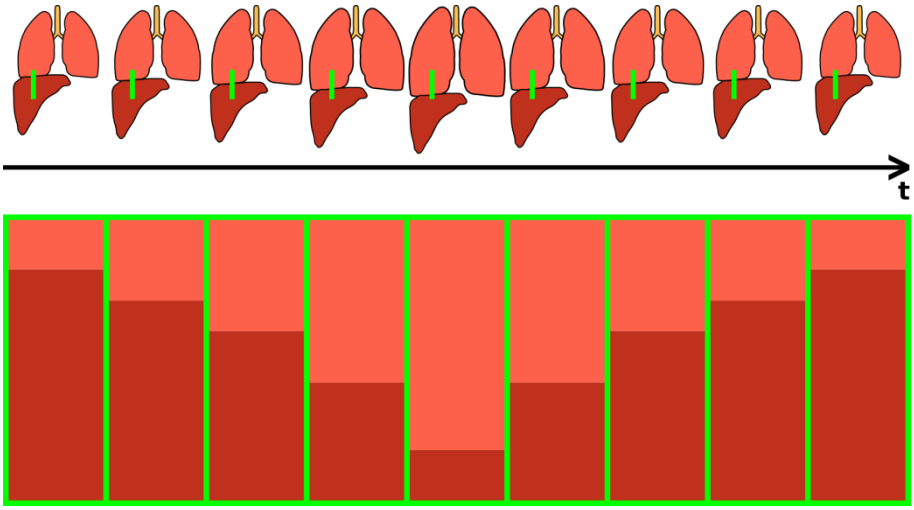

Figure 2.4: Principle of the 1D navigator. A column of 1D signal (in green, top) is acquired frequently along the acquisition process in an interleaved manner. This gives the possibility to track the motion of one chosen part of the body by representing along time the evolution of this 1D signal (bottom). The process is illustrated here with the motion at the interface between the lung and the liver to follow respiratory motion.

3.2.2. THE MULTI-DIMENSIONAL NAVIGATOR

With the same strategy, 2 or 3D navigators can be acquired during the actual MR image acquisition in order to measure at the same time different directional components of motion[117] [118] [119] [120] [121]. More complex navigators, even if they are usually not mentioned as such, can be acquired during the imaging process. One of the most famous special navigators was implemented in the PROspective Motion correction technique (PROMO)[122]. In this technique, three orthogonal 2D MR images are acquired in an interleaved manner with the acquisition of the image k-space and with a sufficient temporal rate. By analyzing in 'real-time' the series of orthogonal 2D images with a Kalman filter, it was shown that the rigid motion of the head could be prospectively corrected by re-scanning the

[117] Michael Lustig et al., "Butterfly: A Self Navigating Cartesian Trajectory," ISMRM 2007.
[118] Zhuo Wu Fu et al., "Orbital Navigator Echoes for Motion Measurements in Magnetic Resonance Imaging," *Magnetic Resonance in Medicine* 34, no. 5 (1995): 746–53, https://doi.org/10.1002/mrm.1910340514.
[119] Yasser M. Kadah et al., "Floating Navigator Echo (FNAV) for in-Plane 2D Translational Motion Estimation," *Magnetic Resonance in Medicine* 51, no. 2 (2004): 403–7, https://doi.org/10.1002/mrm.10704.
[120] Edward Brian Welch et al., "Spherical Navigator Echoes for Full 3D Rigid Body Motion Measurement in MRI," *Magnetic Resonance in Medicine* 47, no. 1 (2002): 32–41, https://doi.org/10.1002/mrm.10012.
[121] André J. W. van der Kouwe, Thomas Benner, and Anders M. Dale, "Real-Time Rigid Body Motion Correction and Shimming Using Cloverleaf Navigators," *Magnetic Resonance in Medicine* 56, no. 5 (2006): 1019–32, https://doi.org/10.1002/mrm.21038.
[122] Nathan White et al., "PROMO: Real-Time Prospective Motion Correction in MRI Using Image-Based Tracking," *Magnetic Resonance in Medicine* 63, no. 1 (January 2010): 91–105, https://doi.org/10.1002/mrm.22176.

motion artifacted k-space lines and by adjusting in real-time the position encoding gradients and RF pulses, as explained in 2.4.2.

3.2.3. 0D NAVIGATOR

With the same 'ND navigator-echoes' formalism, it is even possible to define a 0D navigator-echo. To do so, only one given point either in the Fourier space or in the image space should be acquired. Because of the direct access to image k-space offered by MRI, the simplest way to obtain this 0D navigator is to acquire the exact same k-space point throughout the acquisition, with a sufficient temporal rate and by interleaving the acquisition of this 0D navigator with the acquisition of the image k-space. The most accessible k-space point, which is also certainly the easiest to analyze, is the one located at the center of k-space. Many studies were focused on the acquisition of such a 0D navigator at the center of k-space either by directly acquiring this special point in k-space[123], or a FID curve[124], without any position encoding gradient, or by analyzing the maximum signal of a gradient echo obtained through the acquisition of a central k-space line[125], or even half of a central k-space line[126]. In these two last cases, the k-space line is not acquired to obtain a projection of the image, as seen above with 1D navigator-echoes, but to estimate the signal obtained at the k-space center, which is supposed to be measured when the maximum signal intensity of the echo is reached. For that reason, even if those techniques are based on the acquisition of a 1D k-space signal, only a 0D navigator is extracted from it.

The signal used as a 0D navigator is usually referred to as k-space center because of the location where the measurement is performed in image k-space. It is also usually referred to as DC-signal because this component corresponds to the complex signal baseline or direct component of the MR image. In this approach, it is necessary to clearly distinguish this k-space center signal, used as a navigator, with the signal value found at the center of the spatial Fourier transform of any final reconstructed image. The first reason is because the navigation signal is acquired apart from the imaging data (the navigators and the image k-space data are acquired separately, in an interleaved manner). The second reason is because the spatial average complex signal of the final MR image (or the complex signal found at the center of its k-space, which is the same from the Fourier point of view) will be impacted by a possible signal averaging (if the center of k-space is acquired several times with a radial or interleaved spiral trajectory, for example) and by a possible motion correction strategy applied before or during the image reconstruction step. For those reasons, every time the terms center k-space or DC-signal are mentioned in the field of motion navigation, we will be careful about what this signal represents exactly.

3.2.4. CONCEPT OF SELF-NAVIGATOR

The distinction between the center of k-space in the final image and the one used as a navigator can be even more clouded by directly extracting the navigator from the acquired image k-space, and not by measuring it as a separate step from the imaging process. This practice is usually referred to as self-navigation, and the extracted navigator is called self-navigator. If a gating process is applied from such a navigator, this process will usually be referred to as self-gating. The easiest way to do it is to acquire a 0D self-navigator thanks to the use of a k-space trajectory that

[123] Anja C. S. Brau and Jean H. Brittain, "Generalized Self-Navigated Motion Detection Technique: Preliminary Investigation in Abdominal Imaging," *Magnetic Resonance in Medicine* 55, no. 2 (February 2006): 263–270, https://doi.org/10.1002/mrm.20785.

[124] Martin Buehrer et al., "Prospective Self-Gating for Simultaneous Compensation of Cardiac and Respiratory Motion," *Magnetic Resonance in Medicine* 60, no. 3 (2008): 683–90, https://doi.org/10.1002/mrm.21697.

[125] Mark E. Crowe et al., "Automated Rectilinear Self-Gated Cardiac Cine Imaging," *Magnetic Resonance in Medicine* 52, no. 4 (2004): 782–88, https://doi.org/10.1002/mrm.20212.

[126] Edwin Heijman et al., "Comparison between Prospective and Retrospective Triggering for Mouse Cardiac MRI," *NMR in Biomedicine* 20, no. 4 (2007): 439–47, https://doi.org/10.1002/nbm.1110.

frequently samples the same k-space point throughout the entire image acquisition process. This is the case if a radial trajectory[127] or a trajectory composed of interleaved undersampled spiral segments[128] is implemented for the MR imaging process, for example. It is even possible to extract a ND self-navigator with N > 0 if the imaging trajectory gives this possibility[129] [130] [131] [132]. Again we should be careful about what is referred to as self-navigation and self-gating in the literature because many papers label their techniques with these expressions even if the navigator under consideration is not extracted directly from the imaging data. In the following, we will consider the 'self' prefix only if the navigator is extracted from the image k-space data (see **Figure 2.5**).

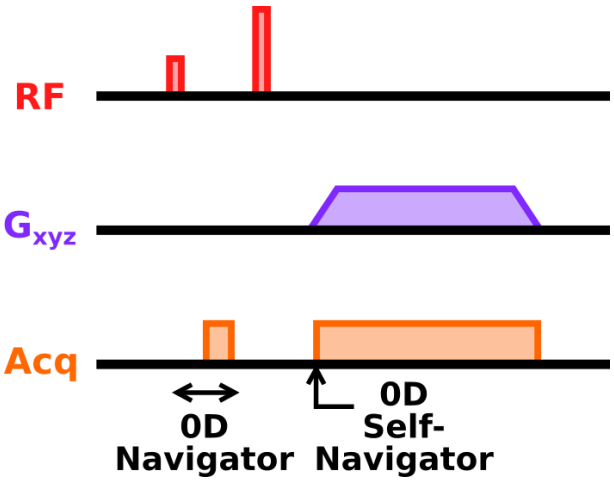

Figure 2.5: Illustration of the difference between a navigator and a self-navigator, here in the 0D case and for a radial pulse sequence. Whereas the navigator needs the application of special pulses to be acquired, the self-navigator is directly extracted from the imaging data.

3.2.5. SOURCES OF SIGNAL VARIATION IN 0D NAVIGATION AND SELF-NAVIGATION

The signal obtained at the center of k-space, either through the implementation of a standard 0D navigator or a 0D self-navigator, is particularly interesting because its complex value represents the complex mean MR signal amplitude of an image that would have been acquired in 'real-time', or instantaneously, and in which all the physiological motions would be frozen. If the spatial configuration of spins changes because of motion (a deformation of biological tissue, for example), the DC-signal will normally change in the general case.

---

[127] Nara S. Higano et al., "Retrospective Respiratory Self-Gating and Removal of Bulk Motion in Pulmonary UTE MRI of Neonates and Adults," *Magnetic Resonance in Medicine* 77, no. 3 (March 2017): 1284–1295, https://doi.org/10.1002/mrm.26212.

[128] Gary H. Glover and Song Lai, "Self-Navigated Spiral FMRI: Interleaved versus Single-Shot," *Magnetic Resonance in Medicine* 39, no. 3 (1998): 361–68, https://doi.org/10.1002/mrm.1910390305.

[129] Li Feng et al., "XD-GRASP: Golden-Angle Radial MRI with Reconstruction of Extra Motion-State Dimensions Using Compressed Sensing," *Magnetic Resonance in Medicine* 75, no. 2 (February 2016): 775–788, https://doi.org/10.1002/mrm.25665.

[130] Wenwen Jiang et al., "Motion Robust High Resolution 3D Free-Breathing Pulmonary MRI Using Dynamic 3D Image Self-Navigator," *Magnetic Resonance in Medicine*, October 2017, https://doi.org/10.1002/mrm.26958.

[131] Marta Tibiletti et al., "Respiratory Self-Gated 3DUTE for Lung Imaging in Small Animal MRI," *Magnetic Resonance in Medicine* 78, no. 2 (August 2017): 739–745, https://doi.org/10.1002/mrm.26463.

[132] Chunlei Liu et al., "Self-Navigated Interleaved Spiral (SNAILS): Application to High-Resolution Diffusion Tensor Imaging," *Magnetic Resonance in Medicine* 52, no. 6 (2004): 1388–96, https://doi.org/10.1002/mrm.20288.

Here is a non-exhaustive list of physical effects that may explain the evolution of the DC-signal with motion:

- **Biological tissue going in and out of the excitation volume:** The excitation volume is controlled both by the sensitivity profile of the excitation coil and by the pulse sequence prescriptions, and in particular the position and width of the slice or slab which is excited. If the biological tissue moves relatively to this excitation volume (through plane motion in 2D imaging, for example), the volume and nature of excited tissue will not be the same at each repetition. This therefore leads to a mean MR signal changing with motion along the imaging process.

- **Displacement of tissue within the sensitivity profile of the reception coil:** Each reception coil element is characterized by a sensitivity profile. This profile is usually modelled as a 3D complex scalar function giving, at each spatial position, the sensitivity of the coil element to the MR signal. The MR signal acquired and reconstructed to one given location can thus be seen as the product of the actual MR signal produced locally with the local value of this sensitivity profile. Usually, and in particular for surface reception coils, the sensitivity profile of one reception element is not spatially uniform within the excited volume presented above. For that reason, if the biological tissue moves within this excitation volume, the measured MR signal coming from this tissue can be modified, even if the actual MR signal produced by this tissue remains the same.

- **Change of the electromagnetic load of the reception coil:** When a biological tissue is installed close to a reception coil element, the resonance frequency and the quality factor of this element are shifted, and these changes depend on the position, size, shape and electromagnetic properties of the biological tissue under consideration. If a motion occurs during the imaging process, the resonance frequency and quality factor of the reception coil element can therefore vary over time, which thus changes its global sensitivity to MR signal depending on motion, and therefore produces motion dependent variations in the DC-signal.

- **Motion of the reception coil itself:** If the reception coil is set in contact with the patient's body and if the internal motion of organs generates external mechanical effects, the reception coil may move during the acquisition process. This is particularly the case because of respiratory motion if a flexible array of surface coils is used to perform thoracic imaging in free-breathing. In this case, the coil elements move relatively to the magnet bore and may even bend because of motion. These effects modify the sensitivity profile of the coil element but also its resonance frequency and quality factor, which leads to a sensitivity to MR signal modulated because of the internal motion of organs.

- **Change of tissue MR properties with motion:** Because of motion, the MR properties of tissues can change. For example, it was shown that the T_2^* values in the lung parenchyma decrease with lung inflation[133]. For that reason, if the acquisition of the DC-signal is subject to a T_2^* contrast (if the duration between the RF excitation and the acquisition of the DC-signal is long, for example), the DC-signal value will change along time because of motion.

- **Variation of B_0 homogeneity with motion:** During a motion, because of the displacement of interfaces between tissues with different magnetic susceptibilities, the B_0 field may change as a function of the motion field along the image acquisition process. As a consequence, the phase component of the DC-signal may vary with motion, in particular if the time between RF excitation and DC-signal acquisition is long.

[133] Rebecca J. Theilmann et al., "Quantitative MRI Measurement of Lung Density Must Account for the Change in T 2* with Lung Inflation," *Journal of Magnetic Resonance Imaging* 30, no. 3 (September 2009): 527–534, https://doi.org/10.1002/jmri.21866.

3.2.6. ADVANTAGES OF USING 0D SELF-NAVIGATORS

0D navigators are sensitive to both respiratory and cardiac motions. At first glance, it may seem complicated to distinguish the two sources of variation but, thanks to the usual difference between respiratory motion frequency (around 0.2-0.3 Hz in human) and cardiac motion frequency (around 1 Hz in human) it is usually easy to separate both sources with a bandpass filtering[134]. Moreover, this DC-signal is extracted from every coil element of the array usually employed to perform thoracic MR imaging, with some coil elements closer to the heart or the diaphragm and therefore more sensitive to one of both types of motion, a whole set of actually different surrogate signals can be used[135]. These considerations are exactly the same for navigators and self-navigators based on ND image projections obtained through the frequent sampling of the same k-space lines for example[136] [137] [138] [139]. The third and last interest of using such 0D navigators is the possibility to use them in any motion correction technique thanks to their great simplicity of acquisition and processing, even in the case of a prospective gating[140].

To finish, 0D self-navigators have a particular advantage in comparison to standard 0D navigators in the fact that no extra element needs to be added to the pulse sequence. In a self-navigation method, the navigator is directly extracted from the imaging data. Thanks to this, the complexity of the pulse sequence is not increased, the scan time is not modified, the SAR remains the same and the obtained signal is perfectly synchronized with the MR acquisition of each view. Nevertheless, for temporal resolution issue, the pulse sequence needs to be adapted to such an intrinsic navigation technique, by featuring a radial or a spiral trajectory for example.

We will study in the following the possibility to use self-navigation through the extraction of 0D self-navigators in our UTE and ZTE pulse sequences. Moreover, we will also see the requirements and the limits of those techniques. Furthermore, we will also study the degrees of freedom offered by k-space trajectory design to optimize both the detection of motion and the final image quality. This is the first necessary step to perform thoracic MR images free of respiratory and cardiac motion artifacts.

---

[134] Bassem Hiba et al., "Cardiac and Respiratory Double Self-Gated Cine MRI in the Mouse at 7 T," *Magnetic Resonance in Medicine* 55, no. 3 (March 2006): 506–513, https://doi.org/10.1002/mrm.20815.

[135] Stefan Weick et al., "DC-Gated High Resolution Three-Dimensional Lung Imaging during Free-Breathing," *Journal of Magnetic Resonance Imaging* 37, no. 3 (2013): 727–32, https://doi.org/10.1002/jmri.23798.

[136] Jing Liu et al., "Respiratory and Cardiac Self-Gated Free-Breathing Cardiac CINE Imaging with Multiecho 3D Hybrid Radial SSFP Acquisition," *Magnetic Resonance in Medicine* 63, no. 5 (May 2010): 1230–1237, https://doi.org/10.1002/mrm.22306.

[137] Peng Hu et al., "Motion Correction Using Coil Arrays (MOCCA) for Free-Breathing Cardiac Cine MRI," *Magnetic Resonance in Medicine* 66, no. 2 (2011): 467–75, https://doi.org/10.1002/mrm.22854.

[138] Davide Piccini et al., "Respiratory Self-Navigation for Whole-Heart Bright-Blood Coronary MRI: Methods for Robust Isolation and Automatic Segmentation of the Blood Pool," *Magnetic Resonance in Medicine* 68, no. 2 (2012): 571–79, https://doi.org/10.1002/mrm.23247.

[139] Tao Zhang et al., "Robust Self-Navigated Body MRI Using Dense Coil Arrays," *Magnetic Resonance in Medicine* 76, no. 1 (July 1, 2016): 197–205, https://doi.org/10.1002/mrm.25858.

[140] Pascal Spincemaille et al., "Kalman Filtering for Real-Time Navigator Processing," *Magnetic Resonance in Medicine* 60, no. 1 (2008): 158–68, https://doi.org/10.1002/mrm.21649.

SECTION 2 SNIF: A SELF-NAVIGATOR INTELLIGENT FILTER TO CORRECT THE UTE DC-SIGNAL FROM OFF-CENTER AND SPIN-HISTORY ARTIFACTS

FOR SELF-NAVIGATION AND SELF-GATING IN MRI, SELF-NAVIGATORS ARE EXTRACTED FROM THE MEASUREMENTS OF THE K-SPACE CENTER MAGNITUDE/PHASE OR REAL/IMAGINARY PARTS, CALLED DC-SIGNAL. THIS EXTRACTION IS USUALLY MADE THROUGH A TEMPORAL FREQUENCY ANALYSIS TO SEPARATE BETWEEN RESPIRATORY AND CARDIAC MOTION COMPONENTS. HOWEVER, THIS SIGNAL OFTEN CONTAINS ARTIFACTS. THIS SECTION INTRODUCES A SELF-NAVIGATOR INTELLIGENT FILTER (SNIF), A METHOD TO MODEL THE PHYSICAL ORIGIN OF THE K-SPACE CENTER ARTIFACTS TO ESTIMATE THEM AND THUS MORE ACCURATELY REMOVE THEM. THE RESULTS OF THIS PROJECT WERE PRESENTED ORALLY AT ISMRM 2018 IN PARIS.

1. PURPOSE OF SNIF

Ultrashort Echo-Time (UTE) pulse sequences were shown to advantageously deal with the short T_2^* values of the lung parenchyma and physiological motions inherent to thoracic imaging[141] [142] [143] [144]. UTE sequences feature very short RF excitation pulses and 2D or 3D radial samplings of the k-space, which yield very short echo times (TE) between the RF excitation and the signal acquisition at the k-space center, down to a few tens of microseconds. These times are very short compared to most standard Cartesian pulse sequences – an order of magnitude or two shorter – so the SNR of measured DC-signals can be largely improved in short T_2^* tissues. Moreover, today MR systems enable very rapid readouts of radii (also called spokes) in k-space, preventing from a strong k-space attenuation in the high spatial frequencies domain and thus a low-pass spatial filtering of the images[145] [146].

Furthermore, because the k-space sampling is radially performed, the DC-signal is sampled every repetition. If it were possible to instantaneously acquire a whole MR image, the complex DC-signal value measured at the k-space center would be equal to the mean complex amplitude of this instantaneous image. If the imaged object were moving, instantaneous images acquired along this motion would move accordingly and the corresponding DC-signal value would evolve correspondingly. Also, as RF excitation and signal readout are performed in a relatively short

[141] P. D. Gatehouse and G. M. Bydder, "Magnetic Resonance Imaging of Short T2 Components in Tissue," *Clinical Radiology* 58, no. 1 (January 2003): 1–19, https://doi.org/10.1053/crad.2003.1157.
[142] Michael Garwood, "MRI of Fast-Relaxing Spins," *Journal of Magnetic Resonance*, Frontiers of In Vivo and Materials MRI Research, 229 (April 2013): 49–54, https://doi.org/10.1016/j.jmr.2013.01.011.
[143] Kevin M. Johnson et al., "Optimized 3D Ultrashort Echo Time Pulmonary MRI," *Magnetic Resonance in Medicine* 70, no. 5 (November 2013): 1241–1250, https://doi.org/10.1002/mrm.24570.
[144] Nicholas S. Burris et al., "Detection of Small Pulmonary Nodules with Ultrashort Echo Time Sequences in Oncology Patients by Using a PET/MR System," *Radiology* 278, no. 1 (July 2015): 239–246, https://doi.org/10.1148/radiol.2015150489.
[145] J. M. Wild et al., "MRI of the Lung (1/3): Methods," *Insights into Imaging* 3, no. 4 (August 2012): 345–353, https://doi.org/10.1007/s13244-012-0176-x.
[146] R.Todd Constable and John C. Gore, "The Loss of Small Objects in Variable TE Imaging: Implications for FSE, RARE, and EPI," *Magnetic Resonance in Medicine* 28, no. 1 (November 1992): 9–24, https://doi.org/10.1002/mrm.1910280103.

time, we can implement short repetition times (TR), hence frequent samplings of the DC, in order to match the motion state evolution. Then, a 1D signal giving information about the motion state of the lung and/or the heart can usually be extracted out of the DC-signal. This signal is usually referred as a self-navigator[147] [148].

The self-navigators inherently depend on several concomitant physical effects: the motion of the organs in and out of the sensitive region of the coil elements, the change in the coil element load as well as the evolution of tissue MR parameters throughout the motion, … The self-navigators are not a measure of the motion itself, like the evolution of the deformation fields of the tissues with time, but they are a surrogate signal following its evolution[149] [150]. Nevertheless, a bijective relationship is often assumed between this signal and the deformation fields: to one value of the self-navigator, a unique deformation field is associated, which is wrong in general because two different deformation fields can lead to the same average signal in the image, and thus to the same self-navigator value.

In most studies, two steps are implemented to extract the self-navigators from the DC-signal: i) separation of respiratory and cardiac information and ii) filtering of high-frequency noise. The latter noise is observed when a quasi-random choice of spoke-orientation is selected for k-space sampling along the image acquisition (computationally-random[151] or golden-angle based[152] [153]). Both steps are usually performed through a temporal frequency analysis because respiratory and cardiac motions can be approximated by quasi-periodic motions with different characteristic low frequencies. The method consists in band-pass filtering the DC-signal to separate the information related to each motion and to reduce the background noise[154] [155] [156] [157] [158] [159]. It holds as long as the physiological motions are quasi-periodic, which is seldom the case over a few-minute acquisition in healthy

[147] Marta Tibiletti et al., "Respiratory Self-Gated 3DUTE for Lung Imaging in Small Animal MRI," *Magnetic Resonance in Medicine* 78, no. 2 (August 2017): 739–745, https://doi.org/10.1002/mrm.26463.
[148] Nara S. Higano et al., "Retrospective Respiratory Self-Gating and Removal of Bulk Motion in Pulmonary UTE MRI of Neonates and Adults," *Magnetic Resonance in Medicine* 77, no. 3 (March 2017): 1284–1295, https://doi.org/10.1002/mrm.26212.
[149] J. R. McClelland et al., "Respiratory Motion Models: A Review," *Medical Image Analysis* 17, no. 1 (January 2013): 19–42, https://doi.org/10.1016/j.media.2012.09.005.
[150] Robert Grimm et al., "Self-Gated Radial MRI for Respiratory Motion Compensation on Hybrid PET/MR Systems," in *Medical Image Computing and Computer-Assisted Intervention – MICCAI 2013* (Springer, Berlin, Heidelberg, 2013), 17–24, https://doi.org/10.1007/978-3-642-40760-4_3.
[151] Wenwen Jiang et al., "Motion Robust High Resolution 3D Free-Breathing Pulmonary MRI Using Dynamic 3D Image Self-Navigator," *Magnetic Resonance in Medicine*, October 2017, https://doi.org/10.1002/mrm.26958.
[152] Li Feng et al., "XD-GRASP: Golden-Angle Radial MRI with Reconstruction of Extra Motion-State Dimensions Using Compressed Sensing," *Magnetic Resonance in Medicine* 75, no. 2 (February 2016): 775–788, https://doi.org/10.1002/mrm.25665.
[153] Grimm et al., "Self-Gated Radial MRI for Respiratory Motion Compensation on Hybrid PET/MR Systems."
[154] Grimm et al., "Self-Gated Radial MRI for Respiratory Motion Compensation on Hybrid PET/MR Systems."
[155] Jiang et al., "Motion Robust High Resolution 3D Free-Breathing Pulmonary MRI Using Dynamic 3D Image Self-Navigator."
[156] Feng et al., "XD-GRASP."
[157] Jing Liu et al., "Respiratory and Cardiac Self-Gated Free-Breathing Cardiac CINE Imaging with Multiecho 3D Hybrid Radial SSFP Acquisition," *Magnetic Resonance in Medicine* 63, no. 5 (May 2010): 1230–1237, https://doi.org/10.1002/mrm.22306.
[158] Jean Delacoste et al., "A Double Echo Ultra Short Echo Time (UTE) Acquisition for Respiratory Motion-Suppressed High Resolution Imaging of the Lung," *Magnetic Resonance in Medicine*, August 2017, https://doi.org/10.1002/mrm.26891.
[159] Bassem Hiba et al., "Cardiac and Respiratory Double Self-Gated Cine MRI in the Mouse at 7 T," *Magnetic Resonance in Medicine* 55, no. 3 (March 2006): 506–513, https://doi.org/10.1002/mrm.20815.

subjects. It obviously fails in patients with breathing difficulties or cardiac arrhythmia. As the filtering method is only based on the supposed frequency content of the DC-signal, the origin and the nature of the high-frequency noise are not integrated in the filtering process.

In this section, we introduce SNIF, a Self-Navigator Intelligent Filter designed to suppress the high frequency noise by considering its physical origin in the context of 3D-UTE with radial sampling in random order. SNIF assumes that this noise is a measurement bias that results from two different physical artifacts:

1. An off-center artifact as the DC-signal measurement is not performed exactly at the center of k-space because of overall system imperfections (B_0 inhomogeneity, gradient delays, …), and

2. A spin-history artifact as the transverse magnetization states of previous repetitions influence the current magnetization state.

The two artifacts were modeled and their intrinsic measurement was implemented for each MR acquisition. Thereafter, on the basis of their physical origin and not on assumed frequency contents, SNIF can knowingly remove both contributions out of the signal. From this advanced process, we hope to extract more reliable respiratory and cardiac self-navigators. Compared to more common techniques, we expect those new self-navigators to better correspond to the underlying motion fields in the patient's thorax and be less dependent on acquisition biases. In the perspective of retrospective motion correction, it is known that the quality of this correction step highly depends on the quality of the surrogate signals, which encourages us to further improve the self-navigator extraction process.

2. THEORY AND UNDERLYING NUMERICAL METHODS

2.1. MODELLING OFF-CENTER AND SPIN-HISTORY ARTIFACTS

Let S_{DC} be the DC signal measured at the expected center of k-space, recorded by a given reception coil element in a radial MR pulse sequence. It corresponds to the first sampled data point along each center-out radial readout. For a subject lying still in the MR bore, presumably motionless, we write this signal S_0. If this measurement were performed at the theoretical center of k-space with no added noise source, say the ground truth, S_0 would remain constant and equal to the mean intensity of the image acquired with each coil element. Because of hardware and pulse sequence imperfections, the first data point is never experimentally sampled at the theoretical center of k-space. This leads to an off-center artifact characterized by a variation of the recorded S_0 value along the acquisition, which depends on both the readout gradient direction and the subject's morphology. Moreover, in the general case, the DC-signal also depends on cumulative former transverse magnetization states reached in preceding sequence repetitions. It introduces a spin-history effect in the recorded signal. This effect was modelled by a convolution kernel $h = [h_{N_{Rep}} \dots h_3\ h_2\ h_1\ h_0]$, where N_{Rep} is the number of relevant preceding sequence repetitions which influence the current measurement. Each one lasts TR and h_0 corresponds to the current repetition. Thereby, the DC-signal is a sum of the back-shifted and re-weighted S_0 signal, $S_0 \star \mathrm{h}$, where $\star$ is the discrete convolution operator. In other words, the effect of previous magnetization states on the current DC-signal is here assumed to be linearly dependent on S_0 values recorded before.

If the subject is now animated by a low-amplitude motion, the effect of this motion on the DC-signal can be modelled as a small additive contribution to S_0, written S_m. The DC-signal S_{DC} can then be written:

$$S_{DC} = (S_m + S_0) \star h \qquad \textbf{Eq. 2.2}$$

S_0 is the motion-less component of the DC-signal; and S_m is the motion component of the DC-signal from which self-navigators should be extracted.

For a quasi-random off-centered radial sampling of the image k-space, which is the case when the entire 2D or 3D k-space is uniformly sampled with an order of spokes ruled by randomness or a law that aims at maximizing the uniformity of k-space sampling within any small number of successive spokes (based on the golden ratio[160] or shifted orthogonal directions[161], for example), S_0 can be considered as a noise containing information within a broad range of frequencies. In comparison, if the motion has a time evolution characterized by a quasi-period $T \gg N_{\text{rep}}TR$ (in the case of a quasi-periodic motion), the motion state does not change much from one repetition to the other. This inequality is experimentally verified for respiratory and cardiac motions for most short TR pulse sequences ($TR < 10\ ms$) because the spin-history effects depends mainly on a small number of previous repetitions (h can be characterized by a small number of values, namely N_{Rep} is small, as demonstrated later). For that reason, **Eq. 2.2** can be simplified as:

$$S_{DC} = S_m + S_0 \star h \qquad \textbf{Eq. 2.3}$$

where $S_0 \star \mathrm{h}$ constitutes an additive noise.

2.2. ESTIMATION OF THE OFF-CENTER AND SPIN-HISTORY ARTIFACTS TERMS

Every spoke of a 3D 'kooshball' trajectory is characterized by two angles in spherical coordinates: a polar angle, θ, and an azimuthal angle, φ (see **Figure 2.6**). S_{DC} is processed to extract $\hat{S}_0$, an estimation of the k-space off-center artifact S_0, with a method based on the C^1-constrained interpolation of k-space data from the time domain to a (θ, φ) representation of k-space. Then, data are filtered by applying successively median, sliding window, and Gaussian low-pass filters before being interpolated back from (θ, φ) into the time domain (see **Figure 2.6a-d**). The different filters cited above were applied in this special order and with their characteristic parameters (sliding window width, spatial frequency cutoff, …) tuned manually in order to remove the noise without degrading the pattern varying slowly along θ and φ. This manual tuning process was performed on the data acquired by several representative reception channels and the same parameters were then used for the entire dataset. Note that this method can be easily transposed to 2D imaging by interpolating data in the polar representation of k-space along θ only.

The estimated convolution kernel $\hat{h}$ was then extracted by deconvolving the original DC-signal S_{DC} with $\hat{S}_0$. With $\star^{-1}$ as deconvolution operator, and thanks to the commutative property of convolution, **Eq. 2.3** leads to:

$$S_{DC} \star^{-1} \hat{S}_0 = \hat{S}_m \star^{-1} \hat{S}_0 + \hat{h} \star \hat{S}_0 \star^{-1} \hat{S}_0 \qquad \textbf{Eq. 2.4}$$

To solve this problem, a deconvolution algorithm was adapted by fitting the general model $\hat{S}_0 \star \tilde{h}$ to the signal S_{DC} in the least squares sense. $\hat{S}_0$ is known and the coefficients of $\tilde{h}$ are the fitting parameters. The optimization process leads to the equality between the kernel $\tilde{h}$ and $S_{DC} \star^{-1} \hat{S}_0$. As $\hat{S}_m$ and $\hat{S}_0$ are not physically correlated, the solution for $\hat{S}_m \star^{-1} \hat{S}_0$ out of the deconvolution algorithm is expected to be very close to a null vector. Moreover,

[160] Stefanie Winkelmann et al., "An Optimal Radial Profile Order Based on the Golden Ratio for Time-Resolved MRI," *IEEE Transactions on Medical Imaging* 26, no. 1 (January 2007): 68–76, https://doi.org/10.1109/TMI.2006.885337.

[161] Hee Kwon Song, Lawrence Dougherty, and Mitchell D. Schnall, "Simultaneous Acquisition of Multiple Resolution Images for Dynamic Contrast Enhanced Imaging of the Breast," *Magnetic Resonance in Medicine* 46, no. 3 (n.d.): 503–9, https://doi.org/10.1002/mrm.1220.

$\hat{S}_0 \star^{-1} \hat{S}_0$ yields, also as expected, a solution very close to a Dirac ($\tilde{h}_0 \approx 1$ and $\tilde{h}_{n\neq 0} \approx 0$). Hence, [3] is simplified to $\tilde{h} \approx \hat{h}$, which provides the estimation of h we want to extract. $\hat{S}_0$ and $\hat{h}$ being known, the DC-signal S_{DC} can be corrected with SNIF and the motion component can be estimated by calculating $\hat{S}_m = S_{DC} - \hat{S}_0 \star \hat{h}$ (see **Figure 2.6e**).

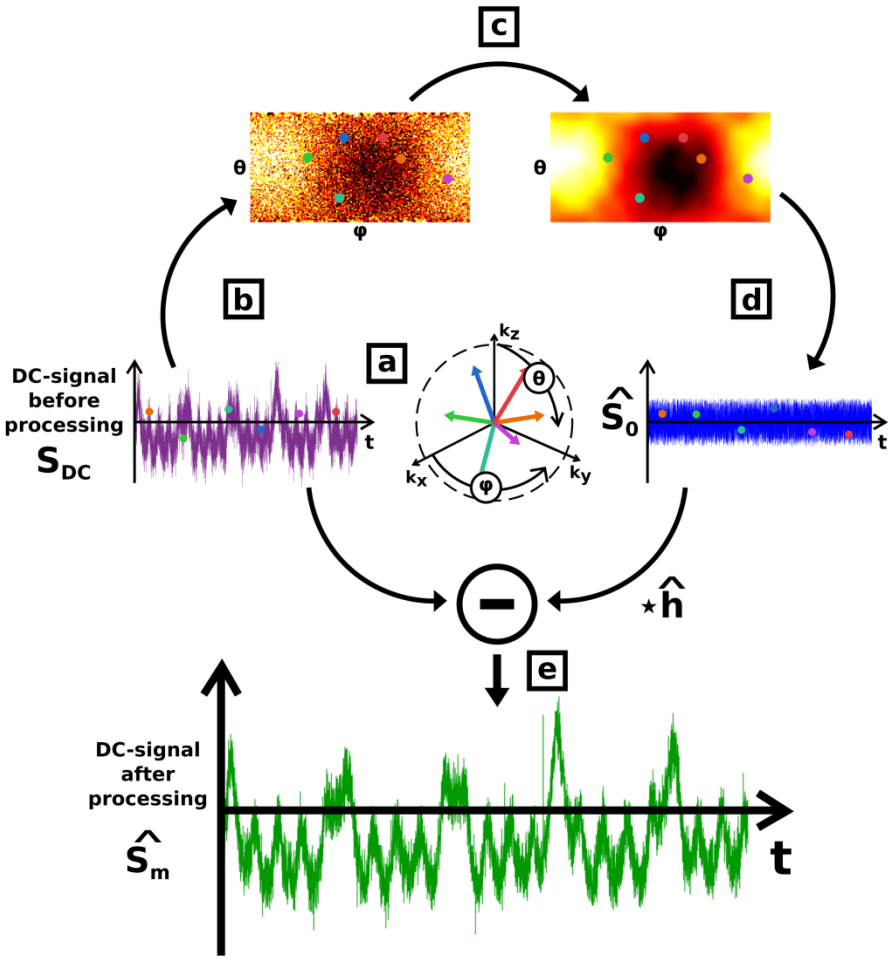

Figure 2.6: SNIF extraction of the off-center component $\hat{S}_0$ from S_{DC} and its role in the correction process: a) Assignment of a pair of angular coordinates (θ, φ) to each DC-signal data point; b) Interpolation and regridding of the DC-signal along θ and φ: motion and spin-history components appear as noise in this matrix and the off-center component appears as a slowly varying pattern along θ and φ; c) Smoothing of the resulting matrix to keep only the off-center component; d) Inverse interpolation process to extract the $\hat{S}_0$ signal: motion information and spin-history artifact are removed; e) Filtering of S with SNIF: $\hat{h}$ is estimated from S_{DC} and $\hat{S}_0$, and the convolution of $\hat{S}_0$ with $\hat{h}$ is subtracted from the original DC-signal S_{DC}, leading to $\hat{S}_m$.

3. VALIDATION METHODS

Thoracic MR acquisitions were performed on a 3.0 T scanner (Signa PET/MR, GE Healthcare, Waukesha, WI, USA) on a freely breathing healthy human volunteer, equipped with a 30-channel thoracic coil for signal reception, a pneumatic abdominal respiratory belt and an oximeter to record the global temporal features of respiratory and

cardiac motions. Tissue RF excitation was performed with the body coil of the MR scanner. The research protocol was approved by the local committee.

A 3D-radial (kooshball) UTE sequence with a random order of spoke orientations was implemented with $TE = 100$ µs, $TR = 2$ ms, FOV $= (32 \times 32 \times 22.4)$ cm^3, Voxel size $= (1.3 \times 1.3 \times 1.3)$ mm^3, full k-space sampling, RF spoiling and ramp-sampling. It resulted in an acquisition of $N_{\text{spokes}} = 150{,}806$ for a total scan time of 5 min 2 s. To build the random order of the spokes, a radial k-space trajectory was first estimated to ensure k-space uniform sampling with respect to the θ and φ angles (see **Figure 2.6a**). Then, each spoke was randomly permuted one and another up to a total of N_{spokes} permutations.

In the experiment, S_{DC} was the complex value of the first acquired data point for each spoke at a given reception channel. The analysis was carried out separately on real and imaginary parts for each of the 30 coil channels. To correct for the spin-history artifact, $N_{\text{rep}} = 50$ previous repetitions were considered for the complex convolution kernel $\hat{h}$, leading to $\hat{h} = [\hat{h}_{50} \dots \hat{h}_3\ \hat{h}_2\ \hat{h}_1\ \hat{h}_0]$. We will verify retrospectively that this value is sufficient in our experimental conditions.

The efficiency of SNIF was evaluated on the SNR of the first three and first two harmonics of the respiratory and cardiac self-navigators respectively, measured on the absolute spectra of DC-signal real and imaginary parts. The reference fundamental frequencies were set for both motions by analyzing the temporal Fourier transforms of the traces provided by the abdominal belt and the photoplethysmography system (PPG). This system outputs a surrogate signal for cardiac motion from an oximetry measurement at the patient's finger. SNR was inferred at each motion harmonic and for each reception channel from the ratio between (1) the amplitude of the local Gaussian fit curves to the absolute value of the DC-signal temporal Fourier transform and (2) the amount of background noise, provided by an affine regression of the same spectrum. Fitting was performed on absolute spectra of DC-signal real and imaginary parts separately. The model used to fit our data was then:

$$|Spectrum(f)| = \alpha + \beta f + \sum_{\substack{i=\{R1,R2,\\ R3,C1,C2\}}} \gamma_i \exp\left(-\frac{(f-f_i)^2}{2{\sigma_i}^2}\right) \qquad \textbf{Eq. 2.5}$$

where $\alpha + \beta f$ is the affine model of the background noise, and where the Gaussian functions of the variable f, centered on f_i and of width σ_i, refer to the first three respiratory motion harmonics $R1$-3 and the first two cardiac motion harmonics $C1$-2. α, β, γ_i, and σ_i, with $i = \{R1, R2, R3, C1, C2\}$, are the fitting parameters and f_i values are estimated from the abdominal belt and PPG sensor traces as described above (chosen as independent physiological motion measurement systems). The SNR for the harmonic i is then:

$$SNR_i = 1 + \frac{\gamma_i}{\alpha + \beta f_i} \qquad \textbf{Eq. 2.6}$$

4. QUANTITATIVE AND QUALITATIVE RESULTS

Figure 2.7 shows a detail of a typical DC-signal extracted from one of the 30 reception channels before and after the correction of off-center and spin-history artifacts by SNIF. This reception channel was chosen as it was able to measure signal variations related to both respiratory and cardiac motions. **Figure 2.8** shows the DC-signal associated spectra obtained before and after SNIF. **Figure 2.9** shows an overview of the processing efficiency of SNIF for all reception channels.

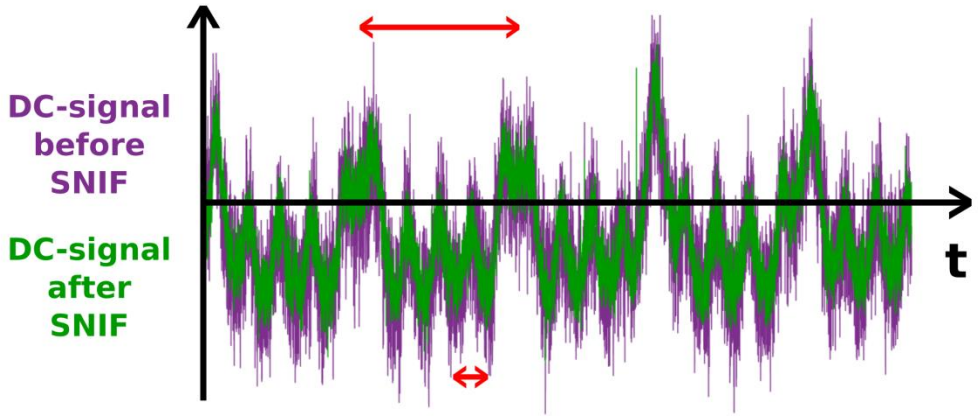

Figure 2.7: Twenty seconds detail for a reception channel of the DC-signal real part before (magenta) and after (green) SNIF with both off k-space-center and spin-history artifacts corrections with $N_{\text{rep}} = 50$. The noticeable reduction of the amount of apparent noise enables a better depiction of the respiratory (long red arrow) and cardiac (short red arrow) motion-related oscillations. A N_{rep} value comprised between 0 and 50 would lead to traces with intermediate amounts of noise.

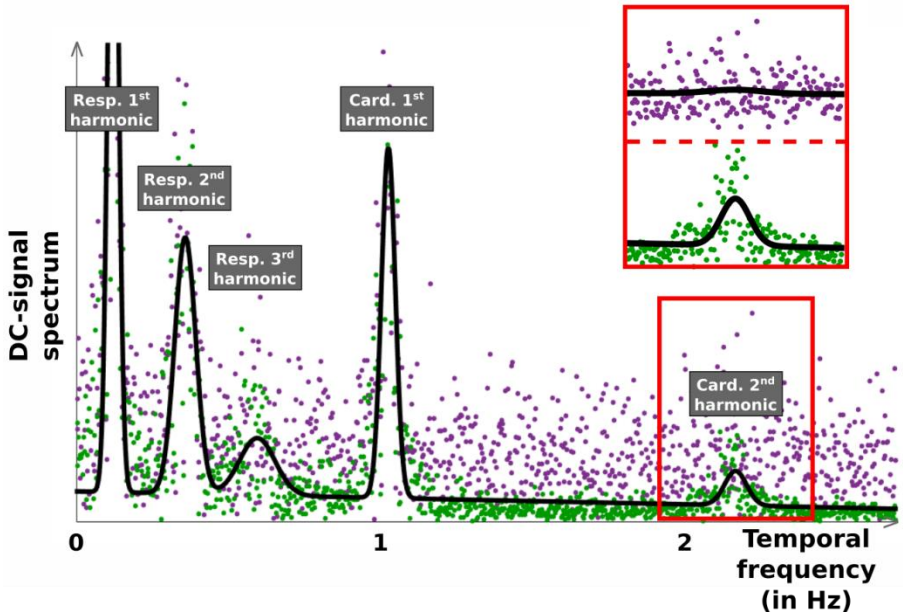

Figure 2.8: Comparison of the absolute DC-signal imaginary part spectrum before (magenta) and after (green) SNIF, for one given reception channel (the comparison similarly holds for the real part). The black curve is the multi-Gaussian fit of the corrected signal (green) with affine regression of the background noise as a basis for SNR estimation of each motion harmonic. The close-up focuses onto the cardiac motion 2nd harmonic (red frame), which is revealed by SNIF whereas it is not distinguishable from the noise without SNIF. Respiratory and cardiac motion fundamental frequencies were extracted from the Fourier analysis of abdominal belt and PPG sensor traces.

On **Figure 2.7**, we see an improvement of the DC-signal after the application of SNIF. When both artifacts are corrected, the amount of noise decreases, enabling a far better depiction of the DC-signal oscillations related to both respiratory and cardiac motions. It is particularly striking for cardiac motion-related oscillations that become easily recognizable with SNIF.

On **Figure 2.8**, after applying SNIF, we observe both the global energy conservation for each motion harmonic and the decrease of the background noise around each peak. Some motion harmonics, hidden by the noise before correction, are revealed: SNIF discriminates motion information from off-center and spin-history noise. On **Figure 2.9**, we see that each correction step in SNIF increases the SNR of each harmonic for almost every channel (standard deviation bars above 1), with SNR gains up to 3.

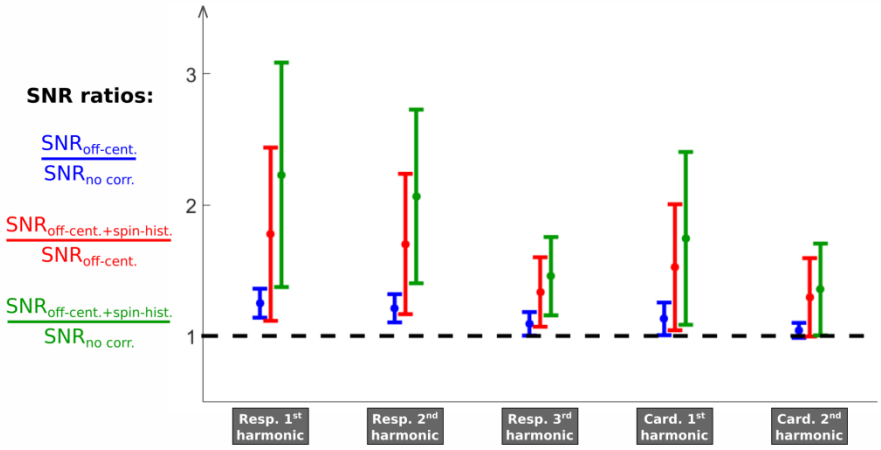

Figure 2.9: Representation of the mean ± standard deviation over the 30 reception channels of SNR ratios for both real and imaginary parts of the DC-signal: i) after and before the correction of the off-center artifact only (blue), ii) after and before the correction of the spin-history artifact only (red), and iii) after and before the correction of both artifacts (green), for the first three harmonics of the respiratory self-navigator and the first two harmonics of the cardiac self-navigator. The unity black dotted line is the threshold above which the SNR is improved.

5. DISCUSSION AND PERSPECTIVES

The underlying theory of SNIF is built on several strong assumptions. The first one is the existence of an off-center component. When represented in a (θ, φ) coordinate system, the acquired data show a coherent but non-uniform pattern that stands out of what can be named as noise (see **Figure 2.6**). On one hand, this noise can be easily understood as respiratory and cardiac motions, but also spin-history effects lose any coherence while represented in (θ, φ) because of the quasi-random order of spokes orientations during the image acquisition. On the other hand, the subject's MR image is experimentally spatially continuous, so is its spatial Fourier representation. Thereof, a smooth pattern can be observed and extracted out of the k-space. Non-coherent components in k-space (like motion and spin-history artifacts but also electronic and numerical noises) are easily low-pass filtered in (θ, φ). First, the resulting data pattern corresponds to what should be obtained for motionless subject at the average position of the overall subject's motion. Second, if data were acquired at the exact center of k-space, with a random order of spoke orientations totally decorrelated with the subject's motions, (θ, φ) data pattern observed in **Figure 2.6** would be uniform. Hence, the observed non-uniformity of the extracted pattern supports the assumption that data were acquired off k-space center. As a matter of fact, after the extraction of the $\hat{h}$

coefficients, the value of $\hat{h}_0$ is experimentally close to 1, which sustains the method used to estimate S_0 and the weight of the correction term for the off-center artifact $\hat{h}_0$ represents (see **Figure 2.10**).

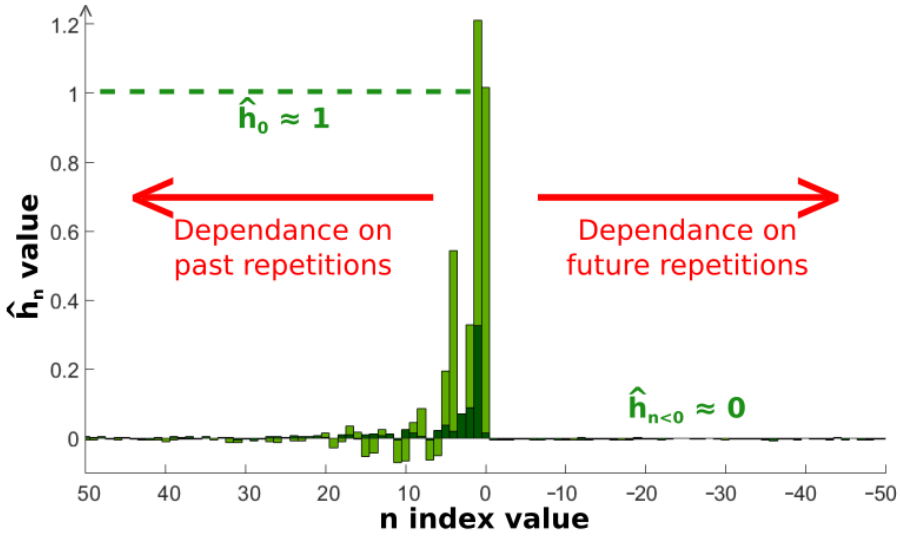

Figure 2.10: Representation for one reception channel of the values estimated for $\hat{h}$ by deconvolving the original DC-signal S_{DC} with $\hat{S}_0$, with the real part of $\hat{h}$ represented in light green and the imaginary part in dark green. For the sake of clarity, in order to verify the coherence of what is computed, the correlation coefficients $\hat{h}_n$ were estimated for positive n values (left part of the graph), corresponding to a correlation with the past repetitions (spin-history effect), but also for negative n values (right part of the graph), which would correspond to a non-physical correlation with future repetitions. First, we observe that $\hat{h}_0$ is very close to 1, which confirms the right extraction of $\hat{S}_0$. Second, we observe non-zero complex $\hat{h}_n$ values for positive n, confirming the existence of a spin-history effect. These weights globally fade as n increases. Furthermore, $\hat{h}_n$values are close to zero for negative n, which is physically expected: at a given repetition, and considering the randomized order of spokes orientations, the transverse magnetization state cannot be correlated with transverse magnetization states reached later in future repetitions.

The second assumption, which states the influence of spin-history, is ascertained by the outcomes of the deconvolution process yielding the estimation $\hat{h}$ of h. The coefficients of $\hat{h}$ at negative indexes ($\hat{h}_{-1}$, $\hat{h}_{-2}$, …), which could support a backward dependence of S_{DC} on future values of $\hat{S}_0$, are experimentally negligible (see **Figure 2.10**) with respect to the coefficients of $\hat{h}$ at positive indexes ($\hat{h}_1$, $\hat{h}_2$, …). Therefore, the current magnetization state is effectively influenced by past magnetization states but not by future ones, in accordance with the causality principle.

The third assumption considers that the spin-history artifact follows a linear model based on the convolution kernel h. It is fair as the spin-history effect can be seen as a cumulative perturbation, which depends on the transverse magnetization states of preceding sequence repetitions. Every transverse magnetization states are supposed to be proportional to the S_0 values at the same repetition time, with h exhibiting the coefficients of proportionality between the S_0 values and the correction terms for the N_{rep} preceding repetitions taken into account to estimate and correct the spin-history artifact.

Finally, a fourth assumption is made by introducing the motion component S_m as an additional term in the measured DC-signal. It is easily justified when both off-center and spin-history artifacts are neglected. In this case,

the mean amplitude $S_{DC}(t)$ of an image that would be acquired instantaneously at t is the sum of i) the mean image intensity without motion $\langle S_0(t)\rangle = S_0$ and ii) the motion correction term $S_m(t)$: $S_{DC}(t) = S_0 + S_m(t)$. The last term characterizes the variation of S around S_0 related to the subject's motion. Experimentally, when off-center and spin-history artifacts cannot be neglected, the mean image amplitude without motion ($S_0(t)$) is not constant anymore but it evolves with the off-center jitter and cumulates the weighted preceding transverse magnetizations through convolution with h, leading to **Eq. 2.2**. This equation is simplified to **Eq. 2.3** and the spin-history effect is correctly estimated as long as $T \gg N_{\text{rep}}TR$, namely as long as the motion characteristic time T is much longer than the spin-history characteristic time, which is fulfilled here with $N_{\text{rep}} = 50$, $TR = 2$ ms, $T_{\text{cardiac}} \geq 500$ ms, and $T_{\text{resp}} \geq 3000$ ms for healthy adults. Moreover, in **Figure 2.10**, we retrospectively observe that the value $N_{\text{rep}} = 50$ is experimentally enough as the $\hat{h}_{40\leq n\leq 50}$ coefficients are very low compared to $\hat{h}_{0\leq n\leq 10}$ values in terms of both real and imaginary parts. For that reason, a value $N_{\text{rep}} > 50$ would not extract a better self-navigator and would increase unnecessarily the post-processing time and complexity.

The abdominal belt and PPG traces provide global and limited information on the organ motions. The single measurements, carried at the surface of the body, are not straightforwardly related to the complex internal organ motions. For example, the measurement with the abdominal belt relies on air pressure changes when the periphery of the patient's thorax or abdomen varies over the respiratory cycle. Moreover, proprietary real-time signal processing is usually performed on those measurements, by applying for example adaptive gains to always keep the same mean motion amplitude displayed on the control screen. Here, the outcomes of the abdominal belt and PPG are minimally used for data analysis only to estimate peak fundamental frequencies of respiratory and cardiac motions in order to increase the confidence we can have on the multi-Gaussian fitting process. They would not be required otherwise.

The strength of SNIF relies on a relatively simple theory, which does not rely on neither the MR properties of the imaged tissues nor the Bloch equations that describe the underlying phenomena. Every supporting assumption and every related processing step can be justified in SNIF in regard to the experimental conditions. Moreover, the two computational methods to estimate S_0 (leading to $\hat{S}_0$) and h (leading to $\hat{h}$) are both theoretically and experimentally supported; they yield direct estimation and suppression of off-center and spin-history effects. Concerning the remaining noise experimentally observed (see **Figure 2.7**), one solution would be to remove it with a more standard method (linear bandpass filtering, for example).

The correction of biases in self-navigator was studied in several recent papers[162] [163]. Those methods are more general, in the sense that they remove the artifacts from both the self-navigator and the final images. Also, they are usually not limited to quasi-random trajectories. However, to our knowledge, SNIF is the only one to enable the correction of both the off-center and the spin-history effects. Moreover, the underlying model proposed by those other methods is often more complicated (the relationship between signals acquired by different reception channels needs to be taken into account, for example), and the principle and use of the correction pipeline are usually not as simple as for SNIF (a calibration scan can be required, for example). To reduce the effects of spin-history, phyllotaxis trajectories may be considered[164]. However, these more advanced trajectories are not as adapted as those featuring a quasi-random sampling of k-space in the perspective of retrospective motion

[162] Guido Buonincontri et al., "Trajectory Correction for Free-Breathing Radial Cine MRI," *Magnetic Resonance Imaging* 32, no. 7 (September 1, 2014): 961–64, https://doi.org/10.1016/j.mri.2014.04.006.

[163] Anagha Deshmane et al., "Self-Calibrated Trajectory Estimation and Signal Correction Method for Robust Radial Imaging Using GRAPPA Operator Gridding," *Magnetic Resonance in Medicine* 75, no. 2 (2016): 883–96, https://doi.org/10.1002/mrm.25648.

[164] Davide Piccini et al., "Spiral Phyllotaxis: The Natural Way to Construct a 3D Radial Trajectory in MRI," *Magnetic Resonance in Medicine* 66, no. 4 (October 1, 2011): 1049–56, https://doi.org/10.1002/mrm.22898.

correction. This is particularly true with retrospective gating methods because of the non-uniform sampling of k-space resulting from each retrospective gate in non-quasi-random trajectories.

SNIF is thus robust and applicable to any 2D or 3D radial MR acquisition, whatever acquisition parameters are selected, as long as quasi-random order of spoke orientations is designed and the condition $T \gg N_{\text{rep}} TR$ is verified, which is the case for most short TR standard pulse sequences, and especially for the UTE sequence performed here. In an ideal situation where there would be neither off-center nor spin-history artifacts, where S_0 would then be time-independent and h would be a Dirac, SNIF would not alter the DC-signal. In other words, SNIF can only improve the extraction of the MR-embedded self-navigators from the DC-signal, before applying a standard Fourier or non-linear band-pass filtering, provided the DC-signal is blurred by off-center and spin-history effects. SNIF does not degrade useful lung or heart motion information but, to the contrary, extract a signal more closely related to the internal motion field inside the thorax because the sources of biases are understood, modelled and filtered with SNIF.

6. CONCLUSION

This work shows the great potential of SNIF: by mere modeling of the physics underlying the MR measurement during a quasi-random 2D- or 3D-radial acquisition, we are able to suppress noise, which results from off k-space center and spin-history artifacts, and to more accurately extract respiratory and cardiac self-navigators out of the acquisition DC-signal. Many studies, where respiratory and/or cardiac self-navigation is used, analyze the DC-signal through its frequency content. A standard low-pass filter is then applied to discriminate high frequency noise and low frequency motion-related signals. However, low frequency noise still blurs the motion information. By considering the origin of the noise, modeling its creation during the MR acquisition and calculating it thanks to this model through computational methods, we showed that SNIF could remove it ‘intelligently’, resulting in the extraction of motion information that was previously hidden within the noise and then un-extractable by using linear filters.

To our knowledge, this is the first time such an approach is used to filter out the noise from MR DC-signal. By following more accurately respiratory and cardiac motions, a potentially more accurate motion artifact correction on images can be envision in MR but also in simultaneous PET/MR acquisitions. This study also showed the relative simplicity to obtain a surrogate signal for respiratory and cardiac motions with 3D UTE. In the next section of this chapter, we will discover that the problem is totally different for the ZTE pulse sequence.

SECTION 3 SNOZE: A SELF-NAVIGATOR FROM OFF-CENTER ZTE EVOLUTION

THIS STUDY AIMS AT SHOWING THE FEASIBILITY OF MR-EMBEDDED RESPIRATORY MOTION TRACKING IN ZTE LUNG IMAGING THROUGH A TECHNIQUE NAMED SNOZE, FOR SELF-NAVIGATOR FROM OFF-CENTER ZTE EVOLUTION. IT WAS SHOWN THAT THE MOTION INFORMATION IN A MOVING PHANTOM AS WELL AS IN FREE-BREATHING HUMAN VOLUNTEERS AND PATIENTS COULD BE EXTRACTED FROM THE OFF-CENTER K-SPACE DATA SAMPLED DURING A ZTE ACQUISITION. THIS EXTRACTION IS MADE WITH A DESCENT ACCURACY AND PRECISION IN TIME AND IN AMPLITUDE WITH RESPECT TO A RESPIRATORY BELT MEASUREMENT. THIS NEW INTRINSIC MOTION FOLLOW-UP METHOD COULD BE USEFUL FOR RETROSPECTIVE MOTION CORRECTION OF SIMULTANEOUSLY ACQUIRED PET/MR IMAGES. THE RESULTS OF THIS PROJECT WERE PRESENTED ORALLY AT ESMRMB 2016 IN VIENNA, AUSTRIA, AS AN ELECTRONIC POSTER AT ISMRM 2017 IN HONOLULU, USA, AND AT MANY OTHER FRENCH AND INTERNATIONAL CONFERENCES AND MEETINGS (SFRMBM, RITS, …).

1. PURPOSE OF SNOZE

In the previous section, we have seen that high quality self-navigators could be extracted from the frequently sampled center of k-space in Ultrashort Echo-Time (UTE) acquisitions, referred to as DC-signal. This remains true for any radial pulse sequence featuring k-space readouts starting at the center of k-space and finishing in the outer k-space. In this case, the DC-signal is extracted from the first signal value measured at the beginning of each spoke. This remains true also for any radial pulse sequence featuring k-space readouts starting in the outer k-space and finishing at the symmetrical outer k-space position, and going through k-space center. In this second case, the DC-signal is extracted from the signal value measured at mid-time of the readout, usually where the signal magnitude is maximum because of the gradient echo occurring at this exact moment. Those self-navigators can be used to track the physiological motion of the lung and/or the heart in order to perform prospective or retrospective motion correction, which avoids the emergence of motion artifacts in the images, as explained in 2.3.4 in the first section of this chapter.

In the first chapter of this manuscript, another pulse sequence was supposed to deal interestingly well with the short T_2^* values found in the lung parenchyma: the Zero Time-Echo (ZTE) pulse sequence. It was shown that ZTE is in reality very similar to UTE: both pulse sequences feature a similar 3D radial trajectory in k-space (usually referred to as 'kooshball'), both enable the measurement of rapidly decaying MR signals thanks to the ultrashort TE (which can reach 0 in ZTE in term of final image contrast), and both are able to perform fast 3D acquisitions with a fine voxel size (around 1 mm) and a relatively short scan time (from several tens of seconds to minutes). However, they feature one important difference: in ZTE, to reach $TE = 0$, the readout gradients need to be applied during the application of the RF excitation pulse and the data acquisition is started as soon as possible after that. This is not the case in UTE, for which the readout gradients are ramped-up and down just after tissue excitation. This results to a 'hole' located at the center of k-space and where the data cannot be measured (see **Figure 2.11**).

To solve this problem, either another acquisition is performed to acquire those missing data (with techniques referred to as WASPI or PETRA, for example) or an estimation of those data is performed as a post-processing step,

as explained in the previous chapter. In the ZTE pulse sequence provided by GE Healthcare and available on PET/MR systems on which our experiments were performed, the WASPI method was implemented: at the beginning of the acquisition, a ZTE acquisition similar to the one described above (in particular with the same RF excitation and timings parameters) but with a reduced number of spokes and attenuated amplitudes of readout gradients is performed. It leads to the measurement of the missing central region of k-space before the acquisition of the outer k-space. In standard conditions, the number of spokes acquired with the WASPI sequence (acquiring the center region of k-space) is 64 times lower than the number of spokes acquired with the RUFIS sequence (acquiring the off-center region of k-space). The name RUFIS is given in reference to the original paper introducing this technique[165].

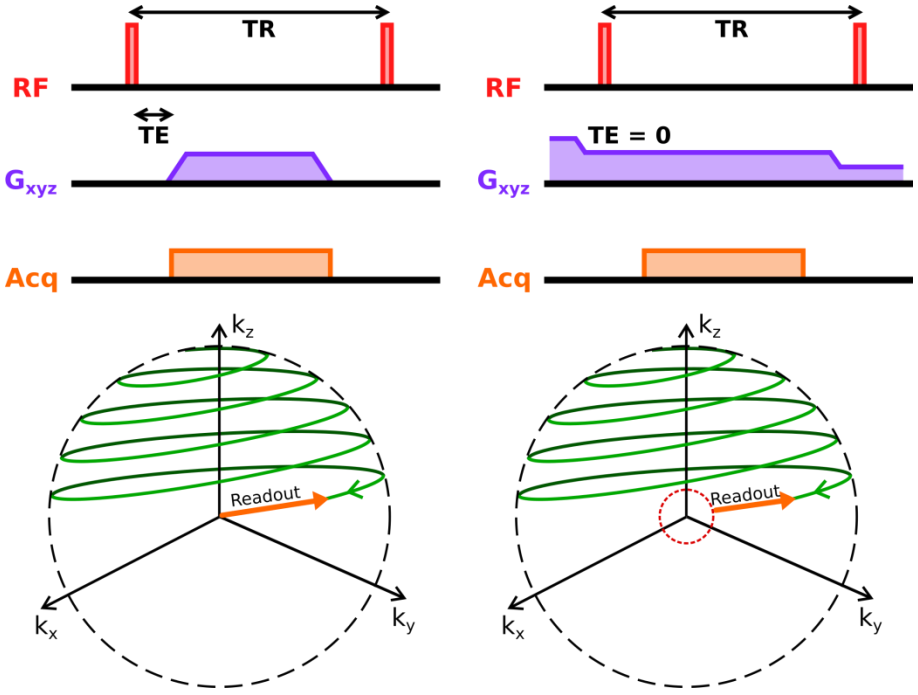

Figure 2.11: Reminder of the differences between UTE (left) and ZTE (right) pulse sequences in terms of pulse sequence chronograms (top) and k-space trajectory.

Thanks to these two separate pulse sequences applied successively, there is no missing data in k-space anymore. This make possible the acquisition of MR signals coming from short T_2^* tissues, as UTE would do. However, the problem is far more complicated for self-navigation, which was the second advantage of UTE for lung imaging. Because the central and peripheral regions of k-space are acquired during separate steps with very different scan times (a few seconds for the WASPI acquisition and around one to several minutes for the RUFIS acquisition for thoracic imaging in practice), the center of k-space, source of DC-signal, is not sampled frequently during the most important part of the acquisition, contrary to UTE. For that reason, self-navigation methods based on DC-signal time evolution cannot be directly implemented in ZTE because this DC-signal is only acquired during the first seconds of each acquisition (and not even at the exact center of k-space in practice). During the application of the RUFIS sequence, the first signal value measured at the beginning of each spoke corresponds to a position off the k-

[165] David P. Madio and Irving J. Lowe, "Ultra-Fast Imaging Using Low Flip Angles and Fids," *Magnetic Resonance in Medicine* 34, no. 4 (October 1995): 525–529, https://doi.org/10.1002/mrm.1910340407.

space center and located on a k-space sphere, at a positon given by the orientation of the spoke under consideration.

In the following, we will see what is possible to extract from those off-center points in terms of self-navigation with SNOZE, a technique that enables the extraction of a Self-Navigator from the Off-center ZTE Evolution. The objective of SNOZE is to extract from k-space data a surrogate signal similar to the one that would be obtained from the center k-space in UTE, but without having access to the actual DC-signal evolution along the acquisition.

2. THEORY AND UNDERLYING NUMERICAL METHODS FOR SNOZE

2.1. THEORETICAL AND EXPERIMENTAL CONSIDERATIONS FOR SNOZE

As seen previously with SNIF, any off-centered k-space data acquired on a moving object will depend on three different components:

- **A signal baseline:** It was written S_0 and corresponded to the off-centered signal that would be acquired without neither motion nor spin-history effects.
- **A self-navigator signal:** It was written S_m and corresponded to a surrogate signal related to any motion occurring in the subject. As seen for a human volunteer above, the self-navigator contains information from both respiratory and cardiac motions.
- **A spin-history term:** It was written h and corresponded to the effects of residual transverse magnetization from previous repetitions on the measurement performed during the current repetition.

Contrary to the UTE pulse sequence presented above, ZTE pulse sequences cannot feature a quasi-random order of k-space spokes orientations. Indeed, to perform the RF excitation pulse at the same time as the readout gradient, the usual solution is to create a continuous readout gradient that evolves smoothly along the pulse sequence repetitions by performing small gradient increments before each new RF excitation. The gradient increments should remain small for two reasons:

- In order to reach rapidly stable gradient values before each RF pulse, and
- In order to keep the SNR in the final image as high as possible without using additional spoiling gradients at the end of each repetition (in fact, the readout gradients acts as spoiling gradients too).

Because of the smooth gradient transitions between repetitions, we can therefore suppose S_0 to vary slowly along time: S_0 is not a white noise anymore and only contains low temporal frequency components. Moreover, thanks to the spoiling property of continuous readout gradients presented above, the smoothing filter characterized by h can be supposed to have weak effects: the kernel h can therefore be described correctly with a small number of components (N_{Rep} is small) and the spin-history effect at one given repetition only depends on a small number of previous repetitions. These two properties, which are the slowly varying nature of S_0 and the small numerical support of h, make it possible to assume that $S_0 \star h \approx S_0$. The model described in the previous part for SNIF would thus leads to the following relationship:

$$S_{DC} = S_m + S_0 \qquad \textbf{Eq. 2.7}$$

Note that this expression is a very simplified model and won't be used directly. We just write it here to understand the close relationship between SNIF and SNOZE, in the sense that a signal related to motion (S_m) can be separated from an off-center signal (S_0), but without taking into account any spin-history effects. The total signal S_{DC} cannot be called DC-Signal anymore because of the distance in k-space between the actual center of k-space and the position where this signal is measured. In the following, this signal will thus be referred to as pseudo DC-Signal and written $S_{pseudoDC}$. This pseudo DC-signal corresponds to k-space points located on the red dotted sphere in **Figure 2.11**, and examples of pseudo DC-signals are given in **Figure 2.12**.

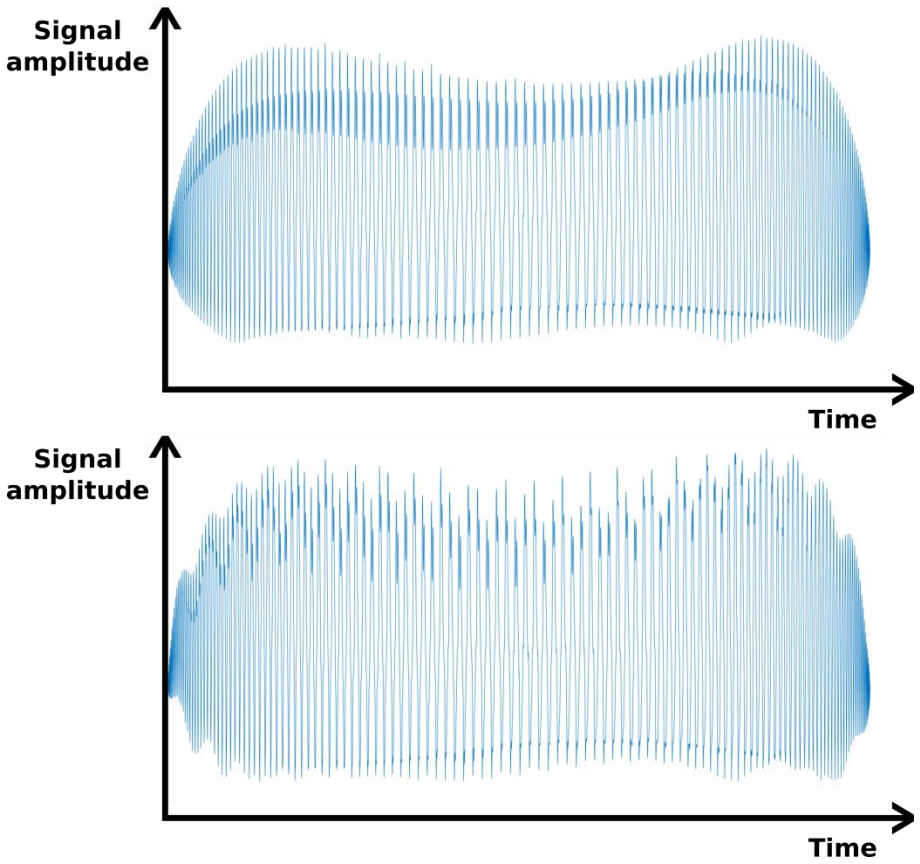

Figure 2.12: Time evolution of the pseudo DC-signal $S_{pseudoDC}$ magnitude obtained on a water phantom without (top) and with (bottom) a periodic translational motion of the phantom during the MRI acquisition. This motion was characterized by a temporal period of 3.5 seconds and an amplitude of 30 mm, which is in the order of magnitude of a usual respiratory motion. In both signals, we observe a rapid and complex oscillation corresponding to the off-center term (S_0), and an oscillating term with a larger temporal period, that only appears on the second signal, and that corresponds to the motion term (S_m).

The problem now is to separate those two signals S_m and S_0. Let us have a look to **Figure 2.12**, which represents the magnitude of the pseudo DC-signal $S_{pseudoDC}$ acquired on a water phantom. This is the signal acquired by one reception coil element when the water phantom is static or performs a periodic translational motion. We observe a signal rapidly varying along time, and more particularly at the beginning and at the end of the ZTE acquisition. Those oscillations are related to the evolution of the φ angular coordinate of the spokes in the trajectory featured by our ZTE pulse sequence (see **Figure 2.11**). At the beginning and at the end of the RUFIS acquisition, when the θ angular coordinate of the spokes are close to 0 and π radians, a small number of spokes are acquired every time φ

covers a range of width 2π (or, explained with hands, every time 'one turn' is performed), resulting to a fast angular frequency along φ at the beginning and at the end of the acquisition. To the contrary, at mid-time of the acquisition, when the angular coordinate θ of the spokes is close to $\pi/2$, a much larger number of spokes are acquired during 'one turn' along the φ angular coordinate, resulting in a lower angular frequency along this coordinate. It explains why the fundamental frequency of the oscillations observed in the pseudo DC-signal varies along the acquisition by first decreasing between the beginning and mid-time of the acquisition, and then re-increasing from mid-time to the end of the acquisition. This rapidly oscillating signal is thus highly dependent on the k-space trajectory followed along the acquisition and on the fact that the data were acquired off the k-space center: if the same data were acquired exactly at center k-space, the measured signal wouldn't depend on the spoke orientation, as seen previously with SNIF. This oscillating signal thus corresponds to S_0. Moreover, we observe a second oscillation modulating the main one described above when a motion is performed. This oscillation is related to the periodic translational motion of the phantom and doesn't seem to depend much on the spoke orientation at first glance. This second signal therefore corresponds to the signal S_m described above.

These two oscillatory signals, the rapidly oscillating off-center signal S_0 and the more slowly varying signal S_m related to physiological motions, are thus totally intricate. At first glance, it seems challenging to separate those two signals from the temporal representation of $S_{pseudoDC}$: because the main temporal frequency of S_0 changes along time, it is not possible to make a simple Fourier analysis, and some frequency components of interest in S_m may share common representative frequencies with S_0. For that reason, a more advanced extraction strategy needs to be considered.

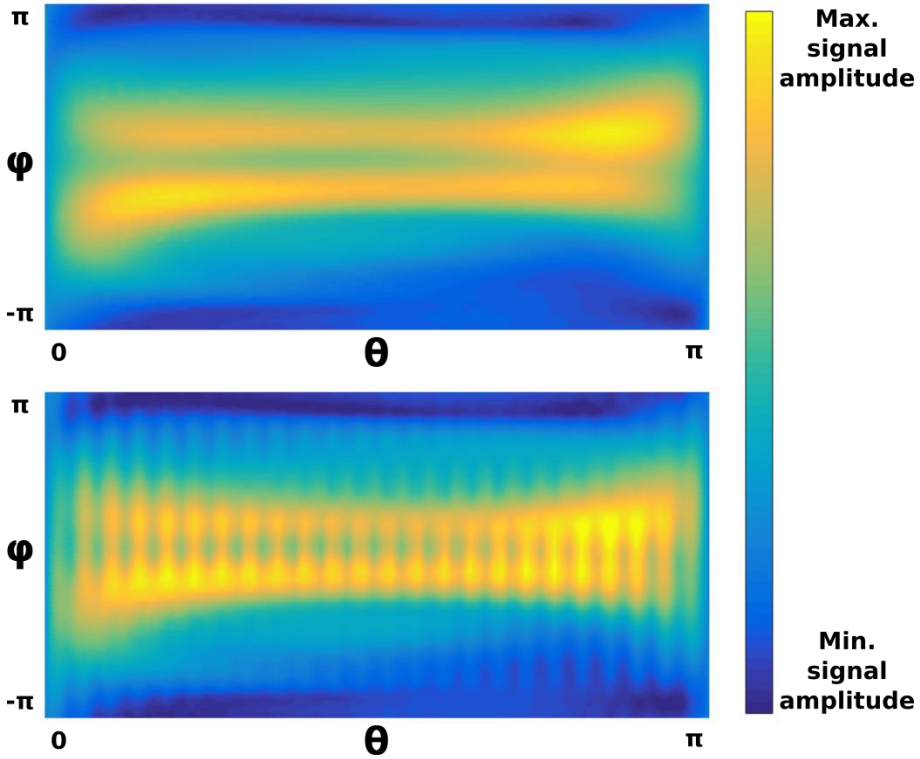

Figure 2.13: Representation of the same data as in **Figure 2.12** but interpolated in the 2D (θ, φ) space through a color-scale (right), for the phantom experiment without (top) and with (bottom) periodic translational motion. In this representation, the rapidly oscillating pattern of S_0 is converted into a 2D pattern varying slowly along θ and φ, and the oscillations corresponding to S_m are more clearly visible now along θ and are more easily distinguishable from S_0.

If the pseudo DC-Signal $S_{pseudoDC}$ is now represented as a 2D (θ, φ) matrix representation, as proposed for SNIF, we obtain the 2D images represented in **Figure 2.13**. Two remarks can be made on this representation:

- The rapid variations discussed above with a temporal frequency varying along the acquisition are now spread over a range of φ angles of width 2π (chosen between $-\pi$ and π) and over a range of θ angles of width π (chosen between 0 and π). For that reason, those oscillations now appear as a slowly varying 2D pattern along the coordinates θ and φ. This pattern is the same as the one observed with SNIF and from which S_0 was extracted. One needs to imagine that those components represent the real part (the imaginary part would give a similar representation) of the Fourier coefficients of the image at one given absolute spatial frequency (proportional to the radius of the sphere where the data is missing during the RUFIS acquisition) and along the different spatial directions that can be followed in k-space (each direction being defined by a couple of angular coordinates (θ, φ)).

- Because the θ coordinate of the spokes vary continuously and monotonically from 0 to π between the beginning and the end of the acquisition, a one-to-one relationship can be made between the time at which each spoke is acquired and its θ coordinate. Said differently, a parallel can be drawn between the evolution of time and the evolution of θ. For that reason, the signal S_m is now observed as a 2D pattern varying slowly along φ and varying quite rapidly along θ because of the periodic motion of the phantom (or because of the pseudo-periodic respiratory motion occurring in the volunteer's thorax). In SNIF, because the acquisition was performed with a quasi-random order of spokes orientations, there was therefore a total incoherence between the time evolutions of physiological motions and (θ, φ) coordinates for the spokes. In SNIF, the variations related to motions in the 2D (θ, φ) representation were thus random and seen as a noise. To the contrary, with the standard k-space trajectory featured by ZTE, θ evolves continuously and monotonically with time. For that reason, the continuous evolution of any surrogate signal along time is still continuous once represented as a function of θ.

Through the 2D (θ, φ) representation proposed above (see **Figure 2.13**), and in comparison to the 1D representation along time (see **Figure 2.12**), it is thus far easier to distinguish between the signal component related to the subject under consideration and understood by the off-center sampling of signal in k-space (S_0), and the signal component related to the physiological motions performed by the subject (S_m). In particular, those two components are easy to distinguish thanks to their distinct characteristic frequency components along the coordinate θ: S_0 varies relatively slowly along θ whereas S_m varies quite rapidly as a function of the same angular coordinate. This consideration is the foundation on which SNOZE is based to extract a surrogate signal related to motion (S_m) from the pseudo DC-Signal acquired at the beginning of each spoke during the RUFIS acquisition ($S_{pseudoDC}$). Let us now describe the implementation of SNOZE.

2.2. NUMERICAL METHODS IMPLEMENTED FOR SNOZE

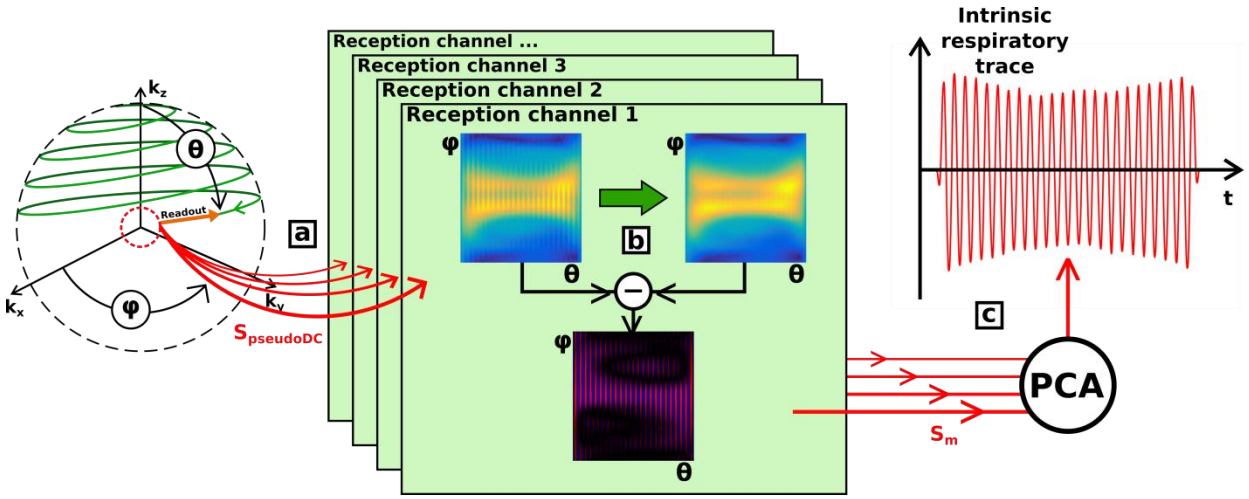

Figure 2.14: Schematic description of SNOZE. a) Interpolation of off-center k-space data from the time space to the (θ, φ) spherical coordinates space ; b) High-pass filtering along θ, performed thanks to a low-pass filtering and a subtraction with the original data ; c) Application of a Principal Component Analysis (PCA) to extract the final respiratory surrogate signal.

In our implementation of SNOZE, the MR data acquired thanks to the ZTE pulse sequence proposed by GE Healthcare were processed using Matlab. In our implementation, three steps were followed to extract the respiratory surrogate signal of interest (see **Figure 2.14**):

a. **Extraction of the pseudo DC-Signal $S_{pseudoDC}$ and interpolation in the (θ, φ) space:** Once the acquisition is performed, the first off-center point of each spoke acquired in k-space during the RUFIS acquisition is extracted: this gives the pseudo DC-Signal $S_{pseudoDC}$. As it was done with the DC-Signal in SNIF, the 1D time representation of $S_{pseudoDC}$ is mapped onto the (θ, φ) space, θ and φ representing respectively the polar and azimuthal angle coordinates of the spokes in the 3D k-space. Note that $S_{pseudoDC}$ was here chosen to be the absolute value of the complex pseudo DC-Signal. The processing pipeline described below would also be applicable to its real and/or imaginary part(s), or even to its phase after the application of a phase unwrapping step. We chose the absolute value because it was experimentally the more sensitive component in terms of modulations caused by physiological motions. Note also that, because θ doesn't evolve linearly with time, we chose a non-uniform interpolation grid along the θ axis in order to obtain discretization steps uniformly allocated in time between the beginning and the end of the RUFIS acquisition. This process was performed separately for each reception channel coil used for MR signal acquisition, as it was done with SNIF.

b. **Non-linear high-pass filtering along θ:** This high-pass filtering is technically performed by subtracting to the 2D (θ, φ) representation of $S_{pseudoDC}$ a non-linearly low-pass filtered version of the same matrix along each constant φ line (see **Figure 2.14**). Once again, this process was performed separately for each reception channel. Concerning the non-linear low-pass filtering cited above, it was performed through a local piecewise least-squares weighted regression with a 2nd order polynomial model. The local fitting was performed on a sliding window with a time width set to 10 seconds by default (to be sure to suppress all the variations related to respiratory motion, which usually feature a period of 3-5 seconds). This time width is controllable by the user if needed. This filter was experimentally chosen for its ability to remove

completely the oscillations related to physiological motion (related to S_m) and keep the background off-center signal intact (related to S_0). Thanks to the high-pass filtering performed by subtraction, we obtain at the end of the process data only representing physiological motion information (S_m).

c. **Combination into one or several respiratory surrogate signals:** A this point, we give to the user the possibility to extract either one global respiratory trace from all reception channels or one trace per reception coil element. The exact same processing pipeline is applied in both cases. The only difference is made on the data analyzed by each pipeline: either the 2D matrices for all reception channels or only the matrix obtained from the data acquired by one given reception coil, with the process repeated identically for each channel. As it might be observed in **Figure 2.14**, each line of the 2D (θ, φ) matrix does not represent exactly a true surrogate signal: for certain lines, the signal polarity sometimes reverses in comparison with the true respiratory motion, leading to a reverse interpretation of those signals in terms of inspirations and expirations. Moreover, the matrix lines show modulation patterns affecting the respiratory oscillations. These modulation patterns essentially result from the directional sensitivity of the off-center k-space data carrying the motion information. Indeed, the Fourier coefficient sampled at spherical coordinates (r, θ, φ), with r being the radius of the missing data sphere in ZTE k-space, represents the amplitude of the harmonic component of spatial frequency inversely proportional to r and oscillating along the k-space orientation given by (θ, φ). From symmetry considerations along orientations orthogonal to this direction, this coefficient is only sensitive to motions occurring in the direction (θ, φ). Because breathing is characterized by a complex motion (deformation of tissues in different directions of space), various spatial components of the motion field can be probed as the direction of acquired spokes evolves along the imaging process. Even if further development may be pursued to integrate this directional sensitivity in SNOZE, we decided to combine all the motion components occurring in all directions into one global surrogate signal (per reception channel or for all channels). To do so, and to overcome the effects of modulation and polarity reversal discussed above, without compromising the generality of the method, we decided to use a combination method based on a Principal Component Analysis (PCA)[166]. Explained with hands, PCA is an algorithm able to extract the 'main' trends and the most representative behaviors within a dataset composed of many observations of different variables. Adapted to our situation, if each time point, or θ coordinate, represents one variable, and if each φ coordinate (and each reception channel if only one global surrogate signal is extracted) represents one observation, it is possible to estimate the most common representative observations in the dataset in terms of values taken by the different variables, and therefore the most representative respiratory surrogate signals extracted from our 2D (θ, φ) representation of S_m. The main output of the PCA algorithm is a square matrix with a size equal to the number of variables and containing ordered series of the most representative combinations of variable values within the set of observations; these new variables are called the principal components (PC). In our case, different respiratory surrogate signals are obtained and ordered in term of representativeness (i.e. explained variance) of the dataset. The first two or three PCs obtained are experimentally what we expect as a surrogate signal. Polarity reversal may occur in those signals but this problem can be corrected easily now because the reversal occurs at known and repeatable positions (experimentally observed at one-half, one-third, … of the total signal duration). Once the polarity corrected, the PCs signals can be summed to give the respiratory surrogate signal of interest. The number of PCA output signals taken into account to create this final respiratory surrogate signal can be chosen by the user. The last step consists in re-interpolating this surrogate signal onto the right temporal grid (for example, one data point per pulse sequence repetition) in order to use it for motion correction purposes.

[166] Hervé Abdi and Lynne J. Williams, "Principal Component Analysis," *Wiley Interdisciplinary Reviews: Computational Statistics* 2, no. 4 (2010): 433–59, https://doi.org/10.1002/wics.101.

Some measurement and processing artifact, as undesired signal amplifications, may appear in the final respiratory surrogate signal at data points corresponding to the beginning and the end of the RUFIS acquisition. These artifacts have three causes:

- The first one is related to the fact that, at the beginning and at the end of the acquisition, the motion is only probed along axis z (corresponding to the direction of spokes when $\theta = 0$ or $\theta = \pi$ radians). Experimentally, we have observed that the best solution to follow respiratory motion was to orientate the axis z along the anterior-posterior axis of the patient. However, the components of the motion field along this direction remain usually low in amplitude for a standard breathing pattern, in particular compared to the motion components along the superior-inferior axis.

- The second one is related to the higher oscillatory frequency of S_0 at the beginning and the end of the acquisition (see **Figure 2.12**). This has effects on the interpolation step in the 2D (θ, φ) space.

- The third one is related to edge effects at the beginning and at the end of the data matrix. Indeed, to perform the low-pass filter at one given time point (see **Figure 2.14b**), data measured before and after this time point are needed. For that reason, low-pass filtering may be less accurate at the beginning and the end of the acquisition.

However, those artifacts are predictable and repeatable. For that reason, correction terms, as attenuation masks for example, were designed empirically and implemented to correct at least partially those measurement biases.

3. VALIDATION METHODS

The ZTE pulse sequence was used on a GE Signa PET/MR 3.0 T system (GE Healthcare, Waukesha, WI, USA). To make the images, a FOV of size (35×35×20) cm^3 was used. RF excitation was performed with hard RF pulses with a flip angle equal to 2° and applied with the body coil featured by the MRI machine, and signal readout was performed with a half-bandwidth equal to 31.25 kHz. Signal acquisition was performed with a GE GEM 30-channel thoracic coil array. Concerning the k-space trajectory, each segment contained 64 spokes and each spoke was composed of 256 sample points. The repetition time TR was chosen equal to 2.55 ms. For each image acquisition, it resulted in the acquisition of 33792 spokes during the RUFIS acquisition (and 640 during the WASPI acquisition, but not used here) and the total scan time was equal to 88s.

Several experiments were performed on different subjects with the exact same pulse sequence. In total, three types of subjects were studied:

- **A rectangular water phantom:** This phantom was periodically moved along the bore axis with different motion amplitudes and periods. The phantom was a plastic container of volume (33×22×16) cm^3 filled with water and gadolinium. Its motion was generated by the translational motion of the MRI bed itself on which the phantom was installed during the experiment, and automated thanks to a computer script created for this purpose. The motion amplitudes ranged from 20 mm to 40 mm, and their periods from 3 seconds to 5 seconds. To create a moving phantom under a non-moving reception coil, the 30-channel reception system was installed against the inside of the MRI bore in order to stay motionless. For each choice of motion amplitude and period, the ZTE acquisition was only performed once, except for the acquisition at motion amplitude of 30 mm and motion period of 3.5 seconds, which was repeated three times for repeatability verification.

- **Five healthy human volunteers breathing freely:** The population was composed of two women and three men, with an age of (28 ± 3) years. For each volunteer, three repetitions of the same acquisition were performed to verify the repeatability of the measurement.

- **Two lung cancer patients breathing freely:** Only one acquisition was performed for each patient because of timing constraint in the clinical protocol.

In each experiment, motions of interest were externally recorded with a respiratory belt. Concerning the human studies, the respiratory belt was set in a standard clinical routine way. Concerning the phantom experiments, because the motion was generated by a periodic translational motion of the MRI bed, we attached one extremity of the belt at the feet extremity of the bed and the second extremity of the belt on a non-moving part of the MR scanner. Human experiments were part of the research protocol PROMISE (PET/MR in Oncology and inflaMmatory process - Clinical trial 100 035 2015-A01431-48) at SHFJ (I2BM, DRF, CEA) and led by Dr. Michael Soussan. For each ZTE acquisition, one global respiratory surrogate signal was extracted from the k-space data thanks to the processing pipeline detailed in **Figure 2.14**. Concerning the tuning of SNOZE parameters, it was chosen to take into account the first three components extracted with the PCA and to create only one global respiratory trace from all the reception channels as output for SNOZE.

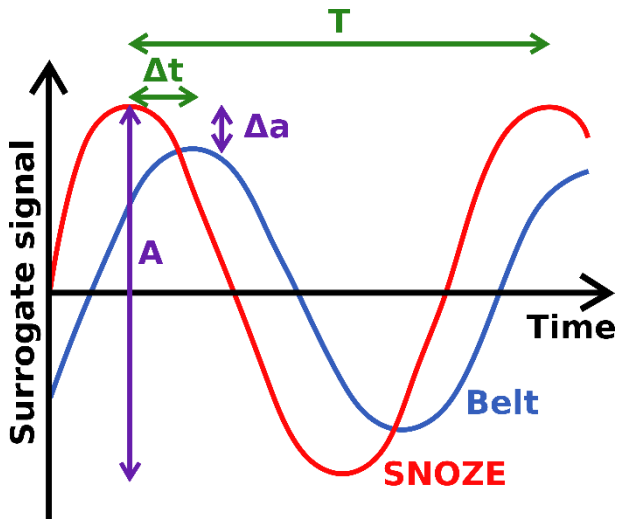

Figure 2.15: Variables used in the definitions of the Coefficient of Similarity in Time (or CST) and the Coefficient of Similarity in Amplitude (or CSA).

The relevance of this global respiratory surrogate signal was challenged with the outcome of the respiratory belt. The intrinsic respiratory trace extracted with SNOZE and the gold standard trace given by the respiratory belt were qualitatively and quantitatively compared and analyzed for each subject and each repetition. Concerning the qualitative analysis, we decided to compare both surrogate signals visually, and comment and discuss on their similarities and differences. Concerning the quantitative analysis, the accuracy of motion tracking was estimated by comparison with the trace given by the respiratory belt through the calculation of two similarity coefficients (see **Figure 2.15**):

- **The Coefficient of Similarity in Time, or CST:** This coefficient is calculated from the mean ratio over the motion periods between the time offset Δt between the extrema of the traces given by SNOZE and the respiratory belt, and the local motion period T estimated from the respiratory belt:

$$CST = \langle 1 - \frac{\Delta t}{T} \rangle_{Motion\ periods} \quad \textbf{Eq. 2.8}$$

- **The Coefficient of Similarity in Amplitude, or CSA:** This coefficient is calculated from the mean ratio over the motion periods between the amplitude difference Δa between the extrema of the traces given by SNOZE and the respiratory belt, and the local motion amplitude A estimated from the respiratory belt:

$$CSA = \langle 1 - \frac{\Delta a}{A} \rangle_{Motion\ periods} \quad \textbf{Eq. 2.9}$$

Before calculating these two coefficients, the traces given by the belt and SNOZE were co-registered with an affine model. For each estimation of CST or CSA, the standard deviation between motion periods was also computed to express the dispersion of these two metric . A last remark: the intrinsic respiratory trace was extracted with SNOZE by applying a high-pass filter (see above). This high-pass filter has the effect to suppress the low frequency components of this surrogate signal. To be able to compare the traces obtained from the belt and from SNOZE, and to be able to calculate the two coefficients CST and CSA correctly, the same high-pass filter was applied to the respiratory trace given by the belt. Moreover, the two traces were registered together before CST and CSA calculations.

4. QUANTITATIVE AND QUALITATIVE RESULTS

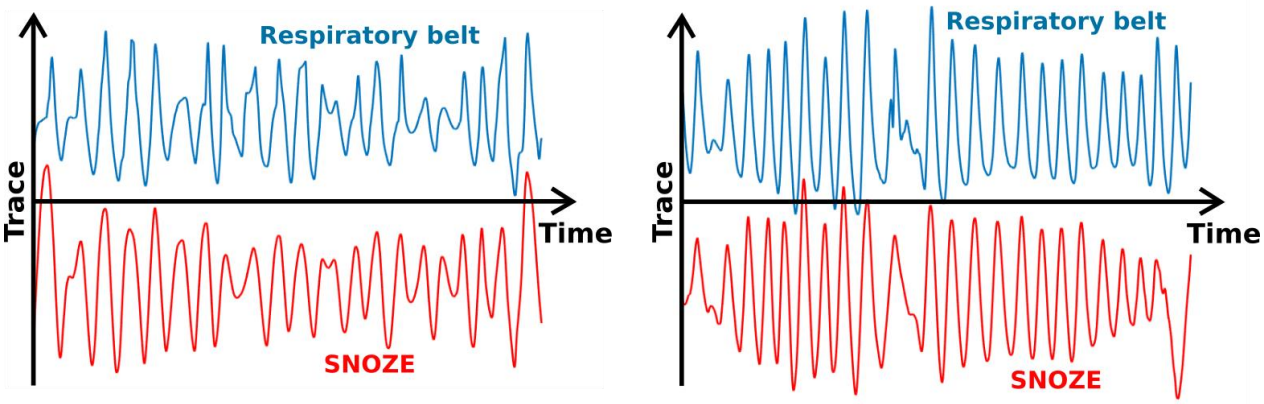

Figure 2.16: Time evolution of the respiratory surrogate signals extracted from the respiratory belt (in blue) and SNOZE (in red) for the first (left) and the second (right) patients. Along the temporal axis, we represented the traces obtained for the 88 s of ZTE acquisition.

Let us first compare qualitatively the respiratory traces given by SNOZE and the respiratory belt. The different traces obtained for the two lung cancer patients are represented in **Figure 2.16**. Qualitatively speaking, the traces obtained from both techniques are very similar for each patient. The surrogate signals provided by the belt and SNOZE remain in phase during the entire scan duration, and the motion amplitudes represented by the two curves are visually similar at each motion period. It is particularly interesting to consider the time periods when the breathing pattern is particularly irregular: even if an apnea or a breathing blip occurs, SNOZE remains able to follow the evolution of the respiratory pattern with visually the same reactivity compared to the respiratory belt (see **Figure 2.16**, patient 2). We chose to represent in priority the surrogate signals obtained for the two patients because their breathing patterns were less regular both in terms of motion period and amplitude (large inter cycle

variations, apnea, …). The value of SNOZE in terms of motion tracking can therefore be more easily evaluated from a qualitative point of view from the respiratory traces obtained for patients.

The Coefficients of Similarity in Time and Amplitude for the phantom, CST and CSA, are plotted with respect to the motion amplitude and period in **Figure 2.17**. On this figure, we observe that motion information obtained with SNOZE is very similar to the information obtained with the respiratory belt, both in terms of motion amplitude and phase, and over a range of motion periods and amplitudes close to the ones usually observed in the lung parenchyma in free-breathing humans. The values for CST and CSA are all around 0.92, which is very close to the value 1 that would represent a perfect correspondence, with a dispersion of approximatively 10 % between periods within each acquisition. To verify the repeatability of the measurement, the acquisition for a motion period of 3.5 seconds and amplitude of 30 mm was repeated three times in the exact same conditions. The results were shown to be repeatable with a variation of 0.10 % for CST and 0.11 % for CSA, which represent a great repeatability.

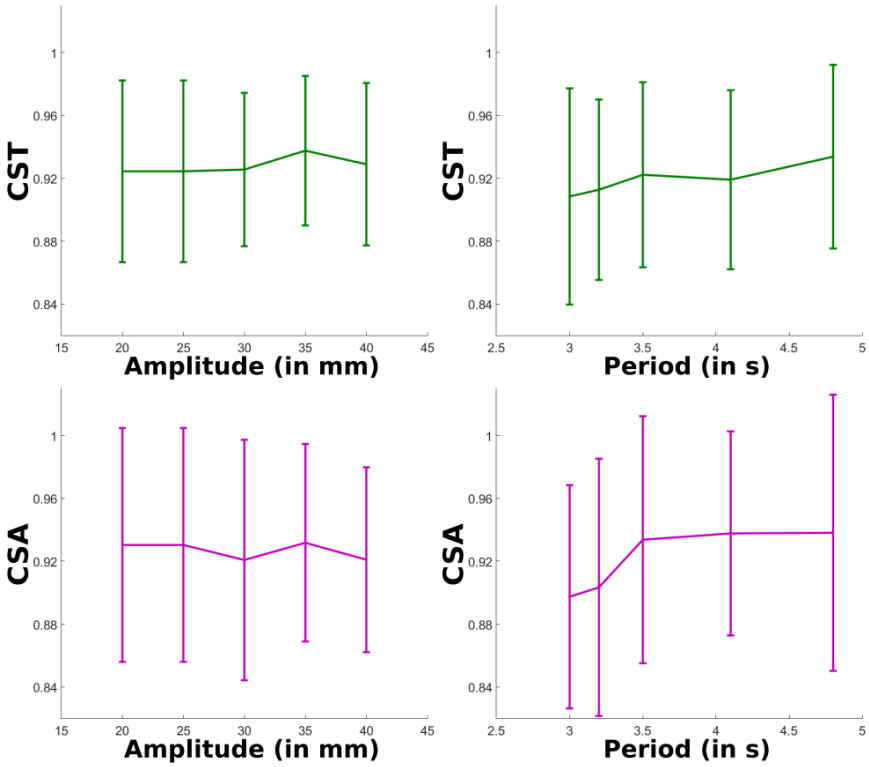

Figure 2.17: Evolution of the CST (top, in green) and the CSA (bottom, in magenta) as a function of the motion amplitude (left) and the motion period (right) of a water phantom in periodic translational motion.

For the human volunteers, the respiratory traces obtained with SNOZE and the respiratory belt are also very similar. The similarity in terms of motion phase resulted, for the five volunteers, in a CST of 0.89 +/- 0.03, thus very close to 1 and with a low dispersion. This dispersion, calculated as explained above thanks to a standard deviation between motion periods, expresses here at the same time the variability between motion periods, between the three acquisition repetitions for each volunteer and between the volunteers. The similarity in terms of motion amplitude resulted in a CSA of 0.88 +/- 0.04. Once again, this value is close to 1 and with a low dispersion between motion periods, repetitions and volunteers.

Concerning now the two lung cancer patients, quantitatively speaking, the values for CST and CSA are a bit lower, but remain largely acceptable. For the first patient, we obtain a CST equal to 0.84 +/- 0.13 and a CSA equal to 0.79 +/- 0.22. For the second patient, we obtain a CST equal to 0.87 +/- 0.10 and a CSA equal to 0.89 +/- 0.08. Note that, because it was not possible to perform several acquisitions on each patient, the dispersion expressed for the CST and CSA values only represent the variability between motion periods.

5. DISCUSSION, PERSPECTVES AND CONCLUSION FOR SNOZE

The information extracted from off-center k-space data accurately follows the motion as recorded with the respiratory belt over a large range of motion amplitudes and periods in the periodically-moving phantom. It also faithfully reports the physiological respiratory motion for both volunteers and patients, as supported by the values close to 1 with low dispersion for CST and CSA. These phantom and *in vivo* results actually sustain the sensitivity to the motion embedded in the MR data. However, the methodology proposed by SNOZE suffers from several limitations. The different drawbacks of this method are discussed in this section.

The first drawback I want to discuss is related to the lack of precision and accuracy of SNOZE at the beginning and the end of the ZTE acquisition. This problem can easily be seen in **Figure 2.16** at the end of the respiratory trace obtained with SNOZE for the second patient. We observe that, for the last seconds of acquisition, the trace obtained with SNOZE is totally different from the one obtained with the respiratory belt. As explained above, the precision in the measurement of the surrogate signal with SNOZE is compromised because of the spoke orientation at the beginning and the end of the ZTE acquisition, because of the trajectory behavior at these moments and because of the difficulties to apply correctly a smoothing filter (edge effect). However, these elements cause problems in measurement accuracy too, which can be severe and not reproducible between acquisitions. Moreover, they are difficult to correct retrospectively with an attenuation mask, for example.

The second drawback concerns the dependence on spokes orientation and therefore the sensitivity of SNOZE to different components of motions depending on the measurement direction. This problem is largely attenuated thanks to the use of the PCA algorithm. The PCA gives the possibility to extract a representative respiratory trace for the different directions contained in the coronal plane (which is experimentally orthogonal to the z axis) and defined by their different φ values. However, because θ varies continuously and monotonically between the values 0 and π from the beginning to the end of the acquisition, the direction of each spoke is different from the others, and the motion component sampled at each instant of the acquisition has never the same direction. A different evolution for the coordinate θ of spokes is difficult to consider because first, the gradients should vary continuously between spokes, and second, the current implementation of SNOZE is based on the fact that θ varies continuously and monotonically along time, so as to be able to establish a one-to-one relationship between the time and the spoke coordinate θ.

The last weakness of this method is its blindness to motions featuring high temporal frequency. This is the case for cardiac motion, for example, which cannot be assessed with SNOZE and the acquisition parameters we chose for our experiments. As a reminder, the motion is detected along the evolution of spoke coordinate θ, and all the signal values for all coordinates φ are taken into account for any motion state. However, in our experimental conditions, when θ is equal to $\pi/2$, it takes 364 spokes for the coordinates φ to cover a range of values of width 2π, or in other words, to make 'one turn' of k-space trajectory. With a TR equal to 2.55 ms, it therefore takes $364 \times 2.55 \approx 930\ ms$ to explore all the possible values of φ when θ equals $\pi/2$. Note that this is the worst case because, when θ gets closer to 0 or π, turns in the trajectory are covered in shorter time periods, as explained above. However, this explains why it is difficult to detect motions with a short temporal period, in particular in the order of 1 second or lower, which is usually the case for the cardiac motion. Furthermore, if the motion period is

too large, motion can also be difficult to detect. Indeed, the motion component S_m is extracted from the background off-center component S_0 thanks to a filtering process based on their supposed difference in frequency content along the variable θ. In the 2D (θ, φ) representation, the signal related to S_m is supposed to contain only higher frequency components in comparison to S_0. If now the physiological motion frequency of interest is too low (for example, with a period ≥ 10 seconds, which is equal to the time span of the sliding window used by the low-pass filter), the frequency components related to S_m and S_0 are mixed and cannot be differentiated anymore, which prevent the extraction of a surrogate signal only related to motion and not to off-center components.

One point in our validation methods deserves some discussion. This concerns the use of the respiratory belt as a gold standard to follow respiratory motion. A first thing to consider is that the respiratory belt is a system largely used in clinical medical imaging routine to limit motion artifacts. However, its use is often limited to prospective gating in the field of MR imaging. As explained in 3.1 in the first section of this chapter, the surrogate signal provided by the belt may not reflect exactly the internal motion of organs for several reasons. The first one is the fact that the respiratory belt is an external measurement system outputting a signal that only depends on the external effects of internal motions. Even if those external effects are usually highly correlated to organ motions, they can be explained by other physiological phenomena (for example, the contraction of abdominal muscles), and some internal motion patterns may not have external effects (for example, a purely diaphragmatic breathing will not affect much the motion of the thoracic chest). The second one concerns the position of the belt. Because the system is sensitive to the change in size of the body part to which the belt is attached, the surrogate signal can vary a lot with the belt position along the superior-inferior axis of the patient. Studies have shown that the correlation between the belt signal and the actual motion field can vary between a thoracic and an abdominal position for the belt[167]. The third one is the fact that respiratory bellows usually work thanks to air pressure variations and air displacements. If air leaks occur, the measurement data given by the belt may be biased. As well, if the belt is not attached correctly around the patient's body, the surrogate signal values can shift and the sensitivity of the system can vary during the acquisition process. Finally, the output signal provided by the respiratory belt system featured by most MRI machines today is usually subject to proprietary real-time signal processing. This can consist, for example, in the application of adaptive gains to always keep the same mean surrogate signal amplitude displayed on the control screen.

These considerations compromise the supposed one-to-one relationship between the motion field and the surrogate signal provided by the belt, and thus the use of the belt signal as a gold standard. It also encourages us to find another method to measure the evolution of the motion field along the imaging process. Nevertheless, several studies have shown the close relationship between the signal of the belt and the internal motion of organs[168]. To avoid the comparison with the belt, the solution would be to include a navigator between the different segments of the ZTE acquisition (between readout gradient ramp-down at the end of one segment and the ramp-up of the gradient at the beginning of the next segment). This possibility was tested for the ZTE pulse sequence[169], but this navigator is not implemented yet in the ZTE product sequence and thus needs further development. Moreover, as explained above, the use of a navigator is not a perfect solution (increase of pulse sequence complexity, increase of scan time, …). Other solutions would be the use of spirometry or optical system to follow motion but, once again, with their advantages and drawbacks.

---

[167] Claudio Santelli et al., "Respiratory Bellows Revisited for Motion Compensation: Preliminary Experience for Cardiovascular MR," *Magnetic Resonance in Medicine* 65, no. 4 (2011): 1097–1102, https://doi.org/10.1002/mrm.22687.

[168] Bruno Madore et al., "A New Strategy for Respiration Compensation, Applied toward 3D Free-Breathing Cardiac MRI," *Magnetic Resonance Imaging* 24, no. 6 (July 1, 2006): 727–37, https://doi.org/10.1016/j.mri.2006.01.009.

[169] Yuji Iwadate et al., "Silent Navigator–Triggered Silent MRI of the Abdomen," *Magnetic Resonance in Medicine* 79, no. 4 (April 2018): 2170–2175, https://doi.org/10.1002/mrm.26869.

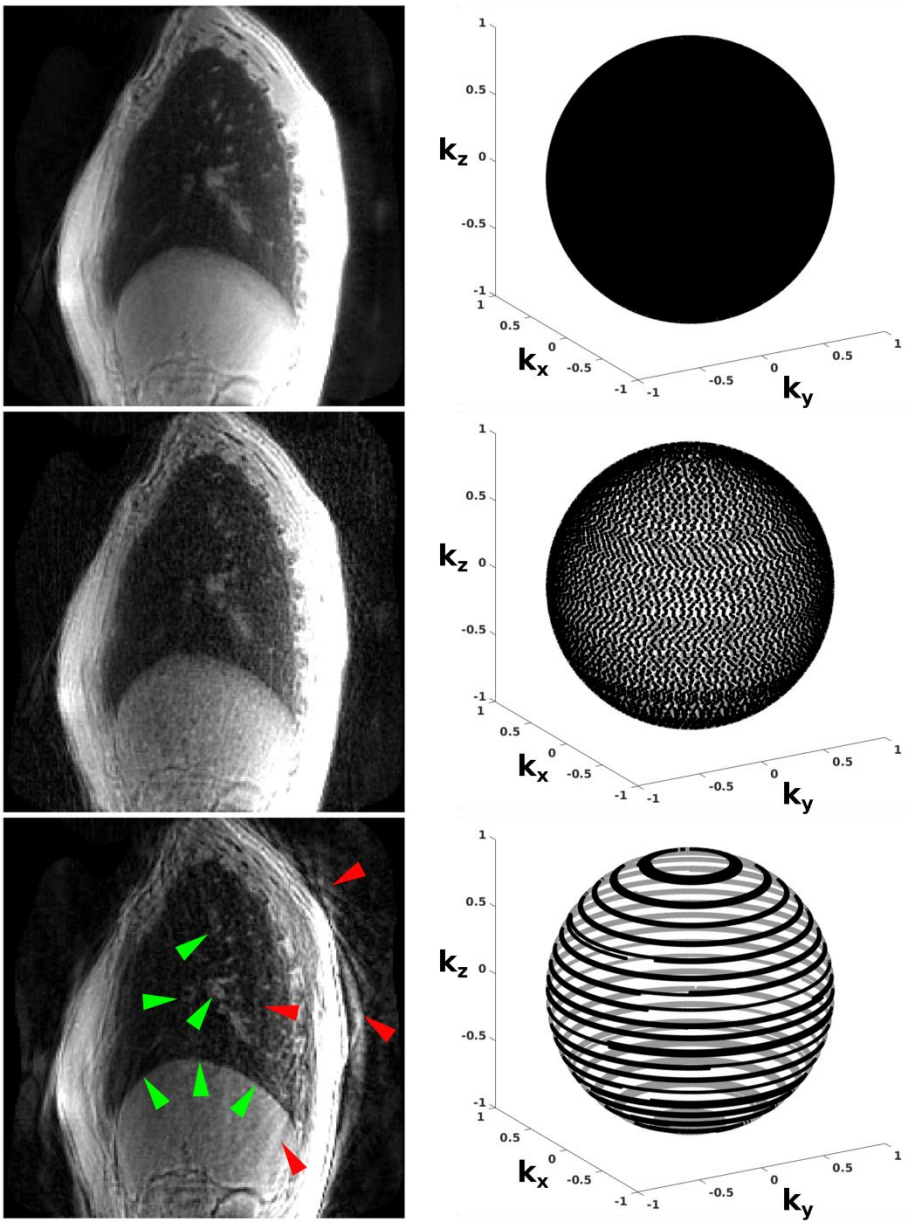

Figure 2.18: Representation of a sagittal slice of a thoracic ZTE image acquired on a healthy human volunteer breathing freely, and reconstructed from the full dataset, with no motion correction (top), from 30% of the dataset chosen uniformly in the k-space (middle) and from 30% of the dataset corresponding to the deflated lung state at each motion period (retrospective gating, bottom). On the right of each lung image, the spokes chosen for image reconstruction are represented as dots on a unit sphere, each dot representing the orientation of one spoke in the 3D k-space. Green arrows represent locations in the image where motion correction is clearly visible (higher image sharpness, details made visible, …) and red arrows represent location where spatially coherent under-sampling artifacts are visible. The presence of those artifacts can be understood by observing the highly inhomogeneous coverage of k-space in the retrospectively gated case. This is clear in comparison with the case where the same amount of data was extracted uniformly in k-space, and for which the under-sampling artifacts look more like a background noise.

The last discussion point concerns one of the final goals of our work: respiratory motion correction to avoid the presence of motion artifacts in the final image. As explained in the first section of this chapter, the detection of one or several surrogate signals is only one step of any motion correction procedure, and the motion correction step itself needs to be implemented in a prospective or a retrospective manner. **Figure 2.18** shows three images reconstructed from the same dataset obtained on a healthy human volunteer. One was obtained by reconstructing the image from the full dataset, without taking into account the respiratory motion. The second one was obtained by taking only into account 30% of the spokes taken uniformly in the k-space. Finally, the third one was obtained by taking 30% of the data too, but corresponding to the spokes acquired when the lung is deflated, which occurs at the end of each expiration (retrospective gating). All these images were reconstructed with the toolbox BART, which will be described in details later.

On the first two images reconstructed without motion correction, we observe motion artifacts, as expected in this case (image smoothing). On the third image obtained with a retrospective gating, the motion artifacts disappear but a new type of artifact appears. We observe the apparition of spatially coherent under-sampling artifacts, related to the fact that only 30% of the total k-space data is taken into account. The spatial coherence of those artifacts is problematic because of the possible confusion between real anatomical structures and those artifacts. Under-sampling artifacts appear in the second image too because the same number of spokes was taken into account for the final image reconstruction. However, those artifacts appear more as a background noise instead of spatially coherent structures, and therefore alter less the clinical interpretation of the final image.

We understand the apparition of spatially coherent under-sampling artifacts in the third case by looking at the global organization of the spokes taken into account for the reconstruction. These graphical representations only concern the RUFIS acquisition, not the WASPI one. In the two first cases, the spokes taken into account for image reconstruction are uniformly distributed in the 3D k-space. However, in the third case, their distribution creates regions fully sampled and other totally empty of information in k-space. This means that no image information is available for large continuous sets of k-space coordinates, where sometimes a lot of useful information is contained. This explains those structured artifacts in the final image. Nevertheless, in the second case, the real lack of information is found in the high spatial frequencies region, but uniformly along all k-space directions. This explains why the under-sampling artifacts appear as a high frequency noise in this case. The holes of missing data appearing in k-space are directly related, first, to the shape of the trajectory used to acquire the raw k-space data, and second, to the motion correction method, retrospective gating, which is maybe the simplest one. The use of a more advanced motion correction method, that would not throw out data but use all the acquired data instead, would surely lead to far better results. Nevertheless, it would be valuable to find a robust solution to the first problem, which is the inadequacy of the k-space trajectory featured by our ZTE pulse sequence for retrospective gating, because it could make motion correction easier and lead to better results with more advanced methods.

In the next section, a solution to this problem is presented.

SECTION 4 AZTEK: ADAPTIVE ZERO TE K-SPACE TRAJECTORIES

BECAUSE OF SHORT SIGNAL LIFETIMES AND RESPIRATORY MOTION, 3D MR LUNG IMAGING IS STILL CHALLENGING TODAY. ZERO TE (ZTE) PULSE SEQUENCES ARE PROMISING AS THEY OVERCOME THE PROBLEM OF SHORT T_2^*. NEVERTHELESS, BECAUSE OF THE CONTINUOUS READOUT GRADIENTS THEY REQUIRE, THEIR K-SPACE TRAJECTORIES ARE NON-OPTIMAL FOR RETROSPECTIVE GATING. WE PROPOSE AZTEK, A 3D RADIAL TRAJECTORY FEATURING SEVERAL TUNING PARAMETERS TO ADAPT THE ACQUISITION TO ANY MOVING ORGAN WHILE KEEPING A SMOOTH TRANSITION BETWEEN CONSECUTIVE SPOKES. THE INCREASE IN IMAGE QUALITY WAS VALIDATED WITH STATIC AND MOVING PHANTOM EXPERIMENTS, AND DEMONSTRATED WITH DYNAMIC THORACIC IMAGING PERFORMED ON A HUMAN VOLUNTEER AND LUNG CANCER PATIENTS. THIS NEW TRAJECTORY WAS PRESENTED AT ISMRM 2019 IN MONTREAL AS AN ELECTRONIC POSTER.

1. PURPOSE OF AZTEK

Lung is a challenging organ for proton MRI because of the short T_2^* values of its parenchyma and because of respiratory motion. 3D radial Ultrashort Echo-Time (UTE)[170] and Zero Echo-Time (ZTE)[171] pulse sequences, because of the very short TE values they feature, were shown to be particularly adapted to short signal lifetime tissues. Nevertheless, whereas the readout gradient is ramped up and down at each repetition in UTE, with no requirements on the k-space trajectory, this gradient must remain continuous in ZTE, only allowing small angular increments between repetitions[172].

The trajectory chosen by GE Healthcare for their implementation of the ZTE pulse sequence was introduced previously in this manuscript. This trajectory is composed of two main parts: the WASPI sequence, which acquires the central region of k-space, and the RUFIS sequence, which acquires the peripheral region of k-space. In this part, we will only consider the RUFIS trajectory because it covers the greatest part of the acquisition time, and therefore is more directly affected by the motion of organs during data acquisition. However, the same work and analysis could also be performed for the WASPI trajectory, as its spokes are generally chosen with the same type of trajectory as RUFIS. The k-space trajectory for the RUFIS acquisition is a standard 3D radial 'kooshball' where the different spokes are acquired along directions varying continuously along time. The first spoke is acquired along direction $+z$, or $\theta = 0$ in spherical coordinates, and the last spoke is acquired along direction $-z$, or $\theta = \pi$ radians. All the other spokes are acquired with an angular coordinate θ varying continuously and monotonically between 0 and π radians, and thus varying slowly along the acquisition, and with an angular coordinate φ increasing

[170] Damian J. Tyler et al., "Magnetic Resonance Imaging with Ultrashort TE (UTE) PULSE Sequences: Technical Considerations," *Journal of Magnetic Resonance Imaging* 25, no. 2 (February 1, 2007): 279–89, https://doi.org/10.1002/jmri.20851.

[171] David P. Madio and Irving J. Lowe, "Ultra-Fast Imaging Using Low Flip Angles and Fids," *Magnetic Resonance in Medicine* 34, no. 4 (October 1995): 525–529, https://doi.org/10.1002/mrm.1910340407.

[172] M. Weiger and K. P. Pruessmann, "MRI with Zero Echo Time," in *EMagRes* (John Wiley & Sons, Ltd, 2007), http://onlinelibrary.wiley.com/doi/10.1002/9780470034590.emrstm1292/abstract.

continuously with a 2π-periodicity in order to cover uniformly the 3D k-space in terms of spokes orientations. This choice of trajectory was made for several reasons:

- The radial nature of the trajectory was chosen because it gives the possibility to encode signal coming from short T_2^* tissues in the most central parts of k-space. This part is known to correspond to low spatial frequency components in the image, and thus to the components controlling the contrast of the image. To be able to visualize the short T_2^* tissues in the image, it is therefore important for those tissues to create contrast in the image.

- This continuous succession of spokes gives the possibility to acquire several spokes during one segment, which is a group of spokes during which the readout gradient is varying continuously. This feature is important to achieve $TE = 0$, as explained in the previous chapter. To evolve continuously, the gradient steps applied between pulse sequence repetitions along the three gradient axes of the MRI machine need to be low in amplitude. This gives the possibility to make rapid changes in term of gradient field, to avoid strong oscillation of the gradient field before each repetition and to avoid the apparition of eddy currents.

- Because successive spokes are applied with very close directions in k-space, the actual readout gradient during the acquisition of one spoke acts as a gradient spoiler for the transverse magnetization produced during the acquisition of the previous spokes. This gives the possibility to obtain images with a SNR which is not reduced by residual transverse magnetization effects and without the addition of supplementary spoiling gradients. This leads to the possibility to achieve very short TR values (between 1 and 2 ms in practice), and thus to acquire 3D MR images in relatively short scan times compared to more standard pulse sequences based on gradient or spin echo, for example.

Unfortunately, this strategy usually leads to trajectories covering non-uniformly the k-space after retrospective gating, as seen at the end of the previous section about SNOZE. We have seen that the holes created in k-space by performing retrospective gating are regions where no information is available about the image to reconstruct. Those signal voids lead to strong spatially coherent artifacts in the final image, which can be confused with actual anatomical structures or lesions. Those artifacts would look like a background noise if the spokes were covering more uniformly the k-space.

To overcome this problem, we propose AZTEK, an adaptive trajectory suited to ZTE requirements and respiratory resolved lung imaging. As we will see, the radial nature of the trajectory remains unchanged, but the succession of spoke orientation is designed to comply better with retrospective gating without compromising its applicability in ZTE imaging and without changing the spoiling properties of readout gradients. Thanks to its design characteristics, this new trajectory can even be adapted to any motion pattern, as it will be discussed in the next parts.

2. DEVELOPMENT OF A NEW ZTE K-SPACE TRAJECTORY

2.1. THE DISTRIBUTION OF SPOKES IN AZTEK

Every spoke of a 3D 'kooshball' trajectory is characterized by two angles in spherical coordinates: a polar angle, θ, and an azimuthal angle, φ. In the standard ZTE sequence, k-space is sampled more rapidly along φ than θ (see **Figure 2.19a**). In AZTEK, we switch the angle orders such that k-space sampling is performed more rapidly along θ than φ (see **Figure 2.19b**). In this case, constant-φ half-circle arcs joining at the two poles, and with θ ranging from 0 to π radians, are obtained. To avoid oversampling around the poles, θ steps are modulated accordingly from one

spoke to another, and θ values on two spatially adjacent arcs are shifted with a golden ratio basis to ensure sampling uniformity. Let us see more closely how those two features are implemented.

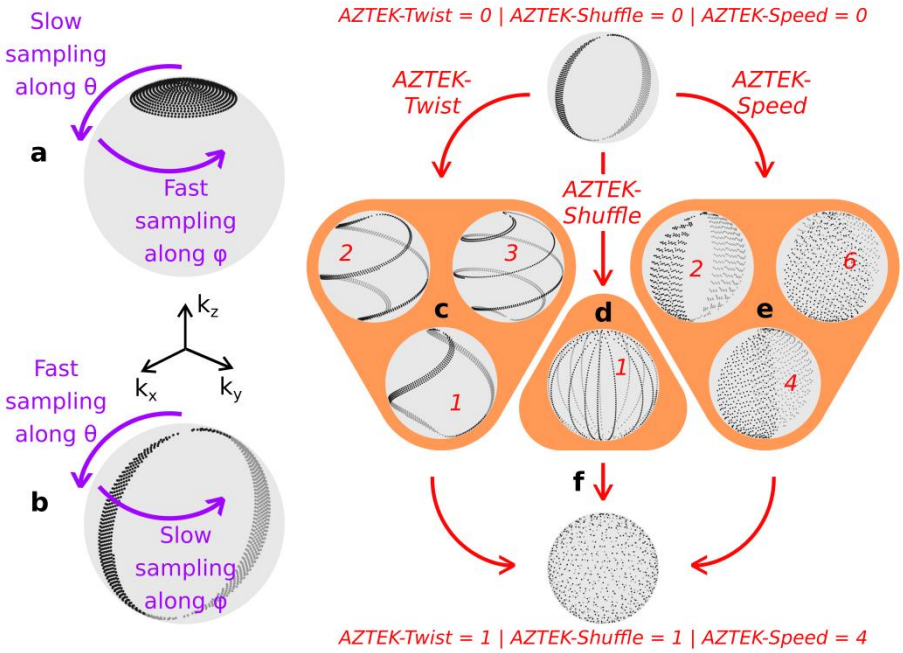

Figure 2.19: Schematic representation of the possibilities offered by AZTEK trajectories in comparison with standard trajectories.

Let N_θ and N_φ be the number of spokes on each arc and the total number of arcs in the trajectory, respectively. If N_{Spokes} is the total number of spokes for the trajectory, the two previous numbers verify the relationship:

$$N_\theta N_\varphi = N_{Spokes} \qquad \textbf{Eq. 2.10}$$

A good method to be sure that the spokes are uniformly covering the k-space is to ensure the equality between all their Voronoi cell areas on a unit sphere in the 3D k-space. This Voronoi cell for one given spoke can be defined as the continuous set of points included on a unit sphere and that are closer to this spoke compared to any other spoke. By using the expression of an infinitesimal surface in spherical coordinates, the surface of the Voronoi cell for one given spoke can be well approximated as:

$$S_{Cell} = \sin(\theta)\,\Delta\theta(\theta,\varphi)\,\Delta\varphi(\theta,\varphi) \qquad \textbf{Eq. 2.11}$$

where, $\Delta\theta(\theta,\varphi)$ and $\Delta\varphi(\theta,\varphi)$ represent the angular steps in term of polar and azimuthal angular coordinates respectively between a spoke located at angular coordinates (θ,φ) and any direct neighbor spoke located on the same arc for $\Delta\theta(\theta,\varphi)$ and on an adjacent arc for $\Delta\varphi(\theta,\varphi)$. From the description of the philosophy of AZTEK trajectories, it can be understood that $\Delta\varphi(\theta,\varphi)$ does not depend neither on θ nor on φ, and is thus given by:

$$\Delta\varphi = \frac{2\pi}{N_\varphi} \qquad \textbf{Eq. 2.12}$$

Moreover, $\Delta\theta$ can be defined as a continuous function of θ only, and that does not depend on φ because the angular coordinate θ of any spoke needs to be defined thanks to a law that does not depend on the arc itself in

order to ensure the uniformity of k-space covering. For that reason, $\sin(\theta)\,\Delta\theta(\theta)$ needs to be constant for any spoke of the trajectory. This leads, for any arc of the trajectory, to a distribution function controlling the distribution of the spokes along the arc, given by:

$$\rho(\theta) = \frac{\sin(\theta)}{\int_0^{\pi} \sin(\theta')\,d\theta'} = \frac{\sin(\theta)}{2} \qquad \textbf{Eq. 2.13}$$

Explained with hands, along any arc, the spokes will need to be more densely distributed around the coordinate $\theta = \pi/2$ radians (which gives the maximum of the distribution) than close to the poles, defined by $\theta = 0$ and $\theta = \pi$ radians (which give the minimum of the distribution). The idea is now to find a method to distribute N_θ spokes along one arc. This consists in defining N_θ values of θ spanned between 0 and π radians and that respect the distribution $\rho(\theta)$. A numerical method exists to perform this and is usually referred to as inverse transform sampling. To do so, we need to calculate the cumulative distribution function P corresponding to the density probability function ρ defined in **Eq. 2.13**. We obtain:

$$\mathrm{P}(\theta) = \int_0^{\theta} \rho(\theta')\,d\theta' = \frac{1-\cos(\theta)}{2} \qquad \textbf{Eq. 2.14}$$

The next step consists in calculating the inverse function of P, written P^{-1}. We obtain:

$$\mathrm{P}^{-1}(\xi) = \cos^{-1}(1-2\xi) \qquad \textbf{Eq. 2.15}$$

The inverse transform sampling technique consists in defining N_θ values ξ_j, with j varying from 0 to $N_\theta - 1$, comprised between 0 and 1 and chosen along a uniform density distribution. The simplest is to define N_θ uniformly spaced values, with a spacing $\Delta\xi = 1/N_\theta$. We thus obtain $\xi_j = j\Delta\xi$, for j varying from 0 to $N_\theta - 1$. By calculating their transform through P^{-1}, a suite of θ_j values comprised between 0 and π radians is obtained with the expected probability distribution given by ρ. By doing so, we ensure to uniformly cover the k-space with the N_{Spokes} spokes.

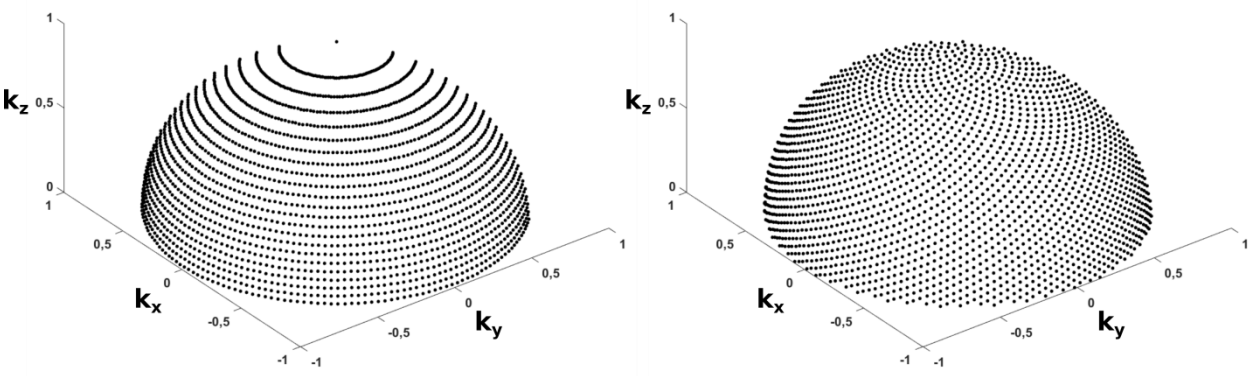

Figure 2.20: Representation of the spokes orientations on the unit sphere in k-space without (left) and with (right) the golden ratio correction of θ coordinates between spatially adjacent arcs. We observe that the circular artifacts disappear thanks to the correction. This leads to far more uniform k-space coverage.

However, if the exact same suite (ξ_j) is used for every arc of the trajectory, circular shapes of constant θ_j values will cover the unit sphere introduced above (see **Figure 2.20**). This is particularly problematic close to the poles where the distance between spokes is large along the angular coordinate θ ($= \Delta\theta(\theta) \propto 1/\sin(\theta)$, which is large close to the poles) but short along the angular coordinate φ ($= \sin(\theta)\,\Delta\varphi$, which is short close to the poles). This

leads to an over-density of spokes along those circles and voids in-between. To correct this, we are using a strategy based on the golden ratio. The golden ratio is defined as:

$$GR = \frac{1+\sqrt{5}}{2} \quad \textbf{Eq. 2.16}$$

If k is an integer index varying from 0 to $N_\varphi - 1$, we re-define the previous suite of ξ values as:

$$\xi_{jk} = j\Delta\xi + \left(\frac{k}{GR}\right)[1] \quad \textbf{Eq. 2.17}$$

In the previous formula, the 1 between brackets is a modulo operator for the ratio between k and GR. Explained differently, we extract the decimal part of k/GR, which is thus comprised between 0 and 1. The use of the golden ratio in the definition of ξ_{jk} makes the spokes from spatially adjacent arcs well distributed, and the final distribution of spokes in the 3D k-space is now uniform (see **Figure 2.20**).

2.2. THE THREE TUNING PARAMETERS OF AZTEK

Thanks to this new way to define a 3D radial k-space trajectory, AZTEK offers three degrees of freedom to control the spoke sequence and explore the k-space:

- Each arc can be twisted by modulating φ as a function of θ. This gives the possibility to 'twist' each arc joining the two poles in order to explore more directions in the 3D k-space when the trajectory goes from one pole to the other. However, if the arcs are twisted, more spokes are acquired on each arc in order to keep low amplitude gradient transitions between spokes. To perform this twisting, we implemented the parameter *AZTEK-Twist*, which represents the rate of φ shifting as a function of θ. More quantitatively speaking, if *AZTEK-Twist* is set equal to 0, the angular coordinate φ remains constant on each arc as the angular coordinate θ evolves from 0 to π radians (see **Figure 2.19b**). If now *AZTEK-Twist* is set equal to 1, the angular coordinate φ is increased continuously and monotonically of π radians on each arc as the angular coordinate θ evolves from 0 to π radians (see **Figure 2.19c**).

- Any increment can be applied for φ when a pole is reached. It gives the possibility to explore a greater diversity of directions in the 3D k-space with a small number of arcs (whereas *AZTEK-Twist* was implemented to explore a greater diversity of directions within one arc). To perform this tunable change of arc orientation, we implemented the parameter *AZTEK-Shuffle*, which is the fraction of the golden angle applied as φ shift. More quantitatively speaking, if *AZTEK-Shuffle* is set to 0, the arcs are successively applied with a minimal change in trajectory direction (and thus a change in the angular coordinate φ very close to π radians) every time a pole is reached (see **Figure 2.19b**). If now *AZTEK-Shuffle* is set to 1, the arcs are successively applied with an increment of angular coordinate φ equal to the golden angle ($\approx 111.25°$) between the end of one arc and the beginning of the next one (see **Figure 2.19d**).

- Interleaved θ reading can be performed to cover more rapidly a great number of directions in k-space. This is made possible by acquiring only a small number of equally spaced spokes on each arc for the entire trajectory and to acquire the missing spokes during successive repetitions of the trajectory. Technically speaking, the idea is to define the full trajectory as described from now (which is just an ordered list of readout gradient instructions along directions x, y and z), but to read it by skipping at each readout a given number of spokes before reading the next one. Once the end of the gradients list is reached, the idea is to go back at the beginning of the list and read the missing spokes with the same interleaving

strategy. This process is repeated until all the spokes of the list are read. To control this possibility, we implemented the parameter *AZTEK-Speed* which indicates the number of spokes that are skipped between two successive readouts. More quantitatively speaking, if *AZTEK-Speed* is set to 0, no spokes are skipped and the ordered list of readout gradients is read continuously from the beginning to the end (see **Figure 2.19b**). If now *AZTEK-Speed* is set to 1, one spoke is skipped after each readout and the ordered list of readout gradients is scanned twice: a first time to read the spokes of odd indexes and a second time to read those of even indexes (see **Figure 2.19e**).

The three parameters *AZTEK-Twist*, *AZTEK-Shuffle* and *AZTEK-Speed* control three different trajectory effects and can be seen as independent degrees of freedom to define the final k-space trajectory. For that reason, these three parameters can be jointly tuned to obtain a final trajectory adapted to the targeted motion dynamics and which uniformly covers the k-space along any retrospective motion gate (see **Figure 2.19f**). This explains why the word 'adaptive' was chosen to qualify this trajectory: as discussed later, we will study the possibility to choose optimally the values for the three tuning parameters in order to obtain, after the application of any retrospective motion gate for a given motion pattern, a sub-trajectory that uniformly covers the entire 3D k-space. We hope, thanks to this possibility, to optimize the quality for any retrospectively gated image by adapting the trajectory to the time evolution of the motion field under consideration.

2.3. THE TECHNICAL DEVELOPMENT OF AZTEK

More technically speaking, AZTEK was implemented as a C function that takes as input only five arguments:

- An integer variable corresponding to the total number of spokes.
- A float variable corresponding to an attenuation factor ranging from 0 to 1, and that scales the amplitude of the final readout gradient instructions. This argument is particularly useful to define the k-space trajectories of RUFIS (this argument is set equal to 1) and WASPI (this argument is set equal to $1/8$ for example).
- A float variable controlling *AZTEK-Twist*.
- A float variable controlling *AZTEK-Shuffle*.
- An integer variable controlling *AZTEK-Speed*.

As outputs, this function returns three 1D arrays with a size equal to the number of spokes and containing the list of integer instruction amplitudes for the readout gradients along directions x, y and z. Those outputs are of the same type as those returned by the built function calculating the standard trajectory for the product ZTE pulse sequence proposed by GE Healthcare. This built function is called in the EPIC source code of the ZTE pulse sequence (EPIC being the programming language used to develop pulse sequences on GE MR and PET/MR scanners). The function defining AZTEK was thus called similarly and a switch variable was implemented to choose between standard or AZTEK trajectories. This switch, as well as the variables controlling the parameters *AZTEK-Twist*, *AZTEK-Shuffle* and *AZTEK-Speed*, were made available on the user interface in order to choose their values at pulse sequence prescription time, just before the acquisition of the images.

3. VALIDATION METHODS

ZTE acquisitions with the standard and adaptive AZTEK trajectories were performed with a GE Signa PET/MR 3.0 T machine (GE Healthcare, Waukesha, WI, USA) on a GE textured water phantom, on one human volunteer breathing freely and two lung cancer patients breathing freely. The choice of trajectory (standard or AZTEK) was the same for both RUFIS and WASPI acquisitions. The human studies on volunteers were validated by the local ethics committee and the human studies on patients were part of the IMAHTEP protocol led by Dr. Florent Besson. Images of the phantom were acquired both in static and dynamic modes. Concerning the dynamic mode, the phantom was put into motion by periodically translating the patient bed during the acquisition with an amplitude of 30 mm and a time period of 5 s, as it was done in the previous section for SNOZE.

For the experiments on the water phantom, the ZTE acquisitions were performed with a cubic FOV of 28 cm, an isotropic voxel size of 1.4 mm and a flip angle of 4°. For this experiment, the body coil featured by the MR scanner was used both as the transmitter and receiver. For the experiments on the human volunteer and the lung cancer patients, the ZTE acquisitions were performed with a cubic FOV of 32 cm, an isotropic voxel size of 1.6 mm and a flip angle of 3°. In human, a GE GEM 30-channel thoracic coil was used for signal reception. In the different experiments, motions were monitored with an abdominal belt. In particular, for the phantom experiments, the motion of the MRI bed was followed thanks to the same technique as described above for the validation of SNOZE. For all the pulse sequences applied, the TR was equal to 1.97 ms and the readout bandwidth was ±31.2 kHz. The WASPI acquisition consisted in the acquisition of 1024 spokes while the RUFIS acquisition consisted in the acquisition of 40000 spokes, and the total scan duration was 1 min 25 s.

For each acquisition, motion correction was performed by selecting a given percentage of the data in the RUFIS acquisition which corresponds to one given extremal motion state: one of the two extremal positions was chosen for the phantom studies and the deflated lung state (end expiration) was chosen for the human studies. However, all the data obtained during the WASPI acquisition was taken into account. All the images were reconstructed with the BART toolbox[173] (Berkeley Advanced Reconstruction Toolbox), which gives the possibility to perform parallel imaging and compressed sensing reconstructions of non-cartesian k-spaces. For the phantom acquisitions performed with only one reception channel (body coil), a Non-Uniform FFT (NUFFT) algorithm proposed in BART was used for reconstruction without any regularization. For human acquisitions performed with the 30-channel thoracic coil, a parallel imaging and l1-wavelet compressed sensing algorithm was used in combination with an ESPIRiT autocalibration step that aims at estimating the coils sensitivity profiles directly from the MR data. Two iterations and a regularization parameter equal to 0.005 for the l1-wavelet term were prescribed for the image reconstruction in human. For all the reconstructions, only radial density compensation was considered to correct for the non-uniform k-space sampling. The possibilities offered by this toolbox and the principles of parallel imaging and compressed sensing will be discussed more in details in the next chapter.

4. RESULTS

Figure 2.21 and **Figure 2.22** show respectively the static phantom images and the dynamic phantom retrospectively gated images obtained with both standard and AZTEK trajectories. **Figure 2.23** and **Figure 2.24** show respectively the gated images obtained from the volunteer and the lung cancer patients with the same k-space trajectories.

[173] Martin Uecker, *Mrirecon/Bart: Version 0.4.03* (Zenodo, 2018), https://doi.org/10.5281/zenodo.1215477.

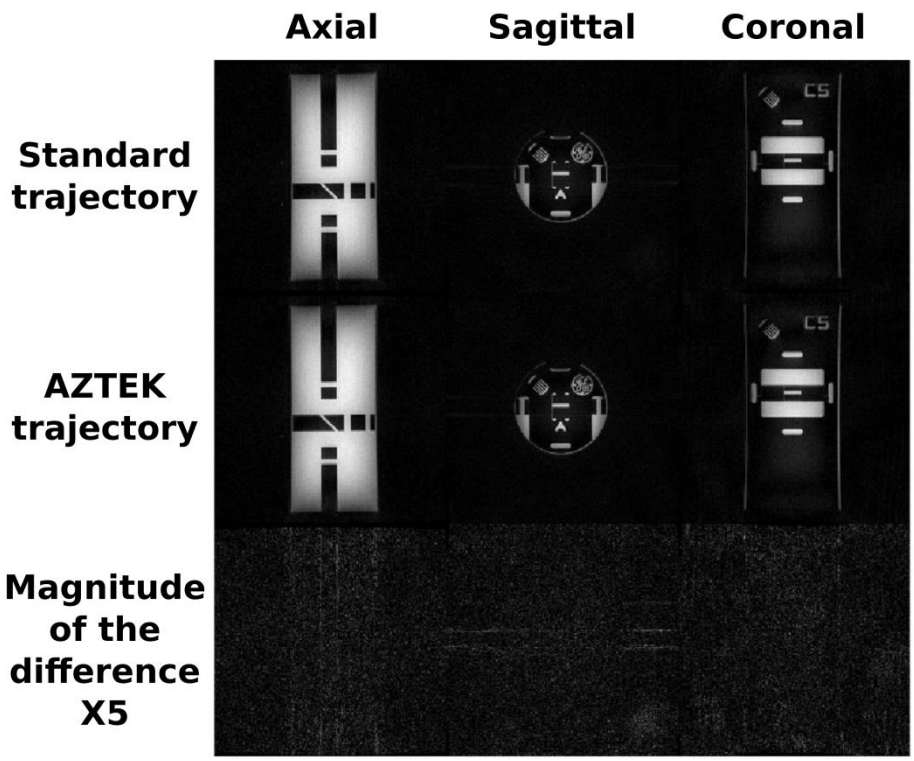

Figure 2.21: Representation of three orthogonal slices of a static water phantom image acquired with the standard trajectory (top), the AZTEK trajectory (middle) and their difference in absolute value (bottom). The orientations of the slices (Axial, Sagittal and Coronal) are given as if a patient was lying supine and head first on the MRI bed. The AZTEK parameters values were *AZTEK-Twist* = 1, *AZTEK-Shuffle* = 1 and *AZTEK-Speed* = 4.

In **Figure 2.21**, three orthogonal image slices of the static water phantom acquired with the standard trajectory (first row) and with the AZTEK trajectory (second row) set with *AZTEK-Twist* = 1, *AZTEK-Shuffle* = 1 (to obtain a golden angle shift between consecutive arcs) and *AZTEK-Speed* = 4. In the bottom row, the amplified absolute difference of the two rows above is represented. We observe a comparable image quality with the two trajectories and along any spatial orientation. These images were reconstructed from the full dataset (the 40000 spokes of the RUFIS acquisition) and with neither motion correction (the phantom was static) nor data decimation. These results confirm that both trajectories, the standard trajectory and the AZTEK one, give similar results in the static case. No artifacts appear in the images and no degradation in SNR is observed.

In **Figure 2.22**, three orthogonal image slices of the dynamic water phantom acquired with the standard and AZTEK trajectories when the phantom is animated by a periodic translational motion (along the direction represented by the red arrows). The first row represents the raw images, obtained by taking into account the full dataset (the 40000 spokes of the RUFIS acquisition). In this case, severe motion artifacts are observed, as expected. The rows two and three represent the images after motion correction with retrospective gating. The gate corresponds to 15% of the data acquired at one extreme position of the phantom. In this case, the motion artifacts observed in the first row disappear. In the fourth row, the fully sampled static image is represented for comparison with the previous motion corrected images. We observe a clear increase in retrospectively gated image quality with AZTEK in comparison to with the standard trajectory. Coherent under-sampling artifacts, which were clearly visible in the retrospectively gated images acquired with the standard trajectory, are not observed anymore if the image is acquired with the AZTEK trajectory. With the use of AZTEK, under-sampling artifacts appear as a high frequency

background noise instead. Contrary to the coherent under-sampling artifacts obtained with the standard trajectory, this high frequency noise is not as troublesome for the diagnostic quality of the final image: this noise doesn't hide the details in the phantom, and it does not create fake structures in the final image.

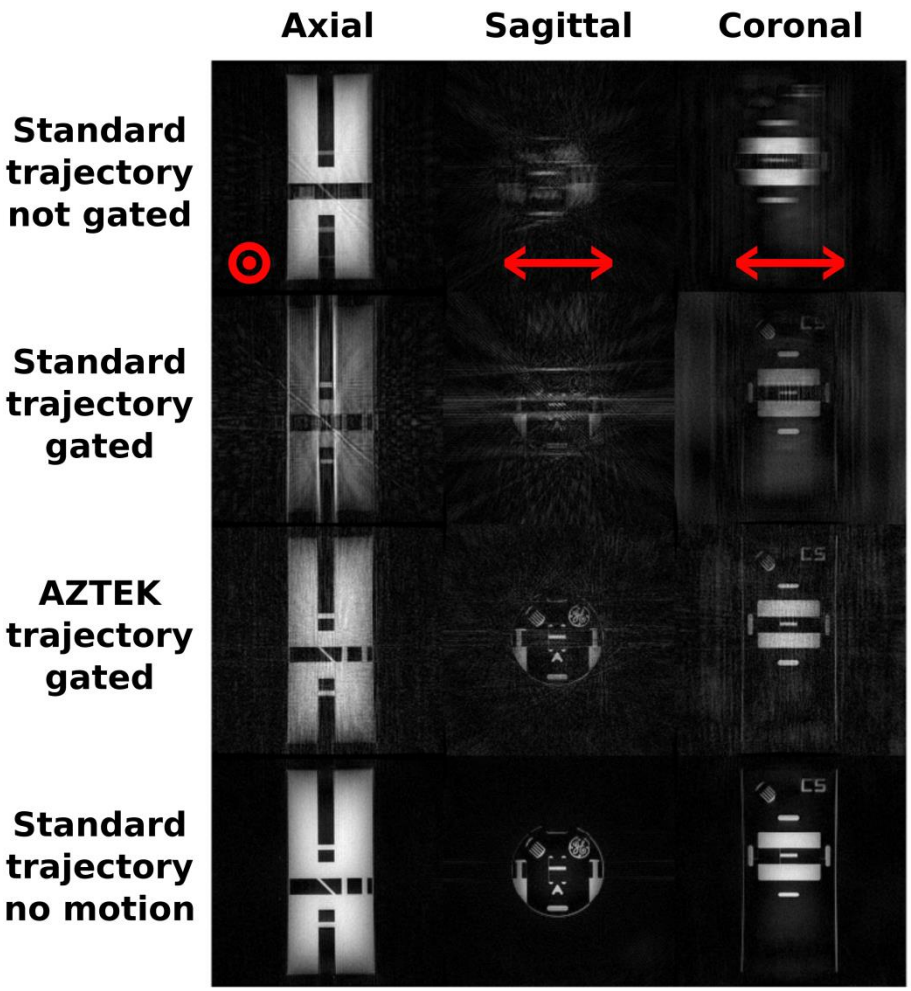

Figure 2.22: Representation of three orthogonal image slices of a moving water phantom acquired with the standard trajectory without (top) and with (top-middle) motion correction, with the AZTEK trajectory and motion correction (middle-bottom) and the corresponding fully sampled image of the static phantom for comparison (bottom). The orientation of motion is given by the red arrows. The orientations of the slices (Axial, Sagittal and Coronal) are given as if a patient was lying supine and head first on the MRI bed. The AZTEK parameters values were *AZTEK-Twist* = 1, *AZTEK-Shuffle* = 1 and *AZTEK-Speed* = 4.

In **Figure 2.23**, three views of a retrospectively-gated ZTE thoracic image acquired on our freely breathing volunteer with the standard and AZTEK trajectories are represented. These images are here observed with a maximum intensity projection over a few slices. The gates were chosen to keep 50% of data corresponding to the deflated lung state. The corresponding k-space trajectories obtained after gating are represented on the right of each row. Green arrows point out details in the lung that are clearly observable when the adaptive trajectory is implemented but hidden by spatially coherent artifacts with the standard trajectory. Once again, we observe the advantage of having a uniformly covered k-space after retrospective gating in term of final image quality and diagnostic value.

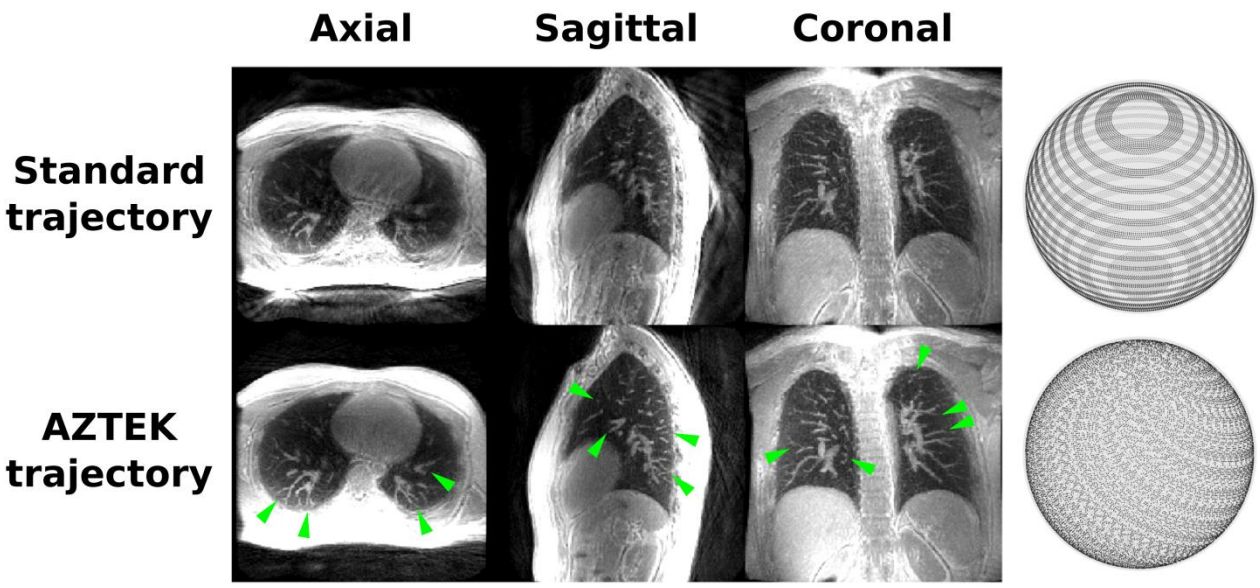

Figure 2.23: Representation of three orthogonal slices of a retrospectively gated image obtained on the healthy human volunteer and acquired with the standard trajectory (top) and the AZTEK trajectory (bottom). The 50 % of data corresponding to the end of expiration were taken for image reconstruction. Details that are more easily visible in the lung thanks to AZTEK are pointed out thanks to the green arrows. On the right are represented the positions of the spokes on a unit sphere after the application of the retrospective gate for each trajectory. The AZTEK parameters were *AZTEK-Twist* = 1, *AZTEK-Shuffle* = 1 and *AZTEK-Speed* = 4.

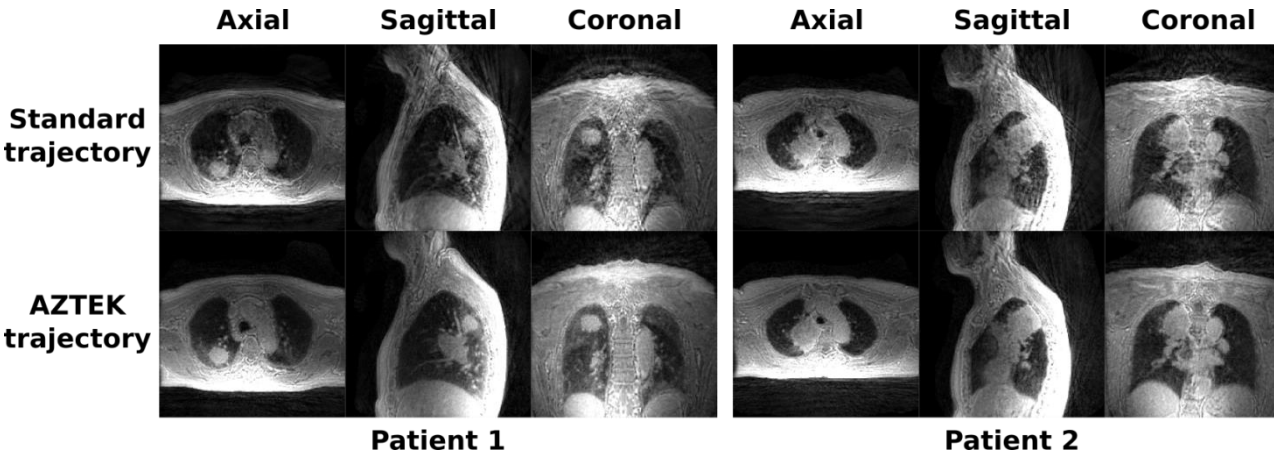

Figure 2.24: Representation of ZTE images obtained for two lung cancer patients through three orthogonal slices centered on the lung tumor. For each patient, the images acquired with the standard and the AZTEK trajectories are represented. Motion correction and image reconstruction were performed with the same method as for the healthy human volunteer. With the AZTEK trajectory, the lung tumor is more clearly visible: thanks to the lower amount of spatially coherent under-sampling artifacts, the tumor borders are sharper and the lesion can be more easily depicted from the background lung parenchyma and surrounding vessels.

In **Figure 2.24**, the same types of images are obtained for the two lung cancer patients. By comparing the images obtained thanks to the standard and the AZTEK trajectories, the same conclusions can be drawn. In particular, if we observe the primary tumor of those patients (located for both patients in the apical region of the right lung), we

observe a better delineation of the tumor borders and a more uniform signal inside the lesion thanks to AZTEK. It is now easier to differentiate between the tumor and the surrounding vessels, to estimate the size and extent of the tumor and to study the texture inside the lesion. The clinical value of retrospectively gated ZTE imaging of the lung is therefore increased thanks to AZTEK.

5. DISCUSSION, PERSPECTIVES AND CONCLUSION FOR AZTEK

5.1. DISCUSSION ON AZTEK

We observe comparable static image qualities between the standard and the AZTEK trajectories. With motion, spatially coherent under-sampling artifacts observed on gated images with the standard trajectory are not observed anymore with AZTEK. The same result is obtained on human, where some details in the lung become more clearly visible with the use of our adaptive trajectory. AZTEK shows similarities with phyllotaxis trajectories[174]. However, it offers more flexibility and adaptability on the spoke sequence, while ensuring readout gradient continuity along time and overall uniform angular density in k-space.

5.2. IDEAS AND PERSPECTIVES FOR FUTURE WORK

A next step for this project would be to evaluate the actual uniformity of k-space coverage along θ and φ with AZTEK, to compare it with the standard trajectory and to correct any problem of angular uniformity by adapting the density compensation matrix in the reconstruction process. This would definitely lead to a greater final image quality. Future work will focus on the adaptation of AZTEK to any moving organ, for example, by learning its motion characteristics before the acquisition. Let us see in the following how it would be possible to perform this adaptation.

5.2.1. THE AUTOMATIC ADAPTATION OF AZTEK TO ANY MOTION PATTERN

The idea would be to find the best set of *AZTEK-Twist*, *AZTEK-Shuffle* and *AZTEK-Speed* parameters to ensure a uniform angular coverage of k-space along any motion gate for a given moving organ. Thanks to first empirical tests, I have observed that the uniformity of k-space coverage for one given motion gate can vary a lot when the three AZTEK parameters are modified. As a result, for one given set of AZTEK tuning parameters, the visual uniformity in k-space coverage was highly dependent on both the timing characteristics of the motion (periodicity, quasi-period, …) and the characteristic parameters of the retrospective gates chosen for motion correction (percentage of data taken into account, rejection of data for abnormal respiratory patterns, …). For the study presented just above, I just chose the parameters so as to obtain visually uniform k-space coverage for a standard respiratory motion pattern (quasi-periodic, with a quasi-period around 4-5 seconds, …) and for a standard retrospective gating (take all the data for which the respiratory belt gives a trace below a given threshold, without data rejection, …).

I think that the problem is quite challenging because it would be necessary to consider several parameters for the optimization: motion characteristics, but also FOV, voxel size, TR and scanner limits that can affect the choice of trajectory characteristics and how it can be played along time. It is also necessary to be careful at the usability of the optimal set of parameter: the gradient transitions between repetitions need to remain low in terms of gradient step amplitude (and thus, *AZTEK-Speed* cannot be set too high for example). Finally, one needs to take into account

[174] Davide Piccini et al., "Spiral Phyllotaxis: The Natural Way to Construct a 3D Radial Trajectory in MRI," *Magnetic Resonance in Medicine* 66, no. 4 (October 1, 2011): 1049–56, https://doi.org/10.1002/mrm.22898.

the possible decrease in SNR in the final image if residual transverse magnetization effects appear during the image acquisition process.

One way to perform this adaptation would be the following:

1. Estimate the main trajectory characteristics from the organ to scan and the scanner itself (number of spokes, gradient amplitudes, readout time of each spoke, …).

2. Extract before the acquisition a surrogate signal of the motion (from the abdominal belt, for example) during several representative periods of motion.

3. Create a fake surrogate signal of duration equal to the desired scan time and that would share the same signal characteristics as the surrogate signal acquired just before. One simple way to do it would consist in replicating the previous acquired surrogate signal several times to reach the desired scan time.

4. Define several fake retrospective gates from this fake motion monitoring signal. This step should be done with the same retrospective gating algorithm as used in the actual motion correction process.

5. Try to find the best values for *AZTEK-Twist*, *AZTEK-Shuffle* and *AZTEK-Speed* to optimize the uniformity of k-space coverage for this set of fake retrospective gates. This could be implemented by defining a 'trajectory uniformity metric', with a value that decreases when the uniformity of k-space coverage increases for the different fake gates, and then by optimizing the three trajectory parameters to minimize this metric. This 'trajectory uniformity metric' could be defined from an analysis of the angular density of spokes in k-space after applying the fake retrospective gates. This can be done by estimating the dispersion of the surfaces of the different Voronoi cells introduced above, or through a PSF analysis for example. Several constraints would be needed in the optimization process to avoid large gradient increments between spokes and to avoid artifacts coming from residual transverse magnetization (which depend on the trajectory but also on the MR properties of the organ under consideration). These constraints could be included in the 'trajectory uniformity metric' by increasing its value if too large gradient increments are needed between successive spokes. Another possibility would be to include these constraints in a regularization term that would need to be minimized during the optimization process.

6. Scan the organ of interest with the adapted AZTEK trajectory, by supposing that the motion will have the same characteristics as the surrogate signal used for the optimization process.

5.2.2. THE ADAPTATION OF SNOZE TO AZTEK

SNOZE is an algorithm that aims at extracting an intrinsic respiratory surrogate signal from the off-center k-space data in the RUFIS acquisition (see previous section). This algorithm is based on the fact that the angular coordinate θ of the acquired spokes evolves slowly, continuously, and monotonically during the entire ZTE acquisition (or more precisely, its RUFIS part), whereas the angular coordinate φ rapidly increases during the acquisition. This is true for the standard trajectory and we demonstrated the applicability of the method in phantoms studies and in human volunteers and patients. In AZTEK, the roles of θ and φ are inverted. In the simplest configuration of AZTEK (*AZTEK-Twist* $= 0$, *AZTEK-Shuffle* $= 0$ and *AZTEK-Speed* $= 0$), θ rapidly varies while φ slowly varies during the entire ZTE acquisition. In this special case, SNOZE would run by also inverting the roles of θ and φ in SNOZE. Yet, if one of the tuning parameters is set different to 0, SNOZE cannot be used to track the respiratory motion anymore. It is a problem because AZTEK becomes efficient when the three tuning parameters are adapted to the motion pattern and the motion correction technique.

In the following, I introduce prospective solutions, which were only rapidly tested, or sometimes neither tested nor implemented. One thing we can be sure of is that a new motion tracking method cannot be based on the continuous evolution of one angular coordinate in the trajectory because, in the general case, no angular coordinate will evolve slowly, continuously and monotonically with the use of an AZTEK trajectory. We therefore need to find a totally different solution. One idea discussed with our collaborators and co-authors at GE Healthcare (Dr. Anne Menini and Dr. Florian Wiesinger, in particular) was to include a 0D navigator (or even a 1D navigator, as proposed recently by Iwadate *et al.*[175]) between ZTE segments. I developed in the ZTE source code the possibility to acquire one FID at the beginning of each segment, without any motion encoding gradient. However, during the few tests I made with this 0D navigator, the obtained surrogate signal was not very stable, maybe because of residual transverse magnetization effects. Maybe the addition of a spoiler gradient before the acquisition of the FID would solve the problem. This possibility needs to be further explored. However, in my sense and as explained above, this technique is not a self-navigation method: the surrogate signal is extracted from data acquired apart from the imaging data. For that reason, the pulse sequence is more complex, the acquisition of the imaging data may be disturbed and the scan time is increased.

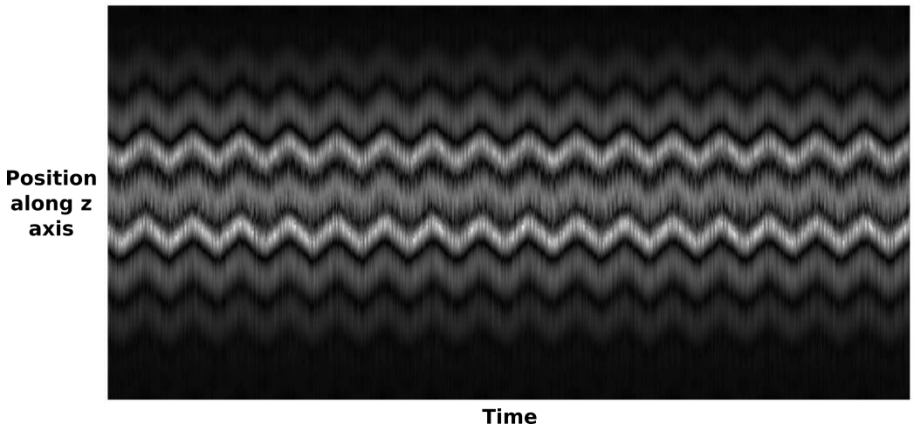

Figure 2.25: Time evolution of the image projections along axis z acquired with the AZTEK trajectory during a RUFIS sequence. We clearly observe oscillations corresponding to the periodic translational motion of a water phantom along axis z, as it would be observed with a standard 1D navigator. The acquisition of such a 1D projection-based self-navigator is made possible thanks to the AZTEK trajectory that frequently samples spokes along $+z$ and $-z$ directions during the whole imaging process.

Another solution, which is a pure self-navigation technique this time, can be considered thanks to the configuration of the AZTEK trajectory. As we have seen, at the end of each arc (and at the beginning of the next one), the AZTEK trajectory reaches a pole in the 3D k-space representation on a unit sphere (the $+z$ and $-z$ poles alternatively). Those poles are reached many times during the acquisition, whatever the choice of *AZTEK-Twist*, *AZTEK-Shuffle* and *AZTEK-Speed*. The only thing that changes when *AZTEK-Twist* and *AZTEK-Speed* are tuned is the time frequency at which those poles are reached. This feature is interesting in terms of motion tracking because each spoke acquired along $+z$ or $-z$ direction represents half the 1D Fourier transform of the image projection on the axis z. For that reason, if z is oriented along a representative direction of motion (for example, the superior-inferior direction for respiratory motion), and if the poles are reached at a sufficient time frequency, it is possible to extract directly from the imaging data a 1D self-navigator based on 1D image projections. I tested this possibility, but I was only able to

[175] Yuji Iwadate et al., "Silent Navigator–Triggered Silent MRI of the Abdomen," *Magnetic Resonance in Medicine* 79, no. 4 (April 2018): 2170–2175, https://doi.org/10.1002/mrm.26869.

detect motion from a phantom in translational motion for the moment, with z oriented along the direction of this motion (see **Figure 2.25**). However, I think that this method should be explored further because it gives the possibility to extract quite easily (in theory, at least) a 1D self-navigator directly from the imaging data and without any complex extraction algorithm (in comparison to SNOZE, for example).

A last solution, that needs to be implemented and tested, would consist in adapting SNOZE to AZTEK. Because no simple relationship can be exploited between the time and any given angular coordinate, the idea would be to interpolate our off-center data on a 3D matrix instead of a 2D one, with the third dimension representing the time (see **Figure 2.26**). In this 3D (θ, φ, t) representation, and thanks to the k-space exploration properties of AZTEK explained above, we can hope to have no large empty regions in terms of data content in this 3D matrix. Because AZTEK is able to explore a lot of different directions in k-space during short durations, one full 2D matrix can be obtained at each time step, provided that the discretization steps chosen for θ, φ and t are not too small. In this case, the signal oscillations related to respiratory motion are seen along the time dimension t, and not along θ anymore. Theoretically, this situation would lead to several advantages:

- The first advantage is that, in this situation, it is not necessary to extract a motion component (S_m) from a background off-center signal (S_0). Indeed, the background off-center signal was representing the variations along θ and φ of the signal sampled at one given spatial frequency off k-space center. Moreover, the time t and the angular coordinate θ were mixed in the previous method, which led to the mixing of information between S_m and S_0. In the new method I propose, the term corresponding to S_0 would only vary along θ and φ, whereas S_m varies along time. For that reason, the separation between S_m and S_0 would be easier compared to the original SNOZE algorithm. In particular, it would not be necessary to use the high-pass filter that was originally designed to separate the two components. This modification should remove the low temporal frequency limit in motion sensitivity discussed for SNOZE.

- The second advantage is closely linked to the first one and is related to the drawbacks of the high-pass filtering step of SNOZE, but also to the shape of the trajectory itself. As a reminder, the high-pass filtering step of SNOZE was composed of the application of a low-pass filter followed by a subtraction. It was explained in the previous section that the output of the low-pass filter was usually biased at the beginning and the end of the acquisition respectively because of the lack of data before the beginning and after the end. Moreover, because the standard k-space trajectory was exploring essentially one special k-space direction at the beginning and the end of the acquisition, respectively the directions $+z$ and $-z$, the sensitivity to motion could be very different during those time periods. Furthermore, because φ was varying more rapidly at the beginning and the end of the acquisition, the sensitivity to motion could be further biased. We have seen that those effects were predictable and repeatable to some point, and attenuation masks could be designed to correct the effects. However, motion information was sometimes totally lost and it was not possible to recover it. With the new technique explained just above, the problem doesn't appear anymore because the trajectory is far different and the low-pass filter is now useless (we do not need to separate between low and high temporal frequency components anymore). For that reason, if a 3D (θ, φ, t) matrix scheme is used with an acquisition made with the AZTEK trajectory, the sensitivity to motion should theoretically be the same at any time point along the acquisition.

- The third advantage is related to the fact that, if discretization steps along θ, φ and t are not chosen to small, a motion information along a great number of directions in space becomes available at each time step. Indeed, one 2D (θ, φ) matrix is obtained at each time step t with this new technique. Moreover, the signal evolution along time at angular coordinates (θ, φ) is related to motion components occurring along

this particular direction. For that reason, if this technique works, a 3D self-navigator would be available for ZTE imaging.

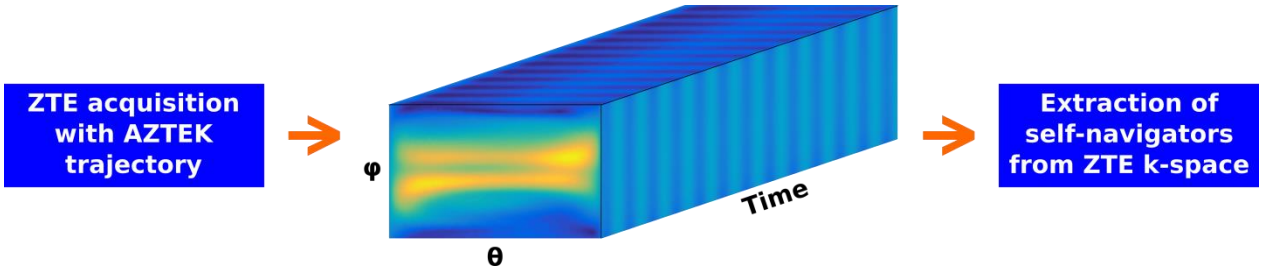

Figure 2.26: Schematic description of a possible adaptation of SNOZE to the use of AZTEK trajectories and based on an interpolation in a 3D (θ, φ, t) domain. Motion is now observed only along time and can even be discretized along different spatial directions thanks to the dimensions θ and φ.

This last technique has therefore the great advantages to be a purely self-navigating technique, that is not limited in terms of low temporal frequency motion components (but limited in high frequency components for sure), that gives a directional information about the physiological motions (which is a more detailed information compared to a 0 or 1D self-navigator), and based on a trajectory that can be adapted to any motion pattern to optimize the final image quality. The real question remains the actual angular and temporal resolution of such a 3D self-navigator. In my opinion, the logical way to choose the discretization step sizes along θ, φ and t would be to give the priority to time, in order to have a sufficient measurement rate to follow correctly the time evolution of the motion field. Once the time step size is optimized, the angular step sizes along θ and φ need to be chosen to avoid over-interpolation (by using a grid size larger than the actual information content) but that optimizes the possibility to probe the motion field along a maximal number of directions in space.

In conclusion, this study shows the great potential of AZTEK for 3D dynamic ZTE lung imaging. This trajectory is able to uniformly sample the k-space for any arbitrary retrospective respiratory motion gate, while preserving static image quality, improving dynamic image quality and guarantying smooth readout gradient transitions between spokes, which makes it appropriate to ZTE.

CHAPTER 3 - 3D MAGNETIC RESONANCE SPIROMETRY

THE DIRECT ASSESSMENT OF BIOLOGICAL FUNCTION CAN BE A SENSITIVE WAY TO EVALUATE THE PATHOPHYSIOLOGICAL STATE OF AN ORGAN. MOREOVER, WE HAVE SEEN THAT LUNG FUNCTION DEPENDS ON LUNG MECHANICAL BEHAVIOR AND PROPERTIES. THESE TWO ASPECTS OF RESPIRATORY MECHANICS SUPPORT THE DEPLOYMENT OF MECHANICAL BIOMARKERS FOR MOST LUNG DISEASES. IN THIS CHAPTER, WE WILL STUDY HOW TO EXPLOIT THE FIRST ASPECT OF RESPIRATORY MECHANICS: THE MECHANICAL BEHAVIOR OF THE LUNG. TO DO SO, WE WILL IMPLEMENT A GLOBAL IMAGE ACQUISITION AND POST-PROCESSING STRATEGY, REFERRED TO AS 3D MAGNETIC RESONANCE SPIROMETRY.

SECTION 1 MR IMAGE-BASED ASSESSMENT OF LUNG FUNCTION

IN THE FIRST CHAPTER OF THIS MANUSCRIPT, WE HAVE SEEN THAT LUNG DISEASES ARE USUALLY RELATED TO THE IMPAIRMENT OF LUNG FUNCTION, AND CAN BE RELATED TO ALTERATIONS IN MECHANICAL BEHAVIOR IN MANY CASES. THANKS TO ITS POSSIBLE SPATIAL AND TEMPORAL RESOLUTIONS, WE HAVE SEEN THAT MRI IS A POWERFUL TOOL TO NON-INVASELY PERFORM ANATOMICAL IMAGING AND FOLLOW ALONG TIME THE DEFORMATIONS OF BIOLOGICAL TISSUES. BEFORE STUDYING HOW TO ESTIMATE BIOMARKERS OF LUNG FUNCTION FROM LOCAL LUNG MECHANICAL BEHAVIOR *IN VIVO* WITH MRI, METHODS BASED ON THE MR MEASUREMENT OF PULMONARY VENTILATION AND/OR PERFUSION WILL BE DISCUSSED, AND A DISTINCTION WILL BE MADE BETWEEN THOSE BASED ON THE MEASUREMENT OF MATTER CONCENTRATIONS AND THOSE BASED ON THE MEASUREMENT OF MOTION FIELDS.

1. METHODS BASED ON THE MEASUREMENT OF MATTER CONCENTRATIONS AND MOTION FIELDS FOR THE ASSESSMENT OF LUNG FUNCTION

In this subsection, we will review the techniques based on, first, the measurement of matter concentrations in the lung and, second, the measurement of motion fields in the organ. The term 'matter' may refer to components, cells, molecules, either in gas or liquid substances, and 'motion' may refer to either the deformation of elastic bodies, the speed at which the blood flows into the pulmonary circulatory system or at which the gas flows into the airways. Both families of techniques will aim at assessing, at the regional level, the quality of the different processes that ensure lung function: ventilation, gas transfer and perfusion. As we will see, the quality of gas transfer through the alveolus-capillary membranes is more difficult to evaluate than ventilation and perfusion with MRI.

This approach was adopted because, as seen in the first chapter of this manuscript, lung function is ensured by different types of circulation processes: a circulation of gas in ventilation and gas transfer, and a circulation of blood in perfusion. From a physicist's point of view, any circulation process can be characterized by a flow, which is the amount of a given physical quantity that went through a given region per unit of time. In our case, ventilation and perfusion circulation processes could therefore be characterized by the notions of local gas and blood flows or, more accurately, by the notions of local gaseous dioxygen and red blood cell flows, for example. These flows depend on the two quantities discussed just above: the concentration of matter (dioxygen in the gas, red blood cells in a given capillary, …) and their motion properties (deformation of surrounding tissues and speed of the fluids, in particular). However, these two quantities are not always well defined when they are measured with MRI, and the measured information is often incomplete. Moreover, these two quantities may be measured more or less directly, depending on the underlying MR-based method. Nevertheless, they are both at the basis of lung function and the measurement of one of them can lead to useful information for the assessment of the pulmonary pathophysiological state.

Successively, for both families of methods, we will describe the techniques designed to estimate blood circulation and perfusion in the lung, pulmonary gas ventilation and, when possible, gas diffusion through the alveolus-capillary membrane. The physical principles supporting these techniques, either based on the estimation of

concentrations of matter or motion fields, are deeply investigated in the excellent book MRI of the lung by Kauczor *et al.*[176], which offers a wide overview on the forefront research in pulmonary MRI but also on the actual clinical practices. Moreover, other recent articles and reviews are more particularly focused on the measurement of lung ventilation and perfusion with MRI[177]. The descriptions given for the different techniques explained below were partly inspired by these publications.

After these presentations, a particular attention will be given to the techniques belonging to the second family, those based on the measurement of motion fields, because they are closer to our interest in respiratory mechanics, and in particular in the mechanical behavior of the lung. As a remark, concentrations and amounts of matter are not totally extraneous to the concept of lung mechanics as this matter composes and characterizes the system under consideration. However, in terms of mechanical behaviors of the lung, we will exclusively focus on motions in the organ. Finally, as explained in the next sections, it will even be possible to measure concentrations and amounts of matter (regional quantities of gas in the lung, in particular) from techniques based on the analysis of motion fields (deformation of the lung parenchyma in our case).

2. METHODS BASED ON THE MEASUREMENT OF MATTER CONCENTRATIONS IN THE LUNG

2.1. TECHNIQUES TO MEASURE BLOOD CIRCULATION AND PERFUSION IN THE LUNG

2.1.1. MAGNETIC RESONANCE ANGIOGRAPHY TECHNIQUES

The different methods that aim at studying blood flows in the human body with MRI are gathered under the general term MR Angiography, or MRA. As discussed rapidly in the first chapter of this manuscript, several techniques are available to perform MRA in the lung and most of them rely on the concentration of a given substance injected in the blood, or directly on the quantity of blood flowing in the pulmonary vessels. One of the most common MRA methods is based on the injection of a T_1 shortening gadolinium agent[178] [179] [180] [181]. By acquiring two images in apnea, one with gadolinium in the vascular system and the other without, and by subtracting these two images, an image is obtained of all the elements of the vascular system reached by the gadolinium agent. The signal obtained in this final image will be directly related to the concentration of gadolinium in the blood vessel. In order to make each image in apnea and to solve the problem of short T_2/T_2^* of the lung, the acquisition is usually performed thanks to a rapid gradient echo pulse sequence, either with gradient spoiling (SPGR) or exploiting the free-precession of spins between repetitions (SSFP), and featuring short TE values (around 2 ms). Ultrashort Echo-Time pulse sequences can also be exploited for this application.

---

[176] Hans-Ulrich Kauczor and Mark Oliver Wielpütz, eds., *MRI of the Lung*, 2nd ed., Diagnostic Imaging (Springer International Publishing, 2018), https://www.springer.com/us/book/9783319426167.

[177] Grzegorz Bauman and Monika Eichinger, "Ventilation and Perfusion Magnetic Resonance Imaging of the Lung," *Polish Journal of Radiology* 77, no. 1 (2012): 37–46.

[178] Hiroto Hatabu, "MR Pulmonary Angiography and Perfusion Imaging: Recent Advances," *Seminars in Ultrasound, CT and MRI*, Pulmonary, 18, no. 5 (October 1, 1997): 349–61, https://doi.org/10.1016/S0887-2171(97)90012-3.

[179] James F.M. Meaney et al., "Diagnosis of Pulmonary Embolism with Magnetic Resonance Angiography," *New England Journal of Medicine* 336, no. 20 (May 15, 1997): 1422–27, https://doi.org/10.1056/NEJM199705153362004.

[180] Ashu Gupta et al., "Acute Pulmonary Embolism: Diagnosis with MR Angiography," *Radiology* 210, no. 2 (February 1, 1999): 353–59, https://doi.org/10.1148/radiology.210.2.r99fe53353.

[181] Hakan Mutlu et al., "Gadolinium-Enhanced 3D MR Angiography of Pulmonary Hypoplasia and Aplasia," *American Journal of Roentgenology* 187, no. 2 (August 1, 2006): 398–403, https://doi.org/10.2214/AJR.04.1664.

Because the MR signal is usually increased thanks to the T_1 shortening effect of gadolinium, this technique is classified as a 'bright blood' MRA technique. Other 'bright blood' MRA techniques are available for the lung, and are not dependent on the injection of a contrast agent. For example, the same type of pulse sequences can be used to exploit the inflow effect in MR signal to produce Time-Of-Flight MRA images[182]. This bright signal coming from the vascular system was observed in the ZTE images presented in chapter 2 and will be observed also in UTE images later in this manuscript[183]. Another technique is based on the exploitation of the large T_2/T_1 contrast between lung parenchyma (low T_2/T_1) and blood (large T_2/T_1) available in bSSFP images[184]. A last 'bright blood' technique is based on the natural contrast obtained in ECG-triggered FSE pulse sequences[185], and the possibility to obtain a lung perfusion contrast by comparing images triggered on systolic and diastolic heart motion phases[186].

Other MRA techniques, usually referred to as 'black blood' MRA, give images where the arteries and veins are observable because of their low signal in comparison to the high signal of the surrounding tissue. However, because the MR signal coming from the lung parenchyma is low for most proton MR techniques, 'black blood' lung MRA seems very challenging and is not even reported in the literature. In the lung, 'black blood' techniques are essentially used for flow artifact removal, for artery wall imaging or for the better detection of pulmonary nodules in thoracic MRI.

Several MR angiography techniques are therefore available for the lung and are promising for the diagnosis of pulmonary embolism. However, only the largest arteries and veins are observed with MRA, not the capillaries surrounding the pulmonary alveoli because those capillaries are smaller than the usual voxel size in MRI. To be able to see these capillaries, decreasing the voxel size is not an acceptable solution as it would only lead to longer scan times and noisier images. MR angiography is therefore limited for the study of functional processes because lung function is made through gas exchange at the capillary level. For that reason, techniques able to give information about those capillaries and on the characteristics of the blood flowing into them are required to fully evaluate lung perfusion. Those methods are usually referred to as perfusion weighted MRI methods.

2.1.2. PERFUSION WEIGHTED MRI TECHNIQUES

As for MR angiography, several techniques exist to perform perfusion MRI in the lung[187]. The most spread one is referred to as Dynamic Contrast Enhanced MRI (DCE-MRI), and was demonstrated on many studies to estimate

[182] Jean-Pierre Laissy et al., "Pulmonary Time-of-Flight MR Angiography at 1.0 T: Comparison between 2D and 3D Tone Acquisitions," *Magnetic Resonance Imaging* 13, no. 7 (January 1, 1995), https://doi.org/10.1016/0730-725X(95)02001-A.

[183] Hatsumi T. C. Nielsen et al., "Ultra-Short Echo-Time 2D Time-of-Flight MR Angiography Using a Half-Pulse Excitation," *Magnetic Resonance in Medicine* 41, no. 3 (1999): 591–99, https://doi.org/10.1002/(SICI)1522-2594(199903)41:3<591::AID-MRM23>3.0.CO;2-R.

[184] Christopher J. François et al., "Pulmonary Vein Imaging with Unenhanced Three-Dimensional Balanced Steady-State Free Precession MR Angiography: Initial Clinical Evaluation," *Radiology* 250, no. 3 (March 1, 2009): 932–39, https://doi.org/10.1148/radiol.2502072137.

[185] Mitsue Miyazaki et al., "Non-Contrast-Enhanced MR Angiography Using 3D ECG-Synchronized Half-Fourier Fast Spin Echo," *Journal of Magnetic Resonance Imaging* 12, no. 5 (2000): 776–83, https://doi.org/10.1002/1522-2586(200011)12:5<776::AID-JMRI17>3.0.CO;2-X.

[186] Kazuyoshi Suga et al., "Potential of Noncontrast Electrocardiogram-Gated Half-Fourier Fast-Spin-Echo Magnetic Resonance Imaging to Monitor Dynamically Altered Perfusion in Regional Lung," *Investigative Radiology* 37, no. 11 (November 2002): 615.

[187] Thomas Henzler et al., "Diffusion and Perfusion MRI of the Lung and Mediastinum," *European Journal of Radiology*, Diffusion and Perfusion of the Body, 76, no. 3 (December 1, 2010): 329–36, https://doi.org/10.1016/j.ejrad.2010.05.005.

lung perfusion[188] [189] [190]. In this technique, the same type of protocol is used as for contrast-enhanced lung MRA with the same type of pulse sequences (short TE gradient echo or UTE). However, instead of acquiring only one image showing a vascular hyper-intensity, multiple images are acquired as fast as possible in order to follow along time the evolution of MR signal in the lung parenchyma. This evolution is explained by the contrast-enriched blood flowing in the many capillaries found in each image voxel. The time evolution of the MR signal at each voxel location is then analyzed thanks to a semi-quantitative (leading to parameters like the Mean Transit Time, or MTT) or quantitative models (which outputs parameters like the regional blood flow and the regional blood volume). Information on perfusion at the alveolar scale is therefore obtained, and not only at large arteries and veins locations. However, this measurement strongly depends on the acquisition protocol (image acquisition rate, injection rate of the contrast agent, …) and on the model chosen for the analysis.

Another contrast agent based perfusion MRI method is called Dynamic Susceptibility Contrast MRI (DSC-MRI), and is based on the MR signal decrease related to the ${T_2}^*$ shortening effect of a bolus of gadolinium. In this case, the pulse sequence should be ${T_2}^*$ weighted and not T_1 weighted. However, this technique is not used for perfusion measurement in the lung, certainly because lung parenchyma ${T_2}^*$ values are naturally short and MR signals are low in amplitude, which would lead to a very weak sensitivity in the perfusion measurement.

Another perfusion weighted MRI method, which is not based on the injection of an extrinsic contrast agent, is referred to as Arterial Spin Labelling (ASL). In this technique, two images are acquired with the application of a spin-saturation band. For the first one, the saturation band is applied at upstream location relatively to the lung perfusion blood (in a main pulmonary artery of the lung, for example) before the acquisition of imaging data. For the second one, the same saturation band is applied symmetrically to the first one relatively to the imaging FOV. By subtracting these two images, a perfusion contrast is obtained in the organ under consideration and the inflowing perfusion blood plays the role of an intrinsic contrast agent in this situation. The signal intensity in the final image will be strongly related to the amount of blood in each voxel and at each time-stamp.

This technique was shown to be applicable to the lung in order to measure pulmonary perfusion[191]. However, the results usually obtained are noisier in comparison to lung DCE-MRI because the subtraction image suffers from a low SNR in the two subtracted images. Moreover, any quantification of perfusion in terms of regional blood flow or volume will depend on both the acquisition process and the analysis model. Furthermore, because two images are needed to create the final perfusion image at each time-stamp, the technique is sensitive to motion artifacts. To solve this problem, lung ASL techniques based on the acquisition of a single image were recently developed[192].

---

[188] Hiroto Hatabu et al., "Pulmonary Perfusion: Qualitative Assessment with Dynamic Contrast-Enhanced MRI Using Ultra-Short TE and Inversion Recovery Turbo FLASH," *Magnetic Resonance in Medicine* 36, no. 4 (1996): 503–8, https://doi.org/10.1002/mrm.1910360402.

[189] Hiroto Hatabu et al., "Quantitative Assessment of Pulmonary Perfusion with Dynamic Contrast-Enhanced MRI," *Magnetic Resonance in Medicine* 42, no. 6 (1999): 1033–38, https://doi.org/10.1002/(SICI)1522-2594(199912)42:6<1033::AID-MRM7>3.0.CO;2-7.

[190] Yoshiharu Ohno et al., "Quantitative Assessment of Regional Pulmonary Perfusion in the Entire Lung Using Three-Dimensional Ultrafast Dynamic Contrast-Enhanced Magnetic Resonance Imaging: Preliminary Experience in 40 Subjects," *Journal of Magnetic Resonance Imaging* 20, no. 3 (2004): 353–65, https://doi.org/10.1002/jmri.20137.

[191] David A. Roberts et al., "Pulmonary Perfusion: Respiratory-Triggered Three-Dimensional MR Imaging with Arterial Spin Tagging—Preliminary Results in Healthy Volunteers," *Radiology* 212, no. 3 (September 1, 1999): 890–95, https://doi.org/10.1148/radiology.212.3.r99se35890.

[192] Eberhard D. Pracht et al., "Single-Shot Quantitative Perfusion Imaging of the Human Lung," *Magnetic Resonance in Medicine* 56, no. 6 (2006): 1347–51, https://doi.org/10.1002/mrm.21091.

2.2. TECHNIQUES TO MEASURE LUNG VENTILATION

Several techniques are today available for the assessment of pulmonary ventilation with MRI, but most of them are only available in research laboratories. Maybe the most advanced one is based on the MR imaging of a gas that would fill the whole respiratory airways during normal breathing maneuvers. This gas should, at the same time, be able to produce a MR signal and remain safe for human. In this case, the signal measured with MRI would be directly proportional to the amount of gaseous tracer present in each voxel and therefore reflect the quality of local lung ventilation.

2.2.1. HYPERPOLARIZED HELIUM-3 MRI

One of the first and most promising one is certainly ^{3}He, which possesses a spin one-half similarly to proton[193] [194] [195]. However, the MR signal produced by breathing a mixture of ^{3}He and dioxygen is usually too low to produce a valuable MR image in a time duration adapted to breath-hold. For that reason, it is necessary to prepare the gas before MRI during a step referred to as hyperpolarization. During this preparatory step, the atoms composing the gas are led out of their thermal equilibrium spin state to reach a state of increased polarization, with a larger majority of atoms in the same spin state. This is usually performed thanks to an optical pumping method[196]. After the administration of such a hyperpolarized gas in the patient's lungs, the MR signal is now several orders of magnitude larger in amplitude compared to the non-hyperpolarized case. To obtain the images, fast gradient echo pulse sequences, like SPGR or SSFP, are usually employed either with a constant flip angle (CFA) or a variable flip angle (VFA) strategy to manage the signal decay as the views are acquired, because of progressive polarized ^{3}He consumption[197]. Moreover, low B_0 fields are usually preferred for this type of acquisitions as the polarization does not depend on the magnetic field strength[198].

At the end of the imaging process, the image obtained during one breath-hold provides direct information on regional pulmonary ventilation, as the MR signal obtained in one voxel is proportional to the number of ^{3}He atoms inside it (in a good approximation). Moreover, if rapid MRI sequences are used, it is possible to perform dynamic hyperpolarized ^{3}He imaging. This gives the possibility to study the temporal evolution of gas inside the lung during several breathing cycles as the hyperpolarized gas is administered ('wash-in')[199] and as the patient is breathing room air after the helium administration ('wash-out')[200]. More advanced applications, based on ^{3}He diffusion MRI, can even be designed in order to quantify microstructural aspects of the lung parenchyma, and therefore be

[193] M Ebert et al., "Nuclear Magnetic Resonance Imaging with Hyperpolarised Helium-3," *The Lancet* 347, no. 9011 (May 11, 1996): 1297–99, https://doi.org/10.1016/S0140-6736(96)90940-X.
[194] Anselm J. Deninger et al., "Quantitative Measurement of Regional Lung Ventilation Using 3He MRI," *Magnetic Resonance in Medicine* 48, no. 2 (2002): 223–32, https://doi.org/10.1002/mrm.10206.
[195] Edwin J. R. van Beek et al., "Functional MRI of the Lung Using Hyperpolarized 3-Helium Gas," *Journal of Magnetic Resonance Imaging* 20, no. 4 (2004): 540–54, https://doi.org/10.1002/jmri.20154.
[196] G. Tastevin, "Optically Polarized Helium-3 for N.M.R. Imaging in Medicine," *Physica Scripta* 2000, no. T86 (2000): 46, https://doi.org/10.1238/Physica.Topical.086a00046.
[197] Martin H. Deppe and Jim M. Wild, "Variable Flip Angle Schedules in BSSFP Imaging of Hyperpolarized Noble Gases," *Magnetic Resonance in Medicine* 67, no. 6 (2012): 1656–64, https://doi.org/10.1002/mrm.23155.
[198] E. Durand et al., "CPMG Measurements and Ultrafast Imaging in Human Lungs with Hyperpolarized Helium-3 at Low Field (0.1 T)," *Magnetic Resonance in Medicine* 47, no. 1 (2002): 75–81, https://doi.org/10.1002/mrm.10047.
[199] Hooman Hamedani et al., "Regional Fractional Ventilation by Using Multibreath Wash-in 3He MR Imaging," *Radiology* 279, no. 3 (January 18, 2016): 917–24, https://doi.org/10.1148/radiol.2015150495.
[200] Martin H. Deppe et al., "Combined Measurement of Pulmonary Inert Gas Washout and Regional Ventilation Heterogeneity by MR of a Single Dose of Hyperpolarized 3He," *Magnetic Resonance in Medicine* 65, no. 4 (2011): 1075–83, https://doi.org/10.1002/mrm.22709.

sensitive to microstructure alterations, as in emphysema for example[201]. However, hyperpolarized ^{3}He MRI is not as accessible as proton MRI, in particular because dedicated hardware (transmit and receive coils tuned at Larmor frequency of helium, hyperpolarization setup, gas administration system, …), trained staff and costly helium-3 tracer gas are needed for the imaging protocol.

2.2.2. FLUORINATED GASES MRI

To overcome the need of hyperpolarization and all the challenges it raises to the imaging protocol, another gas can be investigated. Over the last decades, many research projects were conducted to image fluorinated gases, which correspond to molecules partly composed of ^{19}F (SF_6, CF_4, C_2F_6, …)[202] [203]. It can be shown that a sufficient MR signal can be obtained with signal averaging techniques to produce a MR image in a reasonable amount of time, if the voxel size and the TR are properly chosen (large voxel size of several millimeters and short TR depending on the fluorinated gas under consideration). Similarly as with ^{3}He, ventilation parameters can be extracted from static (breath-hold) and dynamic MR imaging of fluorinated gases[204], and diffusion MRI can even be used to probe the microstructure of the lung parenchyma[205]. However, special pieces of hardware, as dedicated coils for RF excitation and data acquisition, are still needed to perform such applications.

2.2.3. OTHER METHODS FOR VENTILATION MEASUREMENT IN MRI

To finish with MR imaging techniques designed to assess pulmonary ventilation locally, other techniques are still under research and are not ready for short term use in clinical practice. For example, techniques based on proton imaging of the lung under the administration of gadolinium aerosols[206] [207], or even under the infusion of water-in-perfluorocabon emulsions[208], were proposed to locally quantify ventilation parameters in the lung. Also, other gases can be investigated, as krypton for example[209] [210].

---

[201] G. Peces-Barba et al., "Helium-3 MRI Diffusion Coefficient: Correlation to Morphometry in a Model of Mild Emphysema," *European Respiratory Journal* 22, no. 1 (July 1, 2003): 14–19, https://doi.org/10.1183/09031936.03.00084402.

[202] Jesús Ruiz-Cabello et al., "Fluorine (19F) MRS and MRI in Biomedicine," *NMR in Biomedicine* 24, no. 2 (2011): 114–29, https://doi.org/10.1002/nbm.1570.

[203] Marcus J. Couch et al., "Inert Fluorinated Gas MRI: A New Pulmonary Imaging Modality," *NMR in Biomedicine* 27, no. 12 (2014): 1525–34, https://doi.org/10.1002/nbm.3165.

[204] Wolfgang Günther Schreiber et al., "Dynamic 19F-MRI of Pulmonary Ventilation Using Sulfur Hexafluoride (SF6) Gas," *Magnetic Resonance in Medicine* 45, no. 4 (2001): 605–13, https://doi.org/10.1002/mrm.1082.

[205] José M. Pérez-Sánchez et al., "In Vivo Diffusion Weighted 19F MRI Using SF6," *Magnetic Resonance in Medicine* 54, no. 2 (2005): 460–63, https://doi.org/10.1002/mrm.20569.

[206] Patrick Haage et al., "Feasibility of Pulmonary Ventilation Visualization With Aerosolized Magnetic Resonance Contrast Media," *Investigative Radiology* 40, no. 2 (February 2005): 85.

[207] Hongchen Wang et al., "Aerosol Deposition in the Lungs of Spontaneously Breathing Rats Using Gd-DOTA-Based Contrast Agents and Ultra-Short Echo Time MRI at 1.5 Tesla," *Magnetic Resonance in Medicine* 75, no. 2 (2016): 594–605, https://doi.org/10.1002/mrm.25617.

[208] Ming Qiang Huang et al., "MRI of Lungs Using Partial Liquid Ventilation with Water-in-Perfluorocarbon Emulsions," *Magnetic Resonance in Medicine* 48, no. 3 (2002): 487–92, https://doi.org/10.1002/mrm.10231.

[209] Galina E. Pavlovskaya et al., "Hyperpolarized Krypton-83 as a Contrast Agent for Magnetic Resonance Imaging," *Proceedings of the National Academy of Sciences* 102, no. 51 (December 20, 2005): 18275–79, https://doi.org/10.1073/pnas.0509419102.

[210] Zackary I. Cleveland et al., "Hyperpolarized 83Kr MRI of Lungs," *Journal of Magnetic Resonance* 195, no. 2 (December 1, 2008): 232–37, https://doi.org/10.1016/j.jmr.2008.09.020.

2.3. METHODS TO SIMULTANEOUSLY MEASURE LUNG VENTILATION, GAS TRANSFER AND PERFUSION

Let us discover several methods able to estimate at the same time blood perfusion and air ventilation in the lung, and also sometimes gas diffusion through alveolar septal walls. One evident possibility is to combine two techniques during the same MRI exam, one designed to measure perfusion and the second one to measure ventilation. For example, it can be performed by studying two different nuclei[211]. However, those techniques will not be considered here as they are just composed of two independent measurements. Only methods that are intrinsically sensitive to both functional processes will be described.

2.3.1. TECHNIQUES BASED ON THE OXYGEN-RELATED T_1 SHORTENING IN THE LUNG

The simultaneous study of ventilation and perfusion is actually possible in hyperpolarized ^{3}He imaging and ^{19}F MRI, as the T_1 values of those elements are highly dependent on the concentration of dioxygen in their environment. Indeed, because of their paramagnetism, dioxygen molecules in the close environment of the gaseous tracer gas shortens the T_1 of helium or fluorine[212]. For that reason, by quantifying the T_1 of the imaged gas (with T_1 weighted imaging or T_1 mapping pulse sequences, for example), it is possible to extract an information on the partial pressure of dioxygen present locally in the alveoli, and therefore deduce the quantity of dioxygen that has diffused through the alveoli walls and/or was diluted in the perfusion blood[213] [214]. This strategy thus leads to an indirect estimation of gas transfer and/or blood perfusion, and therefore gives an idea of the quality of gas exchange processes regionally inside the lungs, in complement to the ventilation information discussed in 2.2.

Another technique that was deeply investigated to inform on the quality of gas exchange processes is referred to as oxygen enhanced lung MRI[215] [216] [217]. The first direct advantage of this technique is its great availability, because standard gaseous dioxygen is used as a contrast agent and the imaging process is based on the MR signals emitted by protons in the lung parenchyma. For that reason, this technique can be implemented on most modern clinical MRI systems available in hospitals. Once again, as seen just above, this technique exploits the T_1 shortening effect of dioxygen explained by the paramagnetism of O_2. However, the image is acquired from protons present naturally in the lung parenchyma, and this can be performed with any standard short or ultrashort TE pulse sequence. If this

[211] David A. Lipson et al., "Pulmonary Ventilation and Perfusion Scanning Using Hyperpolarized Helium-3 MRI and Arterial Spin Tagging in Healthy Normal Subjects and in Pulmonary Embolism and Orthotopic Lung Transplant Patients," *Magnetic Resonance in Medicine* 47, no. 6 (2002): 1073–76, https://doi.org/10.1002/mrm.10172.

[212] B. Saam, W. Happer, and H. Middleton, "Nuclear Relaxation of 3He in the Presence of O2," *Physical Review A* 52, no. 1 (July 1, 1995): 862–65, https://doi.org/10.1103/PhysRevA.52.862.

[213] A. J. Deninger et al., "Quantification of Regional Intrapulmonary Oxygen Partial Pressure Evolution during Apnea by 3He MRI," *Journal of Magnetic Resonance* 141, no. 2 (December 1, 1999): 207–16, https://doi.org/10.1006/jmre.1999.1902.

[214] Natalie L. Adolphi and Dean O. Kuethe, "Quantitative Mapping of Ventilation-Perfusion Ratios in Lungs by 19F MR Imaging of T1 of Inert Fluorinated Gases," *Magnetic Resonance in Medicine* 59, no. 4 (2008): 739–46, https://doi.org/10.1002/mrm.21579.

[215] Robert R. Edelman et al., "Noninvasive Assessment of Regional Ventilation in the Human Lung Using Oxygen–Enhanced Magnetic Resonance Imaging," *Nature Medicine* 2, no. 11 (November 1996): 1236, https://doi.org/10.1038/nm1196-1236.

[216] Christian J. Müller et al., "Pulmonary Diffusing Capacity: Assessment with Oxygen-Enhanced Lung MR Imaging—Preliminary Findings," *Radiology* 222, no. 2 (February 1, 2002): 499–506, https://doi.org/10.1148/radiol.2222000869.

[217] Yoshiharu Ohno et al., "Dynamic Oxygen-Enhanced MRI Reflects Diffusing Capacity of the Lung," *Magnetic Resonance in Medicine* 47, no. 6 (2002): 1139–44, https://doi.org/10.1002/mrm.10168.

pulse sequence is sufficiently T_1 weighted, an increase of MR signal is observed depending on the local partial pressure of dioxygen. By applying a block paradigm composed of the successive and repetitive inhalation of pure dioxygen and room air[218], or even mixtures with different concentrations of O_2[219], and by acquiring successively images with the exact same rapid T_1 weighted pulse sequence, it is possible to follow along time the evolution of oxygen uptake in the lung either by analyzing in a pixel-wise manner the evolution of MR signal[220] or by quantifying the T_1 values locally inside the organ[221].

More advanced acquisition and post-processing techniques aim at estimating more complex potential biomarkers, as the Oxygen Transfer Function (OTF)[222], for example. However, the information extracted with this technique is at the same time rich but limited, in the sense that the MR signal enhancements were shown to depend at the same time on ventilation, septal diffusion and perfusion. It is therefore difficult to separate the contributions of each aspect. However, more challenging techniques, based on the quantification of O_2 concentration related T_2^* shortening in the lung parenchyma, are also investigated and may better distinguish the ventilation component from the gas transfer and perfusion ones[223] [224].

In the following, two techniques that are really able to separate between those different physiological processes will be described.

2.3.2. HYPERPOLARIZED XENON-129 MRI

First, in the field of hyperpolarized gases, imaging of ^{129}Xe is one of the most promising techniques concerning the simultaneous quantification of ventilation, perfusion and gas transfer[225] [226] [227]. Its hyperpolarization, administration and imaging are done in the same manner as ^{3}He with dedicated hardware parts, and this gas is able to give information on lung ventilation, as ^{3}He does. However, xenon can be dissolved in blood and soft tissues, and it

[218] Olaf Dietrich, "Oxygen-Enhanced Imaging of the Lung," in *Parallel Imaging in Clinical MR Applications*, ed. Stefan O. Schoenberg, Olaf Dietrich, and Maximilian F. Reiser, Medical Radiology (Berlin, Heidelberg: Springer Berlin Heidelberg, 2007), 429–40, https://doi.org/10.1007/978-3-540-68879-2_38.

[219] Peter M. Jakob et al., "Assessment of Human Pulmonary Function Using Oxygen-Enhanced T1 Imaging in Patients with Cystic Fibrosis," *Magnetic Resonance in Medicine* 51, no. 5 (2004): 1009–16, https://doi.org/10.1002/mrm.20051.

[220] Qun Chen et al., "Oxygen Enhanced MR Ventilation Imaging of the Lung," *Magnetic Resonance Materials in Physics, Biology and Medicine* 7, no. 3 (December 1, 1998): 153–61, https://doi.org/10.1007/BF02591332.

[221] Simon M. F. Triphan et al., "Oxygen Enhanced Lung MRI by Simultaneous Measurement of T1 and T2* during Free Breathing Using Ultrashort TE," *Journal of Magnetic Resonance Imaging* 41, no. 6 (2015): 1708–14, https://doi.org/10.1002/jmri.24692.

[222] Julius Renne et al., "Noninvasive Quantification of Airway Inflammation Following Segmental Allergen Challenge with Functional MR Imaging: A Proof of Concept Study," *Radiology* 274, no. 1 (September 8, 2014): 267–75, https://doi.org/10.1148/radiol.14132607.

[223] Eberhard D. Pracht et al., "Oxygen-Enhanced Proton Imaging of the Human Lung Using T2*," *Magnetic Resonance in Medicine* 53, no. 5 (2005): 1193–96, https://doi.org/10.1002/mrm.20448.

[224] Kathrin R. F. Hemberger, Peter M. Jakob, and Felix A. Breuer, "Multiparametric Oxygen-Enhanced Functional Lung Imaging in 3D," *Magnetic Resonance Materials in Physics, Biology and Medicine* 28, no. 3 (June 1, 2015): 217–26, https://doi.org/10.1007/s10334-014-0462-3.

[225] Ana-Maria Oros and N. Jon Shah, "Hyperpolarized Xenon in NMR and MRI," *Physics in Medicine and Biology* 49, no. 20 (September 2004): R105–R153, https://doi.org/10.1088/0031-9155/49/20/R01.

[226] Samuel Patz et al., "Hyperpolarized 129Xe MRI: A Viable Functional Lung Imaging Modality?," *European Journal of Radiology*, Pulmonary Functional Imaging, 64, no. 3 (December 1, 2007): 335–44, https://doi.org/10.1016/j.ejrad.2007.08.008.

[227] John P. Mugler and Talissa A. Altes, "Hyperpolarized 129Xe MRI of the Human Lung," *Journal of Magnetic Resonance Imaging* 37, no. 2 (2013): 313–31, https://doi.org/10.1002/jmri.23844.

exhibits a different chemical shift in gas, blood and tissues, and red blood cells[228]. By employing special acquisition protocols, using for example chemical shift saturation[229] or inversion[230] pulses and Dixon methods[231] to separate between components with different resonance frequencies, and by exploiting adapted models exhibiting the different components at the alveolar level[232], it is possible to quantify specifically ventilation, gas transfer and perfusion terms in the resulting MR signals. It is also possible to gather them and calculate more complex potential biomarkers, as the local alveolar surface-area-to-volume ratio, as demonstrated in soft porous materials[233]. However, most of the drawbacks related to hyperpolarized gases imaging (see 2.2.1) are retrieved in hyperpolarized xenon imaging.

2.3.3. FOURIER DECOMPOSITION PULMONARY MRI

Second, in the field of non-contrast enhanced proton imaging, a technique referred to as Fourier decomposition pulmonary MRI seems very promising in order to measure simultaneously ventilation and perfusion components in the lung[234]. This technique is even more accessible compared to oxygen-enhanced MRI as it is also based on proton MRI but with no need of any extrinsic contrast agent. As seen previously, the physical properties of lung parenchyma (ρ, T_1, T_2^*) can temporally evolve during the acquisition process because of microstructural changes (inflation of alveoli, increase of the surface between air and parenchyma, …) and because of gas composition evolution inside the alveoli. This evolution concerns in particular the dioxygen present inside the alveoli because its partial pressure is function of ventilation, but also of gas exchange quality, which also depends on septal diffusion and pulmonary perfusion. These changes in physical properties of tissues affect directly the MR signals they produce during the free-breathing imaging process.

The idea under Fourier decomposition pulmonary MRI is to follow locally and along time this evolution of MR signal and to separate the sources of signal variation explained by ventilation from those explained by perfusion. To be able to follow the signal evolution along time, a fast MR pulse sequence, as a bSSFP sequence for example, is used to acquire multiple times a 2D image at the exact same location in the lung. After co-registering non-rigidly these series of images, the pixel-wise separation between signal variations caused by ventilation and perfusion is based on the different modulation frequencies for those components, controlled respectively by the respiratory and cardiac frequencies. As seen in Chapter 2 with SNIF, those two components can be easily separated thanks to a

[228] John P. Mugler et al., "Simultaneous Magnetic Resonance Imaging of Ventilation Distribution and Gas Uptake in the Human Lung Using Hyperpolarized Xenon-129," *Proceedings of the National Academy of Sciences* 107, no. 50 (December 14, 2010): 21707–12, https://doi.org/10.1073/pnas.1011912107.

[229] Samuel Patz et al., "Human Pulmonary Imaging and Spectroscopy with Hyperpolarized 129Xe at 0.2T," *Academic Radiology* 15, no. 6 (June 1, 2008): 713–27, https://doi.org/10.1016/j.acra.2008.01.008.

[230] Iga Muradyan et al., "Single-Breath Xenon Polarization Transfer Contrast (SB-XTC): Implementation and Initial Results in Healthy Humans," *Journal of Magnetic Resonance Imaging* 37, no. 2 (2013): 457–70, https://doi.org/10.1002/jmri.23823.

[231] Iga Muradian et al., "Hyperpolarized 129Xe Human Pulmonary Gas Exchange with 3-Point Dixon Technique," ISMRM 2006.

[232] Samuel Patz et al., "Diffusion of Hyperpolarized129Xe in the Lung: A Simplified Model Of129Xe Septal Uptake and Experimental Results," *New Journal of Physics* 13, no. 1 (January 2011): 015009, https://doi.org/10.1088/1367-2630/13/1/015009.

[233] J. P. Butler et al., "Measuring Surface-Area-to-Volume Ratios in Soft Porous Materials Using Laser-Polarized Xenon Interphase Exchange Nuclear Magnetic Resonance," *Journal of Physics: Condensed Matter* 14, no. 13 (March 2002): L297–L304, https://doi.org/10.1088/0953-8984/14/13/103.

[234] Grzegorz Bauman et al., "Non-Contrast-Enhanced Perfusion and Ventilation Assessment of the Human Lung by Means of Fourier Decomposition in Proton MRI," *Magnetic Resonance in Medicine* 62, no. 3 (September 2009): 656–664, https://doi.org/10.1002/mrm.22031.

simple Fourier analysis. By calculating the pixel-wise power spectrum of MR signal time evolution and by representing in each pixel the area under the respiratory and cardiac peaks, qualitative maps of ventilation and perfusion are respectively obtained.

To reach more quantitative results, several recent studies propose to estimate physical parameters thanks to more advanced post-processing methods for this technique[235] [236] [237]. Moreover, comparison with hyperpolarized ^{3}He ventilation measurements[238] and more standard V/Q assessment methods, as V/Q SPECT for example[239], were conducted very recently. Several pulse sequence improvements were also proposed to increase the speed, the robustness and the quantification potential of this method[240] [241], and a 3D version was recently developed based on a UTE pulse sequence[242].

2.3.4. CONCLUSION ON THE SIMULTANEOUS STUDY OF VENTILATION, GAS TRANSFER AND PERFUSION

The two methods described just above, hyperpolarized ^{129}Xe MRI and Fourier decomposition MRI, are therefore two promising techniques to measure during the same imaging protocol both ventilation and perfusion components of lung function, and also septal diffusion in xenon imaging. However, those measurement methods are not easy to perform: they either require the use of an extrinsic tracer gas and special expensive hardware parts, or imply a lot of strong assumptions (3D motion fields estimated from the elastic registration of 2D images, multiple sources of image contrast variations in Fourier decomposition MRI not always related to matter concentrations, …) or hypothetic underlying microscopic behavior models to expect a quantitative measurement of ventilation and perfusion.

In the next subsection, another category of methods will be studied. Instead of being based on the estimation of the concentrations of a given substance (extrinsic contrast agent, non-proton tracer gas, dioxygen, …), these techniques are based on the assessment of deformation and velocity fields inside the lung. This measurement will be performed at the regional scale through the voxel-wise assessment of these motion components. Let us discover

---

[235] Åsmund Kjørstad et al., "Quantitative Lung Ventilation Using Fourier Decomposition MRI; Comparison and Initial Study," *Magnetic Resonance Materials in Physics, Biology and Medicine* 27, no. 6 (December 1, 2014): 467–76, https://doi.org/10.1007/s10334-014-0432-9.

[236] Åsmund Kjørstad et al., "Quantitative Lung Perfusion Evaluation Using Fourier Decomposition Perfusion MRI," *Magnetic Resonance in Medicine* 72, no. 2 (2014): 558–62, https://doi.org/10.1002/mrm.24930.

[237] Åsmund Kjørstad et al., "Non-Invasive Quantitative Pulmonary V/Q Imaging Using Fourier Decomposition MRI at 1.5T," *Zeitschrift Für Medizinische Physik* 25, no. 4 (December 1, 2015): 326–32, https://doi.org/10.1016/j.zemedi.2015.02.002.

[238] Dante P. I. Capaldi et al., "Free-Breathing Pulmonary 1H and Hyperpolarized 3He MRI: Comparison in COPD and Bronchiectasis," *Academic Radiology* 22, no. 3 (March 1, 2015): 320–29, https://doi.org/10.1016/j.acra.2014.10.003.

[239] Grzegorz Bauman et al., "Pulmonary Functional Imaging: Qualitative Comparison of Fourier Decomposition MR Imaging with SPECT/CT in Porcine Lung," *Radiology* 260, no. 2 (August 1, 2011): 551–59, https://doi.org/10.1148/radiol.11102313.

[240] André Fischer et al., "SElf-Gated Non-Contrast-Enhanced FUnctional Lung Imaging (SENCEFUL) Using a Quasi-Random Fast Low-Angle Shot (FLASH) Sequence and Proton MRI," *NMR in Biomedicine* 27, no. 8 (2014): 907–17, https://doi.org/10.1002/nbm.3134.

[241] D. M. R. Corteville et al., "Fourier Decomposition Pulmonary MRI Using a Variable Flip Angle Balanced Steady-State Free Precession Technique," *Magnetic Resonance in Medicine* 73, no. 5 (2015): 1999–2004, https://doi.org/10.1002/mrm.25293.

[242] L. Mendes Pereira et al., "UTE-SENCEFUL: First Results for 3D High-Resolution Lung Ventilation Imaging," *Magnetic Resonance in Medicine* 81, no. 4 (2019): 2464–73, https://doi.org/10.1002/mrm.27576.

how the mechanical behavior of the lung can be exploited to extract quantitative parameters describing lung function, and therefore potential biomarkers of the pulmonary pathophysiological state.

3. TECHNIQUES BASED ON THE MR MEASUREMENT OF MOTION FIELDS IN THE LUNG

3.1. MOTION-BASED ASSESSMENT OF LUNG PERFUSION WITH MRI

3.1.1. PHASE CONTRAST MRA

Concerning blood circulation, another MR Angiography (MRA) technique rapidly cited in the first chapter of this manuscript is Phase Contrast (PC) MRA[243] [244]. This technique consists in measuring locally the velocity of flowing liquids (the blood in the case of angiography) thanks to a MR pulse sequence featuring at each sequence repetition a motion encoding bipolar gradient between the RF excitation pulse and the data acquisition window. The use and the effect of a motion encoding bipolar gradient will be largely demonstrated and discussed in the last chapter of this manuscript. The only thing to understand now is that the phase of our MR image reaches a value that depends linearly on the local velocity of tissue or liquid at each voxel location. Because the motion encoding gradient measures only the velocity component along its direction, several gradient directions (three orthogonal directions are theoretically sufficient) can be used to probe the velocity field in different directions of space.

It is thus possible to obtain, thanks to PC MRA, a velocity map for the different arteries and veins going through the pulmonary parenchyma. The application of such a strategy for the lung was demonstrated in several studies[245] [246], and comparisons with other perfusion measurement methods based on the injection of a radionuclide were made[247]. However, the technique remains challenging in free-breathing because of respiratory motion, which is encoded too. Moreover, it is usually limited to the main pulmonary arteries and veins, as for other MRA methods.

In the general case, it is even possible to use higher order motion encoding gradients to probe higher order motion components. Therefore, tripolar motion encoding gradients can be exploited to obtain blood acceleration maps, for example[248] [249].

[243] M. F. Walker, S. P. Souza, and C. L. Dumoulin, "Quantitative Flow Measurement in Phase Contrast MR Angiography.," *Journal of Computer Assisted Tomography* 12, no. 2 (1988): 304–13.
[244] C. L. Dumoulin et al., "Three-Dimensional Phase Contrast Angiography," *Magnetic Resonance in Medicine* 9, no. 1 (1989): 139–49, https://doi.org/10.1002/mrm.1910090117.
[245] Alex J. Barker et al., "Four-Dimensional Flow Assessment of Pulmonary Artery Flow and Wall Shear Stress in Adult Pulmonary Arterial Hypertension: Results from Two Institutions," *Magnetic Resonance in Medicine* 73, no. 5 (2015): 1904–13, https://doi.org/10.1002/mrm.25326.
[246] Raluca G. Chelu et al., "Cloud-Processed 4D CMR Flow Imaging for Pulmonary Flow Quantification," *European Journal of Radiology* 85, no. 10 (October 1, 2016): 1849–56, https://doi.org/10.1016/j.ejrad.2016.07.018.
[247] S. Sridharan et al., "Assessment of Differential Branch Pulmonary Blood Flow: A Comparative Study of Phase Contrast Magnetic Resonance Imaging and Radionuclide Lung Perfusion Imaging," *Heart* 92, no. 7 (July 1, 2006): 963–68, https://doi.org/10.1136/hrt.2005.071746.
[248] Jean-Pierre Tasu et al., "Acceleration Mapping by Fourier Acceleration-Encoding: In Vitro Study and Initial Results in the Great Thoracic Vessels," *Magnetic Resonance in Medicine* 38, no. 1 (1997): 110–16, https://doi.org/10.1002/mrm.1910380116.
[249] Felix Staehle et al., "Three-Directional Acceleration Phase Mapping of Myocardial Function," *Magnetic Resonance in Medicine* 65, no. 5 (2011): 1335–45, https://doi.org/10.1002/mrm.22744.

3.1.2. INTRA-VOXEL INCOHERENT MOTION (IVIM) MRI

As seen just above, MRA does not give complete information on pulmonary perfusion. Indeed, only the larger lung vessels are accessible with MRA. To really assess perfusion in an organ, a measurement of the mechanical behavior of blood in the small capillaries surrounding each alveolus should be investigated. Because each MRI voxel usually contains a great number of blood capillaries, and because there is no preferential direction for those small vessels, diffusion-like motion of blood can be assumed in each voxel. This pseudo-diffusion motion of blood in small capillaries is usually referred to as Intra-Voxel Incoherent Motion (IVIM)[250] [251] [252].

This pseudo-diffusion motion can be studied as any true diffusion motion of water molecules thanks to diffusion MRI, which also employs motion encoding gradients but which affect the magnitude image. Thanks to the use of several different amplitudes of motion encoding gradients (usually referred to as multi-b diffusion imaging[253]), it is possible to isolate the effect of micro-perfusion from the other sources of contrast, in particular from the true diffusion of water molecules in the surrounding parenchyma. It is therefore possible to estimate a 'diffusion' coefficient (sometimes called pseudo-diffusion coefficient and written D^* in this special case) quantifying the motion properties of blood at microscopic scale, but also a perfusion fraction quantifying the relative volume of perfusion blood present locally. Therefore, this method gives access to the mechanical behavior of blood in the capillaries, but also to relative quantities of blood inside each voxel.

In the lung, this technique has essentially been used recently for the characterization of lung tumors[254] [255] [256] and other types of lung lesions[257], but not a lot for perfusion assessment in the parenchyma, certainly because of the low SNR obtained in proton imaging of the lung tissues. However, this technique might be promising in order to assess directly the mechanical behaviors related to lung perfusion at the local scale, in particular at lower magnetic fields for which T_2^* is longer.

---

[250] D Le Bihan et al., "MR Imaging of Intravoxel Incoherent Motions: Application to Diffusion and Perfusion in Neurologic Disorders.," *Radiology* 161, no. 2 (November 1, 1986): 401–7, https://doi.org/10.1148/radiology.161.2.3763909.

[251] D Le Bihan et al., "Separation of Diffusion and Perfusion in Intravoxel Incoherent Motion MR Imaging.," *Radiology* 168, no. 2 (August 1, 1988): 497–505, https://doi.org/10.1148/radiology.168.2.3393671.

[252] Denis Le Bihan and Robert Turner, "The Capillary Network: A Link between Ivim and Classical Perfusion," *Magnetic Resonance in Medicine* 27, no. 1 (1992): 171–78, https://doi.org/10.1002/mrm.1910270116.

[253] Kishor Karki et al., "Estimation of Optimalb-Value Sets for Obtaining Apparent Diffusion Coefficient Free from Perfusion in Non-Small Cell Lung Cancer," *Physics in Medicine and Biology* 60, no. 20 (September 2015): 7877–7891, https://doi.org/10.1088/0031-9155/60/20/7877.

[254] Li-li Wang et al., "Intravoxel Incoherent Motion Diffusion-Weighted MR Imaging in Differentiation of Lung Cancer from Obstructive Lung Consolidation: Comparison and Correlation with Pharmacokinetic Analysis from Dynamic Contrast-Enhanced MR Imaging," *European Radiology* 24, no. 8 (August 1, 2014): 1914–22, https://doi.org/10.1007/s00330-014-3176-z.

[255] Hisanobu Koyama et al., "Value of Diffusion-Weighted MR Imaging Using Various Parameters for Assessment and Characterization of Solitary Pulmonary Nodules," *European Journal of Radiology* 84, no. 3 (March 1, 2015): 509–15, https://doi.org/10.1016/j.ejrad.2014.11.024.

[256] Mei Yuan et al., "Comparison of Intravoxel Incoherent Motion Diffusion-Weighted MR Imaging with Dynamic Contrast-Enhanced MRI for Differentiating Lung Cancer from Benign Solitary Pulmonary Lesions," *Journal of Magnetic Resonance Imaging* 43, no. 3 (2016): 669–79, https://doi.org/10.1002/jmri.25018.

[257] Chenggong Yan et al., "Use of Intravoxel Incoherent Motion Diffusion-Weighted MR Imaging for Assessment of Treatment Response to Invasive Fungal Infection in the Lung," *European Radiology* 27, no. 1 (January 1, 2017): 212–21, https://doi.org/10.1007/s00330-016-4380-9.

3.2. MOTION-BASED ASSESSMENT OF LUNG VENTILATION WITH MRI

3.2.1. METHODS BASED ON THE DYNAMICS OF HYPERPOLARIZED GASES

As far as lung ventilation is concerned, the same phase contrast technique as presented above for MRA (see 3.1.1) can be used to estimate the flow velocity of hyperpolarized helium in the lung[258]. Of course, this technique could be implemented for other tracer gases. In comparison to what was presented in the previous section, instead of estimating ventilation through the MR signal amplitude produced by the tracer gas (which is proportional to its local concentration), the gas velocity is directly measured in the airways here. Nevertheless, because of the exploitation of a non-proton gas, the measurement of ventilation remains less accessible and less straightforward in comparison to methods based on proton imaging.

3.2.2. METHODS BASED ON THE DYNAMICS OF LUNG WALLS AND RESPIRATORY MUSCLES

It would be great to measure directly lung ventilation from proton MR imaging. Many studies have exploited the great contrast between the lung parenchyma and its surrounding tissues, in addition to the possible high temporal image acquisition rate that can be reached today in 2D imaging (several images per second), in order to study lung mechanics.

This was done either by studying the time evolution of lung volumes[259] [260] or by studying the behavior of respiratory muscles (diaphragm[261] and intercostal muscles in the chest wall[262] mainly). In these studies, the measurement of lung ventilation can even be associated to global spirometry measurements, thanks to the use of MR compatible spirometers[263]. In this situation, a simultaneous ventilation measurement from a gold standard lung function testing machine and a MRI based method is performed. However, those techniques are usually limited to 2D imaging and aim at studying the lung as a whole. They are only able to distinguish between the mechanical behaviors of the left and right lungs, which is yet an improvement compared to standard spirometry and plethysmography. However, it is not possible to obtain true regional information on how the lung inflates and deflates along the respiratory cycle.

The feasibility of true regional ventilation estimation from proton MRI was recently investigated through two main strategies.

---

[258] Ludovic de Rochefort et al., "Phase-Contrast Velocimetry with Hyperpolarized 3He for in Vitro and in Vivo Characterization of Airflow," *Magnetic Resonance in Medicine* 55, no. 6 (2006): 1318–25, https://doi.org/10.1002/mrm.20899.

[259] Christian Plathow et al., "Evaluation of Chest Motion and Volumetry During the Breathing Cycle by Dynamic MRI in Healthy Subjects: Comparison With Pulmonary Function Tests," *Investigative Radiology* 39, no. 4 (April 2004): 202, https://doi.org/10.1097/01.rli.0000113795.93565.c3.

[260] Andy J. Swift et al., "Rapid Lung Volumetry Using Ultrafast Dynamic Magnetic Resonance Imaging During Forced Vital Capacity Maneuver: Correlation With Spirometry," *Investigative Radiology* 42, no. 1 (January 2007): 37, https://doi.org/10.1097/01.rli.0000250735.92266.6b.

[261] Shigeru Kiryu et al., "Quantitative Analysis of the Velocity and Synchronicity of Diaphragmatic Motion: Dynamic MRI in Different Postures," *Magnetic Resonance Imaging* 24, no. 10 (December 1, 2006): 1325–32, https://doi.org/10.1016/j.mri.2006.08.009.

[262] Tetsuri Kondo et al., "A Dynamic Analysis of Chest Wall Motions with MRI in Healthy Young Subjects *," *Respirology* 5, no. 1 (2000): 19–25, https://doi.org/10.1046/j.1440-1843.2000.00221.x.

[263] M. Eichinger et al., "Magnetic Resonance-Compatible-Spirometry: Principle, Technical Evaluation and Application," *European Respiratory Journal* 30, no. 5 (November 1, 2007): 972–79, https://doi.org/10.1183/09031936.00040607.

3.2.3. METHODS BASED ON THE ASSESSMENT OF LOCAL LUNG DEFORMATIONS THROUGH SPIN-TAGGING TECHNIQUES

The first one consists in creating artificial contrast in the proton lung MR image by tagging a grid inside the thorax with spatially selective spin saturation techniques[264] [265] [266]. These spin-tagging techniques are usually based on the SPAtial Modulation of Magnetization technique, or SPAMM[267], or the association of magnetic field gradients to Delays Alternating with Nutations for Tailored Excitation RF pulse trains, or DANTE[268] [269]. These techniques were primarily developed to study the mechanical behavior of the myocardium[270] but were more recently adapted to the mechanical behavior of the lung.

Thanks to the long T_1 values available in the lung parenchyma, it was shown that such a grid could still be visible 1 second after the application of the tagging pulse. By interleaving the application of this tagging pulse with the rapid acquisition of 2D MR images (usually performed thanks to fast gradient echo short TE pulse sequences, like SPGR) and by analyzing the regional deformation of this grid along the free-breathing respiratory motion of the subject as a post-processing step, it is possible to deduce the local deformation of the lung, calculate regional volume expansions, represent regional spirometry-like flow-volume loops and estimate mechanical strain parameters. The use of spin-tagging techniques was also demonstrated on hyperpolarized gas imaging techniques[271] [272].

However, the use of such spin-tagging preparation pulses leads to more complex pulse sequences, with longer total scan times and higher SAR values. These drawbacks are not found in the second category of techniques presented below.

---

[264] Qun Chen et al., "Ultrafast MR Grid-Tagging Sequence for Assessment of Local Mechanical Properties of the Lungs," *Magnetic Resonance in Medicine* 45, no. 1 (January 1, 2001): 24–28, https://doi.org/10.1002/1522-2594(200101)45:1<24::AID-MRM1004>3.0.CO;2-6.

[265] Vitaly J. Napadow et al., "Determination of Regional Pulmonary Parenchymal Strain during Normal Respiration Using Spin Inversion Tagged Magnetization MRI," *Journal of Magnetic Resonance Imaging* 13, no. 3 (March 1, 2001): 467–74, https://doi.org/10.1002/jmri.1068.

[266] Abram Voorhees et al., "Magnetic Resonance Imaging-Based Spirometry for Regional Assessment of Pulmonary Function," *Magnetic Resonance in Medicine* 54, no. 5 (November 1, 2005): 1146–54, https://doi.org/10.1002/mrm.20682.

[267] L Axel and L Dougherty, "MR Imaging of Motion with Spatial Modulation of Magnetization.," *Radiology* 171, no. 3 (June 1, 1989): 841–45, https://doi.org/10.1148/radiology.171.3.2717762.

[268] Gareth A Morris and Ray Freeman, "Selective Excitation in Fourier Transform Nuclear Magnetic Resonance," *Journal of Magnetic Resonance (1969)* 29, no. 3 (March 1, 1978): 433–62, https://doi.org/10.1016/0022-2364(78)90003-3.

[269] Timothy J. Mosher and Michael B. Smith, "A DANTE Tagging Sequence for the Evaluation of Translational Sample Motion," *Magnetic Resonance in Medicine* 15, no. 2 (1990): 334–39, https://doi.org/10.1002/mrm.1910150215.

[270] Jinah Park, Dimitri Metaxas, and Leon Axel, "Analysis of Left Ventricular Wall Motion Based on Volumetric Deformable Models and MRI-SPAMM," *Medical Image Analysis* 1, no. 1 (March 1, 1996): 53–71, https://doi.org/10.1016/S1361-8415(01)80005-0.

[271] John R. Owers-Bradley et al., "MR Tagging of Human Lungs Using Hyperpolarized 3He Gas," *Journal of Magnetic Resonance Imaging* 17, no. 1 (2003): 142–46, https://doi.org/10.1002/jmri.10226.

[272] Jing Cai et al., "Dynamic MRI of Grid-Tagged Hyperpolarized Helium-3 for the Assessment of Lung Motion During Breathing," *International Journal of Radiation Oncology*Biology*Physics* 75, no. 1 (September 1, 2009): 276–84, https://doi.org/10.1016/j.ijrobp.2009.03.051.

3.2.4. METHODS BASED ON THE ASSESSMENT OF LOCAL LUNG DEFORMATION THROUGH THE ELASTIC REGISTRATION OF MR IMAGES

The second strategy is very similar to the first one and aims at estimating regional ventilation parameters by non-elastically registering the same type of dynamic MR images. However, instead of relying on the deformation of artificial contrasted shapes generated by spin-tagging, this technique is based on the registration of contrasted elements naturally present in the MR lung images[273] [274]. These contrasted elements are, of course, the physical limits of the organ, which corresponds mainly to the pleural space, but also the numerous arteries and veins observed in the lung parenchyma. It was observed, as expected, that the image registration process was more difficult in lung regions lacking of this type of contrasted elements, and was therefore more difficult in distal lung regions compared to medial lung regions, which are highly perfused by clearly visible large blood vessels.

Compared to the first one, this technique has the advantage to be less dependent on special pulse sequences (featuring a SPAMM or DANTE + gradient preparation technique) but is now dependent on the presence of local contrasted elements, fiducial landmarks, borders, that gives the possibility to register correctly the dynamic MR images. With such a technique, the possibility to draw a spirometry-like flow-volume loop for any given imaged region of the lung was demonstrated.

This last technique has globally two advantages:

- It is highly accessible, in the sense that it is only based on MR proton imaging and on a very standard type of MR pulse sequences: fast gradient echo and short TE pulse sequences.
- It measures lung ventilation only on a mechanical behavior basis. It means that the only required information is the local displacement of each parcel of lung tissue, which can be directly assessed with dynamic lung imaging and several post-processing steps.

However, because this technique relies on dynamic lung imaging, which is able to follow the mechanical behavior of the lung with a sufficient temporal rate, only one image slice can usually be considered because of the scan time constraints imposed by 2D multi-slice or 3D imaging (it is challenging today to obtain 3D images within scan times below 1 second, which is too long to study respiratory dynamics in freely breathing human subjects[275]). This constraint was the same for the spin-tagging based techniques presented in 3.2.3.

Nevertheless, lung mechanics cannot be fully captured from only one image slice. The first reason is because only one small region of the lung is investigated: the regions in front of and behind the slice under consideration are not studied, and it is therefore not possible to measure the regional ventilation in these regions. This problem can be weakened by repeating the experiment on several different image slices, but all the slices are not obtained neither in 'real-time' nor for the same respiratory cycles in this case. The second reason is because the estimation of motion fields is only possible within the image plane, and through plane motion is not accessible. The lack of tissue displacement information along this third dimension of space can lead to strong biases in the estimation of

[273] James Gee et al., "Characterization of Regional Pulmonary Mechanics from Serial Magnetic Resonance Imaging Data1," *Academic Radiology* 10, no. 10 (October 1, 2003): 1147–52, https://doi.org/10.1016/S1076-6332(03)00329-5.

[274] Tessa A. Sundaram and James C. Gee, "Towards a Model of Lung Biomechanics: Pulmonary Kinematics via Registration of Serial Lung Images," *Medical Image Analysis*, ITK, 9, no. 6 (December 2005): 524–537, https://doi.org/10.1016/j.media.2005.04.002.

[275] Christian Plathow et al., "Evaluation of Lung Volumetry Using Dynamic Three-Dimensional Magnetic Resonance Imaging," *Investigative Radiology* 40, no. 3 (March 2005): 173.

ventilation. This problem can be mitigated by choosing a coronal or a sagittal imaging plane, and by considering that through plane motion is negligible compared to motion components along the superior-inferior axis.

Kolb *et al.* have recently extended 3D dynamic lung images covering the respiratory cycle and from which they would be able to estimate, at any spatial position and at any moment of the respiratory cycle, the same ventilation properties as estimated with spirometry. This possibility was approached by employing retrospectively gated 3D radial stack-of-stars gradient-echo imaging with golden-angle spacing to obtain series of respiratory motion corrected images throughout the respiratory cycle[276]. The lung model-based segmentation and registration strategy they introduce seems very promising. However, in their first results, it remains difficult to evaluate the capabilities of this method in terms of local ventilation measurement inside the lung in free-breathing. As an example, they show flow-volume loops estimated with their method, but only for the left lung, its upper lobe and its lower lobe. They do not present results with a spatial discretization size below the lobar scale. This is not enough if the detection and characterization of small (around 1 cm) and localized lesions or defects in the lung parenchyma are investigated. Finally, more advanced parameters related to local mechanical behavior (strain components, …) were not measured in their project.

However, thanks to its supposed ability to locally characterize ventilation and strain behavior in the lung during free-breathing, this type of method is expected to be more sensitive and more specific to localized lung defects and diseases (emphysema, radiation fibrosis, lung cancer, any affection causing pulmonary shunts, …) and/or to understand the origin of a given affection (Related to the diaphragm or the chest wall? Unilateral or bilateral? …).

This 3D strategy has many interesting features:

- **the method is new:** the first and only article published in 2016,
- **accessible:** it is based on proton imaging, it uses standard pulse sequences, and most parts of the process are composed of standard post-processing tasks,
- **and very promising:** the method gives the ability to fully assess local ventilation and advanced mechanical behavior features of the lung at any spatial position in the organ and at any time point along the respiratory cycle, in spite of rather poor original spatial resolution.

Further work is needed to really appreciate the diagnostic potential of this technique. In the following, we will introduce a global strategy and framework to analyze the mechanical behavior of the lung, based on retrospectively self-gated 3D UTE imaging of the lung, reconstructed with parallel imaging considerations and compressed sensing priors, and coupled with automatic lung segmentation, elastic image registration, and linear numerical analysis. The objective of this project is to obtain a 3D voxel-wise information of pulmonary ventilation (regional volume expansion, regional air flow, …) and strain (principal strain directions, strain anisotropy, …) throughout the entire respiratory period and with a sufficient time resolution within the breathing cycle. Our project shares a lot of similarities with the work proposed by Kolb *et al.*, but we tried to go further in terms of lung MR imaging (use of a UTE pulse sequence), image registration and segmentation (which are not related to any presupposed model) and parameter extraction (extraction of anisotropic and hysteretic behaviors occurring inside the lung). We gathered all those possibilities under the name 3D Magnetic Resonance Spirometry.

[276] Christoph Kolb et al., "Regional Lung Ventilation Analysis Using Temporally Resolved Magnetic Resonance Imaging," *Journal of Computer Assisted Tomography* 40, no. 6 (December 2016): 899, https://doi.org/10.1097/RCT.0000000000000450.

SECTION 2 PRINCIPLES AND METHODS FOR 3D MAGNETIC RESONANCE SPIROMETRY

THIS SECTION INTRODUCES THE BASIC PRINCIPLES WE INVESTIGATED AND THE MAIN METHODS WE DEVELOPED TO PERFORM 3D MAGNETIC RESONANCE SPIROMETRY. THIS TECHNIQUE CAN BE SEEN AS THE MR BASED THREE-DIMENSIONAL ADAPTATION OF STANDARD SPIROMETRY (WHICH CAN BE CONSIDERED AS A '0-DIMENSIONAL' OR NON-SPATIALLY SELECTIVE TECHNIQUE). WITH OUR IMPLEMENTATION OF 3D MR SPIROMETRY, A SPIROMETRY-LIKE FLOW-VOLUME LOOP CAN BE DRAWN FOR ANY RESPIRATORY PATTERN AND FOR ANY REGION OF THE LUNG INSTEAD OF THE ENTIRE ORGAN. MOREOVER, MORE ADVANCED BIOMECHANICAL PARAMETERS CAN BE EXTRACTED, AS LOCAL PRINCIPAL STRAIN DIRECTIONS AND STRAIN ANISOTROPY. AS EXPLAINED IN THE PREVIOUS SECTION, THANKS TO ITS SPATIAL SENSITIVITY, WE HOPE THIS TECHNIQUE TO BE MORE SENSITIVE AND MORE SPECIFIC TO A GREAT NUMBER OF LUNG DISEASES, AND IN PARTICULAR TO LOCALIZED LUNG AFFECTIONS. IN THE NEXT SECTION, WE WILL INTRODUCE THE DIFFERENT STEPS WE DEVELOPED TO BUILD OUR TECHNIQUE AND DISCUSS THE CHOICES WE MADE. FOR THE SAKE OF CLARITY, THE DIFFERENT STEPS DEVELOPPED IN THE FOLOWING ARE REPRESENTED IN THE PIPELINE CHART BELOW, AND EACH SUBSECTION OF THE PRESENTATION WILL REFER TO ONE OR SEVERAL OF THESE STEPS. THIS WORK WAS PRESENTED AT ISMRM 2019 IN MONTREAL AND WAS AWARDED *SUMMA CUM LAUDE* BY THE ORGANIZING COMMITTEE.

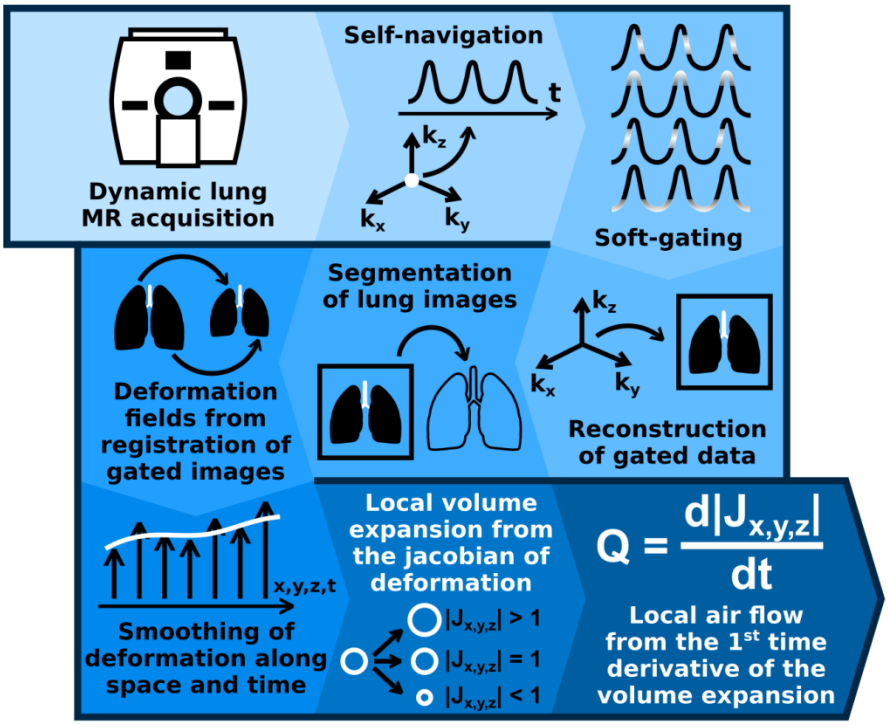

1. DYNAMIC FREE-BREATHING THORACIC UTE ACQUISITION

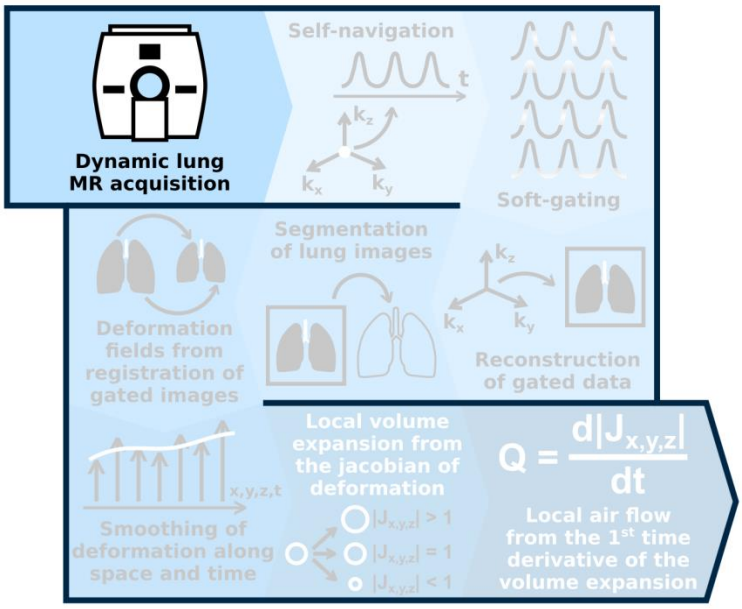

1.1. CHOICE BETWEEN UTE AND ZTE PULSE SEQUENCES

The first step of our 3D Magnetic Resonance Spirometry technique consists in acquiring 3D images of the full lung while the subject is freely breathing. Because the assessment of local lung mechanical behavior will be made from the landmarks, details and contrasts present in the MR signal of the lung parenchyma, the first requirement is to obtain a sufficient MR signal from the lung. In this perspective, two pulse sequences, Ultrashort Echo-Time (UTE) and Zero Echo-Time (ZTE), were proposed and deeply covered in Chapters 1 and 2. Moreover, we have seen that those two pulse sequences deal particularly well with respiratory motion (robustness to motion artifacts, possibility to perform self-navigation and retrospective self-gating, …). For our application, we decided to use the UTE pulse sequence because of its simplicity compared to ZTE:

- The k-space is acquired in only one step in UTE, whereas it is acquired in two separate steps in ZTE: one for the central region and one for the peripheral region of k-space.
- In UTE, the center k-space is acquired directly at each pulse sequence repetition, which is not the case in ZTE. This strongly simplifies self-navigation.
- In UTE, the spokes can be chosen in any direction order, and even in a random order if desired. In ZTE, as seen in Chapter 2 with AZTEK, the k-space trajectory must remain ‘smooth’, in the sense that the change in direction between two successive spokes cannot be too large.

1.2. CHOICE OF K-SPACE TRAJECTORY AND RESIDUAL TRANSVERSE MAGNETIZATION SPOILING METHOD

The standard trajectory provided by our UTE pulse sequence is very similar to the standard trajectory of ZTE. With the variables defined in the previous chapter, the standard trajectory featured by our UTE sequence is characterized by a θ spoke angular coordinate varying slowly, continuously and monotonically from 0 to π, while

the φ spoke angular coordinate varies rapidly during the imaging process, describing 'turns' during the acquisition. This trajectory is very interesting in terms of final image SNR thanks to the spoiling property of readout gradients: because readout gradient direction varies slowly along pulse sequence repetitions, residual transverse magnetization remaining from previous repetitions is further dephased by current readout gradients, which avoids the generation of stimulated echoes. However, as seen in the previous chapter, this trajectory is very bad for motion correction, and in particular for retrospective gating: 'holes' empty of data are generated in k-space besides fully sampled regions. This usually results in coherent under-sampling artifacts in the final retrospectively gated image.

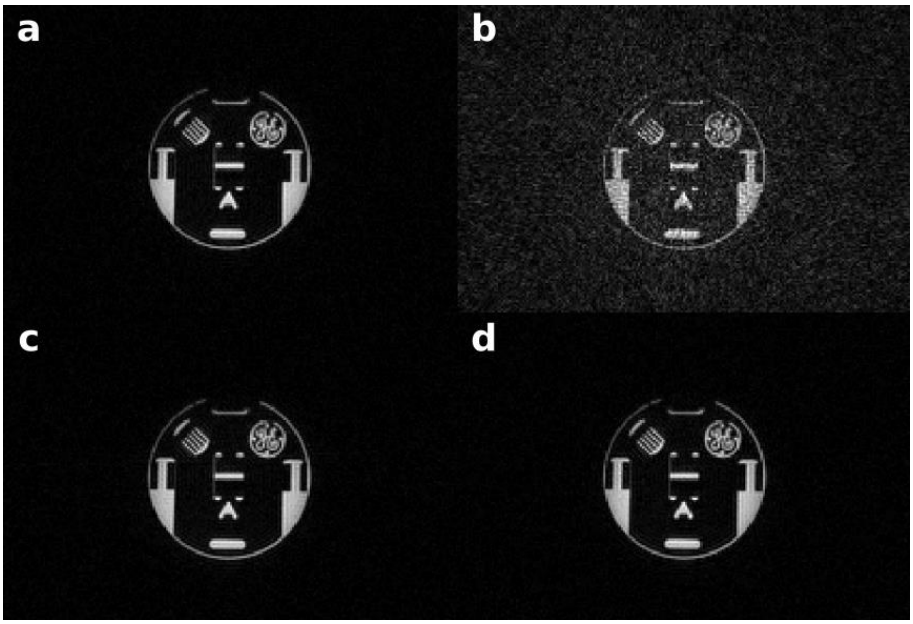

Figure 3.1: Images of a water phantom obtained with the UTE pulse sequence with different k-space trajectories and spoiling strategies. a) Standard trajectory, which features an 'auto-spoiling' property but which is not adapted to retrospective motion gating, $TR = 2$ ms; b) Random temporal order of spokes orientations without gradient spoiling: the trajectory is adapted to retrospective motion gating but the 'auto-spoiling' property is lost and the SNR is therefore decreased, $TR = 2$ ms; c) Random temporal order of spokes orientations with gradient spoiling at the end of each repetition: the SNR is recovered but the TR is increased to 3.88 ms because of this supplementary gradient pulse, which increases the total scan time; d) AZTEK trajectory with no gradient spoiling (*AZTEK-Twist* = 1, *AZTEK-Shuffle* = 1 and *AZTEK-Speed* = 4): this trajectory is adapted to retrospective motion gating and features an 'auto-spoiling' property, which preserves the SNR without increasing the total scan time, $TR = 2$ ms.

Fortunately, we have seen in the previous chapter that a quasi-random order of spoke orientations could be implemented instead of continuously varying directions of spokes. In our UTE pulse sequence, this was implemented by considering the standard trajectory described just above and by performing N_{Spokes} permutations between randomly chosen pairs of spokes, with N_{Spokes} being the number of spokes required for a given image prescription. This type of trajectory is far better compared to the standard one in terms of retrospective gating quality because, in the general case, any retrospective respiratory motion gate will lead to an under-sampled but uniformly covered k-space with such a trajectory. In the final image, the under-sampling artifacts will look more like a homogeneous background noise instead of spatially coherent under-sampling artifacts. This final result is much better in terms of diagnostic value of the image: instead of creating fake structures or hiding anatomical details, an easier separation between the high frequency pseudo-random noise and the coherent anatomical structures can

be made by the user. As explained thereafter, it will even be possible to attenuate this noise during the reconstruction step thanks to compressed sensing priors, which tend to preserve anatomical details. However, because the spokes are now played in a pseudo-random order along the acquisition, the spoiling property of the readout gradients in lost. This is problematic because it decreases the SNR in the final image (see the difference between **Figure 3.1a** and **b**). With this trajectory, one solution to recover an acceptable SNR would be to add spoiling gradients at the end of each repetition (see **Figure 3.1c**), which increases the minimal achievable TR from 2 ms to 3.88 ms in our configuration. Another technique would be to acquire more spokes to perform signal averaging, which increases the total scan time. We cannot accept this increase in scan time because oversampled 3D k-space volumes will be needed for our 3D MR Spirometry application, and this usually takes several minutes if a fine final voxel size is required.

The AZTEK trajectory features inherent spoiling and is adapted to retrospective respiratory gating.: the sufficiently continuous spoke evolution offers a gradient spoiling property to the readout gradient (see **Figure 3.1d**) without leaving unsampled data regions in the final retrospectively gated k-space. Moreover, future work on this trajectory will probably give the possibility to adapt its tuning parameters, *AZTEK-Twist*, *AZTEK-Shuffle* and *AZTEK-Speed*, to any respiratory motion evolution pattern thanks to motion learning and parameter optimization steps performed before the acquisition. For these reasons, AZTEK seems to be one of our best choices in terms of k-space trajectory. As a verification step, with basic parameters for AZTEK, the final image SNR is close to the one obtained either with the standard trajectory or a pseudo-random order of spokes and the application of gradient spoilers (see **Figure 3.1**). In the following, we will therefore consider the AZTEK trajectory for UTE acquisitions and 3D MR Spirometry applications.

1.3. CHOICE OF PULSE SEQUENCE PARAMETERS

For 3D MR Spirometry, we want a full 3D assessment of lung function in the entire volume of the organ. For that reason, we chose a large Field Of View (FOV) of 32 cm along the superior-inferior axis, of 32 cm along the left-right direction and of 21 cm along the anterior-posterior direction. To detect small details inside the lung parenchyma (small arteries and veins, in particular), we chose an isotropic voxel size of 1.5 mm. This size was found to be a good compromise between a fine spatial resolution to observe small anatomical details, a sufficient SNR to separate them from the background noise and acceptable acquisition times (around 11 minutes). The RF excitation was performed with a hard/square RF pulse, without any slice or slab selection gradient, but with phase cycling according to a quadratic law to spoil the remaining transverse magnetization. However, no gradient spoiling strategy was needed thanks to the AZTEK trajectory. TR as small as 2 ms was achieved. The flip angle, 3°, was optimized according to the chosen TR and the long T_1 values in the lung parenchyma along Ernst angle law[277].

To reach such FOV and voxel sizes, each spoke was composed of 192 readout points spread from the center of k-space to the periphery. The readout bandwidth was equal to ± 100 kHz. It is important to set such a large readout bandwidth at the expense of additional noise in order to reduce transverse relaxation effects during readout, which would lead to a decrease in SNR and a degradation of the effective spatial resolution below the voxel size in short $T_2{}^*$ tissues. Ramp-sampling was implemented in the pulse sequence: instead of waiting for the readout gradient to stabilize before reading the MR signal, readout starts as the frequency encoding gradient starts ramping up to its target value. This gives the possibility to sample the first point of each spoke as close as possible from the center of k-space, but also to reach a minimal value for TE of 12 µs. For each spoke, the first 42 points were acquired during readout gradient ramp-up.

[277] R. R. Ernst and W. A. Anderson, "Application of Fourier Transform Spectroscopy to Magnetic Resonance," *Review of Scientific Instruments* 37, no. 1 (January 1, 1966): 93–102, https://doi.org/10.1063/1.1719961.

Because we plan to correct for respiratory motion with a retrospective gating technique, we need to oversample the k-space data in order to obtain enough data in each final retrospective gate. Experimentally, we observe that an oversampling factor around 3 in the number of spokes was a satisfying compromise between the final retrospectively gated image quality and the total scan time for human studies. A modification was done to the original pulse sequence source code in order to tune this oversampling factor as desired. We therefore acquired 322709 spokes instead of 108637, which is the number of spokes calculated for a normal k-space sampling density in this configuration. With this number of spokes, we set the three tuning parameters of AZTEK in order to uniformly cover the k-space for a usual respiratory motion gate. We found the values: *AZTEK-Twist* = 1, *AZTEK-Shuffle* = 1 and *AZTEK-Speed* = 31. All these settings resulted in a total acquisition time of 10 minutes and 51 seconds.

All the acquisitions were performed on a GE Signa PET/MR 3.0 T machine (GE Healthcare, Waukesha, WI, USA). During the imaging process, the subject was lying supine with a respiratory belt around the waist to follow his or her respiratory motion along the imaging process. RF excitation was transmitted by the body coil of the PET/MR machine and a 30-channel GE GEM thoracic coil array was used for signal reception.

2. SELF-NAVIGATOR, MOTION GATES, SOFT-GATING WEIGHTS, AND GATED-AVERAGE RESPIRATORY CYCLE

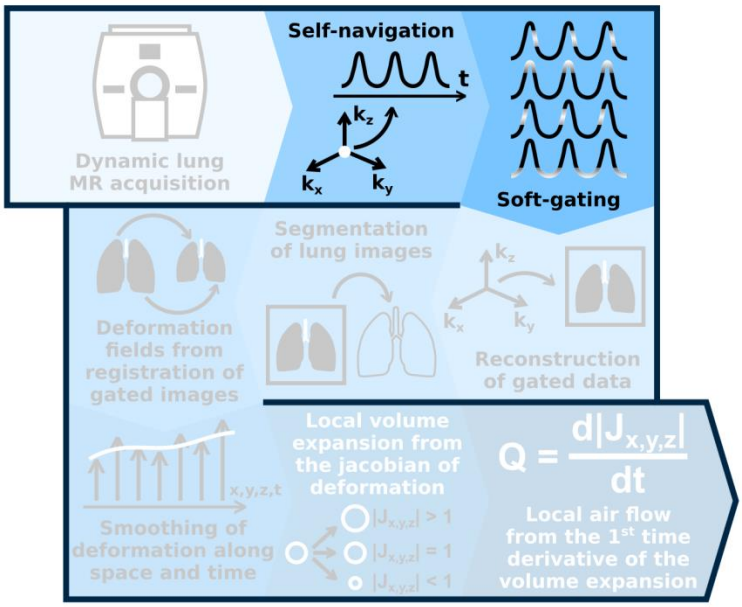

The first step of the motion correction process calls for the definition of a surrogate signal and the calculation of required information out of the MR signal for motion correction. Here, we will also set a method to give a time-stamp to each motion gate. We will come up with the definition of a gated-average respiratory cycle. To simplify the motion correction process, the physiological motion of the heart was neglected here as our radial pulse sequence is very robust to motion artifacts (in particular to motion ghosting, as explained in the previous chapter) and as physiological cardiac motion has only weak secondary effects in terms of lung parenchyma deformation, in

comparison with respiratory motion[278] (in particular far away from the heart). A great part of the total heart motion is actually caused by breathing. Therefore, only a surrogate signal for respiratory motion is required for 3D MR Spirometry. However, cardiac motion could be accounted to further study perfusion with ventilation.

2.1. EXTRACTION OF A RESPIRATORY SELF-NAVIGATOR

The respiratory self-navigator was extracted from the real and imaginary parts of the first point acquired at the beginning of each spoke, for each of the 32 channels of the thoracic reception coil array. After processing those DC-signals with SNIF (see Chapter 2), they were processed one by one to correct for any affine signal shift along time. This was done by fitting on each curve an affine model and by subtracting this adapted model to the original curve. The processed DC-signals were then analyzed by Principal Component Analysis (PCA), as done in SNOZE (see Chapter 2), to extract the first principal component, which corresponds to the respiratory motion, hence to produce a single surrogate signal. This signal was eventually smoothed to remove the remaining high-frequency noise, signed correctly to obtain low values for deflated and high values for inflated lung states, and slightly de-trended to remove any remaining artefactual trend. This process, implemented on Matlab, is fully automatic and it was identically applied to every dataset. The final surrogate signal could be visually compared to the one given by the respiratory belt.

2.2. DEFINITION OF MOTION GATES AND SOFT-GATING WEIGHTS

Motion correction was performed by retrospective self-gating as developed in Chapter 2 with AZTEK. Indeed, we have seen in the previous chapter that very promising image qualities could be reached in retrospectively gated ZTE images acquired with AZTEK. This retrospective gating technique consists in classifying our spokes into different motion bins, each one corresponding to a target motion amplitude. In our situation, we associate this motion amplitude to the amplitude of the respiratory self-navigation signal extracted just above. This constitutes the one-to-one relationship discussed in the previous chapter between the actual motion field and the surrogate signal: to each value of the surrogate signal, we suppose a unique corresponding motion field. For the motion binning process, we want to have a control on the amplitude position and width of each bin. Moreover, because we want to study precisely the mechanisms of breathing, and in particular differentiate the inspiratory phase to the expiratory phase, the sign of the time derivative of the surrogate signal was used to differentiate the inspiratory and expiratory phases and corresponding bins. Thirty-two gates (or bins) were defined to achieve high enough temporal resolution over the respiratory cycle (16 for the inspiratory phase and 16 for the expiratory phase). Because we chose an oversampling factor of only 3, we decided to implement a view-sharing strategy[279]. This sliding window method consists in sharing each spoke between several motion bins so as to exploit the motion field similarity between successive gates and therefore obtain a better SNR in final images, without degrading too much the quality in motion correction.

[278] Yvette Seppenwoolde et al., “Precise and Real-Time Measurement of 3D Tumor Motion in Lung Due to Breathing and Heartbeat, Measured during Radiotherapy,” *International Journal of Radiation Oncology*Biology*Physics* 53, no. 4 (July 15, 2002): 822–34, https://doi.org/10.1016/S0360-3016(02)02803-1.

[279] Jeffrey Tsao and Sebastian Kozerke, “MRI Temporal Acceleration Techniques,” *Journal of Magnetic Resonance Imaging* 36, no. 3 (September 1, 2012): 543–60, https://doi.org/10.1002/jmri.23640.

The retrospective self-gating was improved by soft-gating processing[280] [281] [282]. This consists in weighting the different spokes comprised in the same gate with coefficients reflecting their probability to be part of the gate. For example, the spokes that were acquired at a motion amplitude very close to the target motion amplitude of the bin ('acquired at the center of each gate segment') will be associated to larger weight values than spokes acquired at motion amplitudes different from the target motion amplitude of the bin ('acquired on the border of each gate segment'). This soft-gating strategy can be well associated with the previously described 'hard'-gating strategy (where the weights are either 0 or 1 from a soft-gating point of view) and is particularly adapted to the view-sharing strategy. Also, it would be valuable to discard some spokes that would be acquired at outlying motion states, in particular during extremal motion phases. This can happen for example if the subject takes a deep inspiration or blows more air than usually during expiration. If data acquired in those exceptional situations is taken into account in the reconstruction process, this would lead to motion artifacts in the images acquired at inflated and deflated lung states.

To finish, the image obtained at the end of expiration (deflated lung state) will be taken as a reference for the remaining steps of the 3D MR Spirometry processing pipeline. Because this dynamic state corresponds to a quiescent motion phase[283], with usually low respiratory motion rates (presence of a 'plateau' in the surrogate signal), it leads to a weak amount of residual motion artifacts. Moreover, lower air-tissue interface surface leads to decreased magnetic susceptibility effects. Furthermore, it could be valuable to increase the number of spokes for the bin corresponding to this special motion state as it would lead to a better reference image quality without adding any supplementary motion artifact. However, the same number of spokes is required between the other bins in order to obtain the same image quality after reconstruction for these gates, in order to avoid processing biases in the following steps. All these elements need to be controlled in the gating process.

The parameters (number of gates, amplitude positions and width of motion bins, number of spokes in each gate, number of spokes for the reference gate, separation of inspiratory and expiratory bins, and outlying data upper and lower thresholds) were controlled in a unique Matlab function to fully process the surrogate signal. In particular the target amplitude positions of the gates along both inspiratory and expiratory phases can be adjusted with a slider between 0 and 1. When it is set to 0, the bins are set for a uniform distribution of the target amplitudes, from the lower (deflated lung) to the upper amplitude threshold (inflated lung). When it is set to 1, the bins are set for a uniform distribution of the spoke density, such that more bins are dedicated to the quiescent phase at the end of expiration, when the lung is deflated, compared to the inflated lung state. Then every spoke (1 to N_{Spokes}) is associated to one or several motion bins (because of view-sharing) and are associated to soft-gating weight values (taking real values from 0 to 1). A Gaussian function centered on the target amplitude of each motion bin was chosen to calculate those soft-gating weights. The width of this Gaussian function was adapted for each motion bin in order to keep the same amount of data in each gate and therefore keep the same image quality in terms of SNR. As the numbers of gates along inspiratory and expiratory motion phases were set equal, each inspiratory phase has its 'equivalent' bin (same target amplitude) in the expiratory phase. The only exception is made for the bins at the

[280] Tao Zhang et al., "Fast Pediatric 3D Free-Breathing Abdominal Dynamic Contrast Enhanced MRI with High Spatiotemporal Resolution," *Journal of Magnetic Resonance Imaging* 41, no. 2 (2015): 460–73, https://doi.org/10.1002/jmri.24551.

[281] Joseph Y. Cheng et al., "Free-Breathing Pediatric MRI with Nonrigid Motion Correction and Acceleration," *Journal of Magnetic Resonance Imaging* 42, no. 2 (2015): 407–20, https://doi.org/10.1002/jmri.24785.

[282] Wenwen Jiang et al., "Motion Robust High Resolution 3D Free-Breathing Pulmonary MRI Using Dynamic 3D Image Self-Navigator," *Magnetic Resonance in Medicine*, October 2017, https://doi.org/10.1002/mrm.26958.

[283] Yvette Seppenwoolde et al., "Precise and Real-Time Measurement of 3D Tumor Motion in Lung Due to Breathing and Heartbeat, Measured during Radiotherapy," *International Journal of Radiation Oncology*Biology*Physics* 53, no. 4 (July 15, 2002): 822–34, https://doi.org/10.1016/S0360-3016(02)02803-1.

end of inspiration (inflated lung) and expiration (deflated lung), both composed of spokes corresponding to inspiratory and expiratory phases. All the process described above is fully automatic and was observed to be very robust across experiments.

2.3. DEFINITION OF A GATED-AVERAGE RESPIRATORY CYCLE

Now the motion gates and soft-gating weights are calculated, we can define a gated-average respiratory cycle. The definition of this gated-average respiratory cycle simply consists in giving to each motion bin a time-stamp, with a 0 reference time given to the deflated lung state, which is taken as a reference. To do so, we implemented another fully automatic Matlab function that takes as input the TR of the UTE pulse sequence, the spoke indexes for each motion bin and their soft-gating weights, and returns a vector containing the time-stamps in units of seconds. For each motion bin, this function cuts the list of spoke indexes into continuous segments of indexes and calculates from the TR and the soft-gating weights in each segment the average time duration between this segment and the previous deflated lung state segment. In this process, soft-gating weights should be seen as probabilities to be part of the bin. A single time-stamp is then given to each motion bin by calculating the average time duration between segments weighted by the mean soft-gating weight of each segment. We took care to calculate also the average time duration between two successive deflated lung states, which defines the average respiratory motion cycle. Logically, this time duration is equal to the average temporal pseudo-period of the respiratory motion under consideration. Each motion bin is therefore associated to one representative time-stamp with reference to the deflated lung state. These time-stamps will be useful for calculations involving the time in the next post-processing steps.

3. RECONSTRUCTION OF RETROSPECTIVELY SOFT-GATED UTE IMAGES

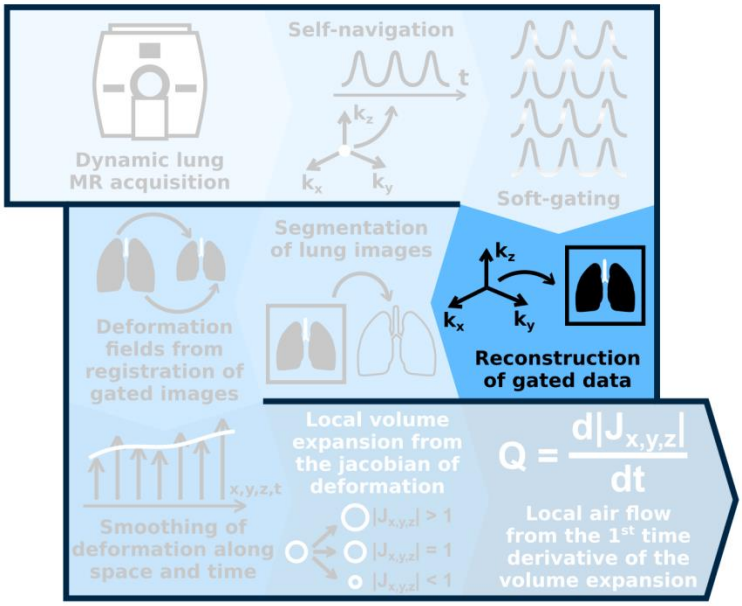

In this subsection, we will reconstruct MR image for each computed motion bin/gate. Because data were acquired radially in the 3D k-space, a standard inverse discrete 3D Fast Fourier Transform (FFT) cannot be used. This type of algorithm can only be used for data acquired on a Cartesian grid, where the data-points in k-space are equally spaced along each of the three k-space orthogonal dimensions. For that reason, a more advanced reconstruction algorithm will be needed.

To perform non-Cartesian reconstructions, we will use the open source Berkeley Advanced Reconstruction Toolbox (BART)[284]. This toolbox is still under development at Berkeley University and features a great diversity of tools for MRI reconstruction and digital image processing. In particular, this toolbox proposes several advanced reconstruction algorithms and strategies adapted to non-Cartesian trajectories and datasets acquired through multiple coils, as we will see.

3.1. PRINCIPLES OF NON-CARTESIAN MRI RECONSTRUCTION

The simpler way to reconstruct non-Cartesian k-spaces is to use a gridding algorithm[285] [286]. This algorithm consists in representing the non-Cartesian dataset on a Cartesian grid, on which an inverse FFT is then applied to perform the reconstruction. The BART toolbox gives the possibility to reconstruct a set of raw MR data with a gridding algorithm, which is a particular application of its *nufft* algorithm. The Non-uniform Fast Fourier Transform[287] (NuFFT) is more general in the sense that it gives the possibility to apply the inverse transform too (from a Cartesian image to a non-Cartesian k-space) and it is possible to perform these forward and inverse transforms in an iterative way and with a regularization term, as explained later.

However, in complement to the k-space data matrix and the list of k-space positions at which the data points were acquired, another element is required to perform the reconstruction correctly. This element is the matrix containing the k-space density compensation factors. Indeed, in the case of a non-Cartesian sampling scheme, the density of acquired points is not uniform in the entire k-space. In particular, for our radial k-space sampling strategy, the density of k-space points will be higher in the central region of k-space than in periphery. If this radially non-uniform density is not corrected, severe image artifacts will appear in the image (low spatial frequency components will be over-represented in our case because the density is larger in the low frequency compared to the high frequency region). Those radial correction coefficients can be calculated by knowing precisely the readout gradient fields performed during data acquisition. In particular, we have to be careful to the fact that several data points are acquired during readout gradient ramp-up.

To perform more accurately the reconstruction step, angular density compensation needs to be implemented too in order to consider the non-uniform angular density of spokes for each gate. However, this secondary correction step hasn't been performed for our experiments. In future work, in complement to radial density compensation, angular density compensation adapted to each motion bin will be implemented in order to increase further the quality of the final image. This global density compensation factor for each k-space data-point could be estimated thanks to the calculation of a 3D Voronoi diagram for example (see Chapter 2, AZTEK). In this situation, the density associated to a given point would be estimated as the inverse volume of the 3D Voronoi cell of this data-point. Another way to estimate this global density compensation factor would be to divide the radial compensation term defined just above with the area of the 2D Voronoi cell on a unity sphere and for the corresponding spoke, as discussed in the previous chapter.

---

[284] Martin Uecker, *Mrirecon/Bart: Version 0.4.03* (Zenodo, 2018), https://doi.org/10.5281/zenodo.1215477.

[285] J. D. O'Sullivan, "A Fast Sinc Function Gridding Algorithm for Fourier Inversion in Computer Tomography," *IEEE Transactions on Medical Imaging* 4, no. 4 (December 1985): 200–207, https://doi.org/10.1109/TMI.1985.4307723.

[286] J. I. Jackson et al., "Selection of a Convolution Function for Fourier Inversion Using Gridding (Computerised Tomography Application)," *IEEE Transactions on Medical Imaging* 10, no. 3 (September 1991): 473–78, https://doi.org/10.1109/42.97598.

[287] J. A. Fessler and B. P. Sutton, "Nonuniform Fast Fourier Transforms Using Min-Max Interpolation," *IEEE Transactions on Signal Processing* 51, no. 2 (February 2003): 560–74, https://doi.org/10.1109/TSP.2002.807005.

3.2. PRINCIPLES OF PARALLEL IMAGING AND COMPRESSED SENSING IN MRI

In a direct first approach, with Non-uniform Fast Fourier Transform (NuFFT), data acquired for each of the 30 reception channels can be pre-compensated with the radial density compensation factors mentioned in 3.1 and separately reconstructed with the NuFFT algorithm proposed by BART. The 30 mono-channel images can then be combined with a root-sum-of-square, which, for a subset of one given motion bin, yields the lung image presented in **Figure 3.2**. Only a subset of the total motion bin is used here to fully illustrate a situation of strong under-sampling. On this image, beyond the expected low SNR in the lung, motion correction appears effective, but a lot of noise-like under-sampling artifacts are visible. Those under-sampling artifacts obviously result from the small number of spokes chosen out of the bin for reconstruction (9,450), which is well below the normally required number of spokes in a non-under-sampled situation (108,637). Once again, this low number of spokes was chosen here only for illustration purposes. To cope for under-sampling artifacts and noise, we advantageously make use of parallel imaging and compressed sensing available in BART.

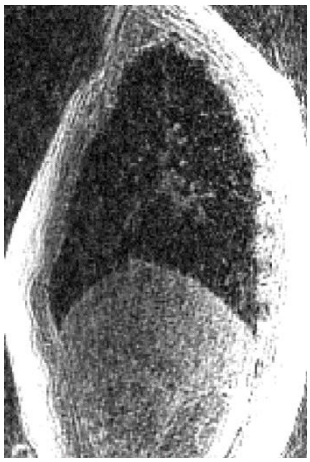

Figure 3.2: Sagittal view of a lung image reconstructed with NuFFT from a small subset of the first motion bin (deflated lung state). Each dataset acquired by each of the 30 reception channels was reconstructed separately and the final image was generated thanks to a root-sum-of-squares method.

3.2.1. PARALLEL IMAGING

The first concept is usually referred to as parallel imaging[288] [289]. It consists in exploiting the redundancy of data acquired through the different reception elements of the coil array. Indeed, two adjacent reception coil elements effectively acquire very close images at the same time, but modulated differently and showing uncorrelated background noise. The modulation pattern is proper to each reception channel element and is usually called sensitivity profile. It can be demonstrated that the non-uniform sensitivity profiles of the coil elements can act as position encoding elements, as it is done by frequency and phase encoding gradients in most MR pulse sequences. Many algorithms were developed to take into account the redundancy of data between coil elements during the reconstruction process, and are therefore able to generate satisfying image qualities from under-sampled data combined to the information of coil sensitivity profiles. The first examples of parallel imaging in the literature

[288] Klaas P. Pruessmann, "Encoding and Reconstruction in Parallel MRI," *NMR in Biomedicine* 19, no. 3 (2006): 288–99, https://doi.org/10.1002/nbm.1042.

[289] Katherine L. Wright et al., "Non-Cartesian Parallel Imaging Reconstruction," *Journal of Magnetic Resonance Imaging : JMRI* 40, no. 5 (November 2014): 1022–1040, https://doi.org/10.1002/jmri.24521.

showed the possibility to correct the strong aliasing artifacts for a regularly under-sampled Cartesian dataset, which would not be possible if the acquisition was made with only one reception channel.

The parallel imaging reconstruction algorithms can roughly be divided into two main categories: those which perform the correction in the image space (the most famous one is probably SENSE[290]) and those which perform the correction in the k-space (one of the first algorithm of this type was SMASH[291]). It can be shown that these two categories of algorithms share a lot of similarities actually, and aim at resolving the same type of problem with different strategies. However, they both need to have precise and accurate information on coil sensitivity profiles. These sensitivity profiles can be measured locally thanks to hardware systems designed for this purpose[292], or calculated in the entire image field-of-view by imaging an homogeneous phantom[293], or by dividing the image obtained with each reception channel by the same image acquired thanks to the body coil[294], or by the image obtained by calculating the root-sum-of-square of the coil images[295], for example. Those measurements are however prone to errors and usually need further image acquisitions. Hopefully, autocalibrated methods were developed, and aim at estimating the coil sensitivity profiles (or the k-space correlations between the different channels) directly from the imaging k-space data. One of the most famous methods using intrinsically this strategy is GRAPPA[296]. More recent and advanced methods aim at estimating the sensitivity profiles from the k-space data, as the ESPIRiT[297] method, for example.

3.2.2. COMPRESSED SENSING

The second useful concept for our problem is usually referred to as compressed sensing[298] [299] [300]. This concept aims at exploiting the sparsity of the image in a given mathematical representation to enable the reconstruction of acceptable quality images from under-sampled (or compressed) data. Indeed, MR images are usually sparse (described with a low amount of coefficients far below the number of voxels) once the image is transformed mathematically to another representation: wavelet transform and gradient usually lead to images with a low amount of high valued voxels and a lot of zeros. Some images, as certain contrast enhanced angiograms, are even

[290] Klaas P. Pruessmann et al., "SENSE: Sensitivity Encoding for Fast MRI," *Magnetic Resonance in Medicine* 42, no. 5 (1999): 952–62, https://doi.org/10.1002/(SICI)1522-2594(199911)42:5<952::AID-MRM16>3.0.CO;2-S.

[291] Daniel K. Sodickson and Warren J. Manning, "Simultaneous Acquisition of Spatial Harmonics (SMASH): Fast Imaging with Radiofrequency Coil Arrays," *Magnetic Resonance in Medicine* 38, no. 4 (1997): 591–603, https://doi.org/10.1002/mrm.1910380414.

[292] Luc Darrasse and Ghazi Kassab, "Quick Measurement of NMR-coil Sensitivity with a Dual-loop Probe," *Review of Scientific Instruments* 64, no. 7 (July 1, 1993): 1841–44, https://doi.org/10.1063/1.1144020.

[293] Sodickson and Manning, "Simultaneous Acquisition of Spatial Harmonics (SMASH)."

[294] Pruessmann et al., "SENSE."

[295] Kevin F. King, Calibration method for use with sensitivity encoding MRI acquisition, United States US6559642B2, filed May 9, 2001, and issued May 6, 2003, https://patents.google.com/patent/US6559642B2/en.

[296] Mark A. Griswold et al., "Generalized Autocalibrating Partially Parallel Acquisitions (GRAPPA)," *Magnetic Resonance in Medicine* 47, no. 6 (June 2002): 1202–1210, https://doi.org/10.1002/mrm.10171.

[297] Martin Uecker et al., "ESPIRiT—an Eigenvalue Approach to Autocalibrating Parallel MRI: Where SENSE Meets GRAPPA," *Magnetic Resonance in Medicine* 71, no. 3 (March 2014): 990–1001, https://doi.org/10.1002/mrm.24751.

[298] Michael Lustig, David Donoho, and John M. Pauly, "Sparse MRI: The Application of Compressed Sensing for Rapid MR Imaging," *Magnetic Resonance in Medicine* 58, no. 6 (December 2007): 1182–1195, https://doi.org/10.1002/mrm.21391.

[299] M. Lustig et al., "Compressed Sensing MRI," *IEEE Signal Processing Magazine* 25, no. 2 (March 2008): 72–82, https://doi.org/10.1109/MSP.2007.914728.

[300] Sairam Geethanath et al., "Compressed Sensing MRI: A Review," *Critical Reviews in Biomedical Engineering* 41, no. 3 (2013): 183–204.

sparse directly in the image domain. This transform sparsity can be exploited in the reconstruction process by minimizing iteratively the L1 norm of the transformed image (wavelet transform or gradient of the image usually) at the same time as a data consistency term (usually the L2 norm of the difference between acquired data and the non-uniform Fourier transform of the current image estimation). It can be demonstrated that the L1 term enforces the transform sparsity along the successive image estimations and this can be performed through a non-linear optimization algorithm. It has been shown that better image quality could be obtained if the original under-sampling artifacts were incoherent in the transformed space. In this case, compressed sensing plays a denoising role during the reconstruction process.

3.2.3. THE COMBINED EFFECT OF PARALLEL IMAGING AND COMPRESSED SENSING ON NON-SPATIALLY COHERENT UNDER-SAMPLING ARTIFACTS

These two previous concepts, parallel imaging and compressed sensing, can be implemented together in the same reconstruction algorithm and are both well suited to our situation. In particular, parallel imaging is largely supported here by the 30-channel thoracic coil array. With an AZTEK trajectory, the under-sampling artifacts for any usual motion bin are incoherent in the image space, and therefore are also incoherent in usual sparsifying transformed spaces (wavelet space or image gradient space for example), which favors compressed sensing. **Figure 3.3** shows the same image as in **Figure 3.2** but reconstructed thanks to the *pics* (Parallel Imaging and Compressed Sensing) generalized iterative reconstruction algorithm proposed by BART[301]. In more details, this algorithm performs the reconstruction thanks to an iterative SENSE method, and we chose a compressed sensing strategy based on the minimization of the L1 norm of the 3D wavelet transform of the image. Concerning the sensitivity profiles of the coil elements, they were estimated directly from the imaging k-space dataset thanks to the ESPIRiT method also proposed by BART. In the images reconstructed with parallel imaging and compressed sensing, we observe that the under-sampling artifacts observed in **Figure 3.2** are strongly attenuated.

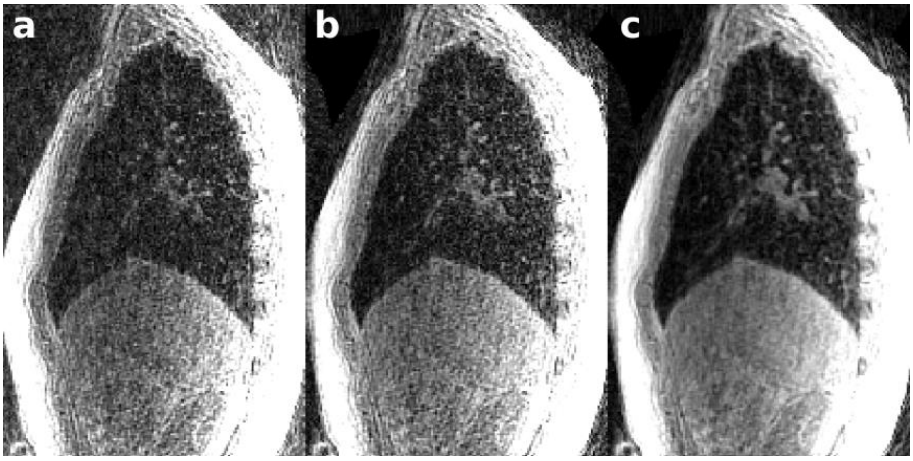

Figure 3.3: Same view of the image represented in **Figure 3.2** but reconstructed with different methods. a) Reconstruction with a NuFFT (same image as in **Figure 3.2**); b) Reconstruction with a direct (1 iteration) SENSE method featuring parallel imaging but no compressed sensing; c) Reconstruction with an iterative (5 iterations) SENSE method featuring parallel imaging and wavelet based compressed sensing (regularization parameter equal to 0.005 for compressed sensing).

[301] Martin Uecker et al., "The BART Toolbox for Computational Magnetic Resonance Imaging," n.d., 1.

3.3. CHOICE OF AN IMAGE RECONSTRUCTION STRATEGY FOR 3D MR SPIROMETRY

For 3D MR Spirometry, the reconstruction was carried over the full dataset of each motion bin thanks to two iterations and a regularization parameter equal to 0.005 (to weight the compressed sensing L1 regularization term regarding to the data consistency L2 term in the iterative process). This same reconstruction process was performed separately for each of the 32 motion bins estimated in the previous section. Note that, during preliminary reconstruction experiments (not reported here), it was considered to exploit sparsity in the motion phase dimension (between motion bins) by considering that the finite difference between consecutive gates was leading to sparsity. To do so, the L1 norm of the gradient transform along the gate index dimension was considered, leading to a Total Variation (TV) regularization in the dimension of motion phase. However, this joint reconstruction of the 32 motion bins with two L1 regularization terms (one implying wavelet transform in space and the other one TV along successive motion phases) led to unpractical reconstruction times and deceiving results, essentially because the deformation of the lung parenchyma between successive gates remained large and led to motion blurring. However, future work would need to be continued in this direction in order to improve further final image quality.

Finally, after the reconstruction, each image was processed to retrospectively account for the non-linearity effects of position encoding gradients with GE Orchestra reconstruction toolbox. At the end, we obtain 32 3D lung images corrected from both respiratory motion and position encoding gradients non-linearity effects. These 32 images represent the lung at different instants of a representative respiratory cycle or gated-average respiratory cycle. Along this cycle, 16 images correspond to the inspiration maneuver (from the deflated to the inflated state) and the 16 other images representing the expiration maneuver (from the inflated state to the deflated state).

4. 3D IMAGE SEGMENTATION OF LUNG PARENCHYMA, VASCULAR TREE AND AIRWAYS

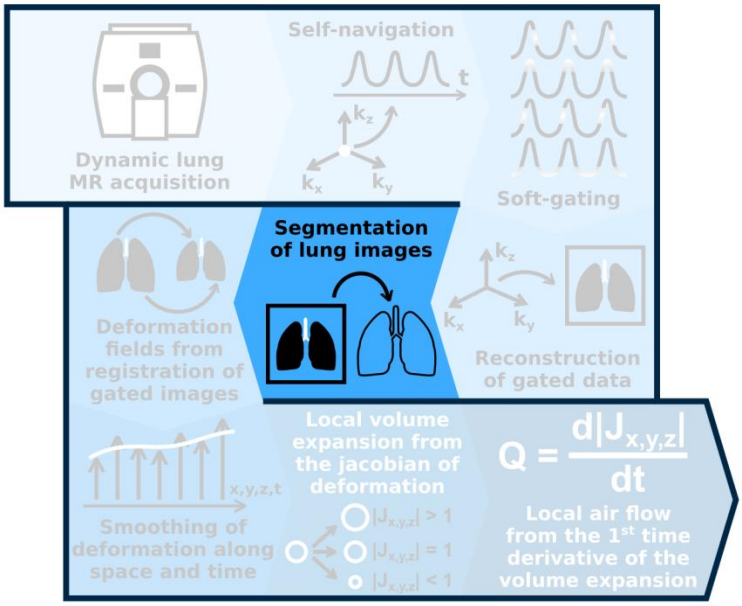

4.1. MOTIVATION FOR THE DEVELOPMENT OF A LUNG SEGMENTATION ALGORITHM

In this step, a dedicated algorithm is developed to segment the lung along with the parenchyma, the vascular tree (arteries, veins) and the large airways (trachea, primary bronchi, next generations of bronchi). Such segmentation is motivated by four main reasons:

- In the next processing steps, slipping boundary conditions will be considered at the periphery of the organ.
- Voxel gas volumes and flows will be estimated from lung images. They will be normalized and compared to global measurements averaged over the whole lung.
- Results will be regionally analyzed in the parenchyma, without taking into account the large airways (which are functional dead spaces), but also close to the larger arteries and veins of the vascular tree.
- Ventilation maps will be superimposed onto the anatomical lung image.

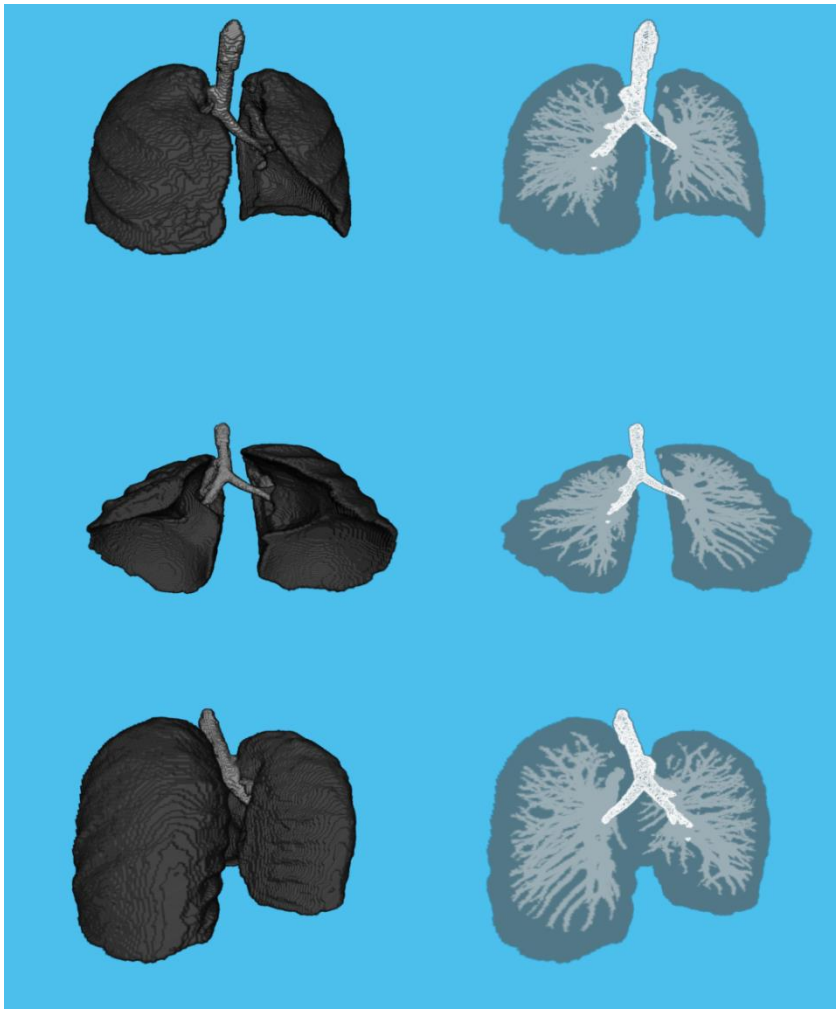

Figure 3.4: Opaque and transparent 3D views of the masks returned by the automatic lung segmentation algorithm. Three different masks are obtained at the end of the segmentation process: a mask of the lung parenchyma (dark grey), a mask of the vascular tree (light grey) and a mask of the large airways (white).

A representative lung mask obtained with the developed algorithm is represented in **Figure 3.4**. In the different opaque and transparent representations, we observe a precise depiction of the three elements mentioned above: the lung parenchyma, the vascular tree and the large airways. All the segmentation process was developed on Matlab and the representations of **Figure 3.4** were generated by a 3D viewer available on Matlab (*volumeViewer*).

4.2. IMPLEMENTATION OF THE LUNG SEGMENTATION ALGORITHM

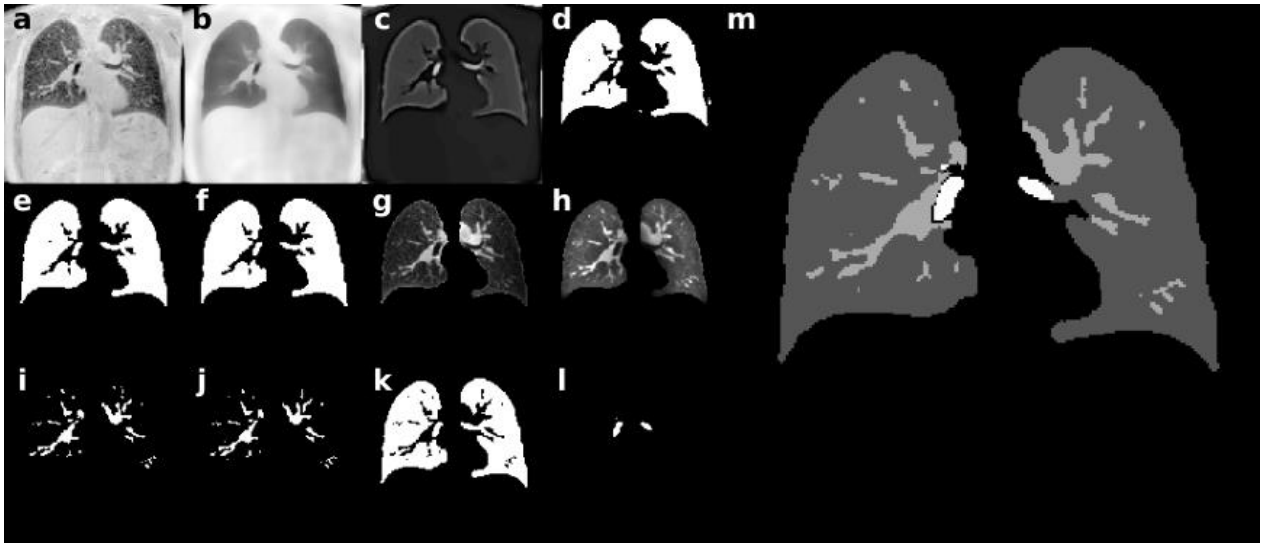

Figure 3.5: Coronal views of the main steps followed by the automatic lung segmentation algorithm.

In the following are listed the main segmentation steps and a global overview of the methods employed to perform the segmentation as desired:

1. **Segmentation of the entire organ:** This step is based on the very large image contrast between the lung parenchyma and large airways (low MR signal, appear dark) and the surrounding tissues like the liver, the spleen, the muscles, or fat (high MR signal, appear bright). An intensity-based thresholding is therefore possible to separate between inside and outside the lung. Care is taken to discard the other parts of the image which generate low MR signal (background, digestive track gas, bones, …). The thoracic image (see **Figure 3.5a**) is first denoised without spatial resolution loss thanks to a Total Variation (TV) denoising algorithm in BART (see **Figure 3.5b**). The edges of the organ were sharpened by using morphological filters and the global intensity of the image was corrected to account for the effects of inhomogeneous reception coil sensitivity profiles (see **Figure 3.5c**). The lung mask was then extracted by automatic thresholding (see **Figure 3.5d**) and only the largest connected component was kept in order to remove other low MR signal regions that were selected during the threshold process (see **Figure 3.5e**). To finish, holes present inside the mask (corresponding mostly to structures of the vascular tree) are filled by morphological filters (see **Figure 3.5f**). A global mask corresponding to the entire organ (parenchyma, vasculature and airways) is therefore obtained.

2. **Segmentation of the vascular tree:** As for the entire organ, the segmentation of the vascular tree is made possible thanks to the large MR contrast between the bright blood vessels and the dark lung parenchyma. The global mask obtained just above is multiplied to the thoracic image (see **Figure 3.5g**). The result is then uniformized, denoised, and the signal at the borders of the lung is attenuated in order to avoid its

segmentation (see **Figure 3.5h**). As before, the denoising is performed thanks to a TV denoising algorithm. The vascular tree is segmented by automatic thresholding (see **Figure 3.5i**) and by selecting only the largest connected components to remove small segmented structures that does not correspond to vasculature (see **Figure 3.5j**). Before performing the third segmentation step, this vasculature mask is removed from the global lung mask obtained during the first step (see **Figure 3.5k**).

3. **Segmentation of the large airways:** The segmentation of the large airways is easy for the trachea and the primary bronchi because they have already been segmented during the first segmentation step. However, the segmentation process is far more difficult for the next generations of bronchi because the contrast between these elements and the surrounding parenchyma is low and their diameter decreases as they go deeper inside the organ, until they reach a diameter close to the voxel size which does not permit to detect them anymore. To perform this segmentation, we adapted an active contour algorithm and applied it to the global lung mask removed from the vascular tree, as calculated previously. Once initialized in the trachea, this algorithm propagates a segmentation contour in the trachea, primary and secondary bronchi and automatically stops according to a regularization process based on the smoothness of the contour (see **Figure 3.5l**). After performing last tiny adaptations between this new mask and the other masks obtained just above, the airway mask is removed from the global lung mask. This global lung mask becomes therefore a lung parenchyma mask and we obtain the three desired masks: the lung parenchyma mask, the vascular tree mask and the large airways mask (see **Figure 3.5m**).

At the end of such a segmentation process, a visual verification is made in order to confirm the relevance of the segmentation of the three elements in the entire lung.

5. ESTIMATION OF THE RESPIRATORY MOTION INDUCED DEFORMATION FIELDS

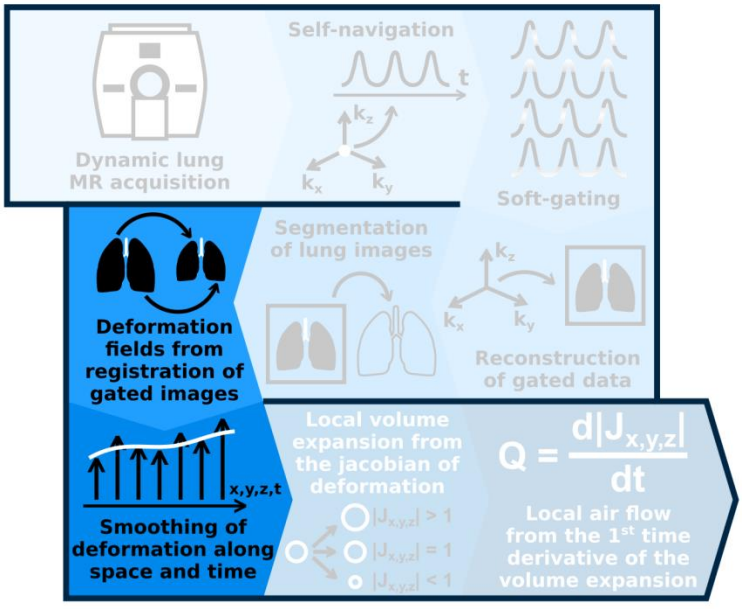

5.1. FROM IMAGE REGISTRATION TO PHYSICAL DEFORMATION FIELDS IN BIOLOGICAL TISSUES

This subsection describes the key post-processing step of the technique where the mechanical behavior of the lung during breathing is inferred from the images. As seen in the previous chapter, the mechanical behavior of the lung can be described at the macroscopic scale with a time varying 3D motion (or displacement) field $\vec{u}(X,Y,Z,t)$. In the Lagrangian point of view, at an arbitrary time t_0 (real or virtual), we consider the infinitesimal volumes of material localized at continuous spatial positions $\vec{R} = \begin{bmatrix} X \\ Y \\ Z \end{bmatrix}$ and we follow along time the evolution of their new spatial position $\vec{r}(X,Y,Z,t) = \vec{R} + \vec{u}(X,Y,Z,t)$. As a definition, at the reference time-point t_0, $\vec{u}(X,Y,Z,t_0) = \vec{0}$ at each spatial position (X,Y,Z). $\vec{r}$ is usually referred to as the deformation field, and it is necessary to make the difference between this deformation field and the motion or displacement field $\vec{u}$, even if both fields are strongly linked to each other.

In the lung, an easy way to define and consider this motion field is to take a phase of the pseudo-periodic lung motion as unique real reference time-point t_0. Every time this reference motion phase occurs, the lung returns to the reference state and the motion field $\vec{u}$ is zero everywhere in the organ. As the motion field is only considered at discrete motion phases materialized by the 32 motion gates, the reference phase is taken at one of these gates. These considerations generally fail because respiratory motion is neither pseudo-periodic nor reproducible. Nevertheless, they especially hold here because inspiratory and expiratory motion phases are separately considered. Therefore, the non-reproducibility between inspiratory and expiratory phases is taken into account. Moreover, outlying motion states are discarded for the image reconstruction, as explained in 2.2. This results in an acceptable reproducibility between motion periods in terms of data taken into account for motion field estimation.

As explained in 2.2, the motion state reached at the end of each expiration maneuver is used as the reference motion phase. Regional pulmonary motion fields $\vec{u}$ were estimated everywhere in the lung from the motion-corrected thoracic images with respect to the reference deflated lung state by performing elastic registration of the 31 images representing the lung throughout the gated-average respiratory cycle upon the deflated lung reference image. For each of the 31 image registration steps, the deflated lung image is involved, which explains the importance to take into account the image showing the best quality as a reference image.

In the general case, image registration consists in deforming one of the images, called the 'moving image', to fit it to the other one, called the 'fixed image'. In our case, the fixed image is the reference deflated lung image, and the moving image is one of the reconstructed 31 images to be deformed so to fit as much as possible to the deflated lung state. Even if the principle of registration or spatial normalization is easy to understand, the underlying implementation of elastic spatial normalization is complex. Usually, the method consists in iteratively estimating the motion field that transforms the fixed image to the moving image until a maximum of similarity between the two images is found. To calculate the similarity between the two images at one given iteration, a set of spatial coordinates $\vec{R}$ is first chosen in the fixed image domain. Then, their transformed spatial coordinates are calculated thanks to the motion field estimated at the iteration under consideration. These new positions $\overrightarrow{r'}$ correspond to the equivalents of $\vec{R}$ but in the moving image space. To finish, the fixed image values are interpolated at positions $\vec{R}$, the moving image values are interpolated at positions $\overrightarrow{r'}$ and a similarity metric between the two images is computed from those two sets of data. An image registration problem is therefore inherently an optimization problem (which tries to minimize the similarity metric calculated between the two images) and the transformation goes from the fixed image domain to the moving image domain. At the end of the process, any point in the fixed image can be mapped to one given position in the moving image, and the displacement components can be

calculated at any fixed image position. In particular, these displacement components can be calculated at each voxel position in the fixed image domain.

Therefore, the displacement of the 'piece of material' present inside any fixed image voxel is directly assessed, and the three spatial components of $\vec{u}$ are therefore directly obtained at each voxel position in the fixed image domain. If the estimation process would perfectly assess the actual physical motion field, we would obtain $\overrightarrow{r'} = \vec{r}$ at the last iteration step and the vector field characterizing the optimal spatial transform would exactly correspond to $\vec{u}$. Moreover, because all the information is inherently mapped to the fixed image domain, all our future calculations and representations of regional volume expansions, air flows and mechanical behavior parameters will be shown as images and parametric maps in the reference deflated lung state. Furthermore, it means that only one lung segmentation will be necessary (see 4.2), and this segmentation will be performed in this deflated lung image. It supports the fact that the motion phase taken as a reference should be associated to the best image quality, as explained in 2.2.

5.2. IMAGE REGISTRATION FEATURES PROPOSED BY THE ELASTIX TOOLBOX

The image registration was performed with the open source Elastix toolbox[302]. The image registration implementations proposed by this toolbox mostly exploit those featured by the well-known Insight Segmentation and Registration Toolkit (ITK). Elastix acts as a wrapper around the image registration methods proposed by ITK and gives the possibility to use and compare them easily and with the same formalism. Moreover, because we wanted to implement all our post-processing tasks on Matlab, we used Elastix through the open source toolbox ElastixFromMatlab (https://sourcesup.renater.fr/elxfrommatlab/), which is itself a wrapper around Elastix. It gives the possibility to use Elastix components as standard Matlab functions, which can therefore be incorporated into any Matlab script and manipulate Matlab matrices as inputs and outputs.

With Elastix, any property describing the image registration process can be chosen from several possible choices. Moreover, most parameters describing the registration process can be tuned freely. Here is a non-exhaustive description of the registration properties that can be modified, of the main parameters that can be tuned and of the choices we made for our 3D MR Spirometry application:

- **Type of transform:** Elastix proposes several types of parametric transforms defined from the fixed to the moving image (non-parametric transforms, as diffeomorphic demons[303] for example, are not proposed by Elastix). Of course, the toolbox proposes standard rigid transformations composed of translations and/or rotations only, which is usually sufficient to correct head motion between independent acquisitions for example. The toolbox proposes also transformations that supposes simple object deformations, as a scaling or a shear transformation. Finally, Elastix proposes elastic transformations, which give the possibility to perform more complex deformations with different behaviors at the local scale. A B-splines transform (based on the deformation of a grid of transform points) and a Thin-plate splines transform (based on the association of an affine model and the registration of user-defined landmarks) are proposed. As a remark, the toolbox gives the possibility to compose several transforms together. For example, it is

[302] S. Klein et al., "Lt;Emphasis Emphasistype="mono" Gt;Elastix Lt;/Emphasis Gt;: A Toolbox for Intensity-Based Medical Image Registration," *IEEE Transactions on Medical Imaging* 29, no. 1 (January 2010): 196–205, https://doi.org/10.1109/TMI.2009.2035616.

[303] Tom Vercauteren et al., "Diffeomorphic Demons: Efficient Non-Parametric Image Registration," *NeuroImage*, Mathematics in Brain Imaging, 45, no. 1, Supplement 1 (March 1, 2009): S61–72, https://doi.org/10.1016/j.neuroimage.2008.10.040.

possible to perform first an affine transform and then a B-splines transform. For our application, in order to make the registration process fully automatic (without the need to manually prescribe landmarks) and to reflect the local deformations of the lung parenchyma, we decided to use a B-splines transform. An isotropic distance of 20 voxels (30 mm in real size) was chosen between the control points of the 3D grid. This value was found to be a good compromise between, in one hand, registration complexity, sensitivity to the image noise and total processing time (which decrease with the distance between control points) and, in the other hand, the possibility to detect localized mechanical behaviors (which increases with the distance between control points).

- **Similarity metric:** This similarity metric is a function taking as inputs the fixed image, the moving image and a transform that is supposed to link both images. This function returns a value that converges to 0 as the similarity between the two registered images at given sample points increases. Different methods are proposed to measure the similarity between the values sampled in both images. The most straightforward one is based on mean-square difference, and aims at registering together regions with similar image intensities. More advanced ones, as *Mutual Information*[304] for example, are based on the probability distribution of intensities in both images, and are able to register images from similar or different modalities. It is also possible to register binary masks by using *Kappa Statistic*. For our application, we chose the *Normalized Mutual Information*. Indeed, when different levels of inflation are reached in the lung, the MR signal usually decreases because of both tissue density and potential T_2^* decrease. Some details, like small blood vessels, may even become invisible because of susceptibility effects and enhanced motion artifacts at increased lung volumes. For that reason, it is preferable to use a metric that supposes a relationship that goes beyond the similarity in image intensities. Experimentally, we found better visual results with *Normalized Mutual Information* compared to the simple *Mutual Information*.

- **Image sampler:** To calculate the similarity metric, a given number of couples of points need to be considered, with one point in the fixed image and the other one being registered to it in the moving image. One possibility is to choose the positions of all the voxels in the fixed image and their corresponding ones in the moving image. However, this leads to long computation times for a result that could be obtained far more easily. This is why the user can choose the image sampler, which is the program that chooses the points in the image that participates to similarity measurement calculation. The user can also choose the number of points to sample at each iteration. In the sampler itself, the user can either choose the points on the full or an under-sampled grid, or choose them randomly either on the image grid or at random positions that can fall between voxel locations. For our application, we chose this last option as it was shown to facilitate image registration, in particular with a similarity measurement based on mutual information[305]. At each iteration, we observed that the selection of 10,000 couples of sample points led satisfying visual results. It significantly reduces the computing time in regard to the 212×212×142=6,382,042 voxels of the lung images. However, an interpolation method needs to be chosen in this case as the chosen points can fall outside voxel locations in the fixed image. At each iteration of the registration process, a new set of points was randomly chosen.

- **Image interpolator:** A method to interpolate values between voxel positions needs to be chosen. These interpolations will be performed to sample the intensity in the moving image domain after applying the

[304] F. Maes et al., "Multimodality Image Registration by Maximization of Mutual Information," *IEEE Transactions on Medical Imaging* 16, no. 2 (April 1997): 187–98, https://doi.org/10.1109/42.563664.
[305] Philippe Thévenaz, Michel Bierlaire, and Michaël Unser, "Halton Sampling for Image Registration Based on Mutual Information," *Sampling Theory in Signal and Image Processing* 7, no. 2 (2008): 141–71.

transformation, but also in the fixed image domain if the sampler chooses points that do not fall onto image grid positions. The easiest way to interpolate is to choose the nearest neighbor voxel, which is light in term of computation time but that can lead to deceiving results. A true interpolation thanks to the calculation of an interpolation function is therefore preferable. However, interpolating with a high order function often leads to long computation times relatively to the improvement in the final result. Usually, a linear first order interpolation is sufficient and this is what we chose for our application. However, to calculate the final transformed moving image after the estimation of the optimal transform, a 3rd order B-splines interpolation is used to obtain an improved final image quality.

- **Optimizer:** The optimizer corresponds to the optimization method that aims at finding the transform parameters that minimize the similarity metric for the fixed and moving images. Standard optimization methods, as *Quasi-Newton* and *Gradient descent*, are available in Elastix. For our application, we decided to use an *Adaptive stochastic gradient decent*[306], which is more robust than the standard gradient descent and gave satisfying results in our case. For each resolution of the multi-resolution procedure described thereafter, 300 iterations of this optimization algorithm were performed.

- **Type of multi-resolution strategy:** In the field of image registration, a well-known strategy to perform complex elastic image registration procedures is to use a multi-resolution strategy[307]. As described above, one way to do it consists in composing several transforms from the simpler one (mere translation, for example) to the more complex one (B-splines, for example). Another way to do it is to start the registration with simpler images, which contain fewer details and which are therefore easier to register. Then, the image complexity is progressively increased. This can be done by starting the registration with smoothed images and/or uniformly under-sampled images (by taking only one pixel over two or three, for example). In our application, we decided to perform the registration with four smoothing levels of the fully sampled images, both for the fixed and moving images. We observed that this strategy strongly helped the convergence and the robustness of the global registration process, even by initializing it with the identity transform.

5.3. MANAGEMENT OF SLIDING MOTIONS IN THE IMAGE REGISTRATION PROCESS

We have observed during our experiments that the B-splines transform was particularly efficient to model the spatially continuous deformation field evolving in the lung parenchyma during breathing. However, the motion field is not purely spatially continuous in the thorax. In particular, we observe a sliding motion between the lung and the thoracic cage, and also between the lung and the heart. This sliding motion is particularly problematic between the lung and the thoracic cage because both the pulmonary vascular tree and the ribs surrounding the lungs act as landmarks for the registration process. The registration algorithm will therefore try to find a spatially continuous deformation field between the lung parenchyma and the thoracic cage with the B-spline transform model, which is wrong anatomically speaking. First, this problem was addressed by performing registration on masked images, with point sampling only performed in regions where the lung was present. To do so, the segmentation algorithm presented in the previous subsection was very useful. However, the results were deceiving because the contrasted limit between the lung and its surrounding tissues was actually important for image registration. Indeed, because a small amount of blood vessels are visible distally in the lung parenchyma, image

[306] Stefan Klein et al., "Adaptive Stochastic Gradient Descent Optimisation for Image Registration," *International Journal of Computer Vision* 81, no. 3 (August 28, 2008): 227, https://doi.org/10.1007/s11263-008-0168-y.
[307] Hava Lester and Simon R. Arridge, "A Survey of Hierarchical Non-Linear Medical Image Registration," *Pattern Recognition* 32, no. 1 (January 1, 1999): 129–49, https://doi.org/10.1016/S0031-3203(98)00095-8.

registration is difficult in those regions without considering the spatial limits of the organ. This issue was then addressed with more advanced masks, which included the borders of the organ but not the external elements acting as landmarks. These more advanced masks led to a better registration but with mismatches, in particular in the posterior part of the lung where the ribs are clearly visible. To solve this problem, Kolb *et al.*[308] used a totally different approach by performing joint lung segmentation and image registration thanks to a pre-designed lung model. In this case, the registration process only estimates the motion field inside the lung parenchyma and does not take into account any external image landmark. However, this process asks for the development of such a lung model and can lead to strong errors if this model is not correct (for example, if the patient was subject to lung resection). This approach is therefore attracting but less general compared to one based on image registration.

Figure 3.6: Sagittal representation of a typical thoracic MR image before (left) and after (right) a saturation process designed to remove features (ribs and intercostal muscles pointed out by red arrows) that might easily be used as landmarks and lead to wrong deformation fields in the lung parenchyma after image registration with a purely elastic model.

The best solution we found to solve this problem was to perform registration on images for which high MR signal values were saturated above a given threshold. Indeed, the structures present in the lung (parenchyma, blood vessels and airways) usually show lower MR signal values than elements surrounding the lung (intercostal muscles, fat, heart, liver, …). For that reason, if the voxels showing a MR signal superior to a well-chosen signal threshold are set to this threshold value, it is possible to saturate the signal of tissues around the lung and thus make the previously described external landmarks invisible, while preserving the contrasted border between lung parenchyma and surrounding tissues. At the end of this saturation process, the image is multiplied by a gain related to the saturation threshold so as to re-expand the image within the full dynamic window (see **Figure 3.6**).

[308] Christoph Kolb et al., "Regional Lung Ventilation Analysis Using Temporally Resolved Magnetic Resonance Imaging," *Journal of Computer Assisted Tomography* 40, no. 6 (December 2016): 899, https://doi.org/10.1097/RCT.0000000000000450.

Therefore, if elastic registration is performed between saturated fixed and moving images, registration will perform correctly in the lung parenchyma, relying on internal landmarks (blood vessels, large airways, …) and on contrasted organ limits, but without taking into account the external landmarks (ribs, heart, intercostal muscles, …). For that reason, it will be possible to find a correct deformation field inside the lung, independent of external landmarks. However, the deformation field estimated outside the lung will obviously be irrelevant as there is no landmark anymore to correctly perform the registration in those regions. This technical solution has the advantage to be very simple, as it only involves one simple supplementary image processing step, and it gives the possibility to use the image registration procedures featured by Elastix.

5.4. FILTERING OF SPATIAL TRAJECTORIES FOLLOWED BY ELEMENTARY LUNG VOLUMES

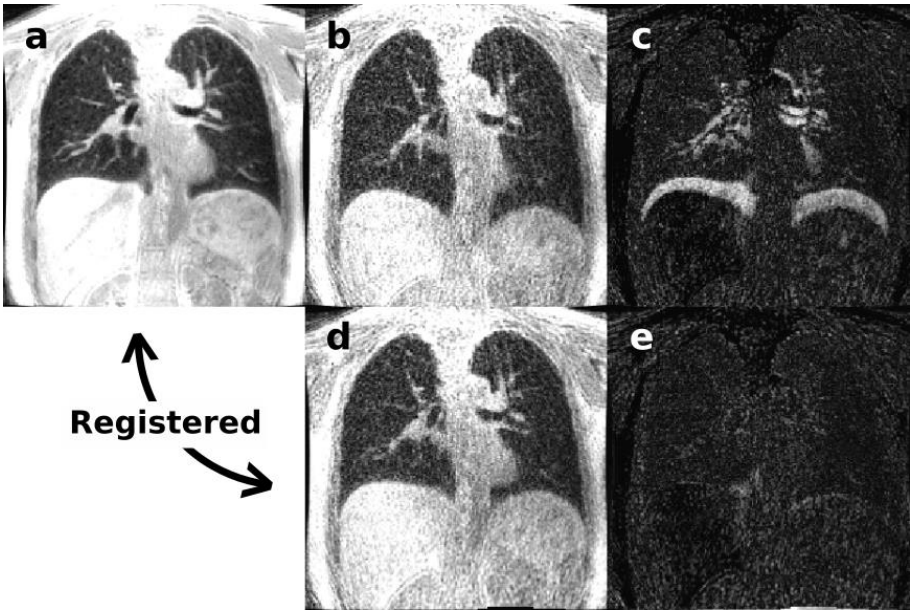

Figure 3.7: Coronal views of the images processed by Elastix. a) Reference image gated at the end of expiration; b) Image gated at the end of inspiration; c) Absolute difference between images a and b; d) Transformed image resulting from the registration of image b on image a; e) Absolute difference between images a and d.

The quality of the registration process is often good with every pair of images (see **Figure 3.7**). Yet, tracking the resulting motion fields throughout the respiratory cycle is less robust along the 32 images. The 3D spatial trajectory followed by an elementary piece of lung tissue is usually noisy, which is not really the smoothly-continuous local motion that is expected (see **Figure 3.8**, blue curve). This noise can be even more problematic when more advanced parameters are calculated from temporal derivatives of these motion fields. As we will see in the next section, the calculation of those derivatives will be performed thanks to standard finite difference methods. A promising way to solve this problem would be to use a registration procedure that registers together the 32 images. We tried to solve the problem by considering a 4D B-spline model, the same as presented in 5.2, but extended to the motion phase dimension too, and for which periodic boundary conditions were considered along this fourth dimension to ensure the temporal pseudo-periodicity of the motion field. These tests led to very long computation times and deceiving results: the local trajectories were smoother in their 3D representations, as expected, but it resulted to a decreased registration quality for individual images. Another attempt consisted in filtering the images with a TV denoising algorithm to remove the noise inside the lung parenchyma without degrading the spatial resolution of the image (to keep all the internal landmarks). However, the final trajectories

were still noisy. We finally used a filter developed by the laboratory CREATIS in Lyon (France) and designed, amongst others, to smooth 3D curves[309]. Thanks to this algorithm, we obtained smooth curves that remained close to the original ones (see **Figure 3.8**, red curve). However, future work should focus on the implementation of a true groupwise registration approach, like the one proposed by Metz *et al.*[310], in order to register together the 32 motion corrected images with separate 3D B-splines models and a regularization term that enforces smoothness in the time evolution of the deformation field. This recent method showed promising results in the case of lung image registration.

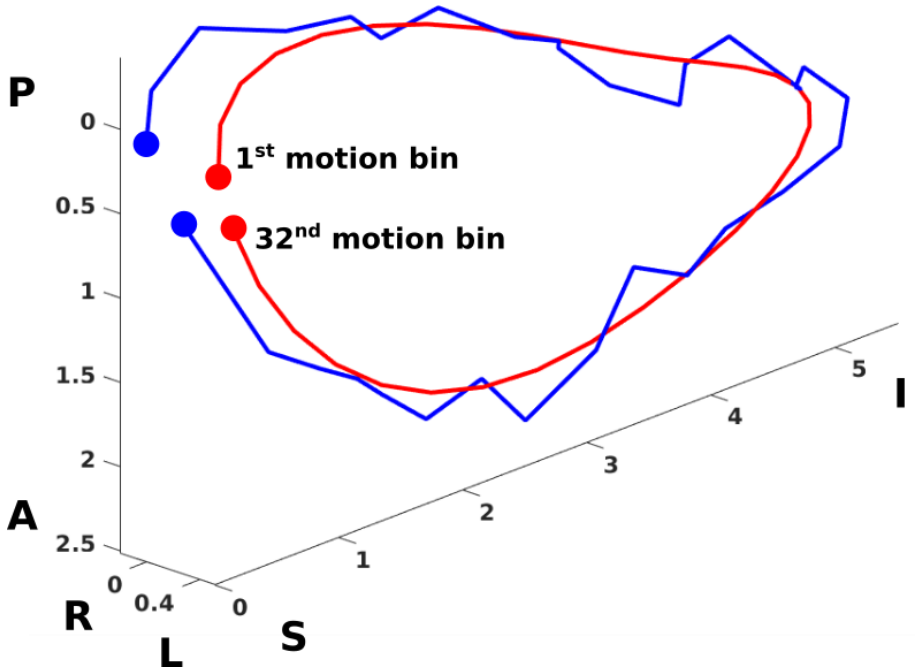

Figure 3.8: 3D representation of the trajectory followed by an elementary piece of lung parenchyma along the gated-average respiratory cycle. The trajectory returned by the registration process is represented in blue, whereas its filtered version is represented in red. The distances along Anterior-Posterior (AP), Left-Right (LR) and Superior-Inferior (SI) are expressed in voxel units.

We therefore extracted the time evolution of the 3D deformation field of the lung parenchyma, $\vec{r}$, at the voxel scale (1.5 mm), and at every gate throughout the breathing cycle. Moreover, time-stamps were given to each of the 32 motion gates and automatic lung segmentation was performed on the reference deflated lung image. It sets the grounds for 3D MR spirometry.

[309] "Smoothn - File Exchange - MATLAB Central," accessed October 24, 2018, https://www.mathworks.com/matlabcentral/fileexchange/25634.

[310] C. T. Metz et al., "Nonrigid Registration of Dynamic Medical Imaging Data Using ND+t B-Splines and a Groupwise Optimization Approach," *Medical Image Analysis* 15, no. 2 (April 1, 2011): 238–49, https://doi.org/10.1016/j.media.2010.10.003.

SECTION 3 QUALITATIVE AND QUANTITATIVE OBSERVATIONS ON THE FIRST EXPERIMENTAL RESULTS OF 3D MAGNETIC RESONANCE SPIROMETRY

IN THE PREVIOUS SECTION, WE HAVE DESCRIBED AN IMAGE ACQUISITION AND POST-PROCESSING PIPELINE TO EXTRACT THE MR-BASED DEFORMATION FIELDS OF THE LUNG PARENCHYMA THROUGHOUT THE RESPIRATORY CYCLE. WE ASSUMED A PSEUDO-PERIODIC RESPIRATORY MOTION, WHICH IS FAIR AS LONG AS INSPIRATORY AND EXPIRATORY MOTION PHASES WERE DIFFERENTIATED, AND DATA ACQUIRED DURING OUTLYING MOTION MANEUVERS WERE DISCARDED FOR THE FINAL IMAGE RECONSTRUCTION. IN THE FOLLOWING, WE WILL SEE WHAT TYPE OF ADVANCED PARAMETERS CAN BE EXTRACTED FROM THESE MOTION FIELDS. ADVANCED ASPECTS OF LUNG MECHANICAL BEHAVIOR WILL BE ASSESSED. QUANTITATIVE VENTILATION PARAMETERS AND REGIONAL FLOW-VOLUME LOOPS, SIMILAR TO THOSE OBTAINED IN STANDARD SPIROMETRY, WILL BE DETERMINED TRIDIMENTIONALLY INSIDE THE LUNG PARENCHYMA.

1. HYSTERETIC BEHAVIOR OF THE DEFORMATION FIELD INSIDE THE LUNG

1.1. VALIDATION CONDITIONS OF 3D MR SPIROMETRY

Three-dimensional Magnetic Resonance Spirometry was challenged on a healthy human volunteer (male, 26 years old). UTE acquisitions were performed during the same imaging session and the volunteer was asked to perform three different types of breathing patterns as he laid supine in the PET/MRI system:

- **A normal breathing pattern:** The volunteer was asked to breathe as spontaneously as possible.
- **A thoracic breathing pattern:** The volunteer was asked to breathe mostly with the intercostal muscles and without the diaphragm to perform the respiratory maneuvers.
- **A diaphragmatic breathing:** The volunteer was asked to breathe mostly with the diaphragm and without the intercostal muscles to perform the respiratory maneuvers.

The motion corrected images obtained at the end of inspiration and expiration are presented in **Figure 3.9**. The normal breathing pattern was performed after the two other ones, and the volunteer told us that he fell asleep during this third acquisition. This explains why the motion amplitude is lower in the images representing the normal breathing in comparison to thoracic and diaphragmatic breathing. From another point of view, it ensures us that this motion pattern was a genuine reflex breathing pattern, without any conscious control from the volunteer. Besides, it was difficult to obtain the same respiratory amplitude between thoracic and diaphragmatic breathings, and this will be observed in the next results.

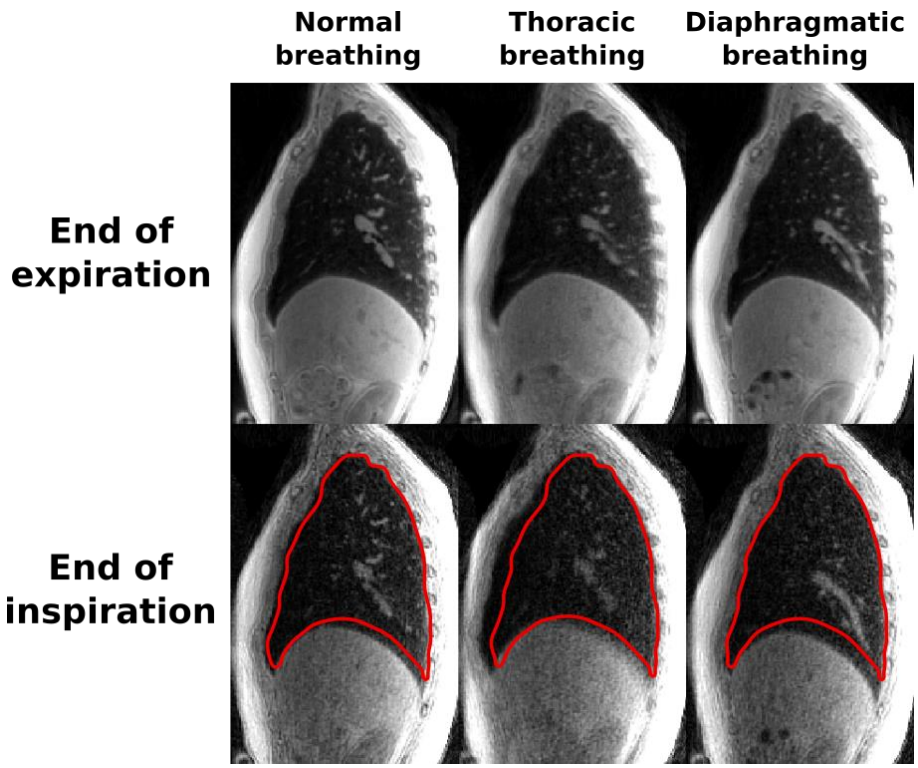

Figure 3.9: Sagittal views of the thoracic images retrospectively gated at the end of expiration (top) and at the end of inspiration (bottom) for the normal (left), thoracic (middle) and diaphragmatic (right) breathing patterns. On each end inspiratory image, the red curve depicts the border of the lung observed in the corresponding expiratory state shown above and exacerbates clearly the respective motions of the diaphragm and the thoracic wall for each breathing pattern.

1.2. THE CONCEPT OF MOTION HYSTERESIS

At the end of the previous section, we have plotted the trajectory followed by an elementary piece of lung parenchyma during an average respiratory cycle. From a mathematical modeling point of view, this trajectory is the path defined by the vector $\vec{r}(X, Y, Z, t)$, which represents the position of the elementary lung volume located at position $\vec{R} = \begin{bmatrix} X \\ Y \\ Z \end{bmatrix}$ at the end of expiration. This vector was measured for the different time-stamps t associated to the 32 gates chosen throughout the average respiratory cycle. We observe that the trajectory describes a closed loop with a different path for the inspiration and the expiration (see **Figure 3.8** at the end of the previous section). It means that the elementary volume of lung tissue under consideration does not follow the same trajectory during inspiratory and expiratory maneuvers. This type of behavior is usually referred to as hysteresis. When the total lung volume increases during inspiration, $\vec{r}$ defines a first path, whereas, when the total lung volume decreases during expiration, $\vec{r}$ defines a different path. We need to be careful because a lot of hysteretic phenomena can be observed in the lung, as we will see below. For that reason, it is important to name clearly each of them. The phenomenon described just above will be referred to as motion hysteresis.

1.3. ANALYSIS OF MOTION HYSTERESIS WITH 3D MR SPIROMETRY

Figure 3.10 shows a small selection of trajectories (1 out of 100) obtained in sagittal and coronal planes. As said above, we observe that these trajectories describe closed loops everywhere in the lung. We observe that these trajectories are nearly 2D trajectories included in the sagittal plane for the three types of breathing. However, the shape and the amount of motion hysteresis vary a lot throughout the lung and for the different types of breathing. In normal breathing, we observe practically no motion hysteresis. This might be explained by the low amplitude respiratory motion performed by the subject during the image acquisition process. For normal breathing, the trajectories show an elongated shape oriented diagonally in the sagittal plane, with a principal direction of motion both along the superior-inferior and the anterior-posterior directions. For the thoracic and diaphragmatic breathings, these trajectories are mainly oriented respectively along the anterior-posterior direction and along the superior-inferior direction, and the amount of motion hysteresis varies a lot throughout the organ.

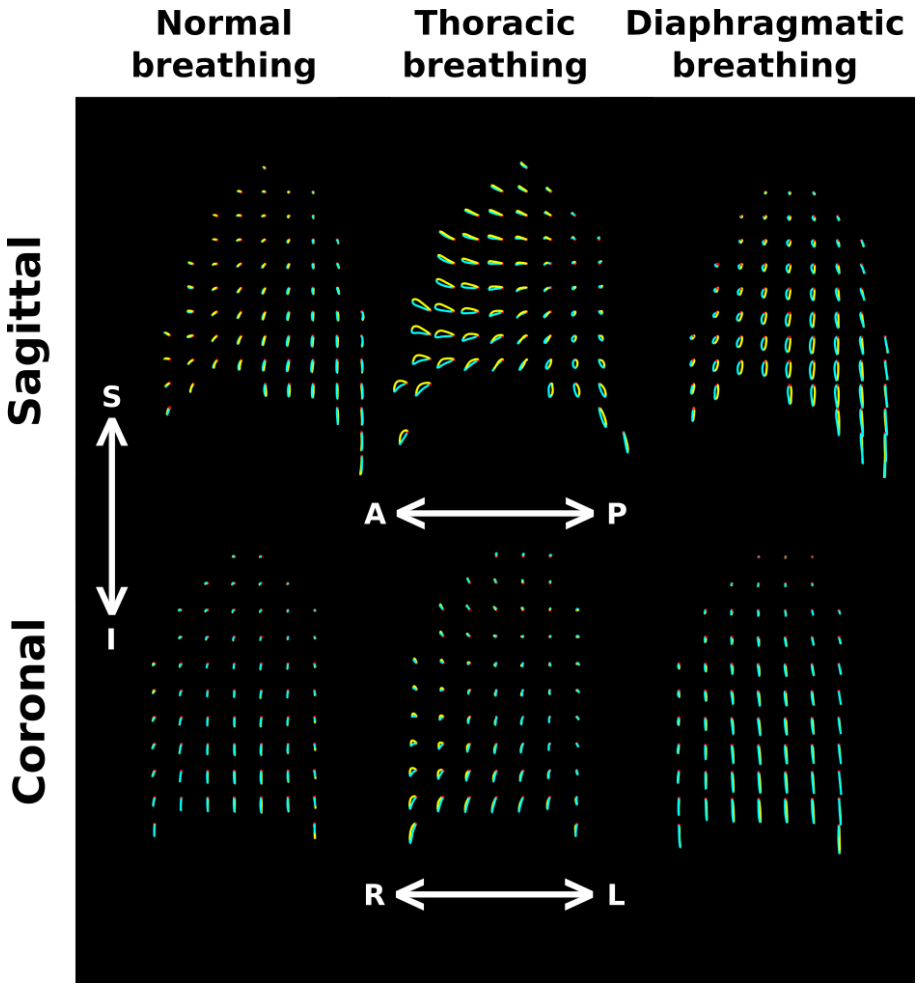

Figure 3.10: Sagittal (top) and coronal (bottom) views of the trajectories (1 out of 100) followed by elementary volumes of the right lung parenchyma located at red dots positions at the end of expiration. These trajectories are pictured for the normal (left), thoracic (middle) and diaphragmatic (right) breathing patterns. In each trajectory, the inspiration phase is represented in yellow and the expiration phase is represented in blue.

Globally, for the three types of breathing patterns, motion amplitude and hysteresis are larger in the inferior regions of the lung compared to the superior ones. In the case of thoracic breathing, they are larger in the anterior regions of the lung compared to the posterior ones. Finally, in the case of diaphragmatic breathing, we observe that the inspiratory parts of the trajectories are posterior to the expiratory parts everywhere in the lung. In the case of thoracic breathing, we observe a very different situation: the inspiratory parts are superior to the expiratory parts. Considering both the main direction and the orientation of the loops, it could also explain why a few amount of motion hysteresis is observed in the case of normal breathing: if this normal breathing is generated by the action of the diaphragm combined to the action of the intercostal muscles, the trajectories should logically be comprised between the two extreme cases just discussed. We therefore obtain trajectories oriented diagonally and showing a low amount of motion hysteresis in the case of normal breathing. This explanation may be too obvious and simple in regard to the complexity of the underlying phenomena, but it is a way to apprehend the results.

Lung motion hysteresis was observed in a large number of research studies, first by performing distance measurements between points localized at the surface of excised lungs[311], but also with 4D Computed Tomography (4D-CT)[312 313 314]. The quantification of the hysteretic motion of the lung is of particular importance for radiotherapy planning, as a lung tumor will not follow the same trajectory during inspiratory and expiratory phases[315 316]. In these studies, most of the trajectories present the same characteristics as the ones observed in our normal and diaphragmatic breathing patterns: the trajectory is elongated along the superior-inferior direction, is mainly comprised in the sagittal plane and the inspiratory trajectory is posterior to the expiratory trajectory. This similarity is encouraging as the measurements performed in the different 4D-CT research studies were usually performed with subjects in the supine position and freely-breathing, which is a breathing situation usually controlled by the action of the diaphragm rather than the thoracic cage. Our test with a thoracic breathing shows that totally different trajectories are followed in this case, with a main orientation along the anterior-posterior axis instead of the superior-inferior axis. To our knowledge, this is the first time such a comparison is made at the local motion scale between the different types of breathing patterns.

1.4. ADVANCED CHARACTERIZATION OF MOTION HYSTERESIS LOOPS

The motion hysteresis can be characterized with additional parameters that can be extracted from the followed trajectories. First, at each voxel position, the perimeter and the area of the trajectory can be computed. The calculation of the perimeter is straightforward as it is just the sum of the lengths of the different segments joining the 32 individual positions for each reference location. For the area, it is a little bit more difficult as the curve is quasi-planar but it is not fully included in a 2D plane. The solution we found was to define a center point for each

[311] B. A. Hills, "Geometric Irreversibility and Compliance Hysteresis in the Lung," *Respiration Physiology* 13, no. 1 (October 1, 1971): 50–61, https://doi.org/10.1016/0034-5687(71)90064-8.
[312] Vlad Boldea et al., "4D-CT Lung Motion Estimation with Deformable Registration: Quantification of Motion Nonlinearity and Hysteresis," *Medical Physics* 35, no. 3 (2008): 1008–18, https://doi.org/10.1118/1.2839103.
[313] Guanglei Xiong et al., "Tracking the Motion Trajectories of Junction Structures in 4D CT Images of the Lung," *Physics in Medicine and Biology* 57, no. 15 (July 2012): 4905–4930, https://doi.org/10.1088/0031-9155/57/15/4905.
[314] Benjamin White et al., "Distribution of Lung Tissue Hysteresis during Free Breathing," *Medical Physics* 40, no. 4 (2013): 043501, https://doi.org/10.1118/1.4794504.
[315] Yvette Seppenwoolde et al., "Precise and Real-Time Measurement of 3D Tumor Motion in Lung Due to Breathing and Heartbeat, Measured during Radiotherapy," *International Journal of Radiation Oncology*Biology*Physics* 53, no. 4 (July 15, 2002): 822–34, https://doi.org/10.1016/S0360-3016(02)02803-1.
[316] Shinichiro Mori et al., "Four-Dimensional Measurement of Lung Tumor Displacement Using 256-Multi-Slice CT-Scanner," *Lung Cancer* 56, no. 1 (April 1, 2007): 59–67, https://doi.org/10.1016/j.lungcan.2006.11.011.

trajectory (for example, the center of mass of the 32 points defining the trajectory) and to calculate the sum of the areas for the triangles defined by two trajectory points and this center point. From these two measurements, the perimeter P and the area A of the loop, it is possible to calculate a circularity metric C, defined as:

$$C = \frac{4\pi A}{P^2} \qquad \textbf{Eq. 3.1}$$

This circularity metric C takes values from 0 to 1 as a function of the shape of the trajectory of perimeter P and area A, with a value 0 for loops of null area and a value 1 for perfect circles. **Figure 3.11** represents the P, A and C maps for the three types of breathing. Once again, we observe very different results for the three types of breathing patterns. In normal breathing, the trajectories are more circular in the superior part of the lung. The same result is obtained in diaphragmatic breathing, but with larger C values and more importantly pronounced in the anterior part of the lung. Finally, for thoracic breathing, the circularity is increased in the posterior and inferior parts of the lung.

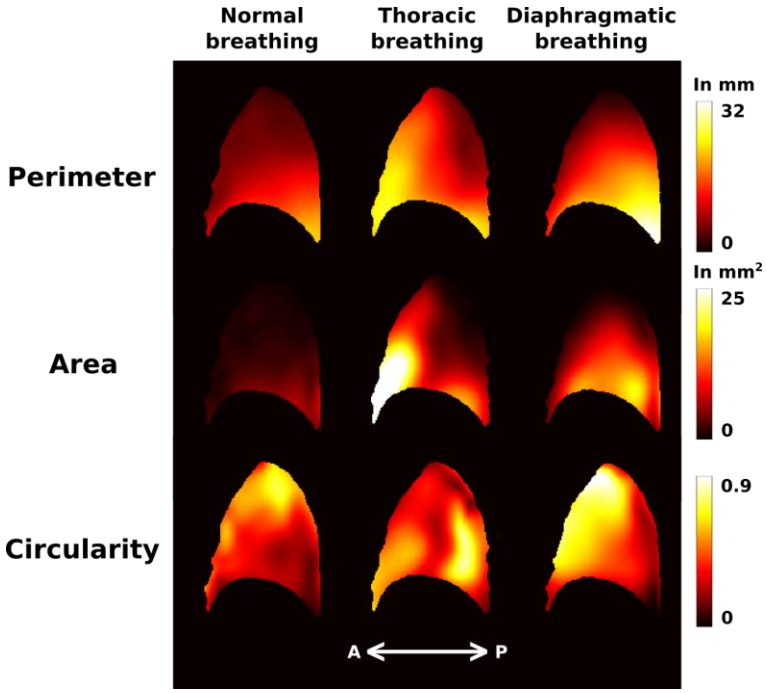

Figure 3.11: Sagittal views of local motion trajectory perimeter (top), area (middle) and circularity (bottom) for the three types of breathing patterns: normal breathing (left), thoracic breathing (middle) and diaphragmatic breathing (right).

These first results are quite impressive. They show a high sensitivity of the technique to the local motions of the lung parenchyma. They announce high potentials for the 3D MR Spirometry technique. However, those trajectories hide complex phenomena which are difficult to sort out. Indeed, they effectively describe the local motion of the lung parenchyma but they also contain bulk translation and rotation components in addition to the local strain components. Even if bulk translation and rotation components can be interesting, in particular in a context of motion tracking and correction in medical imaging or in radiotherapy planning, they are not very informative here about respiratory mechanics and are not directly significant in terms of lung function. In the following, we will see how to process those data to remove bulk translation and rotation components, and only keep tissue strain

components. Furthermore, we will see how to extract valuable physical quantities from these deformation components, always in the perspective of assessing lung function and mechanical behavior.

2. RELATIONSHIP BETWEEN LOCAL AND GLOBAL VENTILATIONS IN THE LUNG ALONG THE RESPIRATORY CYCLE

In this subsection, we will study the next step of our pipeline chart:

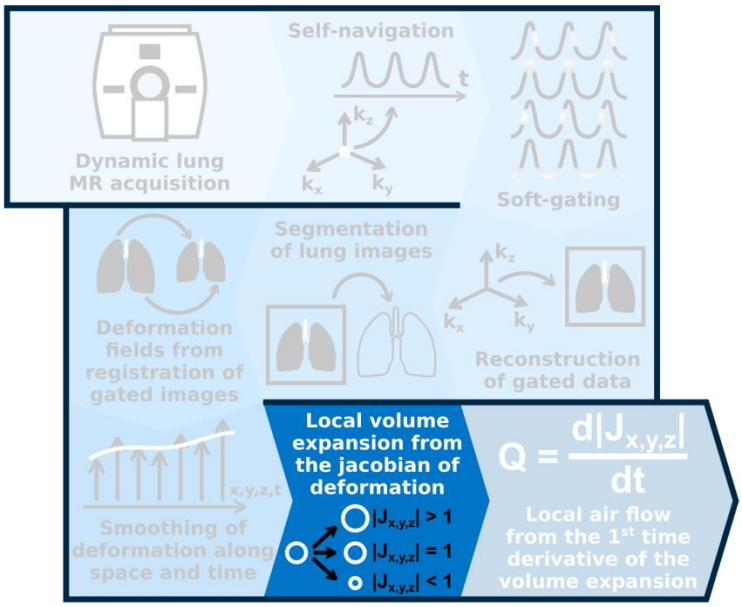

As said in the previous subsection, the deformation vector field $\vec{r}$ contains local tissue strain components, but also bulk motion components of the organ. In order to extract information of interest regarding lung mechanics, it will be necessary to separate those two types of motion components.

2.1. BULK TRANSLATION AND ROTATION COMPONENTS REMOVAL THROUGH THE CALCULATION OF THE JACOBIAN OF THE DEFORMATION FIELD

2.1.1. INTRODUCTION OF THE DEFORMATION GRADIENT TENSOR

We observe that a bulk translation is a motion component characterized by a spatially uniform motion field $\vec{u}$. It means that if we calculate the first spatial derivative of such a field, or the gradient of each of its spatial components, a null vector field should be obtained. In the general case, such a calculation on $\vec{r}$ would give a new field free of translation components, with only bulk rotation and local tissue strain components. However, $\vec{r}$ is a 3D vector field, thus equivalent to three scalar fields r_x, r_y and r_z, representing respectively the components of $\vec{r}$ along the orthogonal spatial directions x, y and z. Therefore, a full tridimensional spatial derivation of these three vector fields leads to nine scalar components that can be stored in a 3×3 tensor.

For that reason, we can define the deformation gradient tensor, written F, as following:

$$F = \frac{d\vec{r}}{d\vec{R}} = \begin{bmatrix} \frac{dr_x}{dR_x} & \frac{dr_x}{dR_y} & \frac{dr_x}{dR_z} \\ \frac{dr_y}{dR_x} & \frac{dr_y}{dR_y} & \frac{dr_y}{dR_z} \\ \frac{dr_z}{dR_x} & \frac{dr_z}{dR_y} & \frac{dr_z}{dR_z} \end{bmatrix} = I + \frac{d\vec{u}}{d\vec{R}} \quad \textbf{Eq. 3.2}$$

In the previous expression, I represents the identity tensor. For a pure translational motion, $F = I$ for any translational amplitude. Therefore, F is insensitive to bulk translations. However, it is still sensitive to bulk rotations. $\frac{d\vec{r}}{d\vec{R}}$ and $\frac{d\vec{u}}{d\vec{R}}$ should be seen here as simplified and compact ways to write tensors.

2.1.2. INTRODUCTION OF THE JACOBIAN OF THE DEFORMATION FIELD

It can be demonstrated that F can be written as:

$$F = RU \quad \textbf{Eq. 3.3}$$

where R is a rotation matrix and U is a symmetric matrix containing only strain components. In the next subsection, we will see how to properly calculate a matrix that only reflects those strain components. However, it is possible to calculate from F a parameter which only depends on strain and not on pure rotation. F is sometimes called Jacobian matrix of the deformation field, as this matrix reflects all the first partial derivatives of a multi variables and multi components function. Here, because we have three variables (X, Y and Z) and three components (along x, y and z directions), we have seen in **Eq. 3.2** that F is expressed as a 3×3 square matrix. A determinant can therefore be calculated for this matrix. This determinant, called Jacobian of the deformation field (or simply Jacobian in the following) and written J, verifies:

$$J = det(F) = det(RU) = det(R)det(U) = det(U) \quad \textbf{Eq. 3.4}$$

Thanks to the properties of the determinant and the definition of a rotation matrix, we observe that J only depends on deformation components.

2.1.3. INTERESTING PROPERTIES OF THE JACOBIAN FOR THE QUANTIFICATION OF LOCAL PULMONARY VENTILATION

It can be demonstrated that J represents the relative increase of volume of an infinitesimal sample of tissue centered at the location where F was calculated. If δV_0 represents this elementary volume in the reference state, before any deformation, and δV the elementary volume after deformation, it can be shown that:

$$J = \frac{\delta V}{\delta V_0} \quad \textbf{Eq. 3.5}$$

As seen in Chapter 1, the lung parenchyma is composed of a mixture of tissue and gas, with proportions that vary throughout the respiratory cycle. The cells composing the lung tissue are mainly composed of water, which can be considered as an incompressible material at scales and forces found in human physiology. It is therefore possible, for pure lung tissues (without gas), to change their shape but not change their volume. For that reason, any variation of J values in the lung parenchyma can only arise from changes in gas volume. Moreover, considering the forces and pressures found in human lung physiology, we can assume that the gas inside the organ is also incompressible. Furthermore, variations in temperature between the human body and its external environment are

usually too low to induce remarkable gas volume changes. For that reason, the volume of a sample of gas inside the lung will be directly proportional to the number of molecules that composes the sample, and any volume variation of a given sample of lung parenchyma will be directly proportional to the variation of the quantity of gas inside this sample.

Therefore, it leads to the following conclusion:

- If $J > 1$, a given quantity of gas has inflated locally the organ compared to the reference state (which was chosen when the lung was deflated at the end of expiration).
- If $J < 1$, a given quantity of gas has left the lung locally. The organ is therefore locally deflated compared to the reference state.
- If $J = 1$, the local quantity of gas is the same as the one observed in the reference state.

J is therefore an interesting quantity to estimate lung ventilation. It is calculated directly from F, which can be evaluated from the deformation field $\vec{r}$ everywhere in the lung thanks to finite differences methods at each voxel location. Moreover, $\vec{r}$ is estimated from image registration methods between the reference image and one of the 31 images corresponding to the different motion bins. For that reason, J estimates quantitatively local lung ventilation at each voxel location in the lung and for each of the 31 time-stamps chosen throughout the respiratory cycle. However, because deformation fields were estimated thanks to a B-splines model, which is characterized by a control grid, the spatial resolution of the J maps is closer to the grid size than the image voxel size. However, as we chose a grid size of 20 voxels, which corresponds to 30 mm, it leads to a quite fine spatial resolution for the ventilation measurements in comparison to the total size of a usual human lung, with around 105 B-splines control points throughout the organ.

One important remark is that J does not depend on local absolute gas content in the reference motion phase. As seen in the first chapter of this manuscript, at the end of expiration (reference motion phase), the lung still contains around 2 liters of gas, which are spread non-uniformly in the entire organ. Moreover, a forced expiratory maneuver can still be performed by the subject to blow its expiratory reserve volume. Even at the end of such a forced expiratory maneuver, around half a liter of gas is kept in the lung, corresponding to the residual volume of the subject. J is therefore only sensitive to the local relative variation of gas quantity in comparison with the reference state. This consideration is important because it means that regional gas volume variations measured with J should be considered as relative volume expansions of pre-inflated lung tissues. The extracted volume will never reflect the absolute gas volume locally present in the lung tissue.

This is not such a problem because we want to estimate ventilation, which is primarily characterized by a gas circulation process in the alveoli (to bring dioxygen and evacuate carbon dioxide). Therefore, this process only depends on gas volume variations within each respiratory cycle, and not on the absolute quantities of gas present in the organ. In other words, and in an extreme situation, an inflated region of the lung with no regional volume change (and therefore no circulation of gas, as in gas trapping phenomena for example) is useless in term of lung function because no gas exchange is possible in this region. For that reason, J reflects particularly well regional lung ventilation.

2.2. STUDY OF REGIONAL VENTILATION WITH 3D MR SPIROMETRY

2.2.1. EVOLUTION OF REGIONAL VOLUME EXPANSIONS ALONG THE BREATHING CYCLE

Figure 3.12 shows the J maps obtained for the three types of breathing patterns at eight different phases of the respiratory cycle. We observe that the estimated values of J globally vary a lot between breathing patterns because of the difference in breathing amplitudes discussed in 1.1. However, for each breathing pattern and everywhere in the lung, we observe that J values increase monotonically during the inspiration phase and decrease monotonically during expiration, which is what is expected. Moreover, for each breathing pattern and for each time-stamp, we observe that J is not uniformly distributed within the organ. In all breathing types, we observe J values higher in the inferior regions of the lung compared to superior regions. Moreover, they reach large values in the posterior region of the lung, which is expected as it corresponds to the gravity dependent region for a subject laid supine. As discussed earlier, the dependent regions are known to ventilate better in the field of lung physiology. Furthermore, we observe a slight ventilation increase in the anterior region of the lung for thoracic breathing in comparison to normal and diaphragmatic breathing. We will study further the ventilation distribution along the anterior-posterior axis of the lung later in this manuscript. A clear difference between the different types of breathing is difficult to appreciate at this point, in particular because only one subject was studied and because the global lung volumes are not the same at the end of inspiration for the different types of breathing.

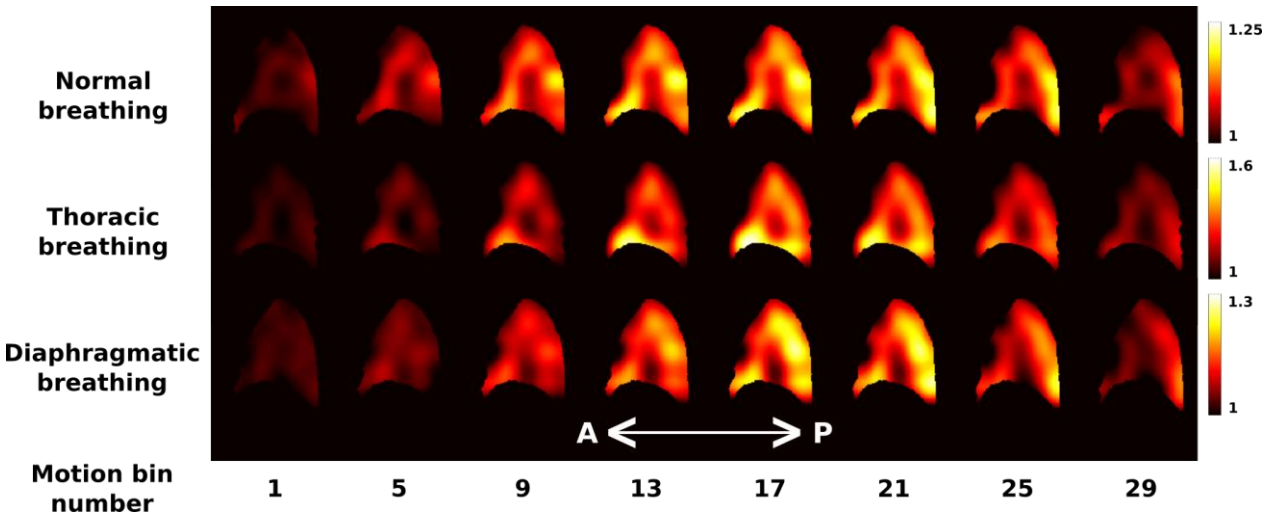

Figure 3.12: Representation of 8 out of 32 sagittal views (1 out of 4) showing the evolution of the J map throughout the gated-average respiratory cycle for the normal (top), thoracic (middle) and diaphragmatic (bottom) breathing patterns.

2.2.2. CALCULATION OF GLOBAL VOLUME EXPANSIONS FROM LOCAL VOLUME EXPANSIONS

To discuss further the local J values, the total lung volume expansions at each phase of the respiratory cycle must be calculated for comparison purposes. This could be obtained by performing 3D lung segmentation for each of the 32 images, count the voxels in each mask and calculate ratios between these numbers of voxels in any image and in the reference image. In this case, the quantity, J_T, similar to J, would be obtained for the entire lung. However, this method would be very long to perform, as 32 individual image segmentations would be needed, with several minutes of computation for each segmentation procedure with our algorithm. Of course, a more time efficient method could be investigated, as with a better implementation of the segmentation algorithm or with an efficient

groupwise segmentation of the 32 lung volumes together. Nevertheless, a far easier method exists. Because J is the map of volume expansions represented in the reference frame, J_T can be calculated by computing the mean of the J values inside the reference lung mask. In this case, only the reference image must be performed. This segmentation returns three masks: the lung parenchyma, the vascular tree and the large airways. To calculate J_T, we decided to choose the mask corresponding to the union of the lung parenchyma and the vasculature, without taking into account the large airways. Indeed, the large airways correspond to anatomical dead spaces occupying a large volume (in particular the trachea and the primary bronchi) and which therefore should not be taken into account in ventilation calculations. However, we chose to take into account the vasculature mask because it is spread everywhere in the organ and represents objects with sizes largely below the size of the B-splines grid. If M_{P+V} represents the set of voxels either corresponding to lung parenchyma or vasculature in the reference image, and if (X, Y, Z) represents the spatial coordinates of voxels in this reference frame, J_T can be calculated from J at each time-stamp t through:

$$J_T(t) = \frac{1}{|M_{P+V}|} \sum_{\substack{(X,Y,Z) \\ \subset M_{P+V}}} J(X, Y, Z, t) \qquad \textbf{Eq. 3.6}$$

where $|\cdot|$ represents the cardinal operator, which counts the number of pixels of value 1 in a binary mask. During the development of 3D Magnetic Resonance Spirometry, we verified that the total volume expansions found with this method were in accordance with the volumes measured directly with lung segmentation. Along the respiratory cycle, we found a mean deviation around 2% between the total volume expansions estimated from segmentation and those estimated from the integration of J.

2.2.3. THE 1966 MILIC-EMILI'S EXPERIMENT AND THE 'ONION SKIN DIAGRAM'

A famous study carried out by Milic-Emili *et al.* in 1966[317] consisted in asking to seated healthy human volunteers to breathe a mixture of room air and gamma-emitting radioactive ^{133}Xe and to make breath-holds at specific lung volumes. Twelve scintillation counters were positioned along the superior-inferior axis of the volunteer to measure for each breath-hold the quantity of gamma rays emitted by ^{133}Xe from the different regions in the lung. The breath-hold steps were spread from the residual capacity to the total lung capacity, and total lung volumes were measured with a spirometer at the same time as the measurements of regional volumes. These regional volumes were supposed to be proportional to the concentration of xenon, which was estimated by its gamma emission measured by each scintillation counter and converted into a concentration of gas along a normalization procedure. It was therefore possible to plot the evolution of the regional lung volumes, measured by each scintillation detector, as a function of the global lung volume, measured by the spirometer. Several important conclusions were made from this study:

- The absolute regional volume of gas is always larger in the superior regions of the lung than in the inferior ones.
- The slope of the curve is lower for the superior regions of the lung compared to the inferior regions of the lung.
- A concavity is observed in the curves for superior regions, while a convexity is observed for inferior regions.

[317] J. Milic-Emili et al., "Regional Distribution of Inspired Gas in the Lung," *Journal of Applied Physiology* 21, no. 3 (May 1966): 749–759, https://doi.org/10.1152/jappl.1966.21.3.749.

These results were summarized in a diagram usually referred to as the 'Onion skin diagram' because of its shape (see **Figure 3.13**). However, these measurements were only made during breath-holds performed after the inhalation of gas. These measurements were not performed in dynamic mode with a separation between inspiratory and expiratory phases.

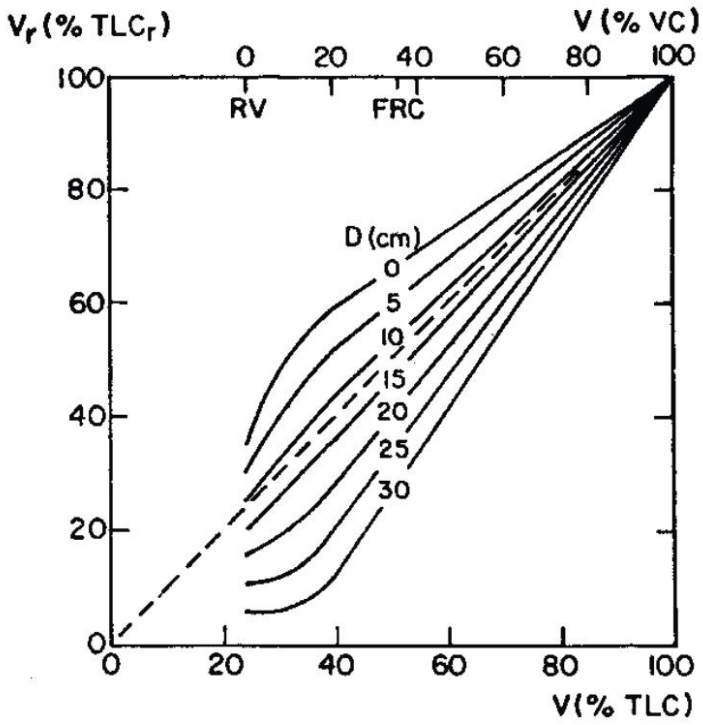

Figure 3.13: The 'Onion skin diagram' as measured experimentally and published by Milic-Emili *et al.* in 1966. In this diagram, V_r represents the normalized regional volume, whereas V represents the normalized global volume of the lung. The quantity D represents the distance along the superior-inferior axis and from the apex of the lung where the normalized regional volume was measured. Note that the measurement was performed on the full range of total lung volume, from the Residual Volume (RV) to the Total Lung Capacity (TLC).

2.2.4. COMPARISON BETWEEN LOCAL AND GLOBAL LUNG VOLUME EXPANSIONS ALONG THE RESPIRATORY CYCLE

We reproduced the Milic-Emili's experiment in dynamic mode with 3D MR Spirometry technique because, as we have seen, we can measure the regional lung volume expansion (J) and compare it to the total lung volume expansion (J_T) for the entire respiratory cycle. Moreover, instead of plotting the curve $J = f(J_T)$ in a voxelwise manner, we can degrade the resolution, simulate the presence of scintillation counters and calculate an average curve for different slabs of lung tissue along the superior-inferior axis. To do so, we separated the lung volume into five slabs of equal width along the superior-inferior axis and represented, for each slab, the mean J value as a function of J_T. We performed this for the three types of respiratory patterns presented in 1.1. These curves are represented in **Figure 3.14**.

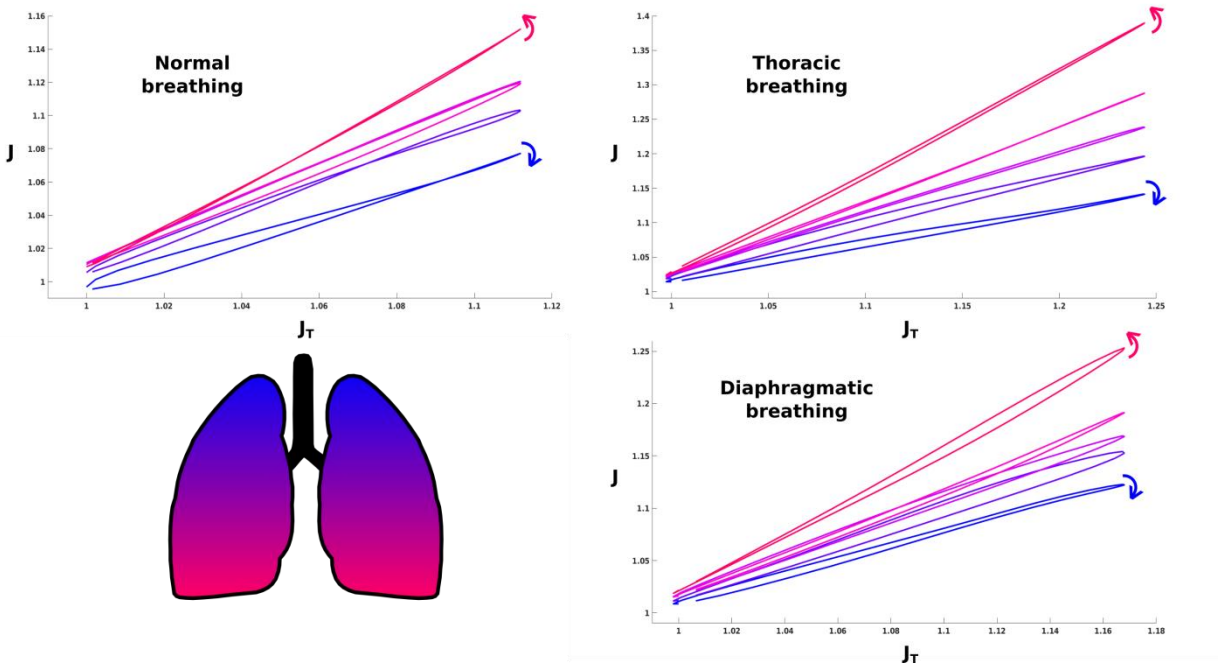

Figure 3.14: Representation of $J = f(J_T)$ in different regions along the superior-inferior axis of the lung for normal, thoracic and diaphragmatic breathing patterns. The color-scale in the bottom right hand corner represents which region of the lung is represented by each curve, and the arrows represent the way the curves are followed with time.

In the curves represented in **Figure 3.14**, we cannot observe the first result presented by Milic-Emili *et al.* (higher regional volumes in superior regions of the lung) because, as explained in 2.1.3, we do not have access to the absolute volume of gas present inside the lung. We can only measure the volume expansion from the reference lung state. For that reason, all the curves have the same origin, which is $J = J_T = 1$ for the point corresponding to the end of expiration. However, the second result is clearly observed (higher $J = f(J_T)$ slope for inferior regions of the lung), even if the curves are vertically shifted compared to the 1966 experiment because of the previous remark. We also slightly observe something similar to the third result (concavity of the curves in superior regions and convexity in inferior regions). These slight effects can be seen more clearly in the cases of thoracic and diaphragmatic breathing patterns, certainly because the amplitudes of breathing were higher in those two cases. However, the observation of this third result should be more robustly validated. The observation of this concavity or convexity was not evident as the subject was laid supine (whereas he was seated in the 1966 experiment) and the breathing volumes between inspiration and expiration were close to the tidal volume (whereas it ranges from the residual volume to the total lung capacity in the 1966 experiment). To visualize our results in the 'Onion skin diagram', our curves are approximatively comprised between 45 and 55 percent of TLC concerning the total lung volume. Within this range of values, the curves are nearly linear in the 'Onion skin diagram'. Further experiments should be carried out to verify this result with 3D MR Spirometry.

A different additional result appears in the curves of **Figure 3.14**: the hysteresis of J as a function of J_T. This result is not accessible in the experiment of Milic-Emili *et al.* because, as explained 2.2.3, the measurements were done during breath-holds, and not in dynamic mode with separation of inspiratory and expiratory phases. This hysteresis phenomenon differs from the one observed for local motion trajectories (see **Figure 3.10**). This new hysteresis phenomenon will be referred to as ventilation hysteresis in the following. This hysteresis is particularly clear for

thoracic and diaphragmatic motions, certainly because of their larger breathing amplitudes. We observe that $J = f(J_T)$ curves appear as open loops, which are drawn clockwise in superior regions and counterclockwise in the inferior regions. It means that, for any total lung volume, regional ventilation is higher during inspiration than during expiration in superior regions, whereas regional ventilation is lower during inspiration than during expiration in inferior regions of the lung.

Two years later, in 1968, Milic-Emili's research team conducted the same type of experiment (same technique, same conditions) to compare inspiratory and expiratory phases[318] in the 'Onion skin diagram'. However, their results were not conclusive as they found the same $J = f(J_T)$ curve for inspiratory and expiratory maneuvers. At the end of the article, they explain that two phenomena are in competition in their experiment:

- They explain that lung compliance, which is the ability of the lung to change its volume when the air pressure is increased, has major effects on the uniformity of lung ventilation: when the compliance of the lung increases, the uniformity of volume expansion in the lung decreases. However, it is known that lung compliance is lower during inspiration than during expiration, leading to a hysteresis phenomenon in the pressure-volume curve of the lung (which is another hysteresis phenomenon). This pressure-volume curve is the evolution of the total lung volume as a function of the transpulmonary pressure, and has been largely studied to characterize the mechanical hysteretic properties of the lung[319]. This hysteretic phenomenon has been explained by the presence of pulmonary surfactant in the alveoli[320]. This pulmonary surfactant exhibits hysteretic surface tension properties when the surface of lung alveoli increases and decreases[321]: surface tension is lower during expiration than during inspiration, which avoids alveolar collapsus at the end of expiration[322]. However, the link between the two types of hysteresis is not straightforward[323] and hysteresis in the pressure-volume curve can be explained by other factors[324]. As this leads to a lower compliance of the lung during inspiration, regional volume expansion should be more uniform than during expiration, which would lead to higher regional volume expansions in superior regions and lower expansions in inferior regions during inspiration in comparison to expiration.

- Because of gravity, alveoli are more expanded in apical region than in basal regions. In this case, the basal region is called the dependent region, as seen in Chapter 1, and ventilates better[325]. The article explains

[318] P W Sutherland, T Katsura, and J Milic-Emili, "Previous Volume History of the Lung and Regional Distribution of Gas.," *Journal of Applied Physiology* 25, no. 5 (November 1, 1968): 566–74, https://doi.org/10.1152/jappl.1968.25.5.566.

[319] Eduardo Salazar and John H. Knowles, "An Analysis of Pressure-Volume Characteristics of the Lungs," *Journal of Applied Physiology* 19, no. 1 (January 1, 1964): 97–104, https://doi.org/10.1152/jappl.1964.19.1.97.

[320] J. Mead, J. L. Whittenberger, and E. P. Radford, "Surface Tension as a Factor in Pulmonary Volume-Pressure Hysteresis," *Journal of Applied Physiology* 10, no. 2 (March 1957): 191–196, https://doi.org/10.1152/jappl.1957.10.2.191.

[321] John A. Clements, "Surface Tension of Lung Extracts," *Proceedings of the Society for Experimental Biology and Medicine* 95, no. 1 (May 1, 1957): 170–72, https://doi.org/10.3181/00379727-95-23156.

[322] R. J. King, "Pulmonary Surfactant," *Journal of Applied Physiology* 53, no. 1 (July 1, 1982): 1–8, https://doi.org/10.1152/jappl.1982.53.1.1.

[323] "(191p) Lung Hysteresis: Its Origins and the Role of Pulmonary Surfactant | AIChE Academy," accessed March 7, 2019, https://www.aiche.org/conferences/aiche-annual-meeting/2011/proceeding/paper/191p-lung-hysteresis-its-origins-and-role-pulmonary-surfactant.

[324] J. D. Escolar and A. Escolar, "Lung Hysteresis: A Morphological View.," *Histology and Histopathology* 19, no. 1 (January 2004): 159–66, https://doi.org/10.14670/HH-19.159.

[325] A C Bryan, J Milic-Emili, and D Pengelly, "Effect of Gravity on the Distribution of Pulmonary Ventilation.," *Journal of Applied Physiology* 21, no. 3 (May 1, 1966): 778–84, https://doi.org/10.1152/jappl.1966.21.3.778.

that it constitutes a counter effect to the first one, and it would explain why they haven't seen any difference between regional ventilations during inspiration and expiration.

In our experiment, the situation is very different because the subject is lying supine, and therefore gravity does not act along the superior-inferior axis but along the anterior-posterior axis. In this case, and if the explanation given above holds, we would only observe the first effect but not the second one. This would explain why we observe higher ventilation during inspiration than during expiration in apical regions and lower ventilation during inspiration than during expiration in basal regions. Once again, this hypothesis should be verified for a population and in other experimental conditions to be fully validated. However, the same type of ventilation hysteresis was observed in more recent studies based on 4D-CT[326], which supports our results, but the spatial dependence of the hysteresis has not been studied yet.

Ventilation hysteresis may have strong links with lung compliance, but also with the presence and properties of lung surfactant, which are at the heart of lung mechanics and lung function. A deeper exploration and exploitation of this ventilation hysteresis phenomenon observed on $J = f(J_T)$ curves might lead, for example, to the quantitative measurement of valuable parameters that may describe lung compliance and/or pulmonary surfactant effects on regional lung ventilation. We can therefore envision the measurement of the same parameters as the ones resulting from the standard pressure-volume curves but without any invasive pressure measurement and with a spatial sensitivity that is not reached in gold standard techniques. Once again, further studies, modeling and experiments are needed to verify these hypotheses.

3. ANISOTROPIC DEFORMATION OF THE LUNG PARENCHYMA

In the previous subsection, we calculated J, the local Jacobian of the deformation field. We explained that this metric was taking values equal to the relative volume expansion of an elementary piece of lung tissue with respect to a reference inflation state. We also demonstrated why J was an interesting metric of local lung ventilation, and we showed that its evolution as a function of the total lung volume expansion, J_T, could lead to rich information in terms of lung function. However, J is an isotropic measurement, in the sense that it reflects how the tissue inflates locally, but not how its shape changes. In particular, we do not know with J from which directions of tissue deformation the volume increases or decreases. To obtain such information, we need to compute more developed metrics.

3.1. ASSESSMENT OF THE GREEN-LAGRANGE STRAIN TENSOR WITH 3D MR SPIROMETRY

3.1.1. INTRODUCTION OF THE GREEN-LAGRANGE STRAIN TENSOR

In **Eq. 3.2**, we introduced F, a 3×3 tensor representing the deformation gradient, and which could be written $\frac{d\vec{r}}{d\vec{R}}$ in a simplified and compact format. We have seen that this tensor was free of bulk translational information, but contained information on both bulk rotation and local strain. It is even possible to write it as the product of a rotation matrix and a symmetric matrix containing only pure local strain components (see **Eq. 3.3**).

[326] Shinjiro Miyawaki et al., "A 4DCT Imaging-Based Breathing Lung Model with Relative Hysteresis," *Journal of Computational Physics* 326 (December 1, 2016): 76–90, https://doi.org/10.1016/j.jcp.2016.08.039.

To analyze in more details how the tissue locally deforms and see if there are preferential orientations in this local deformation, it is first necessary to remove the rotation components to keep only the strain ones. It can be easily done by calculating $F^T F$:

$$F^T F = (RU)^T RU = U^T R^T RU = U^T U \quad \textbf{Eq. 3.7}$$

Rotation components are therefore removed as the transpose of a rotation matrix, R^T, is equal to its inverse, R^{-1}. From this expression and the knowledge of F, several definitions of pure strain tensors can be given and calculated. In the following, we will use the definition of the Green-Lagrange strain tensor, written ε^G:

$$\varepsilon^G = \frac{1}{2}(F^T F - I) \quad \textbf{Eq. 3.8}$$

By using the Einstein summation convention, its expression as a function of the displacement components gives:

$$\varepsilon_{ij}^G = \frac{1}{2}\left(\frac{\partial u_i}{\partial R_j} + \frac{\partial u_j}{\partial R_i} + \frac{\partial u_k}{\partial R_j}\frac{\partial u_k}{\partial R_j}\right) \quad \textbf{Eq. 3.9}$$

As a reminder, in the previous expression, $R_x = X$, $R_y = Y$ and $R_z = Z$. In this tensor, the diagonal terms (ε_{ii}^G) represent strain components characterized by deformation gradients oriented in the same direction as the deformation itself, which results in what we would call 'contraction/compression' or 'expansion/stretching'. However, the non-diagonal terms (ε_{ij}^G, with $i \neq j$) represent strain components characterized by deformation gradients oriented orthogonally to the deformation itself, which results in what we would call 'shear deformation'. The relationship between such tensor terms, compression and shear will be largely discussed in the next chapter where we will see that the rigorous definitions of compression and shear are more complicated. Moreover, as we can see in the previous expression, ε^G is symmetric, which means that $\varepsilon_{ij}^G = \varepsilon_{ji}^G$. For that reason, 6 different strain maps (ε_{xx}^G, ε_{yy}^G, ε_{zz}^G, ε_{xy}^G, ε_{yz}^G and ε_{xz}^G) can be calculated at any phase of the respiratory cycle. These maps are represented in **Figure 3.15** for the inflation state obtained at the end of inspiration and for the three breathing patterns.

3.1.2. RELATIONSHIP BETWEEN THE GREEN-LAGRANGE STRAIN TENSOR AND THE JACOBIAN OF THE DEFORMATION FIELD

From **Eq. 3.4**, it can be shown that J can be well approximated for small strains by the following formula:

$$J \approx 1 + \varepsilon_{xx}^G + \varepsilon_{yy}^G + \varepsilon_{zz}^G \quad \textbf{Eq. 3.10}$$

It means that ε_{xx}^G, ε_{yy}^G and ε_{zz}^G represent the strain contributions to the regional increase in lung volume along directions x, y and z (chosen here to be respectively superior-inferior, left-right and anterior-posterior directions). Thanks to ε_{xx}^G, ε_{yy}^G and ε_{zz}^G maps, it is therefore possible to estimate the ventilation anisotropy within the lung. Moreover, the maps ε_{xy}^G, ε_{yz}^G and ε_{xz}^G poorly contribute to regional ventilation but reflect how the lung is locally affected by shear-like deformation.

3.1.3. COMPARISON OF THE GREEN-LAGRANGE STRAIN TENSOR ELEMENTS FOR THE THREE TYPES OF BREATHING PATTERNS

In **Figure 3.15**, we observe that the maps obtained for the diagonal terms (ε_{xx}^G, ε_{yy}^G and ε_{zz}^G) are very interesting because the strains along superior-inferior, left-right and anterior-posterior directions are not contributing to the same extent to the local lung ventilation. We can therefore say that ventilation is anisotropic in the lung. Moreover,

we observe that these contributions of strain along the three main directions of space are not the same for our three types of breathing patterns. For normal breathing, we observe that the strain components contributing to ventilation are made essentially along superior-inferior and anterior-posterior axes. However, for thoracic breathing, the contribution is essentially along the anterior-posterior axis, whereas it is along the superior-inferior axis for diaphragmatic motion. For the three types of breathing, the strain contribution along the left-right direction is always lower.

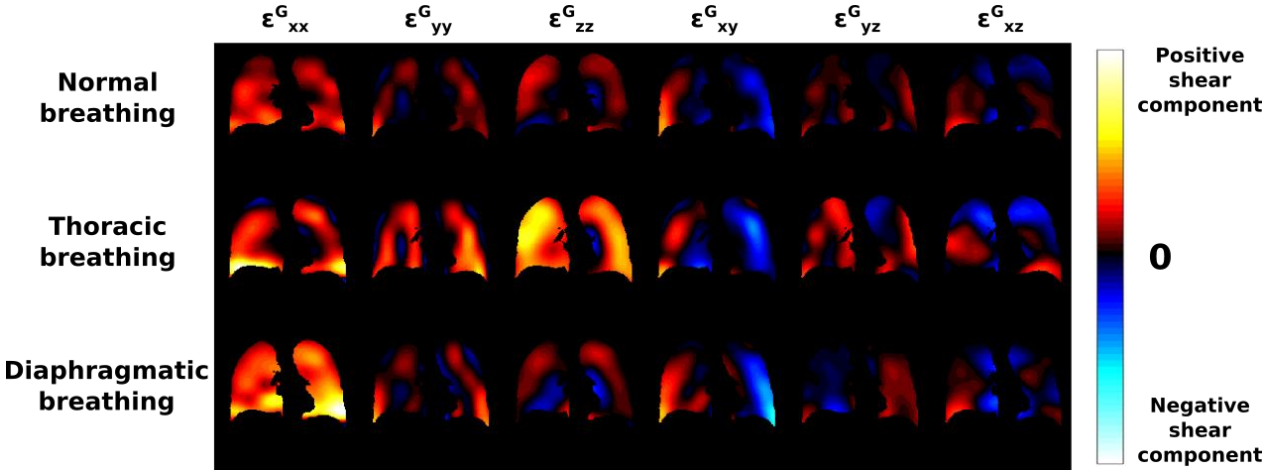

Figure 3.15: Coronal views of the different components of the Green-Lagrange strain tensor for normal, thoracic and diaphragmatic breathing patterns.

Concerning the non-diagonal components of the Green-Lagrange strain tensor (ε^G_{xy}, ε^G_{yz} and ε^G_{xz}), the comparison between the three respiratory patterns is less obvious, but they probably contain interesting information in terms of regional lung mechanics. Indeed, it has been demonstrated that extreme mechanical conditions that would be reached during breathing, in particular if the patient is subject to mechanical ventilation, can damage lung tissue and cause deformation- or ventilator-induced lung injuries[327] [328]. The precise and accurate quantification of the characteristics of such extreme deformations (amplitude, anisotropy, deformation rate, …) might be useful to diagnose and localize this type of injuries.

3.2. ASSESSMENT OF VENTILATION ANISOTROPY WITH 3D MR SPIROMETRY

3.2.1. DIAGONALIZATION OF THE GREEN-LAGRANGE STRAIN TENSOR

As observed in **Figure 3.15**, regional lung ventilation is anisotropic in the sense that the strain components that cause ventilation are not the same in the different directions of space and depend on the lung anatomy and on the breathing pattern. However, to study more quantitatively ventilation anisotropy, the expression of the Green-Lagrange strain tensor in the reference frame of the MR image is not the best one (with x, y and z corresponding to global anatomical orientations). To really appreciate the anisotropic deformation and make the difference

[327] Didier Dreyfuss and Georges Saumon, "Ventilator-Induced Lung Injury," *American Journal of Respiratory and Critical Care Medicine* 157, no. 1 (January 1, 1998): 294–323, https://doi.org/10.1164/ajrccm.157.1.9604014.
[328] Daniel J. Tschumperlin, Jane Oswari, and And Susan S. Margulies, "Deformation-Induced Injury of Alveolar Epithelial Cells," *American Journal of Respiratory and Critical Care Medicine* 162, no. 2 (August 1, 2000): 357–62, https://doi.org/10.1164/ajrccm.162.2.9807003.

between 'contraction/expansion' and pure 'shear' terms in the strain tensor, it would be more convenient to adapt the basis locally to the actual regional tissue deformation. As being a linear combination of real and symmetric matrices, the Green-Lagrange strain tensor is real and symmetric too. According to the spectral theorem, an orthonormal basis exists in which the Green-Lagrange strain tensor is a diagonal matrix. It means that, in this new basis, the local deformation can be interpreted only as deformation gradient components oriented along the direction of the deformation components themselves. If we consider an elementary sphere of material before deformation, it will be transformed into an ellipsoid having its main axes oriented along these new orthogonal basis directions, with some of its main radii that has increased in size (which could be seen as an 'oriented expansion') and/or others that has decreased (which could be seen as an 'oriented contraction'). However, as it will be explained in the next chapter, the deformation will usually be composed of a mixture of compression and shear in the continuum mechanics sense.

Regionally, after calculating the basis in which the local Green-Lagrange strain tensor is diagonal, we obtain:

$$\varepsilon^G = \begin{bmatrix} \varepsilon_I^G & 0 & 0 \\ 0 & \varepsilon_{II}^G & 0 \\ 0 & 0 & \varepsilon_{III}^G \end{bmatrix} \qquad \textbf{Eq. 3.11}$$

In the previous expression, ε_I^G, ε_{II}^G and ε_{III}^G are the main strain values, or eigenvalues of the Green-Lagrange strain tensor, and the new basis is chosen such that $\varepsilon_I^G > \varepsilon_{II}^G > \varepsilon_{III}^G$. Note that the diagonalization process needs to be performed for each voxel location as the main directions of deformation may differ throughout the organ. This process can be performed straightforwardly and rapidly with Matlab. At the end of the procedure repeated for each voxel location in the organ, all the information presented in **Figure 3.15** through six maps (ε_{xx}^G, ε_{yy}^G, ε_{zz}^G, ε_{xy}^G, ε_{yz}^G and ε_{xz}^G) is now 'compressed' into three maps only (ε_I^G, ε_{II}^G and ε_{III}^G), which has the advantage to simplify the visualization of the results but has the inconvenient to make them less directly related to usual anatomical axes. To understand along which axes the principal deformations are made, one has to refer to the local eigenvectors.

3.2.2. COMPARISON OF THE GREEN-LAGRANGE STRAIN EIGENVALUE MAPS

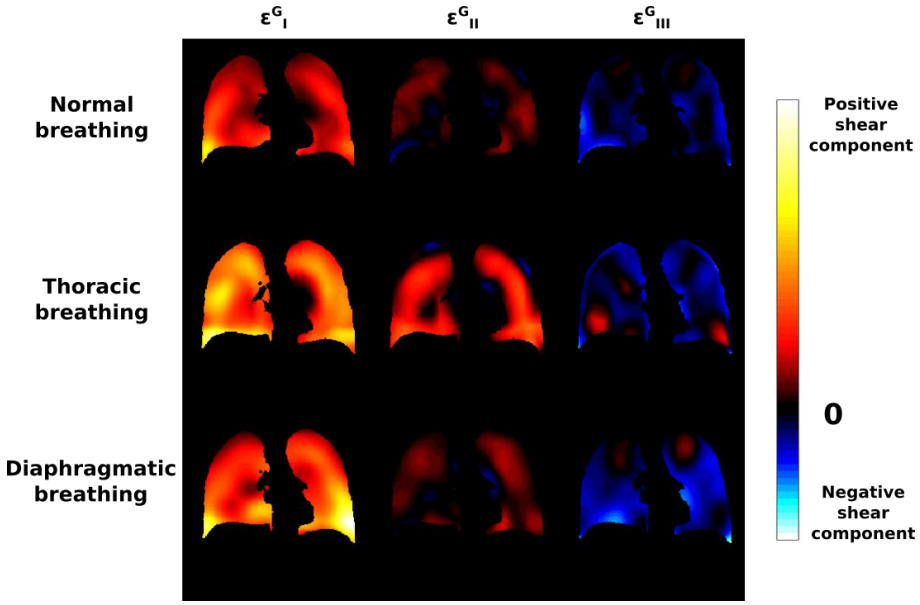

Figure 3.16: Coronal views of the three principal strain components for normal, thoracic, and diaphragmatic breathing patterns.

The maps representing ε_I^G, ε_{II}^G and ε_{III}^G for the three breathing patterns and calculated at the end of inspiration are shown in **Figure 3.16**. We observe once again that the local lung deformation is anisotropic because, at each given location, ε_I^G, ε_{II}^G and ε_{III}^G show very different values. More precisely, we observe that tissue locally expands along two principal directions and contracts along the third one almost everywhere in the organ. For thoracic breathing, the secondary expansion is more strongly pronounced than for normal and diaphragmatic breathings.

3.2.3. INTRODUCTION OF METRICS FOR THE CHARACTERIZATION OF LOCAL LUNG VENTILATION ANISOTROPY

The idea of using such quantities defined along three orthogonal directions (ε_I^G, ε_{II}^G and ε_{III}^G, or ε_{xx}^G, ε_{yy}^G and ε_{zz}^G) instead of one (J for example) was already proposed many years ago to study the anisotropic behavior of the lung[329]. However, to study more quantitatively ventilation anisotropy, and in particular the level and the type of this anisotropy at the local scale, it is possible to calculate metrics that gather at each voxel location the values of ε_I^G, ε_{II}^G and ε_{III}^G into one real number that 'answers' quantitatively to one given question.

The question can be: What is the 'amount' of local ventilation anisotropy? To answer this question, let us first take the example of the elementary sphere of material introduced in 3.2.1. As explained above, this elementary sphere takes the shape of an ellipsoid oriented along the three eigenvectors found by diagonalizing the Green-Lagrange strain tensor. It can be shown that the ratio between one main radius of the ellipsoid after and before deformation is given by $\lambda_i = \sqrt{1 + 2\varepsilon_i^G}$, with $i = I, II, III$. It can be shown that λ_I, λ_{II} and λ_{III} are actually the square-rooted eigenvalues of $F^T F$. Thanks to their strong relationship with the characteristics of regional deformation field, λ_I, λ_{II} and λ_{III} are particularly suited to the calculation of the metric of interest. A first metric proposed in the literature to measure the amount of anisotropy is the Anisotropic Deformation Index, or ADI, given by:

$$ADI = \sqrt{\left(\frac{\lambda_I - \lambda_{II}}{\lambda_{II}}\right)^2 + \left(\frac{\lambda_{II} - \lambda_{III}}{\lambda_{III}}\right)^2} \qquad \textbf{Eq. 3.12}$$

However, this index is not always suitable for two main reasons:

- It takes values from 0 (isotropic) to $+\infty$ (infinitely anisotropic), which can lead to difficult image representations with a given color-scale, in particular if a comparison is made between cases where the amount of anisotropy can vary a lot from one region of the lung to the other, or from one patient to another. It would be preferable to have a value that would vary significantly from 0 to 1 in usual situations. Of course, this problem can be solved easily by transforming this value through a monotonic and bounded function (like the arctangent function, for example).

- This expression is biased as it explicitly implies that $\lambda_I > \lambda_{II} > \lambda_{III}$. A term in $\lambda_I - \lambda_{III}$ should be added for symmetry reason.

For these two reasons, the Fractional Anisotropy, or FA, as it is used in Diffusion Tensor Imaging (DTI) MRI, may be preferred. The anisotropy analysis shares a lot of similarities with the current problem:

$$FA = \sqrt{\frac{(\lambda_I - \lambda_{II})^2 + (\lambda_{II} - \lambda_{III})^2 + (\lambda_I - \lambda_{III})^2}{2\left({\lambda_I}^2 + {\lambda_{II}}^2 + {\lambda_{III}}^2\right)}} \qquad \textbf{Eq. 3.13}$$

[329] T. A. Wilson, "Nonuniform Lung Deformations," *Journal of Applied Physiology* 54, no. 6 (June 1, 1983): 1443–50, https://doi.org/10.1152/jappl.1983.54.6.1443.

This expression have the great advantage to return values comprised between 0 (isotropic) and 1 (infinitely anisotropic) and to be purely symmetrical. Therefore, this expression does not suppose to have the λ_i values ranked in a special order. The Fractional Anisotropy is therefore more straightforward to compute and to display with any color-scale. However, as we will see thereafter, the information provided by ADI and FA are very similar and both answer to our initial question with close precision and accuracy.

We can also question the 'shape' the anisotropic tissue deformation takes. A 2D anisotropic phenomenon could be described with only one metric (as the 2D equivalents of ADI or FA for example) indicating if the 'shape' of the deformed object is more a circle or an elongated ellipse. However, in 3D, a given value of this first metric can correspond to very different situations. For example, it is possible to find cases where equal values of FA and ADI are obtained for $\lambda_I \gg \lambda_{II} \approx \lambda_{III}$, leading to a 'rod-shaped' deformation state, and $\lambda_I \approx \lambda_{II} \gg \lambda_{III}$, leading to a 'slab-shaped' deformation state. For that reason, a second metric is needed to fully understand the underlying 3D anisotropic deformation occurring inside the lung. One way to do it is to define a Slab-Rod Index, or SRI, like this one:

$$SRI = \frac{2}{\pi} arctan\left(\frac{\lambda_{III}(\lambda_I - \lambda_{II})}{\lambda_{II}(\lambda_{II} - \lambda_{III})}\right) \quad \textbf{Eq. 3.14}$$

The previous expression returns a value comprised between 0 (perfect rod-shape) and 1 (perfect slab-shape) and supposes $\lambda_I > \lambda_{II} > \lambda_{III}$. As previously said for FA, this type of bounded metric is ideal to be represented on a 2D map with a color-scale. Whereas FA is inspired by DTI-MRI, ADI and SRI were proposed a few years ago in an article focused on the 3D characterization of regional lung deformation[330] (itself inspired by rock characterization methods employed in geology). These two metrics were used afterwards in other studies in the same domain, in particular for the extraction and quantification of biomechanical parameters of the lung in 3D[331] [332] and 4D-CT[333].

3.2.4. CHARACTERIZATION AND COMPARISON OF VENTILATION ANISOTROPY FOR THE THREE TYPES OF BREATHING PATTERNS

Figure 3.17 represents the ADI, FA and SRI maps obtained at the end of inspiration for our three types of breathing. Once again, differences are observed between the three types of breathing. In particular, a larger amount of anisotropy is obtained in the inferior parts of the lung for normal and diaphragmatic breathings, whereas anisotropy is more uniformly shared within the lung for thoracic breathing. However, the fractional anisotropy values remain low: ($FA = 0.0640 \pm 0.032$) for normal breathing, ($FA = 0.102 \pm 0.035$) for thoracic breathing and ($FA = 0.0953 \pm 0.037$) for diaphragmatic breathing. Concerning the 'shape' of the anisotropic deformation, it seems that diaphragmatic breathing is globally best characterized by a rod-shape ($SRI = 0.611 \pm 0.20$) than thoracic breathing ($SRI = 0.548 \pm 0.23$) (which can be observed in **Figure 3.16**), whereas normal breathing is somewhere between the two behaviors ($SRI = 0.562 \pm 0.24$) but without strong statistical

[330] Ryan Amelon et al., "Three-Dimensional Characterization of Regional Lung Deformation," *Journal of Biomechanics* 44, no. 13 (September 2, 2011): 2489–95, https://doi.org/10.1016/j.jbiomech.2011.06.009.
[331] Sanghun Choi et al., "Registration-Based Assessment of Regional Lung Function via Volumetric CT Images of Normal Subjects vs. Severe Asthmatics," *Journal of Applied Physiology* 115, no. 5 (June 6, 2013): 730–42, https://doi.org/10.1152/japplphysiol.00113.2013.
[332] Nariman Jahani et al., "Assessment of Regional Non-Linear Tissue Deformation and Air Volume Change of Human Lungs via Image Registration," *Journal of Biomechanics* 47, no. 7 (May 7, 2014): 1626–33, https://doi.org/10.1016/j.jbiomech.2014.02.040.
[333] Nariman Jahani et al., "Assessment of Regional Ventilation and Deformation Using 4D-CT Imaging for Healthy Human Lungs during Tidal Breathing," *Journal of Applied Physiology* 119, no. 10 (August 27, 2015): 1064–74, https://doi.org/10.1152/japplphysiol.00339.2015.

significance. All the FA and SRI values above were given as (mean $\pm$ standard deviation) over the entire lung mask corresponding to the parenchyma and the vascular tree. As previously mentioned, note that the maps for ADI and FA give similar information on the amount of anisotropy, but not with the same scale. Both metrics can therefore be used to quantify the amount of anisotropy but FA is better for parameter mapping representation.

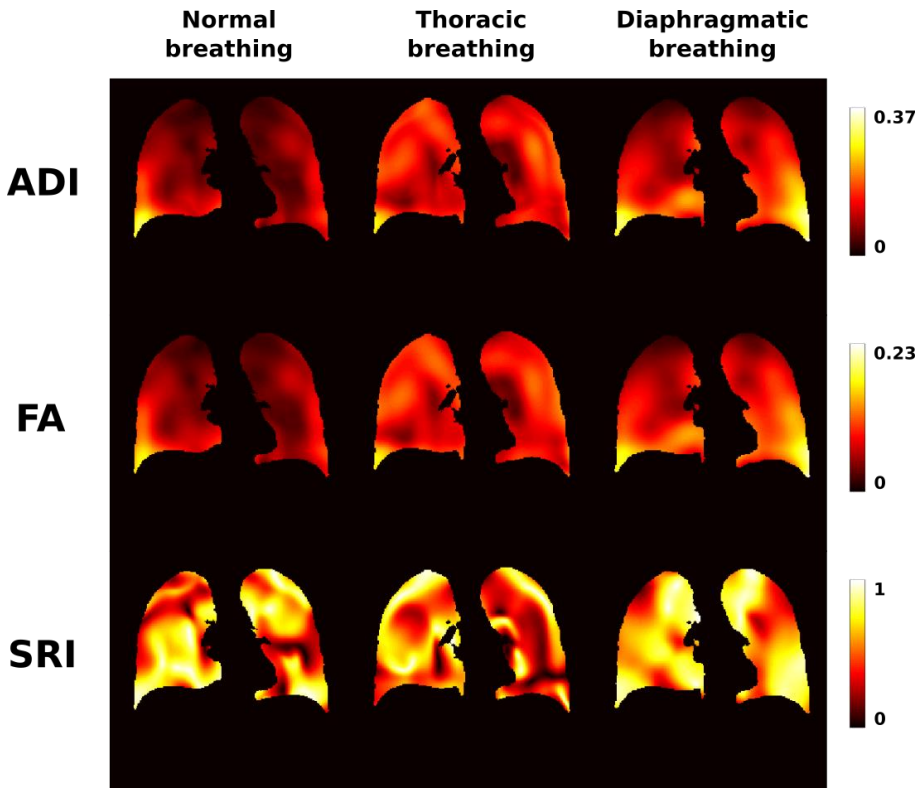

Figure 3.17: Coronal views of ADI, FA and SRI maps for normal, thoracic, and diaphragmatic breathing patterns.

3.2.5. EVOLUTION OF VENTILATION ANISOTROPY ALONG THE RESPIRATORY CYCLE

Anisotropy metrics may also evolve along the breathing cycle and show hysteretic behaviors. They can be plotted as a function of the global volume expansion of the lung. No interesting results were observed for SRI. However, particularly interesting curves were observed for FA (or ADI, the behavior is the same) and represented in **Figure 3.18** for the three types of breathing patterns. On these $FA = f(J_T)$ curves, we first observe that the amount of anisotropy generally increases with the global lung volume expansion. Moreover, we observe a gradient of FA from the superior to the inferior regions of the lung for the three types of breathing, but less pronounced in thoracic breathing, as already observed in **Figure 3.17**. Besides, we observe an hysteresis phenomenon: for the different types of breathing and for all regions of the lung, the amount of ventilation anisotropy is higher during inspiration than during expiration. Recently, Jahani *et al.*[334] reported the same results for ADI in their 4D-CT experiments, as well as an increased non-linearity of the curve in inspiration compared to expiration, as observed here on **Figure 3.18**.

[334] Nariman Jahani et al., "Assessment of Regional Ventilation and Deformation Using 4D-CT Imaging for Healthy Human Lungs during Tidal Breathing," *Journal of Applied Physiology* 119, no. 10 (August 27, 2015): 1064–74, https://doi.org/10.1152/japplphysiol.00339.2015.

The larger amount of ventilation anisotropy in inspiration compared to expiration may be related to the active nature of the inspiratory maneuver (contraction of the diaphragm and/or intercostal muscles, which 'pulls' the lung parenchyma and causes an asymmetry in the deformation process), whereas expiration is passive (the lung tissue goes back to its equilibrium state, with no preferential direction for the deformation process). Finally, it seems that a relationship exists between the amount of hysteresis (the area of the loop) and the amount of tissue deformation: in thoracic breathing, loops for apical regions (where tissue deformation is larger, as observed in **Figure 3.10**) show a larger area than those for basal regions, whereas the contrary is observed for diaphragmatic breathing. Once again, in normal breathing, we are somewhere between these two extreme types of breathing.

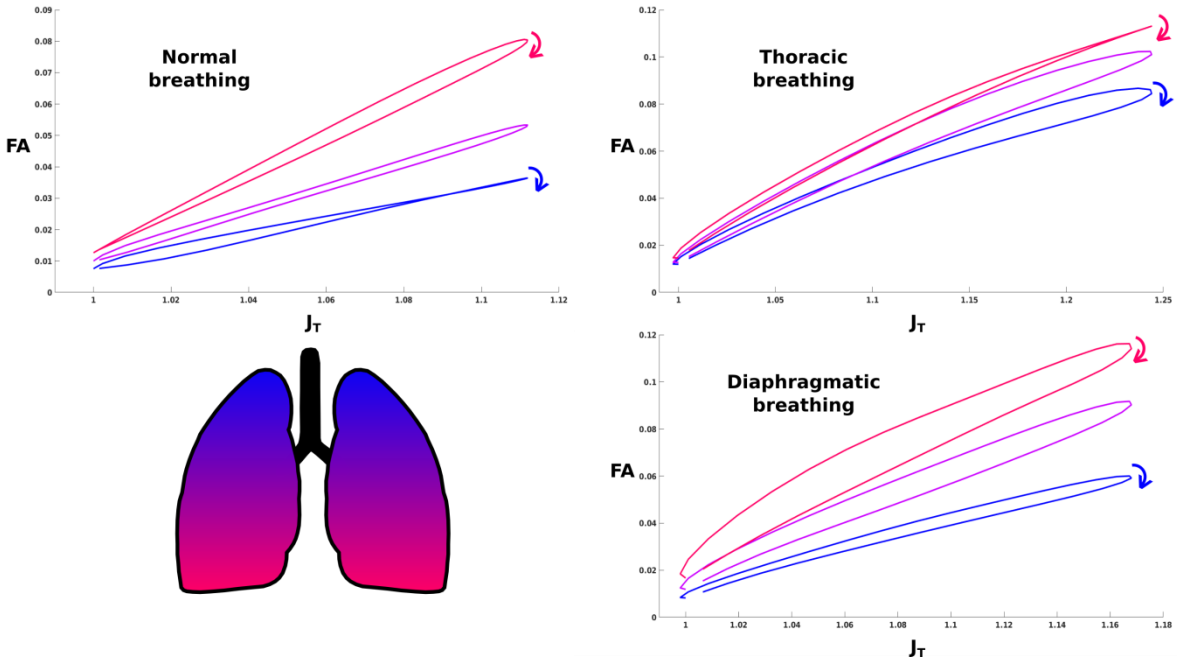

Figure 3.18: Representation of $FA = f(J_T)$ in different regions along the superior-inferior axis of the lung for normal, thoracic, and diaphragmatic breathing patterns. The color-scale in the bottom right hand corner represents which region of the lung is represented by each curve, and the arrows represent the way the curves are drawn along time.

The study of regional ventilation anisotropy seems promising and complementary to the study of regional 'isotropic' ventilation. A set of new parameters are accessible and seem dependent on the anatomy of the lung and on the type of breathing. It would be valuable to validate the aforementioned conclusion with other volunteers and observe if these parameters are sensitive to the pathophysiological state of patients' lung in, and therefore verify if they could be used as biomarkers for lung diseases.

4. CALCULATION OF FLOW-VOLUME LOOP MAPS

Until now, we only considered parameters measured at given time-points, which correspond to the different motion bins chosen at the beginning of the post-processing procedure designed for 3D MR Spirometry. Even if we have studied how they evolve along the ventilation cycle, it does not mean that the time has been taken into account yet, as actual time evolution of the initial proposed parameters has not been studied so far. In this last

subsection, we will introduce the notion of time and therefore make possible what is promised from the beginning of this chapter under the name of the technique: 3D spirometry.

This lies in the last step of the pipeline chart.

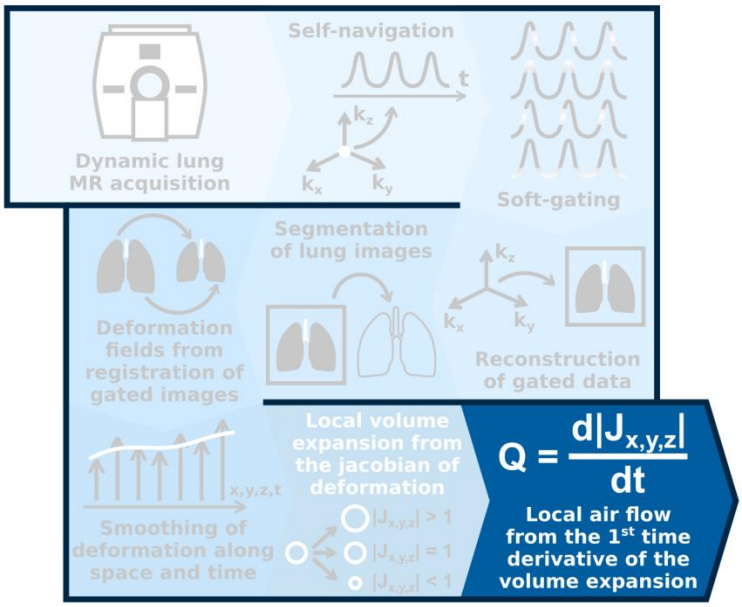

4.1. INTRODUCTION OF THE TIME IN 3D MR SPIROMETRY

In the perspectives of 3D MR spirometry application, time is a central variable for the dynamic of lung motion. Many previous studies have shown that the time variations of parameters measured from the lung are relevant to assess the pathophysiological state of the organ. Maybe the most obvious example is spirometry, for which the representation of the gas flow as a function of the gas volume inside the lung during a forced expiration is very sensitive to obstructive lung diseases. Even if those data are not plotted against time, time is embedded in the gas flow that is the first time derivative of gas volume inside the lung.

More generally, it has been shown that the lung does not behave in the same way in static and dynamic regimes, and changes in lung mechanical behavior have been observed between different breathing rates. These changes are largely explained by the resistance of air ducts, which is the ratio between the pressure difference at both ends of the duct and the gas flow inside[335]. This airway resistance is highly dependent on the local anatomy, and in particular on the geometry of the air ducts[336]. Moreover, its values are highly altered by some obstructive lung diseases, like COPD[337] or asthma[338] for example. To finish, differences in the resistance of small neighbor air ducts

[335] Arthur B. DuBois, Stella Y. Botelho, and Julius H. Comroe, "A NEW METHOD FOR MEASURING AIRWAY RESISTANCE IN MAN USING A BODY PLETHYSMOGRAPH: VALUES IN NORMAL SUBJECTS AND IN PATIENTS WITH RESPIRATORY DISEASE 1," *Journal of Clinical Investigation* 35, no. 3 (March 1, 1956): 327–35, https://doi.org/10.1172/JCI103282.

[336] William A. Briscoe and Arthur B. Dubois, "The Relationship Between Airway Resistance, Airway Conductance and Lung Volume in Subjects of Different Age and Body Size12," *Journal of Clinical Investigation* 37, no. 9 (September 1, 1958): 1279–85, https://doi.org/10.1172/JCI103715.

[337] James C. Hogg, Peter T. Macklem, and W. M. Thurlbeck, "Site and Nature of Airway Obstruction in Chronic Obstructive Lung Disease," *New England Journal of Medicine* 278, no. 25 (June 20, 1968): 1355–60, https://doi.org/10.1056/NEJM196806202782501.

can produce microscopic air flow effects dephased from the macroscopic respiratory cycle, as in *pendelluft* processes[339].

4.2. ESTIMATION OF FLOW-VOLUME LOOP MAPS WITH 3D MR SPIROMETRY

4.2.1. ESTIMATION OF REGIONAL PULMONARY GAS FLOWS

In 2.3 in the previous section, we have associated to each motion bin a time-stamp estimated from a gated-average respiratory cycle. Those time-stamps give the mean time duration between any motion bin and the reference deflated lung state that occurs at each breathing cycle. By re-interpolating the data on a regular 1D time grid or by using weighted finite difference methods, it is possible to calculate the first (and even the second, third, …) time derivative(s) of all the physical and mathematical quantities that can be computed from the time varying 3D deformation field of the lung parenchyma. For the sake of clarity and readability of this manuscript, we will neither discuss all the first time derivatives of all the parameters extracted from the beginning of the section (even if it would be interesting and valuable to observe the regional tissue velocities and accelerations, as well as the shear rate fields within the lung), nor study if they exhibit any hysteretic behavior. Instead, we will only focus on the first time derivative of the regional volume expansion.

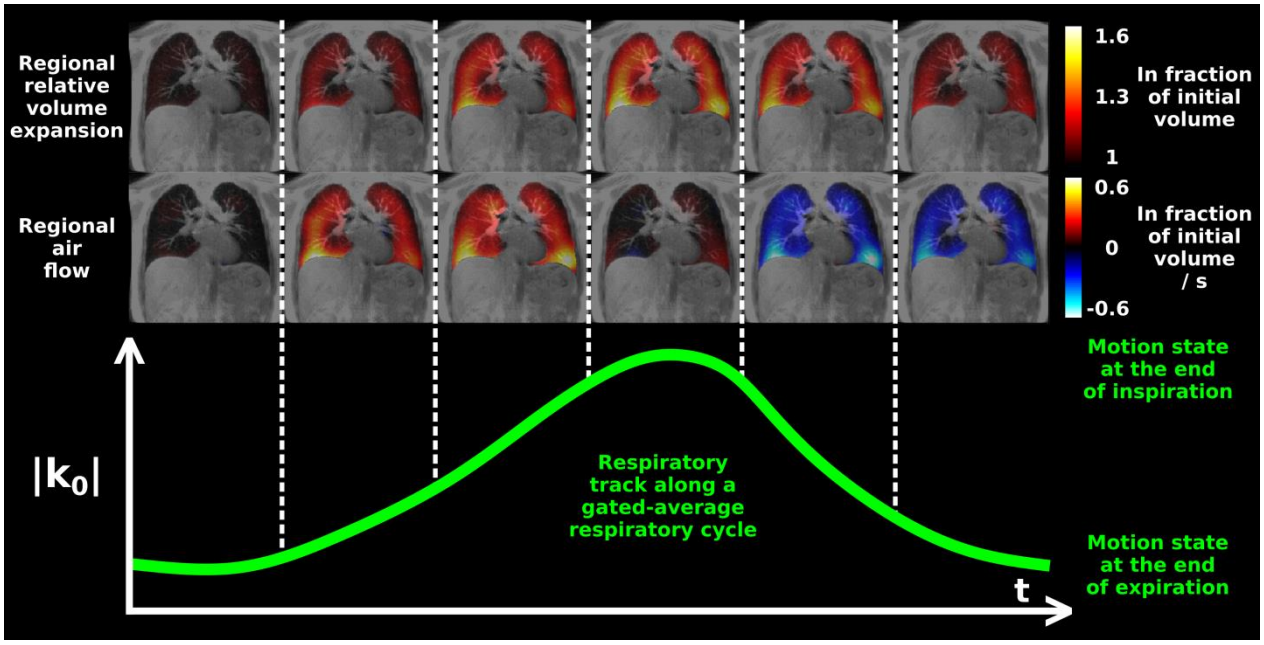

Figure 3.19: Representation of the regional volume expansion (J) and regional air flow (Q) along the gated-average respiratory cycle. This average cycle is represented as the average DC signal values (used as respiratory surrogate signal for retrospective gating) over the different respiratory cycles. Regional volume expansions are expressed relatively to local volumes in the reference state (end of expiration), as explained in the definition of the Jacobian.

As a reminder, this quantity was extracted with J, the Jacobian of the deformation field, and was shown to be a satisfying representation of the regional lung ventilation (i.e. gas volume change). By calculating its first time

[338] Elizabeth M. Wagner et al., "Peripheral Lung Resistance in Normal and Asthmatic Subjects," *American Review of Respiratory Disease* 141, no. 3 (March 1, 1990): 584–88, https://doi.org/10.1164/ajrccm/141.3.584.
[339] Arthur B. Otis et al., "Mechanical Factors in Distribution of Pulmonary Ventilation," *Journal of Applied Physiology* 8, no. 4 (January 1, 1956): 427–43, https://doi.org/10.1152/jappl.1956.8.4.427.

derivative, written $Q = \frac{dJ}{dt}$, we therefore obtain a measurement of the regional air flow discussed in 4.1 in the definition of the airway resistance. Q is therefore a quantity of potential great interest for the study of lung physiology. In **Figure 3.19**, we represent the time evolution of the regional air flow maps (Q) with their corresponding ventilation maps (J) along the gated-average respiratory cycle. Logically, we observe that the regional air flow is positive when the regional volume expands, and is negative in the case of a regional deflation. As it is the case for local volume expansion, we observe a spatially uneven distribution of regional air flow, which is certainly explained by several factors (breathing pattern, local lung anatomy, gravity, global lung inflation level, …).

4.2.2. REPRESENTATION OF 3D FLOW-VOLUME LOOP MAPS

On **Figure 3.20**, local curves $Q = f(J)$ reveal the evolution of local gas flow as a function of local gas volume. Such outcome is well known in the field of lung physiology as being the main information returned by standard spirometers for the entire organ. With our technique, the same measurement is made at the regional scale and in 3D, hence the name of the technique: 3D Magnetic Resonance Spirometry. A regional flow-volume loop can therefore be plotted at each voxel position to represent the contribution of any local volume of lung parenchyma to the global spirometry result, which can be directly computed here by averaging over the organ every local measurement (see **Figure 3.20**).

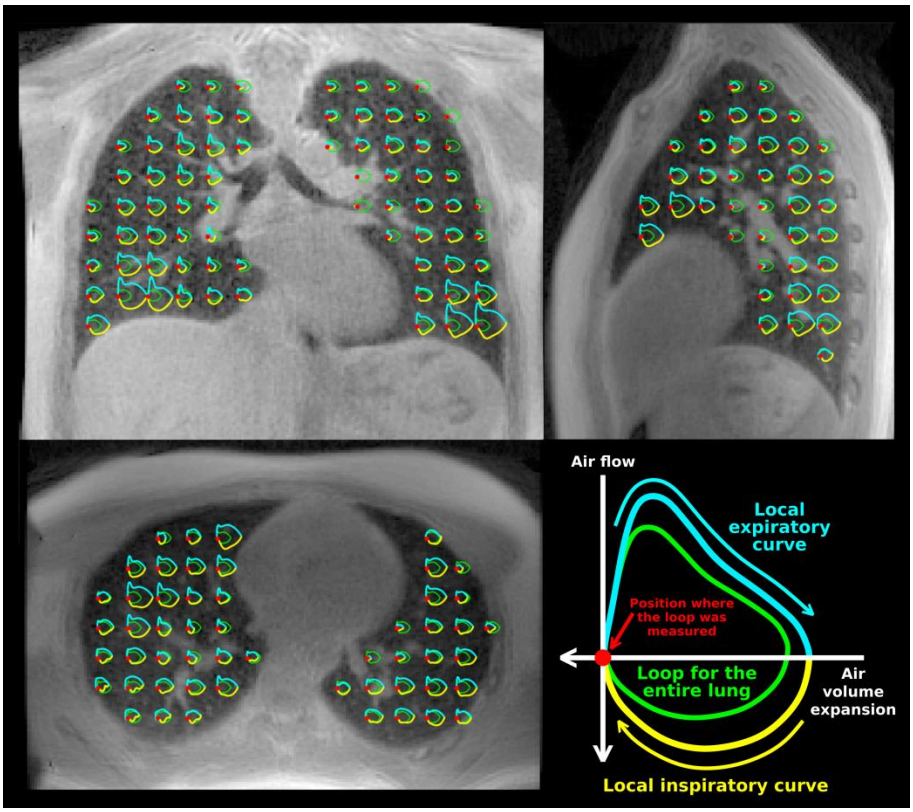

Figure 3.20: Axial, sagittal and coronal views of the 3D UTE image at the end of expiration and over which are superimposed the regional flow-volume loops estimated with 3D MR Spirometry. For each local loop, the global loop representing the flow-volume relationship for the entire lung is also drawn for reference. In the bottom right hand corner, we represented the color and axis conventions for the representation of local and global loops.

For this representation, we used the same conventions as the ones used in standard spirometry: expiratory volumes and flows are chosen to be positive, contrary to what would be conventionally chosen in physics. In this representation, we observe loops similar to those usually observed in standard spirometry. By comparing the local loops (represented in yellow and blue, respectively for inspiratory and expiratory phases) and the one obtained for the total lung volume (represented in green), we observe a variability of the sizes and shapes of the loops throughout the lung, as expected for the different breathing patterns from previous observations.

4.2.3. COMPARISON BETWEEN THE FLOW-VOLUME LOOP MAPS FOR THE THREE TYPES OF BREATHING PATTERNS

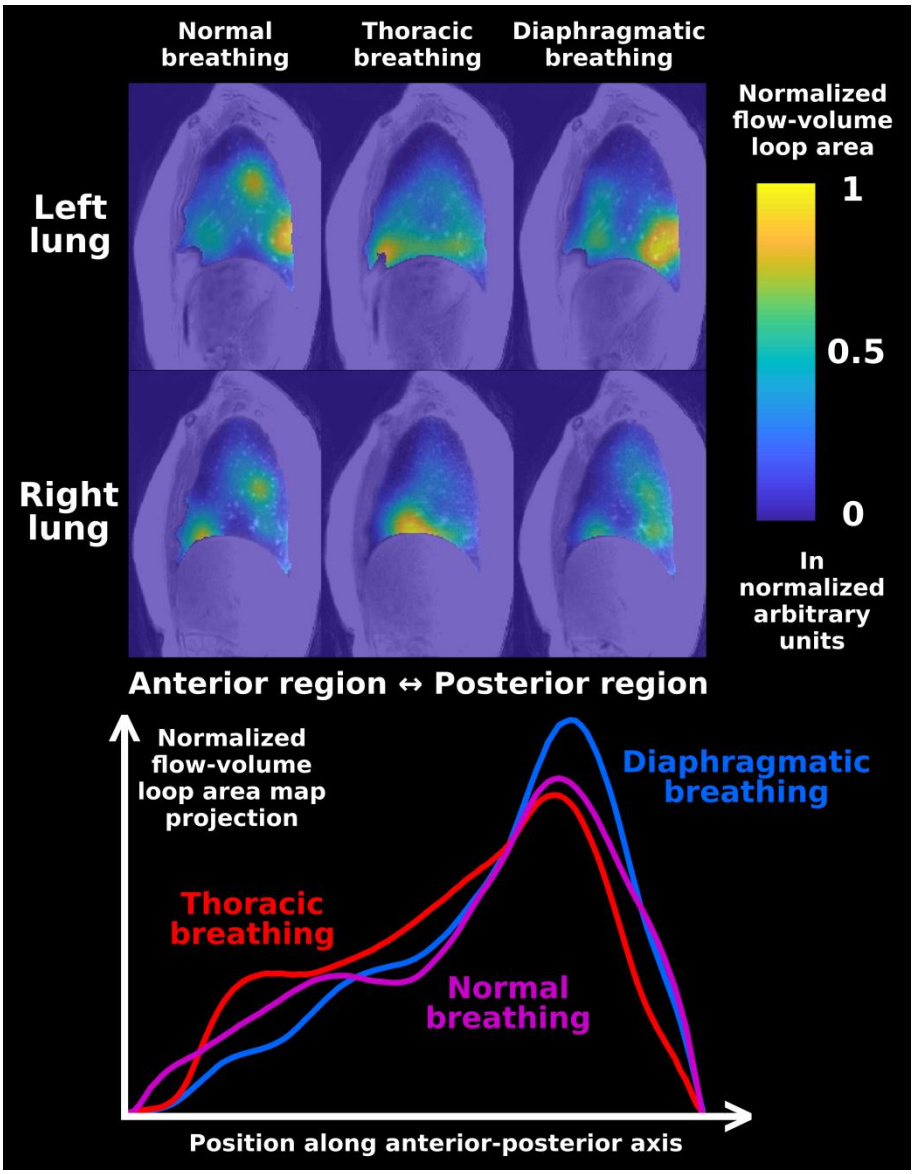

Figure 3.21: Sagittal slices of normalized flow-volume loop area maps and projections of these 3D area maps on the anterior-posterior axis for the three types of breathing patterns. Normalization was performed separately over each slice for sagittal views of area maps and over the entire lung volume for area maps projections to compensate for global tidal volume and air flow differences between the three types of breathing patterns.

A great number of parameters can be extracted from these loops: the area, the perimeter, the slope at the end of the expiratory curve and the linearity of this part of the curve. Even more advanced metrics can also be calculated by combining several of these parameters, as a measure of the circularity of the loop from its area and perimeter for example, as it was proposed in **Eq. 3.1** for local tissue trajectories. Yet, to quantitatively compare the three types of breathing patterns, the mere area of the regional flow-volume loops was singled out as a representative parameter of these regional loops. The corresponding parametric maps are represented in **Figure 3.21** for the three types of breathing patterns. In these maps, the area is larger in anterior parts of the lung in thoracic breathing whereas it is larger in posterior parts of the lung for diaphragmatic breathing. In normal breathing, the area seems more evenly distributed throughout the organ. To observe the difference, data were projected onto the anterior-posterior axis to represent the result as a 1D curve for each breathing pattern. As expected, the distribution of flow-volume loop area is retrieved in the curves, and the normal breathing curve is somewhere in-between the curves for thoracic and diaphragmatic breathing patterns. This observation can be understood when considering that, for the volunteer, in normal breathing, both thoracic and diaphragmatic forces contribute.

5. DISCUSSION, PERSPECTIVES AND CONCLUSION FOR 3D MR SPIROMETRY

5.1. DISCUSSION

As we have seen in the course of this chapter, 3D Magnetic Resonance Spirometry is not just a 3D spirometry technique. From the pulmonary deformation fields extracted out of MR lung images, it is possible to determine the trajectory followed by each elementary volume of lung parenchyma, compute the different components of tissue strain, quantify the amount and nature of strain anisotropy, measure the regional volume expansion from a given reference state, estimate local gas flow as the first time derivative of the local volume expansion, and study the evolution of these parameters as a function of more global ones, like the total lung volume or the time for example. Three-dimensional MR Spirometry is therefore far richer than standard spirometry concerning the number and nature of parameters that it can provide. This novel technique may be highly valuable for lung physiology but also for lung pathology. We chose to refer to ‘Spirometry’ because it is today one of the most common exams in clinical routine to assess lung ventilation as a part of lung function.

Our technique demonstrates the advantage to measure directly the mechanical pulmonary behavior in order to estimate local lung function. Thanks to a direct quantification of parameters and simple underlying models linking the deformation fields and the quantities of interest (mainly based on spatial and temporal derivatives, and on multidimensional representations), we have access to a great variety of relevant parameters that exhibits how the lung locally behaves but also how it ensures air ventilation at the regional scale and at any time-point of the respiratory cycle. The best strength of our technique is to be based on 3D motion corrected MR images, namely on complete 4D dataset. Of course, it gives the possibility to quantify the parameters listed just above everywhere in the lung, but the main advantage is the technique dimensionality to quantify these parameters from the actual 3D motion field of the lung parenchyma. This last aspect is very important because, from a Lagrangian point of view, each elementary volume of lung tissue follows a trajectory in a 3D space. If this trajectory is extracted from a space with a lower number of dimensions (2D MR images or 2D projection images, for example), the information is automatically incomplete and could lead to quantification biases. Furthermore, the measurement of the different parameters in the entire organ offers great perspectives in terms of intra-subject and extra-subject normalization (by dividing a parameter by its average value over the entire organ, or by fitting the final parametric maps onto a representative atlas of the human lung, for example).

Nevertheless, the technique presents an important drawback that is MRI. The equipment is far more cumbersome than a standard spirometer. It is not available in a pulmonology department and might not be in the near future. The exam is more expensive and the measurement of the parameters is carried from a dataset acquired in a total scan time around 11 minutes. Even if improvements in the image acquisition procedure are possible to reduce the total scan time and even if compromises can be found between this duration and the final image quality (voxel size, SNR, under-sampling artifacts, …), it will be difficult to achieve the acquisition of a sufficient amount of data in less than several tens of seconds. This minimal scan time involves an acquisition over several quasi-periods of nominal respiratory motion, which implies the averaging of data coming from different respiratory cycles, even if a more advanced motion correction procedure is implemented. However, it is well understood today that respiratory motion is not fully reproducible from one motion period to the other. For that reason, a 'real-time' 3D imaging strategy would be preferred for our application, as it can be approached with modern 4D-CT techniques[340]. However, if inspiration and expiration phases are separated and if the outlying motion states are discarded in the post-processing steps, the main part of the problem is solved, in particular with a final voxel size above 1 mm. Moreover, contrary to 4D-CT, retrospectively gated MRI is safe for the patient in terms of ionizing radiation and the number of motion gates is not limited. Furthermore, the final quality of motion corrected UTE images and the quantity of landmarks observable in the lung tend to be more and more similar to what can be obtained in motion corrected CT[341].

'Real-time' MR spirometry have been proposed a few years ago[342], but only with 2D coronal images and with a very low temporal resolution (7 time-stamps per respiratory period), by exploiting grid tagging to create artificial structures in the lung parenchyma. The same strategy was proposed to study lung mechanics a few years before by the same research group[343] [344]. In these cases, the extracted deformation field is included in the coronal plane and therefore discards any component of motion along the anterior-posterior axis (which can be important in term of displacement amplitude, as seen in the case of thoracic breathing for example). In their work, the measurement of gas volumes and flows is therefore biased by not considering this motion component. Other groups proposed multi-slice 2D acquisitions in the sagittal plane, which seems far better for the estimation of motion fields, either by using dynamic grid-tagging in ^{3}He MRI[345] or by studying static images at different levels of lung inflation obtained during breath-holds[346] [347]. In the first case, it is still based on grid-tagging and it brings the difficulties (but also the

[340] M. Endo et al., "Development of Real 4D CT with Real-Time Reconstruction and Display," in *IEEE Nuclear Science Symposium Conference Record, 2005*, vol. 5, 2005, 2603–6, https://doi.org/10.1109/NSSMIC.2005.1596871.

[341] Nicholas S. Burris et al., "Detection of Small Pulmonary Nodules with Ultrashort Echo Time Sequences in Oncology Patients by Using a PET/MR System," *Radiology* 278, no. 1 (July 2015): 239–246, https://doi.org/10.1148/radiol.2015150489.

[342] Abram Voorhees et al., "Magnetic Resonance Imaging-Based Spirometry for Regional Assessment of Pulmonary Function," *Magnetic Resonance in Medicine* 54, no. 5 (November 1, 2005): 1146–54, https://doi.org/10.1002/mrm.20682.

[343] Qun Chen et al., "Ultrafast MR Grid-Tagging Sequence for Assessment of Local Mechanical Properties of the Lungs," *Magnetic Resonance in Medicine* 45, no. 1 (January 1, 2001): 24–28, https://doi.org/10.1002/1522-2594(200101)45:1<24::AID-MRM1004>3.0.CO;2-6.

[344] Vitaly J. Napadow et al., "Determination of Regional Pulmonary Parenchymal Strain during Normal Respiration Using Spin Inversion Tagged Magnetization MRI," *Journal of Magnetic Resonance Imaging* 13, no. 3 (March 1, 2001): 467–74, https://doi.org/10.1002/jmri.1068.

[345] Jing Cai et al., "Dynamic MRI of Grid-Tagged Hyperpolarized Helium-3 for the Assessment of Lung Motion During Breathing," *International Journal of Radiation Oncology*Biology*Physics* 75, no. 1 (September 1, 2009): 276–84, https://doi.org/10.1016/j.ijrobp.2009.03.051.

[346] James Gee et al., "Characterization of Regional Pulmonary Mechanics from Serial Magnetic Resonance Imaging Data1," *Academic Radiology* 10, no. 10 (October 1, 2003): 1147–52, https://doi.org/10.1016/S1076-6332(03)00329-5.

advantages) of hyperpolarized gases MRI. In the second case, as the images are made in static mode, all the dynamic aspects of lung mechanics are lost, which is detrimental in regard to what was discussed previously.

To my opinion, the best work which has been carried in the field is the one published by Kolb *et al.* in 2016[348]. By using retrospectively self-gated 3D MRI in free-breathing, their research project is very close to our 3D MR Spirometry technique. The main difference is in the post-processing tasks: instead of segmenting and registering the images separately and without any prior, they propose a joint segmentation and registration task based on a supposed 3D lung model. The use of such a model may play a regularization role in the process (instead of filtering the extracted motion fields) but supposes a standard lung shape, which fails in the case of a preclinical study or in the diagnosis of patients that underwent lung surgery. Their study goes further in terms of validation processes, as several patients were studied and comparisons were made with 3D and 4D-CT. However, their study is less advanced in the fact that only ventilation parameters were prospected, and nothing about strain, hysteresis or anisotropy is mentioned in the article.

5.2. PERSPECTIVES

It is important to consider that every acquisition or post-processing step of our 3D MR Spirometry technique can be improved. Non-exhaustively, scan-time can be reduced, imaging parameters can be further optimized to increase the final image quality, other surrogate signals can be added to perform a better motion binning, and registration can be performed with a more adapted motion model coupled with a regularization process to obtain spatially and temporally smooth deformation fields. This smoothness is important because it represents what we expect from physiological deformation fields and because most advanced parameters introduced in this chapter were defined as spatial and/or temporal derivatives of the motion field and are calculated directly from these motion fields by finite difference techniques. These techniques are known to be very sensitive to the noise present in the initial data, and therefore lead to estimations of derivatives with an amplified amount of noise, which can compromise the precision and even sometimes the accuracy of the final result.

The fact that all the parameters presented in this chapter are extracted from the same motion field is also source of discussion. We have seen that a lot of parameters can be extracted and several of them show anisotropic and hysteretic properties (and both properties sometimes). However, as they are all extracted from the same initial vector field, we can expect them to carry the same information in certain cases. All the useful information is contained in the deformation fields actually, but as we have seen, it is really helpful to extract well defined parts of this information to only focus on known physical quantities (local volume expansion, for example) or one precise mechanical behavior (strain components free of bulk translation and rotation components, for example).As all the parameters are extracted from the same motion field, it is not really surprising to observe several hysteretic behaviors as information redundancy may appear. Here are my thoughts and my recommendations for the choice of parameters:

- **Choose parameters that have a physical meaning:** As it was seen, many parameters can be extracted and many behaviors can be studied by plotting one parameter against another one, or by calculating the successive time or spatial derivatives of any parameter. More advanced metrics can even be calculated by

[347] Tessa A. Sundaram and James C. Gee, "Towards a Model of Lung Biomechanics: Pulmonary Kinematics via Registration of Serial Lung Images," *Medical Image Analysis*, ITK, 9, no. 6 (December 2005): 524–537, https://doi.org/10.1016/j.media.2005.04.002.

[348] Christoph Kolb et al., "Regional Lung Ventilation Analysis Using Temporally Resolved Magnetic Resonance Imaging," *Journal of Computer Assisted Tomography* 40, no. 6 (December 2016): 899, https://doi.org/10.1097/RCT.0000000000000450.

combining several of these parameters. However, it is important to really consider and understand what they represent. To me, the best way to do it is to refer to basic sciences in order to make the appropriate choice of parameters and define them accordingly. For example, J is clear to me as it represents the regional relative volume expansion in the tissue. However, its spatial gradient has less sense to me as a physicist.

- **Validate the quantification of these parameters:** Even if the quantification method is based on the assessment of lung mechanical behavior, the estimation of each parameter is never totally direct. Several steps (image registration, calculation of derivatives, …) are needed and errors can accumulate through the estimation process. Even if the parameter has a physical or physiological meaning, its estimated value can be totally wrong because of the propagation of measurement biases and errors. It is therefore important to find methods to verify the precise and accurate quantification of each parameter. For example, I consider the comparison discussed in 2.2.2 between the total lung volume expansions J_T obtained with segmentation and with the integration of J to be good practice. Numerical simulations, tests made with controlled phantoms and parallel comparison with gold standard measurement methods can also be useful to verify the quality of the quantification process.

- **Verify if the parameters carry useful information on lung physiology and/or pathology:** Even if the extracted parameters are interesting from a physical point of view, and even if they are extracted precisely and accurately, it is important to keep in mind that the final goal is to study the pathophysiology of the organ: its function or even detect, localize and characterize pathological alterations in the clinical environment. An example is the first time derivative of tissue displacement, which is interesting from a physicist point of view as it represents the local velocity of lung tissue. However, its interest is not straightforward in terms of lung pathophysiology. From the physiologist point of view, it is definitely more relevant to extract local strain components and eventually calculate strain rates. To make the best choices, it is important to create links between physicists and medical doctors to find the parameters that both have a physical and a physiological meaning, and then to conduct tests *in vivo* in healthy and diseased subjects to verify the relevance of these choices.

The application of 3D MR Spirometry in the clinical field and its comparison with standard spirometry must be carried with the different experimental conditions in mind. As described in Chapter 1, standard spirometry is performed on seated subjects through forced respiratory cycles for sensitivity and normalization purposes, whereas 3D MR Spirometry is performed on lying subjects with more spontaneous respiratory cycles. It seems difficult to perform our technique with forced respiratory cycles as many successive cycles are needed throughout the entire image acquisition process. However, we can wonder if 3D MR Spirometry would not be as sensitive or even more sensitive to lung diseases thanks to the possibility to locally assess lung ventilation. In the case of localized emphysema for example, we can expect great differences between the flow-volume loops measured in the diseased tissue and in its surrounding healthy tissue, even during breathing patterns involving tidal air volumes. If this equal or increased sensitivity is verified, added to the great advantage to localize diseased tissues, it would bring valuable benefits compared to standard spirometry. Indeed, because it requires forced and controlled breathing cycles, standard spirometry is only applicable with cooperative patients. If our technique is at least as sensitive and specific as standard spirometry, it could be performed with non-cooperative patients, like young children or patients with whom interaction is not possible. We could also consider an acquisition with a silent ZTE pulse sequence, instead of the UTE, in order to perform the exam on sleeping patients.

Finally, it may have been noticed that the PET side of the PET/MR machine hasn't been used in our 3D Magnetic Resonance Spirometry experiments. However, promising possibilities are offered by such a multi-modality machine

in the perspective of measuring complementary ventilation parameters, as the absolute regional gas volume in the lung (with gaseous radioactive tracers), or other components of lung function, as regional pulmonary perfusion for example (with the injection of intravenous radioactive tracers).

5.3. CONCLUSION

The information provided by 3D MR Spirometry is not complete with respect to the lung function. As reminded at the beginning of this chapter, information on lung perfusion and gas transfer would be valuable. These other parameters could be acquired within the same exam, either during another MR acquisition (DCE-MRE, for example), or even along the same acquisition process thanks to a PET/MR imaging exam with the injection of a radioactive tracer able to give quantitative information on organ perfusion. For the study of lung mechanical behavior, the motion field and all the parameters that can be extracted from it are not sufficient for a complete analysis of the respiratory mechanics. Indeed, no information on forces (pressures, stresses, …) comes with 3D MR Spirometry. It is problematic because, as explained in the first chapter of this manuscript, mechanics is the field of physics that studies the behavior of physical bodies when subjected to forces. We will see in the next and last chapter that pulmonary forces can be indirectly estimated from the displacement fields and the mechanical properties of the lung.

CHAPTER 4 - 3D MAGNETIC RESONANCE ELASTOGRAPHY OF THE LUNG

IN THIS CHAPTER, WE WILL INTRODUCE THE BASIC CONCEPTS OF CONTINUUM MECHANICS AND SEE HOW MECHANICAL PROPERTIES CAN BE LOCALLY MEASURED IN BIOLOGICAL TISSUES THANKS TO TWO MEDICAL IMAGING MODALITIES: ULTRASOUND ELASTOGRAPHY AND MAGNETIC RESONANCE ELASTOGRAPHY, OR MRE. WE WILL THEN SEE THE GREAT CHALLENGES PRESENTED BY MRE FOR THE LUNG AND PROPOSE A TOTALLY NEW PARADIGM TO PERFORM LUNG MRE THANKS TO AN ORIGINAL PULSE SEQUENCE WE HAVE DEVELOPED. THE FIRST RESULTS OBTAINED IN PHANTOMS AND *IN VIVO* WILL BE PRESENTED AT THE END OF THIS CHAPTER.

SECTION 1 INTEREST AND METHODS TO MEASURE THE VISCOELASTIC PROPERTIES OF ORGANS

IN THE PREVIOUS CHAPTER, WE HAVE STUDIED THE MECHANICAL BEHAVIOUR OF THE LUNG PARENCHYMA IN TERMS OF TIME VARYING DEFORMATION FIELDS AND OTHER QUANTITIES DERIVED FROM THEM: MOTION HYSTERESIS, LOCAL GAS VOLUME, LOCAL GAS FLOW AND TISSUE STRAIN. THE UNDERLYING VISCOELASTIC PROPERTIES OF THE LUNG PARENCHYMA SHOULD BE MEASURED TO FULLY CHARACTERIZE THE RESPIRATORY MECHANICS AND THE OVERALL PATHOPHYSIOLOGY OF THE LUNG. IN THIS FIRST SECTION, WE WILL CLARIFY HOW TO DEFINE AND UNDERSTAND THE VISCOELASTIC PROPERTIES OF ORGANS. IN PARTICULAR, WE WILL STUDY THREE DIAGNOSTIC TECHNIQUES TO ASSESS THEM: ORGAN PALPATION, ULTRASOUND ELASTOGRAPHY, AND MAGNETIC RESONANCE ELASTOGRAPHY.

1. FROM ORGAN PALPATION AND FUNDAMENTAL CONCEPTS OF CONTINUUM MECHANICS TO THE QUANTITATIVE ASSESSMENT OF VISCOELASTIC PROPERTIES IN BIOLOGICAL TISSUES WITH ULTRASOUND IMAGING

In this section, the viscoelastic properties of biological tissues will be introduced in parallel with different ultrasound elastography techniques. This simultaneous introduction is not obligatory as ultrasound elastography will be minimally implemented for the study of lung mechanical properties. However, the illustration of the different notions of continuum mechanics with ultrasound elastography techniques directly exploiting these concepts is, in my opinion, an interesting approach to pave the way for the medical imaging of mechanical properties of tissues in general. Following the definition of the vocabulary, the concepts and the different steps that need to be implemented for the imaging process, the regional assessment of mechanical properties will then be explored through magnetic resonance with MR elastography, a strategy better suited to pulmonary imaging.

1.1. NOTION OF YOUNG'S MODULUS AND ITS DIRECT MEASUREMENT WITH ULTRASOUND ELASTOGRAPHY TECHNIQUES

Organ palpation is a widely spread diagnosis technique in the medical field. Thanks to the sensitivity of his or her fingers and his or her clinical experience, the medical practitioner is able to detect the abnormal stiffness of an organ or the presence of suspicious heterogeneous masses inside a biological tissue. With its simplicity and low cost, this technique remains qualitative, highly operator dependent and can only be performed on superficial or accessible organs (thyroid, breast, prostate, …). As it was seen at the beginning of this manuscript, the lung is enclosed inside the thoracic cage, which makes lung palpation impossible. For that reason, to evaluate *in vivo* the stiffness of the lung parenchyma or the presence of a lesion with mechanical properties that differs from its surrounding environment, another strategy will be needed.

1.1.1. THE THOMAS YOUNG'S EXPERIMENT

From a physicist's point of view, palpation reminds the experiments performed by the British physicist Thomas Young (1773-1829) to study the mechanical behavior of pieces of elastic materials when an external force was

applied to them (see **Figure 4.1**). The principal result of these experiments was the proportionality relationship between the uniaxial surface force applied to the piece of elastic material along one direction x, written σ_{xx} and usually called stress, to the relative change of its length along this same axis, written ε_{xx} and called strain. The stress is usually expressed in Pascal whereas the strain is a dimensionless quantity, as seen in the previous chapter. The first x index in the stress or strain symbols refers to the orientation of the vector normal to the surface to which the force is applied or from which the strain is defined, and the second one to the direction along which the stress or strain is oriented. Here, those two directions are thus the same. The stress and strain are therefore oriented normally to the surface of the material.

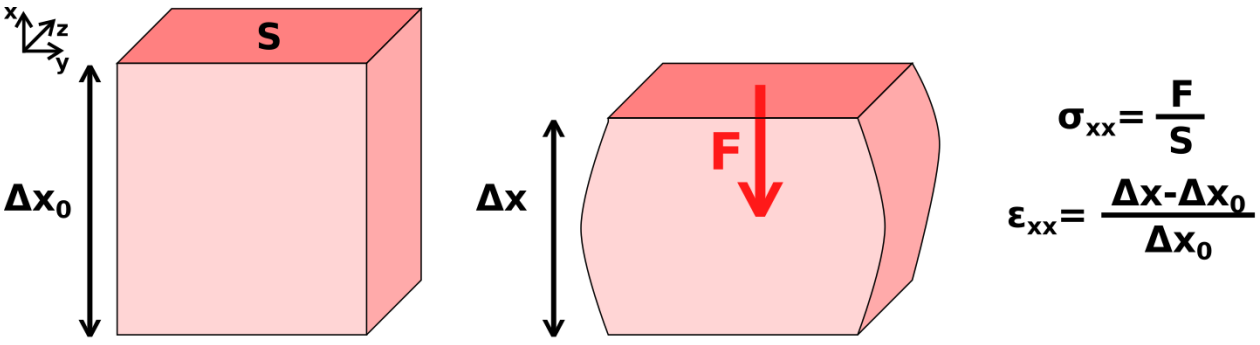

Figure 4.1: Thomas Young's experiment to measure the Young's modulus E.

This relationship, called the Hooke's law, is usually written:

$$\sigma_{xx} = E\,\varepsilon_{xx} \qquad \textbf{Eq. 4.1}$$

with E, a scalar parameter expressed in Pascal (or kPa in usual biological tissues), being the apparent stiffness of the material as a compression or a traction is performed on it. It thus characterizes the amount of stress needed on a piece of purely elastic material to reach a given strain. E, which is usually called modulus of elasticity, or Young's modulus[349], is therefore the physical quantity to which the medical practitioner is sensitive when a palpation exam is performed on a patient: a small deformation is applied to the tissue under examination and, thanks to the sensitivity of her or his fingers, the medical practitioner can estimate the recoil force generated by the deformed tissue, which is equal to the force she or he creates her or himself to deform the tissue in the quasi-static case.

The Hooke's law links together a force, a mechanical property and a strain. In the previous chapter, the local strain components appearing inside the lung parenchyma during the breathing cycle were measured. It would be very interesting to also measure the mechanical property as it would give us the possibility to map the internal forces (internal pressures, local stress, …) inside the organ, and therefore give us all the information needed to completely study the respiratory mechanics.

[349] A. P. Sarvazyan et al., "Biophysical Bases of Elasticity Imaging," in *Acoustical Imaging*, ed. Joie Pierce Jones, Acoustical Imaging (Boston, MA: Springer US, 1995), 223–40, https://doi.org/10.1007/978-1-4615-1943-0_23.

1.1.2. SMALL STRAIN APPROXIMATION

Only small displacement will be considered in this chapter (experimentally several tens of micrometers are produced for elastography). For that reason, we do not need to use the Green-Lagrange strain tensor ε^G. As a reminder, this tensor was defined as:

$$\varepsilon^G = \frac{1}{2}(F^T F - I) \qquad \textbf{Eq. 4.2}$$

where F is the deformation gradient tensor, which can be compactly written $\frac{d\vec{r}}{d\vec{R}}$. The different components of ε^G can therefore be written:

$$\varepsilon^G_{ij} = \frac{1}{2}\left(\frac{\partial u_i}{\partial R_j} + \frac{\partial u_j}{\partial R_i} + \frac{\partial u_k}{\partial R_j}\frac{\partial u_k}{\partial R_j}\right) \qquad \textbf{Eq. 4.3}$$

with $R_x = X$, $R_y = Y$ and $R_z = Z$. In the assumption of small displacements, strain components remain small ($\ll 1$) an it is possible to neglect the quadratic term in the expression just above. In this case, it is possible to define an infinitesimal strain tensor, written ε, as an approximation of the Green-Lagrange strain tensor for small strains:

$$\begin{aligned} \varepsilon_{ij} &= \frac{1}{2}\left(\frac{\partial u_i}{\partial R_j} + \frac{\partial u_j}{\partial R_i}\right) \\ &= \varepsilon^G_{ij} - \frac{1}{2}\frac{\partial u_k}{\partial R_j}\frac{\partial u_k}{\partial R_j} \\ &\approx \varepsilon^G_{ij} \end{aligned} \qquad \textbf{Eq. 4.4}$$

Furthermore, it can be shown that:

$$\varepsilon = \frac{1}{2}(F + F^T) - I \qquad \textbf{Eq. 4.5}$$

In the rest of this chapter, strain will refer to this infinitesimal strain. The following expressions are usually used to designate each of its components:

$$\begin{aligned} \varepsilon &= \begin{bmatrix} \varepsilon_{xx} & \varepsilon_{xy} & \varepsilon_{xz} \\ \varepsilon_{yx} & \varepsilon_{yy} & \varepsilon_{yz} \\ \varepsilon_{zx} & \varepsilon_{zy} & \varepsilon_{zz} \end{bmatrix} \\ &= \begin{bmatrix} \varepsilon_{xx} & \frac{\gamma_{xy}}{2} & \frac{\gamma_{xz}}{2} \\ \frac{\gamma_{yx}}{2} & \varepsilon_{yy} & \frac{\gamma_{yz}}{2} \\ \frac{\gamma_{zx}}{2} & \frac{\gamma_{zy}}{2} & \varepsilon_{zz} \end{bmatrix} \end{aligned} \qquad \textbf{Eq. 4.6}$$

In the expression just above, γ_{xy} is just defined as $2\varepsilon_{xy}$.

1.1.3. STATIC ULTRASOUND ELASTOGRAPHY

The Thomas Young's experiment was directly translated to the medical ultrasound imaging field to implement the first imaging technique able to quantify the elasticity of tissues, usually referred to as elastography[350]. In ultrasound

[350] J. Ophir et al., "Elastography: A Quantitative Method for Imaging the Elasticity of Biological Tissues," *Ultrasonic Imaging* 13, no. 2 (April 1, 1991): 111–34, https://doi.org/10.1016/0161-7346(91)90079-W.

imaging, an array of ultrasound transducers is held in contact to the patient's body and sends an ultrasound pulse focused on a small region in the tissue. This process gives the possibility to explore and measure the waves reflected from this region. By repeating this process for the different regions located under the ultrasound probe, it is possible to reconstruct an image representing the amplitude of reflected waves as a function of the spatial position where the reflections occurred. This image is usually called B-mode image.

By acquiring two B-mode images, one with the ultrasound probe just held against the patient's body and another one with the same probe position but by applying a force on the organ under consideration thanks to the probe itself, two B-mode images covering the same region of interest but subject to different stresses will be obtained. By calculating the deformation field between the two images (with a registration algorithm, as seen in the former chapter with 3D Magnetic Resonance Spirometry) and estimating the local strain values from this field, it is possible to obtain a strain image of the tissue. If the strain is lower in a lesion compared to its surrounding tissue, it means that this lesion is stiffer than the surrounding tissue.

This technique thus offers a more quantitative information and a better spatial localization in comparison with palpation. It is available on several commercial ultrasound devices today. Nevertheless, the Young's modulus itself cannot be obtained because the values of the stress in the image FOV are not known. Moreover, this technique suffers from other limitations: like for palpation, the technique is operator dependent and is limited to superficial organs. In addition, during the application of the stress field, the boundary conditions and the inhomogeneity of the generated field are not taken into account. Some research groups call this technique 'compression elastography'[351], which is not correct from a physics point of view. It will be explained why later and the name static elastography will be preferred instead.

1.1.4. DYNAMIC ULTRASOUND ELASTOGRAPHY

The technique introduced in 1.1.3 is usually qualified as static or quasi-static because the two images are acquired in a static tissue state without tissue deformation during the imaging process. Other techniques, referred to as dynamic techniques, were also developed and enable a better control of the applied stress:

- **Acoustic Radiation Force Imaging (ARFI)[352]:** In this technique, the probe of the ultrasound imaging machine focusses an ultrasonic wave at one given location in the biological tissue (see **Figure 4.2**). Because of the transfer of momentum between the acoustic wave beam and the tissue, a force usually referred to as radiation pressure is generated at the focal spot and deforms slightly the tissue at this exact location[353]. After the generation of this deformation, the ultrasonic probe switches to imaging mode, enabling the measurement of the deformation amplitude and its evolution along time thanks to a speckle-tracking technique[354]. The local mechanical properties of the tissue are then extracted from this deformation amplitude and evolution. To obtain an image, the same procedure is repeated for different positions of the focal spot.

[351] Rui Prado-Costa et al., "Ultrasound Elastography: Compression Elastography and Shear-Wave Elastography in the Assessment of Tendon Injury," *Insights into Imaging* 9, no. 5 (October 1, 2018): 791–814, https://doi.org/10.1007/s13244-018-0642-1.
[352] Kathryn R. Nightingale et al., "On the Feasibility of Remote Palpation Using Acoustic Radiation Force," *The Journal of the Acoustical Society of America* 110, no. 1 (July 1, 2001): 625–34, https://doi.org/10.1121/1.1378344.
[353] Takahi Hasegawa and Katuya Yosioka, "Acoustic-Radiation Force on a Solid Elastic Sphere," *The Journal of the Acoustical Society of America* 46, no. 5B (November 1, 1969): 1139–43, https://doi.org/10.1121/1.1911832.
[354] R. J. Dickinson and C. R. Hill, "Measurement of Soft Tissue Motion Using Correlation between A-Scans," *Ultrasound in Medicine and Biology* 8, no. 3 (January 1, 1982): 263–71, https://doi.org/10.1016/0301-5629(82)90032-1.

- **Vibro-acoustography**[355]**:** This technique is carried out by focusing two ultrasonic transducers at the same focal spot in the biological tissue. These two transducers are sending an ultrasonic wave with a frequency difference $\Delta\omega$. It results in an interference phenomenon at the focal spot and, because of the radiation pressure effect at this location, the tissue at the focal spot vibrates at the frequency $\Delta\omega$, creating an acoustic wave that can be measured with a reception transducer. By sweeping the focal spot over a range of $\Delta\omega$ frequencies and by repeating the experiment for different focal spot locations, it is possible to find at each measurement point a fundamental resonance frequency, which was shown to be related to the Young's modulus[356].

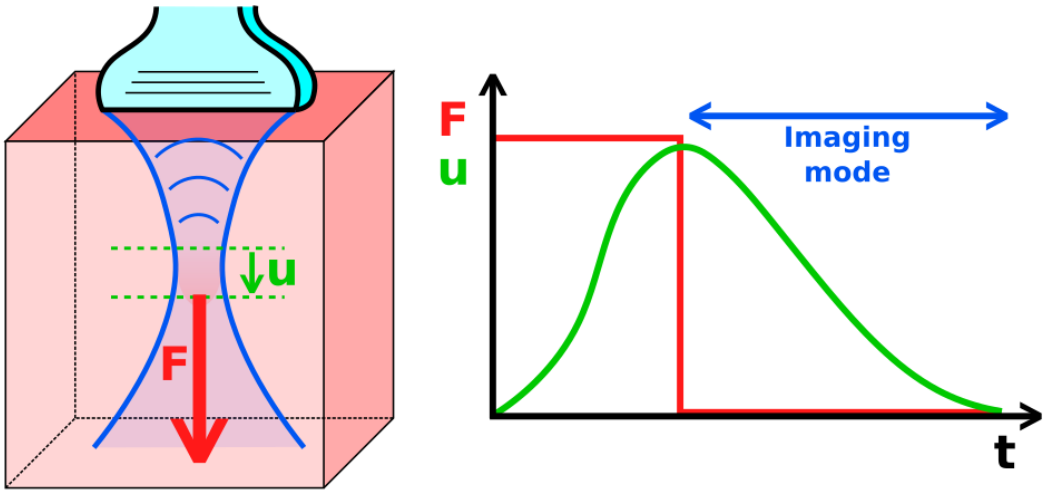

Figure 4.2: Principle of Acoustic Radiation Force Impulse (ARFI) imaging.

In the two methods presented above, the force applied to the biological tissue is more accurately controlled because the relationship between the radiation force and the parameters characterizing the propagation and focus of the acoustic wave is known[357]. Moreover, the ultrasound probe can be controlled with a great precision. This makes the two previous techniques less operator dependent than static elastography. Nevertheless, because of the necessity to focus intense ultrasound beams in the medium, a lot of energy is deposited, leading to heating problems[358]. Moreover, because those two techniques perform a pointwise acquisition, the acquisition time can be long. In ARFI for example, a time duration comprised between 10 and 25 ms is needed to perform one measurement point, which leads to a total acquisition time of several seconds to cover a 1.5 cm square FOV with a 1 mm isotropic planar resolution. Furthermore, even if the quantity measured here depends on the Young's modulus, it depends on a great number of other acquisition and material parameters and properties. The

[355] Mostafa Fatemi and James F. Greenleaf, "Ultrasound-Stimulated Vibro-Acoustic Spectrography," *Science* 280, no. 5360 (April 3, 1998): 82–85, https://doi.org/10.1126/science.280.5360.82.

[356] Mostafa Fatemi and James F. Greenleaf, "Application of Radiation Force in Noncontact Measurement of the Elastic Parameters," *Ultrasonic Imaging* 21, no. 2 (April 1, 1999): 147–54, https://doi.org/10.1177/016173469902100205.

[357] Kathryn Nightingale et al., "Acoustic Radiation Force Impulse Imaging: In Vivo Demonstration of Clinical Feasibility," *Ultrasound in Medicine & Biology* 28, no. 2 (February 1, 2002): 227–35, https://doi.org/10.1016/S0301-5629(01)00499-9.

[358] M. L. Palmeri and K. R. Nightingale, "On the Thermal Effects Associated with Radiation Force Imaging of Soft Tissue," *IEEE Transactions on Ultrasonics, Ferroelectrics, and Frequency Control* 51, no. 5 (May 2004): 551–65, https://doi.org/10.1109/TUFFC.2004.1320828.

quantification of E is therefore far to be accurate. For that reason, if a quantitative mapping of E is required, an advanced understanding of the underlying physics and the consideration of other imaging strategies will be needed.

1.2. ULTRASOUND ELASTOGRAPHY TECHNIQUES BASED ON THE IMAGING OF SHEAR WAVES PROPAGATION IN TISSUES

The Young's modulus E has the great advantage to be intuitive: the Thomas Young's experiment is simple to set up and very close to the medical practice of palpation, and the Hooke's law is very simple to understand. Nevertheless, E is not sufficient to understand what really happens in terms of deformations inside a purely elastic medium and can hide a mixture of different physical phenomena like:

- **Compression**, which refers to a change of volume for a piece of elastic material without any change of its shape, and
- **Shear**, which refers to a change of shape for a piece of elastic material without any change of its volume.

These mechanical changes can be better understood with two other mechanical moduli.

1.2.1. NOTIONS OF COMPRESSION AND BULK MODULUS

The first one is called bulk modulus, usually written K. It characterizes pure material compression (see **Figure 4.3**).

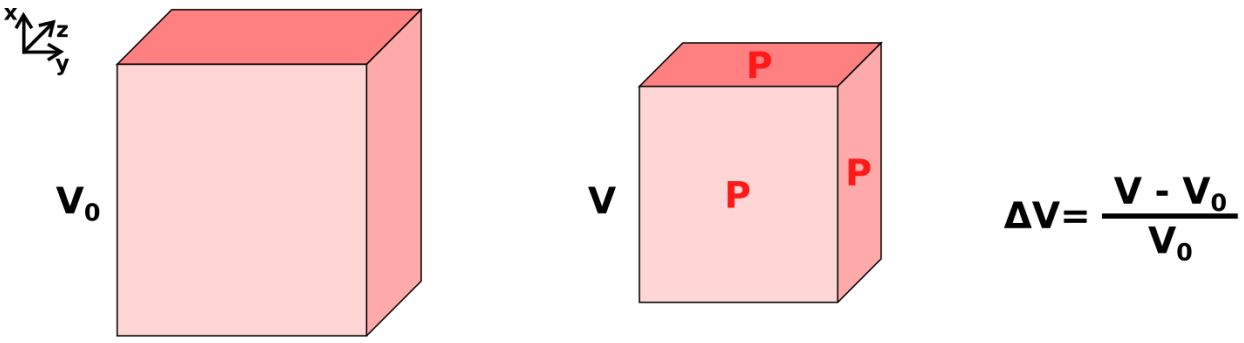

Figure 4.3: Compression experiment to define the bulk modulus K.

K represents the proportionality coefficient between the external pressure applied on a piece of purely elastic material, written P, and its relative change of volume, written ΔV:

$$P = -K\Delta V \qquad \textbf{Eq. 4.7}$$

K represents for the material its resistance to volume change when an isostatic pressure is applied.

1.2.2. NOTIONS OF SHEAR AND SHEAR MODULUS

The second one is called shear modulus, or second coefficient of Lamé. It is usually written μ and characterizes pure material shear (see **Figure 4.4**).

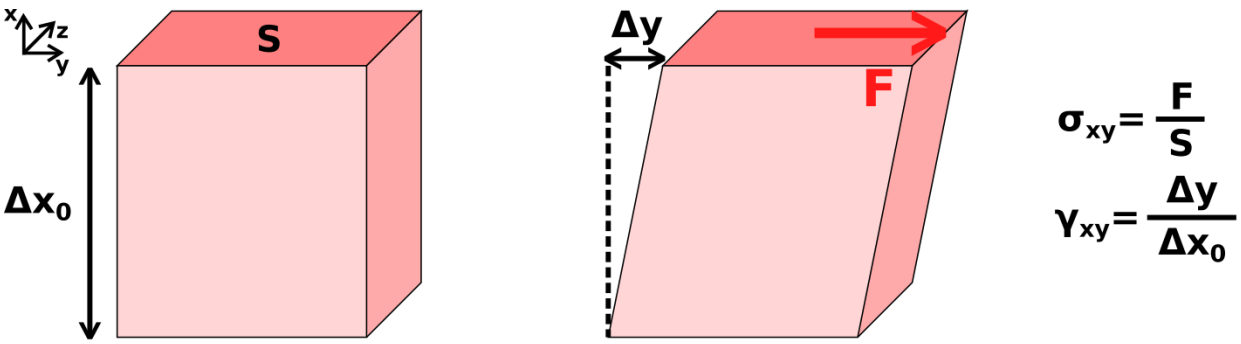

Figure 4.4: Shear experiment to define the shear modulus μ.

μ represents the proportionality coefficient between a shear stress applied on a piece of material, written σ_{xy}, and the resulting shear strain, written γ_{xy} in **Eq. 4.6**:

$$\sigma_{xy} = \mu\gamma_{xy} \qquad \textbf{Eq. 4.8}$$

For the material, μ represents its resistance to isovolumetric shape change when a shear stress is applied to it. γ_{xy} corresponds to a gradient along x of a displacement of material along y.

1.2.3. RELATIONSHIP BETWEEN THE YOUNG'S MODULUS, THE BULK MODULUS AND THE SHEAR MODULUS IN SOFT BIOLOGICAL TISSUES

These two quantities, K and μ, are not as easy to measure as E, but they have the advantage to independently describe compression and shear respectively, which imply distinct underlying physical phenomena. Moreover, E can be expressed as a function of K and μ:

$$E = \frac{9K\mu}{3K + \mu} \qquad \textbf{Eq. 4.9}$$

This equation confirms that, despite its simplicity, the result of Thomas Young's experiment expresses two distinct physical effects. Nevertheless, in soft biological tissues, K is usually much higher than μ: the order of magnitude for K is usually the gigapascal, whereas the order of magnitude for μ is the kilopascal.

Sometimes, the biological tissues are said 'incompressible', which is wrong but considered as a good approximation to simplify some problems. In particular, this large difference between the two values gives the possibility to simplify the previous formula between E, K and μ for biological tissues:

$$E \approx \frac{9K\mu}{3K} = 3\mu \qquad \textbf{Eq. 4.10}$$

This leads to the following conclusion: for soft biological tissues, E and μ can be considered as similar parameters in the sense that E results mostly from tissue shear strain. During palpation, the medical practitioner thus creates a pure shear strain field in the nearly incompressible organ under consideration, which is not trivial at first glance because of the quasi-uniaxial force he or she generates, which can sometimes be mistakenly called 'compression', and this is why the term 'compression elastography' found in several publications is not well suited.

More interestingly, this conclusion also means that E will be estimated with rather good accuracy from pure shear experiments.

1.2.4. PROPAGATION OF COMPRESSION AND SHEAR WAVES IN SOFT BIOLOGICAL TISSUES

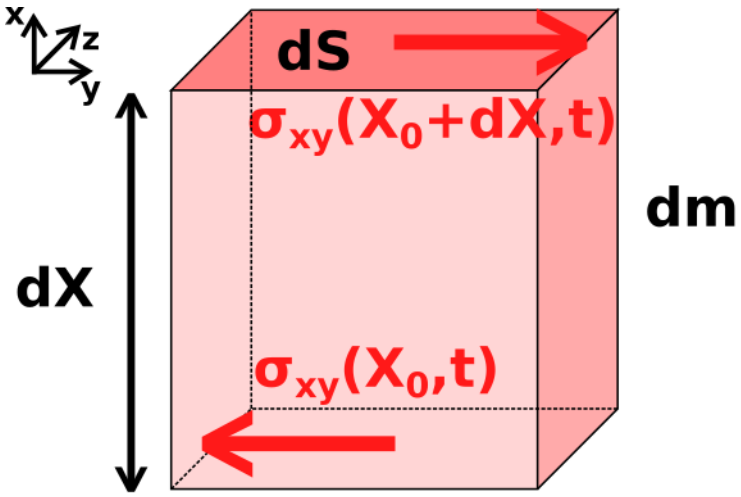

Figure 4.5: Dynamic physical quantities related to an elementary volume of elastic material during a shear experiment.

We consider the same shear experiment as seen in 1.2.2 in a semi-infinite, homogeneous, isotropic and purely elastic material, with the x direction being normal to the surface of the semi-infinite material under consideration, and with a force applied along the y direction, but in the dynamic case and not in the quasi-static case anymore. This consideration means that σ_{xy} and γ_{xy} can now vary along time. To solve this problem, an elementary volume of mass dm is considered, with a surface orthogonal to the x direction equal to dS and comprised between the positions X_0 and $X_0 + dX$ along the x axis (see **Figure 4.5**). The Newton's second law of motion applied to this particle gives:

$$\begin{aligned} dm\frac{\partial^2 u_y}{\partial t^2}(X_0,t) &= \left(\sigma_{xy}(X_0+dX,t)-\sigma_{xy}(X_0,t)\right)dS \\ &\approx \frac{\partial \sigma_{xy}}{\partial X}(X_0,t)dSdX \end{aligned} \qquad \textbf{Eq. 4.11}$$

The expression just above links the acceleration of this elementary volume of matter, its mass and the forces applied on the surfaces located at positions X_0 and $X_0 + dx$. $u_y(X_0,t)$ represents here the displacement of the particle of matter from its original equilibrium position X_0 at time t (Lagrangian point of view). By introducing the density ρ of the material and the relationship defining the shear modulus μ seen in **Eq. 4.8**, it gives:

$$\rho\frac{\partial^2 u_y}{\partial t^2}(X_0,t) = \mu\frac{\partial \gamma_{xy}}{\partial X}(X_0,t) \qquad \textbf{Eq. 4.12}$$

Given the differential definition of shear strain components without rigid body rotations, as seen in the previous chapter, and because there is no displacement along direction x, we have:

$$\begin{aligned} \gamma_{xy} &= \frac{\partial u_x}{\partial Y}+\frac{\partial u_y}{\partial X} \\ &= \frac{\partial u_y}{\partial X} \end{aligned} \qquad \textbf{Eq. 4.13}$$

Therefore, the equation becomes:

$$\frac{\partial^2 u_y}{\partial X^2} - \frac{1}{{c_S}^2}\frac{\partial^2 u_y}{\partial t^2} = 0 \qquad \textbf{Eq. 4.14}$$

with:

$$c_S = \sqrt{\frac{\mu}{\rho}} \qquad \textbf{Eq. 4.15}$$

A wave equation for the shear components of displacement (orthogonal to the direction of propagation) is easily recognized. This type of wave is usually called shear wave (or secondary wave, or S-wave) and c_S is the velocity of those waves in the purely elastic material.

If the problem is solved for the compression components (along the direction of propagation) instead, a new wave equation is obtained, characterizing the evolution of a compression wave (or primary wave, or P-wave) that propagates at a velocity c_P given by:

$$\begin{aligned} c_P &= \sqrt{\frac{K + \frac{4\mu}{3}}{\rho}} \\ &\approx \sqrt{\frac{K}{\rho}} \end{aligned} \qquad \textbf{Eq. 4.16}$$

for biological tissues, because $K \gg \mu$. This also leads to $c_P \gg c_S$.

Therefore, if a mechanical excitation is performed at the surface of a biological tissue, two wave patterns are created and superimpose in the general case:

- A compression wave, which propagates rapidly (around 1500 m/s in most soft biological tissues).
- A shear wave, which propagates slowly (around several m/s in most soft biological tissues).

Even if those relationships were demonstrated for a semi-infinite homogeneous medium, they still can be considered in a medium of finite volume with a heterogeneous content in terms of density ρ and mechanical properties K and μ, as far as the characteristic length for the evolution of these quantities remains large compared to the characteristic length of the wave pattern (for example, the wavelength in the case of a monochromatic wave). If this condition is verified locally in the biological tissue, the compression wave propagates at a velocity depending only on the local density and bulk modulus, and the shear wave propagates at a velocity depending only on the local density and shear modulus. Otherwise, the principal effects of the organ boundaries and the tissue heterogeneities appear as wave reflections and mode conversions[359].

[359] Ernest L. Madsen, H. John Sathoff, and James A. Zagzebski, "Ultrasonic Shear Wave Properties of Soft Tissues and Tissuelike Materials," *The Journal of the Acoustical Society of America* 74, no. 5 (November 1, 1983): 1346–55, https://doi.org/10.1121/1.390158.

1.2.5. ULTRASOUND ELASTOGRAPHY TECHNIQUES BASED ON THE PROPAGATION OF SHEAR WAVES

The wave propagation phenomenon and the direct link between shear wave velocity and shear modulus, which is itself highly related to the Young's modulus, opens the door to a new family of ultrasound elastography techniques, referred to as oscillatory techniques when they are based on the generation of temporally continuous and harmonic perturbations (vibro-acoustography is an oscillatory technique), or transient techniques when they are based on a pulsed perturbation (ARFI is a transient technique). These two families are sub-families of the dynamic elastography family. The oscillatory and transient techniques based on shear wave imaging are all based on the same three experimental steps:

- **Step 1:** Creating an acoustic wave at the surface or from the inside of the biological tissue. This wave thus propagates from this source into the surrounding tissue.
- **Step 2:** Recording along time the displacement field induced by the propagation of this wave in the biological tissue
- **Step 3:** Reconstructing from the recorded displacement fields a map of μ.

Most of the different dynamic elastography methods essentially differ either on wave generation (type of source, position of this source, type of generated wave, …), displacement wave tracking (number of image dimensions, pointwise or full-field imaging) and reconstruction (time-of-flight, rheological modelling, …). The major different methods developed during the last 20 years are listed and described below[360]:

- **Sonoelasticity imaging**[361] [362]**:** This oscillatory technique is based on the ultrasound Doppler measurement (which is originally designed to measure blood flow velocities) of vibrations induced by monochromatic acoustic waves externally generated and propagating inside the biological tissue to the targeted organ. With such Doppler measurements, it was shown that stiffer regions vibrate with a lower motion amplitude, giving the possibility to detect lesions in tissue thanks to the amplitude of vibration different between the lesion and its surrounding medium. This technique has the advantage to make possible the detection of mechanical inhomogeneities that are not visible with standard B-mode imaging. Nevertheless, even if theoretical demonstrations were made to explain the phenomenon[363], the specificity of this technique remains limited in the sense that E is not quantified and the change in motion amplitude can be related to other phenomena (the viscosity of the tissue for example, as explained later).

[360] J. -L. Gennisson et al., "Ultrasound Elastography: Principles and Techniques," *Diagnostic and Interventional Imaging*, Ultrasound elastography, 94, no. 5 (May 1, 2013): 487–95, https://doi.org/10.1016/j.diii.2013.01.022.
[361] Robert M. Lerner, S. R. Huang, and Kevin J. Parker, "'Sonoelasticity' Images Derived from Ultrasound Signals in Mechanically Vibrated Tissues," *Ultrasound in Medicine and Biology* 16, no. 3 (January 1, 1990): 231–39, https://doi.org/10.1016/0301-5629(90)90002-T.
[362] K. J. Parker et al., "Tissue Response to Mechanical Vibrations for 'Sonoelasticity Imaging,'" *Ultrasound in Medicine & Biology* 16, no. 3 (January 1, 1990): 241–46, https://doi.org/10.1016/0301-5629(90)90003-U.
[363] L. Gao et al., "Sonoelasticity Imaging: Theory and Experimental Verification," *The Journal of the Acoustical Society of America* 97, no. 6 (June 1, 1995): 3875–86, https://doi.org/10.1121/1.412399.

- **1D transient elastography**[364] [365] [366]**:** This technique consists in generating a shear wave transient pulse (of short duration) in an elastic medium and in following its propagation thanks to a 1D ultrasound imaging system only composed of one piezoelectric transducer able to send focused ultrasound pulses and record the echoes generated during their propagation in the medium. This practice is commonly referred to as M-mode measurements. The shear wavefront creates a modulation in the A-mode signal (created by the echoes measured along one line in the tissue), giving the possibility to follow its propagation along time if the A-mode acquisition is repeated at a sufficient temporal rate (its 2D space-time representation constitutes the aforementioned M-mode measurement). This is made possible by the fact that the modulation wave is a shear wave, propagating at velocities of a few meters per seconds, whereas the waves created and recorded in a M-mode acquisition are compression waves, propagating at a velocity around 1500 m/s, as seen in 1.2.4. A lot of A-mode acquisitions can therefore be performed during the propagation of the shear perturbation in the elastic medium. By tracking the time evolution of the shear wave pulse, its velocity can be estimated, leading directly to a measurement of the shear modulus μ by assuming a tissue density ρ equal to 1 g/cm^3. A measurement of the Young's modulus E can therefore be obtained by multiplying μ by 3. A commercial medical device based on this technique, and called the FibroScan®, is developed and commercialized by the company Echosens and used for the diagnosis of liver fibrosis[367] [368].

- **ARFI-SWS**[369]**:** This technique is an extension of the ARFI technique presented in 1.1.4. Instead of tracking the local displacement and relaxation of tissue as an acoustic radiation force is applied, ARFI-SWS follows along time the propagation of the transient shear wave created when this force is applied for a short time (around 1 ms). As seen previously with 1D transient elastography, the elasticity is estimated from the velocity at which the shear wave propagates (hence the name of the method, SWS standing for Shear Wave Speed). This technique is therefore a particular case of the Shear Wave Elasticity Imaging (SWEI) theoretically studied a few decades ago[370]. Nevertheless, the usual image acquisition rate for a standard 2D ultrasound imaging system is low (around 50 Hz). Moreover, the shear wavefront obtained usually is not plane, the displacement amplitude is low and the attenuation of the shear wave can be consequent.

[364] S. Catheline et al., "Diffraction Field of a Low Frequency Vibrator in Soft Tissues Using Transient Elastography," *IEEE Transactions on Ultrasonics, Ferroelectrics, and Frequency Control* 46, no. 4 (July 1999): 1013–19, https://doi.org/10.1109/58.775668.

[365] L. Sandrin et al., "Shear Elasticity Probe for Soft Tissues with 1-D Transient Elastography," *IEEE Transactions on Ultrasonics, Ferroelectrics, and Frequency Control* 49, no. 4 (April 2002): 436–46, https://doi.org/10.1109/58.996561.

[366] Jean-Luc Gennisson et al., "Transient Elastography in Anisotropic Medium: Application to the Measurement of Slow and Fast Shear Wave Speeds in Muscles," *The Journal of the Acoustical Society of America* 114, no. 1 (July 1, 2003): 536–41, https://doi.org/10.1121/1.1579008.

[367] Laurent Sandrin et al., "Transient Elastography: A New Noninvasive Method for Assessment of Hepatic Fibrosis," *Ultrasound in Medicine & Biology* 29, no. 12 (December 1, 2003): 1705–13, https://doi.org/10.1016/j.ultrasmedbio.2003.07.001.

[368] Laurent Castéra et al., "Prospective Comparison of Transient Elastography, Fibrotest, APRI, and Liver Biopsy for the Assessment of Fibrosis in Chronic Hepatitis C," *Gastroenterology* 128, no. 2 (February 1, 2005): 343–50, https://doi.org/10.1053/j.gastro.2004.11.018.

[369] Kathryn Nightingale, Stephen McAleavey, and Gregg Trahey, "Shear-Wave Generation Using Acoustic Radiation Force: In Vivo and Ex Vivo Results," *Ultrasound in Medicine & Biology* 29, no. 12 (December 1, 2003): 1715–23, https://doi.org/10.1016/j.ultrasmedbio.2003.08.008.

[370] Armen P Sarvazyan et al., "Shear Wave Elasticity Imaging: A New Ultrasonic Technology of Medical Diagnostics," *Ultrasound in Medicine & Biology* 24, no. 9 (December 1, 1998): 1419–35, https://doi.org/10.1016/S0301-5629(98)00110-0.

For those reasons, this technique needs more developed image acquisition schemes and remains limited to small FOV (typically a few millimeters).

- **2D transient elastography**[371]**:** In this technique, the shear wave pulse is generated by an external vibrator surrounding the ultrasound imaging probe, and its propagation is followed with 2D echography in ultrafast mode: instead of acquiring one 2D image through the repeated generation of focused ultrasounds and echo measurement to cover the full image surface, only a few plane waves are generated[372] and the echoes are recorded to create the full image. This technique gives the possibility to reach image acquisition rates above 10,000 Hz instead of the usual 50 Hz. The shear wave propagation can therefore be followed in 'real-time' and the Young's modulus, estimated through local wave velocity calculation. *In vivo* application on breast tumor detection was promising but difficult because of the volume and weight of the entire system[373] (ultrasound probe + external vibrator).

- **Supersonic Shear Imaging (SSI)**[374]**:** The SSI technique combines the advantages of both ARFI-SWS and 2D transient elastography. Instead of generating a shear wave through the application of acoustic radiation pressure on one focused spot in the tissue, leading to a non-plane wavefront, the focus spot generating this force is spatially shifted along a line with a shift velocity higher than the shear wave velocity. It leads to the generation of a Mach cone that appears as a plane wavefront in the image plane. The energy of this conic wave is less spatially dispersed and geometrically attenuated than the spherical wave generated in ARFI-SWS, leading to a better detectability of the wavefront in a larger image FOV. Once generated, the propagation of this wavefront is followed by the ultrafast imaging mode presented just above, enabling 'real-time' wavefront tracking thanks to a time-of-flight method, from which a velocity map and thus a Young's modulus map can be obtained. This technology, initially developed at the Institut Langevin in Paris, was exploited by the company Supersonic Imagine in their ultrafast diagnostic ultrasound imaging device, the Aixplorer®. This technique was validated in numerous studies, in particular for the detection and characterization of breast lesions[375] [376] [377], the study of liver fibrosis[378] and the anisotropic properties

[371] L. Sandrin et al., "Shear Modulus Imaging with 2-D Transient Elastography," *IEEE Transactions on Ultrasonics, Ferroelectrics, and Frequency Control* 49, no. 4 (April 2002): 426–35, https://doi.org/10.1109/58.996560.

[372] M. Tanter et al., "Ultrafast Compound Imaging for 2-D Motion Vector Estimation: Application to Transient Elastography," *IEEE Transactions on Ultrasonics, Ferroelectrics, and Frequency Control* 49, no. 10 (October 2002): 1363–74, https://doi.org/10.1109/TUFFC.2002.1041078.

[373] J. Bercoff et al., "In Vivo Breast Tumor Detection Using Transient Elastography," *Ultrasound in Medicine & Biology* 29, no. 10 (October 1, 2003): 1387–96, https://doi.org/10.1016/S0301-5629(03)00978-5.

[374] J. Bercoff, M. Tanter, and M. Fink, "Supersonic Shear Imaging: A New Technique for Soft Tissue Elasticity Mapping," *IEEE Transactions on Ultrasonics, Ferroelectrics, and Frequency Control* 51, no. 4 (April 2004): 396–409, https://doi.org/10.1109/TUFFC.2004.1295425.

[375] Mickael Tanter et al., "Quantitative Assessment of Breast Lesion Viscoelasticity: Initial Clinical Results Using Supersonic Shear Imaging," *Ultrasound in Medicine & Biology* 34, no. 9 (September 1, 2008): 1373–86, https://doi.org/10.1016/j.ultrasmedbio.2008.02.002.

[376] David O. Cosgrove et al., "Shear Wave Elastography for Breast Masses Is Highly Reproducible," *European Radiology* 22, no. 5 (May 1, 2012): 1023–32, https://doi.org/10.1007/s00330-011-2340-y.

[377] Wendie A. Berg et al., "Shear-Wave Elastography Improves the Specificity of Breast US: The BE1 Multinational Study of 939 Masses," *Radiology* 262, no. 2 (February 1, 2012): 435–49, https://doi.org/10.1148/radiol.11110640.

[378] Éric Bavu et al., "Noninvasive In Vivo Liver Fibrosis Evaluation Using Supersonic Shear Imaging: A Clinical Study on 113 Hepatitis C Virus Patients," *Ultrasound in Medicine & Biology* 37, no. 9 (September 1, 2011): 1361–73, https://doi.org/10.1016/j.ultrasmedbio.2011.05.016.

of muscle[379] (by making measurement with the ultrasonic probe oriented along different directions). More recently, a 3D imaging mode was implemented on the Aixplorer®, providing the possibility to follow the shear wavefront evolution in a 3D volume[380].

- **Comb-push Ultrasound Shear Elastography (CUSE)**[381]**:** This more recent technique uses the same technical innovations as SSI (radiation pressure and ultrafast imaging) but, instead of generating waves with a rapidly shifted focused ultrasound beam before the image acquisition, the wave pattern is generated by sending unfocused ultrasound waves only from a subset of the piezoelectric elements used for imaging. The wave velocity is then estimated with a time-of-flight method.

1.2.6. PARAMETRIC RECONSTRUCTION IN SHEAR WAVE ULTRASOUND ELASTOGRAPHY

For any oscillatory or transient dynamic elastography method, a reconstruction step is needed to estimate the E or μ map from the images representing the wave pattern that propagates inside the biological tissue along time. Globally, and as for many numerical problem resolutions, two families of methods exist[382]:

- **Methods based on the direct resolution of the inverse problem** (from the 'consequence' to the 'cause'), that directly try to deduce the E map from the wave pattern. It is usually based on the inversion of the wave propagation equation. This is the case of the time-of-flight method[383] used in SSI, for example. These methods are usually fast and simple but are sensitive to the noise present in the original images.

- **Methods based on the iterative resolution of the forward problem** (from the 'cause' to the 'consequence') to find the best solution for the inverse problem. Those methods usually try to iteratively find the best E map by minimizing a metric depending on both the acquired data and calculated data from an estimation of the mechanical properties and try to improve these estimations. These methods are usually based on advanced numerical methods (finite elements[384], …) and are usually more robust against the noise in comparison to direct reconstruction methods. However, they are usually slower and often need more information at the beginning (boundary conditions, …).

[379] Jean-Luc Gennisson et al., "Viscoelastic and Anisotropic Mechanical Properties of in Vivo Muscle Tissue Assessed by Supersonic Shear Imaging," *Ultrasound in Medicine & Biology* 36, no. 5 (May 1, 2010): 789–801, https://doi.org/10.1016/j.ultrasmedbio.2010.02.013.
[380] Jean Provost et al., "3D Ultrafast Ultrasound Imaging in Vivo," *Physics in Medicine & Biology* 59, no. 19 (2014): L1, https://doi.org/10.1088/0031-9155/59/19/L1.
[381] P. Song et al., "Comb-Push Ultrasound Shear Elastography (CUSE): A Novel Method for Two-Dimensional Shear Elasticity Imaging of Soft Tissues," *IEEE Transactions on Medical Imaging* 31, no. 9 (September 2012): 1821–32, https://doi.org/10.1109/TMI.2012.2205586.
[382] Kathryn Nightingale, Stephen McAleavey, and Gregg Trahey, "Shear-Wave Generation Using Acoustic Radiation Force: In Vivo and Ex Vivo Results," *Ultrasound in Medicine & Biology* 29, no. 12 (December 1, 2003): 1715–23, https://doi.org/10.1016/j.ultrasmedbio.2003.08.008.
[383] Mickael Tanter et al., "Quantitative Assessment of Breast Lesion Viscoelasticity: Initial Clinical Results Using Supersonic Shear Imaging," *Ultrasound in Medicine & Biology* 34, no. 9 (September 1, 2008): 1373–86, https://doi.org/10.1016/j.ultrasmedbio.2008.02.002.
[384] M. M. Doyley, P. M. Meaney, and J. C. Bamber, "Evaluation of an Iterative Reconstruction Method for Quantitative Elastography," *Physics in Medicine & Biology* 45, no. 6 (2000): 1521, https://doi.org/10.1088/0031-9155/45/6/309.

1.2.7. COMPARISON BETWEEN TRANSIENT TECHNIQUES AND OSCILLATORY TECHNIQUES

Shear wave fields obtained from transient methods are far easier to analyze than those obtained in oscillatory methods, essentially for two reasons:

- The first one is related to the superposition between compression and shear wave patterns in oscillatory methods. Because the mechanical excitation is continuously applied during the imaging process, compression and shear wave patterns are measured. The measured wave pattern comprises both shear and compression waves, the latter depending not on E but K. This wave superposition thus biases the reconstruction step. In transient techniques, as the image is acquired after the generation of displacement waves, the compression wave has already travelled away out of the FOV because it propagates much faster than the shear wave (see 1.2.4) such that only the shear wave remains visible in transient techniques.

- The second one is related to the wave reflections that can appear at the boundaries of the organ of interest. In continuum mechanics, when an acoustic wave reaches the interface between two media featuring different mechanical properties, the energy of the wave is split between a reflected wave, which propagates back in the medium, and a refracted wave, which goes through the interface. When several waves are propagating in the same medium along different directions (which can arise in a closed cavity because of reflections, as in an organ for example), a wave interference pattern showing a standing wave (that does not propagate) becomes usually visible. Because the assessment of E is usually based on the measurement of wave velocity, it is more challenging to perform elastography from a non-propagative standing wave. For transient techniques, the displacement field can be captured before the shear wave gets reflected at the boundary. The shear wave velocity can therefore be estimated from its 'first pass' in the biological tissue, without considering the images after the moment when the first reflections appear.

1.3. VISCOSITY AND VISCOELASTICITY IN ULTRASOUND ELASTOGRAPHY

In the previous presentation of the physical concepts and their exploitation to measure the elasticity of biological tissues (see 1.1 and 1.2), we made the hypothesis that our biological medium was a purely elastic medium. It means that when a stress is applied to such a material, a strain appears, and this strain is directly proportional to the stress applied with a proportionality coefficient driven by the bulk modulus K and, essentially for biological tissues, by the shear modulus μ. More importantly, this relationship does not depend on time: at each time point of the experiment, the relationship between the stress and the strain does not depend on what happened before this time point. For example, the stress might have been constant from the beginning of the experiment or linearly increased from this starting time, the final result remains the same: the final strain field only depends on the final stress and on the shear modulus distribution in the material (and also on the bulk modulus in a more general case). The deformation state reached by the material is therefore an equilibrium state that can only change if the stress or the moduli change too. Furthermore, if the stress is released, the material recovers its initial shape. However, this is not true for most biological tissues in the human body.

1.3.1. NOTIONS OF VISCOSITY AND VISCOELASTICITY IN SOFT BIOLOGICAL TISSUES

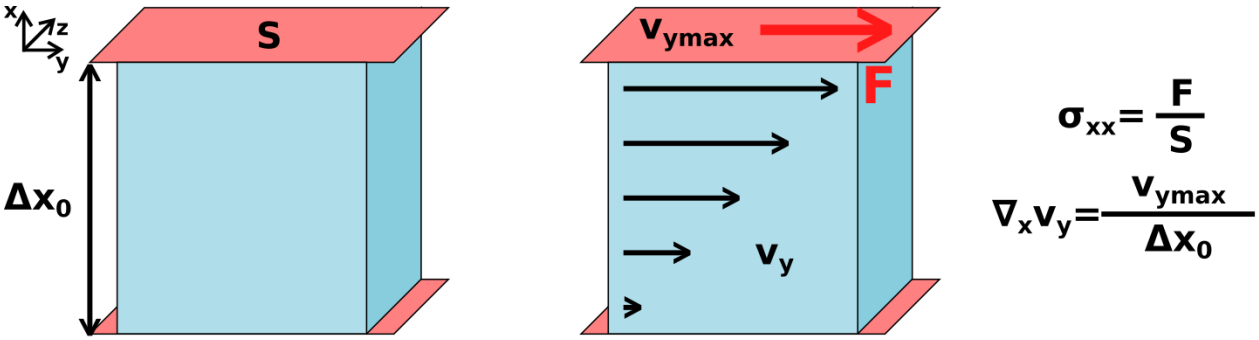

Figure 4.6: Shear experiment on a viscous liquid performed to define its viscosity η.

Biological tissues do not only have an elasticity property but also a viscosity property. They are usually referred to as viscoelastic. At the atomic scale, viscosity is explained by the diffusion of momentum inside the biological tissue, in particular through the diffusion of atoms or molecules in the material microstructure. At the macroscopic scale, it results in a frictional energy loss for the material every time a deformation occurs[385]. Moreover, if the strain is not constant, because the mean diffusion distance depends on the time given to the atoms or molecules to cover this distance, the amount of frictional energy loss directly depends on the strain rate. For that reason, even if the stress is the same at the end of two given shear experiments on the same type of material, the final result in terms of strain fields can be different if the strain rate evolution along the two experiments were not the same.

The easiest way to understand the notion of viscosity is to consider a liquid because the shear modulus μ of a liquid is equal to 0: when a transverse stress is applied to a liquid, this material deforms until the application of the stress stops. Moreover, to simplify the problem, only Newtonian materials will be considered, which are materials featuring a viscosity that does not depend on their strain rate. In this case, we consider a shear stress applied thanks to a moving plate located at the surface of such a liquid and with an infinite surface, and a similar static plate parallel to the first one and delimitating the infinite volume of liquid taken into consideration for this experiment. In this situation, a stationary velocity field is reached everywhere in the fluid with a maximum velocity at the contact of the moving plate and with a decrease of velocity as the flowing material is located far from this surface and close to the static one (see **Figure 4.6**). This velocity gradient, written $\nabla_x v_y$, which is uniform in the volume of liquid under consideration when the equilibrium is reached, is directly proportional to the surface force applied with the moving plate, written σ_{xy}, through this relationship:

$$\sigma_{xy} = \eta \nabla_x v_y \qquad \textbf{Eq. 4.17}$$

with η being the viscosity of the fluid, expressed in Pascal·seconds (Pa·s). This expression remains the same locally if the spatial evolution of v_y is not linear globally.

To understand the generation of this velocity gradient, the origin of viscosity should be reminded. It comes from the spatial diffusion of momentum through the diffusion of atoms or molecules in the material. Because of this diffusion phenomenon, if an atom or molecule in the liquid is put in motion by the moving plate, it diffuses in the fluid, goes away from the moving plate and puts in motion other atoms and molecules. The final equilibrium result

[385] Marc A. Meyers and Krishan Kumar Chawla, *Mechanical Behavior of Materials*, 2nd ed (Cambridge ; New York: Cambridge University Press, 2009).

is a fluid in motion everywhere with a local velocity depending on the proximity of the fluid atoms or molecules to the moving plate.

In **Eq. 4.17**, v_y verifies:

$$v_y = \frac{\partial u_y}{\partial t} \qquad \textbf{Eq. 4.18}$$

with u_y the component of displacement along the direction y. Moreover, γ_{xy} was defined as:

$$\gamma_{xy} = \frac{\partial u_y}{\partial X} \qquad \textbf{Eq. 4.19}$$

The relationship defining η is thus equivalent to:

$$\sigma_{xy} = \eta \frac{\partial \gamma_{xy}}{\partial t} \qquad \textbf{Eq. 4.20}$$

For purely viscous Newtonian fluids, the velocity gradient is therefore equal to the shear strain rate. Because the viscosity property of fluids is observed in viscoelastic materials, this explains why the result of a shear experiment on those materials will depend on the evolution of strain rate. This can be observed clearly in the graphic representation of the evolution of strain as a function of the applied stress. Whereas this representation is linear for a purely elastic solid, without any dependence on the strain rate, this representation will usually be different for a viscoelastic material. A mechanical cycle composed of the application of a stress and its release on a viscoelastic material will thus draw a loop on the representation of σ_{xy} as a function of γ_{xy} (see **Figure 4.7**). It can even be shown that the area of this hysteresis loop is proportional to the energy dissipated during the mechanical cycle because of frictional losses, and which is dissipated by conversion into heat.

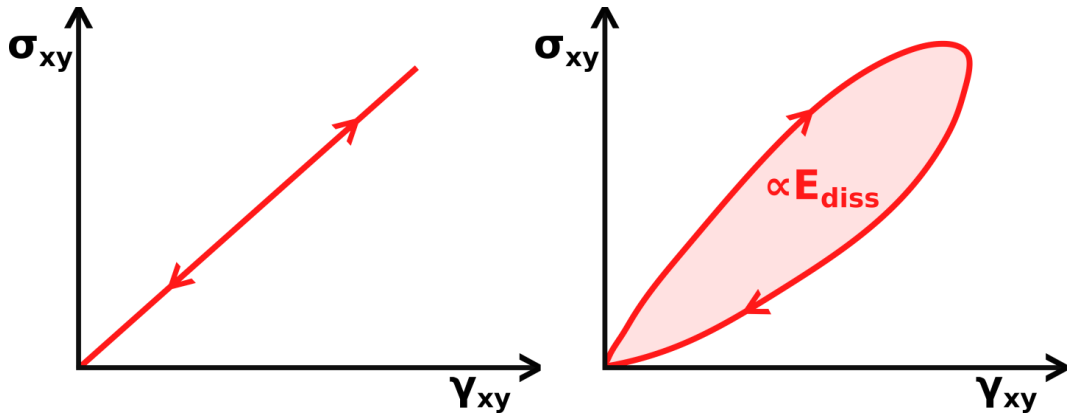

Figure 4.7: Graphical representation of σ_{xy} as a function of γ_{xy} for a purely elastic material (left) and for a viscoelastic material (right).

1.3.2. CONSEQUENCES OF THE VISCOSITY IN ULTRASOUND ELASTOGRAPHY

In the previously described medical imaging applications, viscosity will have a major impact on the quantification of E because of the shear wave attenuation it causes. Experimentally, this viscosity related attenuation can be associated to other attenuation processes, as those related to the geometry of wavefronts, or to the micro-reflections of waves propagating in heterogeneous media. Because viscosity results in frictional losses, the energy

that propagates in a medium through the propagation of shear strain decreases along space. This effect results in a decrease of the wave amplitude along the propagation path. This will have many consequences on the imaging process, with the three main ones described here:

- **The image FOV is reduced:** Because of the attenuation of shear waves in viscoelastic media, and because most dynamic methods are based on the measurement of shear wave velocity in an entire volume of tissue, the FOV is usually limited to the regions in which the waves remain visible. For example, this is one of the reasons why the ARFI-SWS technique is only limited to FOV of a few millimeters.

- **Only low frequency mechanical excitation can be used:** It can be shown that the linear attenuation coefficient characterizing the attenuation of shear waves increases with the temporal frequency of the excitation. Because of this effect, only shear waves with a frequency comprised between a few hertz and a few hundreds of hertz can be used in human practice.

- **Most standard reconstruction methods assume purely elastic tissues:** In oscillatory methods, parametric reconstruction strategies based on the inversion of the wave equation can lead to biased results when the attenuation of the displacement amplitude is not taken into account. Moreover, in transient methods, because the material is usually excited with a shear wave pulse of short duration, a mechanical excitation featuring a large bandwidth of shear wave frequencies is sent in the material. The shape of the wavefront tracked in the ultrasound images will usually spread along the propagation as the different frequency components propagate at different speed in a viscoelastic medium. Besides, the transient pulse usually loses more rapidly its high frequency components along the propagation path. Once again, this might bias the estimation of the local shear wavefront velocity, leading to errors in the value of E.

1.3.3. MEASUREMENT OF VISCOSITY IN ULTRASOUND ELASTOGRAPHY

Some reconstruction techniques take into account viscosity[386] to map the viscosity η in the FOV at the same time as E. This opportunity is valuable as viscosity was shown to be a biomarker of interest for some diseases[387]. To take into account viscosity in the reconstruction process, two main strategies can be followed:

- The first one consists in using a rheological model, which links σ_{xy}, γ_{xy} and their time derivatives. The two main rheological models are the Maxwell Model, that considers the viscoelastic material as if it was composed of a purely elastic component and a purely viscous component set in series, and the Kelvin-Voigt model, that consider those two same components in parallel. These two models do not describe perfectly all the viscoelastic materials but many other more complicated models exist.

- The second one consists in defining a shear modulus mathematically represented as a complex number, and not a real number. This complex modulus, usually called dynamic modulus and written G^*, is defined as the ratio between σ_{xy} and γ_{xy} when those two quantities are represented as oscillatory components at one given temporal frequency through their complex exponential representation. For purely elastic materials, because no experimental dephasing occurs between the shear stress and strain components. Their ratio is thus real and equal to the shear modulus μ. For a purely viscous fluid, because a dephasing of

[386] S. Catheline et al., "Measurement of Viscoelastic Properties of Homogeneous Soft Solid Using Transient Elastography: An Inverse Problem Approach," *The Journal of the Acoustical Society of America* 116, no. 6 (December 1, 2004): 3734–41, https://doi.org/10.1121/1.1815075.

[387] Thomas Deffieux et al., "Investigating Liver Stiffness and Viscosity for Fibrosis, Steatosis and Activity Staging Using Shear Wave Elastography," *Journal of Hepatology* 62, no. 2 (February 1, 2015): 317–24, https://doi.org/10.1016/j.jhep.2014.09.020.

$\frac{\pi}{2}$ experimentally occurs between the two components (because $\frac{\partial \gamma_{xy}}{\partial t} = i\omega_{Motion}\gamma_{xy} = \omega_{Motion}\gamma_{xy}e^{i\frac{\pi}{2}}$ for a given motion angular frequency ω_{Motion}). Their ratio is thus a pure imaginary number equal to $i\eta\omega_{Motion}$. For a viscoelastic material, because of the dual mechanical behavior between a purely elastic material and a purely viscous fluid, G^* has both non-zero real and imaginary parts and can be written $G^* = G' + iG''$. G' is usually called storage modulus, and represents approximatively the elastic property of the viscoelastic material, whereas G'' is usually called loss modulus and represents approximately its viscous property. The advantage of introducing G^* is that it can be defined for any viscoelastic material (even for purely elastic or viscous materials) and the problem does not depend anymore on a rheological model. The inconvenience is that G' and G'' do not represent intrinsic mechanical properties of the material as they depend on the oscillation frequency chosen to measure them.

In both reconstruction strategies to recover the viscoelastic properties of a biological tissue, because the characteristic quantities highly depend on time, the measurement at different oscillation frequencies or the differentiation of the tissue response for its different frequency components is usually performed, and sometimes referred to as shear wave spectroscopy[388].

This review on the main ultrasound techniques to perform elastography gave us the possibility to understand better the notion of mechanical properties in organs (Young's modulus E and viscosity η) and to understand the different strategies that can be used to measure them (static, oscillatory and transient methods). Nevertheless, as explained in the first chapter of this manuscript and reminded at the beginning of this chapter, lung is enclosed in the thoracic cage. This makes the use of ultrasound techniques very challenging for this organ. Moreover, the lung is not the only difficultly accessible organ in the human body: for example, it is impossible to perform palpation or ultrasound elastography non-invasively in the human brain. However, it was seen previously that magnetic resonance imaging can be a valuable tool for the characterization of lung function, in particular concerning the possibility of motion tracking and the exploitation of motion fields for quantification purposes. More generally, this technique is well adapted to any remote, internal or difficultly accessible organ. Let us see in the following how it is possible to perform elastography with a MRI machine.

2. MAGNETIC RESONANCE ELASTOGRAPHY (MRE)

Magnetic Resonance Elastography (MRE) refers to an elastography technique based on magnetic resonance imaging. As it was the case above for elastography techniques based on ultrasound imaging, the goal of MR elastography is to measure the mechanical properties of biological tissues (the Young's modulus E and sometimes the viscosity η). Standard MRE can be classified as a dynamic oscillatory technique. For that reason, a continuous oscillatory mechanical wave is generated inside the biological tissue using an external actuator, and the MR images are used to follow the propagation of those waves along time. The measured wave pattern can therefore be exploited afterwards to estimate the mechanical properties of the organ under consideration with a given spatial resolution. The imaging process is therefore quite similar to those covered above with shear wave ultrasound elastography techniques.

In the previous subsection, it was explained that dynamic oscillatory elastography is always performed along three steps in echography: wave generation, image acquisition and E map reconstruction. Similarly, these same three steps will be described for MR elastography, and the great possibilities offered by this technique will be figured out,

[388] T. Deffieux et al., "Shear Wave Spectroscopy for In Vivo Quantification of Human Soft Tissues Visco-Elasticity," *IEEE Transactions on Medical Imaging* 28, no. 3 (March 2009): 313–22, https://doi.org/10.1109/TMI.2008.925077.

but also the limitations and the simplifications to make so as to estimate quantitatively the mechanical properties of biological tissues. Most of the elements explained below are largely developed in the reference papers[389] [390].

2.1. SHEAR WAVE GENERATION INSIDE THE ORGANS IN MR ELASTOGRAPHY

The generation of shear wave is highly organ dependent. To perform MR elastography, a continuous shear wave needs to be generated inside the organ under consideration. In this subsection, only active MR elastography techniques are considered, in which shear waves are externally applied to the organ, in opposition with passive elastography techniques, where the shear waves are generated through natural physiological processes[391] (pulsatile blood flow, physiological motions, …). Usually, a monochromatic continuous shear wave is generated during the whole imaging process thanks to an external excitation system. In some advanced application, a continuous multi-frequency wave can be generated and exploited[392].

To be able to estimate the mechanical properties of a region in the organ, this region needs to be 'irradiated' by the shear wave. For that reason, the type and geometry of mechanical excitation system, but also the mechanical excitation frequency, need to be chosen as a function of the size of the organ under consideration, of the distance between the mechanical excitation system and this organ and of the viscosity of the tissues in the propagation path. For example, in the case of the liver, which is a large organ, mechanical frequencies of a few tens of Hertz and usually under 100 Hz are employed[393] [394] [395]. For smaller organs, like the breast, the kidneys or even the ocular globe, and for most preclinical studies, frequencies from several hundreds of Hertz to several thousands of Hertz are usually employed[396] [397] [398] [399].

To generate the waves themselves, any technique able to generate a mechanical wave pattern in the organ of interest should be considered (see **Figure 4.8**). Moreover, any part of the mechanical excitation system close to the MR scanner needs to be MR compatible. Non-exhaustively, in the literature, it is possible to find mechanical

[389] R. Muthupillai et al., "Magnetic Resonance Elastography by Direct Visualization of Propagating Acoustic Strain Waves," *Science* 269, no. 5232 (September 29, 1995): 1854–57, https://doi.org/10.1126/science.7569924.
[390] A. Manduca et al., "Magnetic Resonance Elastography: Non-Invasive Mapping of Tissue Elasticity," *Medical Image Analysis* 5, no. 4 (December 2001): 237–254, https://doi.org/10.1016/S1361-8415(00)00039-6.
[391] Karim G. Sabra et al., "Passive in Vivo Elastography from Skeletal Muscle Noise," *Applied Physics Letters* 90, no. 19 (May 7, 2007): 194101, https://doi.org/10.1063/1.2737358.
[392] Patrick Asbach et al., "Assessment of Liver Viscoelasticity Using Multifrequency MR Elastography," *Magnetic Resonance in Medicine* 60, no. 2 (2008): 373–79, https://doi.org/10.1002/mrm.21636.
[393] Laurent Huwart et al., "Liver Fibrosis: Non-Invasive Assessment with MR Elastography," *NMR in Biomedicine* 19, no. 2 (2006): 173–79, https://doi.org/10.1002/nbm.1030.
[394] Olivier Rouvière et al., "MR Elastography of the Liver: Preliminary Results," *Radiology* 240, no. 2 (August 1, 2006): 440–48, https://doi.org/10.1148/radiol.2402050606.
[395] Sudhakar K. Venkatesh et al., "MR Elastography of Liver Tumors: Preliminary Results," *American Journal of Roentgenology* 190, no. 6 (June 1, 2008): 1534–40, https://doi.org/10.2214/AJR.07.3123.
[396] Alexia L. McKnight et al., "MR Elastography of Breast Cancer: Preliminary Results," *American Journal of Roentgenology* 178, no. 6 (June 1, 2002): 1411–17, https://doi.org/10.2214/ajr.178.6.1781411.
[397] Christine U. Lee et al., "MR Elastography in Renal Transplant Patients and Correlation with Renal Allograft Biopsy: A Feasibility Study," *Academic Radiology* 19, no. 7 (July 1, 2012): 834–41, https://doi.org/10.1016/j.acra.2012.03.003.
[398] Daniel V. Litwiller et al., "MR Elastography of the Ex Vivo Bovine Globe," *Journal of Magnetic Resonance Imaging* 32, no. 1 (2010): 44–51, https://doi.org/10.1002/jmri.22217.
[399] E. H. Clayton, J. R. Garbow, and P. V. Bayly, "Frequency-Dependent Viscoelastic Parameters of Mouse Brain Tissue Estimated by MR Elastography," *Physics in Medicine & Biology* 56, no. 8 (2011): 2391, https://doi.org/10.1088/0031-9155/56/8/005.

excitation systems made of a vibrating membrane or an ergonomic piece adapted to a natural cavity of the body, which is driven by pressure waves generated by a loudspeaker and guided through a tubular waveguide, or MR compatible mechanical actuators driven electromagnetically or piezoelectrically[400]. Each system has its own advantages and drawbacks[401] and the system needs to be adapted both to the organ of interest and the mechanical frequencies to explore.

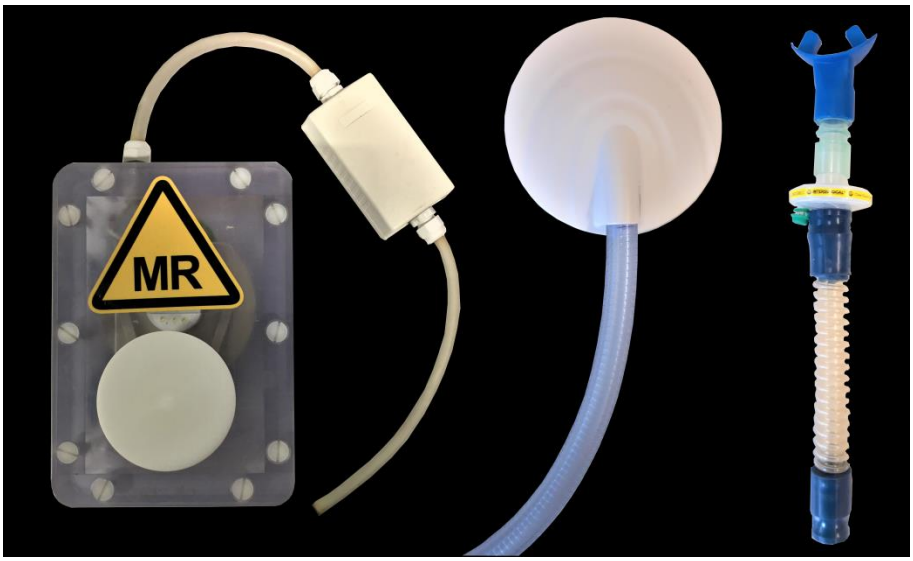

Figure 4.8: Three examples of mechanical excitation systems used in our laboratory. From left to right, a MR compatible electromechanical actuator, a vibrating membrane (for liver elastography for example) and a flexible tubular mouthpiece (for brain or lung elastography, for example). The first system is active, while the two others are passive and need therefore to be driven by an active pressure generator (made of a loudspeaker enclosed in a cabinet for example). These two last elements are usually referred to as mechanical coupling systems.

2.2. PROBING SHEAR WAVES IN MR IMAGES

Thanks to the sub-millimeter spatial resolution offered by ultrasound imaging, from a few tens to several hundreds of micrometers, and thanks to the very high image frame rate obtained through ultrafast ultrasound imaging, that can reach several tens of thousands images per second, the mechanical deformation induced by shear waves can directly be observed in 'real-time' in the ultrasound images and its spatio-temporal evolution studied through successive image comparison (with speckle-tracking methods, for example). In MRI, because the spatial resolution of images rarely goes below 1 mm, and because several seconds to several minutes are usually needed to acquire an exploitable image, shear wave evolution cannot be followed directly in the complex MR image in 'real-time'. This problem is partially solved through the use of a technical addition to any standard MRI pulse sequence: a motion encoding gradient synchronized to the mechanical excitation system and applied at each MR repetition between the RF excitation and data acquisition (see **Figure 4.9**).

[400] Kai Uffmann et al., "Design of an MR-Compatible Piezoelectric Actuator for MR Elastography," *Concepts in Magnetic Resonance* 15, no. 4 (2002): 239–54, https://doi.org/10.1002/cmr.10045.
[401] K. Uffmann and M. E. Ladd, "Actuation Systems for MR Elastography," *IEEE Engineering in Medicine and Biology Magazine* 27, no. 3 (May 2008): 28–34, https://doi.org/10.1109/EMB.2007.910268.

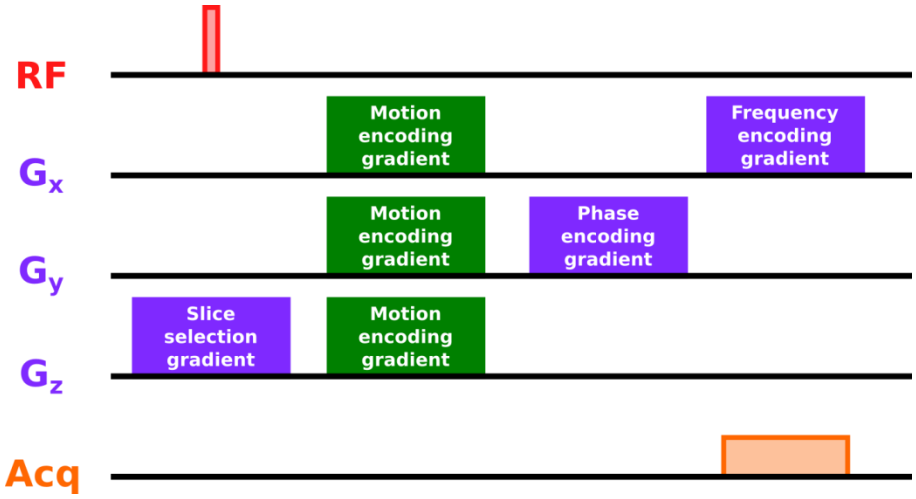

Figure 4.9: Sequence chronogram of RF and gradient pulses in MRE.

2.2.1. MOTION ENCODING GRADIENT

A motion encoding gradient (MEG), sometimes called motion sensitizing gradient, is at least composed of two lobes of magnetic field gradient applied along one given direction. More sophisticated motion encoding gradients are composed of more than two lobes of gradient, but their role is similar and will not be discussed here. Moreover, only 'trapezoid' gradient lobes will be considered. They are composed of a linear gradient ramp-up, a plateau and a linear gradient ramp-down, even if more complicated gradient shapes can be implemented. For such a bipolar motion encoding gradient, the first important characteristic feature is the absolute 'area' equality between the two lobes. The 'area' of a gradient pulse is the result of its integral value along time, and it can easily be visualized graphically on usual pulse sequence chronograms. The second important characteristic feature of such a motion encoding gradient is that it creates a zero net dephasing for any non-moving spin located in the image FOV. To perform this, two possible situations are usually encountered:

- If the second lobe is applied after the first one with no RF pulses between them, the two gradient lobes need to be opposite in sign.
- If a 180° RF pulse is applied between the two gradient lobes, the dephasing of any non-moving spin generated by the first lobe is retrieved with an opposite sign after the application of the refocusing pulse. For that reason, the exact same gradient lobe with the same sign can be applied to rewind the spin dephasing.

In both cases, the final result for non-moving spins is the same: the dephasing accumulated during the application of the first lobe is totally cancelled by the application of the second lobe. If a spin is now animated by a motion (caused by the flow of a biological fluid, the diffusion of water molecules inside the tissue, the deformation of biological tissue, …) with a non-zero velocity component in the direction of the motion encoding gradient and between the application of the two gradient lobes, the phase of its Larmor precession accumulated during the application of the first lobe is not totally compensated by the application of the second lobe. In particular, if a given spin moves toward the direction of decreasing magnetic fields during the application of the bipolar gradient, the magnetic field is higher during the application of the first 'positive' lobe than during the application of the second

'negative' lobe: the total dephasing generated by the motion encoding gradient is thus positive. If the spin moves now in the opposite direction, the total dephasing will be negative.

2.2.2. QUANTITATIVE EXPLAINATION OF A MOTION ENCODING GRADIENT

More quantitatively speaking, the dephasing $\Delta\varphi$ accumulated by a spin isochromat (group of spins that behaves similarly) following a spatial trajectory $\vec{u}(t)$ during the application of any time varying gradient shape $\vec{G}(t)$ starting at time t_0 and with a duration ΔT_{MEG} is given by:

$$\Delta\varphi = \gamma \int_{t_0}^{t_0+\Delta T_{MEG}} \vec{G}(t) \cdot \vec{u}(t) dt \qquad \textbf{Eq. 4.21}$$

From this relationship, if all the parameters characterizing the bipolar gradient are correctly controlled, valuable quantitative parameters characterizing the trajectory of a spin can be obtained from the phase of this moving spin. For example, if the spin is animated by a uniform and rectilinear motion, it can be shown from the previous formula that $\Delta\varphi$ is proportional to its velocity, and the component of this velocity parallel to the motion encoding gradient direction can be quantitatively calculated from the different geometrical and gradient related parameters. For that reason, if now such a gradient is applied at each pulse sequence repetition between the RF excitation of spins and the MR data sampling (see **Figure 4.9**), and if the motion of spins repeats exactly at each pulse sequence repetition, an image depending on $\Delta\varphi$ can be obtained.

If S is the complex image obtained after the application of a standard MR pulse sequence, the complex image obtained with the exact same pulse sequence (same TE, same TR, …) but with the addition of a MEG, and with the condition that the motion of spins remains exactly the same at each MEG application, can be written:

$$S_{MEG} = Se^{i\Delta\varphi} \qquad \textbf{Eq. 4.22}$$

with $\Delta\varphi$ defined as in **Eq. 4.21** for the MEG and the motion under consideration. If a map depending only on the dephasing $\Delta\varphi$ is required, without any dependency on the original background phase, one solution is to perform the exact same acquisition as previously but with opposite signs for both MEG lobes. In this case, S_{-MEG} is obtained and depends similarly on $-\Delta\varphi$. Therefore, a map giving the $\Delta\varphi$ value at each voxel can be obtained by calculating:

$$\Delta\varphi = \frac{Arg\left(\frac{S_{MEG}}{S_{-MEG}}\right)}{2} \qquad \textbf{Eq. 4.23}$$

where Arg corresponds to the function extracting the argument (or angle, or phase) of a complex number. From this $\Delta\varphi$ map, a quantitative map giving at each voxel location the value of a parameter of interest related to spin motion can be calculated (a spin velocity map, for example).

2.2.3. MOTION ENCODING GRADIENT TO MEASURE A DISPLACEMENT

Three remarks need to be taken into account to perform the quantification of a mechanical parameter of interest:

- The first remark concerns the possibility to measure the information of interest. Even if S does not appear anymore in the previous expression of $\Delta\varphi$ (**Eq. 4.23**), S_{MEG} and S_{-MEG} are both proportional to S. If S equals zero in a region of the image (for example, if the proton density ρ equals zero, or if ${T_2}^*$ is extremely short, or both), the phase in the image is not definite and therefore $\Delta\varphi$ cannot be calculated, even if this region is moving. Motion quantification thus depends first on our ability to acquire a MR signal from the tissue under consideration.

- The second remark is related to the motion itself. A motion encoding gradient encodes all the motions happening along its encoding direction. For example, if the organ under consideration is animated by a physiological motion (respiratory motion or cardiac motion, for example), this can create a shift of value in the $\Delta\varphi$ map. Moreover, water molecules are animated by a diffusion motion explained by thermal agitation and that can be modeled by a random walk. At the scale of one voxel, an experimentally great number of water molecules are following their own random walk, each of them experiencing their own environmental magnetic field evolution during the application of the MEG. Because the signal in one voxel is equal to the sum of signals created by all the spins located inside this voxel, with each one having their own phase decorrelated from the other spins because of diffusion, it results in a signal magnitude attenuation which is comparable to a T_2/T_2^* effects. In this case, the MR phase is not impacted directly, but because of this attenuation, the SNR of S_{MEG} and S_{-MEG} are lower compared to the one of S. This effect degrades the SNR of $\Delta\varphi$ and thus alters the precision, and sometimes the accuracy, of motion quantification. This decrease in signal magnitude is the main phenomenon exploited in diffusion MRI. However, in the quantification of motions generated for elastography, diffusion and generally other types of motions can make the measurement process more challenging. Nevertheless, these unpredicted motions do not usually repeat at each application of the MEG, leading to data averaging effects. Moreover, the time evolution characteristics of these unattended motions make sometimes the MEG poorly sensitive to them. Those two effects usually attenuate the problem of parasite motions.

- The third and last remark is directly related to the mathematical representation of the phase of complex numbers. When the Arg function presented in **Eq. 4.23** is applied to a complex number, an angle always comprised in the same range of width 2π ($[0,2\pi[$ or $]-\pi,\pi]$ usually) is obtained. For that reason, the argument of S_{MEG}/S_{-MEG}, which should be equal to $2\Delta\varphi$, is in fact obtained with values comprised exclusively in this type of interval. This is totally correct mathematically speaking because the angles φ and $\varphi + 2\pi$ are equivalent when they represent the argument of a complex number. Nevertheless, when those angles are the basis of a quantification technique in experimental physics, this artifact must be corrected. This limit in phase representation is usually called phase wrapping. When a phase map (for example, a MR phase image) is displayed graphically thanks to a continuous color-scale, this phase wrapping is usually observed as abrupt phase transitions between two neighbor voxels having values close to the two limits of the 2π-width range, which usually contrast with the smoothly spatially varying phase that is expected. To correct this effect, a phase image can be post-processed with a phase unwrapping algorithm, usually based on a supposed spatial continuity of phase values[402].

We have seen the possibilities of motion encoding gradients to make our MR image sensitive to a given motion, but also the possible quantification biases we have to be careful with. It was also explained that MR elastography is based on the possibility to track a shear displacement in biological tissue thanks to MRI. If the use of MEG is obviously an efficient strategy to encode the wave pattern into the MR phase image, one very important consideration needs to be taken into account to perform this properly: as motion needs to remain the same at each MEG repetition, synchronicity between the mechanical excitation system and the MEG is primordial. Two types of synchronicities can be explored.

[402] M. Costantini, "A Novel Phase Unwrapping Method Based on Network Programming," *IEEE Transactions on Geoscience and Remote Sensing* 36, no. 3 (May 1998): 813–21, https://doi.org/10.1109/36.673674.

2.2.4. TEMPORAL POSITION SYNCHRONICITY

The necessity for the motion to repeat exactly at each MEG application would be a challenging constraint if transient mechanical phenomena were considered. However, in standard MR elastography, tissue motion is induced thanks to the propagation of a monochromatic shear wave with a frequency between a few tens to several thousands of Hertz. For that reason, because any elementary volume of tissue experiences a cyclic motion during the whole image acquisition at a motion period in the same order of magnitude than the usual repetition time TR in standard MR pulse sequences (between several milliseconds to several hundreds of milliseconds), this necessity is not a challenge anymore, but it remains a constraint.

If the MEG is always applied at the same time duration after the RF excitation (which is usually the case), one sufficient condition is that TR equals a multiple of the shear wave temporal period. If T_{Motion} is this period, TR needs to verify:

$$TR = NT_{Motion} \qquad \textbf{Eq. 4.24}$$

with N being a non-zero integer number. From an experimental point of view, fixing TR as a multiple of the motion period is not sufficient to keep the exact same motion pattern at each repetition. Because of pulse sequence and hardware imperfections, and because of numerical roundings of time positions and durations of pulse sequence elements, the N value in the relationship between TR and T_{Motion} just above is not exactly an integer number experimentally. This leads to a progressive shift of the wave pattern along the repetitions of MEG. A simple technical solution to solve this problem is to prescribe a desired T_{Motion} value for a given pulse sequence. This pulse sequence then adapts its time parameters as a function of this prescribed motion period, and returns at the end of the calculation an experimental value for T_{Motion}, which can therefore be prescribed directly on the mechanical excitation system and represents the actual motion period. Moreover, to be sure to keep the exact same wave pattern at each MEG repetition, the usual technique is to program in the pulse sequence the generation of a trigger pulse which will be sent on one given output of the MRI system at each sequence repetition. This trigger is employed to synchronize the generation of packets of N motion periods (sometimes called bursts) at each pulse sequence repetition to avoid any temporal shift between the mechanical excitation system and the MRE pulse sequence.

These three technical strategies, which are the correct setting of TR, the adaptation of the temporal period of motion and the generation of a trigger, make the synchronization between the MEG and the motion field very robust to constraints in terms of temporal position of MRI pulses but also to technical imperfections. The only drawback concerns the total scan time of the MRE pulse sequence: because of those timing constraint between motion and pulse generation, the chronogram of pulse sequence elements cannot be as optimized as it can be for a standard MRI pulse sequence in order to reduce the total scan time, in particular if the motion frequency is low (large T_{Motion} of several tens of milliseconds). Automatically, TR is always longer than the MEG duration, which leads to important consequences in terms of total scan times.

2.2.5. TEMPORAL FREQUENCY SYNCHRONICITY

Contrary to the synchronicity in temporal position, which was mandatory to achieve MR elastography acquisitions, the exact synchronicity in temporal frequency between the shear wave and the MEG is not necessary, but should be clearly understood in order to control the sensitivity of motion encoding in MR elastography. As it was defined for the oscillatory motion with T_{Motion}, a temporal 'period' can be defined for the bipolar MEG: written T_{MEG}, it is defined as the double of the time duration between the centers of the two MEG lobes. Moreover, if those two

lobes are considered to have an absolute amplitude of G_0 ($+G_0$ for the first lobe and $-G_0$ for the second lobe) and both have a duration of ΔT_{Lobe}.

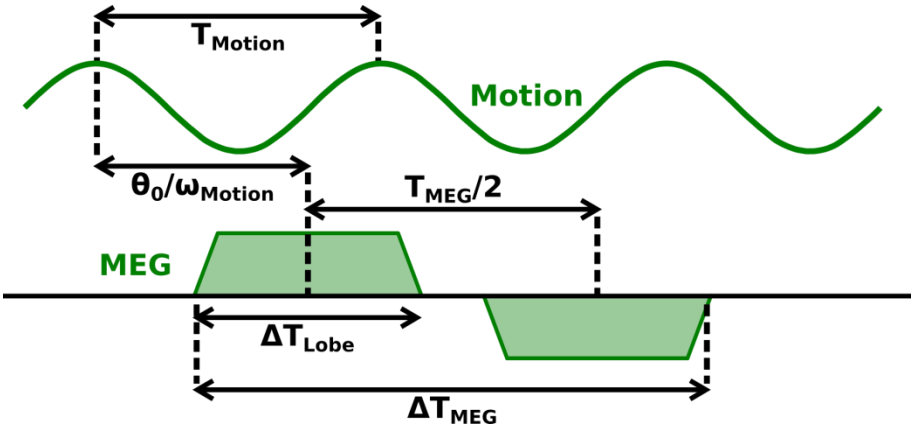

Figure 4.10: Schematic representation of a bipolar MEG applied during the generation of a motion.

Let us consider a spin isochromat moving along the direction of the MEG as a result of the propagation of a shear wave. Its displacement, $u(t)$, follows the oscillation:

$$u(t) = u_0 \cos\left(\frac{2\pi}{T_{Motion}} t + \theta_0\right) \qquad \textbf{Eq. 4.25}$$

with θ_0 being the motion phase reached at the center of the first MEG lobe, chosen here to be the time origin of the problem (see **Figure 4.10**). If the two MEG lobes are simplified as rectangular gradient pulses instead of trapezoid pulses (ramp-up and ramp-down times are considered equal to 0), the integration of the previous expression giving $\Delta\varphi$ as a function of $G(t)$ and $u(t)$ (see **Eq. 4.21**) gives:

$$\Delta\varphi = \underbrace{\frac{2\gamma G_0 u_0 T_{Motion}}{\pi}}_{a} \underbrace{\sin\left(\pi \frac{\Delta T_{Lobe}}{T_{Motion}}\right)}_{b} \underbrace{\sin\left(\frac{\pi}{2}\frac{T_{MEG}}{T_{Motion}}\right)}_{c} \underbrace{\cos\left(\theta_0 + \frac{\pi}{2}\left(\frac{T_{MEG}}{T_{Motion}} - 1\right)\right)}_{d} \qquad \textbf{Eq. 4.26}$$

As indicated below the formula, the expression can easily be decomposed into the product of 4 terms a, b, c and d. The terms a, b and c can be interpreted as weights for the term d, which is the wave pattern to be encoded into the MR phase image. Indeed, if T_{MEG} and T_{Motion} are fixed for the entire pulse sequence (which is always the case in standard elastography), the term d becomes a dephased cosine of the local motion phase θ_0 in the biological tissue of interest. If this d signal can be measured for every voxel of the image, the wave pattern for a given motion phase is obtained. If T_{MEG} equals T_{Motion}, the dephasing term in d equals 0 and $\Delta\varphi$ has the same phase θ_0 as u.

Let us now study one by one the three weighting terms, which essentially set the motion sensitivity of the measurement:

a) First, the dephasing $\Delta\varphi$ encoded in the MR phase evolves linearly with the motion amplitude u_0. It is also proportional to the absolute gradient amplitude G_0 and to the period of motion T_{Motion}. Hence, to increase the motion sensitivity, it is better to use large gradient amplitudes. However, the dependence in motion period can be compensated in practice by applying several synchronous bipolar MEG that accumulate motion induced dephasing (proportionally to the number of bipolar

MEG repetitions) at high motion frequencies, without impacting the total motion encoding duration in comparison with lower motion frequencies.

b) The second term governs the weighting related to the duration of each MEG lobe with respect to the motion period. A maximum weight equal to 1 is obtained for a lobe duration equal to half the motion period:

$$\Delta T_{Lobe} = \frac{T_{Motion}}{2} \qquad \textbf{Eq. 4.27}$$

c) This term governs the weighting related to the period of the MEG with respect to the motion period. A maximum weight equal to 1 is obtained for a MEG period exactly equal to the motion period:

$$T_{MEG} = T_{Motion} \qquad \textbf{Eq. 4.28}$$

Because of the periodicity of this term (sine function), this maximum weight can also be obtained for longer MEG periods.

2.2.6. MAXIMISATION OF MOTION SENSITIVITY

In conclusion, the most efficient configuration to encode a monochromatic motion with a bipolar MEG in terms of encoding sensitivity is obtained with a total MEG duration ΔT_{MEG} equal to the motion period T_{Motion} and composed of two lobes of equal duration $\Delta T_{Lobe} = \frac{\Delta T_{MEG}}{2}$ (see **Figure 4.11** for the illustration in a gradient echo pulse sequence).

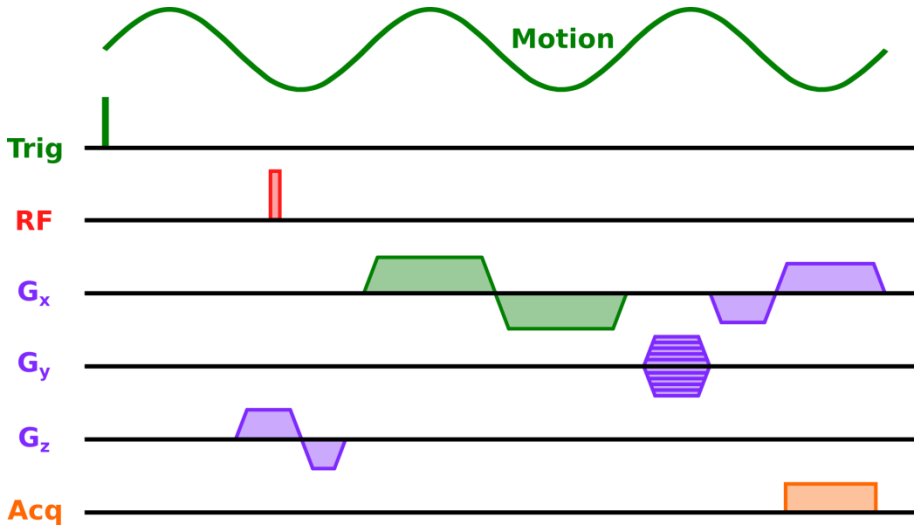

Figure 4.11: Representation of a gradient echo based MRE pulse sequence.

This type of gradient pulse is very common in standard elastography exams based on gradient echo sequences. For MRE acquisitions based on spin echo sequences, the usual technique to optimize the schedule of pulses is to use one MEG lobe before and one after the refocusing RF pulse applied between the RF excitation and the acquisition window, the two lobes having the same sign in this case (see 2.2.1). In spin echo sequences, because a MEG as shown in **Figure 4.11** cannot be played (because of the refocusing pulse applied between the two lobes), a usual way to reach the same encoding sensitivity is to apply the two lobes but with a duration between the end of the

first lobe and the beginning of the second lobe equal to a multiple of the motion period. This solution leaves the time necessary to apply the refocusing pulse between the two MEG pulses.

The synchronicity between the temporal frequencies of motion and MEG gives the maximal motion encoding sensitivity in most clinical cases, but this is not mandatory. As explained in 2.2.5, a lack of synchronicity in temporal frequency results in a reduced dephasing, hence sensitivity, in comparison with the synchronous case. In particular applications, it can even be valuable to set the MEG parameters out of the theoretical 'optimal' solution. Indeed, as explained in 2.2.3, the MEG is sensitive to all motions (respiratory motion, for example). For that reason, for a moving organ, a long MEG duration can make the MRE sequence very sensitive to this physiological motion. Moreover, because the MEG is applied at each sequence repetition between tissue excitation and data sampling, its duration acts as a lower bound for the TE. For short T_2/T_2^* tissues (like the lung for example), this TE value can thus become too long to acquire the MR image with a sufficient SNR. Furthermore, the MEG duration acts as a lower bound for the TR too. For that reason, and in particular for low motion frequencies and 3D acquisitions, the total scan time can become clinically unadapted in a situation of maximal sensitivity. For the three reasons explained just above, it can therefore be valuable to set the MEG parameters out of the theoretical 'best' solution and set its total duration lower that the 'optimal' one. This practice is usually referred to as fractional encoding, and the convenience of this technique was demonstrated in the elastography of the heart, which suffers from motion of tissue and blood, as well as quite short T_2/T_2^* values around 30-40 ms[403].

The application of a MEG as presented above enables the acquisition of MR images with a phase resulting from, first, the phase that would be obtained if no motion encoding gradient were performed, and second, the phase $\Delta\varphi$ that is proportional to the local motion amplitude. It is the displacement field, $u(t)$, along the direction defined by the MEG at one given motion phase, which can be computed upon the unwrapped $\Delta\varphi$ maps.

2.3. EXTRACTION OF THE MECHANICAL PROPERTIES OF THE ORGAN

2.3.1. LOCAL FREQUENCY ESTIMATION ALGORITHM

A direct extraction of the mechanical properties from the displacement field maps can be performed through the application of the so-called Local Frequency Estimation (LFE) algorithm[404] [405]. This very simple and direct algorithm was the first one proposed for MR elastography and is based on the estimation of the local shear wavelength at each voxel location in the unwrapped $\Delta\varphi$ or $u(t)$ map. Thanks to its simplicity, it will constitute the basis for future discussions on MR elastography reconstruction.

It is performed thanks to a filter specially designed for this purpose. Like in ultrasound elastography, this is theoretically sufficient to obtain the shear velocity maps: because the temporal motion period is known (T_{Motion}), the local value of shear wavelength λ_S is sufficient to calculate the local shear wave velocity c_S through:

$$c_S = \frac{\lambda_S}{T_{Motion}} \qquad \textbf{Eq. 4.29}$$

[403] Jens Rump et al., "Fractional Encoding of Harmonic Motions in MR Elastography," *Magnetic Resonance in Medicine* 57, no. 2 (February 2007): 388–395, https://doi.org/10.1002/mrm.21152.

[404] H. Knutsson, C.- Westin, and G. Granlund, "Local Multiscale Frequency and Bandwidth Estimation," in *Proceedings of 1st International Conference on Image Processing*, vol. 1, 1994, 36–40 vol.1, https://doi.org/10.1109/ICIP.1994.413270.

[405] Armando Manduca et al., "Image Processing for Magnetic-Resonance Elastography," in *Medical Imaging 1996: Image Processing*, vol. 2710 (Medical Imaging 1996: Image Processing, International Society for Optics and Photonics, 1996), 616–24, https://doi.org/10.1117/12.237965.

As ρ can be approximated to 1 g/cm^3 in most biological tissues, the map of μ values throughout the organ of interest can be obtained according to $\mu = \rho {c_s}^2$ (see **Eq. 4.15**). If required, the Young's modulus can then be obtained by calculating $E = 3\mu$ (see **Eq. 4.10**).

2.3.2. LIMITS OF THE LFE ALGORITHM

The LFE algorithm was shown to be moderately sensitive to the phase image noise. Nevertheless, the LFE algorithm suffers from many drawbacks:

- In its first implementation, LFE was estimating the local wavelength from a single 2D phase image. This method is accurate only if the wave actually propagates within the image plane and if the direction of the motion encoding gradient is orthogonal to the image plane. However, if the wave propagates locally in a direction which is not parallel to the image plane, the local wavelength is overestimated, which results in overestimated values of shear velocity and shear modulus.

- Because LFE estimates the parametric map from the measurement of only one motion component oriented along one direction, no motion may be seen in some regions of the organ, even if a motion field exists. However, the μ values can be assessed only if a wave is detected, which requires that a non-zero motion component exists in the direction of the MEG. More generally, if the local $\Delta\varphi$ values are small in a given region, it can be hard to detect its spatial variation because of the phase noise and eventual biases coming from the background phase.

- Moreover, because the estimation of μ is based on the analysis of an oscillatory pattern, it can be shown that the spatial resolution of the parametric map provided by LFE is always lower than the voxel size and depends on the local wavelength. More quantitatively speaking, the spatial resolution given by LFE is approximatively equal to λ_S. If elastography is performed on a material composed of two different media with different homogeneous μ values, separated by a neat boundary, the parametric map reconstructed with LFE shows a blurred frontier between the two media. The distance between the position of the boundary and the first locations in one of the two media where the measured values of μ are correctly estimated is approximatively equal to half the wavelength in this medium. In a biological tissue, a mass smaller than the shear wavelength and with an elasticity different from its surrounding environment is visible, but its elasticity value cannot be assessed accurately through LFE.

- Because only one motion phase is studied, it is not possible to say in which direction the wave propagates. For that reason, it is not possible to say if the observed wave pattern is composed of only one wave or several ones propagating in different directions (several sources, reflections, …). For that reason, the observed pattern can result from the interference of several waves, leading to standing wave patterns in the tissue, and making the accurate reconstruction of a parametric map difficult with LFE.

- Because standard elastography is an oscillatory technique based on the continuous generation of a shear wave, the observed wave pattern is composed of both shear and compression components in the general case. The compression component usually appears as a very long wavelength pattern. Because of this superposition of the two types of waves, the solution obtained through LFE can be biased.

- LFE only measures the local wavelength, from which a wave velocity and thus a shear modulus can be obtained. However, this method does not estimate the local wave attenuation, and is therefore not able to estimate the local tissue viscosity.

In the following, strategies to address the different issues raised just above will be presented.

2.3.3. 3D IMAGING WITH 3D MOTION ENCODING

To address the issue of wavelength overestimation[406], which is common to all MR elastography reconstruction techniques that are based on 2D acquisitions, it is necessary to acquire 3D data. As seen in the first chapter of this manuscript, it can be done either by acquiring several k-spaces corresponding to several organ slices, or by acquiring directly a 3D k-space corresponding to a volume of biological tissue. In this case, a 3D MR phase image is obtained, and the wave pattern can therefore be observed along the three dimensions of space. For that reason, this configuration gives the possibility to properly estimate the motion wavelength.

To address the issue of null motion components along the MEG direction, additional acquisitions can be performed, first, at different phases of the motion and, second, along different MEG directions to record potentially non-zero components of the displacement field. Because $\Delta\varphi$ was shown to be proportional to the displacement component along the MEG axis, three acquisitions with three non-coplanar MEG directions are mathematically sufficient to obtain the full 3D displacement field $\vec{u}$. Nevertheless, because the measurement of $\Delta\varphi$ is challenged by different sources of noise, the three MEG directions are usually chosen along the axes of a 3D orthogonal basis. Furthermore, if the accuracy in the measurement of $\vec{u}$ needs to be increased, more MRE acquisitions with other MEG directions can be performed. From this process, and by knowing precisely the characteristics of the MEG (shape, amplitude, and duration), a quantitative measurement of $\vec{u}$ can be obtained.

2.3.4. ACQUISITION AND PROCESSING OF DIFFERENT MOTION DYNAMICS

The problem of low spatial resolution explained in 2.3.2 is inherent to LFE: because the estimation of local frequency is based on the application of linear filters to the $\Delta\varphi$ map, one way to perform it is by convolving $\Delta\varphi$ with a kernel that covers, for each voxel location, a given area depending on the filter characteristics and support. Explained with hands, the kernel needs to 'see' a sufficient amount of information to estimate the wavelength. For that reason, the kernel support needs to cover an area with a minimal size given by the wavelength to estimate. Because the local wavelength is not known before applying the filter, several filters with different characteristics, forming a bank of filters sensitive to different local wavelengths, are tested. The poor spatial resolution is therefore related to the area of the kernel support. To increase the spatial resolution of the μ map, another reconstruction strategy must be investigated.

Several MR phase images can be recorded at different motion phases within the mechanical time period. The acquisitions at different motion phases are usually called phases or dynamics. This last term will be preferred in the following to avoid confusion between the different 'phases' involved in the topic (MR phase image, phase encoding, motion phase, etc.). The usual number of dynamics in MRE exams is at least 4 (4 and 8 dynamics are very common in the literature). To choose the motion phase corresponding to one dynamic in terms of pulse sequence prescription, the trigger that controls the synchronicity in time position between the pulse sequence and the mechanical excitation system is usually shifted such that everything else is kept unchanged. For each dynamic, the image contrast is expected to be the same.

If a LFE reconstruction was then applied separately on each wave pattern obtained at each dynamic, several μ maps with the same spatial resolution would be obtained, leading maybe to a better confidence on the result but

[406] U. Hamhaber et al., "Three-Dimensional Analysis of Shear Wave Propagation Observed by in Vivo Magnetic Resonance Elastography of the Brain," *Acta Biomaterialia* 3, no. 1 (January 1, 2007): 127–37, https://doi.org/10.1016/j.actbio.2006.08.007.

not to a better spatial resolution. Because the displacement field is obtained for several motion phases within one motion period, and because the motion at each voxel location is sinusoidal, with a given local amplitude and phase, these amplitudes and phases can be estimated at each voxel location by Fourier filtering the data along the dimension of dynamics (by keeping only the Fourier component corresponding to the expected motion frequency). The Fourier coefficient extracted is a complex number. For that reason, two real maps can be extracted from this complex map:

- A map representing the local wave amplitudes, written u_0,
- A map representing the wrapped shear wave phases, calculated as the arguments of the complex numbers extracted just above. After applying a phase unwrapping algorithm, a shear wave phase map, written θ, is obtained. These values increase along any shear wave propagation path.

Because the same MR elastography acquisition is usually performed along different MEG directions, a motion component in a direction j ($j = x, y, z$ for example) is obtained and can be written with the notations introduced just above:

$$u_j = u_{0j} e^{i\theta_j} \quad \textbf{Eq. 4.30}$$

From those two new maps, while assuming a purely elastic medium for the moment, two elastography reconstruction strategies can be considered:

- **The Phase Gradient (PG) method**[407]**:** Locally, along the direction of shear wave propagation, the phase of this wave can be written as:

$$\theta = \theta_0 + \frac{2\pi}{\lambda_S} s \quad \textbf{Eq. 4.31}$$

  In the expression just above, s designates the curvilinear abscissa along the propagation path, which is the distance travelled by the wave from a given origin along its propagation path. If only one wave pattern is propagating through the organ of interest (no overlapping waves), the amplitude of the gradient of θ, written $\left|\vec{\nabla}\theta\right|$, is given by:

$$\left|\vec{\nabla}\theta\right| = \frac{2\pi}{\lambda_S} \quad \textbf{Eq. 4.32}$$

  Therefore, the same local shear wavelength as obtained through a LFE reconstruction is obtained, but with a major difference: instead of being measured directly from the wave pattern observed in the $\Delta\varphi$ map at one given dynamic, for which large area filter kernels are needed, λ_S is estimated more easily by calculating the gradient of the θ map, which can be obtain at each voxel location from its direct neighbor voxels thanks to the finite differences method. For that reason, the spatial resolution becomes closer to the voxel size. The only drawback of this technique is its increased sensitivity to noise because of the finite difference calculation of local spatial derivatives on noisy data, which tends to amplify this noise in comparison to the useful information. This problem can be attenuated by pre-smoothing the θ map or calculating differently the local derivatives (based on local fitting, for example).

[407] A. Manduca et al., "Magnetic Resonance Elastography: Non-Invasive Mapping of Tissue Elasticity," *Medical Image Analysis* 5, no. 4 (December 2001): 237–254, https://doi.org/10.1016/S1361-8415(00)00039-6.

- **The Algebraic Inversion of the Differential Equation (AIDE) method**[408]**:** The 3D generalization of **Eq. 4.14** describing shear wave propagation in a homogeneous and purely elastic medium leads to the following partial differential equation:

$$\Delta\vec{u} - \frac{1}{{c_S}^2}\frac{\partial^2\vec{u}}{\partial t^2} = 0 \qquad \textbf{Eq. 4.33}$$

We usually consider that, in the neighborhood of each voxel, the biological tissue is assumed to be homogeneous such that the local wave equation holds. Because $\vec{u}$ locally varies sinusoidally with an angular frequency $\omega_{Motion} = \frac{2\pi}{T_{Motion}}$, it can be represented as a monochromatic complex exponential. In this situation, the partial differential equation written just above can be transformed in a simple 2nd order differential equation, usually referred to as Helmholtz equation:

$$\Delta\vec{u} + \frac{{\omega_{Motion}}^2}{{c_S}^2}\vec{u} = 0 \qquad \textbf{Eq. 4.34}$$

As it was done with the gradient, the Laplacian of $\vec{u}$ can be calculated through the finite differences method. Because the spatial components of this Laplacian can be calculated separately from the corresponding components of $\vec{u}$, any of those components along the direction j ($j = x, y, z$) can lead to a local estimation of μ through:

$$\mu = \Re\left(-\rho{\omega_{Motion}}^2\frac{u_j}{\Delta u_j}\right) \qquad \textbf{Eq. 4.35}$$

where $\Re$ extracts the real part of a complex number. As compression waves are not considered in the reconstruction process, this method based on the inversion of the Helmholtz equation is usually referred to as 'Incompressible AIDE'. More advanced AIDE reconstruction processes involve compression terms in the calculation, which couples the different components of motion and makes the estimation process more complicated.

In AIDE, in comparison with PG, similar benefits in terms of spatial resolution are obtained (but lower in AIDE because of the second spatial derivative). As PG, AIDE is sensitive to the noise and the same techniques to solve this problem are applicable to AIDE in the same way as PG. Usually, the AIDE technique exploits not only the real part of the inverted wave equation, but also its imaginary part, as explained later.

A lot of other reconstruction methods exist, in particular those based on finite element modeling[409] and other using regularization[410]. Moreover, techniques designed to assess the mechanical anisotropy of tissues were developed[411]. These advanced methods will not be discussed further in this manuscript.

[408] Travis E. Oliphant et al., "Complex-Valued Stiffness Reconstruction for Magnetic Resonance Elastography by Algebraic Inversion of the Differential Equation," *Magnetic Resonance in Medicine* 45, no. 2 (2001): 299–310, https://doi.org/10.1002/1522-2594(200102)45:2<299::AID-MRM1039>3.0.CO;2-O.

[409] Elijah E. W. Van Houten et al., "Three-Dimensional Subzone-Based Reconstruction Algorithm for MR Elastography," *Magnetic Resonance in Medicine* 45, no. 5 (2001): 827–37, https://doi.org/10.1002/mrm.1111.

[410] M. McGarry et al., "Including Spatial Information in Nonlinear Inversion MR Elastography Using Soft Prior Regularization," *IEEE Transactions on Medical Imaging* 32, no. 10 (October 2013): 1901–9, https://doi.org/10.1109/TMI.2013.2268978.

2.3.5. NOTION OF DIRECTIONAL FILTERING

The superposition of waves propagating in different directions can be differentiated on multi-dynamics data. A Fourier transform can be applied to the $\Delta\varphi$ maps both in the spatial and temporal dimensions. For 3D $\Delta\varphi$ maps at different dynamics, a 4D k-space data matrix (3 spatial dimensions + 1 dynamic dimension) is thus obtained. It can be shown that the information corresponding to wave propagating in different directions is stored in different regions of this 4D k-space. For that reason, a mask or, more generally, a linear filter in the frequency domain, can be applied to this 4D k-space to keep only the information related to the waves propagating in one given direction and remove the information related to the other waves. After this filtering and the application of an inverse Fourier transform, only waves propagating along the filtered direction is obtained, and the reconstruction methods presented in 2.3.4 can be applied directly on this new displacement field map. This technique is usually referred to as directional filtering, and was first proposed for MR elastography[412] and then adapted to ultrasound elastography[413]. This step is particularly critical for the phase gradient method because motion phase map cannot be exploited if several waves propagate in the organ. A usual way to use directional filters is to extract the displacement field maps for a set of directional filters and run a reconstruction algorithm on those filtered displacement field maps. A unique μ map can then be calculated as a weighted average of the different μ maps obtained from the previous step.

2.3.6. COMPRESSION WAVES IN ELASTOGRAPHY RECONSTRUCTION

As explained in 1.2.7, because of the great difference between the compressional and shear wave velocities, compressional wave patterns are not recorded in transient elastography techniques. However, in continuous oscillatory techniques, the recorded displacement fields result in general from the superimposition of the two types of waves. In certain reconstruction methods, because of the large wavelength difference between the two types of waves, the displacement field created by the compression wave is either neglected (as it was done in the reconstruction methods presented until now), or filtered out as a low spatial frequency component[414]. Another proposed method consists in applying the curl operator, written $\overrightarrow{rot}$, to the motion field $\vec{u}$ to obtain the field $\vec{q}$ such that:

$$\vec{q} = \overrightarrow{rot}(\vec{u}) \qquad \textbf{Eq. 4.36}$$

[411] R. Sinkus et al., "High-Resolution Tensor MR Elastography for Breast Tumour Detection," *Physics in Medicine and Biology* 45, no. 6 (2000): 1649, https://doi.org/10.1088/0031-9155/45/6/317.

[412] A. Manduca et al., "Spatio-Temporal Directional Filtering for Improved Inversion of MR Elastography Images," *Medical Image Analysis*, Medical Image Computing and Computer Assisted Intervention, 7, no. 4 (December 2003): 465–473, https://doi.org/10.1016/S1361-8415(03)00038-0.

[413] T. Deffieux et al., "On the Effects of Reflected Waves in Transient Shear Wave Elastography," *IEEE Transactions on Ultrasonics, Ferroelectrics, and Frequency Control* 58, no. 10 (October 2011): 2032–35, https://doi.org/10.1109/TUFFC.2011.2052.

[414] Dieter Klatt et al., "Noninvasive Assessment of the Rheological Behavior of Human Organs Using Multifrequency MR Elastography: A Study of Brain and Liver Viscoelasticity," *Physics in Medicine & Biology* 52, no. 24 (2007): 7281, https://doi.org/10.1088/0031-9155/52/24/006.

As the compressional wave is curl free, $\vec{q}$ is free of any compression components[415], and thus it verifies the Helmholtz equation related to the curl field of the shear wave component only. A more accurate μ map can therefore be obtained by calculating:

$$\mu = \Re\left(-\rho\omega_{Motion}{}^2 \frac{q_i}{\Delta q_i}\right) \quad \textbf{Eq. 4.37}$$

No motion term is neglected in the calculation, and this method is performed theoretically without any bias. The only weakness of this method is that, because the curl operator is usually calculated through a finite difference method, it tends to amplify the noise relatively to the information of interest, as it was seen for the gradient. Moreover, it decreases a bit the final spatial resolution in the μ map.

2.3.7. VISCOSITY IN MR ELASTOGRAPHY

Shear viscosity in the organ can be extracted along two main approaches:

- Instead of taking into account only the real part in the inversion of the wave equation proposed by AIDE, as it was done for the Helmholtz equation just above for example, it is possible to keep the resulting complex value and refer it to the dynamic modulus introduced in 1.3.3:

  $$G^* = -\rho\omega_{Motion}{}^2 \frac{q_i}{\Delta q_i} \quad \textbf{Eq. 4.38}$$

  In this case, a storage modulus and a loss modulus are obtained. It was shown that these two moduli can be directly used as potential biomarkers[416] or integrated in a rheological model to extract a shear modulus μ and a viscosity η[417].

- In addition, it is possible to perform MRE acquisitions at several motion frequencies and to fit the results on a given rheological model[418] or just study the dispersion of the dynamic modulus components[419] [420].

Usually, the assessment of both the shear elasticity and viscosity is more difficult technically speaking than the assessment of only one 'elasticity' modulus, which is often a shear elasticity modulus biased by viscosity effects.

To conclude on this section, we have seen that MR elastography is a very rich and promising diagnostic technique able to estimate quantitatively the mechanical parameters of biological tissues, which is not possible with

[415] Ralph Sinkus et al., "Viscoelastic Shear Properties of in Vivo Breast Lesions Measured by MR Elastography," *Magnetic Resonance Imaging*, Proceedings of the Seventh International Conference on Recent Advances in MR Applications to Porous Media, 23, no. 2 (February 1, 2005): 159–65, https://doi.org/10.1016/j.mri.2004.11.060.
[416] Philippe Garteiser et al., "MR Elastography of Liver Tumours: Value of Viscoelastic Properties for Tumour Characterisation," *European Radiology* 22, no. 10 (October 1, 2012): 2169–77, https://doi.org/10.1007/s00330-012-2474-6.
[417] Sinkus et al., "Viscoelastic Shear Properties of in Vivo Breast Lesions Measured by MR Elastography."
[418] Patrick Asbach et al., "Assessment of Liver Viscoelasticity Using Multifrequency MR Elastography," *Magnetic Resonance in Medicine* 60, no. 2 (2008): 373–79, https://doi.org/10.1002/mrm.21636.
[419] E. H. Clayton, J. R. Garbow, and P. V. Bayly, "Frequency-Dependent Viscoelastic Parameters of Mouse Brain Tissue Estimated by MR Elastography," *Physics in Medicine & Biology* 56, no. 8 (2011): 2391, https://doi.org/10.1088/0031-9155/56/8/005.
[420] Maxime Ronot et al., "Assessment of Portal Hypertension and High-Risk Oesophageal Varices with Liver and Spleen Three-Dimensional Multifrequency MR Elastography in Liver Cirrhosis," *European Radiology* 24, no. 6 (June 1, 2014): 1394–1402, https://doi.org/10.1007/s00330-014-3124-y.

palpation. Moreover, the method is adapted to many internal organs, which is not often possible with ultrasound elastography.

SECTION 2 DEVELOPMENT OF A MRE PULSE SEQUENCE ADAPTED TO THE LUNG

MAGNETIC RESONANCE ELASTOGRAPHY SEEMS TO BE THE MOST PROMISING TECHNIQUE TO ASSESS THE VISCOELASTIC PROPERTIES OF THE LUNG. IN THIS SECTION, WE DISCUSS THE CHALLENGES IN LUNG MR ELASTOGRAPHY, PROPOSE A NEW ELASTOGRAPHY PULSE SEQUENCE AND EXPLORE ITS POTENTIAL FOR THE LUNG.

1. CHALLENGES FOR LUNG MRE

As seen in the first chapter of this manuscript, lung MRI is a very challenging task because of low tissue density of the organ, short T_2^* in the lung parenchyma and elastic respiratory motion. In this subsection, we will understand why MR elastography of the lung is even more challenging.

1.1. GENERATION OF SHEAR WAVES INSIDE THE LUNG

A first challenge of lung MR elastography concerns the generation of propagating shear wave throughout the organ. Two main strategies can be undertaken:

- The first one consists in using a standard vibrational system composed of a vibrating membrane connected at the end of a pressure wave generator (see **Figure 4.8**, in the middle), or being composed of a MR compatible mechanical actuator driven electromagnetically or piezoelectrically (see **Figure 4.8**, on the left). This mechanical excitation system can be set against the chest wall or the back and create waves inside the lung by exciting the parenchyma through the thoracic cage.

- The second one consists in sending, thanks to a waveguide, pressure waves inside the lung through the mouth of the subject. In this case, upper airways (trachea, bronchi, …) prolong the waveguide, which helps the waves to propagate throughout the lung (see **Figure 4.8**, on the right). When the sound waves, compression waves in the air, reach the surface of the lung parenchyma, the energy of the wave is transmitted inside the parenchyma, resulting in both compressional and shear waves inside the lung tissue.

Whatever the chosen technique, the system needs to be powerful enough to generate waves that propagate everywhere in the organ. As the lung is a large organ with potential viscous properties, low mechanical frequencies are to be preferred.

1.2. MOTION ENCODING INSIDE THE LUNG

In standard elastography, applying a motion encoding gradient, or MEG, between the RF excitation and data sampling raise two issues in the lung.

1.2.1. MOTION ENCODING WITH SHORT SIGNAL LIFETIMES

For large internal organs like the lung, low excitation frequencies, below 100 Hz, are used for the generation of an oscillatory motion in MR elastography in order to limit wave attenuation at higher temporal frequencies because of tissue viscosity. With standard motion encoding techniques, an excitation frequency of 100 Hz yields a bipolar gradient with a duration of 10 ms. This MEG duration is a lower bound for the TE in the MRE pulse sequence (see **Figure 4.11**). Furthermore, TE should be lower than ${T_2}^*$ in order to achieve a fair SNR in the final image. Yet, the MR signal lifetimes, ${T_2}^*$ values, are short in the lung parenchyma. More precisely, the ${T_2}^*$ value in the lung at 3 T is reported to be between 0.3 and 1 ms in the lung parenchyma[421] [422] [423] [424], and this value was shown to vary only slightly with the inflation state of the lung[425].

Hence, if a standard MEG is inserted between the RF excitation pulse and the acquisition window in the pulse sequence, even in a UTE pulse sequence, the TE is at least equal to 10 ms, which is far too much for the lung. Even if a fractional encoding technique is used to decrease the duration of the MEG, it is not possible to reach TE values below 1 or 2 ms while maintaining motion sensitivity.

1.2.2. MOTION ENCODING WITH RESPIRATORY MOTION

The lung is animated by a pseudo-periodical motion which will be encoded by the MEG even though it is not synchronized with this gradient. Let us consider a particle of lung parenchyma. This particle travels about 2 cm (approximatively the amplitude of motion inside the lung) in 2 s (approximatively half a respiratory motion period). The distance travelled by this particle in a duration of 5 ms (time duration between the centers of the two lobes for the proposed MEG) will be $\frac{2\text{ cm} \times 5\ ms}{2\ s} = 50\ \mu\text{m}$, which is in the same order of magnitude as the typical motion amplitude generated in the organ during MR elastography[426]. For that reason, respiratory motion will be a challenge for MR elastography, not only in terms of motion tracking and correction to avoid motion artifacts in the images, but also because this motion is able to create considerable phase shifts for the spins when breathing occurs

[421] Yoshiharu Ohno et al., "T2* Measurements of 3-T MRI With Ultrashort TEs: Capabilities of Pulmonary Function Assessment and Clinical Stage Classification in Smokers," *American Journal of Roentgenology* 197, no. 2 (August 1, 2011): W279–85, https://doi.org/10.2214/AJR.10.5350.

[422] Jiangsheng Yu, Yiqun Xue, and Hee Kwon Song, "Comparison of Lung T2* During Free-Breathing at 1.5T and 3.0T with Ultrashort Echo Time (UTE) Imaging," *Magnetic Resonance in Medicine : Official Journal of the Society of Magnetic Resonance in Medicine / Society of Magnetic Resonance in Medicine* 66, no. 1 (July 2011): 248–54, https://doi.org/10.1002/mrm.22829.

[423] J. M. Wild et al., "MRI of the Lung (1/3): Methods," *Insights into Imaging* 3, no. 4 (August 2012): 345–353, https://doi.org/10.1007/s13244-012-0176-x.

[424] Kevin M. Johnson et al., "Optimized 3D Ultrashort Echo Time Pulmonary MRI," *Magnetic Resonance in Medicine* 70, no. 5 (November 2013): 1241–1250, https://doi.org/10.1002/mrm.24570.

[425] Rebecca J. Theilmann et al., "Quantitative MRI Measurement of Lung Density Must Account for the Change in T 2* with Lung Inflation," *Journal of Magnetic Resonance Imaging* 30, no. 3 (September 2009): 527–534, https://doi.org/10.1002/jmri.21866.

[426] K. Uffmann and M. E. Ladd, "Actuation Systems for MR Elastography," *IEEE Engineering in Medicine and Biology Magazine* 27, no. 3 (May 2008): 28–34, https://doi.org/10.1109/EMB.2007.910268.

during the application of the MEG. It may result in quantification biases and uncertainties in the following elastography reconstruction processes.

1.3. LUNG DENSITY IN MR ELASTOGRAPHY

A usual assumption in elastography reconstruction is to take ρ, the mass density of the organ, homogeneously equal to 1 g/cm^3 in the organ under consideration. This assumption works very well for a great number of solid organs because they are mostly composed of water. Concerning the lung, this is not the case at all. The lung tissue is commonly assumed to be about ten times lighter than other usual biological tissues[427]. Moreover, its mass density is varying along the respiratory cycle, with lower values at the end of inspiration and larger values at the end of expiration. Furthermore, the values taken by this quantity are very heterogeneous throughout the lung, with high values in non-parenchymatous tissues (trachea, primary bronchi, …), lower values in the lung parenchyma and null values inside the large airways. For that reason, a precise ρ map needs to be assessed in order to obtain quantitative measurements of the mechanical parameters in the lung.

This map can be obtained with CT[428]. Nevertheless, CT irradiates the patient with X-rays and cannot be performed for every respiratory phase. It needs to be performed as a separate step, implying the use of image registration techniques to be able to use the ρ map obtained from CT during the elastography reconstruction step. Another more recent technique proposes to create an artificial CT image from several MR images thanks to a deep learning method[429]. The learning step is made on a bank of MR and CT images. Nevertheless, this technique is only based on a complicated function between features extracted from images of both modalities, and is not based on a direct measurement of the lung density.

A last method, which is in my opinion the most adapted and promising one today for MR elastography of the lung, consists in assuming that lung tissue mass density can be approximated from the proton density of the lung tissue. This can be accepted because lung parenchyma is essentially made of water and air. This proton density can thus be estimated at the same time as the T_2^* by fitting an exponential decay model to a series of lung MR images acquired thanks to a short TE gradient echo sequence[430] [431] or an ultrashort TE sequence[432]. This technique was used recently in several experiments carried out in our lab[433] [434]. I have personally participated to such a project a

[427] J. M. Wild et al., "MRI of the Lung (1/3): Methods," *Insights into Imaging* 3, no. 4 (August 2012): 345–353, https://doi.org/10.1007/s13244-012-0176-x.

[428] André Heremans et al., "Measurement of Lung Density by Means of Quantitative CT Scanning: A Study of Correlations with Pulmonary Function Tests," *Chest* 102, no. 3 (September 1, 1992): 805–11, https://doi.org/10.1378/chest.102.3.805.

[429] Andrew P. Leynes et al., "Direct PseudoCT Generation for Pelvis PET/MRI Attenuation Correction Using Deep Convolutional Neural Networks with Multi-Parametric MRI: Zero Echo-Time and Dixon Deep PseudoCT (ZeDD-CT)," *Journal of Nuclear Medicine*, October 30, 2017, jnumed.117.198051, https://doi.org/10.2967/jnumed.117.198051.

[430] Hiroto Hatabu et al., "T2* and Proton Density Measurement of Normal Human Lung Parenchyma Using Submillisecond Echo Time Gradient Echo Magnetic Resonance Imaging," *European Journal of Radiology* 29, no. 3 (March 1, 1999): 245–52, https://doi.org/10.1016/S0720-048X(98)00169-7.

[431] Rebecca J. Theilmann et al., "Quantitative MRI Measurement of Lung Density Must Account for the Change in T 2* with Lung Inflation," *Journal of Magnetic Resonance Imaging* 30, no. 3 (September 2009): 527–534, https://doi.org/10.1002/jmri.21866.

[432] Osamu Togao et al., "Ultrashort Echo Time (UTE) MRI of the Lung: Assessment of Tissue Density in the Lung Parenchyma," *Magnetic Resonance in Medicine* 64, no. 5 (November 2010): 1491–1498, https://doi.org/10.1002/mrm.22521.

[433] Hongchen Wang et al., "Magnetic Resonance Elastography of Emphysematous Rat Lung in Vivo" (ISMRM, Honolulu, USA, 2017).

few years ago to characterize the MR properties of the brain tissues thanks to multi-echo UTE acquisitions[435], and I think that this technique is the most promising one to date for several reasons:

- The density measurement is non-invasive and not dangerous for the patient.
- It gives a ρ map reflecting the possible great heterogeneity of lung density, which can therefore be corrected during the elastography reconstruction.
- Thanks to motion tracking and correction techniques available in MRI, it is possible to obtain density maps for different motion phases throughout the respiratory cycle.
- Last but not least, the measurement can be performed during the same exam as MR elastography, and even partly at the same time as the MRE acquisitions by exploiting the magnitude MR images that are usually not useful in standard elastography. This last possibility is true in particular if the MRE exam is based on short or ultrashort TE pulse sequences. The application of only one pulse sequence has the advantage to simplify the exam workflow.

After estimating proton density maps along the respiratory cycle in the lung parenchyma, a last conversion step is needed to obtain mass density maps. This can be done by assuming a pre-calibrated linear relationship between proton and mass density. The parameters characterizing this relationship can be estimated by performing the same multi-echo acquisition and model fitting procedure on calibrated materials (for which mass density is well known) or to use a CT reference image.

1.4. LUNG MR ELASTOGRAPHY IN THE LITERATURE

A few studies report successful outcomes in lung MR elastography. These experiments usually fall into two main categories, each one corresponding to a given strategy to overcome the problems related to lung MR elastography described just above.

1.4.1. LUNG MRE BASED ON PROTON IMAGING AND SPIN ECHO PULSE SEQUENCES

The first strategy consists in using a spin echo based MRE pulse sequence[436] [437] [438] [439] [440] [441] [442]. Indeed, the lung parenchyma suffers from very short T_2^* values, around 0.5 milliseconds at 3T, but was shown to have a quite long

[434] Felicia Julea et al., "Magnetic Resonance Elastography Accuracy and Precision in Rat Lung and Liver at 1.5 T" (ISMRM-ESMRMB, Paris, France, 2018).
[435] Tanguy Boucneau et al., "In Vivo Characterization of Brain Ultrashort-T2 Components," *Magnetic Resonance in Medicine* 80, no. 2 (2018): 726–35, https://doi.org/10.1002/mrm.27037.
[436] Kiaran P. McGee et al., "Feasibility of Quantifying the Mechanical Properties of Lung Parenchyma in a Small-Animal Model Using 1H Magnetic Resonance Elastography (MRE)," *Journal of Magnetic Resonance Imaging* 29, no. 4 (April 2009): 838–845, https://doi.org/10.1002/jmri.21720.
[437] Yogesh K. Mariappan et al., "MR Elastography of Human Lung Parenchyma: Technical Development, Theoretical Modeling and in Vivo Validation," *Journal of Magnetic Resonance Imaging* 33, no. 6 (2011): 1351–61, https://doi.org/10.1002/jmri.22550.
[438] Yogesh K. Mariappan et al., "Magnetic Resonance Elastography of the Lung Parenchyma in an in Situ Porcine Model with a Noninvasive Mechanical Driver: Correlation of Shear Stiffness with Trans-Respiratory System Pressures," *Magnetic Resonance in Medicine* 67, no. 1 (2012): 210–17, https://doi.org/10.1002/mrm.22976.
[439] Yogesh K. Mariappan et al., "Estimation of the Absolute Shear Stiffness of Human Lung Parenchyma Using 1H Spin Echo, Echo Planar MR Elastography," *Journal of Magnetic Resonance Imaging* 40, no. 5 (2014): 1230–37, https://doi.org/10.1002/jmri.24479.

T_2 value, comprised between 30 and 80 ms in human[443] [444]. With this type of sequences, the TE can be set to a much longer value and still enable pulmonary MRI. This makes possible the implementation of a MEG between the RF excitation and the data acquisition window. To optimize the timing parameters and the final image quality, the MEG can be split around the refocusing pulse and a fractional encoding strategy can be used. The mechanical frequency was low for human (50 Hz) and higher for preclinical studies (100-300 Hz). The shear waves were induced in human thanks to a mechanical excitation system in contact with the right chest wall.

Nevertheless, in spite of the interesting results reported with this strategy, the scan times involved are usually very long. Even the EPI-based method reports scan times of 30 seconds for only four slices, 4 dynamics and only one motion encoding direction. If the acquisition of a full 3D image of the lung is considered, with more dynamics and with MEG applied along the three dimensions of space, the total scan time would thus become not adapted to clinical practice. Moreover, each acquisition was performed during several breath-holds at one given lung volume or averaged over several respiratory cycles. In this situation, the dynamic evolution of the mechanical properties of the lung during the respiratory cycle cannot be assessed in free-breathing. Furthermore, the Cartesian spin echo pulse sequence doesn't provide any feature to make respiratory motion tracking and/or correction easier (self-navigation, radial sampling of k-space, …).

1.4.2. LUNG MRE BASED ON THE IMAGING OF A TRACER GAS WITH GRADIENT ECHO PULSE SEQUENCES

The second strategy consists in imaging hyperpolarized ^{3}He or ^{129}Xe than ^{1}H to perform lung elastography[445] [446].

Hyperpolarized ^{3}He was proposed in several elastography studies to carry the motion information needed in MRE[447] [448]. A US patent was even deposited for this technique based on ^{3}He or ^{129}Xe as a contrast agent[449]. With

---

[440] John P. Marinelli et al., "Quantitative Assessment of Lung Stiffness in Patients with Interstitial Lung Disease Using MR Elastography," *Journal of Magnetic Resonance Imaging* 46, no. 2 (2017): 365–74, https://doi.org/10.1002/jmri.25579.

[441] Hongchen Wang et al., "Magnetic Resonance Elastography of Emphysematous Rat Lung in Vivo" (ISMRM, Honolulu, USA, 2017).

[442] Felicia Julea et al., "Magnetic Resonance Elastography Accuracy and Precision in Rat Lung and Liver at 1.5 T" (ISMRM-ESMRMB, Paris, France, 2018).

[443] J. M. Wild et al., "MRI of the Lung (1/3): Methods," *Insights into Imaging* 3, no. 4 (August 2012): 345–353, https://doi.org/10.1007/s13244-012-0176-x.

[444] Kevin M. Johnson et al., "Optimized 3D Ultrashort Echo Time Pulmonary MRI," *Magnetic Resonance in Medicine* 70, no. 5 (November 2013): 1241–1250, https://doi.org/10.1002/mrm.24570.

[445] Hans-Ulrich Kauczor et al., "Imaging of the Lungs Using 3he MRI: Preliminary Clinical Experience in 18 Patients with and without Lung Disease," *Journal of Magnetic Resonance Imaging* 7, no. 3 (1997): 538–43, https://doi.org/10.1002/jmri.1880070314.

[446] Bastiaan Driehuys et al., "Imaging Alveolar–Capillary Gas Transfer Using Hyperpolarized 129Xe MRI," *Proceedings of the National Academy of Sciences* 103, no. 48 (November 28, 2006): 18278–83, https://doi.org/10.1073/pnas.0608458103.

[447] B.c. Goss et al., "Magnetic Resonance Elastography of the Lung: Technical Feasibility," *Magnetic Resonance in Medicine* 56, no. 5 (November 2006): 1060–1066, https://doi.org/10.1002/mrm.21053.

[448] Kiaran P. McGee, Rolf D. Hubmayr, and R.l. Ehman, "MR Elastography of the Lung with Hyperpolarized 3He," *Magnetic Resonance in Medicine* 59, no. 1 (January 2008): 14–18, https://doi.org/10.1002/mrm.21465.

[449] Richard L. Ehman et al., Imaging elastic properties of the lung with magnetic resonance elastography, United States US7991449B2, filed April 20, 2006, and issued August 2, 2011, https://patents.google.com/patent/US7991449B2/en.

^{3}He, the T_2^* value in the lung is now around 10 ms[450], enabling the use of gradient echo pulse sequences for MR elastography. This technique was performed on phantoms and ex-vivo lungs with a higher mechanical frequency (100-150 Hz) compared to proton MRE experiments introduced in 1.4.1, and sometimes with a fractional encoding strategy. *In vivo* human experiments were also performed in our research team with pressure waves produced thanks to a loudspeaker and sent in the lung through the subject's mouth at the same time as the hyperpolarized gas thanks to a waveguide[451].

Nevertheless, hyperpolarized gas imaging is costly, both in terms of supplementary hardware (hyperpolarizer, MRI coils, …) and in terms of consumption of contrast agent. Moreover, this type of exam is more challenging to implement than standard proton MRI exams and require a qualified staff to perform the exams. Furthermore, as it was said for proton MRE of the lung in 1.4.1, the studies were essentially performed during breath-holds, preventing the measurement of the different mechanical parameters along the respiratory cycle. To conclude, even with a gradient echo sequence, the total scan time remains long: 52 seconds for only one slice, 4 dynamics and one motion encoding direction. Extended to a full 3D scan of the lung, this scan time can become unpractical clinically speaking, unless large voxel sizes (> 1 cm) are prescribed, as it was done in Santarelli *et al.*.

1.4.3. LIMITATIONS AND PERSPECTIVES

The first results obtained in the field of lung MRE are relevant and prove the feasibility of MR elastography in this challenging organ. Nevertheless, the presented techniques are not flawless, in particular in terms of scan time, contrast mechanisms, and motion correction. Moreover, as seen previously, encoding the motion pattern in the MR phase by inserting a MEG between RF excitation and data acquisition is only possible if the problem of short T_2^* signal decay is corrected (for example, by using a spin echo sequence or exploiting hyperpolarized gas NMR).

Ultrashort Echo-Time (UTE) and Zero Echo-Time (ZTE) pulse sequences may solve the issue of short signal lifetime the acquisition of MR signal just after the RF excitation. However, they do not leave enough time to insert a MEG between the RF excitation pulse and the data acquisition window: the insertion of such a bipolar gradient would result in an increase of TE, which thus exacerbates the problem of short T_2^* decay of signal.

UTE and ZTE pulse sequences and MRE of the lung seem incompatible. In the next subsection, we will explore another strategy to encode motion with an ultrashort or zero echo time acquisition in a MR image.

2. THE MOTION-SENSITIZING MAGNETIZATION PREPARATION (MSPREP) PULSE

2.1. ADVANCED AND INSPIRING MOTION ENCODING STRATEGIES PROPOSED IN THE LITERATURE

As the MEG cannot be inserted between the RF excitation pulse and the acquisition window, it seems evident that it needs to be inserted elsewhere. The solution is to insert the MEG before the RF excitation pulse or after the acquisition window, which is similar because of repetitions in standard MRI pulse sequences. In this case, the MEG would act as a magnetization preparation pulse instead of a standard encoding pulse.

[450] X. Josette Chen et al., "Spatially Resolved Measurements of Hyperpolarized Gas Properties in the Lung in Vivo. Part II: T2*," *Magnetic Resonance in Medicine* 42, no. 4 (1999): 729–37, https://doi.org/10.1002/(SICI)1522-2594(199910)42:4<729::AID-MRM15>3.0.CO;2-2.

[451] Roberta Santarelli, "Helium-3 Magnetic Resonance Elastography of the Lung" (phdthesis, Université Paris Sud - Paris XI, 2013), https://tel.archives-ouvertes.fr/tel-01359197/document.

The first idea we had in this way was to adapt the strategy published ten years ago on DENSE-MRE[452]. In this technique, the two MEG lobes are inserted in two different parts of the MR pulse sequence:

- The first lobe is inserted before the RF excitation pulse between dedicated +90° and -90° RF pulses. With the association of those three components, the longitudinal magnetization is first flipped in the transverse plane. The transverse magnetization is then submitted to the first gradient lobe. At the spin level, this first lobe of gradient generates a dephasing with:
    - the original position of the spin, as any position encoding gradient lobe would do.
    - the shear displacement generated during MR elastography.

  Finally, the -90° pulse is applied and generates a longitudinal magnetization component that is equal to the projection of the prepared transverse magnetization orthogonally to the polarization of this RF pulse. After this preparation, a spoiler gradient is applied to destroy any remaining transverse magnetization component. Just before the RF excitation step, the longitudinal magnetization is therefore modulated in amplitude because of the position of the spins at preparation time, which is a combination of the equilibrium position and the induced displacement at the motion encoding time.

- The second lobe is inserted between RF excitation and data acquisition. At RF excitation time, a fraction of the previously prepared longitudinal magnetization is flipped in the transverse plane and the corresponding spins are dephased thanks to the second MEG lobe. It can be shown that the resulting signal is the sum of three components, with one of the three components having a phase modulated only by the displacement induced by the propagation of the shear wave. It can also be shown that the two other terms can be either attenuated or taken out of the measured k-space with a good choice of acquisition parameters.

Despite its advanced complexity compared to more standard MR elastography sequences, this technique was shown to be particularly adapted to short T_2^* tissues and gives the possibility to reduce the total scan time. Furthermore, such a preparation before the RF excitation pulse is adaptable to any MR pulse sequence, and in particular UTE and ZTE sequences. Nevertheless, the technique does not only involve the insertion of a preparation pulse but also a gradient lobe between the RF excitation pulse and the acquisition window: the problem of short T_2^* is only partially alleviated. A large reduction of the duration ΔT_{Lobe} of the two MEG lobes to reduce the TE, would be detrimental to the motion sensitivity of the sequence.

Another inspiring strategy relies on optimal control[453]. In this case, motion encoding is performed in the MR phase image at the same time as RF excitation thanks to an optimal control approach. However, because of the very long duration of such RF pulses (around 20 ms), it is just impossible to properly excite short T_2^* tissues (because of spin dephasing during the excitation) with this technique. Moreover, it would certainly lead to unpractical total scan times.

[452] Benjamin Robert et al., "Application of DENSE-MR-Elastography to the Human Heart," *Magnetic Resonance in Medicine* 62, no. 5 (2009): 1155–63, https://doi.org/10.1002/mrm.22124.
[453] Pauline M. Lefebvre et al., "Active Control of the Spatial MRI Phase Distribution with Optimal Control Theory," *Journal of Magnetic Resonance* 281 (August 1, 2017): 82–93, https://doi.org/10.1016/j.jmr.2017.05.008.

2.2. INTRODUCTION OF THE MSPREP PULSE

To keep the TE as short as possible, without compromising neither the efficiency of RF excitation nor the total acquisition time, we implemented the same type of motion sensitizing module but as a pure preparation step, without adding anything neither during nor between the RF excitation and the data acquisition. However, a pure preparation before the RF excitation means that only the longitudinal magnetization would be impacted by this preparation. This constraint is not such a problem because the transverse magnetization that creates the MR signal is directly proportional to the longitudinal magnetization existing just before tissue excitation. Rather, this is quite a good idea because the T_1, that controls the evolution of the longitudinal magnetization, is particularly long in the lung. The motion encoding efficiency is therefore not degraded anymore by the shortness of the relaxation time. Thanks to this long T_1, a motion encoding strategy based on a pure preparation of the longitudinal magnetization could thus be performed at a given moment of the imaging process and then kept for a long time during the acquisition, giving the possibility to exploit it along a large number of repetitions in the pulse sequence. This possibility to acquire an important quantity of data from only one encoding step is a high potential source of scan time reduction. The preparation pulse must provide at the same time an exploitable sensitivity to shear waves and a weak dependence on the short $T_2{}^*$ values.

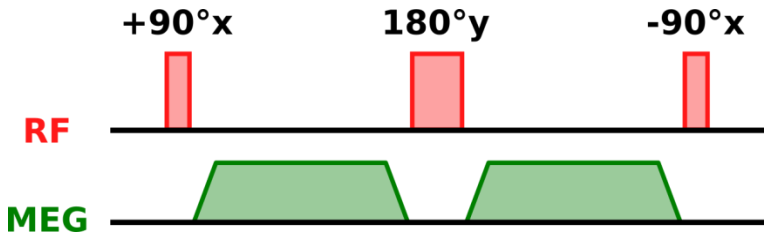

Figure 4.12: The Motion Sensitized magnetization Preparation (MSPREP) pulse.

Such a preparation pulse has already been addressed in the literature but, to our knowledge, never used as a tool to encode a shear wave pattern for MR elastography. This pulse is the Motion-Sensitizing magnetization Preparation pulse, or MSPREP. Chronologically, this pulse is composed of those elements (see **Figure 4.12**):

- **One +90° RF pulse applied along the x direction:** after the application of this pulse, all the existing longitudinal magnetization is flipped in the transverse plane. Just after the application of this pulse, the local $\overrightarrow{M_{xy}}$ vector is thus oriented along y everywhere in the FOV.

- **One motion encoding gradient lobe applied along one chosen encoding direction:** during the application of this gradient pulse, the local $\overrightarrow{M_{xy}}$ vector experiences a global phase shift (because of the initial spin positions and because of the shear displacement, as seen with DENSE-MRE in 2.1) but also a decrease in amplitude because of the dephasing between neighboring spins ($T_2{}^*$ signal decay effect). At this point, the amplitude of $\overrightarrow{M_{xy}}$ is thus very low in the lung because of the short $T_2{}^*$ in the lung parenchyma.

- **One 180° refocusing RF pulse applied along the y direction:** this RF pulse flips all the spins around the y axis. Thanks to this pulse, a spin echo will be created after a time equal to the duration between the +90° and this 180° RF pulse.

- **A second motion encoding gradient lobe exactly identical to the first one:** this gradient pulse will refocus the spin phase shifts accumulated so far and related to their original position but not the ones related to

the motion that occurred between the applications of the two gradient lobes, as seen in the first section of this chapter for standard MRE.

- **One -90° RF pulse applied along the x direction:** this pulse will be applied at the time when the spin echo occurs. It results in the generation of a longitudinal magnetization that is proportional to the projection of $\overrightarrow{M_{xy}}$ on axis x (as explained for DENSE-MRE), with an amplitude that depends only on the displacement of spins from their original position and that occurred between the two gradients lobes. Thanks to the previous application of a 180° RF pulse, the amplitude decay from the beginning of this preparation pulse depends only on the T_2 value in the biological tissue (and not on the T_2^*, thanks to the spin echo).

The very first applications of this type of pulse, but without any gradient lobes, were in NMR spectroscopy to enhance the amplitude of signal created by nuclei with a long T_1 constant[454]. At this time, this pulse was called Driven Equilibrium Fourier Transform, or DEFT. This exact same pulse was used later in MRI as a preparation pulse to add T_2 contrast to gradient echo images[455]. Several years later, gradient lobes were added between the RF pulses, making this pulse sensitive to motion. This DEFT pulse with gradients was thus called Diffusion Preparation, or DP[456], but also Motion-Sensitized Driven-Equilibrium, or MSDE[457], and Motion-Sensitizing magnetization Preparation, or MSPREP[458], and was essentially used to perform efficient black blood MRI thanks to its ability to suppress the signal coming from moving spins. This last name will be kept for the rest of this manuscript because it better reflects the role of this pulse in the context of MR elastography: making tissue magnetization sensitive to motion.

2.3. THEORETICAL ANALYSIS AND ADAPTATION OF MSPREP TO MR ELASTOGRAPHY

If a shear wave is generated inside the biological tissue, and if the two MEG lobes are set to be synchronous both in terms of temporal position and temporal frequency with the mechanical excitation (see 2.2.4 and 2.2.5 in the previous section), it is possible to encode the displacement field directly onto the MR image, as in standard MR elastography. However, the displacement field is now encoded into the MR signal magnitude and not into the signal phase. This MR signal phase is reset to zero immediately after the application of each RF pulse and any phase contrast can thus be generated only between the application of the RF excitation pulse and the data acquisition window. All the theory seen in the first section of this chapter for motion sensitization in MR elastography is thus

[454] Edwin D. Becker, James A. Feretti, and Thomas C. Farrar, "Driven Equilibrium Fourier Transform Spectroscopy. A New Method for Nuclear Magnetic Resonance Signal Enhancement," *Journal of the American Chemical Society* 91, no. 27 (December 1969): 7784–85, https://doi.org/10.1021/ja50001a068.

[455] John P. Mugler, Thomas A. Spraggins, and James R. Brookeman, "T2-Weighted Three-Dimensional MP-RAGE MR Imaging," *Journal of Magnetic Resonance Imaging* 1, no. 6 (1991): 731–37, https://doi.org/10.1002/jmri.1880010621.

[456] Ioannis Koktzoglou and Debiao Li, "Diffusion-Prepared Segmented Steady-State Free Precession: Application to 3D Black-Blood Cardiovascular Magnetic Resonance of the Thoracic Aorta and Carotid Artery Walls," *Journal of Cardiovascular Magnetic Resonance* 9, no. 1 (January 1, 2007): 33–42, https://doi.org/10.1080/10976640600843413.

[457] Jinnan Wang et al., "Improved Suppression of Plaque-Mimicking Artifacts in Black-Blood Carotid Atherosclerosis Imaging Using a Multislice Motion-Sensitized Driven-Equilibrium (MSDE) Turbo Spin-Echo (TSE) Sequence," *Magnetic Resonance in Medicine* 58, no. 5 (2007): 973–81, https://doi.org/10.1002/mrm.21385.

[458] Thanh D. Nguyen et al., "Effective Motion-Sensitizing Magnetization Preparation for Black Blood Magnetic Resonance Imaging of the Heart," *Journal of Magnetic Resonance Imaging* 28, no. 5 (2008): 1092–1100, https://doi.org/10.1002/jmri.21568.

applicable here, with the difference that the dephasing related to the shear motion will be retrieved in the magnitude image and not in the phase image.

However, one slight modification can be proposed to this MSPREP pulse to be more adapted to MR elastography. To understand this modification, let us see what is measured exactly after the application of such a preparation pulse. Let $\Delta\varphi$ be the phase shift induced to $\overrightarrow{M_{xy}}$ because of the shear displacement in the biological tissue. If there are no other sources of dephasing, the longitudinal magnetization obtained just after the application of the -90° pulse along x, written M_z, will be:

$$M_z = M_{z0} e^{-\frac{\Delta T_{MSPREP}}{T_2}} \cos(\Delta\varphi) \qquad \textbf{Eq. 4.39}$$

where M_{z0} is the longitudinal magnetization just before the application of the MSPREP and ΔT_{MSPREP} is its total duration. If a spoiler of duration ΔT_{Spoil} is applied just after the MSPREP to suppress the remaining transverse magnetization, as it was done in DENSE-MRE, the longitudinal magnetization at the end of the spoiler is now:

$$M_z = M_0 + \left(M_{z0} e^{-\frac{\Delta T_{MSPREP}}{T_2}} \cos(\Delta\varphi) - M_0 \right) e^{-\frac{\Delta T_{Spoil}}{T_1}} \qquad \textbf{Eq. 4.40}$$

with M_0 being the longitudinal magnetization in the biological tissue at thermal equilibrium, without any spin saturation effect. If a RF excitation pulse of flip angle α is applied just after the spoiler, a transverse magnetization is generated and is source of MR signal for the MR imaging process. Its amplitude is then:

$$M_{xy}(\Delta\varphi) = \left[M_0 + \left(M_{z0} e^{-\frac{\Delta T_{MSPREP}}{T_2}} \cos(\Delta\varphi) - M_0 \right) e^{-\frac{\Delta T_{Spoil}}{T_1}} \right] \sin(\alpha) \qquad \textbf{Eq. 4.41}$$

If $\Delta\varphi = 0$ (because there is no motion or because the MEG amplitude is null, for example), $M_{xy}(0)$ corresponds to a maximum of transverse magnetization amplitude which results in a maximum magnitude signal for the image. If $\Delta\varphi > 0$, it can be shown that $M_{xy}(\Delta\varphi) < M_{xy}(0)$: the magnitude MR signal is thus attenuated by the presence of a positive shear displacement component along the MEG direction. Now, if the motion induced dephasing is the same as just before but with an opposite sign ($-\Delta\varphi$). Because of the parity of the cosine function, we obtain $M_{xy}(-\Delta\varphi) = M_{xy}(\Delta\varphi)$ for all the values that can be taken by $\Delta\varphi$. With the MSPREP pulse presented above, the motion encoding is thus rectified and it is not possible to distinguish between positive and negative components of motion along the MEG direction.

The solution to this problem would be to change the phase of the -90° RF pulse in the MSPREP. Instead of having a phase equal to 0 (to obtain a -90° RF pulse applied along the direction x), the idea is to set a non-zero phase β for this RF pulse. In this case, the transverse magnetization obtained by applying this new RF excitation pulse is:

$$M_{xy}(\Delta\varphi) = \left[M_0 + \left(M_{z0} e^{-\frac{\Delta T_{MSPREP}}{T_2}} \cos(\Delta\varphi - \beta) - M_0 \right) e^{-\frac{\Delta T_{Spoil}}{T_1}} \right] \sin(\alpha) \qquad \textbf{Eq. 4.42}$$

In this case, it can be shown that $M_{xy}(-\Delta\varphi) \neq M_{xy}(\Delta\varphi)$ for all the values of $\Delta\varphi \neq 0[\pi]$. It is now possible to differentiate between positive and negative components of the displacement along the MEG direction.

However, for any values of $\Delta\varphi$ and β, if we consider a dephasing $\Delta\psi = -\Delta\varphi + 2\beta$, the cosine term gives:

$$\cos(\Delta\psi - \beta) = \cos(\Delta\varphi - \beta) \qquad \textbf{Eq. 4.43}$$

which results to the same equality for $M_{xy}(\Delta\psi)$ and $M_{xy}(\Delta\varphi)$. The exact same result is obtained when $\Delta\psi = \Delta\varphi + 2\pi$. For that reason, if the dephasing $\Delta\varphi$ becomes too large in absolute value, the same MR signal can be obtained for different values of motion components along the MEG direction. In standard elastography, it resulted as a phase wrapping in the MR phase image. Here, the effect is different and concerns the magnitude image. We might perform two acquisitions with different values of β or two different MEGs to discriminate between displacement equality and wrapping artifact.

In this new approach, the image weighting involved when a MSPREP pulse is applied during the propagation of a shear wave is complex. As seen in **Eq. 4.42**, the amplitude of the transverse magnetization created just after the RF excitation depends on the different physical properties of tissues (ρ, T_1, T_2). The signal in the final MR image may be additionally altered by the T_1 dependence of the steady-state which gets established after a sufficient number of repetitions in the sequence. Such effect can be partly suppressed by acquiring two images with the same mechanical excitation and opposite gradient amplitudes, as it is sometimes done in standard MR elastography to remove the background phase.

On the output signal, the displacement field is generally not encoded with a simple linear relationship. It is not proportional to $\Delta\varphi$ but to its cosine. Thereof, if it is recorded at different moment, for different dynamics, the magnitude signal in a voxel does not follow a sinusoidal signal but varies as its cosine as a function of the dynamics. Only if $\Delta\varphi$ remains small in absolute value then the cosine term can be approximated by the following affine relationship:

$$\cos(\Delta\varphi - \beta) \approx \cos(\beta) + \sin(\beta)\,\Delta\varphi \qquad \textbf{Eq. 4.44}$$

The same type of affine relationship is thus obtained between the transverse magnetization and $\Delta\varphi$. In this case, if β is well chosen (we will see later what it means) and if $\left|\frac{\Delta\varphi}{\beta}\right| \ll 1$, the exploitation of the resulting MR magnitude images acquired with MSPREP-MRE is not more difficult than the exploitation of MR phase images acquired with standard MRE.

In conclusion, the MSPREP strategy seems adapted to lung MR elastography. By including motion sensitization gradients in a pure preparation pulse, it is possible to completely separate the 'motion encoding sequence part' from the 'image acquisition sequence part' in the pulse sequence. It therefore gives the possibility to include this preparation pulse in theoretically any pulse sequence, and in particular in UTE or ZTE pulse sequences, which were shown to be well adapted to lung MR imaging, without compromising their basic features and capabilities.

3. DEVELOPMENT OF A MSPREP-UTE PULSE SEQUENCE FOR MRE

3.1. IMPLEMENTATION DETAILS

To test the potentially promising capabilities offered by a MSPREP pulse for lung MRE, we first implemented it in the UTE pulse sequence, which is a little bit more flexible than the ZTE as:

- First, in UTE, the radii in k-space can be chosen in any temporal order, while the angle between two successive spokes must remain small in ZTE.
- Second, in UTE, a preparation pulse can be applied before any repetition, while this preparation pulse can only be applied between two segments in ZTE (group of repetitions during which the readout gradient varies continuously).

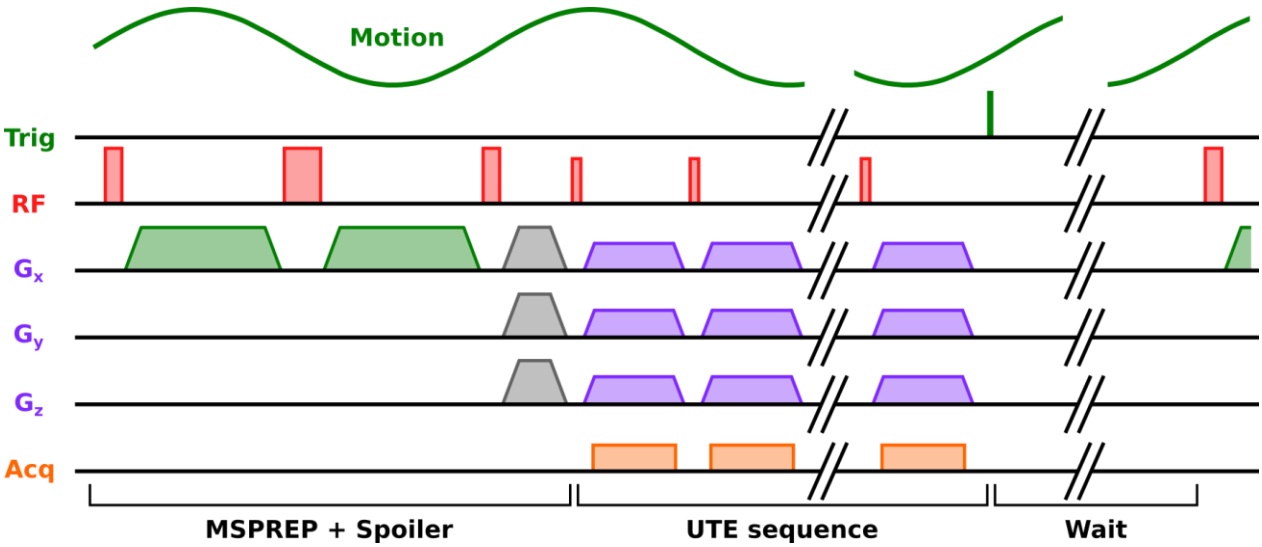

Figure 4.13: Representation of one segment of the MSPREP-UTE pulse sequence and delimitation of its three main parts.

First, in order to explain the implementation of the MSPREP strategy in UTE, while keeping it compatible with the ZTE pulse sequence, we introduce the concept of 'segment' for a MSPREP-UTE sequence (and more generally a MSPREP-MRE pulse sequence, based on UTE, ZTE or any other pulse sequence). In the following, the names written in italic correspond to the names of variables in the GE EPIC (Environment for Pulse programing In C) code source.

For the MSPREP-UTE pulse sequence, a segment is composed of three elements (see **Figure 4.13**):

- **The MSPREP pulse itself followed by a spoiling gradient:** as seen in 2.3, this MSPREP pulse encodes the motion information directly in the longitudinal magnetization of the biological tissue and the spoil is useful to destroy any transverse magnetization remaining after the preparation. Remark that the other preparation pulses originally implemented in the pulse sequence are still usable (chemically selective fat suppression pulse, long T_2 suppression pulse, …). In this case, this supplementary preparation pulse is applied between the MSPREP and the spoil.

- $\boldsymbol{MRE\_TRsPerPrep}$ **repetitions:** each repetition is composed of a RF excitation pulse, readout gradient pulses in the three spatial directions to acquire a radius in a 3D k-space, an acquisition window and, optionally, a spoiler gradient to remove any residual transverse magnetization before the next RF excitation.

- **A waiting period of time:** this period of time of duration $MRE\_WaitTime$ is useful to let the longitudinal magnetization recover before applying a new MSPREP. Indeed, because of the long T_1 values in the lung parenchyma, it can be wise to set a sufficient recovery time in order to have a sufficient SNR in the final MR image. During this waiting period, the only pulse sequence element applied is the trigger sent to synchronize the mechanical excitation system with the MSPREP pulse. If several dynamics are needed, the parameter MRE_NbDyn can be set accordingly, and the dynamic switch is simply done by shifting in time the trigger at the beginning of each dynamic.

This preparation pulse was developed as an additional option to the original UTE pulse sequence. To turn-on the MSPREP option, the parameter MRE_Flag just needs to be set to 1 in the user interface. On this user interface, other useful parameters can be set:

- the desired motion frequency, set with $MRE\_MotionFreq$;
- the MEG direction, chosen by setting MRE_EncDir to 1, 2 or 3, corresponding respectively to the 'frequency encoding direction', the 'phase encoding direction' and the 'slice selection direction' (in GE Healthcare pulse sequences, these three directions need to be prescribed for every pulse sequence, even a 3D radial one);
- the MEG amplitude, chosen by setting $MRE\_EncGradAmp$ between -1 and $+1$, in units of maximal gradient amplitude reachable by the machine;
- fractional encoding, by setting the parameter $MRE\_FracEncRatio$ between 0 and 1. This value represents the ratio between the MEG period, written T_{MEG} in the first section, and the actual motion period, written T_{Motion}. The value 1 thus corresponds to a standard motion encoding procedure ($T_{MEG} = T_{Motion}$).

$MRE\_MotionFreq$ is the user target frequency for the experiment, and not the actual motion frequency to set to the mechanical excitation system. Indeed, because the different RF and gradient boards have their own discrete update times (2 µs for RF boards and 4 µs for gradient boards) that need to be considered in pulse sequence programing, a given desired motion frequency value is not always adapted to a given value of $MRE\_FracEncRatio$. For that reason, the MSPREP parameters are calculated to be adapted as much as possible to the target frequency $MRE\_MotionFreq$, and the actual motion frequency to set to the mechanical excitation system is returned in $MRE\_ActMotionFreq$ with a precision in the order of the µHz. It is adapted to the refreshing rates of the RF and gradient boards. This actual frequency is automatically reduced compared to the target frequency if the prescribed MEG amplitudes cannot be physically achieved because of slew-rate limitations. In this case, the user has the choice either to decrease the motion frequency to the one proposed by the program, to decrease the gradient amplitude to reach an actual frequency very close to the target one, or to increase, if possible, the parameter $MRE\_FracEncRatio$. Another very useful parameter calculated after the sequence prescription and returned to the user is the number of motion periods to send between two triggers. This number can be found in the parameter $MRE\_NbBursts$ and is usually needed to properly set the function generator that drives the mechanical excitation system.

Every parameter of the MSPREP itself and its associated spoiler gradient is tunable with the following guidelines:

- A square/hard RF pulse was implemented to reach the desired flip angle in the lung in the minimal time. By default, the amplitude of this square pulse was set to the maximal B_1 value reachable by the machine, but its value can be changed if needed. For a B_1 amplitude of 0.25 Gauss, the durations of the RF pulses are equal to 236 µs for the +/-90° pulses and 472 µs for the 180° pulse.
- The gradient lobes (MEG lobes and spoiler) were defined as trapezoids with a ramp-up section, a plateau and a ramp-down section. By default, the ramp-up and ramp-down sections were set to have the minimal possible duration with the slew-rate constraint, but their duration can be modified if needed. For a MEG set at the maximal gradient amplitude reachable on the PET/MR system at SHFJ, the minimal ramp-up/ramp-down duration is equal to 628 µs.

For example, the duration between the beginning/end of a RF pulse and the end/beginning of a gradient pulse in the MSPREP can be chosen in order to avoid the application of a RF pulse as the magnetic field is inhomogeneous because of Eddy currents generated by the MEG lobes[459]. This parameter, named $MRE\_RFGradSep$ and set by default to 100 µs, thus indirectly controls the duration of each gradient lobe, defined so far as ΔT_{Lobe}. The β angle introduced in 2.3 can also be prescribed by setting the variable $MRE\_BetaAngle$.

In each segment of the UTE sequence, the code defining the repetitions was not modified. The UTE acquisition itself keeps the same performances with and without the MSPREP option. Only every $MRE\_TRsPerPrep$ repetitions, the repetitions of tissue excitation and data acquisition are paused to apply the waiting period of duration $MRE\_WaitTime$, during which a new trigger is sent before starting a new segment.

3.2. THE CONTINUOUS AND TRANSIENT MSPREP-MR ELASTOGRAPHY MODES

The two possible continuous and transient elastography modes can be chosen by setting the parameter MRE_Mode (see **Figure 4.14**):

- **If $\boldsymbol{MRE\_Mode = 1}$:** The MRE pulse sequence is set to continuous oscillatory mode. This mode is the standard mode in MR elastography: a continuous oscillatory shear wave is generated inside the organ and several phases of the wave pattern, called dynamics, are encoded in MR images. For this mode, the trigger is sent at the very beginning of the waiting period to be sure that the wave pattern has reached a mechanical steady-state before motion encoding and data acquisition. Moreover, the MRE_NbDyn time positions of the trigger are spread within one actual motion period of duration $\frac{1}{MRE\_ActMotionFreq}$.

- **If $\boldsymbol{MRE\_Mode = 2}$:** The MRE pulse sequence is set to transient mode. Whereas this mode is very common in ultrasound elastography, only a few studies relate the use of such a technique[460] [461] [462] [463]. With this mode, instead of sending in the organ a continuous oscillatory wave at one given temporal frequency, a transient wavefront is created within the tissue and this wavefront is followed with the same strategy as standard elastography. In the elastography mode presented just above, it was necessary to synchronize the time position and frequency of the oscillatory motion with the bipolar MEG thanks to a trigger sent at the beginning of the waiting time period. In transient mode, the trigger is inserted at the end of the waiting time period and gives the instruction to the mechanical excitation system to generate an excitation pulse (a square pulse or only one oscillatory period of motion, for example), which results in the generation of a single wavefront. By repeating the process for different time positions of the trigger, the propagation of this wavefront can be tracked with time. Transient elastography can be performed by any MRE pulse sequence actually with proper triggering. Yet, because the wavefront needs to be followed

[459] Wang et al., "Improved Suppression of Plaque-Mimicking Artifacts in Black-Blood Carotid Atherosclerosis Imaging Using a Multislice Motion-Sensitized Driven-Equilibrium (MSDE) Turbo Spin-Echo (TSE) Sequence."
[460] Paul J. McCracken et al., "Mechanical Transient-Based Magnetic Resonance Elastography," *Magnetic Resonance in Medicine* 53, no. 3 (2005): 628–39, https://doi.org/10.1002/mrm.20388.
[461] Rémi Souchon et al., "Transient MR Elastography (t-MRE) Using Ultrasound Radiation Force: Theory, Safety, and Initial Experiments in Vitro," *Magnetic Resonance in Medicine* 60, no. 4 (2008): 871–81, https://doi.org/10.1002/mrm.21718.
[462] Rémi Souchon et al., "Measurement of Pulsatile Motion with Millisecond Resolution by MRI," *Magnetic Resonance in Medicine* 67, no. 6 (2012): 1787–93, https://doi.org/10.1002/mrm.23134.
[463] Lorne W. Hofstetter et al., "Efficient Shear Wave Elastography Using Transient Acoustic Radiation Force Excitations and MR Displacement Encoding," *Magnetic Resonance in Medicine* 81, no. 5 (2019): 3153–67, https://doi.org/10.1002/mrm.27647.

along its entire propagation through the organ (during a time that corresponds usually to several motion periods in standard MR elastography), the expected TR is usually very long. Moreover, because a great number of dynamics need to be acquired, it results in scan times that are unpractical for clinical exams. Here, the waiting time before the application of every MSPREP pulse can be exploited to follow the entire propagation of the shear wavefront by properly setting the time position of the trigger. Besides, the long TR with standard MRE pulse sequences for transient elastography is not an issue anymore in MSPREP-MRE with separate motion encoding magnetization preparation. Moreover, the time efficiency of MSPREP-MRE pulse sequences, which is largely due to the fact that several spokes can be acquired from only one preparation step, gives the possibility to follow the shear wavefront thanks to a great number of motion dynamics without reaching prohibitive scan times. In more general perspectives, this mode is adapted to any organ, which extends further the possibilities of this new MRE pulse sequence.

We have developed and implemented a new preparation pulse on a 3D UTE pulse sequence, the MSPREP, without compromising any of the capabilities of the initial pulse sequence. The development was carried to enable full control of every parameter of the preparation pulse and test this new technique in a great number of configurations.

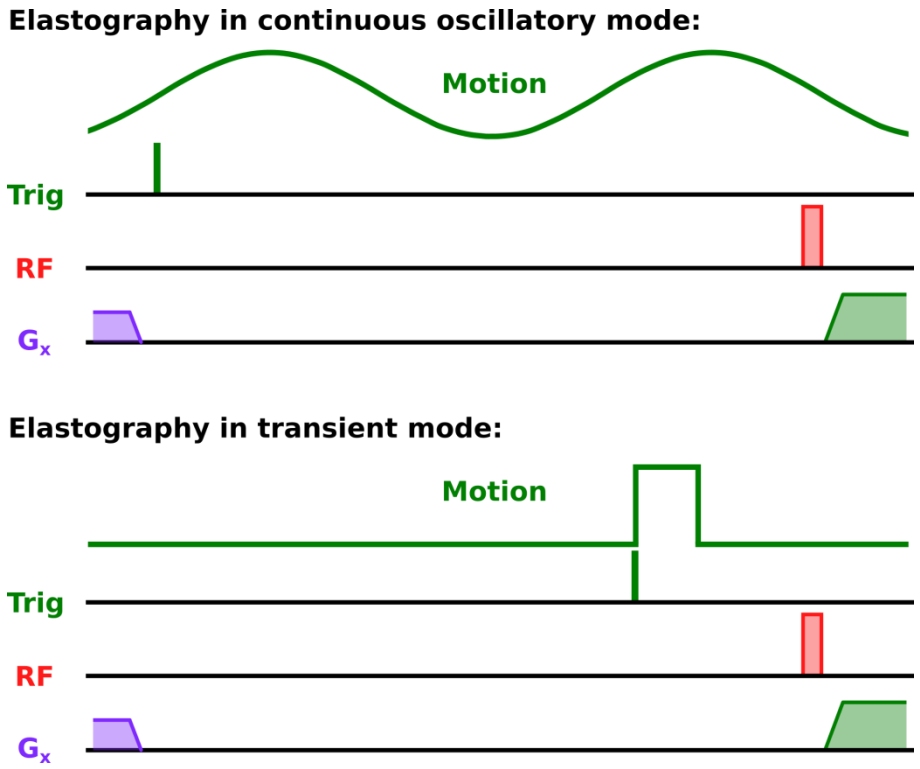

Figure 4.14: Illustration of the two available modes in MSPREP-MRE: the continuous oscillatory mode (upper row) and the transient mode (lower row).

4. ADVANTAGES AND DRAWBACKS OF MSPREP-MRE

The expected advantages and drawbacks of MSPREP-MRE with respect to standard MRE are summarized below to give a broad overview of the possibilities offered by both techniques.

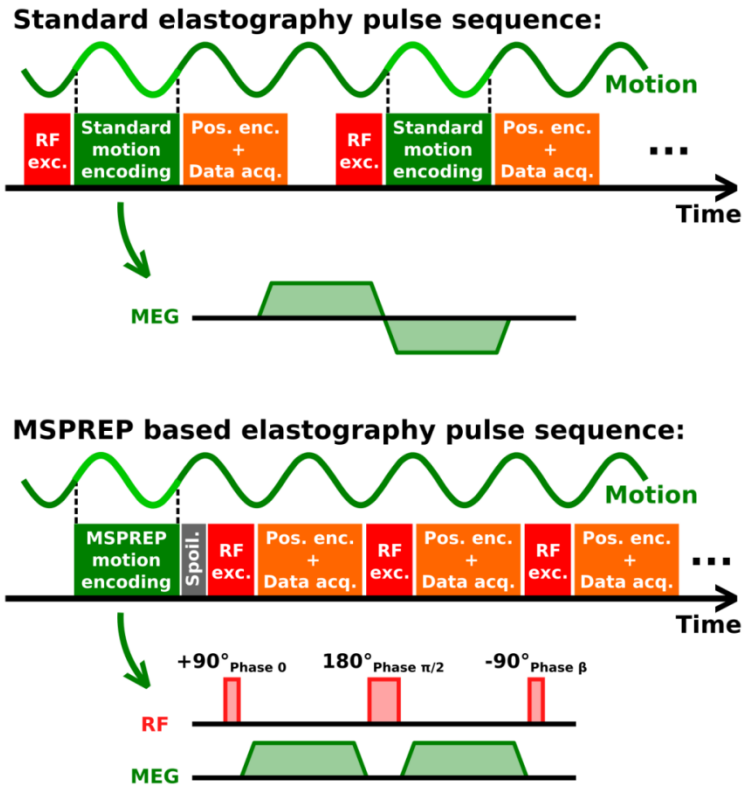

Figure 4.15: Illustration of the time efficiency of MSPREP-MRE in comparison with standard MRE.

Advantages of MSPREP-MRE compared to standard MRE pulse sequences:

- MRE capability to any MRI pulse sequence, and in particular to pulse sequences featuring a very short TE, like UTE and ZTE pulse sequences, which are not usually neither adapted nor used with standard MRE strategies.

- Drastically reduced scan times thanks to a separate magnetization preparation of the motion encoding step. A great number of k-space lines (up to several hundreds, as it will be seen afterwards) can be acquired for only one motion encoding preparation, whereas standard MRE pulse sequences need one MEG after each RF excitation pulse to perform phase modulation, even in EPI (see **Figure 4.15**). For example, with an oscillatory motion at a frequency of 100 Hz, a MSPREP pulse with its spoiler gradient applied during 10 ms, a pulse sequence repetition duration of 2 ms and 300 repetitions per preparation pulse, the total scan time is reduced by a factor of 6 (obtained by calculating $\frac{300\times(10+2)}{10+300\times2}$).

- Efficient standard continuous and transient MR elastography technique without any total scan time increase. For example, in transient mode, if an acoustic pulse needs to be tracked for a propagation

duration of 100 ms, with a MSPREP pulse with its spoiler gradient applied during 10 ms, a pulse sequence repetition duration of 2 ms and 300 repetitions per preparation pulse, the total scan time could be decreased by a factor of 47 (obtained by calculating $\frac{300\times(100+10+2)}{100+10+300\times2}$).

Drawbacks of MSPREP-MRE compared to standard MRE pulse sequences:

- Motion encoding in the magnitude MR image with a multi-parametric weighting dependence (with different physical properties of the biological tissue like ρ, T_1, T_2) beyond induced motion. The acquisition of two images with opposite MEG amplitudes, as it is sometimes done in standard MR elastography, may cope for the complexity.

- Non-linear relationship with the motion (cosine function), whereas standard MRE provides a MR phase image that varies linearly with the motion. This problem can be attenuated by keeping low $\Delta\varphi$ values and a well chosen β angle.

Beyond lung MRE, MSPREP-MRE could advantageously be applied to any other organs, in particular in the cases where time efficiency is critical and/or where the use of a transient method is valuable.

SECTION 3 THE FIRST COMPUTATIONAL AND EXPERIMENTAL RESULTS OBTAINED WITH MSPREP-MRE

IN THE PREVIOUS SECTION, WE PRESENTED THE PRINCIPLES OF A TOTALLY NEW TECHNIQUE TO PERFORM MR ELASTOGRAPHY: THE MOTION-SENSITIZED MAGNETIZATION PREPARATION PULSE, OR MSPREP. THIS PREPARATION PULSE CAN BE ADDED TO ANY STANDARD PULSE SEQUENCE, AND IN PARTICULAR TO UTE AND ZTE PULSE SEQUENCES, WHICH ARE KNOWN TO BE WELL SUITED TO LUNG IMAGING. IN THIS LAST SECTION, WE PERFORMED COMPUTATIONAL SIMULATION TO BETTER UNDERSTAND THE EFFECTS OF SUCH A PREPARATION PULSE ON MR SIGNAL. WE WILL THEN SHOW THE FIRST EXPERIMENTAL RESULTS WE OBTAINED IN PHANTOMS WITH THE PREPARATION PULSE IMPLEMENTED ON A UTE PULSE SEQUENCE.

1. SIMULATION OF THE EFFECTS OF MSPREP ON THE MR SIGNAL

1.1. MOTIVATION FOR COMPUTATIONAL SIMULATION

The MSPREP-UTE MRE pulse sequence is much more complicated compared to the original UTE pulse sequence, without motion encoding step. Trains of standard UTE repetitions (up to several hundred in practice, as described later) are comprised between the MSPREP pulse itself followed by a spoiler gradient on one side, and by a waiting period of time on the other side to let the magnetization recover (up to several hundred of milliseconds, as it will be seen below). The repetition of all these elements during the imaging process leads to a steady-state that depends on the motion itself, on tissue MR properties and on the characteristics of the elements described above (number of UTE repetitions, duration of the waiting period of time, flip angle for the UTE repetitions, phase β of the -90° RF pulse in MSPREP, etc.). The expression **Eq. 4.42** given in the previous section, which describes the evolution of $M_{xy}(\Delta\varphi)$, is therefore only an approximation as it does not take into account the longitudinal magnetization saturation effects, neither between UTE repetitions nor between the repetitions of MSPREP-MRE segments (MSPREP + Spoiler + Train of UTE repetitions + Waiting period of time). Moreover, this derivation did not take any residual transverse magnetization effects between UTE repetitions into account.

To refine the mathematical expression of $M_{xy}(\Delta\varphi)$, first we may assume that there are no residual transverse magnetization effects. The remaining transverse magnetization can be spoiled, either by implementing specially designed spoiler gradients or, better here, by programming continuously varying trajectories, like AZTEK for example. The latter seems to be the best solution to deal with motion, residual transverse magnetization effects and total scan time. However, longitudinal magnetization saturation and recovery effects are still there, and it is difficult to understand the link between the choice in pulse sequence parameters, the sensitivity to motion and the scan time efficiency. Of course, these aspects will highly depend on the MR properties of the tissues under consideration, and in particular their T_1 as it constitutes the relevant parameter in longitudinal magnetization recovery and saturation. However, a precise and accurate understanding of how the sensitivity to motion evolves with tissue characteristics and pulse sequence parameters would be of great interest as it would give the possibility to prescribe the image acquisition process wisely. As a complete mathematical expression for $M_{xy}(\Delta\varphi)$ seems

neither accessible nor intelligible easily, we will develop a computational simulation of the MSPREP-MRE pulse sequence.

1.2. SIMULATION OF THE MSPREP-MRE PULSE SEQUENCE

For the simulation, a variable is allocated to store the longitudinal magnetization value in a given image voxel and another one to store the transverse magnetization in the same voxel. These variables are respectively M_z and M_{xy}. In the image voxel, to keep it simple, we consider only one tissue component, characterized by only one set of MR properties (T_1, T_2, T_2^*, …). However, it would be possible to consider a multi-component tissue defined as a mixture of different components, each one being characterized by a set of MR properties and a fraction characterizing their relative quantity. To represent the beginning of the MR acquisition, we initialize the two magnetization variables with $M_z = M_0 = 1$ and $M_{xy} = 0$. Then, every time an event occurs in the MR pulse sequence (application of a RF pulse and/or a gradient lobe), M_z and M_{xy} are updated as a function of their current value, of the type and characteristics of the event and of the time that went by since the last event.

For example, if a +γ° RF pulse is applied at a time ΔT after the last pulse sequence event, M_z and M_{xy} are updated according to the Bloch equations:

$$M_z \leftarrow \left(M_0 + (M_z - M_0)e^{-\frac{\Delta T}{T_1}}\right)\cos(\gamma) \qquad \textbf{Eq. 4.45}$$

$$M_{xy} \leftarrow M_z \sin(\gamma) \qquad \textbf{Eq. 4.46}$$

Once again, we consider that there is no residual transverse magnetization, which is true in the lung if ΔT is above T_2^* (1-2 ms at 3 T). To fully address the problem, we should solve the Bloch equations at each pulse sequence event as the actual effect of these events on macroscopic magnetization may be different from the simple solution presented just above. For example, if the T_2^* is short (below 1 ms), it is known that large flip angles may not be achieved because of spin dephasing during the application of the RF pulse. Here, we consider the solutions of the Bloch equations for a perfect situation (relaxation times >> duration of the RF pulses).

The dephasing produced by a given displacement field occurring during the application of a given gradient pulse can be analytically calculated (see **Eq. 4.21**). However, the MSPREP pulse will not be completely simulated along the solutions of the Bloch equations. Instead, we will investigate the outcomes directly from the variable $\Delta\varphi$, without considering the motion field at the source of the dephasing. All we want to know here is how this dephasing $\Delta\varphi$ modulates longitudinal and transverse magnetization throughout the entire pulse sequence. The simulation can therefore be run for a set of $\Delta\varphi$ values and we can study the effect of each of these dephasing values on magnetization components along the imaging process.

Throughout the UTE repetitions, the longitudinal magnetization is not in a steady-state. In more standard MRI sequences, a steady-state is reached because a very close set of RF pulses are repeated every TR (usually with TR << T_2). In our situation, a steady-state may be reached between segments (MSPREP + Spoiler + Train of UTE repetitions + Waiting period of time) but not between the UTE repetitions within a given segment. In our computational simulations, the steady-state at the segment level can be reached by looping the simulation over several segments until stable magnetization values are reached. Computationally, we observed that 15 repetitions of the same segment were sufficient to reach the steady-state.

At the level of UTE repetitions within one segment, for a given UTE excitation flip angle FA and TR, the theoretical steady-state longitudinal magnetization reached in a material characterized by T_1 is given by:

$$M_{zss} = M_0 \frac{1 - e^{-\frac{TR}{T_1}}}{1 - \cos(FA)\, e^{-\frac{TR}{T_1}}} \qquad \textbf{Eq. 4.47}$$

This theoretical longitudinal magnetization steady-state is reached just before any new RF excitation pulse only if a sufficient number of UTE repetitions are performed. In standard UTE, this steady-state is experimentally reached after a few hundreds of 'dummy' repetitions (depending on FA, TR and T_1) and is held for the rest of the entire image acquisition process. In our MSPREP-MRE sequence, just before the first UTE repetition of any segment in steady state, longitudinal magnetization M_z is in general out of the M_{zss} steady-state value. It would be a waste to wait for the steady states with 'dummy' acquisitions so to have $M_z = M_{zss}$ everywhere in the image as M_z is modulated by $\Delta\varphi$, which is not uniform over the targeted organ where the shear wave has been induced for elastography purposes. In this situation, two different cases can be studied:

- If $M_z > M_{zss}$ before the first UTE repetition, longitudinal magnetization saturation dominates T_1 relaxation in the evolution of M_z along the following repetitions. For that reason, the signal measured at each UTE repetition decreases along the segment and tends towards M_{zss}.

- If $M_z < M_{zss}$ before the first UTE repetition, T_1 relaxation dominates longitudinal magnetization saturation in the evolution of M_z along the following repetitions. For that reason, the signal measured at each UTE repetition increases along the segment and tends towards M_{zss}.

Thereafter, the final image will be reconstructed from spokes that were not all acquired out of the same initial longitudinal total magnetic moment M_z. The discrepancies can lead to artifacts in the final reconstructed image and therefore degrade the precision and/or the accuracy of the measurement of the motion field.

The sensitivity can be defined as the slope of the curve giving the average M_{xy} estimated at $\Delta\varphi = 0$ over UTE repetitions when steady-state has been reached in a segment. Mathematically speaking, we can write this sensitivity χ as:

$$\chi = \frac{d\langle M_{xy}\rangle_{UTE\ Rep}}{d\Delta\varphi}(\Delta\varphi = 0) \qquad \textbf{Eq. 4.48}$$

This quantity needs to be understood as the variation rate of the MR signal magnitude (proportional to $\langle M_{xy}\rangle_{UTE\ Rep}$) when $\Delta\varphi$ varies around the null value (which corresponds to the null displacement, which is also the time average displacement for a tissue following an oscillatory motion). In the previous section, this slope was approximated to be proportional to $\sin(\beta)$ with a quasi-linear relationship between transverse magnetization and motion induced dephasing (see **Eq. 4.44**) provided $\left|\frac{\Delta\varphi}{\beta}\right| \ll 1$. β could be set to 90° in order to maximize the slope. However, the dependence in $\sin(\beta)$ holds as long as there is no saturation effects. In a more realistic situation, we will see that β should be tuned to a lower value which depends on most of the pulse sequence parameters and tissue characteristics mentioned above. Moreover, if we want to optimize the different parameters of MSPREP-MRE for a given set of tissue characteristics, we should not only take this sensitivity χ into account but also the variability of M_{xy} throughout the different UTE repetitions in any given segment in steady-state. This variability could be approximated independently of the motion as the standard deviation of M_{xy} estimated at $\Delta\varphi = 0$ along UTE repetitions. This quantity, which can be seen as a metric of signal uncertainty/variability, will be written ζ in the following. Both ζ and χ should therefore be optimized by tuning the various parameters of the MSPREP-MRE

pulse sequence. Finally, because we are out of the usual steady-state case known for a standard MRI sequence, the notion of optimal Ernst angle cannot be directly used to maximize the final image SNR. In conclusion, the problem is complex. We then made use of computational simulation to further understand the underlying contrast mechanisms in MSPREP-MRE. The effects of the different sequence parameters were explored to optimize the sensitivity and the precision of the measurement of the induced motion field in the organ of interest.

For the simulations, typical tissue properties of the lung at 3 T were chosen: $T_1 = 1300$ ms and $T_2 = 60$ ms. T_2^* is not taken into account in the simulation as transverse relaxation is governed by T_2 during the MSPREP and we always consider the shortest achievable TE for our acquisition. The term $e^{-\frac{TE}{T_2^*}}$ would therefore only be a non-optimizable multiplicative factor in the final result. We arbitrarily chose the following values for the different relevant tuning parameters:

- $TR = 2\,ms$
- $\beta = 35°$
- $MRE\_TRsPerPrep = 300$
- $MRE\_WaitTime = 513\,ms$
- $FA = FA_{Ernst} = 3.18\,°$

Figure 4.16 shows the evolution of $\langle M_{xy} \rangle_{UTE\ Rep}$ as a function of $\Delta\varphi$. This curve was obtained by repeating the simulation process for different input $\Delta\varphi$ values.

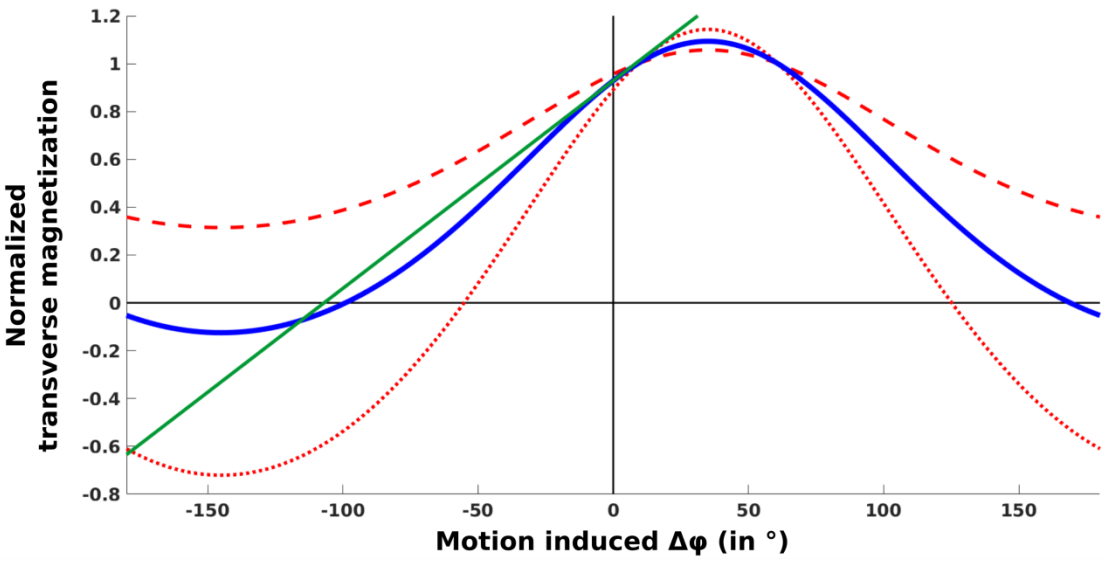

Figure 4.16: Representation of the average transverse magnetization $\langle M_{xy} \rangle_{UTE\ Rep}$ as a function of the motion induced dephasing $\Delta\varphi$ (blue curve), with the transverse magnetization available during the first (red dots) and the last (red dashes) UTE repetitions performed after any MSPREP pulse, and the affine approximation of $\langle M_{xy} \rangle_{UTE\ Rep}(\Delta\varphi)$ around $\Delta\varphi = 0$ (green). We observe that, close to $\Delta\varphi = 0$, we have a quasi-affine relationship between the average transverse magnetization and $\Delta\varphi$ in the range of [-20° +20°]. We also observe that transverse magnetization can vary a lot from the first to the last UTE repetition, which can cause artifacts in the final image.

In **Figure 4.16**, the signals recorded during the first and the last UTE repetitions are shown. These two curves let us appreciate the saturation and/or the T_1 relaxation effects occurring along the UTE repetitions, which could lead to

artifacts in the final image. Finally, we represented the affine curve that shares the same position and slope as $\langle M_{xy} \rangle_{UTE\ Rep}(\Delta\varphi)$ at $\Delta\varphi = 0$. From this curve, the sensitivity χ of our MSPREP-MRE pulse sequence can be estimated.

In **Figure 4.16**, all the curves are normalized by the signal that would be obtained with a standard UTE pulse sequence on the same tissue, with the same TR and with the optimal Ernst angle, given by:

$$FA_{Ernst} = \arccos\left(e^{-\frac{TR}{T_1}}\right) \qquad \textbf{Eq. 4.49}$$

This normalization step gives us the possibility to clearly estimate what can be expected with MSPREP-MRE in comparison with a nominal UTE sequence with the same timing characteristics and tuned with the optimal flip angle.

However, this set of parameters does not necessarily optimize MSPREP-MRE. It is clear for β that the choice we made was not the best as the affine curve tangent to $\langle M_{xy} \rangle_{UTE\ Rep}(\Delta\varphi)$ at $\Delta\varphi = 0$ does not touch the average transverse magnetization curve at its inflexion point (where $\frac{d^2\langle M_{xy} \rangle_{UTE\ Rep}}{d\Delta\varphi^2} = 0$). Moreover, as previously said, the Ernst angle may not be the best choice for FA as no steady-state is reached during a segment. Finally, it is difficult to know if we should increase or decrease the number of repetitions per segment and the wait time. To make the best choice, an optimization procedure on our simulation is therefore needed.

1.3. COMPUTATIONAL MAXIMISATION OF MOTION SENSITIVITY

Here is certainly the best choice to maximize the sensitivity χ: if only one repetition per MSPREP pulse is chosen, very long TR and $MRE\_WaitTime$ (like 10 s for example), $FA = 90\,°$ and $\beta = 90\,°$ approximately, we are sure to produce an image with a large SNR and with the largest χ possible. However, this configuration would lead to extremely long total scan times. Here is therefore a key point for our optimization process: we need to choose first what total scan time we want to spend before optimizing the different MSPREP-MRE parameters. As this total scan time depends on the number of spokes acquired, which depends itself on a number of non-MRE-specific parameters (final voxel and field of view sizes, averaging or under-sampling factor, use of prospective motion correction, …), it is easier to define how much time we want to spend for each spoke on average along the imaging process. This mean spoke duration T_{Spoke} can be defined as:

$$T_{Spoke} = \frac{\Delta T_{MSPREP} + \Delta T_{Spoil} + MRE\_TRsPerPrep \times TR + MRE\_WaitTime}{MRE\_TRsPerPrep} \qquad \textbf{Eq. 4.50}$$

T_{Spoke} is not the TR between UTE repetitions but the average time it takes to acquire one spoke at the level of the entire MSPREP-MRE pulse sequence. However, T_{Spoke} is logically greater than TR, as it clearly appears in the expression written just above. This quantity can therefore be considered as a relevant indicator of the final total scan time, whatever the desired voxel size, motion correction technique, under-sampling factor, … For the simulation, we chose the preparation duration $\Delta T_{MSPREP} = 10$ ms and the spoiling duration $\Delta T_{Spoil} = 2$ ms, which are very close to what we have experimentally implemented.

Before launching any optimization procedure on the simulation, we therefore need to choose a value for T_{Spoke}. To simplify the problem, TR will be fixed to the minimal achievable value in our UTE sequence (2 ms). This choice leads to the solution with the best time efficiency and the lowest amount of signal variability between UTE repetitions (because of saturation and/or T_1 relaxation, as explained above). Once these timing parameters are fixed, it is possible to find the best values for four tuning parameters: β, $MRE\_TRsPerPrep$, $MRE\_WaitTime$ and

FA. To remain simple, the objective of our problem will be to maximize χ, even if a metric implying other parameters (as ζ, for example) could be maximized instead.

χ maximization with β:

The choice of the optimal β is easy. As it can be easily understood, any change in β will only shift horizontally the curve $\langle M_{xy}\rangle_{UTE\ Rep}(\Delta\varphi)$. Moreover, we have seen that the best χ is obtained when the inflexion point of $\langle M_{xy}\rangle_{UTE\ Rep}(\Delta\varphi)$ is reached at $\Delta\varphi = 0$. In the objective function, for any iteration of the optimization process, we just need to choose the value of β that verifies this condition. This can be done, at each iteration, by calculating $\langle M_{xy}\rangle_{UTE\ Rep}$ for different β values and choose the one that maximizes $\frac{d\langle M_{xy}\rangle_{UTE\ Rep}}{d\beta}(\Delta\varphi = 0)$. Thanks to multi-resolution and parallel computing strategies we implemented, this procedure is quite time efficient.

χ maximization with $MRE\_TRsPerPrep$:

The choice of the optimal $MRE\_TRsPerPrep$ follows approximately the same strategy. As it only takes integer values, and as most standard optimization techniques are unadapted to integer parameter optimization, the simplest solution is to test different parameter values and choose the best one. For that reason, at each iteration, we launch the simulation for a set of reasonable $MRE\_TRsPerPrep$ values and use a multi-resolution strategy to find the optimal one.

χ maximization with $MRE\_WaitTime$:

Then, the choice of $MRE\_WaitTime$ is straightforward as it only depends on timing parameter values that were chosen yet, as it can be seen in the definition of T_{Spoke} above.

χ maximization with FA:

Finally, the optimal value for FA was estimated thanks to an unconstrained nonlinear minimization algorithm available on Matlab (Nelder-Mead method, via the 'fminsearch' Matlab function).

This optimization process was repeated for different values of T_{Spoke} ranging uniformly from 2.5 ms to 50 ms with 0.25 ms steps, and different values of T_1 ranging uniformly from 100 ms to 3100 ms with 300 ms steps. The results of the simulation are given in **Figure 4.17**. For each couple of values, optimal values for β, $MRE\_TRsPerPrep$, $MRE\_WaitTime$ and FA were therefore calculated and plotted. These values are optimal in the sense that they maximize χ, the sensitivity of our elastography method. In this figure, we also show the optimal χ values and the corresponding ζ values, the standard deviation of M_{xy} along UTE repetitions at $\Delta\varphi = 0$.

At first glance, the first surprising thing we observe on these curves is their 'tooth' shapes. However, this shape is normal as it reflects non-continuous relationships related to the optimization on an integer parameter. As T_{Spoke} increases, the optimal $MRE\_TRsPerPrep$ can only evolve by integer steps. The minimal change in this parameter (one unit) can have dramatic effects on the evolution of the other optimal parameter values. It is particularly clear for the optimal FA at short T_1 values and long T_{Spoke}: as the number of UTE repetitions change of one unit, the optimal flip angle to set to maximize χ changes of a large amount of degrees. We also observe that the optimal value for FA is always larger than FA_{Ernst}. For example, at $T_1 = 1300\ ms$ and $\Delta T_{Spoke} = 4TR\ = 8\ ms$ (which corresponds to a realistic situation for the lung), the optimal flip angle is 5.43 °, whereas the Ernst angle is 3.18 °. A substantial increase in motion sensitivity and global image SNR can therefore be obtained by tuning the flip angle in UTE repetitions.

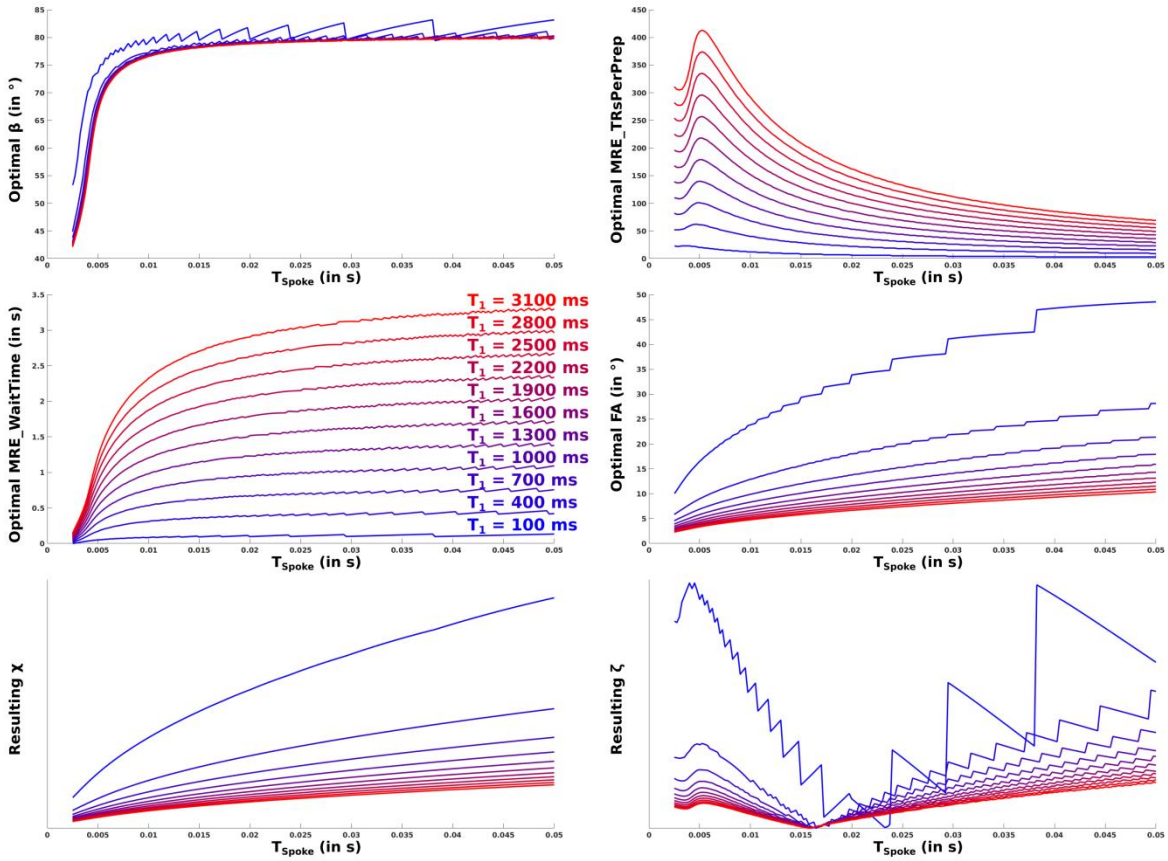

Figure 4.17: Evolution of the optimal values for β, $MRE\_TRsPerPrep$, $MRE\_WaitTime$ and FA as a function of T_{Spoke} for different T_1 values characterizing the tissue under consideration. At the bottom of the figure, we represent in arbitrary units the resulting sensitivity χ and variability ζ metrics in the different situations.

Another interesting result concerns the number of UTE repetitions per segment. Indeed, at low T_{Spoke} values, we could be tempted to set $MRE\_TRsPerPrep$ at a very large value (several hundred or thousands ms) to reach such a time efficiency for the pulse sequence. However, the simulation and optimization results show us that for a representative range of T_1 values found in proton MRI (from 100 ms to 3100 ms approximately), it is not useful to perform more than 450 UTE repetitions per MSPREP pulse. In the case of the lung at 3 T ($T_1 = 1300\ ms$), it is not even useful to go above 180 repetitions per segment. For that reason, instead to tending towards $+\infty$ when $T_{Spoke} \to TR$, $MRE\_TRsPerPrep$ draws a bell-shaped curve showing a maximum number of UTE repetitions for T_{Spoke} comprised between 3.5 and 5.25 ms, depending on the chosen T_1 value. This behavior should be understood like this:

- For large T_{Spoke} values, it is not useful to prescribe a large number of repetitions per MSPREP pulse. The best solution is to exploit the large available waiting time for the longitudinal magnetization to recover after the train of UTE repetitions. Therefore, large values should be prescribed instead for $MRE\_WaitTime$ and low values should be prescribed for $MRE\_TRsPerPrep$. Remark the quasi-plateau reached by $MRE\_WaitTime$, which evolves much more slowly when it reaches values close to the simulated T_1.

- When T_{Spoke} decreases, a lower average amount of time is spent for each spoke. To maximize the sensitivity, the optimization results tell us to increase the number of UTE repetitions per MSPREP pulse and to reduce the waiting period of time after the train of repetitions. Therefore, when T_{Spoke} decreases, $MRE\_TRsPerPrep$ increases and $MRE\_WaitTime$ decreases.

- When T_{Spoke} reaches low values (between 3.5 ms and 5.25 ms), to reduce further the average time spent for each spoke, the optimization results tell us to change the strategy: it is better to reduce $MRE\_TRsPerPrep$ and to reduce further $MRE\_WaitTime$. Indeed, increasing further $MRE\_TRsPerPrep$ would lead to severe saturation and/or T_1 relaxation effects, resulting in decreased χ values. This explains why this bell-shaped curve is observed for $MRE\_TRsPerPrep$.

Interestingly, the optimal β angle does not vary a lot with T_1. Globally, the optimal β decreases slightly as T_1 increases. However, it varies a lot with T_{Spoke}, in particular for values comprised between 2.5 ms and 10 ms. Within this range, the optimal β varies from 42° to 77° approximatively. When ΔT_{Spoke} further increases, the optimal β angle slowly tends towards 90°.

In the curves represented in **Figure 4.16**, T_{Spoke} was equal to 3.75 ms and T_1 was equal to 1300 ms. Hence, the parameters β, $MRE\_TRsPerPrep$, $MRE\_WaitTime$ and FA were not optimized to obtain the best sensitivity χ. After the optimization procedure, we found the optimal parameters for the same T_{Spoke} and T_1:

- $\beta = 53.25\ °$
- $MRE\_TRsPerPrep = 147$
- $MRE\_WaitTime = 245\ ms$
- $FA = 4.30\ °$

In **Figure 4.18**, we represented the same curves as in **Figure 4.16** but with this optimal set of parameters. In this representation, we obtain a better sensitivity χ in comparison with the non-optimized case. However, we also observe a large variation of transverse magnetization along UTE repetitions at $\Delta\varphi = 0$. This large variation is related to the fact that $MRE\_TRsPerPrep$ is still large. We can wonder if it is possible to further decrease the value of this parameter to decrease the variation in transverse magnetization without impacting χ too much.

In **Figure 4.18**, we represented also the evolutions of χ and ζ as a function of the number of repetitions $MRE\_TRsPerPrep$. These two curves were obtained for T_{Spoke} equal to 3.75 ms and T_1 equal to 1300 ms. We observe that χ describes a plateau with its highest value reached for $MRE\_TRsPerPrep = 147$, the optimal value found previously. However, we observe that ζ reaches a large value for this number of repetitions and that it increases quasi-linearly with the number of repetitions around this optimal value. It is therefore possible to choose a lower number of repetitions, for example $MRE\_TRsPerPrep = 90$, that would decrease significantly ζ without impacting too much χ. With this new choice, ζ is reduced to 67% of the value that was found in the 'optimal' case, whereas χ was only reduced to 99% of its best value. The result in term of $\langle M_{xy} \rangle_{UTE\ Rep}(\Delta\varphi)$ is also given in **Figure 4.18**. It was obtained with this new corresponding set of optimal parameters:

- $\beta = 43.37\ °$
- $MRE\_TRsPerPrep = 90$
- $MRE\_WaitTime = 146\ ms$
- $FA = 4.48\ °$

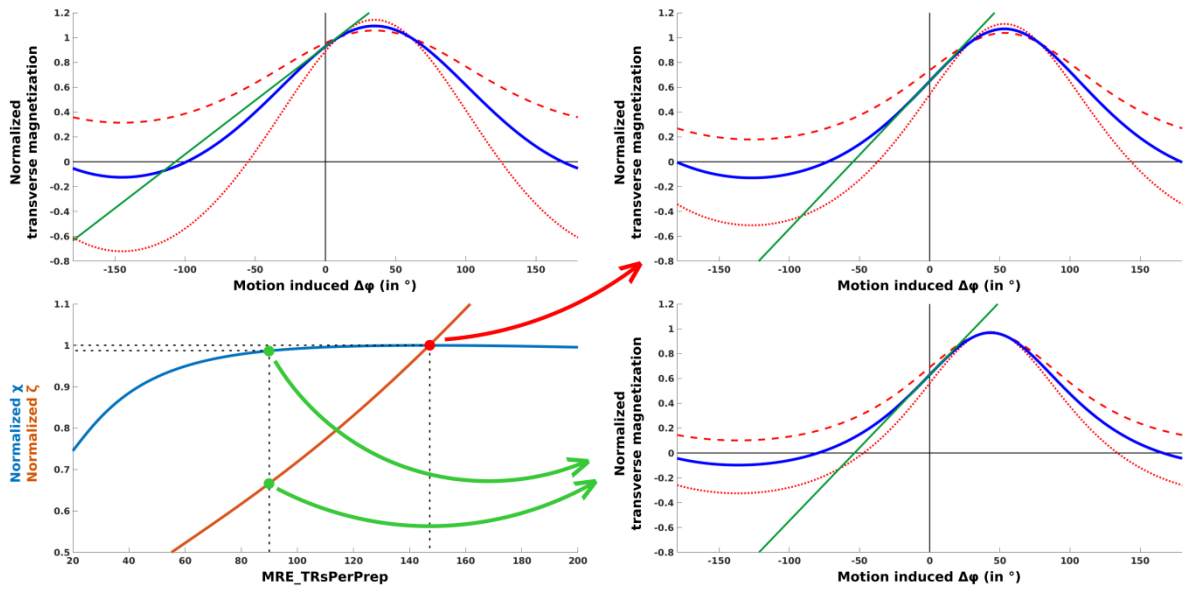

Figure 4.18: Top left-hand corner: same graph as in **Figure 4.16**, reproduced for comparison. Top right-hand corner: representation of the same quantities as in **Figure 4.16**, with the same T_{Spoke} and T_1, but with the tuning parameters set so as to maximize χ. Observe the larger slope obtained for the green curve in comparison to the first graph. In the bottom left-hand corner, we represented the evolutions of χ and ζ (normalized by their value in the optimal situation) as $MRE\_TRsPerPrep$ varies and the other parameters (β, $MRE\_WaitTime$ and FA) are chosen to optimize χ. We observe χ values close to the optimal one at lower $MRE\_TRsPerPrep$ values, while ζ is decreased a lot. This new situation, which seems better in terms of final image quality, is represented in the bottom right-hand corner.

These parameters preserve exactly the average time spent for each spoke, preserve quasi-identically the sensitivity of the technique but reduce drastically the variability of transverse magnetization along UTE repetitions. For that reason, this last set of parameters may be preferred in order to keep an optimal sensitivity to the motion field without introducing image artifacts related to image reconstruction from incoherent spokes. This choice was made manually here in order to understand clearly the interest of taking ζ into account while maximizing χ. Of course, the same type of procedure can be done fully automatically by maximizing a more complex metric during the optimization process. For example, this metric could take the following form:

$$\chi' = \frac{\chi}{\zeta^{\gamma}} \qquad \textbf{Eq. 4.51}$$

where γ is a real coefficient weighting the minimization of ζ. If $\gamma = 0$, $\chi' = \chi$ and we come back to the case where only the sensitivity is optimized, without taking ζ into account. Other parameters, as the range of $\Delta\varphi$ values over which the relationship $\langle M_{xy} \rangle_{UTE\ Rep}(\Delta\varphi)$ can be supposed to be linear, may also be considered during the optimization process. The choice of such a metric to optimize MSPREP-MRE would deserve further research work.

In conclusion, first, primary parameters must be estimated or chosen:

- The MR properties of the tissue under consideration (T_1 in particular).
- The time do to spend on average for each spoke (as T_{Spoke} increases, the quality of measurement may become better and the flexibility in the choice of tuning parameter becomes larger).

- The aspect(s) of the measurement process to optimize (the sensitivity χ seems obvious, but other aspects may be important to avoid image artifacts and/or biases in the measurement of the motion field).

Once these choices are made, the best choice of tuning parameters can be estimated efficiently thanks to computational simulation and optimization.

2. MR ELASTOGRAPHY EXPERIMENTS ON PHANTOMS

The first experimental tests of the MSPREP-UTE pulse sequence were carried on elastic phantoms. The phantoms were mechanically excited thanks to a system developed at the laboratory and for which a patent was applied several years ago[464]. This system consists in a loudspeaker enclosed in a cabinet and driven by a waveform generator and a power amplifier. The pressure waves generated by the enclosed loudspeaker are conducted to the phantom or the organ of interest thanks to a tubular waveguide. The waves are then transmitted to the phantom thanks to an adapted transmission system, depending on the size and shape of the phantom (see **Figure 4.8**).

2.1. MR ELASTOGRAPHY EXPERIMENTS ON HOMOGENEOUS PHANTOMS

The first experiment was carried on a set of calibrated homogeneous phantoms produced by the company CIRS and intended to mimic four different stages of liver fibrosis, from healthy liver to cirrhosis. For the four phantoms, the indicated Young's moduli are the following (with a possible error of ± 4% of the prescribed value, as indicated by CIRS):

- **Phantom 1:** 3.5 kPa
- **Phantom 2:** 11.4 kPa (3.26 times the elasticity of Phantom 1)
- **Phantom 3:** 28.6 kPa (8.17 times the elasticity of Phantom 1)
- **Phantom 4:** 44.8 kPa (12.8 times the elasticity of Phantom 1)

Shear wave velocities were measured in these four phantoms with 1D transient elastography (FibroScan®, see 1.2.5 in the first section of this chapter), ultrasound Supersonic Shear Imaging (SSI, see 1.2.5 in the first section of this chapter) and MR elastography during the Ph.D. thesis of Dr. Jinlong Yue in our laboratory[465]. For the three techniques, the shear wave velocities were shown to be similar (except for the stiffer phantom with the FibroScan®), even with different probes for SSI and at different mechanical excitation frequencies in MRE. However, lower values were found in comparison to the ones prescribed by CIRS. As these experiments were performed several years ago, the internal structure and properties of the phantoms may have changed with time. To evaluate a possible shift in their E values with time, we measured their actual Young's moduli with the SSI technique available on a Aixplorer® system developed by the company Supersonic Imagine. These Young's modulus maps were acquired with a 15-4 ultrasonic probe (which transmits and receives ultrasonic signals at frequencies comprised between 4 and 15 MHz to produce the B-mode images).

[464] "US20130237807A1 - Apparatus and Method for Generating Mechanical Waves into Living Bodies, System and Method for Mapping an Organ or Tissue and System and Method for Characterising the Mechanical Properties of Said Organ or Tissue - Google Patents," accessed April 19, 2019, https://patents.google.com/patent/US20130237807A1/en.

[465] Jinlong Yue, "Magnetic Resonance Elastography and Supersonic Shear Imaging: Simulation, Experimental Comparison and Application to the Characterization of the Liver," 2017.

Here are the values obtained (given as mean ± standard deviation over a region of interest):

- **Phantom 1:** (3.0 ± 0.5) kPa
- **Phantom 2:** (7.9 ± 0.6) kPa (2.63 times the measured elasticity of Phantom 1)
- **Phantom 3:** (18.1 ± 0.7) kPa (6.03 times the measured elasticity of Phantom 1)
- **Phantom 4:** (36.6 ± 2.6) kPa (12.2 times the measured elasticity of Phantom 1)

Therefore, the measured values are lower compared to the prescribed ones. The elasticity ratios in comparison to Phantom 1 are lower too. However, the measured values are similar to those obtained several years ago during the Ph.D. thesis of Dr. Jinlong Yue. In the following, we will take these new elasticity values for comparison with our MSPREP-UTE technique.

All the MRE experiments were performed on the GE Signa PET/MR 3.0 T scanner at SHFJ. Each phantom was scanned three times to encode motion along the three orthogonal directions of space. The phantoms were excited at a mechanical frequency of 80 Hz by attaching the end of the waveguide against the surface of each phantom. During each acquisition, 8 dynamics were acquired along the motion period. For each dynamic, an image with an isotropic voxel size of 1.5 mm and a matrix size of (80 × 80 × 84) voxels was acquired. MR signal was received with an 8-channel head coil. We chose a number of UTE repetitions per MSPREP pulse equal to 200, a waiting time of 200 ms, a flip angle of 3° and a β angle value of 45°. TE was 12 µs and TR was equal to 2 ms. These parameters are not optimal as the experimental run took place before establishing the optimization process.

Here, we suppose to have an affine relationship between the motion amplitude along the encoded direction and the magnitude signal in the image. The E maps were then reconstructed from the linearly-inferred displacement fields with an AIDE-like algorithm (see 2.3.4 in the first section of this chapter) developed on Matlab. Briefly, this reconstruction algorithm tries to invert the Helmholtz equation written in **Eq. 4.34**. The Laplacian and the second time derivative are calculated thanks to finite difference methods. Before this calculation, the series of magnitude images are temporally-filtered (to only keep the component oscillating at excitation frequency), spatially bandpass-filtered (to remove at the same time the background noise and the signal variation coming from compression waves) and directionally filtered along 6 orthogonal directions (as explained in 2.3.5 in the first section of this chapter). For the bandpass-filtering, the convolution kernel in the image domain is the difference between two 3D Gaussian kernels of standard deviations 1 and 2.5 voxels respectively.

For each encoding direction and each directional filter direction, we therefore obtain a ${c_S}^2$ (squared shear wave velocity) map. The Young's modulus E maps are estimated by applying the formula $E = 3\rho{c_S}^2$ for each squared velocity map, with $\rho = 1.03$ as indicated on the technical specifications given by CIRS (provided that this specified value is true and has not evolved from the phantom fabrication process). Then, a final E map is obtained by calculating the average of all the Young's modulus maps obtained previously, weighted at each voxel location by the local motion amplitude observed on the temporally, spatially and directionally filtered magnitude images.

The results of this experiment are shown in **Figure 4.19**. Here are the average Young's moduli values found for each phantom (given as mean ± standard deviation over a region of interest):

- **Phantom 1:** (2.02 ± 0.3) kPa
- **Phantom 2:** (6.51 ± 0.7) kPa (3.22 times the measured elasticity of Phantom 1)
- **Phantom 3:** (14.4 ± 0.8) kPa (7.12 times the measured elasticity of Phantom 1)
- **Phantom 4:** (28.2 ± 1.8) kPa (14.0 times the measured elasticity of Phantom 1)

We observe that the measured Young's moduli values are a little bit lower compared to those measured with the ultrasonic system. The ratios with Phantom 1, however, are a little bit increased. These differences are not surprising as the two methods are not based on the same principles: in MRE, the excitation is done only at one frequency (which is quite low here), whereas a large band of higher mechanical frequencies is sent in ultrasonic shear wave imaging (centered at 300 Hz).

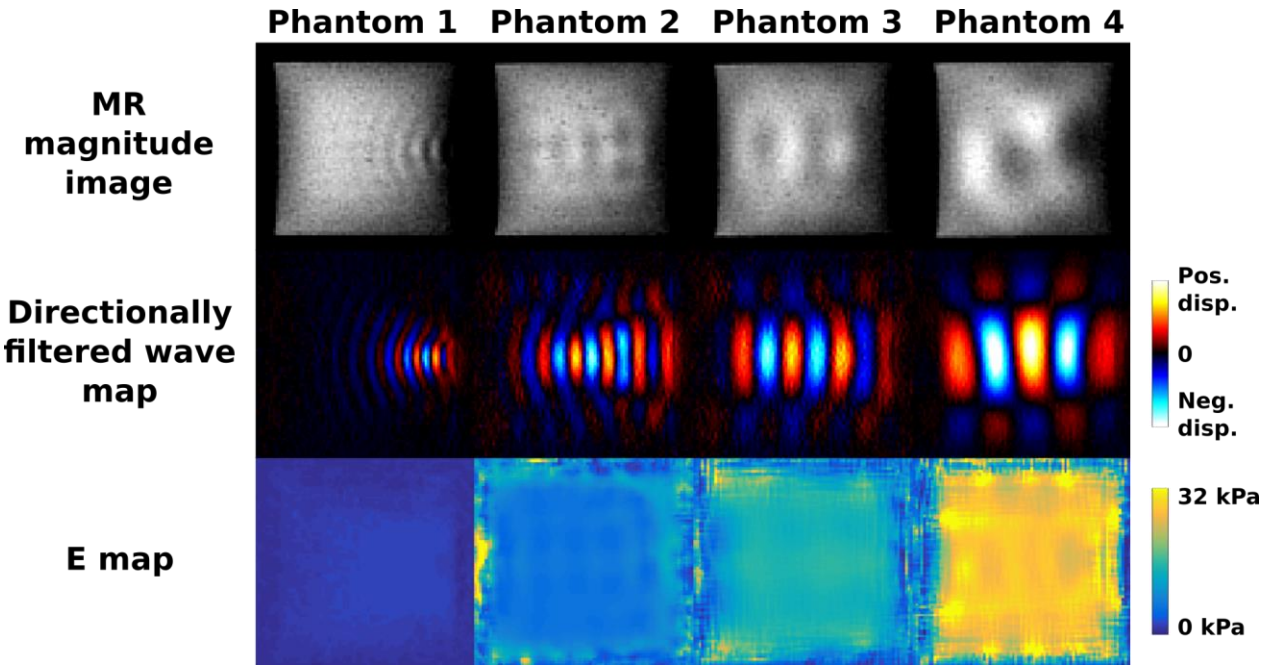

Figure 4.19: MR magnitude images, wave maps directionally filtered along the horizontal direction and Young's modulus maps obtained for the four CIRS liver fibrosis phantoms and excited at 80 Hz.

2.2. MR ELASTOGRAPHY EXPERIMENTS ON AN HETEROGENEOUS PHANTOM

We performed similar experiments on an heterogeneous elastic phantom composed of five stiff ellipsoidal inclusions enclosed in a softer homogeneous elastic medium surrounding them.

This heterogeneous phantom was also developed by the company CIRS. Here are the Young's moduli values measured with a 15-4 probe on the Aixplorer® system (given as mean ± standard deviation over a region of interest):

- **Surrounding medium:** (6.2 ± 0.2) kPa
- **Inclusions:** (11.5 ± 0.5) kPa (1.85 times the measured elasticity of the surrounding medium)

For this experiment, we performed two sets of measurements: one at a mechanical frequency of 150 Hz and the other one at 180 Hz. The experimental conditions and protocol were quite similar to the first experiment, excepted for the tuning parameters: $MRE\_TRsPerPrep = 150$, $MRE\_WaitTime = 100\,ms$, $FA = 5°$ and $\beta = 45°$. Mechanical excitation was performed thanks to a large vibrating membrane connected at the end of the waveguide and set against the surface of the phantom (Resoundant, Rochester, United-States). To ensure the mechanical coupling between the membrane and the phantom, ultrasonic gel was spread between them. As in homogeneous phantoms experiments, signal was received with an 8-channel head coil. The acquisitions were carried with an

isotropic voxel size of 1.3 mm and a matrix size of (92 × 92 × 184) voxels. 8 dynamics were acquired along the motion period and the final E maps were reconstructed with the AIDE-like reconstruction method described in 2.1. These E maps are shown in **Figure 4.20**.

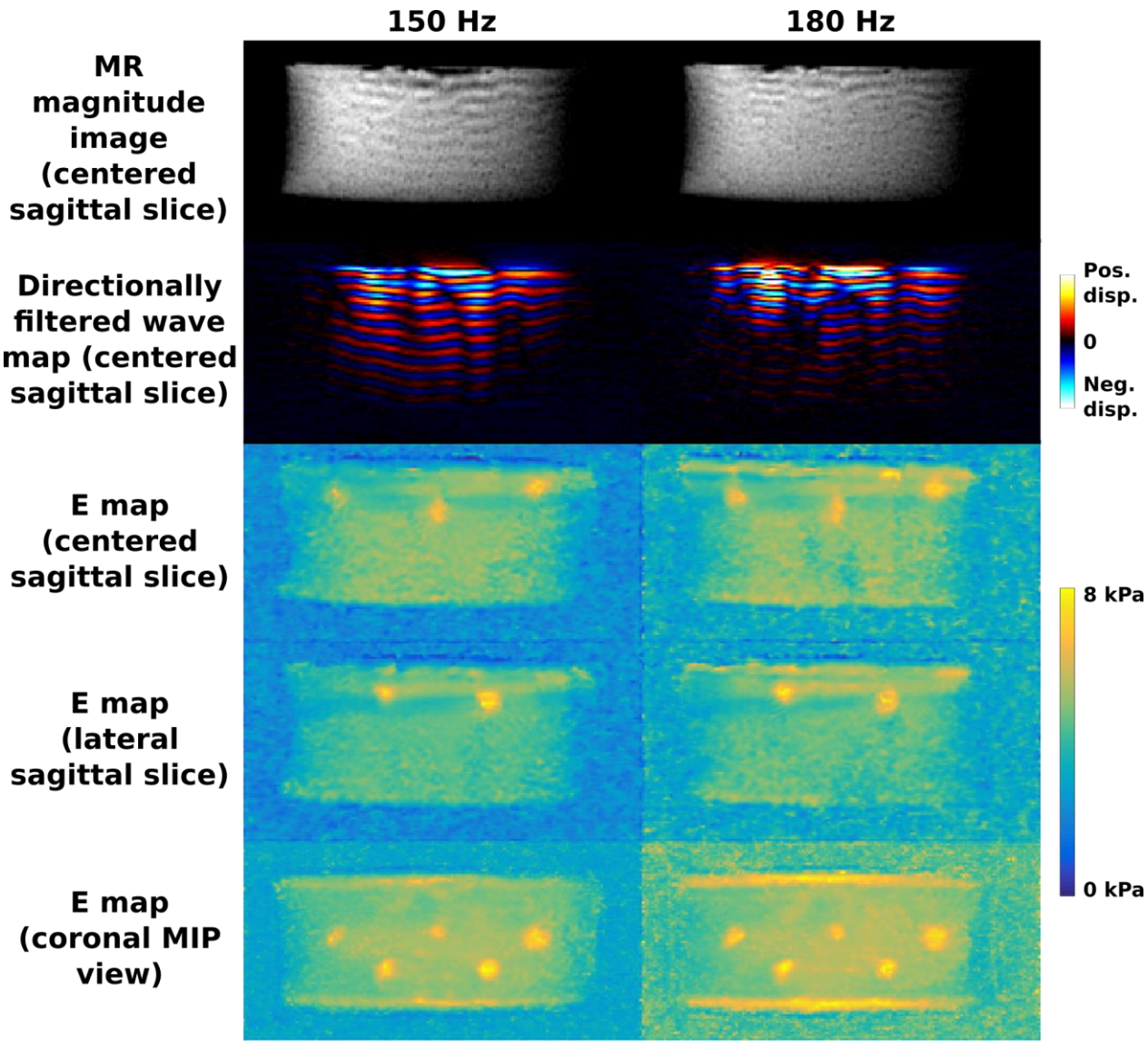

Figure 4.20: MR magnitude images, wave maps directionally filtered along the vertical direction (from the top to the bottom) and Young's modulus maps obtained for the heterogeneous phantom developed by CIRS and excited at 150 and 180 Hz. We chose to represent two sagittal planes containing respectively three and two stiff inclusions. A Maximum Intensity Projection (MIP) in the coronal view clearly depicts the five inclusions. Note the softer band going through the inclusions and visible in the sagittal images: it corresponds to a material discontinuity surface resulting from the phantom fabrication process.

In these E maps, the five stiffer inclusions mentioned previously are clearly depicted. Note that these inclusions are not even visible in the standard UTE image (see **Figure 4.20**, top), which tends to show that MSPREP-UTE is effectively sensitive to the stiffness of the mediums. Quantitatively speaking, the Young's modulus of the surrounding medium was measured to be (5.01 ± 0.4) kPa at 150 Hz and (4.89 ± 0.5) kPa at 180 Hz. Concerning the

inclusions, an average value over a region of interest is more difficult to give as the inclusions are small in comparison to the final spatial resolution in the E map, leading to spatially smoothed Young's modulus maps. It is therefore more correct to consider the peak elasticity value in each inclusion instead of an average value. At 150 Hz, the average ± standard deviation on the maximum values observed in each inclusion gives (8.03 ± 0.9) kPa, whereas it gives (8.40 ± 0.6) kPa at 180 Hz. These values correspond respectively to 1.60 and 1.72 times the measured elasticity of the surrounding medium at 150 and 180 Hz.

The Young's modulus values found at 150 Hz and 180 Hz are therefore very close to each other, both in the inclusions and their surrounding medium. However, these values are lower compared to those found in ultrasound elastography, as it was observed also in the previous experiment on homogeneous phantoms. Concerning the ratios between the elasticities in inclusions and their surrounding medium, their values are close between 150 Hz and 180 Hz but lower compared to those found with the Aixplorer®. Once again, all these differences can be understood because of the great difference between the two methods (continuous vs transient, mono-frequency vs multi-frequency, …). Moreover, as the inclusions are small (between 1 and 2 cm), it is expected to find lower values in MR elastography compared to US elastography because of the larger voxel size and the averaging effect occurring during the elastography reconstruction process. Indeed, the voxel size is 1.3 mm in MR elastography, and the reconstruction of the E map uses smoothing filters and finite difference operators to calculate the derivatives. In particular, the Laplacian is calculated over a (5 × 5 × 5) voxels window, representing a cube of size 6.5 mm, which is relatively large in comparison with the size of the inclusions.

The new elastography technique fulfills the basic expectations of any MR elastography pulse sequence. We were able to quantify the Young's modulus of a homogeneous elastic material and detect stiff inclusions in a softer material. However, the acquisition of MR images in these phantoms was easy, in particular thanks of their relatively long T_2^*. In the homogeneous and heterogeneous CIRS phantoms, we measured a T_2^* ranging between 27 and 48 ms (thanks to several gradient echo acquisitions at different TE values followed by a mono-exponential fit on a region of interest in the final images).

2.3. MR ELASTOGRAPHY EXPERIMENT ON AN ULTRASHORT T_2^* RUBBER PHANTOM

Here, MSPREP-UTE is challenged in short and ultrashort T_2^* materials, where standard MR elastography usually fail. In a large laboratory rubber stopper of diameter 83 mm (see **Figure 4.21**, on the left) the average T_2^* was found equal to 0.826 ms, which is close to the transverse relaxation time in the lung.

The output end of the pressure waveguide was coupled to the surface of the piece of rubber and a 100 Hz mechanical excitation was applied. Signal reception was performed with a 16-channel flexible coil wrapped around the phantom and the waveguide. Finally, a small water phantom was added inside the antenna to ensure a sufficient MR signal for prescan purposes. Excepted for this, we used the exact same imaging protocol as above for the heterogeneous phantom. Unfortunately, we were not able to observe propagative waves inside this phantom. One possibility is that no waves were generated inside the phantom. This may be related to the small size of the phantom (around 8 cm), its important stiffness, which is definitely larger compared to most soft tissues in human, but also its supposed large viscosity. However, we were able to observe a compressional motion inside the phantom with the MSPREP-UTE pulse sequence set with a motion encoding direction parallel to the waveguide. After applying temporal Fourier filtering to select only the signal component modulated at 100 Hz, we were able to generate a 'Motion amplitude' map shown in **Figure 4.21**. Of course, this is not a true motion amplitude map as it only represents the variation in UTE signal related to motion, and does not give access to the absolute motion amplitude.

In **Figure 4.21**, we observe that UTE signal is further modulated close to the waveguide and the modulation amplitude reaches low values close to the other surfaces of the phantom. This means that a localized deformation field is created inside the rubber phantom by the acoustic waves sent through the waveguide, and only little translational motion is observed (which results in a quite uniform modulation of MR signal inside the entire phantom). Even if we were not able to observe shear waves inside the piece of rubber, this result means that we are able to generate and control a deformation field inside the phantom and to encode the resulting micrometric motion fields inside the MR magnitude signal. Unfortunately, we were not able to characterize the piece of rubber with the Aixplorer® system because of the lack of echogenicity of the material.

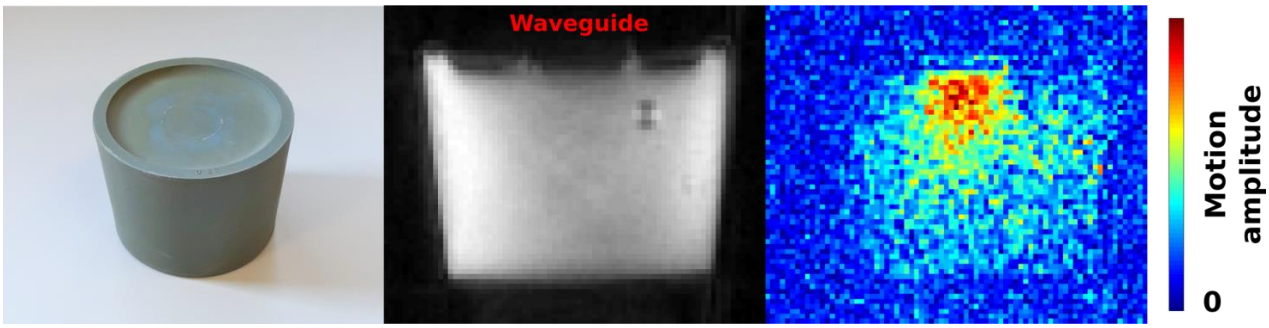

Figure 4.21: Picture of the ultrashort T_2^* rubber phantom, its MR magnitude image and the corresponding 'Motion amplitude' map (which only represents the variation in signal magnitude related to the induced motion). We observe that the motion amplitude is particularly large close to the interface between the phantom and the excitation waveguide. This result proves that it is possible to visualize motion-related signal variations in ultrashort T_2^* materials thanks to our MSPREP-UTE pulse sequence.

The MSPREP-UTE method seems very promising for lung elastography. We have shown its ability to perform MR elastography on homogeneous and heterogeneous calibrated phantoms, but also its ability to encode an externally generated motion inside a very short T_2^* rubber phantom, characterized by a relaxation time close to those found usually in the lung at 3 T. Moreover, as explained at the end of the previous section, our new method has other advantages compared to standard MR elastography pulse sequences. In particular, the total scan time can be much lower with our technique compared to standard methods (see **Figure 4.15**). As an example, in the heterogeneous phantom experiment, the acquisition of each 3D image for one given motion encoding direction and one given dynamic took less than one minute, which is quite impressive for a 3D elastography acquisition with a fine isotropic voxel size. As a comparison, if the acquisition was made thanks to a standard MRE pulse sequence with a similar radial scheme, each k-space spoke would have been acquired in, at least, 11 ms (two times the motion period at 180 Hz). In our experiment, the average time duration spent per spoke, ΔT_{Spoke}, was 2.72 ms, which is four times lower compared to the standard case. Our pulse sequence is therefore very promising for most organs, not only short T_2^* ones, as it solves the common problem of long total scan times in MR elastography. In the lung, we can even envision the acquisition of the whole set of images for elastography in only one breath-hold.

3. *IN VIVO* HEALTHY HUMAN VOLUNTEER EXPERIMENTS

The MSPREP-UTE MRE pulse sequence was tested in human volunteers. We obtained very promising results in a human brain *in vivo* in transient mode. During the image acquisition process, short acoustic pulses of 5 ms were sent in the mouth of the human volunteer (instead of a continuous oscillatory wave, as it was done with the CIRS phantoms above) thanks to the same excitation system as described at the beginning of the previous subsection

equipped with the mouthpiece shown in **Figure 4.8**, on the right of the figure. Motion was encoded thanks to a bipolar MEG with a frequency of 100 Hz and oriented along the anterior-posterior axis. In 5 minutes, we obtained 16 3D images with an isotropic resolution of 5 mm showing the propagation of the pulse through the entire brain of the subject during 80 ms of propagation. 12 out of these 16 images are represented in **Figure 4.22**. If this experiment was performed thanks to a standard elastography sequence, it would have taken approximatively 3 hours and 20 minutes of acquisition, instead of 5 minutes here. This scan time could even be reduced further by optimizing pulse sequence parameters and MR image reconstruction methods. The new method we developed seems therefore totally applicable *in vivo* in human.

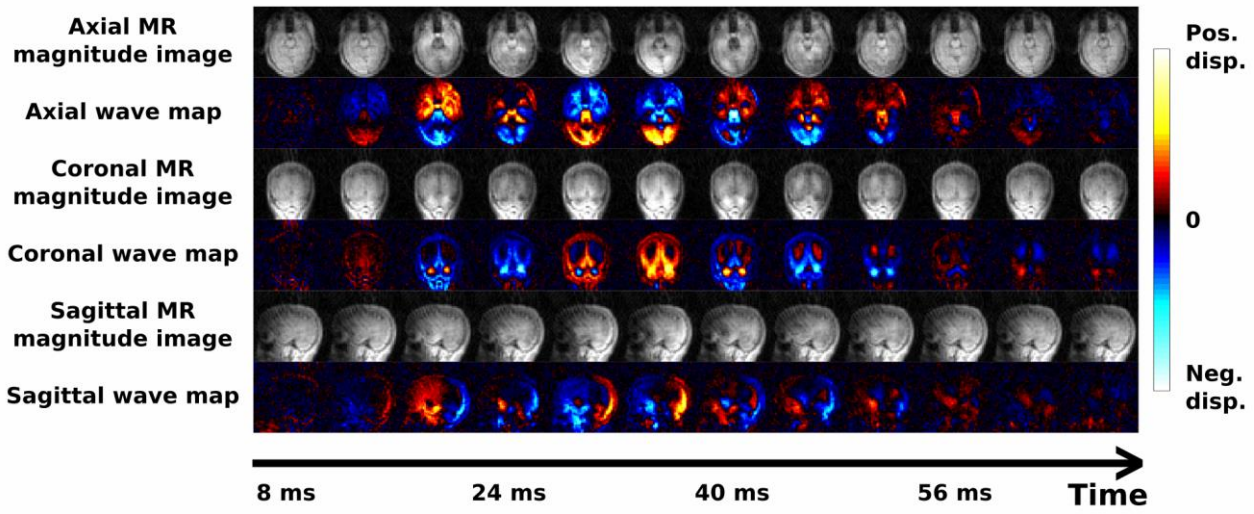

Figure 4.22: Axial, coronal and sagittal views of the same 3D images showing the propagation along time of a 5 ms transient acoustic pulse thanks to the MSPREP-UTE pulse sequence. We observe that coherent and anatomy dependent acoustic modes are created in the entire brain. These modes appear, evolve and fade with time. 12 of the 16 acquired images are shown here.

Unfortunately, we were not able to obtain results in the lung yet. We have tested three types of mechanical excitations: with pressure waves sent from the mouth of the patient, with a vibrating membrane set against the right chest lung and with the same vibrating membrane set against the back between the two scapulae. This last method seems to be the most adapted one in terms of wave transmission inside the thorax. To avoid the effects of respiratory motion, we were able to acquire four dynamics along the induced motion cycle with a coarse voxel size (5 mm isotropic) in only 1 min 25 s, which gives the possibility to acquire the four 3D images in one breath-hold only (with a well-trained and very compliant subject, of course). We also used the simulation and optimization work presented in 1.2 and 1.3 to find the best tuning parameters adapted to the lung. Moreover, we used fractional encoding to reduce the total duration of the MSPREP motion encoding pulse, in particular for low motion frequencies (around 50 Hz). However, no waves could be observed so far.

We plan to perform the same tests at 1.5 T on another MRI machine. It would generally alleviate a series of issues: T_2^* values will be around 1-2 ms instead of 0.5 ms, more homogeneous $\overrightarrow{B_0}$ and $\overrightarrow{B_1}$ fields, which is important to perform correctly the large flip angle RF pulses. We also plan to acquire a lower number of dynamics (like 2) in order to improve the image acquisition process (the voxel size in particular) and see if shear waves can be encoded. Our *in vivo* experiments are thus still in progress, but the method is promising and we really hope to observe shear waves soon, and therefore perform 3D proton MR elastography of the lung. We are confident in the possibility to

do it as spin-tagging techniques are possible in the lung parenchyma at 1.5 T, as discussed at the beginning of the previous chapter (grid-tagging methods were used for the estimation of deformation fields in the lung).

CONCLUSION

Respiratory mechanics is a very rich field in terms of physical phenomena and biomechanical properties to measure. These properties are believed to have a strong relationship with lung function and pathophysiological state. The combined study of the two aspects of respiratory mechanics, mechanical behaviors and mechanical properties of the lung, seems therefore a strategic way to consider for the future of pulmonology. In this work, proton MRI was shown to be one of the best choices as it gives the possibility to explore three-dimensionally, dynamically, non-invasively and relatively easily the thorax, and to measure a great diversity of relevant physical quantities along the respiratory cycle. These parameters, measured with a fine spatial resolution, are potential biomarkers for lung diseases. The techniques we developed are based on the management and the exploitation of dynamic processes occurring inside the organ. Their measurement is performed without ionizing the patient, contrary to 4D-CT for example.

In this manuscript, we have seen that physiological motion is a challenge lung MRI tackles today with a set of robust techniques that track motion and limit the presence of motion artifacts in the final images. It is first in this context that we introduced three innovations that aim at increasing the potential of dynamic Ultrashort Echo Time (UTE) and Zero Echo Time (ZTE) lung imaging: the Self-Navigator Intelligent Filter (SNIF), the Self-Navigator from Off-center ZTE Evolution (SNOZE), and the Adaptive Zero TE K-space Trajectories (AZTEK) all contribute into the exploration of respiratory mechanics with MRI. When properly characterized, respiratory motion itself is an amazing source of information as it constitutes the vital function of the organ and the fundamental aspect of lung mechanical behavior. By measuring the three-dimensional deformation field of the lung parenchyma during breathing, by extracting physical quantities of interest from these vector fields and choosing appropriate ways to present and analyze the results in regard to previous studies on lung physiology, we have established 3D Magnetic Resonance Spirometry as a promising tool for the regional study of the mechanical behavior of the lung *in vivo*. This technique is expected to be sensitive to regional mechanical abnormalities that would be linked to local lung affections. Finally, the measurement of micrometric displacement shear wave fields may be carried with MRI to assess the mechanical properties of this moving, protected, and remote organ. We have developed and implemented a totally new paradigm to perform MR elastography in the lung. With promising first results, this technique may open the research and clinical field in the measurement of pulmonary mechanical properties. More generally, with the advantages this new strategy offers with respect to current methods, it may advantageously be applied to MR elastography in other organs.

Further studies are needed to validate the results obtained in the course of the PhD and to really appreciate their full potential in the clinical field. Next research and development steps are required in terms of technical development (code optimization, ease to use, …), of validation (comparison with gold standard or validated measurement methods, tests on calibrated phantoms, …) and in terms of clinical relevance (sensitivity and specificity to physiological processes and diseases, adaptability to the clinical field with patients, …). This project will be continued as the techniques we developed open the doors to a totally new approach of lung diagnosis, which radically departs from what is undertaken today in pulmonary function testing. This research topic is fairly new (most relevant research articles were published after 2005) as the tools to perform such an exploration are now available to researchers and were largely validated. I personally see this field as a great opportunity for physicists, but also computer scientists, engineers and clinicians to develop a valuable research domain that could totally revolutionize the fields of pulmonology, pulmonary function testing and lung diagnosis. Based on the magnetic resonance imaging of respiratory mechanics, these new approaches could bring valuable diagnosis solutions for disease classification, stadification, and therapy that would increase the chances to efficiently cure patients affected by pulmonary diseases.

université PARIS-SACLAY

ÉCOLE DOCTORALE
Physique et ingénierie : électrons, photons, sciences du vivant (EOBE)

Titre : Imagerie par résonance magnétique de la mécanique respiratoire

Mots clés : Imagerie médicale ; Imagerie par résonance magnétique ; Poumon ; Mouvement ; Elastographie ; Mécanique des milieux continus

Résumé : La fonction respiratoire chez l'homme est indissociable du mouvement de déformation du poumon : les échanges gazeux entre l'organisme et son environnement sont rendus possibles, lors de l'inspiration, par le gonflement des alvéoles du parenchyme pulmonaire, et lors de l'expiration, par un retour passif à l'état d'équilibre statique du poumon. Les propriétés viscoélastiques des tissus pulmonaires jouent un rôle clé dans la fonction même de cet organe. Ces éléments de la mécanique respiratoire pourraient être des biomarqueurs très sensibles de l'état physiopathologique du poumon puisqu'ils dépendent de la structure des tissus et des conditions biologiques qui sont considérablement altérées par la plupart des maladies pulmonaires comme le cancer, l'emphysème, l'asthme ou la fibrose interstitielle.

L'imagerie par résonance magnétique permet aujourd'hui, de manière non-invasive, l'obtention d'images anatomiques tridimensionnelles permettant, grâce aux résolutions spatiales et temporelles accessibles ainsi qu'aux contrastes riches observés au sein des tissus mous, la mesure de l'état de déformation d'un organe à un instant donné. Par ailleurs, par l'application de gradients d'encodage du mouvement, l'élastographie par résonance magnétique permet de suivre, sur la phase du signal de résonance magnétique, la réponse des organes à une contrainte mécanique externe afin de révéler leurs propriétés viscoélastiques, ce qui permet d'envisager l'exploration quantitative et spatialement résolue d'organes profonds que la main du médecin ne peut atteindre.

Dans le poumon, l'IRM conventionnelle est cependant relativement inadaptée : la faible densité tissulaire, les grandes différences de susceptibilité magnétique à l'interface entre le gaz et le tissu et, corrélativement, les très faibles durées de vie du signal de résonance magnétique, conduisent à des rapports signal-à-bruit difficilement exploitables. De plus, les durées des acquisitions IRM tridimensionnelles sont généralement supérieures à la période du mouvement respiratoire, ce qui nécessite de prendre en considération ce mouvement au sein du processus d'imagerie.

Ce projet de thèse, réalisé en collaboration avec GE Healthcare, vise à contourner les limitations citées précédemment en s'appuyant sur des techniques d'acquisition à temps d'écho sub-milliseconde de type UTE et ZTE, associées à des approches originales et innovantes de suivi intrinsèque des mouvements physiologiques ainsi qu'à des techniques de reconstruction d'images quadridimensionnelles tenant compte à la fois du mouvement respiratoire, de la redondance de l'information entre les différents canaux d'acquisition de données et de la parcimonie des images reconstruites à travers certaines représentations mathématiques. L'objectif ultime du projet est le développement et la validation de techniques d'exploration fonctionnelle respiratoire locales et quantitatives, mais aussi d'élastographie dynamique du poumon par résonance magnétique, afin d'extraire les paramètres ventilatoires et les modules viscoélastiques de cisaillement locaux du poumon au cours du cycle respiratoire.

Title: Magnetic resonance imaging of respiratory mechanics

Keywords: Medical imaging ; Magnetic resonance imaging ; Lung ; Motion ; Elastography ; Continuum mechanics

Abstract: The respiratory function in human cannot be separated from the deformation motion of the lung: the gas exchanges between the organism and its environment are made possible, during the inspiration, by the swelling of the alveoli in the pulmonary parenchyma, and during the expiration, by a passive return to the static equilibrium state of the lung. The viscoelastic properties of lung tissue play a key role in the function of this organ. These elements of respiratory mechanics may prove to be very sensitive biomarkers of the pathophysiological state of the lung since they depend on the structure of tissues and biological conditions that are considerably altered by most pulmonary diseases such as cancer, emphysema, asthma or interstitial fibrosis.

Magnetic resonance imaging enables non-invasive measurement of three-dimensional anatomical images that allow, thanks to the accessible spatial and temporal resolutions as well as the rich contrasts observed in the soft tissues, the measurement of the deformation state of an organ at a given moment. Moreover, by applying motion encoding gradients, magnetic resonance elastography gives the possibility to follow, onto to the magnetic resonance phase signal, the mechanical strain response of organs to an external mechanical stress in order to reveal their viscoelastic properties, which makes possible a quantitative and spatially-resolved exploration of deep organs that are nor reachable by the medical doctor's hand.

In the lung, conventional MRI is, however, relatively difficult: the low tissue density, the large differences in magnetic susceptibility at the interface between gas and tissue and, correlatively, the very short lifetimes of the magnetic resonance signal, lead to signal-to-noise ratios that are difficult to exploit. In addition, the durations of three-dimensional MRI scans are generally longer than the period of the respiratory motion, which requires consideration of this motion within the imaging process.

This PhD project, carried out in collaboration with GE Healthcare, aims at circumventing the limitations mentioned above by using UTE and ZTE sub-millisecond echo-time acquisition techniques, combined with original and innovative approaches of intrinsic physiological motions monitoring as well as four-dimensional image reconstruction techniques taking into account the respiratory motion, the redundancy of information between the different data acquisition channels and the sparsity of the reconstructed images through some mathematical representations. The ultimate goal of this project is the development and the validation of local and quantitative techniques to explore the respiratory function, as well as dynamic magnetic resonance lung elastography, in order to extract local ventilation parameters and viscoelastic shear moduli in the lung during the breathing cycle.

Université Paris-Saclay
Espace Technologique / Immeuble Discovery
Route de l'Orme aux Merisiers RD 128 / 91190 Saint-Aubin, France